Stefan Enoch Nicolas Bonod *Editors* 

# Plasmonics

From Basics to Advanced Topics



#### Springer Series in Optical Sciences

#### Volume 167

Founded by H. K. V. Lotsch

Editor-in-Chief: W. T. Rhodes

Editorial Board:
Ali Adibi, Atlanta
Toshimitsu Asakura, Sapporo
Theodor W. Hänsch, Garching
Takeshi Kamiya, Tokyo
Ferenc Krausz, Garching
Bo A. J. Monemar, Linköping
Herbert Venghaus, Berlin
Horst Weber, Berlin
Harald Weinfurter, München

For further volumes: http://www.springer.com/series/624

#### Springer Series in Optical Sciences

The Springer Series in Optical Sciences, under the leadership of Editor-in-Chief William T. Rhodes, Georgia Institute of Technology, USA, provides an expanding selection of research monographs in all major areas of optics: lasers and quantum optics, ultrafast phenomena, optical spectroscopy techniques, optoelectronics, quantum information, information optics, applied laser technology, industrial applications, and other topics of contemporary interest.

With this broad coverage of topics, the series is of use to all research scientists and engineers who need up-to-date reference books.

The editors encourage prospective authors to correspond with them in advance of submitting a manuscript. Submission of manuscripts should be made to the Editor-in-Chief or one of the Editors. See also www.springer.com/series/624

Editor-in-Chief
William T. Rhodes
School of Electrical and Computer Engineering
Georgia Institute of Technology
Atlanta, GA 30332-0250
USA
e-mail: bill.rhodes@ece.gatech.edu

Editorial Board
Ali Adibi
Georgia Institute of Technology
School of Electrical and Computer Engineering
Atlanta GA 30332-0250
USA
e-mail: adibi@ee.gatech.edu

Toshimitsu Asakura Hokkai-Gakuen University Faculty of Engineering 1-1, Minami-26, Nishi 11, Chuo-ku Sapporo, Hokkaido 064-0926 Japan e-mail: asakura@eli.hokkai-s-u.ac.ip

Theodor W. Hänsch Max-Planck-Institut für Quantenoptik Hans-Kopfermann-Straße 1 85748 Garching, Germany

e-mail: t.w.haensch@physik.uni-muenchen.de

Takeshi Kamiya Ministry of Education, Culture, Sports Science and Technology National Institution for Academic Degrees 3-29-1 Otsuka Bunkyo-ku Tokyo 112-0012, Japan e-mail: kamiyatk@niad.ac.jp

Ferenc Krausz
Ludwig-Maximilians-Universität München
Lehrstuhl für Experimentelle Physik
Am Coulombwall 1
85748 Garching, Germany and
Max-Planck-Institut für Quantenoptik
Hans-Kopfermann-Straße 1 85748
Garching Germany
e-mail: ferenc.krausz@mpq.mpg.de

Bo A. J. Monemar
Department of Physics and Measurement Technology
Materials Science Division
Linköping University
58183 Linköping, Sweden
e-mail: bom@ifm.liu.se

Herbert Venghaus Fraunhofer Institut für Nachrichtentechnik Heinrich-Hertz-Institut Einsteinufer 37 10587 Berlin, Germany e-mail: venghaus@hhi.de

Horst Weber Optisches Institut Technische Universität Berlin Straße des 17. Juni 135 10623 Berlin, Germany e-mail: weber@physik.tu-berlin.de

Harald Weinfurter Sektion Physik Ludwig-Maximilians-Universität München Schellingstraße 4/III 80799 München, Germany e-mail: harald.weinfurter@physik.uni-muenchen.de Stefan Enoch · Nicolas Bonod Editors

## **Plasmonics**

From Basics to Advanced Topics



Editors
Stefan Enoch
Institut Fresnel
CNRS
13013 Marseille
France

Nicolas Bonod Institut Fresnel CNRS 13013 Marseille France

ISSN 0342-4111 ISSN 1556-1534 (electronic)
ISBN 978-3-642-28078-8 ISBN 978-3-642-28079-5 (eBook)
DOI 10.1007/978-3-642-28079-5
Springer Heidelberg New York Dordrecht London

Library of Congress Control Number: 2012940267

#### © Springer-Verlag Berlin Heidelberg 2012

This work is subject to copyright. All rights are reserved by the Publisher, whether the whole or part of the material is concerned, specifically the rights of translation, reprinting, reuse of illustrations, recitation, broadcasting, reproduction on microfilms or in any other physical way, and transmission or information storage and retrieval, electronic adaptation, computer software, or by similar or dissimilar methodology now known or hereafter developed. Exempted from this legal reservation are brief excerpts in connection with reviews or scholarly analysis or material supplied specifically for the purpose of being entered and executed on a computer system, for exclusive use by the purchaser of the work. Duplication of this publication or parts thereof is permitted only under the provisions of the Copyright Law of the Publisher's location, in its current version, and permission for use must always be obtained from Springer. Permissions for use may be obtained through RightsLink at the Copyright Clearance Center. Violations are liable to prosecution under the respective Copyright Law.

The use of general descriptive names, registered names, trademarks, service marks, etc. in this publication does not imply, even in the absence of a specific statement, that such names are exempt from the relevant protective laws and regulations and therefore free for general use.

While the advice and information in this book are believed to be true and accurate at the date of publication, neither the authors nor the editors nor the publisher can accept any legal responsibility for any errors or omissions that may be made. The publisher makes no warranty, express or implied, with respect to the material contained herein.

Printed on acid-free paper

Springer is part of Springer Science+Business Media (www.springer.com)

#### **Preface**

The field of plasmonics is built on the resonant interaction of light with the free electrons of a noble metal. The polarizability of the free electron cloud allows particles much smaller than the incoming wavelength to couple efficiently with incoming light. The first application of this wavelength-specific interaction dates back to the Roman Empire with the use of metal particles in coloured glass. Resonant light/matter interactions are however abundant in optical sciences with dielectric spheres and cavities as well as atomic gases; so why has plasmonics triggered so much interest in the last 30 years? If plasmon resonances do not exhibit the highest oscillator strengths, they could exhibit quality factors in the range of interest for many applications and arise in solid-state materials that offer robust chemical and mechanical properties. Furthermore, the negative dielectric permittivity of noble metals at optical frequencies induces a drastic increase of the incoming electromagnetic field in the vicinity of the metal structure. This enhanced light/matter interaction, which occurs at the nanometer scale, sparked a growing interest in metallic nanostructures with the discoveries in 1976 of full-light absorption and in 1977 of surface-enhanced Raman scattering. The development, in the following decade, of surface-enhanced spectroscopy and plasmon-based biosensing has attracted the attention of a broad scientific community ranging from physicists to biochemists. Technical breakthroughs in nanofabrication, electromagnetic modelling and near-field optics added a new momentum to the field of plasmonics at the end of the 1990s with groundbreaking experiments in surface plasmon sub-wavelength optics; in particular, extraordinary optical transmission, plasmon polariton waveguiding and near-field enhancement imaging. During the last decade, the study of plasmon resonances has brought together an electic array of research fields ranging from quantum electrodynamics to electrical engineering for the understanding of light/matter interactions and from solar energy to pharmacology as potential applications. The recent development of metamaterials, optical antennas, nanosensing as well as photothermal cancer therapy make plasmonics one of the most dynamic and exciting research fields of this new millennium.

vi Preface

As the scientific community involved in plasmonics exponentially grows, exhaustive reference textbooks become crucial. The objective of this book is to thoroughly describe the physics of surface plasmons before addressing the most important and promising applications. The number of chapters has been deliberately restricted to offer authors the opportunity to develop their arguments and to detail their subjects while preserving the didacticism of their chapter. It is divided into three parts. Part I addresses surface plasmons polaritons propagating on metallic surfaces. Part II is dedicated to surface plasmons localized on metallic particles together with their applications in spectroscopy, energy production and biophotonics. Part III is devoted to the imaging and nanofabrication of metallic nanostructures.

#### Part I

The first two chapters are written by Daniel Maystre who discovered in 1976 with Hutley the phenomenon of full-light absorption by a nanostructured metal. In Chap. 1, Daniel Maystre describes the major advances of the twentieth century on plasmon surface polaritons propagating on metal surfaces. Chapter 2 is devoted to the Wood anomalies and the total absorption of light. These two discoveries made at intervals of 74 years have strongly impacted the discipline in the twentieth century. How can such a reflective metal absorb light when its surface is structured at a scale around one-tenth of the illuminating wavelength? Daniel Maystre explains in detail the phenomenon from an electromagnetic point of view. After defining the surface plasmon polariton as the complex pole of the scattering operator, he studies the trajectory of this pole in the complex plane as a function of the grating depth.

The publication in 1998 of the unexpected light transmission through a metal film perforated with nanoholes offered a new dynamism to the research on plasmon resonances. The need for convincing explanations of this so-called 'extraordinary' transmission has greatly advanced the knowledge of surface plasmon properties on nanostructured metals. Theoretical works that were carried out throughout the twentieth century by Rayleigh, Fano, Hessel and Oliner were needed to explain the famous Wood's anomalies. Philippe Lalanne and Haitao Liu show in Chap. 3 the interest of these works in the more modern context of the extraordinary light transmission. They discuss the concept of surface wave and define in particular quasi-cylindrical waves. They detail the subtle differences between these surface waves and surface plasmons, before presenting their microscopic theory that was able in 2008 to predict the phenomenon.

Chapter 4 written by Jean-Jacques Greffet is devoted to the theory of surface plasmons. The strength of this chapter is to describe the plasmon dispersion formulas in solid-state physics and electromagnetism formalisms. In the first case, the surface plasmon is described as a collective oscillation of free electrons while, in the second case, the microscopic properties of the metal are 'hidden' in the

permittivity of the metal. The surface plasmon is then defined as a pole of the scattering operator and described as a surface wave propagating at a metal/dielectric interface. Jean-Jacques Greffet explains the term 'polariton' that describes the coupling between an electromagnetic wave and the free electrons. An analysis of the dispersion curves shows the different regimes of propagation between the frequencies ranging from microwave to optical frequencies. He explains the physical content of the dispersion relations for lossy metals. In particular, the divergence of the local density of states and the resolution limit are discussed.

#### Part II

In Chap. 5, Javier Aizpurua and Rainer Hillenbrand introduce surface plasmons localized on metallic particles before presenting their interest in surface-enhanced Raman spectroscopy. The interaction of light with nanoparticles much smaller than the wavelength can be described in the quasistatic approximation. The authors introduce the analytical expressions of the scattering and absorption cross-sections of a dipolar nanoparticle. They describe the higher multipolar modes and the impact of retardation effects before introducing the very important concept of coupled dipoles. The last part of their chapter is devoted to the use of nanoparticles to probe vibrational states of molecules (Surface-Enhanced Raman Spectroscopy and Surface-Enhanced Infrared Absorption). The discovery of the surface-enhanced Raman scattering dates back to 1977 and it initiated the creation of the very active discipline of 'molecular plasmonics'. The authors therefore present the basics of Raman spectroscopy and show the importance of enhancing the optical near field in the vicinity of metal nanoparticles for increasing the Raman signal.

The use of nanoparticles in dielectric materials has been known since antiquity, but it recently experienced a renewed interest with the use of metallic particles in solar cells. Predicting the optical properties of a large ensemble of nanoparticles in a homogeneous medium can be performed by considering the material as homogeneous. The techniques of homogenization of Maxwell-Garnett and Bruggeman are described in Chap. 6, written by Ross McPhedran. These methods were developed in the late nineteenth and early twentieth centuries by renowned scientists such as Clausius, Mossotti, Maxwell, Rayleigh, Lorenz, Lorentz and Maxwell-Garnett. This chapter contains technical sections, but Ross McPhedran carefully highlights the main results and unveils the physics behind the formulas. He shows in particular the resonant character of the effective dielectric permittivity calculated when the metal particles are considered as inclusions in a glass matrix, which proves that the Maxwell-Garnett formulation is able to take into account plasmonic resonances supported by metallic particles. The usefulness of the homogeneization technique is illustrated in the context of photovoltaic and photothermal energy production. Ross McPhedran then discusses cloaking and spasers, two very modern advances that should appear in this book.

viii Preface

Medical diagnosis is the first industrial application of surface plasmons. Chapter 7 written by Romain Quidant is devoted to the promising role of plasmonics in health. He emphasizes the use of metallic particles for the development of light and heat sources for light trapping, biosensing and photothermal cancer therapy. Romain Quidant first shows the importance of the shape of the nanoparticle on the heat power emission spectra calculated numerically using the dyadic Green's function. The maps of heat density are interesting since they differ largely from that of light intensities. He then describes a technique of microscopy capable of measuring the temperature around the nanoparticles. Chapter 5 describes the ability of nanoparticles to focus incident light into tiny volumes, while this chapter uses this property for the optical sensing of proteins or the light trapping of cells and viruses. Combining biosensing and trapping techniques could lead to the design of cost-effective biochips capable of quickly analysing liquid samples. Romain Quidant concludes his chapter with a description of a new therapy against certain cancers based on the heating of metal nanoparticles.

#### Part III

The first seven chapters of this book described the theory of surface plasmons and showed their interest in the enhancement of light/matter interactions, with important applications in nanophotonics and biophotonics. These breakthroughs were made possible by advances in imaging techniques and nanofabrication.

The first direct observation of surface plasmons performed in the mid-1990s is now considered as a key moment in plasmonics history. Alexandre Bouhelier, Gérard Colas des Francs and Jonathan Grandidier write a very detailed chapter on the different techniques of surface plasmon imaging. They distinguish three techniques: near-field optical imaging, far-field optical imaging and electron microscopies. The authors introduce in this chapter the fundamental concept of spatial resolution, and explain the difference between near and far fields before extending these concepts to the temporal resolution needed to observe the dynamics of surface plasmons. Besides these three main techniques of microscopy, the authors present fluorescence microscopy, dark-field microscopy and photochemical imaging. This chapter contains many coloured surface plasmon images which will help the reader understand the nature of surface plasmons.

Plasmonics is at the crossroads of optics and nanotechnology. Electromagnetism modelling and transformational optics lead to original designs of metallic nanostructures that will push the boundaries of nanotechnology. The huge industrial markets of microelectronics have led to massive investments in technological platforms in order to increase the precision of surface patterning. The plasmonics community greatly benefits from the recent progress of nanotechnology, and the last chapter of this book written by Gilles Lérondel, Sergei Kostcheev and Jérôme Plain addresses the different techniques of nanofabrication. They describe in detail the techniques of electron beam lithography, ion beam

Preface

lithography as well as optical lithography. The authors nicely emphasize the growing role that will be played by chemical self-assembly and surface functionalization techniques.

We gratefully thank the authors for their participation in this book. We particularly appreciated the scientific discussions that emerged during this project. Our careful editing of these comprehensive chapters has increased our knowledge and understanding of plasmon resonances. We hope our readers will have the same exciting journey in the field of plasmonics and that it will help them launch novel research ventures.

Marseille, France

Nicolas Bonod Stefan Enoch

#### **Contents**

#### Part I Surface Plasmons Polaritonson Metallic Surfaces

1	Surv	ey of Su	ırface Plasmon Polariton History	3		
	1.1	Introduction				
	1.2	onics and Grating Anomalies	4			
		1.2.1	Discovery of Wood's Anomalies	4		
		1.2.2	The Early Experimental and Theoretical			
			Contributions	5		
		1.2.3	The Explanations in Terms of Surface Waves	5		
		1.2.4	The Experimental and Theoretical Revolutions	6		
		1.2.5	The Failure of Perfect Conductivity Model			
			in the Grating Theory	7		
		1.2.6	The Quantitative Phenomenological Approach	9		
		1.2.7	Other Studies	10		
		1.2.8	Coherent Thermal Emission	11		
	1.3	Plasmo	onics in Nanophotonics	11		
		1.3.1	Extraordinary Transmission Through			
			Subwavelength Holes	12		
		1.3.2	Plasmonics and Metamaterials	14		
		1.3.3	Plasmonics and Near-Field Microscopy	20		
	1.4	on Propagation on Randomly Rough Surfaces,				
		Weak	and Strong Localization of Light	21		
		1.4.1	Enhanced Backscattering (Weak Localization)	22		
		1.4.2	Anderson Localization (Strong Localization)	26		
	1.5	Conclu	usion	28		
	Refe	rences .		29		
2	Theo	ory of W	Vood's Anomalies	39		
	2.1	Introdu	uction	39		
	2.2	Propag	gation of Surface Plasmon Polaritons			
		on a M	Metallic Surface	46		

xii Contents

		2.2.1	Case of the Flat Surface	46		
		2.2.2	Case of the Diffraction Grating	58		
	2.3	Phenor	menological Study of Wood Anomalies	63		
		2.3.1	Pole of the Reflection and Transmission			
			Coefficients	63		
		2.3.2	Zero of the Reflection Coefficient,			
			Phenomenological Formula	64		
		2.3.3	Verification of the Phenomenological Formula			
			from Numerical Results	65		
	2.4	Total A	Absorption of Light by a Diffraction Grating	67		
		2.4.1	Theoretical Demonstration	67		
		2.4.2	Experimental Verification	68		
		2.4.3	Some Applications	70		
	2.5	Further	r Properties of Surface Plasmon Polaritons	71		
		2.5.1	Physical Interpretation and Fundamental Properties			
			of the Zero of the Reflection Coefficient	71		
		2.5.2	Analogy with Guided Waves in Dielectric Films			
			Deposited on Metallic Surfaces	73		
	2.6	Conclu	asion	76		
		Appen	dix 1: Electromagnetic modelling in Two Dimensions	76		
	Refer	rences.		80		
3			at Grating Theories Through the Extraordinary			
	_		nsmission Phenomenon	85		
	3.1		action	85		
	3.2		itial Microscopic Interpretation of Wood's Anomaly	87		
	3.3	-	Question the Initial Plasmonic Interpretation?	89		
		3.3.1	Modern Grating Theory and Local Surface Waves	90		
		3.3.2	Perfectly-Conducting Case	90		
		3.3.3	The Quasi-Cylindrical Wave	92		
	3.4		ning the EOT with Grating Theories	94		
	3.5		scopic SPP Theory	97		
	3.6	The Role of Surface Plasmons in the EOT				
	3.7	Conclusion				
			ISION	101		
4	Refer	rences .				
4	Refer	rences .  oduction		102		
4	Refer	rences . oduction Introdu	to Surface Plasmon Theory	102 105		
4	Refer Intro	rences .  oduction  Introdu  Surface	to Surface Plasmon Theory.	102 105		
4	Refer Intro	ences .  oduction  Introdu  Surface  Introdu	to Surface Plasmon Theory	102 105 105		
4	Refer Intro 4.1 4.2	ences .  oduction  Introdu  Surface  Introdu	to Surface Plasmon Theory	102 105 105 106		

Contents xiii

	4.4		Electromagnetic Wave	111
		4.4.1	Dispersion Relation for the Non-Magnetic Case	111
		4.4.2	Polarization of the Surface Wave	113
		4.4.3	Length Scales of a Surface Wave	114
		4.4.4	Link with Resonances of the Reflection Factor	115
		4.4.5	Generation of a Surface Wave	115
	4.5		Plasmon Polariton	116
		4.5.1	Dielectric Constant of a Metal	116
		4.5.2	Dispersion Relation of a SPP	119
		4.5.3	Electrostatic Limit	123
	4.6	Surface	Phonon Polaritons	123
		4.6.1	Lorentz Model	123
	4.7		ourri of Surfaces Waves: Sommerfeld or Zenneck	
		Modes,	Quasicylindrical or Lateral Wave	124
		4.7.1	Historical Perspective	125
	4.8	Key Pro	operties of SPP	127
		4.8.1	Confinment of the Field	127
		4.8.2	Surface Plasmons Contribution to the Local	
			Density of States	129
		4.8.3	Broad Spectrum and Fast Response	138
	4.9	Surface	Plasmon Polaritons on Lossy Materials	139
		4.9.1	First Interpretation	139
		4.9.2	Representation of the Fields	140
		4.9.3	Implications for LDOS	142
		4.9.4	Implications for Superresolution	
			and Strong Confinment	142
	4.10	Fourier	Optics for SPP	143
		4.10.1	General Representation	144
		4.10.2	Huygens–Fresnel Principle	145
	4.11	Conclus	sion	146
	Refere			146
n	4 11	C 6		
Pa	rt II	Surface	Plasmons Localizedon Metallic Particles	
5	Local	ized Sur	face Plasmons: Basics and Applications	
	in Fie	eld-Enha	nced Spectroscopy	151
	5.1	Localiz	ed Plasmons and Optical Antennas	152
		5.1.1	Surface Plasmon Polaritons Versus Localized Surface	
			Plasmon Polaritons	152
		5.1.2	The Simplest Optical Nanoantenna:	
			A Metallic Nanoparticle	154
		5.1.3	Higher-Order Modes	157
			<del>-</del>	

xiv Contents

		5.1.4 Retardation	159
		5.1.5 Influence of Particle Shape in Plasmon Response	161
		5.1.6 Field Enhancement by Plasmon Coupling	163
		5.1.7 Optical Antennas: From Radiowaves	100
		to Visible Light	166
	5.2	Field-Enhanced Vibrational Spectroscopy	168
	3.2	5.2.1 Concept	169
		5.2.2 SERS	169
		5.2.3 SEIRA	172
		5.2.4 Localized Plasmons in Other Applications	173
	Refe	rences	173
	IXCIC.	tences	1/7
6	Plasi	mons on Separated Particles: Homogenization	
	and	Applications	177
	6.1	Introduction	177
	6.2	Electromagnetic Waves in Structured Systems	178
	6.3	Effective Permittivities and Permeabilities	180
	6.4	Plasmon Resonances in Particle Clusters	188
	6.5	Application of Plasmonic Resonances	
		in Solar Energy Absorbers	190
	6.6	Coated Cylinders and Plasmonic Cloaking	193
	6.7	The Spaser: Cutting our Losses	196
	6.8	Envoi	198
	Refe	rences	198
_	-	N ON BALL NAME OF A	
7		mon Nano-Optics: Designing Novel Nano-Tools	201
		Biology and Medicine	201
	7.1	Optical and Thermal Properties of Plasmonic	• • •
		Metallic Nanoparticles	201
		7.1.1 Nanoscale Light Concentration in MNP	202
		7.1.2 Nanoscale Heat Generation in MNP	202
	7.2	MNP as Nano Light-Sources: Application to Biosensing	
		and Optical Trapping	208
		7.2.1 Enhanced Sensitivity LSP-Based Biosensing	208
		7.2.2 Plasmon-Based Optical Trapping	211
	7.3	MNP as Nano Heat-Sources for Photothermal	
		Cancer Therapy	218
		7.3.1 Toxicity	219
		7.3.2 Cancer Cell Targeting and Latest Advances	
		in Hyperthermia	219
	7.4	Conclusion	220
	Refe	rences	220

Contents xv

Part III Imaging and Nanofabrication	Part III	Imaging	and	Nanofabrication
--------------------------------------	----------	---------	-----	-----------------

8	Imag	ing Sur	face Plasmons	225
	8.1	Introdu	uction	225
	8.2	Optica	l Near-Field Imaging	227
	8.2.1	Near-F	Field Imaging of Propagative Surface Plasmons	227
	8.2.2	Near-F	Field Imaging of Localized Surface Plasmons	230
	8.3	Photoc	chemical Mapping	232
	8.4	Leakag	ge Radiation Microscopy	235
		8.4.1	Leaky Mode Properties	235
		8.4.2	Leakage Radiation Microscopy	240
		8.4.3	Leakage Radiation Microscopy of Surface	
			Plasmon Coupled Emission	242
	8.5	Fluore	scent Probes	244
	8.6	Dark-F	Field Microscopy	245
	8.7		cal Laser Microscopy	248
	8.8		naging with Electrons	251
		8.8.1	Electron-Matter Interaction	252
		8.8.2	Spatially Resolved Electron Energy-Loss	
			Spectroscopy	255
		8.8.3	Cathodoluminescence Microscopy	259
		8.8.4	Photoemission Electron Microscopy	261
		8.8.5	Photon-Induced Electron Microscopy: Highly Resolved	
			Electron Energy-Loss/Gain Spectroscopy Imaging	262
	Refer	ences .		265
9	Nano	fabrica	tion for Plasmonics	269
	9.1	Introdu	uction	269
	9.2	Metho	ds of Nanofabrication and Related Techniques	270
		9.2.1	Lithography: Evolution and Resolution Issue	271
		9.2.2	Electron-Beam Lithography	273
		9.2.3	Complementary and Alternative	
			Lithographic Techniques	278
		9.2.4	Lift-off	282
		9.2.5	Direct Writing	284
		9.2.6	Surface Functionalization	285
	9.3	Structu	ures Fabrication	289
		9.3.1	Metallic Nanostructuring on Planar Surfaces	290
		9.3.2	Metallic Structures Fabrication	
			on a NonPlanar Surface	300
		9.3.3	Metallic Structure Surface Functionalization	303
		9.3.4	Hybrid Nanostructures Fabrication	304

xvi Contents

9.4	Altern	ative Techniques and Emerging Issues	306
	9.4.1	Localized Photochemical Combined	
		Synthesis and Patterning	307
	9.4.2	Material Issues	
	9.4.3	Large-Scale Nanostructuring: Toward Plasmonic	
		Materials (Effective Properties) and Metamaterials	310
	9.4.4	Plasmonic Integration	312
9.5	Summ	ary	314
Refe	rences .		315
Index .			317

### Part I Surface Plasmons Polaritons on Metallic Surfaces

## **Chapter 1 Survey of Surface Plasmon Polariton History**

**Daniel Maystre** 

**Abstract** A huge interest in Surface Plasmon Polaritons (SPPs) was born at the beginning of the twentieth century with the discovery of grating anomalies by Wood. Subsequently, the excitation of SPPs by randomly rough surfaces has initiated fascinating subjects of modern physics like enhanced backscattering or Anderson localization of photons. More recently, this domain has attracted considerable attention since plasmonics is involved in the main domains of nanophotonics: metamaterials, near-field optics, extraordinary transmission through subwavelength holes, second harmonic generation, and surface enhanced Raman scattering. This chapter outlines the main steps in the development of these fields of research.

#### 1.1 Introduction

This chapter deals with the domain of plasmonics that can be defined as the domain of Optics in which the excitation and the propagation of surface plasmons play a key role. Initiated in 1902 by Wood [1], the study of Surface Plasmon Polaritons (SPPs) has been, for a long time, restricted to the study of the so-called Wood's anomalies. These anomalies are observed in the spectrum of light diffracted by diffraction gratings and they manifest themselves by rapid variations in the intensity of the diffracted spectral orders in narrow frequency bands. Wood's anomalies have been considered for all the twentieth century as one of the most fascinating phenomena in optics.

Almost one century after the Wood discovery, plasmonics has attracted a new and considerable attention, in such a way that nowadays, it is considered as a vital part of nanophotonics. Examples of this modern evolution of plasmonics can be found

D. Maystre (⋈)

Institut Fresnel, CNRS, Université d'Aix Marseille, Ecole Centrale Marseille Avenue Escadrille Normandie-Niemen, Campus Universitaire de Saint Jérôme, 13397 Marseille, France

e-mail: daniel.maystre@fresnel.fr

D. Maystre

in the phenomenon of extraordinary transmission of light by subwavelength holes, near-field microscopy, use of SPPs excitation for superlensing or fabrication of very compact, high-speed, low-power and interference-free optical devices for telecommunications industry. Although many studies in plasmonics have been devoted to periodic structures, it must be recalled that numerous studies have analyzed the effect of the excitation of SPPs on non-periodic rough surfaces, especially on randomly rough surfaces. Two phenomena generated by excitation of SPPs by randomly rough surfaces have been particularly investigated both experimentally and theoretically: the enhanced backscattering of light and the Anderson localization of photons. These phenomena are not classified specifically in the frame of optics and must be considered as domains of modern physics, which have been studied by specialists of theoretical physics, electromagnetics, optics, acoustics, and solid-state physics.

The second section will describe the long history of the experimental and theoretical analysis of grating anomalies. The third one will deal with some of the main contributions of plasmonics in nanophotonics: extraordinary transmission through subwavelength holes, metamaterials, and near-field microscopy. Finally, the fourth section will be devoted to the phenomena generated by the propagation of SPPs on randomly rough surfaces.

#### 1.2 Plasmonics and Grating Anomalies

#### 1.2.1 Discovery of Wood's Anomalies

Although the notion of SPP appeared long afterwards, their generation in optics was described at the very beginning of twentieth century. Indeed, the American astronomer Wood observed in 1902 the spectra obtained using an optical grating of a continuous light source produced by an incandescent lamp [1]. He noticed a surprising phenomenon: "I was astounded to find that under certain conditions, the drop from maximum illumination to minimum, a drop certainly of from 10 to 1, occurred within a range of wavelengths not greater than the distance between the sodium lines".

Wood found narrow bright and dark lines in various spectra obtained for different conditions of incidence and made a crucial remark: these lines were present only for p-polarized light, i.e. when the magnetic field is parallel to the grating grooves. At that time, the electromagnetic theory of gratings was at an embryonic stage and thus was quite unable to provide any explanation to these phenomena, which explains that Wood termed them "singular anomalies", concluding that this problem was "one of the most interesting that I have ever met with".

#### 1.2.2 The Early Experimental and Theoretical Contributions

For a good while after the discovery of Wood's anomalies, SPP studies remained intimately related to relief diffraction gratings [2–45]. The interested reader can find detailed descriptions of this early age of plasmonics in [45–50]. Other experimental studies of Wood's anomalies were published by Wood [4, 6] but pretty soon, theoreticians tried to provide interpretations to this surprising phenomenon. The first explanation to the existence of the anomalies was given by Lord Rayleigh [2, 3]. He conjectured that an anomaly in a given spectrum occurs at a wavelength corresponding to the passing-off of a spectrum of higher order, or in other words at the wavelength for which a scattered wave emerges tangentially to the grating surface. Thus, he was inclined to think that the passing-off may be the determining circumstance of any anomaly.

It is quite amazing to notice that this conjecture was not based on the experimental data contained in the paper by Wood, since this paper did not mention the grating period, a necessary parameter (with incidence angle) for calculating the passing-off wavelength from the classical grating formula. Hearing from Wood the value of the grating period, he noticed that his prediction allowed him to find the locations of the anomalies, but with a significant discrepancy of about 5%, which seemed hardly good enough. Rayleigh expressed the hypothesis that this mismatch was the consequence of an imprecise knowledge of the grating period.

For nearly a couple of decades, the interpretation proposed by Rayleigh was not questioned. However, in 1936, Strong published crucial experimental measurements [7]. Strong showed Wood's anomalies for various metallic gratings having the same period. The results implicitly evidenced the influence of the metal on the shape and, much more important, on the location of the anomalies. Bearing in mind that the grating formula is purely geometrical and thus that the metal has no effect on the location of the passing-off, this result must be considered as the first reappraisal of the Rayleigh interpretation.

#### 1.2.3 The Explanations in Terms of Surface Waves

A few years later, U. Fano achieved the first theoretical breakthrough on Wood's anomalies [8]. Observing the published experimental data, Fano distinguished two kinds of anomalies:

- A sharp anomaly, that is an edge of intensity, appears along the spectrum at sharply defined wavelengths governed by the grating formula, using the Rayleigh conjecture
- A diffuse anomaly extends for a wavelength interval from the first one (the edge) to the red (i.e. higher wavelengths) and "consists generally of a minimum and a maximum of intensity (one dark band and one bright band)".

Obviously, the anomaly observed by Wood was not an edge of intensity but a drop and it must be classified in the second kind of anomaly. This remark explains the discrepancy between the predictions made by Rayleigh and the actual locations of the anomalies: the diffuse anomaly does not occur exactly at the passing-off wavelength. Fano explained the diffuse anomaly by "a forced resonance" related to the "leaky waves supportable by the grating". In other words, he explained the diffuse anomaly by the excitation of surface waves propagating along the grating surface. In this chapter, we will denote by "Rayleigh anomaly" the sharp anomaly at the passing-off of a spectrum of higher order. We will see in the following that the remarkable interpretation given by Fano can be considered as the starting point of the modern analysis of Wood's anomalies, even though the connection between the leaky waves of Fano and SPPs was not stated.

Fano's analysis was pursued by Hessel and Oliner which were led to the same conclusions [12]. In addition, these two authors tried, for the first time, to use numerical tools in order to calculate the location and shape of the anomalies. With this aim, they used a model based on the knowledge of the impedance on a straight line located above the grating grooves, assuming this impedance to take simple forms. They were able to explain some properties experimentally known, such as the possibility of anomalies for s-polarized light with very deep gratings [9, 10], or the reluctance of anomalies to merge [11].

The same year, Hagglund and Sellberg achieved a second attempt to analyze the anomalies properties from numerical tools [13]. To this end, they used the electromagnetic theory of perfectly conducting gratings proposed by Rayleigh [51]. This theory assumes that the electromagnetic field above the grating surface can be represented by a sum of plane waves, including inside the grooves. It is well known that it leads to numerical instabilities, except for shallow gratings, for which it can be shown that this theory gives accurate results on intensities scattered by gratings. Unfortunately, in this region of convergence, the agreement with experimental data was only qualitative.

#### 1.2.4 The Experimental and Theoretical Revolutions

At the end of the 1960s and beginning of 1970s occurred two revolutions, which deeply changed the experimental and theoretical tools used for the study of grating anomalies. As regards the experimental means, the use of laser sources and photoresist layers permitted the invention and production of holographic gratings for scientific and industrial purpose [52]. For the first time, the holographic technology provided a rapid and accurate tool for constructing gratings with submicronic periods. As regards the theory, the opportunity of using the first powerful computers and the strong development of the rigorous vector theory of gratings made it possible wide numerical studies of Wood's anomalies and allowed the first successful quantitative comparisons between experimental data and numerical calculations.

In 1972, Maystre elaborated and implemented on a computer a rigorous integral theory of scattering from metallic diffraction gratings, including the possibility of representing the metal by its complex permittivity [16, 17]. It is worth noting that, at that time, this new theory was intended to provide a realistic tool for the optimization of metallic gratings embarked in satellites for spectroscopy in the ultraviolet region, where the conductivity of metals falls down. Indeed, it was widely acknowledged at that time that metallic gratings in the visible and near-infrared regions behave nearly like perfectly conducting surfaces. This hypothesis was based on a simple remark: the reflectivity of metallic planes of aluminium, silver, or gold in these regions exceeds 90 % in general (98 % for silver). Thus it was accepted that the metal can be replaced by a perfectly conducting (impenetrable) material, the intensities computed using this hypothesis being finally multiplied by the reflectivity of the metal. Nevertheless, the new theory was initially applied to metallic gratings in the visible and near-infrared regions, in order to confirm the hypothesis of perfect conductivity of metallic gratings.

## 1.2.5 The Failure of Perfect Conductivity Model in the Grating Theory

The first results were quite surprising. As expected, for s-polarized light, the numerical results confirmed the usual hypothesis: the intensities scattered in various orders can be deduced from those obtained assuming a perfect conductivity of the metals through a simple multiplication factor close to reflectivity of the plane metallic surface. On the other hand, for p-polarized light, strong discrepancies appeared. The obvious and crucial consequence of this unexpected result was the failure in the visible and infrared regions of the perfect conductivity model of gratings for natural light, where the intensities take the average value between both fundamental polarizations.

This result was presented in 1972 by Petit, Maystre, and Nevière in a communication at the International Congress of Optics (I.C.O. IX, Santa Monica, Ca) reported in Ref. [21]. Most of the attendants in this congress expressed serious doubts about the validity of this result: is the new theory valid and is the numerical implementation accurate?. These criticisms can be easily understood: a new theory must be checked not only through numerical tests (energy balance, reciprocity theorem [53, 54]) but also, and above all, by comparison of the numerical results with experimental data. This comparison arose very soon, as we will see.

Indeed, at the same time, at the National Physical Laboratory (Teddington, UK) Hutley was able to make metallic holographic gratings and to measure their nearly sinusoidal profiles using a profilometer (chisel-shaped stylus). He performed measurements of their efficiencies (by definition, the efficiency of a grating in a given order is the ratio of the light intensity in this order to the intensity of the incident wave). He compared this data with theoretical predictions obtained from a rigorous theory of scattering by perfectly conducting gratings elaborated in 1973 by McPhedran and Waterworth [18]. He noticed for p-polarized light a significant

D. Maystre

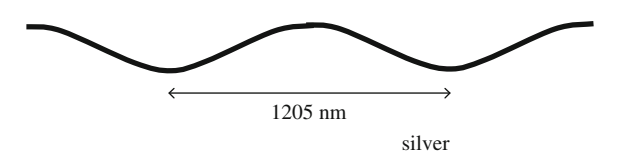


**Fig. 1.1** Profile of the holographic grating made in the National Physical Laboratory (by courtesy of Hutley). The height of the grating is equal to 170 nm

discrepancy between theory and experiment [19, 20] and proposed three possible explanations to this mismatch:

- the finite conductivity of metals,
- an insufficient knowledge of the grating profile, specially of the distortion from a perfectly sinusoidal shape.
- the reluctance of anomalies to merge, this hypothesis being presented by the author as the "perhaps more likely explanation of the discrepancy".

Obviously, the only way to solve the problem was to compare the experimental measurements performed by Hutley with numerical results obtained from the new rigorous theory of metallic gratings. This comparison, suggested by McPhedran, was made in 1974 by Maystre and McPhedran [23, 24, 55]. The profile of the silver holographic grating made by Hutley is shown in Fig. 1.1.

This grating was illuminated by a laser beam with a wavelength equal to 521 nm. Hutley measured the efficiency in the -1 order as a function of incidence [20]. In this chapter, the grating formula writes:

$$\sin(\theta_n) = \sin(\theta) + n\lambda/d, \tag{1.1}$$

with  $\theta$  and  $\theta_n$  being, respectively, the angle of incidence (measured anti-clockwise) and the angle of diffraction in the *n* order (measured clockwise),  $\lambda$  being the wavelength in vacuum, and *d* being the period of the grating.

Figure 1.2 shows the experimental and theoretical results. The nearly symmetrical shape of the curves of efficiency with respect to the Littrow angle  $\theta_L = 12.5^{\circ}$  is a straightforward consequence of the reciprocity theorem [53, 54]. Let us recall that in the Littrow configuration, the -n order (here, n=-1) and the incident wave propagate in opposite directions.

- solid line: experimental data
- dashed lines: theoretical results for a silver grating,
- dashed-dotted line: theoretical results for total scattered efficiency (in all scattered orders) of silver grating.
- dotted line: theoretical results for a perfectly conducting grating.

For s-polarized light, the agreement of both theories with experimental results is excellent. One can notice two Rayleigh anomalies at the passing-off wavelengths shown by arrows. The Rayleigh anomalies hold for p-polarized light, but spectacular

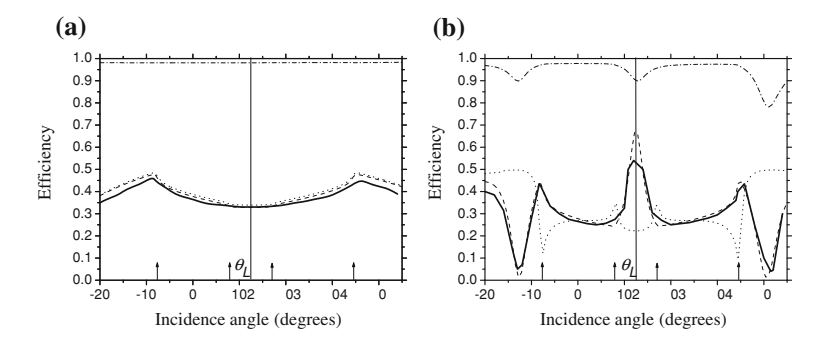


Fig. 1.2 Comparison between experimental efficiencies (by courtesy of Hutley) and theoretical efficiencies in the order -1 (taken from [55]) for a holographic silver grating for s-polarized light (a) and p-polarized light (b). The passing-off incidences are shown by *arrows* and the Littrow (Bragg) position by a *vertical line* 

Wood's anomalies accompanied by significant absorptions (up to 20%) occur. Due to these anomalies, the perfect conductivity model completely fails for this polarization.

#### 1.2.6 The Quantitative Phenomenological Approach

This first successful comparison between experimental and numerical results for metallic gratings in the visible region was followed by many other such comparisons, using the same integral theory or another rigorous grating theory, the differential theory of gratings [56], in such a way that the theoretical warning stated in 1972 about the non-validity of the perfect conductivity model was fully confirmed, at least for wavelengths smaller that  $10 \, \mu m$  [26].

The existence of powerful computer codes able to predict with a precision better than 1% the grating efficiency in the visible and near-infrared regions has permitted wide numerical studies of Wood's anomalies for various grating profiles, metals, and mountings. However, numerical results do not provide simple rules or formulae able to predict the shape and the position of the anomalies in a quantitative manner. This remark explains why attempts were made in order to develop a quantitative phenomenological theory [46, 47]. This theory starts from the basic origin of Wood's anomalies, i.e. the excitation of SPPs, and then uses the theory of analytic functions of the complex variable. It shows that the behavior of the efficiency in the region of anomaly can be quantitatively deduced from the knowledge of a couple of complex parameters: the pole and the zero of the analytic continuation of the complex amplitude of the scattered order (classically defined on the real axis of the incidence angle) in the complex plane.

The pole represents the complex constant of propagation of the SPP on the grating surface. From the knowledge of the pole and of the zero, a very simple

phenomenological formula allows one to predict the efficiency in the region of anomaly with remarkable precision. This phenomenological theory has led to the prediction of a very surprising phenomenon: the total absorption of a p-polarized incident wave by a shallow grating [30], experimentally verified by Hutley and Maystre [31]. The same phenomenon has been generalized to s-polarized light for metallic gratings covered by a thin dielectric layer [41, 42] and to unpolarized light for crossed gratings [43]. The phenomenological theory also applies to perfectly conducting gratings. Although the SPP of a metallic grating tends to a field which is not a surface wave, it has been shown (see Fig. 1.8 of [47]) that this field is associated to a pole and a zero (complex conjugate of the pole), and thus becomes a surface wave again as soon as the perfectly conducting plane is corrugated. It is to be noticed that other phenomenological studies were achieved by Andrewartha et al. for perfectly conducting lamellar gratings [44, 45]. The phenomenological theory also applies to corrugated waveguides.

#### 1.2.7 Other Studies

Other computations have been achieved to study the dispersion of SPPs on a metallic or a semiconductor grating.

An impressive variety of experimental measurements on phase velocity and damping of SPPs on metallic gratings can be found in the studies undertaken by Raether, Pockrand, Kröger, and Kretschmann. These authors illuminated the grating from the bulk side through a prism and used an approximate theory to interpret their results [25, 27–29, 32–35].

It must be noticed that a group working in the Oak Ridge National Laboratory (USA) tried to analyze the properties of SPPs using the microscopic laws of solid-state physics. Such a study has an advantage on macroscopic studies described in the present chapter: it starts directly from the basic origin of SPPs, i.e. a collective electron resonance. It is to be noticed that the same group was at the origin of the discovery of SPPs [57]. Unfortunately, the complexity of the problem led the authors to use a perturbation treatment, in which the anomaly is studied in terms of an interaction between the incoming photon and the collective electron resonance. This analysis was not able accurately to describe the phenomenon, especially for deep gratings, except by tuning the optical constants of metal to fit the measured data [14, 15].

The excitation of SPPs by periodic relief surfaces has remained a key subject of Plasmonics, due to the interest of practical and technological applications in biology (virus detection), telecommunications (phone cards), photovoltaic or solar cells (improvement of efficiency), and many other domains. The interested reader can find the description of some of these studies in [58–85].

#### 1.2.8 Coherent Thermal Emission

Thermal emission of objects like the sun can be observed in current life. Even though thermal emission is made of electromagnetic waves, the blackbody radiation is studied using radiometry. However, this very efficient theory cannot answer too many questions like the coherence of thermal radiation or the electromagnetic properties of the radiated near-field. The development of near-field optics and nanophotonics has encouraged the analysis of these questions. Electromagnetic models of thermal emission have been developed by Rytov [86, 87]. These models constitute efficient tools to merge electromagnetics with thermodynamics and quantum theory and allow one to study thermal emission in the near-field.

It turns out that at large distance (typically greater than  $100\,\mu\text{m}$ ) from a surface of silicon carbide held at 300 K, the spectrum of energy density resembles the Planck function of the blackbody spectrum, with a maximum at a wavelength close to  $10\,\mu\text{m}$ . However, when this distance approaches  $1\,\mu\text{m}$ , the spectrum strongly changes. The energy density increases and the spectrum becomes more and more dominated by a peak located at a wavelength close to  $10\,\mu\text{m}$ . As a consequence, the near-field becomes nearly monochromatic. It is spatially and temporally strongly coherent.

The explanation of this surprising result is that surface waves called "surface phonons", very similar to SPPs, can propagate at the surface of the metal at the wavelength corresponding to the peak. For metals, the surface waves are SPPs and the peak in the spectrum is located in the ultraviolet. Of course these surface waves exponentially decrease and cannot be observed in the far field, at least if the surface is planar. On the other hand, if the surface is periodically corrugated, the surface waves can be radiated at infinity in given directions. In these directions, the thermal emission is nearly monochromatic and strongly coherent [88–93]. This phenomenon is called "coherent thermal emission".

#### 1.3 Plasmonics in Nanophotonics

Recently, plasmonics has attracted considerable attention on new fields of research. This new interest is linked with the strong development of nanophotonics. This domain of Optics is defined as the behavior and properties of light at the nanometer scale, i.e. when the wavelength of light is significantly larger than the size of the basic elements of the optical component (subwavelength scale). One of the major objectives of nanophotonics is to achieve optical instruments that are able to focus the light generated by a point source much tightly than the diffraction limit, also called Rayleigh criterion, in order to obtain strongly subwavelength light localization, i.e. light spots having sizes significantly smaller than the classical resolution of optical instruments (about half a wavelength). Such subwavelength light spots can provide very efficient tools, for example for characterization of surfaces or biological objects.

12 D. Maystre

The other purpose of nanophotonics is to develop very compact, high-speed, low-power, and interference-free optical devices, with revolutionary applications to telecommunications industry. In this chapter, we will mention three domains of nanophotonics where plasmonics is deeply involved: the phenomenon of extraordinary transmission of light through subwavelength holes, the fabrication of superlenses, and the near-field optical microscopy. These domains are described in detail in other chapters of this book.

## 1.3.1 Extraordinary Transmission Through Subwavelength Holes

At first glance, it is very easy to generate a subwavelength light source. It suffices to drill a circular subwavelength hole in a thick metallic screen and to illuminate this screen on one side. The other side of the hole should behave like a subwavelength light source, thanks to the transmitted light. Unfortunately, the elementary laws of electromagnetics show that this light source should be very weak in intensity. Indeed, this hole in the screen is nothing else than a truncated metallic circular waveguide. Assuming perfect conductivity of the metal, it can be shown very easily that the guided field in an infinitely extended waveguide can be represented by modes, these modes being mathematically described by Fourier–Bessel series. Analyzing these series, it turns out that for a given diameter, it exists a cut-off wavelength  $\lambda_c$  above which the light cannot be guided [94]. This wavelength, which corresponds to the TE<sub>11</sub> mode, is given by:

$$\lambda_c \simeq 1.71D,\tag{1.2}$$

with D diameter of the hole. Of course, the hole constitutes a truncated waveguide and thus a part of light can be transmitted at wavelengths greater than  $\lambda_c$  by the tunnelling effect (or in other words through transmission by evanescent modes which are ignored in the current waveguide theory), but this part should be very small and so, the light spot should be very weak in intensity.

Figure 1.3 shows the zero-order transmission of a two-dimensional, periodic, square symmetry array (with period 900 nm) of cylindrical galleries of diameter 150 nm made in a silver thin film of width 200 nm deposited on a quartz substrate [95].

From Eq. (1.2), it can be deduced that the cut-off wavelength  $\lambda_c$  is equal to 256 nm. Obviously, strong peaks of transmission are observed for larger wavelengths. According to the authors of [95], the narrow peak at the left-hand side of the figure is caused by the excitation of the bulk silver plasmon and disappears by increasing the width of silver. The remarkable characteristic of the transmission is the set of peaks which become gradually stronger as the wavelength is increased, each peak

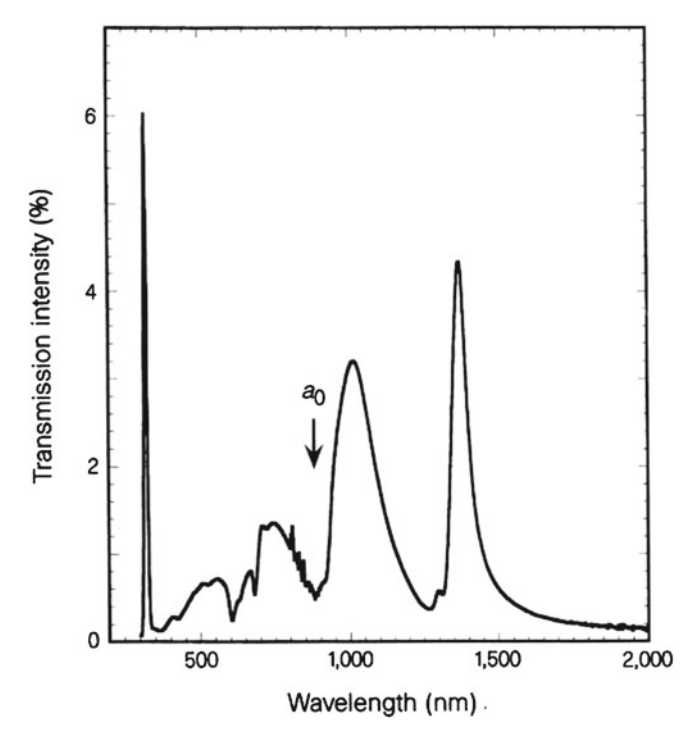


**Fig. 1.3** Extraordinary transmission through an array of circular galleries in a silver film. Reprinted by permission from Macmillan Publishers Ltd: T. W. Ebbesen, H. J. Lezec, H. F. Ghaemi, T. Thio and P. A. Wolff, Nature 391, pp. 667–669 (1998)

occurring just after a drop of transmission. The strongest peak arises at a wavelength equal to 1,370 nm, i.e. more than five times the cut-off wavelength.

Another astounding feature of the figure is that the transmitted efficiency, i.e. the fraction of the incident light which is transmitted, is more than two times larger than the hole area/elementary cell area ratio. It is to be noticed that this surprising property was demonstrated both theoretically and experimentally in a paper published in 1980 [96]. In this paper, it is shown that a perfectly conducting metallic grid with periodically spaced circular galleries can transmit 100% of the incident energy.

The link between the drops/peaks and the excitation of SPPs can be deduced from their locations. For example, a drop/peak occurs in the wavelength range between 850 and 1,000 nm, close to the passing-off wavelength of the (0,1) and (1,0) reflected order, which is equal to 900 nm. The drop-peak between 1,200 and 1,450 nm is close to the passing-off wavelength of the (0,1) and (1,0) orders transmitted inside the quartz.

The paper on extraordinary transmission [95] has been followed by numerous other papers, with the purpose of providing an efficient coupling of an incident light to a nanoconfined mode [97–138]. Experimental studies confirm the phenomenon but

14 D. Maystre

some controversies arose on the theoretical interpretation, especially on the role of SPPs. It is to be noticed that the study of nanophotonic components utilizing channel plasmon polaritons [139] is close to that of enhanced transmission: the ability of SPPs to confine electromagnetic fields is used for the propagation and filtering of optical signals on adequately structured metallic planes.

This phenomenon of extraordinary transmission through subwavelength holes will be studied in detail in another chapter of this book, but let us notice the clear analogy with Wood's anomalies. In both cases, the "anomalies" are caused by the excitation of SPPs on metallic surfaces.

#### 1.3.2 Plasmonics and Metamaterials

One of the major achievements of nanophotonics is the ability to produce subwavelength light sources. This vital result overcomes the classical limit of resolution in optics, also called Rayleigh limit.

In order to outline the origin of this crucial limit, let us recall the expression of the field scattered by a monochromatic light source at frequency  $\omega$ . For the sake of simplicity, we consider the two-dimensional case. The light source is a line current parallel to the *z*-axis of a Cartesian coordinate system xyz, intersecting the xy plane at point S of coordinates  $x_S$  and  $y_S$  (top of Fig. 1.4). Using a time dependency in  $\exp(-i\omega t)$ , it can be shown that the field emitted by this light source is s-polarized, does not depend on z, and is given at a point M of coordinates (x,y,0) by:

$$E^{s} = H_0^{(1)} (kSM), (1.3)$$

where k is the wavenumber in vacuum ( $k = 2\pi/\lambda = \omega/c$ , c is the celerity of light in vacuum) and  $H_0^{(1)}$  is the Hankel function of the first kind and zero order. Such a source is considered as a 2D point source since, due to the singularity of the Hankel function at the origin, the width at half height of the field intensity vanishes. Using the Weyl formula [140], the Hankel function can be expressed in the form:

$$H_0^{(1)}\{kSM\} = \frac{1}{\pi} \int_{\alpha = -\infty}^{+\infty} \frac{1}{\beta(\alpha)} \exp\{ik \left(\alpha(x - x_s) + \beta(\alpha)|y - y_s|\right)\} d\alpha, \quad (1.4)$$

with

$$\beta(\alpha) = \sqrt{1 - \alpha^2} \text{ if } |\alpha| < 1 \text{ or } i\sqrt{\alpha^2 - 1} \text{ if } |\alpha| > 1.$$
 (1.5)

Below the line source,  $y - y_s$  is negative and Eq. (1.4) takes the form:

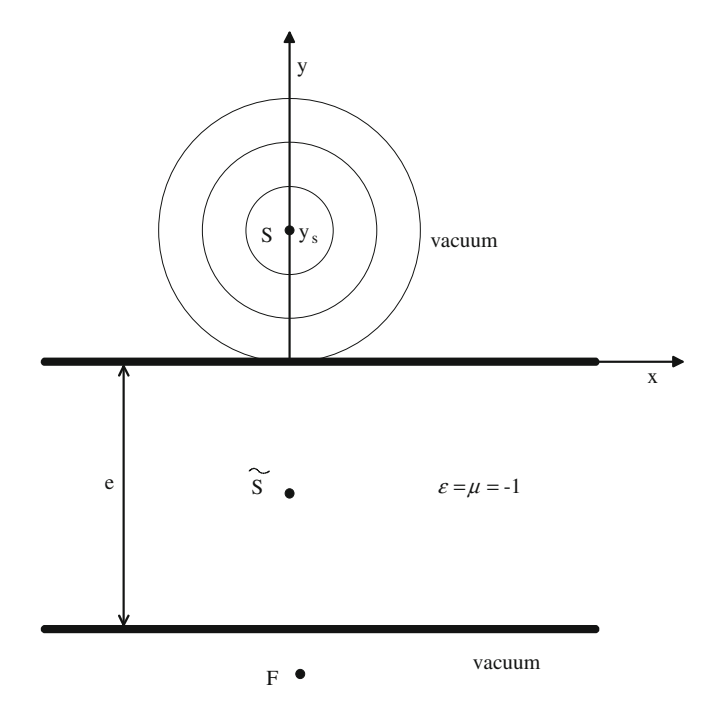


Fig. 1.4 The light emitted by a point source S is focused

$$H_0^{(1)}\{k\text{SM}\} = \frac{1}{\pi} \int_{\alpha = -\infty}^{+\infty} \frac{1}{\beta(\alpha)} \exp\{ik\left(\alpha(x - x_s) - \beta(\alpha)(y - y_s)\right)\} d\alpha. \tag{1.6}$$

It can be deduced that below the light source, the field is described by a sum of plane waves  $\exp\{ik\ (\alpha x - \beta(\alpha)y)\}$  with amplitude  $\frac{\exp\{-ik\alpha x_s + ik\beta(\alpha)y_s\}}{\pi\beta(\alpha)}$ . These plane waves can be decomposed into two categories, according to their propagation factor k on the x-axis. From Eq. (1.5), it turns out that:

- if  $|\alpha| < 1$ , the projection  $-k\beta(\alpha)$  of the wavevector on the y-axis is real and negative. In the following, we call such a wave y-propagating wave,
- if  $|\alpha| > 1$ , this projection is purely imaginary. The plane wave propagates in x only and exponentially decreases in y. It is an evanescent wave.

Let us suppose that an instrument of optics (for example, a cylindrical lens parallel to the light source) is placed below this source in order to obtain an image. After crossing the lens, and assuming that this lens is perfect (which is impossible in practice since it requires an infinite width of the lens), it turns out that all the *y*-propagating plane waves are deviated in order to be in phase and to form an image at the point F conjugate of S with respect to the lens. On the other hand, the evanescent waves will decrease exponentially from the source to the lens, then they will be

16 D. Maystre

scattered by the lens, in such a way that, in practice, they cannot reach the point F. The consequence is that the field below the lens is given by the same expression as in Eq. (1.6), replacing S by F, but now, the integral extends to the finite range  $|\alpha| < 1$ . In the plane  $y = y_F$ , the field is thus given by:

$$E(M) = \frac{1}{\pi} \int_{\alpha=-1}^{+1} \frac{1}{\beta(\alpha)} \exp\{ik\alpha(x - x_F)\} d\alpha.$$
 (1.7)

This integral is equal to a Bessel function of the first kind and zero order [141]:

$$E(M) = J_0 (k(x - x_F)). (1.8)$$

Thus, the field in the image plane is a Bessel function of the first kind and zero order. Since this Bessel function  $J_0(u)$  is not singular and has its first zero for u=2.4, the crucial consequence is that the width  $\Delta x$  of the central light spot is given by  $k\Delta x/2=2.4$ , i.e.  $\Delta x=0.76\lambda$ , i.e. The image is not a point. An intuitive way to explain the vital importance of evanescent waves in focusing devices is to notice that the propagation constant  $k\alpha$  along the x-axis of the evanescent waves generated by a point source is unbounded. Consequently, the transverse wavelength  $\lambda_T=\lambda/\alpha$  (viz. the period on the x-axis) of such an evanescent wave can be very close to 0, thus can be much smaller than the actual wavelength  $\lambda$  of the light emitted by the point source. The existence of these waves of high frequencies in space is a necessary condition to obtain a point source.

Overcoming the Rayleigh limit seems quite impossible since an instrument able to realize this scope must restore at the point image the amplitudes of the evanescent waves contained in the point source. Reconsidering a device initially described and analyzed by Veselago in 1968 [142], Pendry proposed at the very beginning of the twenty-first century a solution to this problem [143]. The perfect lens proposed by Pendry is shown in Fig. 1.4. The 2D point source is placed on the *y*-axis ( $x_s = 0$ ) at the ordinate  $y_s$  and illuminates a slab of a so-called left-handed material, having both relative permittivity and permeability  $\varepsilon$  and  $\mu$  equal to -1. The top and bottom of the slab are located respectively in the planes y = 0 and y = -e.

Using the elementary laws of Electromagnetics, it can be shown that any plane wave  $\exp\{ik(\alpha(x) - \beta(\alpha)y)\}\$  generated by the point source is transmitted below a slab having relative permittivity and permeability  $\varepsilon$  and  $\mu$  with an amplitude  $t(\alpha)$  given by:

$$t(\alpha) = \frac{4p \exp(ik (\gamma(\alpha) - \beta(\alpha))e)}{D},$$
(1.9)

with

$$D = (1+p)^2 - (1-p)^2 \exp(2ik\gamma e), \quad p(\alpha) = \frac{1}{\mu} \frac{\gamma}{\beta}, \quad \gamma(\alpha) = \sqrt{\varepsilon\mu - \alpha^2}. \quad (1.10)$$

When  $\varepsilon$  and  $\mu$  are both equal to -1,  $\gamma$  is equal to  $\beta$ , thus p=-1 and the transmission factor is given by:

$$t(\alpha) = \exp\left(-2ik\gamma(\alpha)e\right). \tag{1.11}$$

Using a new Cartesian coordinate system XYZ of origin F, deduced from xyz by a translation -2e along the y-axis, it emerges that the transmission factor becomes equal to 1. The astounding conclusion is that the amplitudes of both y-propagating and evanescent waves are restored at point F, which is thus a perfect, stigmatic light spot. It can be shown that the point  $\tilde{S}$ , symmetric of S with respect to the top of the slab, constitutes a second point image, located inside the slab. It is worth noting that for a p-polarized field (the electric current being replaced by a magnetic current), Eqs. (1.9), (1.10) and (1.11) hold, except that p is now given by  $p(\alpha) = \frac{1}{\varepsilon} \frac{\gamma}{\beta}$ , but since  $\varepsilon = \mu$ , the final result remains unchanged.

The paper by Pendry has been followed by many controversies [144–152]. It is worth noting that in 1994, it was shown in [153] that quasistatic (low frequency) line sources could have arbitrary sharp images, even though the significance of this discovery was not recognized at the time. Also, it should be noticed that it has been shown that a non-harmonic solution to the problem of transmission by a left-handed material illuminated at t=0 by a sinusoidal field exists, with a linear increase of the field with time [154]. It is possible to understand the physical meaning of this crucial result by considering an equivalent result in electronics.

A sinusoidal tension v(t) on a RLC circuit generates a current j(t) which satisfies the classical equation:

$$v(t) = \frac{q}{C} + L\frac{\mathrm{d}j}{\mathrm{d}t} + Rj,\tag{1.12}$$

with q charge of the capacitor. Taking the derivative of Eq. (1.12) yields:

$$L\frac{\mathrm{d}^2 j}{\mathrm{d}t^2} + R\frac{\mathrm{d}j}{\mathrm{d}t} + \frac{j}{C} = \frac{\mathrm{d}v}{\mathrm{d}t}.$$
 (1.13)

For a harmonic tension, we can use the complex notation and the complex amplitude  $\tilde{j}$  of the current is given by  $\tilde{j} = \tilde{v}/Z$ , with  $\tilde{v}$  being the complex amplitude of the tension v, and the impedance Z of the RLC circuit being given by

$$Z = R + i\left(L\omega - \frac{1}{C_{\omega}}\right). \tag{1.14}$$

When R takes non-null values,  $\tilde{j}$  remains bounded but if R tends to zero, Z tends to zero at the resonance frequency  $\omega_1$  defined by  $LC\omega_1^2$ , thus for this resonance frequency the current is infinite. Intuitively, this result is not surprising since the energy provided by the generator cannot be dissipated. As a consequence, a harmonic solution for the current does not exist at resonance.

Now, let us suppose that the tension starts at t = 0:

18 D. Maystre

$$v(t) = \theta(t)\sin(\omega t). \tag{1.15}$$

We deduce from Eq. (1.13) that:

$$L\frac{\mathrm{d}^2 j}{\mathrm{d}t^2} + \frac{j}{C} = \omega\theta(t)\cos(\omega t). \tag{1.16}$$

This linear differential equation of the second order with right-hand member and initial conditions (j(0)) and dj/dt(0) = v(0)/L = 0 can be solved classically by adding the general solution of the differential equation without right-hand member and a particular solution of the differential equation with right-hand member. The final result is given by:

$$j(t) = \frac{\omega}{L(\omega_1^2 - \omega^2)} (\cos(\omega t) - \cos(\omega_1 t))\theta(t). \tag{1.17}$$

Surprisingly, the solution for  $\omega \neq \omega_1$  contains both frequencies  $\omega$  and  $\omega_1$ , i.e. the frequency of excitation and the resonance frequency. When  $\omega$  is equal to  $\omega_1$ , the right-hand member of Eq. (1.17) is undetermined but the limit of the expression as  $\omega$  tends to  $\omega_1$  exists and is given by:

if 
$$\omega \to \omega_1$$
,  $j(t) \to \frac{1}{2L} t \sin(\omega_1 t) \theta(t)$ . (1.18)

This very simple result shows that the solution oscillates at frequency  $\omega_1$  with a modulus which linearly increases with time. From much more complicated calculations, the same results can be found for left-handed materials. First, the solution for an arbitrary frequency  $\omega$  includes both a term at frequency  $\omega$  and a term at resonance frequency  $\omega_1$  for which  $\varepsilon = \mu = -1$ . Second, the limit of the solution when  $\omega$  tends to  $\omega_1$  oscillates at frequency  $\omega_1$  with a modulus which linearly increases with time. In fact, these results are general for resonance phenomena with lossless devices, and many other examples could be found, for example in mechanics with the lossless harmonic oscillator.

Coming back to the slab, it turns out that the transmitted field in the harmonic problem diverges above F and even inside a part of the slab. It is not the purpose of this chapter to give a detailed description of the state of the art in this domain, but it appears that nowadays, the specialists acknowledge that there does not exist a harmonic solution to the problem of transmission by a left-handed material but that, nevertheless, the device shown in Fig. 1.4 can constitute a "superlens", viz. an instrument able to generate a subwavelength light spot, a fact confirmed by many experimental studies [155–158]. A prerequisite for the fabrication of a superlens is to get both electric and magnetic microresonators periodically spaced, the elementary cell containing a couple of resonators having a strongly subwavelength size. As a consequence, in the visible region, the period of the so-called "metamaterial" must be nanometric, which in practice is very difficult to fabricate. This is the reason

why another way to realize metamaterials and superlenses has been explored in plasmonics.

The plasmonics device, called "poor man superlens" by Pendry, is also a slab, as represented by Fig. 1.4, but now, the material inside the slab is a metal, for example silver or gold. Of course, the width of this slab must be very small in order to avoid a poor transmission factor. We suppose that the permittivity of the slab is close to -1, but the material is not magnetic, thus its permeability is equal to +1. We recall that a metal such as silver has a permittivity close to -1 in the near ultraviolet, around 340 nm. Let us show that such a slab is able to increase exponentially the amplitudes of the evanescent waves for p-polarized light.

Defining the enhancement  $\tau$  of the amplitude of an evanescent wave as the modulus of the ratio of the amplitude of the transmitted evanescent wave at the bottom of the slab (at y=-e), to the amplitude of the incident evanescent wave at y=0, it can be deduced from Eq. (1.9) that:

$$\tau (\alpha) = \frac{4p \exp(ik\gamma (\alpha) e)}{D}.$$
 (1.19)

Let us consider an evanescent wave with a large constant of propagation  $k\alpha$  on the x-axis, in such a way that  $\beta(\alpha)$  and  $\gamma(\alpha)$  given by Eqs. (1.5) and (1.10) are very close to each other:

$$\beta(\alpha) \simeq \gamma(\alpha) \simeq i |\alpha|$$
. (1.20)

We deduce from Eq. (1.10) (replacing  $\mu$  by  $\varepsilon$  since the light is p-polarized) that  $p(\alpha) \simeq -1$ . In these conditions, Eq. (1.19) becomes:

$$\tau(\alpha) \simeq \frac{-4 \exp(-k |\alpha| e)}{(1+p)^2 - 4 \exp(-2k |\alpha| e)}.$$
 (1.21)

Since  $(1 + p)^2$  is very small, the denominator behaves like  $-4 \exp(-2k |\alpha| e)$ , at least for small values of  $k |\alpha| e$ , and thus:

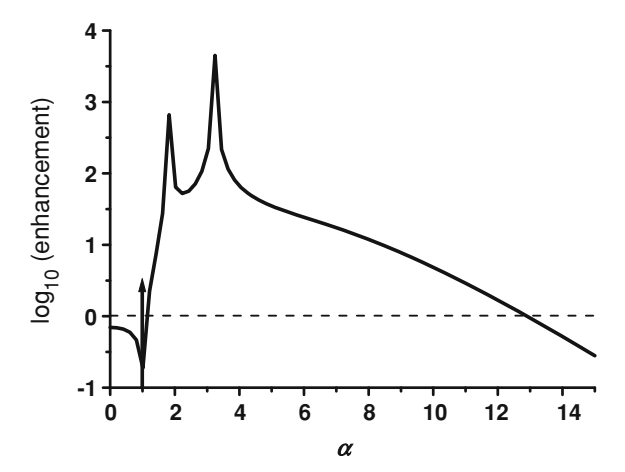
$$\tau(\alpha) \simeq \exp(+k|\alpha|e) \text{ if } (1+p)^2 \ll \exp(-2k|\alpha|e).$$
 (1.22)

If, for a given value of  $k\alpha$ , e is equal to 0, the slab disappears and  $\tau=1$ . Now, if the width e is increased,  $\tau$  increases exponentially as long as the inequality in Eq. (1.22) is satisfied: the amplitude of the transmitted evanescent wave below the slab is greater than that of the incident evanescent wave on the top of the slab. We have drawn in Fig. 1.5 the enhancement factor versus the normalized propagation factor  $\alpha$  for a non-magnetic slab of permittivity -1 and width 50 nm.

Obviously, a strong enhancement is obtained in a wide range of evanescent waves. This enhancement has two poles at  $\alpha=1.8$  and  $\alpha=3.2$ . Is it possible to obtain subwavelength light spots with a device that enhances the evanescent waves in a given range but does not focus the y-propagating waves? A simple demonstration can show

D. Maystre

Fig. 1.5 Enhancement factor of a metallic slab of permittivity -1 and width 50 nm. The *arrow* shows the limit between y-propagating waves (*left*) and evanescent waves (*right*)



that the answer is positive: restricting the constants of propagation of evanescent waves to the couple  $\alpha/k_0=\pm 4$ , it is straightforward to show that the transmitted field creates a system of interferences with a period  $\lambda/8$  containing a bright and a dark band. Thus, the width of a bright band is smaller than  $\lambda/8$ . Consequently, this couple of propagation constants generates a series of subwavelength light lines.

The experimental demonstration of the ability to create a subwavelength imaging process with a thin silver slab has been given by Fang et al. [159]. These authors recorded the images of an array of nanowires and the word "NANO" onto an organic polymer with a resolution close to 60 nm, i.e. one-sixth of the illumination wavelength in the near ultraviolet. This breakthrough was followed by other papers on planar metallic or metallo-dielectric structures [160–166], but most of the studies in this field are now devoted to more complicated metal devices, for example periodic chains of nanometric particles, for use as metamaterial devices or for the purpose of field enhancement [167–174].

#### 1.3.3 Plasmonics and Near-Field Microscopy

The Weyl formula shows that the field emitted by a point source includes evanescent waves with transverse wavelengths  $\lambda_T$  very close to 0. A device like a superlens is able to reproduce a part of these waves in order to generate a subwavelength image. Moreover, it can be conjectured that these waves can be used to characterize objects or surface asperities having sizes much smaller than the wavelength  $\lambda$  of the light, but of the same order as  $\lambda_T$ . From that point of view, a superlens should be an efficient tool for optical characterization. However, another way to generate strong evanescent waves on a nanometric object is to use optical antennas placed very close to this object. If this antenna can produce strong evanescent waves, the

mismatch between the wavelength of light and the dimensions of nanostructures to be characterized will be overcome. This is one of the basic principles of the near-field microscopy [175–193].

It is quite impossible, in practice, to make antennas acting like intense point sources in the visible region: the size of the source is hardly negligible with respect to the wavelength. Indeed, the challenge to make strongly subwavelength antennas generating intense radiated fields seems impossible to win. Plasmonics provides a solution to this problem. SPPs can propagate at the surface of metallic planes or metallic gratings, but they can propagate as well at the surface of metallic particles. When a nanometric metallic particle is illuminated by a monochromatic optical source like the extremity of an optical fiber, a SPP can propagate on its surface with a given propagation constant. In general, the intensity of the field created by this SPP is very small. However, the finite size of the particle plays the same role as the periodicity for diffraction gratings: for a given wavelength of light, a resonance can occur, determined by the particle size, shape, composition and by the local dielectric environment. Due to this resonance, such a "resonant optical antenna" enables the electromagnetic energy produced by the fiber to be concentrated into a subwavelength region. In addition, it provides an optimal conversion of the localized field into a radiated field, which can be used for characterization purpose.

Examples for these relevant field-confining optical probes are subwavelength metallic spheres and sharp metal tips. It is to be noticed that the use of narrow apertures for optical microscopy beyond the limit of diffraction was suggested as early as 1928 by Synge [175]. However, this visionary proposal was far beyond the technical capabilities of the time. In 1972, Ash and Nichols [176] demonstrated in the microwaves region a subwavelength imaging capability and obtained a resolution of  $\lambda/60$ . Then, in the 1980s, two groups won the difficult challenge of extending Synge's concept to the visible region and gave the evidence of the feasibility of nearfield optical microscopy: a research group at IBM Corporation's Zurich laboratory [177–179] and an independent group working at Cornell University [180]. The reader can find in [181–193] some reviews and articles on more recent achievements in that field.

#### 1.4 Plasmon Propagation on Randomly Rough Surfaces, Weak and Strong Localization of Light

The study of phenomena generated by fields on random structures is one of the major domains of analysis of modern physics. In the frame of optics and scattering, phenomena such as enhanced backscattering (or weak localization) or Anderson localization (or strong localization) of light by a set of particles, an inhomogeneous material or randomly rough surfaces have drawn a considerable attention. The reason for this interest lies not only on the attraction for random structures and underlying physics, but also on the vital importance of these phenomena in many practical

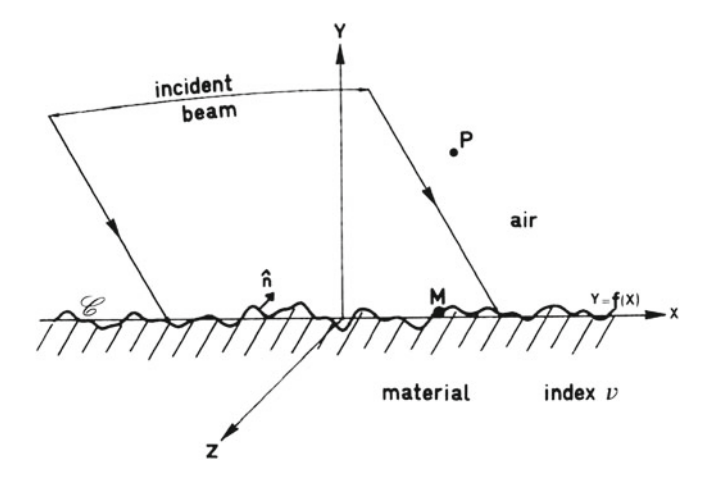


**Fig. 1.6** A randomly rough metallic surface illuminated by an incident beam. Reprinted by permission from OSA:D. Maystre and M. Saillard, Journal of the Optical Society of America A7, p. 983 (1990)

applications of scattering phenomena like RADAR observation, biological tissues characterization, observation of soil, vegetation and sea surfaces, or propagation of laser beams through atmospheric turbulence [194–197].

## 1.4.1 Enhanced Backscattering (Weak Localization)

The experimental observation of enhanced backscattering from randomly rough surfaces has been first reported by Mendez and O'Donnell in 1987 [198]. This phenomenon is manifested by a well-defined peak in the retro-reflection direction in the angular dependence of the intensity of the incoherent light scattered by such a surface. It is explained by the coherent addition of multiply scattered waves, which add in phase in the backward direction only. Every photon scattered from the surface in the backward direction has a time-reversed photon travelling along the same path in the opposite direction. These photons have the same phase at the exit points and thus interfere constructively with each other, resulting in enhanced backscattering.

In the case of metallic rough surfaces with weak corrugations, the propagation of SPPs plays the key role in the interpretation of the phenomenon [199–203]. Figure 1.6 shows the device used for a numerical demonstration of enhanced backscattering. We consider a randomly rough surface y = f(x), invariant with respect to the z-axis of a Cartesian coordinate system xyz. This surface separates the air from a metal of complex index v. Such a non-periodic surface, assumed to be centered  $(\langle y(x) \rangle = 0$ , the averaging process being made by varying x) is classically characterized by its rms  $\sigma$  (random mean square) defined by  $\sigma^2 = \langle y(x)^2 \rangle$ ,

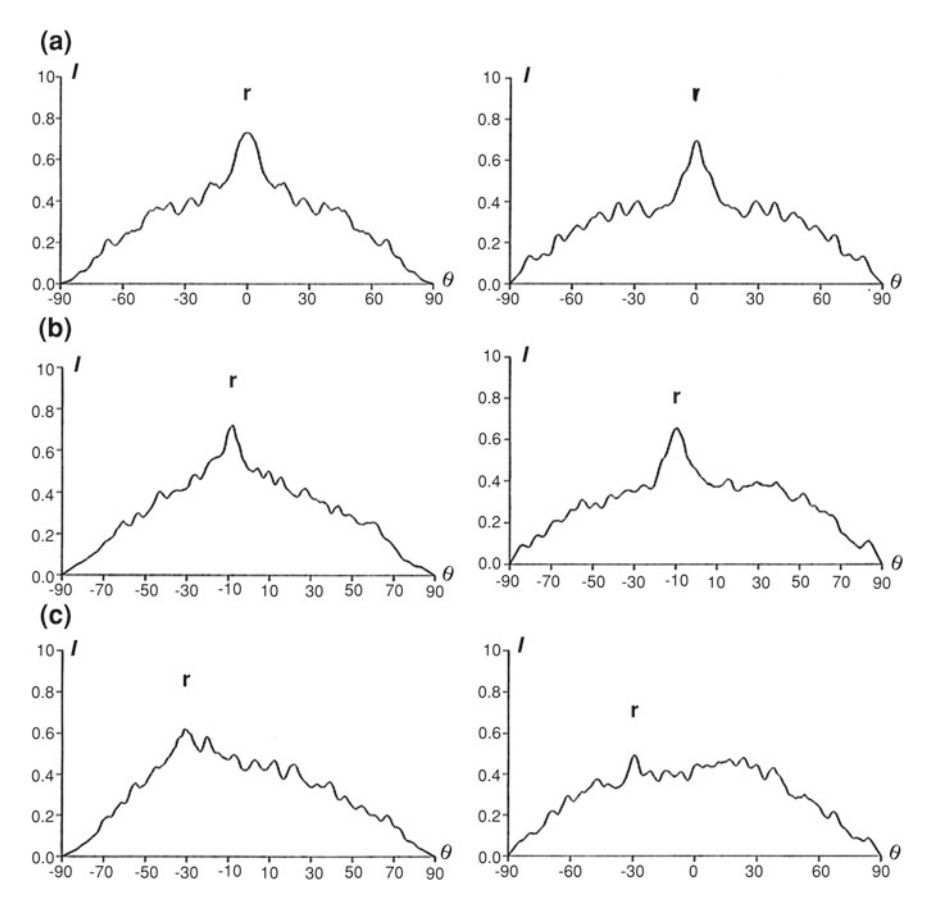
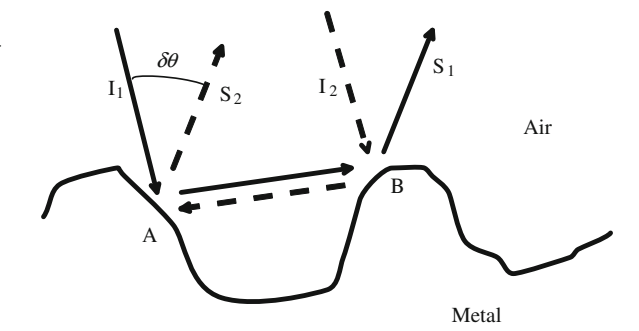


**Fig. 1.7** Scattering intensity versus the scattering angle with a s-polarized (*left*) or p-polarized (*right*) light beam with wavelength 3,392 nm, impinging on a gold randomly rough surface with rms height = 1,950 nm and correlation length 3,570 nm. From the *top* to the *bottom*, the incidence angle is equal to  $0^{\circ}$  (a),  $10^{\circ}$  (b), and  $30^{\circ}$  (c). The *arrows* show the backscattering direction. Reprinted by permission from Taylor & Francis Ltd (http://www.informaworld.com): D. Maystre and M. Saillard, Waves in Random Media 4, 467–485 (1994)

which characterizes the mean height of the surface, and its correlation function  $C(\tau)$  defined by  $C(\tau) = \langle y(x)y(x+\tau) \rangle$ . Assuming a symmetrical correlation function, the correlation length T is defined by C(T) = C(0)/e, with e being the Euler constant. The correlation length characterizes the mean width of the asperities. This metallic surface is illuminated by a light beam, invariant with respect to the z-axis, with wavelength  $\lambda$  and angle of incidence  $\theta$ .

Figure 1.7 represents the mean intensity scattered at infinity by the surface [203]. The results have been obtained from a rigorous theory of scattering by randomly rough surfaces [204, 205]. The mean intensity is defined as an averaging process on a given window of scattering angles, which corresponds to the actual

Fig. 1.8 Heuristic explanation of the enhanced backscattering phenomenon for deep surfaces



measurement process. Indeed, the intensity scattered by a randomly rough surface varies very rapidly with the diffraction angle, at least if the width of the incident beam is large: it is a speckle noise. The averaging process allows one to smooth the intensity pattern, which becomes much clearer. In Fig. 1.7, the width of the incident beam is equal to 1,000 wavelengths and the mean intensity is achieved on a range of scattering angles equal to 4°. The backscattering peak appears for both polarizations, its height decreasing as the angle of incidence is increased.

A heuristic explanation of this retro-reflection peak is given in Fig. 1.8.

First, it must be noticed that the rms height of the surface has the same order of magnitude as the wavelength and the correlation length. This entails that the grooves of the surface are deep. Thus, a ray  $I_1$  striking the surface at a given point A can be scattered toward another point B of the surface and scattered a second time before going to infinity in a given direction (ray  $S_1$ ). The trajectory of this ray is shown by a solid line in Fig. 1.8. A second incident ray  $I_2$ , parallel to  $I_1$  and coherent with it, represented by a dashed line, can strike the surface at point B, be scattered toward the point A and can generate an emerging ray  $S_2$  parallel to  $S_1$ . In general,  $S_1$  and  $S_2$  do not have the same phase, except when the deviation  $\delta\theta$  between the incident and scattered rays vanishes. In that case, the emerging rays are in the backscattering direction and the phases of these emerging rays are identical, due to the reciprocity for reverse paths. As a consequence, the amplitudes of the couple of emerging rays are greater in that direction and it can be shown that the intensity can be enhanced by a factor of 2.

Of course, this explanation does not hold for shallow corrugation. However, a peak of enhanced backscattering can be observed in that case, but only for p-polarized light. Figure 1.9 shows the diffraction pattern of a silver randomly rough surface illuminated by a light beam.

Obviously, a retro-reflection peak can be observed for this very shallow surface. The reflection peak can be observed as well since the surface has properties close to that of a mirror and the scattered field is very small with respect to the specularly reflected one: the speckle is not completely developed, by contrast with what happens in Fig. 1.7. Since the surface is shallow, the heuristic explanation of Fig. 1.8 does not hold. However, the same interpretation can be given, provided that the rays

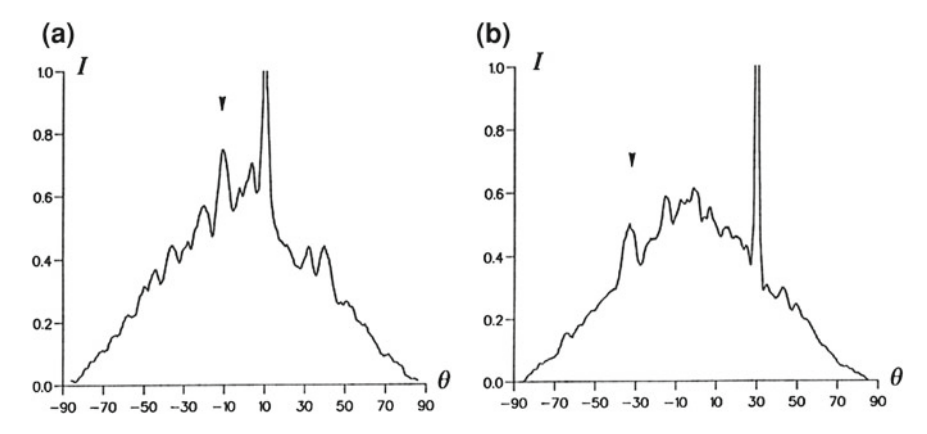


Fig. 1.9 Scattering intensity versus the scattering angle with a p-polarized light beam with wavelength 400 nm, impinging on a silver randomly rough surface with a rms height of 8 nm and a correlation length of 100 nm. The incidence angle is equal to  $10^{\circ}$  at the left-hand side (a) and  $30^{\circ}$  at the right-hand side (b). The arrows show the backscattering direction. Reprinted by permission from Taylor & Francis Ltd (http://www.informaworld.com): D. Maystre and M. Saillard, Waves in Random Media 4, 467–485 (1994)

Fig. 1.10 Picture taken through a window of an airplane, of a glory around the shadow of the airplane onto a cloud layer (by courtesy of Tayeb, Institut Fresnel)



propagating in opposite directions between the points A and B of Fig. 1.8 are replaced by SPPs propagating in opposite directions along the surface. This explanation is consistent with the fact that the phenomenon is not observed for s-polarized light.

The explanation of enhanced backscattering given in Fig. 1.8 can be generalized to a large object (plane, boat. . .) on which multiple reflections of light occur on different parts, or to a set of particles, the points A and B denoting now two different particles of the set. This remark explains why this phenomenon has a vital importance in RADAR observation, propagation of laser beams in turbulent media and meteorology. The phenomenon of enhanced backscattering can be observed in everyday life. It explains the bright halo (glory) around the shadow of an airplane onto a cloud layer (Fig. 1.10).

## 1.4.2 Anderson Localization (Strong Localization)

Anderson localization, also known as strong localization, is manifested by the absence of diffusion of waves in a random structure. Anderson suggested for the first time the possibility of electron localization inside a semiconductor, provided that the degree of randomness of the impurities or defects is sufficiently large [206, 207].

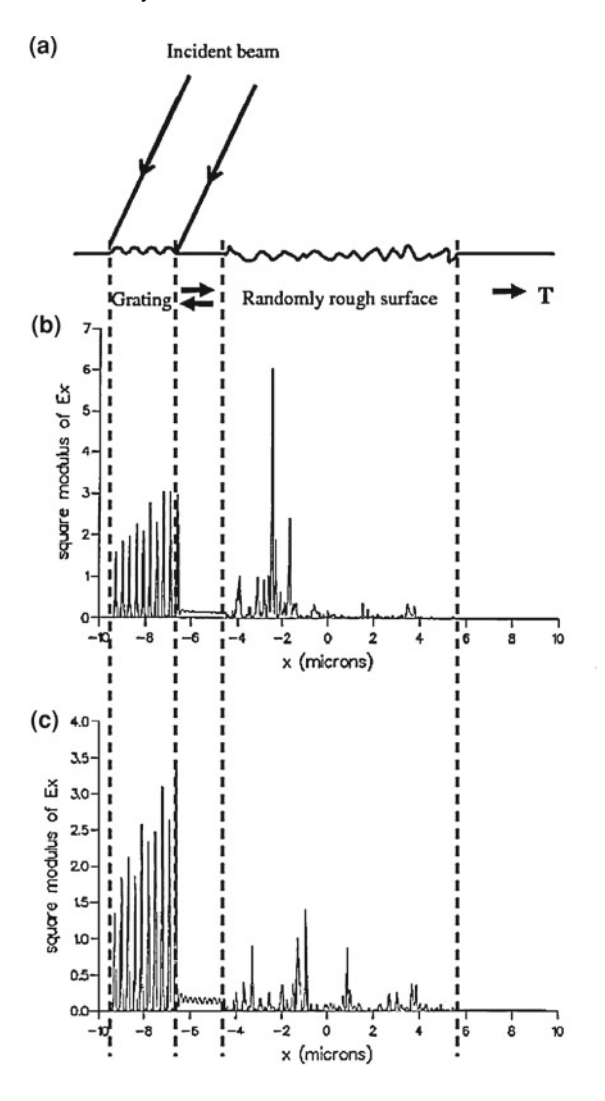
Anderson localization is a general wave phenomenon that applies to electromagnetic waves as well [208–211]. Indeed, in analogy with electron localization, it has been anticipated that in a random strongly scattering optical structure, photons can be trapped in some regions by the constructive interference of waves. These severe interferences can completely halt the waves inside the random medium. Strong localization of light has been analyzed in the frame of plasmonics [212–215].

It can be observed that a SPP propagating on a flat metal surface and striking a randomly corrugated region presents in some parts of this region hot spots generating a strong radiation in the far field and a strong absorption in the metal. As a consequence, the transmitted intensity can become very weak. Figure 1.11, obtained by Saillard and Maystre using an extension of the theory described in [204], illustrates this phenomenon. The silver rough surface (Fig. 1.11a), invariant with respect to the direction of the z-axis (perpendicular to the figure), is composed of a grating and a randomly rough surface, separated by a flat region. The grating is illuminated by an incident beam, invariant with respect to the direction perpendicular to the figure, with p-polarized light. The incidence has been chosen in order to excite at the surface of the grating a SPP propagating to the right of the figure. This SPP is transmitted to the flat region and generates a scattering phenomenon: a part of the incident wave creates in the flat region a system of interferences generated by the reflections on the grating and on the rough surface while another part is transmitted to the rough surface and is shared between absorption inside the metal, scattering at infinity and transmission in the semi-infinite flat region located to the right of the rough surface.

Figure 1.11b and c show the square modulus  $|E_x|^2$  of the x component of the electric field, calculated using an adaptation of our code devoted to scattering from randomly rough surfaces in order to take into account the grating and the flat regions. These two curves are obtained for two different realizations of the rough surface. A randomly rough surface is defined from stochastic features like rms height or correlation function. It is possible to generate a large number of rough surfaces having quite different profiles but the same stochastic parameters. Each of these deterministic rough surfaces is called realization of the rough surface. For example, we can generate such a set of realizations by constructing first a very large rough surface, then by selecting a large set of realizations by cutting the large surface into many smaller parts. We have constructed 100 realizations of the rough surface and selected a couple of them: that corresponding to the smallest (Fig. 1.11b) and largest (Fig. 1.11c) values of SPP transmission T across the rough surface.

In Fig. 1.11b, the transmission is equal to 3 % while it reaches 62 % in Fig. 1.11c. The explanation of this surprising difference can be found in the behavior of  $|E_x|^2$ .

Fig. 1.11 Transmission of an incident SPP generated by a grating across two randomly rough surfaces (a). The transmission in (b) (3%) is much smaller than in (c) (62%), due to the existence of a resonance phenomenon, the strong localization (localiton)



In Fig. 1.11b, in the region close to  $x = -2.5 \,\mu\text{m}$  the field is much larger than in Fig. 1.11c. In this region,  $|E_x|^2$  reaches a value equal to 6, while it never exceeds 1.5 in Fig. 1.11c. Thus, the strong difference between the transmission factors is caused by a resonance phenomenon which occurs for the realization of Fig. 1.11b. This resonance phenomenon generates a large field on the surface, and thus a strong absorption in the metal and a large scattered field in the far field, which entails a small transmission.

Let us try to give a heuristic explanation to this resonance phenomenon. In Fig. 1.12, we have, for simplicity, represented a randomly rough surface by a series of diffraction gratings having different pitches and different heights. An incident

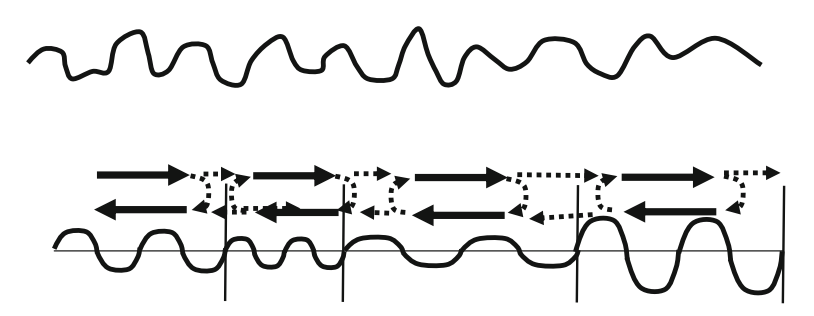


Fig. 1.12 Heuristic explanation of strong localization by randomly rough surfaces

SPP coming from the left-hand side can propagate in the set of gratings but, of course, phenomena of reflection and transmission occur at each transition between two elementary gratings. Thus, the field inside the rough surface results from a very complicated interference system. In some parts of the surface, the interference process may be constructive, in such a way that a resonance arises: the field becomes very strong and cannot escape from this region, except by absorption or radiation. This is the explanation of the hot spot observed in Fig. 1.11b.

Of course, if the rough surface is very large, this resonance phenomenon can occur on several parts of the surface, thus, the variations of T over the different realizations of the surface are small. In Fig. 1.11, the rough surface has a small size, which entails that resonance phenomena can exist or not, depending on the realization. This phenomenon of resonance has been investigated theoretically and numerically in [213, 214]. The field in the resonance region has been termed "localiton", or localized mode, viz. a homogeneous (without incident wave) solution of Maxwell equations decreasing exponentially with time.

### 1.5 Conclusion

Widely developed in the twentieth century, SPP studies have been strongly linked for a long time to the study of grating anomalies, even though the origin of the anomalies from the excitation of SPPs was not discovered before the middle of this century. A considerable number of articles have been published in that domain and nowadays the phenomena of absorption, filtering, and field enhancement associated with anomalies are used in many fields of science, technology, and medicine.

The study of excitation of SPPs from randomly rough surfaces has led to the study of fascinating phenomena of modern physics, namely enhanced backscattering and Anderson localization. These phenomena, which can be observed in the nature, play a crucial role in many fields of technology like RADAR observation, propagation of laser beams in the atmosphere and meteorology.

Recently, plasmonics has raised a new and considerable interest. It is involved in the main domains of nanophotonics like metamaterials, superlensing, near-field optics, or extraordinary transmission through subwavelength holes. It can be conjectured that in the future, the remarkable property of SPPs to concentrate and enhance the electromagnetic field on the nanometer scale will open new fields of applications in science and technology, especially in the domain of photonic circuits, even though the realization of completely plasmonics circuits on subwavelength scale remains a dream at present time.

## References

- R.W. Wood, On a remarkable case of uneven distribution of light in a diffraction grating spectrum. Philos. Mag. 4, 396–402 (1902)
- L. Rayleigh, Note on the remarkable case of diffraction spectra described by Prof. Wood. Philos. Mag. 14, 60–65 (1907)
- L. Rayleigh, On the dynamical theory of gratings. Proc. Royal Soc. (Lond.) 79, 399–416 (1907)
- R.W. Wood, Diffraction gratings with controlled groove form and abnormal distribution of intensity. Philos. Mag. 23, 310–317 (1912)
- L.R. Ingersoll, Some peculiarities of polarization and energy distribution by speculum gratings. Phys. Rev. 17, 493–501 (1921)
- 6. R.W. Wood, Anomalous diffraction gratings. Phys. Rev. 48, 928–936 (1935)
- J. Strong, Effect of evaporated films on energy distribution in grating spectra. Phys. Rev. 49, 291–296 (1936)
- 8. U. Fano, The theory of anomalous diffraction gratings and of quasi-stationary waves on metallic surfaces (Sommerfeld's waves). J. Opt. Soc. Am. 31, 213–222 (1941)
- 9. C.H. Palmer Jr, Parallel diffraction grating anomalies. J. Opt. Soc. Am. 42, 269–276 (1952)
- C.H. Palmer Jr, Diffraction grating anomalies, II, coarse gratings. J. Opt. Soc. Am. 46, 50–53 (1956)
- J.E. Stewart, W.S. Gallaway, Diffraction anomalies in grating spectrophotometers. Appl. Opt. 1, 421–429 (1962)
- A. Hessel, A.A. Oliner, A new theory of Wood's anomalies on optical gratings. Appl. Opt. 4, 1275–1297 (1965)
- J. Hagglund, F. Sellberg, Reflection, absorption, and emission of light by opaque optical gratings. J. Opt. Soc. Am. 56, 1031–1040 (1966)
- R.H. Ritchie, E.T. Arakawa, J.J. Cowan, R.N. Hamm, Surface-plasmon resonance effect in grating diffraction. Phys. Rev. Lett. 21, 1530–1533 (1968)
- J.J. Cowan, E.T. Arakawa, Dispersion of surface plasmons in dielectric-metal coating on concave diffraction gratings. Z. Physik 235, 97–109 (1970)
- D. Maystre, Sur la diffraction d'une onde plane par un réseau métallique de conductivité finie.
   Opt. Commun. 6, 50–54 (1972)
- D. Maystre, Sur la diffraction d'une onde plane électromagnétique par un réseau métallique.
   Opt. Commun. 8, 216–219 (1973)
- R.C. McPhedran, M.D. Waterworth, Properties of diffraction grating anomalies. Opt. Acta 20, 533–547 (1973)
- M.C. Hutley, An experimental study of the anomalies of sinusoidal diffraction gratings. Opt. Acta 20, 607–624 (1973)
- M.C. Hutley, V.M. Bird, A detailed experimental study of the anomalies of a sinusoidal diffraction grating. Opt. Acta 20, 771–782 (1973)

21. R. Petit, D. Maystre, M. Nevière, Practical applications of the electromagnetic theory of gratings, in *Space Optics, Proceedings of the Ninth International Congress of Optics*, vol. 2 (1974), pp. 667–681

- P.M. Van den Berg, J.C.M. Borburgh, Dispersion of surface plasmons in InSb-gratings. Appl. Phys. 3, 55–60 (1974)
- R.C. McPhedran, D. Maystre, A detailed theoretical study of the anomalies of a sinusoidal diffraction grating. Opt. Acta 21, 413–421 (1974)
- R.C. McPhedran, D. Maystre, Theoretical study of the diffraction anomalies of holographic gratings. Nouv. Rev. Optique 5, 241–248 (1974)
- I. Pockrand, Reflection of light from periodically corrugated silver films near the plasma frequency. Phys. Lett. 49A, 259–260 (1974)
- M.C. Hutley, J.P. Verrill, R.C. McPhedran, M. Nevière, P. Vincent, Presentation and verification of a differential formulation for the diffraction by conducting gratings. Nouv. Rev. Optique 6, 87–95 (1975)
- 27. I. Pockrand, Coupling of surface plasma oscillations in thin periodically corrugated silver films. Opt. Commun. 13, 311–313 (1975)
- 28. H. Raether, On the influence of roughness on the optical properties of surfaces: plasma resonance emission and the plasmon dispersion relation. Thin Solid Films 28, 119–124 (1975)
- 29. R. Orlowski, H. Raether, The total reflection of light at smooth and rough silver films and surface plasmons. Surf. Sci. **54**, 303–308 (1975)
- 30. D. Maystre, R. Petit, Brewster incidence for metallic gratings. Opt. Commun. 17, 196–200 (1976)
- 31. M.C. Hutley, D. Maystre, The total absorption of light by a diffraction grating. Opt. Commun. **19**, 431–436 (1976)
- 32. I. Pockrand, H. Raether, Surface plasma-oscillations in silver films with wavy surface profiles—quantitative experimental study. Opt. Commun. 18, 395–399 (1976)
- I. Pockrand, Resonance anomalies in light intensity reflected at silver gratings with dielectric coatings. J. Phys. D Appl. Phys. 9, 2423–2432 (1976)
- E. Kröger, E. Kretschmann, Surface plasmon and polariton dispersion at rough boundaries. Phys. Status Solidi B 76, 515–523 (1976)
- I. Pockrand, H. Raether, Surface plasma oscillations at sinusoidal silver surfaces. Appl. Opt. 16, 1784–1786 (1977)
- C.E. Wheeler, E.T. Arakawa, R.H. Ritchie, Photon excitation of photon surface plasmons in diffraction gratings—effect of groove depth and spacing. Phys. Rev. 13, 2372–2376 (1976)
- J.J. Cowan, E.T. Arakawa, Artificial polarization anomalies from holographic gratings. Opt. Commun. 21, 428–431 (1977)
- 38. R.C. McPhedran, D. Maystre, Theory and solar application of inductive grids. Appl. Phys. (Berlin) **14**, 1–20 (1977)
- 39. D. Maystre, M. Nevière, Quantitative theoretical study on plasmon anomalies of diffraction gratings. J. Opt. 8, 165–174 (1977)
- M. Nevière, D. Maystre, P. Vincent, Determination of leaky modes of a corrugated waveguide—application to the study of anomalies of dielectric coated gratings. J. Opt. 8, 231–242 (1977)
- E.G. Loewen, M. Nevière, dielectric coated gratings—curious property. Appl. Opt. 16, 3009–3011 (1977)
- 42. D. Maystre, M. Nevière, P. Vincent, General theory of anomalies and energy absorption by diffraction gratings and their relation with surface waves. Opt. Acta 25, 905–915 (1978)
- 43. M. Nevière, D. Maystre, G.H. Derrick, R.C. McPhedran, M.C. Hutley, On the total absorption of unpolarized monochromatic light, in *Proceedings of the I.C.O.XI Conference* (Madrid, Spain, 1978), pp. 609–612
- 44. J.R. Andrewartha, J.R. Fox, I.J. Wilson, Resonance anomalies in the lamellar grating. Opt. Acta 26, 69–89 (1979)
- J.R. Andrewartha, J.R. Fox, I.J. Wilson, Further properties of lamellar grating resonance anomaly. Opt. Acta 26, 197–209 (1979)

- 46. R. Petit (ed.), Electromagnetic Theory of Gratings. Topics in Current Physics (Springer, Berlin, 1980)
- D. Maystre, in General Study of Grating Anomalies from Electromagnetic Surface Modes, ed. by A.D. Boardman. Chapter 17 of Electromagnetic Surface Modes (Wiley, New York, 1982)
- 48. M.C. Hutley, *Diffraction Gratings* (Academic Press, New York, 1982)
- 49. H. Raether, Surface Plasmons on Smooth and Rough Surfaces and on Gratings. Springer Tracts in Modern Physics, vol. 111 (Springer, New York, 1988)
- E.G. Loewen, E. Popov, Diffraction Gratings and Their Applications (Marcel Dekker, New York, 1997)
- 51. L. Rayleigh, *The Theory of Sound*, vol. 2 (Dover, New York, 1945)
- D. Rudolph, G. Schmahl, Spektroscopische Beugungsgitter hoher Teilungsgenauigkeit erzeugt mit Hilfe von Laserlicht und Photoresistschichten. Optik 30, 475–487 (1970)
- 53. J.L. Uretsky, The scattering of plane waves from periodic surfaces. Ann. Phys. **33**, 400–427 (1965)
- D. Maystre, R.C. Mc Phedran, Le théorème de réciprocité pour les réseaux de conductivite finie: Demonstration et applications. Opt. Commun. 12, 164–167 (1974)
- 55. D. Maystre, Sur la diffraction et l'absorption par les réseaux utilisés dans l'infrarouge, le visible et l'ultraviolet; applications à la spectroscopie et au filtrage des ondes électromagn?tiques, Thèse d'Etat, Université d'Aix-Marseille (1974)
- 56. M. Nevière, P. Vincent, R. Petit, Sur la théorie du réseau conducteur et ses applications a l'optique. Nouv. Rev. Optique **5**, 65–77 (1974)
- 57. R.H. Ritchie, Plasma losses by fast electrons in thin films. Phys. Rev. 106, 874–881 (1957)
- A. Wirgin, T. López-Rios, Can surface-enhanced Raman scattering be caused by waveguide resonance? Opt. Commun. 48, 416–420 (1984)
- E. Popov, L. Tsonev, D. Maystre, Losses of plasmon surface wave on metallic grating. J. Mod. Opt. 37, 379–387 (1990)
- E. Popov, L. Tsonev, D. Maystre, Lamellar diffraction grating anomalies. Appl. Opt. 33, 5214–5219 (1994)
- E.L. Wood, J.R. Sambles, N.P. Cotter, S.C. Kitson, Diffraction grating characterization using multiplewavelength excitation of surface-plasmon polaritons. J. Mod. Opt. 42, 1343–1349 (1995)
- 62. F. Pincemin, J.-J. Greffet, Propagation and localization of a surface plasmon polariton on a finite grating. J. Opt. Soc. Am. B 13, 1499–1509 (1996)
- W.L. Barnes, S.C. Kitson, T.W. Preist, J.R. Sambles, Photonic surfaces for surface-plasmon polaritons. J. Opt. Soc. Am. A 14, 1654–1661 (1997)
- T. López-Rios, D. Mendoza, F.J. Garcia-Vidal, J. Sánchez-Dehesa, B. Pannetier, Surface shape resonances in lamellar metallic gratings. Phys. Rev. Lett. 81, 665–668 (1998)
- F.J. Garcia-Vidal, J. Sánchez-Dehesa, A. Dechelette, E. Bustarret, T. López-Rios, T. Fournier,
   B. Pannetier, Localized surface plasmons in lamellar metallic gratings. J. Lightwave Technol.
   17, 2191–2195 (1999)
- W.-C. Tan, T.W. Preist, J.R. Sambles, N.P. Wanstall, Flat surface-plasmon-polariton bands and resonant optical absorption on short-pitch metal gratings. Phys. Rev. B 59, 12661–12666 (1999)
- 67. E.A. Smith, R.M. Corn, Surface plasmon resonance imaging as a tool to monitor biomolecular interactions in an array based format. Appl. Spectrosc. **57**, 320A–332A (2003)
- 68. R. Hooper, J.R. Sambles, Surface plasmon polaritons on narrow-ridged short-pitch metal gratings in the conical mount. J. Opt. Soc. Am. 20, 836–843 (2003)
- 69. S.F. Cheng, L.K. Chau, Colloidal gold modified optical fiber for chemical and biochemical sensing. Anal. Chem. **75**, 16–21 (2003)
- E. Hutter, J. Fendler, Exploitation of localized surface plasmon resonance. Adv. Mater. 16, 1685–1706 (2004)
- S. Collin, F. Pardo, R. Teissier, J.L. Pelouard, Efficient light absorption in metalsemiconductor-metal nanostructures. Appl. Phys. Lett. 85, 194–196 (2004)

72. K. Aslan, J.R. Lakowicz, C. Geddes, Plasmon light scattering in biology and medicine: new sensing approaches, visions and perspectives. Curr. Opin. Chem. Biol. 9, 538–544 (2005)

- J.N. Gollub, D.R. Smith, D.C. Vier, T. Perram, J.J. Mock, Experimental characterization of magnetic surface plasmons on metamaterials with negative permeability. Phys. Rev. B 71, 195402 (2005)
- L.K. Chau, Y.F. Lin, S.F. Cheng, T.J. Lin, Fiber-optic chemical and biochemical probes based on localized surface plasmon resonance. Sens. Actuators B 113, 100–105 (2006)
- 75. J.L. Tang, S.F. Cheng, W.T. Hsu, T.Y. Chiang, L.K. Chau, Fiber-optic biochemical sensing with a colloidal gold-modified long period fiber grating. Sens. Actuators B **119**, 105–109 (2006)
- E. Popov, N. Bonod, S. Enoch, Non-Bloch plasmonic stop-band in real-metal gratings. Opt. Express 10, 6241–6250 (2007)
- 77. E. Popov, N. Bonod, S. Enoch, Comparison of plasmon surface waves on shallow and deep metallic 1D and 2D gratings. Opt. Express 15, 4224–4237 (2007)
- 78. N. Bonod, E. Popov, L. Li, B. Chernov, Unidirectional excitation of surface plasmon by slanted grating. Opt. Express 18, 11427–11432 (2007)
- C.D. Chen, S.F. Cheng, L.K. Chau, C.R.C. Wang, Sensing capability of the localized surface plasmon resonance of gold nanorods. Biosens. Bioelectron. 22, 926–932 (2007)
- 80. N. Bonod, E. Popov, R.C. McPhedran, Increased surface plasmon resonance sensitivity with the use of double Fourier harmonic gratings. Opt. Express 16, 11691–11702 (2008)
- J. Le Perchec, P. Quémerais, A. Barbara, T. López-Ríos, Why metallic surfaces with grooves a few nanometers deep and wide may strongly absorb visible light. Phys. Rev. Lett. 100, 066408 (2008)
- 82. N. Bonod, G. Tayeb, D. Maystre, S. Enoch, E. Popov, Total absorption of light by lamellar metallic gratings. Opt. Express 16, 15431–15438 (2008)
- 83. E. Popov, D. Maystre, R.C. McPhedran, M. Nevière, M.C. Hutley, G.H. Derrick, Total absorption of unpolarized light by crossed gratings. Opt. Express 16, 6146–6155 (2008)
- T.V. Teperik, F.J. García De Abajo, A.G. Borisov, M. Abdelsalam, P.N. Bartlett, Y. Sugawara,
   J.J. Baumberg, Omnidirectional absorption in nanostructured metal surface. Nat. Photonics
   2, 299–301 (2008)
- S. Mokapati, F.J. Beck, A. Polman, K.R. Catchpole, Designing periodic arrays of metal nanoparticles for light trapping applications in solar cells. Appl. Phys. Lett. 95, 53115 (2009)
- 86. S.M. Rytov, Correlation theory of thermal fluctuations in an isotropic medium. Sov. Phys. JETP **6**, 130–140 (1958)
- 87. S.M. Rytov, Y.A. Kravtsov, V.I. Tatarskii, *Principles of Statistical Radiophysics* (Springer, Berlin, 1989)
- 88. J.J. Greffet, R. Carminati, K. Joulain, J.P. Mulet, S.P. Mainguy, Y. Chen, Coherent emission of light by thermal sources. Nature **416**, 61–64 (2002)
- 89. C. Henkel, S. Potting, M. Wilkens, Loss and heating of particles in small and noisy traps. Appl. Phys. B **69**, 379–387 (1999)
- 90. F. Marquier, K. Joulain, J.P. Mulet, R. Carminati, J.J. Greffet, Y. Chen, Coherent spontaneous emission of light by thermal sources. Phys. Rev. B 69, 155412 (2004)
- 91. M. Laroche, C. Arnold, F. Marquier, Highly directional radiation generated by a tungsten thermal source. Opt. Lett. **30**, 2623–2625 (2005)
- 92. C. Henkel, K. Joulain, Electromagnetic field correlations near a surface with a nonlocal optical response. Appl. Phys. B **84**, 61–68 (2006)
- 93. J.J. Greffet, C. Henkel, Coherent thermal radiation. Contemp. Phys. 48, 183–194 (2007)
- R.E. Collin, Field Theory of Guided Waves (McGraw-Hill Book Company, New York, 1960),
   p. 195
- 95. T.W. Ebbesen, H.J. Lezec, H.F. Ghaemi, T. Thio, P.A. Wolff, Extraordinary optical transmission through subwavelength hole arrays. Nature **391**, 667–669 (1998)
- P.J. Bliek, L.C. Botten, R. Deleuil, R.C. McPhedran, D. Maystre, Inductive grids in the region of diffraction anomalies: theory, experiment, and applications. IEEE Trans. Microw. Theory Tech. MTT28, 1119–1125 (1980)

- 97. H.F. Ghaemi, T. Thio, D.E. Grupp, T.W. Ebbesen, H.Z. Lezec, Surface plasmons enhanced optical transmission through subwavelengths holes. Phys. Rev. B **58**, 6779–6782 (1998)
- 98. T. Thio, H.F. Ghaemi, H.J. Lezec, P.A. Wolff, T.W. Ebbesen, Surface-plasmon enhanced transmission through hole arrays in Cr films. JOSA B 16, 1743–1748 (1999)
- 99. T.J. Kim, T. Thio, T.W. Ebbesen, D.E. Grupp, H.J. Lezec, Control of optical transmission through metals perforated with subwavelength hole arrays. Opt. Lett. **24**, 256–258 (1999)
- J.A. Porto, F.T. Garcia-Vidal, J.B. Pendry, Transmission resonances on metallic gratings with very narrow slits. Phys. Rev. Lett. 83, 2845–2848 (1999)
- D.E. Grupp, H.J. Lezec, K.M. Pellerin, T.W. Ebbesen, T. Thio, Fundamental role of metal surface in enhanced transmission through subwavelength apertures. Appl. Phys. Lett. 77, 1569–1571 (2000)
- E. Popov, M. Nevière, S. Enoch, R. Reinisch, Theory of light transmission through subwavelength periodic hole arrays. Phys. Rev. B 62, 16100–16108 (2000)
- L. Martin-Moreno, F.J. Garcia-Vidal, H.J. Lezec, K.M. Pellerin, T. Thio, J.B. Pendry, T.W. Ebbesen, Theory of extraordinary optical transmission through subwavelength hole arrays. Phys. Rev. Lett. 86, 1114 (2001)
- 104. A. Krishnan, T. Thio, T.J. Kim, H.J. Lezec, T.W. Ebbesen, P.A. Wolff, J. Pendry, L. Martin-Moreno, F.J. Garcia-Vidal, Evanescently coupled resonance in surface plasmon enhanced transmission. Opt. Comm. 200, 1–7 (2001)
- H.J. Lezec, A. Degiron, E. Devaux, R.A. Linke, L. Martin-Moreno, F.J. Garcia-Vidal,
   T.W. Ebbesen, Beaming light from a subwavelength aperture. Science 297, 820–823 (2002)
- A. Degiron, H.J. Lezec, W.L. Barnes, T.W. Ebbesen, Effects of hole depth on enhanced light transmission through subwavelength hole arrays. Appl. Phys. Lett. 81, 4327–4329 (2002)
- S. Enoch, E. Popov, M. Nevière, R. Reinisch, Enhanced light transmission by hole arrays.
   J. Opt. A 4, S83–S87 (2002)
- Q. Cao, P. Lalanne, Negative role of surface plasmon in the transmission of metallic gratings with very narrow slits. Phys. Rev. Lett. 88, 057403 (2002)
- L. Martin-Moreno, F.J. Garcia-Vidal, H.J. Lezec, A. Degiron, T.W. Ebbesen, Theory of highly directional emission from a single subwavelength aperture surrounded by surface corrugations. Phys. Rev. Lett. 90, 167401 (2003)
- N. Bonod, S. Enoch, L. Li, E. Popov, M. Nevière, Resonant optical transmission through thin metallic films with and without holes. Opt. Express 11, 482–490 (2003)
- F.J. Garcia-Vidal, H.J. Lezec, T.W. Ebbesen, L. Martin-Moreno, Multiple paths to enhance optical transmission through a single subwavelength slit. Phys. Rev. Lett. 90, 213901 (2003)
- W.L. Barnes, A. Dereux, T.W. Ebbesen, Surface plasmon subwavelength optics. Nature 424, 824–830 (2003)
- 113. F.I. Baida, D. Van Labeke, Three-dimensional structures for enhanced transmission through a metallic film: annular aperture arrays. Phys. Rev. B 67, 155314 (2003)
- F.I. Baida, D. Van Labeke, B. Guizal, Enhanced confined light transmission by single subwavelength apertures in metallic films. Appl. Opt. 42, 6811–6815 (2003)
- F.J. Garcia-Vidal, L. Martin-Moreno, H.J. Lezec, T.W. Ebbesen, Focusing light with a single subwavelength aperture flanked by surface corrugations. Appl. Phys. Lett. 83, 4500–4502 (2003)
- A. Degiron, T.W. Ebbesen, Analysis of the transmission process through a single aperture surrounded by periodic corrugations. Opt. Express 12, 3694–3700 (2004)
- 117. W.L. Barnes, W.A. Murray, J. Dintinger, E. Devaux, T.W. Ebbesen, Surface plasmon polaritons and their role in the enhanced transmission of light through periodic arrays of subwavelength holes in a metal film. Phys. Rev. Lett. 92, 107401 (2004)
- E. Popov, M. Nevière, P. Boyer, N. Bonod, Light transmission through single apertures. Opt. Commun. 255, 338–348 (2005)
- 119. A. Degiron, T.W. Ebbesen, The role of localized surface plasmon modes in the enhanced transmission of periodic subwavelength apertures. J. Opt. A 7, S90–S96 (2005)
- J. Dintinger, S. Klein, F. Bustos, W.L. Barnes, T.W. Ebbesen, Strong coupling between surface plasmon-polaritons and organic molecules in subwavelength hole arrays. Phys. Rev. B 71, 035424 (2005)

 S.I. Bozhevolnyi, V.S. Volkov, E. Devaux, T.W. Ebbesen, Channel plasmon-polariton guiding by subwavelength grooves. Phys. Rev. Lett. 95, 046802 (2005)

- H. Rigneault, J. Capoulade, J. Dintinger, J. Wenger, N. Bonod, E. Popov, T.W. Ebbesen, P.F. Lenne, Enhancement of single-molecule fluorescence detection in subwavelength apertures. Phys. Rev. Lett. 95, 117401 (2005)
- 123. E. Popov, M. Neviere, A.L. Fehrembach, N. Bonod, Optimization of plasmon excitation at structured apertures. Appl. Opt. **44**, 6141–6154 (2005)
- E. Popov, M. Neviere, A.L. Fehrembach, N. Bonod, Enhanced light transmission through a circular structured aperture. Appl. Opt. 44, 6898

  –6904 (2005)
- P. Lalanne, J.P. Hugonin, J.C. Rodier, Theory of surface plasmon generation at nanoslit apertures. Phys. Rev. Lett. 95, 902 (2005)
- K.G. Lee, Q.H. Park, Coupling of surface plasmon polaritons and light in metallic nanoslits. Phys. Rev. Lett. 95, 902 (2005)
- 127. J. Bravo-Abad, A. Degiron, F. Przybilla, C. Genet, F.J. Garcia-Vidal, L. Martin-Moreno, T.W. Ebbesen, How light emerges from an illuminated array of subwavelength holes. Nat. Phys. 1, 120–123 (2006)
- D. Van Labeke, D. Gérard, B. Guizal, F. Baida, L. Li, An angle-independent Frequency Selective Surface in the optical range. Opt. Express 14, 11945–11951 (2006)
- 129. J. Wenger, J. Dintinger, N. Bonod, E. Popov, P.F. Lenne, T.W Ebbesen, H. Rigneault, Raman scattering and fluorescence emission in a single nanoaperture: optimizing the local intensity enhancement. Opt. Commun. **267**, 224–228 (2006)
- E. Popov, M. Nevière, J. Wenger, P.-F. Lenne, H. Rigneault, P.C. Chaumet, N. Bonod, J. Dintinger, T.W. Ebbesen, Field enhancement in single subwavelength apertures. J. Opt. Soc. Am. A 23, 2342–2348 (2006)
- 131. C. Genet, T.W. Ebbesen, Light in tiny holes. Nature 445, 39-46 (2007)
- 132. J. Wenger, F. Cochonaud, J. Dintinger, L. Wawreznieck, T.W. Ebbesen, H. Rigneault, D. Marguet, P.-F. Lenne, Diffusion analysis within single nanometric apertures reveals the ultrafine cell membrane organization. Biophys. J. 92, 913–919 (2007)
- 133. F. Lopez-Tejeira, S.G. Rodrigo, L. Martin-Moreno, F.J. Garcia-Vidal, E. Devaux, T.W. Ebbesen, J.R. Krenn, I.P. Radko, S.I. Bozhevolnyi, M.V. Gonzalez, J.C. Weeber, A. Dereux, Efficient unidirectional nanoslit couplers for surface plasmons. Nat. Phys. 3, 324–328 (2007)
- H. Liu, P. Lalanne, Microscopic theory of the extraordinary optical transmission. Nature 452, 728–731 (2008)
- J. Wenger, D. Gerard, J. Dintinger, O. Mahboub, N. Bonod, E. Popov, T.W. Ebbesen, H. Rignault, Emission and excitation contributions to enhanced single molecule fluorescence by gold nanometric apertures. Opt. Express 16, 3008–3020 (2008)
- A.-L. Baudrion, F. de Leon-Perez, O. Mahboub, A. Hohenau, H. Ditlbacher, F.J. Garcia-Vidal, J. Dintinger, T.W. Ebbesen, L. Martin-Moreno, J.R. Krenn, Coupling efficiency of light to surface plasmon polariton for single subwavelength holes in a gold film. Opt. Express 16, 3420–3429 (2008)
- M. Spasenovica, D. van Oosten, E. Verhagen, L. Kuipers, Measurements of modal symmetry in subwavelength plasmonic slot waveguides. Appl. Phys. Lett. 95, 203109 (2009)
- E. Verhagen, L. Kuipers, A. Polman, Field enhancement in metallic subwavelength aperture arrays probed by erbium upconversion luminescence. Opt. Express 17, 14586–14598 (2009)
- V.S. Volkov, S.I. Bozhevolnyi, E. Devaux, J.Y. Laluet, T.W. Ebbesen, Wavelength selective nanophotonic components utilizing channel plasmon polaritons. Nanoletters 7, 880–884 (2007)
- P.M. Morse, H. Feshbach, Methods of Theoretical Physics (Mc Graw Hill Book Company, New York, 1953), p. 823
- M. Abramowitz, I.A. Stegun, Handbook of Mathematical Functions (Dover Publications, New York, 1965)
- 142. V.G. Veselago, The electrodynamics of substances with simultaneously negative values of  $\varepsilon$  and  $\mu$ . Sov. Phys. Uspekhi **10**, 509–514 (1967)

- 143. J.B. Pendry, Negative refraction makes a perfect lens. Phys. Rev. Lett. 85, 3966 (2000)
- G. W'.t Hooft, Comment on negative refraction makes a perfect lens. Phys. Rev. Lett. 87, 249701 (2001)
- 145. J.B. Pendry, Reply. Phys. Rev. Lett. 87, 249702 (2001)
- 146. J.M. Williams, Some problems with negative refraction. Phys. Rev. Lett. 87, 249703 (2001)
- 147. J.B. Pendry, Reply. Phys. Rev. Lett. 87, 249704 (2001)
- P.M. Valanju, R.M. Walser, A.P. Valanju, Wave refraction in negative-index media: always positive and very inhomogeneous. Phys. Rev. Lett. 88, 187401 (2002)
- 149. R.W. Ziolkowski, E. Heyman, Wave propagation in media having negative permittivity and permeability. Phys. Rev. E **64**, 56625 (2001)
- N. Garcia, M. Nieto-Vesperinas, Left-handed materials do not make a perfect lens. Phys. Rev. Lett. 88, 207403 (2002)
- D. Maystre, S. Enoch, Perfect lenses made with left-handed materials: Alice's mirror? J. Opt. Soc. Am. A 21, 122–131 (2004)
- D. Maystre, S. Enoch, R.C. Mc Phedran, Why a harmonic solution for lossless, perfectly homogeneous, left-handed material cannot exist. J. Opt. Soc. Am. A 25, 1937–1943 (2008)
- G.W. Milton, N-A. P. Nicorovici and R.C. McPhedran, Optical and dielectric properties of partially resonant composites. Phys. Rev. B 49, 8479–8482 (1994)
- B. Gralak, A. Tip, Macroscopic Maxwell's equations and negative index materials. J. Math. Phys. 51, 052902 (2010)
- D.R. Smith, W.J. Padilla, D.C. Vier, S.C. Nemat-Nasser, S. Schultz, Composite medium with simultaneously negative permeability and permittivity. Phys. Rev. Lett. 84, 4184 (2000)
- R.A. Shelby, D.R. Smith, S. Schultz, Experimental verification of a negative index of refraction. Science 292, 77 (2001)
- 157. D.R. Smith, How to build a superlens. Science **308**, 502–503 (2005)
- B.-I. Popa, S.A. Cummer, Direct measurement of evanescent wave enhancement inside passive metamaterials. Phys. Rev. E 73, 016617 (2006)
- N. Fang, H. Lee, C. Sun, X. Zhang, Subdiffraction-limited optical imaging with a silver superlens. Science 308, 534–537 (2005)
- D.O. Melville, R.J. Blaikie, Super-resolution-limited diffraction imaging through a planar silver layer. Opt. Express 13, 2127–2134 (2005)
- T. Taubner, D. Korobkin, Y. Urzhumov, G. Shvets, R. Hillenbrand, Near-field microscopy through a SiC superlens. Science 313, 1595 (2006)
- S.A. Ramakrishna, J.B. Pendry, M.C.K. Wiltshire, W.J. Stewart, Imaging the near field. J. Mod. Opt. 50, 1419–1430 (2003)
- 163. P.A. Belov, H. Yang, Subwavelength imaging at optical frequencies using a transmission device formed by a period layered metal-dielectric structure operating in the canalization regime. Phys. Rev. B **73**, 113110 (2006)
- 164. H. Shin, S.H. Fan, All-angle negative refraction and evanescent wave amplification using one-dimensional metallodielectric photonic crystals. Appl. Phys. Lett. 89, 151102 (2006)
- 165. M. Scalora, G. D'Aguanno, N. Mattiucci, M.J. Bloemer, D. de Ceglia, M. Centini, A. Mandatori, C. Sibilia, N. Akozbek, M.G. Cappeddu, M. Fowler, J.W. Haus, Negative refraction and sub-wavelength focusing in the visible range using transparent metallo-dielectric stacks. Opt. Express 15, 508–523 (2007)
- 166. J. Zhang, H. Jiang, B. Gralak, S. Enoch, G. Tayeb, M. Lequime, Towards -1 effective index with one-dimensional metal-dielectric metamaterial: a quantitative analysis of the role of absorption losses. Opt. Express 15, 7720–7729 (2007)
- N. Grigorenko, A.K. Geim, H.F. Gleeson, Y. Zhang, A.A. Firsov, I.Y. Krushchev, J. Petrovic, Nanofabricated media with negative permeability at visible frequencies. Nature 438, 335–338 (2005)
- 168. V.M. Shalaev, W. Cai, U.K. Chettiar, H.-K. Yuan, A.K. Sarychev, V.P. Drashev, A.V. Kildishev, Negative index of refraction in optical metamaterials. Opt. Lett. **30**, 3356–3358 (2005)
- W. Cai, V. Shalaev, Optical Metamaterials: Fundamentals and Applications (Springer, Berlin, 2009)

 J. Aizpurua, A. Rivacoba, N. Zabala, F.J. García de Abajo, Collective excitations in an infinite set of aligned spheres. Surf. Sci. 402–404, 418–423 (1998)

- 171. J. Aizpurua, P. Hanarp, D.S. Sutherland, M. Käll, G.W. Bryant, F.J. García de Abajo, Optical properties of gold nanorings. Phys. Rev. Lett. **90**, 057401 (2003)
- J. Aizpurua, G.W. Bryant, L.J. Richter, F.J. García de Abajo, B.K. Kelly, T. Mallouk, Optical properties of coupled metallic nanorods for field-enhanced spectroscopy. Phys. Rev. B 71, 235420 (2005)
- 173. I. Romero, J. Aizpurua, G.W. Bryant, F.J. García De Abajo, Plasmons in nearly touching metallic nanoparticles: singular response in the limit of touching dimmers, Opt. Express 14, 9988–9999 (2006)
- A.V. Kabashin, P. Evans, S. Pastkovsky, W. Hendren, G.A. Wurtz, R. Atkinson, R. Pollard,
   V.A. Podolskiy, A.V. Zayats, Plasmonic nanorod metamaterials for biosensing. Nat. Mater. 8, 867–871 (2009)
- 175. E.H. Synge, A suggested method for extending microscopy resolution into the ultramicroscopic region. Phil. Mag. 6, 356–362 (1928)
- 176. E.A. Ash, G. Nichols, Super-resolution aperture scanning microscope. Nature **237**, 510–516 (1972)
- 177. D.W. Pohl, W. Denk, M. Lanz, Optical stethoscopy-image recording with resolution  $\lambda/20$ . Appl. Phys. Lett. **44**, 651–653 (1984)
- 178. D.W. Pohl, W. Denk, U. Durig, Optical stethoscopy: imaging with λ/20, in Micron and submicron integrated integrated circuit metrology, in *Proceedings of the SPIE*, vol. 565, 1985, ed. by K.M. Monahan, pp. 56–61
- U. Durig, D.W. Pohl, F. Rohner, Near-field optical scanning microscopy. J. Appl. Phys. 59, 3318–3327 (1986)
- A. Lewis, M. Isaacson, A. Harootunian, A. Murray, Development of a 500-A spatial-resolution light-microscope.
   Light is efficiently transmitted through gamma-16 diameter apertures. Ultramicroscopy 13, 227–231 (1984)
- R. Bachelot, P. Gleyzes, A.C. Boccara, Near-field optical microscope based on local perturbation of a diffraction spot. Opt. Lett. 20, 1924–1926 (1995)
- 182. R. Bachelot, F. H'Dhili, D. Barchiesi, G. Lerondel, R. Fikri, P. Royer, N. Landraud, J. Peretti, F. Chaput, G. Lampel, G.P. Boilot, K. Lahli, Apertureless near-field optical microscopy: a study of the local tip enhancement using photosensitive azo-benzene containing films. J. Appl. Phys. 94, 2060–2072 (2003)
- A. Bouhelier, M.R. Beversluis, L. Novotny, Near-field scattering of longitudinal fields. Appl. Phys. Lett. 82, 4596–4598 (2003)
- 184. Y. Gilbert, R. Bachelot, A. Vial, G. Lerondel, P. Royer, A. Bouhelier, G. Wiederrecht, Photoresponsive polymers for topographic simulation of the optical near-field of a nanometer sized gold tip in a highly focused laser beam. Opt. Express 13, 3619–3624 (2005)
- G. Lévêque, R. Quidant, Channeling light along a chain of near-field coupled gold nanoparticles near a metallic film. Opt. Express 16, 22029–22038 (2008)
- 186. D.W. Pohl, D. Courjon (eds.), *Near Field Optics* (Kluwer, Dordrecht, 1992)
- D. Courjon, Near Field microscopy and Near Field Optics (Imperial College Press, London, 2003)
- J.P. Fillard, Near Field Optics and Nanoscopy (World Scientific Publishing Company, Singapore, 1996)
- M.A. Paesler, J.P. Moyer, Near Field Optics: Theory, Instrumentation and Applications (Wiley Interscience, New York, 1996)
- U.Ch. Fischer, Scanning near-field Optical Microscopy, in Scanning Probe Microscopy. Analytical Methods ed. by R. Wiesendanger (Springer, Berlin, 1998), pp. 161–210
- 191. M. Ohtsu, M. Hori, *Near Field Optics* (Kluwer Academic, New York, 1999)
- 192. L. Novotny, The history of near-field optics, in *Progress in Optics*, vol. 50, Chap. 5, ed. by E. Wolf (Elsevier, Amsterdam, 2007), pp. 137–184
- D. Richards, A.V. Zayats (eds.), Nano-Optics and Near-Field Optical Microscopy (Artech, Boston, 2008)

- M.P. Van Albada, A. Lagendijk, Observation of weak localization of light in a random médium. Phys. Rev. Lett. 55, 2692–2695 (1985)
- P.E. Wolf, G. Maret, Weak localization and coherent backscattering of photons in disordered media. Phys. Rev. Lett. 55, 2696–2699 (1985)
- Y.N. Barabanenkov, Y.A. Kravtsov, V.D. Ozrin, A.I. Saichev, Enhanced backscattering in optics. in *Progress in Optics*, vol. 29, ed. by E. Wolf (Elsevier, New York, 1991), pp. 65–197
- B.A. Van Tiggelen, A. Lagendijk, A. Tip, Problem of light diffusion in strongly scattering medium-comment. Phys. Rev. Lett. 71, 1284–1284 (1993)
- E.R. Mendez, K.A. O'Donnell, Observation of depolarization and backscattering enhancement in light scattering from gaussian random surfaces. Opt. Commun. 61, 91–95 (1987)
- A.A. Maradudin, E.R. Mendez, T. Michel, Backscattering effects in the elastic scattering of p-polarized light from a large amplitude random metallic grating. Opt. Lett. 14, 151–153 (1989)
- J.A. Sanchez-Gil, M. Nieto-Vesperinas, Light scattering from random rough dielectric surfaces. J. Opt. Soc. Am. A 8, 1270–1286 (1991)
- A. Ishimaru, J.S. Chen, P. Phu, K. Yoshitomi, Numerical, analytical, and experimental studies
  of scattering from very rough surfaces and backscattering enhancement. Waves Random
  Media 3, S91–S107 (1991)
- E. Jakeman, Enhanced backscattering through a deep random phase screen. J. Opt. Soc. Am. A 5, 1638–1648 (1988)
- D. Maystre, M. Saillard, Enhanced backscattering and blazing effect from gratings, quasigratings and randomly rough surfaces. Waves Random Media 4, 467–485 (1994)
- M. Saillard, D. Maystre, Scattering from metallic and dielectric rough surfaces. J. Opt. Soc. Am. A 7, 982–990 (1990)
- 205. M. Saillard, D. Maystre, Scattering from random rough surfaces. J. Opt. 19, 173–176 (1988)
- P.W. Anderson, Absence of diffusion in certain random lattices. Phys. Rev. 109, 1492–1505 (1958)
- N.F. Mott, E.A. Davis, Electronic Processes in Non Crystalline Materials, 2nd edn. (Clarendon, Oxford, 1979)
- S. John, Electromagnetic absorption in a disordered medium near a photon mobility edge. Phys. Rev. Lett. 53, 2169–2172 (1984)
- P.W. Anderson, The question of classical localization/ A theory of white paint. Phil. Mag. B 52, 505–509 (1985)
- 210. A.Z. Genack, Optical transmission in disordered media. Phys. Rev. Lett. 58, 2043–2046 (1987)
- 211. P. Sheng, B. White, Z.Q. Zhang, G. Papanicolaou, Wave localization and multiple scattering in randomly-layered media, in *Scattering and Localization of Classical Waves in Random Media*, ed. by P. Sheng (World Scientific, Singapore, 1990), pp. 563–619
- V.D. Freilikher, S.A. Gredeskul, Localization of waves in media with one-dimensional disorder, in *Progress in Optics*, vol. 30, ed. by E. Wolf (North-Holland, Amsterdam, 1992), pp. 137–203
- D. Maystre, M. Saillard, Localization of light by randomly rough surfaces: concept of localiton. J. Opt. Soc. Am. A 11, 680–690 (1994)
- M. Saillard, Random rough surfaces—numerical study of localized electromagnetic surface modes. Appl. Opt. 32, 3354–3361 (1993)
- A.R. McGurn, A.A. Maradudin, V. Celli, Localization effects in the scattering of light from a randomly rough grating. Phys. Rev. B 31, 4866–4871 (1985)

## Chapter 2 Theory of Wood's Anomalies

**Daniel Maystre** 

Abstract Discovered by Wood in 1902, grating anomalies have fascinated specialists of optics for more than one century. Long after the first interpretation given by Rayleigh, Fano has suggested that the origin of anomalies could be found in the excitation of surface waves. This chapter describes the quantitative phenomenological theory of Wood's anomalies developed in the 1970s, based on the interpretation given by Fano and on the macroscopic laws of electromagnetics. This theory leads to a formula giving the efficiency of gratings in the region of anomaly and predicts the phenomenon of total absorption of light by a grating.

#### 2.1 Introduction

In 1902, Wood, observing the spectrum of a continuous light source given by an optical metallic diffraction grating, noticed a surprising phenomenon: "I was astounded to find that under certain conditions, the drop from maximum illumination to minimum, a drop certainly of from 10 to 1, occurred within a range of wavelengths not greater than the distance between the sodium lines" [1]. Wood made a crucial remark: these lines were present only for p-polarized light, i.e. when the magnetic field is parallel to the grating grooves. However, he was unable to provide any interpretation to these phenomena and thus termed them "singular anomalies", concluding that this problem was "one of the most interesting that I have ever met with". Even though the notion of Surface Plasmon Polariton (SPP) appeared more than half a century afterwards, let us give back to Caesar what is Caesar's: Wood must be considered as the initiator of plasmonics.

D. Maystre (⋈)

Institut Fresnel, CNRS, Université d'Aix Marseille, Ecole Centrale Marseille, Avenue Escadrille Normandie-Niemen, Campus universitaire de Saint Jérôme, 13397 Marseille, France

e-mail: daniel.maystre@fresnel.fr

As it will be seen in the following, Wood's discovery immediately raised considerable attention and the fascination of many specialists of optics for the so-called Wood's anomalies never died. Rayleigh proposed the first explanation for the existence of the anomalies [2, 3]: an anomaly in a given spectrum occurs at a wavelength corresponding to the passing-off of a spectrum of higher order, in other words, at the wavelength for which a scattered wave emerges tangentially to the grating surface. The Rayleigh conjecture was considered as a valuable tool for the prediction of Wood's anomalies. Indeed, the famous grating formula:

$$\sin(\theta_n) = \sin(\theta) + n\lambda/d,\tag{2.1}$$

where  $\theta$  is the angle of incidence (measured anticlockwise from the normal to the grating),  $\theta_n$  is the angle of diffraction (measured clockwise),  $\lambda$  is the wavelength in vacuum (which can also be considered as the wavelength in the air) and d is the groove period, allows one to rigorously calculate the diffraction angle of any scattered order n from the grating period, the angle of incidence and the wavelength of light. The passing-off of the order n occurs when  $\sin(\theta_n) = \pm 1$  and thus, from Eq. (2.1), the wavelengths of a spectrum generating the passing-off of a diffracted order are given by:

$$n\lambda/d = -\sin(\theta) \pm 1, \quad n = \pm 1, \pm 2, \pm 3...$$
 (2.2)

Figure 2.1 shows the spectra obtained by Wood for some values of the angle of incidence.

Near-normal incidence ( $\theta = 4^{\circ}12'$ , top of the figure), a bright narrow line appeared in the yellow (about  $\lambda = 610 \, \mathrm{nm}$ ), while a larger dark line was observed in the green (near 520 nm). Decreasing the angle of incidence to 2°37′, these lines approached one another and for angles of incidence of 0°15′ and 0°5′, they came in contact. Finally, at normal incidence, the lines fused and a uniform illumination was observed. With an incidence on the other side of the normal, two lines separated again, corresponding to red and orange. These lines were extremely brilliant up to a certain wavelength where the intensity very suddenly dropped to values close to zero, this fall occurring within a range not greater than the distance between the sodium lines. The paper by Wood did not mention the characteristics of the grating (period, shape, metal) but subsequently, Wood communicated to Rayleigh the period, equal to 1,760 nm. Using Eq. (2.2), Rayleigh was able to check the validity of his conjecture. The calculation predicts that, for an angle of incidence of 4°12′, the anomalies should arise at wavelengths 543.7 nm (n = +3 in Eq. (2.2) with sign +) and 629.6 nm (n = -3 in Eq.(2.2) with sign -). The discrepancy of about 5% with the real location of anomalies in Fig. 2.1 (517 and 609 nm) seems hardly good enough. Rayleigh expressed the hypothesis that this mismatch was the consequence of an imprecise knowledge of the grating period and for 30 years, the Rayleigh conjecture remained unquestioned. The present chapter is devoted to the theory of Wood's anomalies and it is not our purpose to mention all the experimental contributions to this phenomenon. The interested reader can find a survey of these contributions in Chap. 1. However,

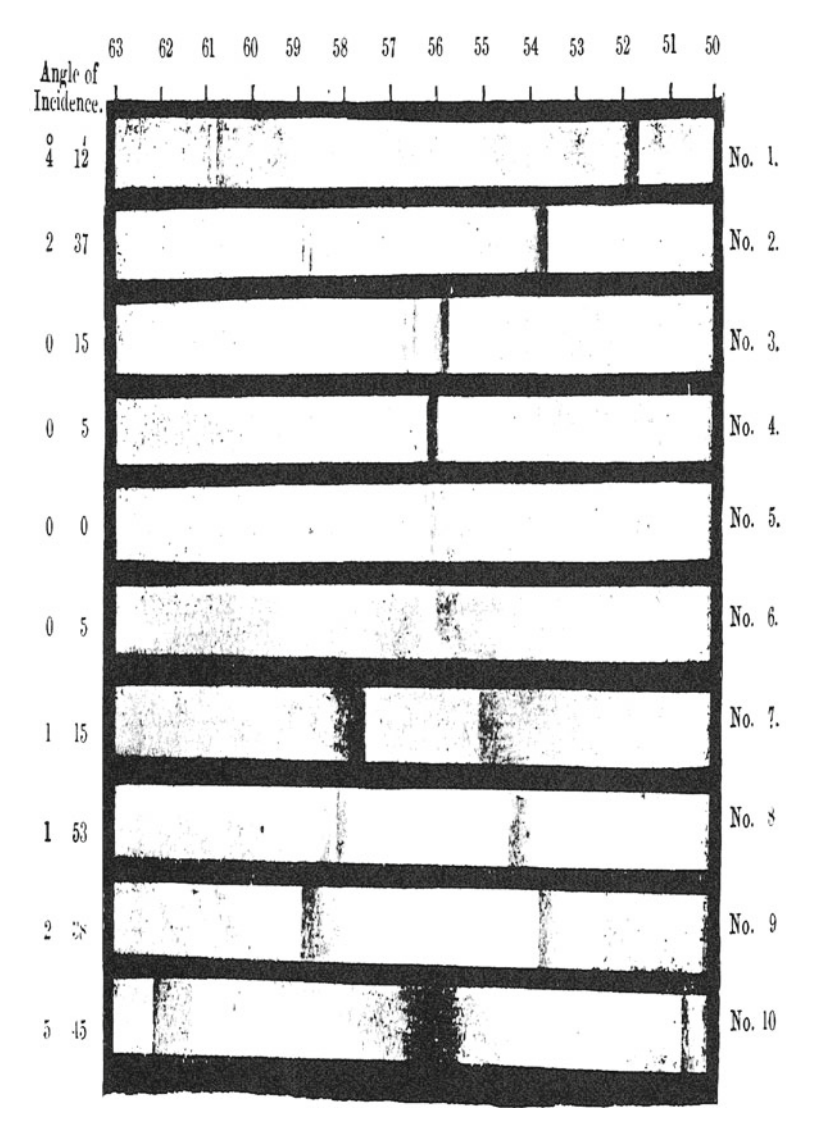


**Fig. 2.1** Spectra of a continuous light source obtained by Wood. The wavelength in nanometers is obtained by multiplying by a factor 10 the numbers shown at the top of the figure. The angles of incidence are, from the *top* to the *bottom*:  $4^{\circ}12'$ ,  $2^{\circ}37'$ ,  $0^{\circ}15'$ ,  $0^{\circ}5'$ ,  $0^{\circ}$ ,  $-1^{\circ}15'$ ,  $-1^{\circ}53'$ ,  $-2^{\circ}38'$  and  $-5^{\circ}45'$ . Reprinted by permission from Taylor & Francis Ltd (http://www.informaworld.com): [1] p. 397

at least one contribution must be cited here since it demonstrated that the Rayleigh prediction is unable to explain some vital experimental results.

Strong [4] showed Wood's anomalies for various metallic gratings having the same period. The results implicitly evidenced the influence of the metal on the shape

of the anomalies and, much more important, on their location. Bearing in mind that the grating formula is purely geometrical and thus that the metal has no effect on the location of the passing-off, this result must be considered as the first reappraisal of the Rayleigh interpretation.

Some years later, Fano achieved the first theoretical breakthrough on Wood's anomalies [5]. Observing the published experimental data, Fano distinguished two kinds of anomalies:

- A sharp anomaly—that is, an edge of intensity—appears along the spectrum at sharply defined wavelengths governed by the grating formula using the Rayleigh conjecture.
- A diffuse anomaly extends for a wavelength interval from the first one (the edge) to the red (i.e. higher wavelengths) and "consists generally of a minimum and a maximum of intensity (one dark band and one bright band)".

So, Fano explained the discrepancy between the theoretical predictions by Rayleigh and the experimental data provided by Wood: the Rayleigh conjecture predicts the location of the sharp anomaly, while obviously the anomaly observed by Wood was the diffuse anomaly. Fano explained the diffuse anomaly by "a forced resonance" related to the "leaky waves supportable by the grating". In the following, we will denote by "Rayleigh anomaly" the sharp anomaly at the passing-off of a spectrum of higher order. We will see in the following that the remarkable analysis by Fano must be considered as the starting point of the modern explanation of Wood's anomalies, even though the connection between the leaky waves mentioned by Fano and SPPs was not stated in the paper. Hessel and Oliner were led to the same conclusions as those stated by Fano [6]. In addition, these two authors used numerical tools in order to calculate the location and shape of the anomalies. Unfortunately, the model used by Hessel and Oliner was based on the knowledge a priori of the electromagnetic impedance (ratio of the tangential components of the electric/magnetic fields) on a straight line located above the grating grooves. Nevertheless, they were able to explain some properties experimentally known, such as the possibility of anomalies for p-polarized light with very deep gratings [7, 8], or the reluctance of anomalies to merge [9].

The modern analysis of Wood's anomalies began at the end of the 1960s and at the beginning of 1970s thanks to two revolutions, which drastically changed the experimental and theoretical tools in the study of gratings. The use of laser sources and photoresist layers permitted the invention and the production of holographic gratings for scientific and industrial purpose [10]. For the first time, the holographic technology provided a rapid and accurate tool for constructing gratings with submicronic periods. At the same time, the opportunity of using the first powerful computers encouraged theoreticians to develop rigorous vector theories of gratings and to implement them on computers. These new and powerful tools allowed for the first time wide numerical studies of Wood's anomalies and led to the first successful quantitative comparisons between experimental data and numerical calculations. As a consequence, the conditions were fulfilled for developing phenomenological

theories of Wood's anomalies and for checking their predictions with numerical and experimental data.

The first rigorous vector theory of gratings able to predict with precision the properties of relief metallic gratings for any shape of the profile in any range of wavelength was achieved by Maystre in 1972 [11, 12]. This theory can be classified as an integral theory since it reduces the problem of scattering by a grating to the solution of an integral equation. It is amazing to notice that, at that time, this new theory was intended to provide a realistic tool for the optimization of metallic gratings embarked in satellites for spectroscopy in the ultraviolet region, where the conductivity of metals falls down. Indeed, it was considered that the grating problem was already solved in the visible and near-infrared regions, using the theory of perfectly conducting gratings [13–17]. It was accepted that the metal can be replaced by a perfectly conducting (impenetrable) material, the efficiencies in the various orders computed using this hypothesis being finally multiplied by the reflectivity of the metal. At first glance, this approximation seems to be justified as the reflectivity of metallic planes of aluminium, silver or gold in these regions exceeds 90% in general. Nevertheless, the new theory was applied to metallic gratings in the visible and near-infrared regions, in order to confirm the hypothesis of perfectly conductivity of metallic gratings in these regions.

As expected, for s-polarized light, the numerical results confirmed the usual hypothesis: the intensities scattered in the various orders can be deduced from those obtained assuming a perfect conductivity of the metals through a simple multiplication factor close to the reflectivity of the plane metallic surface. On the other hand, for p-polarized light, the first results were quite surprising since strong discrepancies appeared. As a consequence of this unexpected result, a crucial conclusion must be stated: for natural light where the intensities take the average value between both fundamental polarizations, the perfect conductivity model for gratings fails. This result was presented in 1972 by Petit et al. in a communication at the International Congress of Optics (I.C.O. IX, Santa Monica, Ca) [18]. Surprisingly for the authors, serious doubts about the validity of this result were expressed by attendants in this Congress. The criticisms were based on two remarks: is the new theory valid? Is the numerical implementation accurate? It must be recognized that these criticisms were justified: numerical tests (energy balance, reciprocity theorem [19, 20]) are not sufficient for checking the validity of the numerical results deduced from a new theory. Above all, the validity of this theory must be checked by successful comparisons of the numerical results with the experimental data.

The reader can find in Chap. 1 a detailed description of the first successful comparison between the experimental results published by Hutley and the calculations performed by Maystre and McPhedran [21] using the new integral theory and the profile of the holographic grating measured by Hutley. The agreement between the experimental and numerical results for both polarizations was all the more remarkable since on similar experimental data published by Hutley, the theory of perfectly conducting gratings previously used by McPhedran and Waterworth led to significant discrepancies for p-polarized light [22–24].

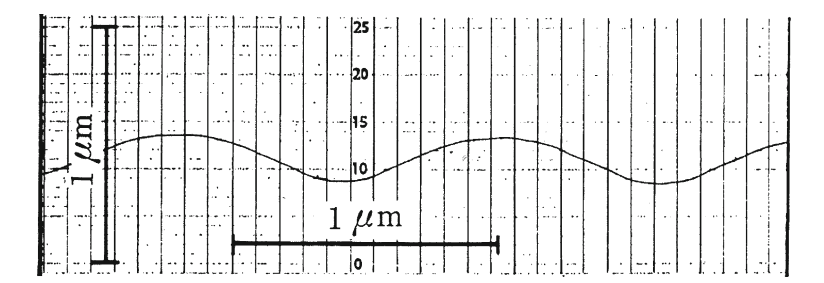


**Fig. 2.2** Profile of a metallic holographic grating with period 1,210 nm made by Hutley, measured using a mechanical profilometer. Notice the nearly sinusoidal shape. Reprinted by permission from Taylor & Francis Ltd (http://www.informaworld.com): [24] pp. 772–776

This first successful comparison between experimental and numerical results for metallic gratings in the visible region was followed by many others, using the same integral theory [25–27] or another rigorous grating theory, the differential theory of gratings [28], in such a way that the theoretical warning stated in 1972 about the non-validity of the perfect conductivity model has been fully confirmed, at least for wavelengths smaller than 10  $\mu$ m.

Figure 2.2 shows the profile of one of the holographic gratings made by Hutley and Fig. 2.3 gives the experimental and theoretical efficiencies of the order -1 and of the total efficiency (sum of all the scattered efficiencies) for one of these gratings, covered with three different metals [27]. For all the three metals, significant absorption peaks can be observed. Two of the three energy curves at a wavelength of 476 nm (silver and aluminium) are rather similar in form, with the third (gold at 476 nm) having greatly broadened absorption regions. It must be noticed that Fig. 2.3 constitutes another indicator as to the accuracy of infinite conductivity model for metals in the visible region. In regions where the energy absorption by gratings can be of the order of 50%, models, which cannot take this absorption into account, must be suspect.

The existence of powerful computer codes that are able to predict with a relative precision better than 1% the grating efficiencies in the visible and near-infrared regions has permitted wide numerical studies of Wood's anomalies. However, numerical results do not provide simple rules or formulae that are able to predict the shape and position of the anomalies in a quantitative manner. The specialist of optics likes to understand the physical origin of the observed phenomena and to use simple rules in order to select the best grating for a given application. As a consequence, attempts were made at developing a quantitative phenomenological theory [29, 30]. The following sections give a detailed description of this theory. It starts from the basic origin of Wood's anomalies, the excitation of SPPs and then uses the theory of analytic functions of the complex variable to express the efficiency of the grating in the region of anomaly in a simple form using two complex parameters only. It will be shown that this phenomenological formula provides a remarkable precision on the efficiencies. Moreover, this formula will show that an incident wave can be absorbed by a grating in totality, due to the excitation of a SPP.

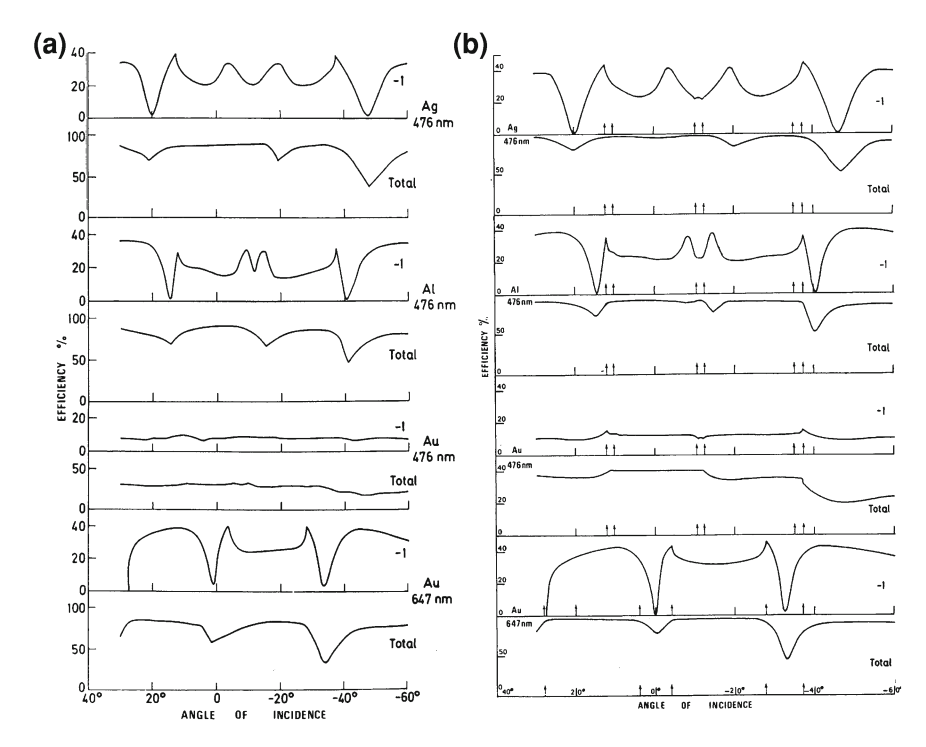


Fig. 2.3 Efficiency curves for the order -1 and total energy curves for three holographic gratings experimental measurements with period 1,210 nm and height 190 nm covered with three different metals illuminated by p-polarized laser beams. a Experimental measurements by Hutley and Bird; b results obtained from the new integral theory. a is reprinted by permission from Taylor & Francis Ltd (http://www.informaworld.com): [24] pp. 772–776

The theory of Wood's anomalies described in this chapter is based on electromagnetics. In other words, it starts from the macroscopic properties of metals through electromagnetic parameters like permittivity and permeability and never takes into account their microscopic structure. On the other hand, a group working in the Oak Ridge National Laboratory, which was at the origin of the discovery of SPPs [31], tried to investigate the properties of SPPs using the microscopic laws of solid-state physics. Such a study has an advantage on macroscopic studies: it starts directly from the basic origin of SPPs, i.e. a collective electron resonance. Unfortunately, the complexity of the problem led the authors to use a perturbation treatment, in which the anomaly is studied in terms of an interaction between the incoming photon and the collective electron resonance. This analysis was not able to accurately describe the phenomenon, especially for deep gratings, except by tuning the optical constants of metal to fit the measured data [32–34].

One can find an impressive amount of experimental measurements on phase velocity and damping of SPPs on metallic gratings in the studies published by Raether, Pockrand, Kröger and Kretschmann. These authors illuminated the grating from

the bulk side through a prism, a device named "total attenuated reflection" by these authors. They compared their experimental measurements with an approximate electromagnetic theory [35–43].

# 2.2 Propagation of Surface Plasmon Polaritons on a Metallic Surface

## 2.2.1 Case of the Flat Surface

## Problem of Scattering by a Flat Surface

In a problem of scattering, an object is illuminated by an incident electromagnetic wave and one wants to determine the total field at any point of space. This total field contains not only the incident field, which is known, but also the scattered field which has been generated by the object, which is unknown. We present in Fig. 2.4 the problem of scattering by a flat metallic surface, in which the scattering object is a metallic half-plane.

An incident plane wave propagating in a lossless dielectric material of optical index  $\nu_1 = \sqrt{\varepsilon_1}$  (with  $\varepsilon_1$  relative permittivity) illuminates a non-magnetic metallic half-plane of complex index  $\nu_2 = \sqrt{\varepsilon_2}$ . The problem of scattering is solved as soon as we know the amplitudes of the reflected and transmitted waves. Indeed, using the complex notation with a time dependence  $\exp{(-i\omega t)}$ , an incident field  $\mathbf{F^i}$  with unit amplitude can be written in the form:

$$\mathbf{F}^{\mathbf{i}} = F^{i} \hat{\mathbf{z}} = \exp\left(ik_{1} \left(\alpha x - \beta y\right)\right) \hat{\mathbf{z}},\tag{2.3}$$

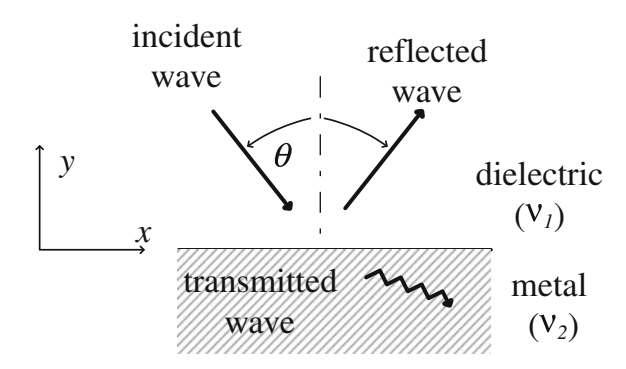
with  $\hat{\mathbf{z}}$  being the unit vector of the z-axis (orthogonal to the xy plane),  $k_1 = k\nu_1 = \frac{2\pi\nu_1}{\lambda}$  wavenumber in the dielectric material (k and  $\lambda$  being, respectively, the wavenumber and the wavelength of light in vacuum), and (see Appendix 1):

$$F^{i} = \begin{cases} \text{incident electric field } E^{i} \text{ for s-polarized light,} \\ \text{incident magnetic field } H^{i} \text{ for p-polarized light,} \end{cases}$$
 (2.4)

$$\alpha = \sin(\theta), \quad \beta = \cos(\theta),$$
 (2.5)

with  $\theta$  being the angle of incidence measured clockwise from the normal to the plane,  $\alpha$  and  $\beta$  being called normalized propagation constants of the wave in the following. It can be easily shown by using Helmholtz equations in both regions and boundary conditions on the interface (Eqs. (2.77) and (2.78)) that the projections on the z-axis of the reflected and transmitted fields  $F^r$  and  $F^t$  can be written as

**Fig. 2.4** The problem of scattering by a flat metallic plane



$$F^{r} = r \exp\left(ik_{1}\left(\alpha x + i\beta y\right)\right),\tag{2.6}$$

$$F^{t} = t \exp(ik_{1}(\alpha x - i\gamma y)), \qquad (2.7)$$

$$\gamma = \sqrt{\nu^2 - \alpha^2}$$
,  $\nu = \nu_2/\nu_1$  relative index of metal. (2.8)

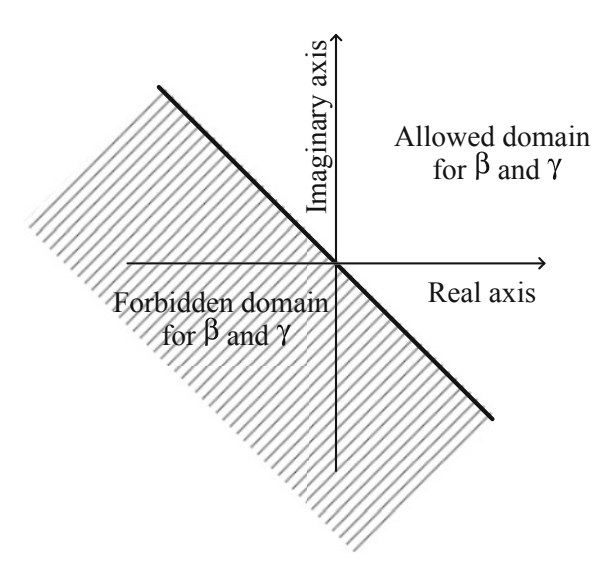
It must be noticed that the relative index  $\nu$  being complex, the definition of  $\gamma$ is ambiguous. In order to choose the determination of  $\gamma$  for complex values of  $\nu$ , let us put forth two remarks. First, if the metal is replaced by a lossless dielectric material, the choice of the determination of  $\gamma$  is quite clear. Indeed, the transmitted wave expressed in Eq. (2.7) must propagate downwards in order to satisfy a radiation condition, thus the real value of  $\gamma$  must be positive. Secondly, let us now assume that  $\nu$  is purely imaginary, thus  $\nu = i\nu''$ . It should be noticed that this assumption is not far from the actual values of indices of metals in the visible region (for example, the index of aluminium at 647 nm is equal to 1.3+i7.1). From this assumption, the value of  $\gamma$  is given by  $\gamma = \sqrt{-\nu''^2 - \alpha^2} = \pm i\sqrt{\nu''^2 + \alpha^2}$  and the choice of determination is quite clear: since the field must decrease in modulus as  $y \to -\infty$ , the imaginary part must be positive. Thus, in order to adopt a determination of  $\gamma$  which applies to any material, the authorized region of the complex plane of  $\gamma$  must include both half-lines defined by Im  $(\gamma) = 0$ , Re  $(\gamma) > 0$  and Re  $(\gamma) = 0$ , Im  $(\gamma) > 0$ . In real life, the index of metals is neither real nor purely imaginary, but its real and imaginary parts are always positive. Thus, a natural way to adopt a general determination for  $\gamma$ is to choose in the complex plane a half-plane containing both the positive real axis (choice of  $\nu$  for a lossless dielectric material) and the positive imaginary axis (choice of  $\nu$  for a purely imaginary index). In the following, we will determine  $\gamma$  from:

$$\operatorname{Re}\left\{\gamma\right\} + \operatorname{Im}\left\{\gamma\right\} > 0,\tag{2.9}$$

or in other words by choosing the value of  $\gamma$  in the half-plane located above the second bisector. Figure 2.5 shows the location of this half-plane in the complex plane.

From Eqs. (2.77) and (2.78), one obtains, using the expressions of the field given by Eqs. (2.3), (2.6), and (2.7):

**Fig. 2.5** Determination of  $\beta$  and  $\gamma$ 



$$1 + r = t$$
 for both polarizations, (2.10)

$$\beta(-1+r) = -\gamma t$$
 for s-polarized light, (2.11)

$$\frac{\beta}{\varepsilon_1}(-1+r) = -\frac{\gamma}{\varepsilon_2}t$$
 for p-polarized light. (2.12)

Solving the linear system of equations expressed in Eqs. (2.10) and (2.11) provides the Fresnel coefficients for s-polarized light:

$$r = \frac{\beta - \gamma}{\beta + \gamma}, \quad t = \frac{2\beta}{\beta + \gamma},$$
 (2.13)

and Eqs. (2.10) and (2.12) yield, for p-polarized light:

$$r = \frac{\beta/\varepsilon_1 - \gamma/\varepsilon_2}{\beta/\varepsilon_1 + \gamma/\varepsilon_2}, \quad t = \frac{2\beta/\varepsilon_1}{\beta/\varepsilon_1 + \gamma/\varepsilon_2}.$$
 (2.14)

These Fresnel coefficients allow one to solve the problem of scattering from a flat interface.

## Problem of Guiding by a Flat Surface: the SPP

Now, we consider a different, but closely related problem: the problem of guiding. The question is to know whether a surface wave can propagate at the surface of the metal. Of course, the answer to this question requires a precise definition of a

guided wave. Classically, a guided wave is a wave propagating along the *x*-axis and satisfying a radiation condition at infinity. In other words:

- if  $y \to +\infty$ , the field must propagate upwards or vanish,
- if  $y \to -\infty$ , the field must propagate downwards or vanish.

First, let us notice that the total field in the guided wave satisfies almost the same conditions as the total field in the scattering problem: it must satisfy Maxwell equations and boundary conditions on the interface. On the other hand, it must satisfy radiation conditions at infinity on both sides of the interface. These radiation conditions make a big difference with the total field in the problem of scattering: in the problem of scattering, the field above the interface contains the incident wave, which does not satisfy the radiation condition since it propagates towards the interface. In other words, a guided wave corresponds to a problem of scattering in which the incident field does not exist. At first glance, such a guided wave should not exist. Indeed, in the scattering problem, the incident energy is shared between the scattered field and the losses inside the metal. On the other hand, in the problem of guiding, there is no incident energy at all, and of course the existence of a field generates losses in the metal. Thus it seems that such a wave cannot satisfy the energy balance. This remark is quite correct as far as the propagation constant of the guided wave is real. If we consider the expressions of the reflected and transmitted waves in the problem of scattering (Eqs. (2.6) and (2.7)), the propagation constant  $k_1\alpha$  is real since it is imposed by the incident plane wave. This requirement does not hold in a problem of guiding and, from a heuristic point of view, it can be conjectured that a surface wave may propagate along the x-axis with an exponentially decreasing amplitude, due to the losses inside the metal. The consequence is that the imaginary part of  $k_1\alpha$  must be positive if its real part is positive.

In conclusion, the search for a surface wave leads to the search for a solution of the field in a scattering problem, but without any incident wave, or in other words, the so-called "homogeneous solution of Maxwell equations". We know that such a solution will have a complex (with positive imaginary part) propagation constant  $k_1\alpha$  along the x-axis. A priori, many possibilities exist according to whether  $\alpha$ , or  $k_1$ , or both have a non-null imaginary part. Here, we will consider that  $k_1$  is real and  $\alpha$  complex. This choice entails that the amplitude of the surface wave decreases in x, but that the frequency  $\omega = k_1/\sqrt{\varepsilon_1\mu_0}$  remains real. Other choices could be made. For example, introducing complex values for both  $\alpha$  (with positive imaginary part) and  $k_1$  (with negative imaginary part) leads, if their product  $k_1\alpha$  is real, to a constant amplitude along the x-axis, but an exponential decrease in  $\exp(-i\omega t)$  of this amplitude with time. The heuristic meaning of such a wave is clear: the losses in the metal generate a decrease in time of the amplitude.

The search for the solution of the guiding problem is straightforward from the Fresnel formulae. In order to cancel the incident wave, it suffices to find a pole of the reflection and transmission coefficients r and t in Eq. (2.13) for s-polarized light or in Eq. (2.14) for p-polarized light. For the s-polarized light, this pole is the root of the denominator of Eq. (2.13), i.e. the solution of  $\beta + \gamma = 0$ . However, since  $\alpha$  is complex, it is necessary to give a precise definition of the determinations of

 $\beta$  and  $\gamma$ . The determination of  $\gamma$  was given yet in Eq. (2.9) but now, the definition of  $\beta$  from the angle of incidence in the problem of scattering (Eq. (2.5)) does not hold. Since the field above the interface must satisfy the Helmholtz equation (Eq. (2.73)), we must impose that  $\alpha^2 + \beta^2 = 1$ , thus:

$$\beta = \sqrt{1 - \alpha^2}.\tag{2.15}$$

Moreover, the field above the interface must satisfy a radiation condition; it must propagate upwards or decrease in amplitude if  $y \to +\infty$ . Consequently, we are led to the same choice as that used for  $\gamma$  in Fig. 2.5, with

$$\text{Re}\{\beta\} + \text{Im}\{\beta\} > 0.$$
 (2.16)

Finally, the solution of the equation  $\beta + \gamma = 0$  requires that  $\beta^2 = \gamma^2$ , thus from Eqs. (2.8) and (2.15),  $\nu^2 = 1$ . The solution  $\nu = +1$  offers no interest since it means that the metal is replaced by the same dielectric material as above the interface. The solution  $\nu = -1$  is not realistic, at least for a non-magnetic material. The conclusion to be drawn from this result is that for s-polarized light, the propagation on a flat metal surface of a guided wave is impossible.

As regards p-polarized light, according to Eq. (2.14) we have to solve the equation:

$$\beta/\varepsilon_1 = -\gamma/\varepsilon_2. \tag{2.17}$$

Taking the root of both members yields, after simplifications:

$$\alpha = \tilde{\alpha}^{\text{plane}} = \pm \nu / \sqrt{1 + \nu^2},\tag{2.18}$$

which entails, according to Eqs. (2.8) and (2.15):

$$\tilde{\beta}^{\text{plane}} = -1/\sqrt{1+\nu^2}, \quad \tilde{\gamma}^{\text{plane}} = \nu^2/\sqrt{1+\nu^2}.$$
 (2.19)

In the symbol  $\tilde{\alpha}^{\text{plane}}$ , the hat "tilde" means that it concerns a guided wave, while the superscript "plane" indicates that the interface is a plane. It can be verified that the values of  $\tilde{\beta}^{\text{plane}}$  and  $\tilde{\gamma}^{\text{plane}}$  obey the determination expressed by Eqs. (2.16) and (2.9) for usual metals (Al, Au, Ag. . .) in the visible or infrared regions, as well as the initial equation (we must recall that we have taken the square of both members of Eq. (2.17) to find the solution), provided that the square root of an arbitrary complex number  $\rho \exp(i\phi)$ , with  $0 \le \phi < 2\pi$ ,  $\rho > 0$ , is, by definition, equal to  $\sqrt{\rho} \exp(i\phi/2)$ .

The two opposite values of  $\alpha$  given by Eq. (2.18) represent the constants of propagation of two waves propagating in opposite directions. This kind of wave is called SPP or sometimes surface plasmon or sometimes surface plasmon oscillation. This wave can be written in the normalized form:

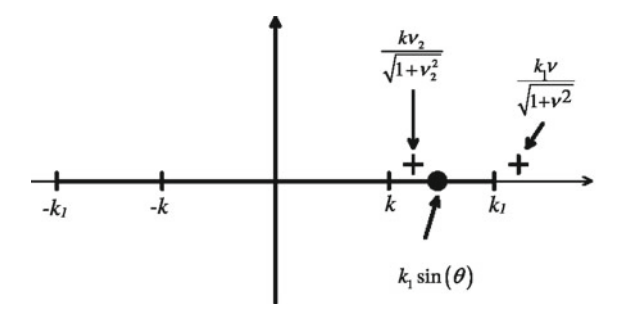


**Fig. 2.6** Constants of propagation along the *x*-axis of a plane wave  $(k_1 \sin(\theta))$ , of a SPP at the interface between a metal of index  $\nu_2$  and a dielectric of index  $\nu_1(k_1\nu/\sqrt{1+\nu^2}, \nu=\nu_2/\nu_1)$ , and of a SPP at the interface between a metal of index  $\nu_2$  and vacuum  $(k\nu_2/\sqrt{1+\nu^2})$ 

$$H = \begin{cases} \exp\left(ik_1\left(\tilde{\alpha}^{\text{plane}}x + \tilde{\beta}^{\text{plane}}y\right)\right) \text{ in the dielectric,} \\ \exp\left(ik_1\left(\tilde{\alpha}^{\text{plane}}x - \tilde{\gamma}^{\text{plane}}y\right)\right) \text{ in the metal.} \end{cases}$$
 (2.20)

For aluminium at 647 nm, the optical index  $\nu_2$  is equal to 1.3 + i7.1 and using fused silica as a dielectric material (index 1.45), the relative index  $\nu$  is equal to 0.89 + i4.9, then:

$$\tilde{\alpha}^{\text{plane}} = 1.019 + i \ 7.6 \ 10^{-3}.$$
 (2.21)

The real part of  $\tilde{\alpha}^{\text{plane}}$  is slightly greater than unity, while its imaginary part is very small. This is a general result for metals in the visible and infrared regions and it explains why SPPs cannot be excited by a plane wave. Indeed, as shown in Fig. 2.6, the propagation constant on the *x*-axis of a plane wave is equal to  $k_1 \sin{(\theta)}$  (circle), thus it is always smaller than  $k_1$  in modulus, in contrast with the real part of  $k_1 \tilde{\alpha}^{\text{plane}}$ . Since the surface is flat, a plane wave cannot excite a field having a significantly different propagation constant and then it cannot excite the SPP.

#### **SPP and Brewster Effect**

In this section, it is shown that the SPP propagating at a metal–dielectric interface may be deduced by continuity from the well-known phenomenon of total transmission of light between two dielectric materials (Brewster effect). Figure 2.7 shows the trajectory of  $\tilde{\alpha}^{\text{plane}} = \nu_2/\sqrt{1+\nu_2^2}$ , normalized propagation constant of the SPP on an air–metal interface, when the imaginary part of the optical index of the metal is varied from zero to infinity, the real part being equal to 1.3, i.e. that of aluminium at 647 nm.

The trajectory, which starts at  $\tilde{\alpha}^{\text{plane}} = 0$  for  $q = +\infty$  (perfectly conducting metal), reaches the point corresponding to aluminium for q = 7.1. Its imaginary part first increases as long as q remains greater than unity, then it decreases and for q = 0,

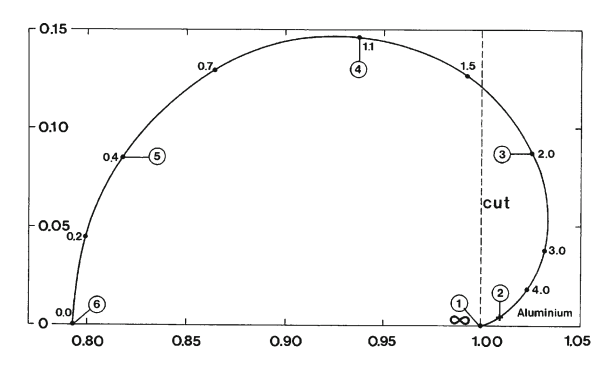


Fig. 2.7 Trajectory of  $\tilde{\alpha}^{\text{plane}} = \nu_2/\sqrt{1+\nu_2^2}$  in the complex plane when  $\nu_2 = 1.3+iq$ , q being varied from  $+\infty$  to 0. The *cross* (point 2) represents the value of  $\tilde{\alpha}^{\text{plane}}$  corresponding to the index of aluminium at  $\lambda = 647$  nm (q=7.1), points l and d correspond, respectively, to the cases of a perfectly conducting metal  $(q=+\infty)$  and a lossless dielectric (q=0). Reprinted by permission from Blackwell Publishing: [30]

 $\tilde{\alpha}^{plane}$  becomes real and equal to 0.793, while  $\tilde{\beta}^{plane}=-1/\sqrt{1+\nu_2^2}=-0.61$  and  $\tilde{\gamma}^{\text{plane}} = \nu_2^2 / \sqrt{1 + \nu_2^2} = 1.03$ . As a consequence, the plasmon waves propagating in air and in dielectric are homogeneous plane waves propagating downwards, according to Eq. (2.20). In conclusion, the wave propagating in air is incident and generates a transmitted wave in the lossless dielectric, without any reflection in the air. Obviously, this limit is nothing else than the field in the Brewster effect. Besides, it should be noticed that in that case, since the fields are represented by plane waves,  $\tilde{\alpha}^{\text{plane}} = \nu_2 / \sqrt{1 + \nu_2^2}$  is nothing else than  $\sin(\theta)$ , the sine of the angle of incidence, which entails that  $\tan(\theta) = \frac{\sin(\theta)}{\sqrt{1 - \sin(\theta)^2}} = \nu_2$ , which is the Brewster formula. At first glance, the strong link between SPP propagation and Brewster effect seems to be surprising. Indeed, by definition, a SPP is a homogeneous solution of Maxwell equations, i.e. a field scattered on both sides of the interface, without any incident wave. By contrast, in the Brewster effect, the field in the air is an incident wave. The explanation of this apparently paradoxical result is given in Fig. 2.8, where the corresponding trajectory of  $\tilde{\beta}^{\text{plane}}$  is represented. It is worth noting that this trajectory, which starts from 0 and ends at -0.61, crosses the second bisector of the complex plane (dashed line). Bearing in mind that a scattered wave is defined as a wave satisfying Eq. (2.16), it emerges that the plasmon wave in the air, which is a scattered wave in the air, continuously becomes an incident wave when the trajectory of  $\tilde{\beta}^{\text{plane}}$ crosses the second bisector.

In order to show the continuous evolution of the wave from the SPP of a perfectly conducting metal to the Brewster effect, we have expressed the field in air (top of Fig. 2.9) and in metal (bottom of Fig. 2.9) in the form  $H = \exp[ik(\mathbf{u_r} + i\mathbf{u_i}) \rho]$  with  $\rho = (x, y)$ . In a lossless dielectric material, the two vectors are orthogonal, a simple consequence of Maxwell equations. The first point corresponds to a perfectly

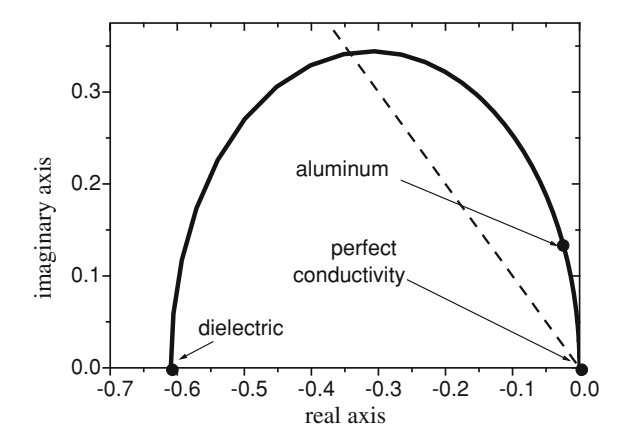


Fig. 2.8 Trajectory of  $\tilde{\beta}^{\text{plane}} = -1/\sqrt{1+\nu_2^2}$  in the complex plane when  $\nu_2 = 1.3 + iq$ , q being varied from 0 to  $+\infty$ . The *dashed line* shows the second bisector in the complex plane

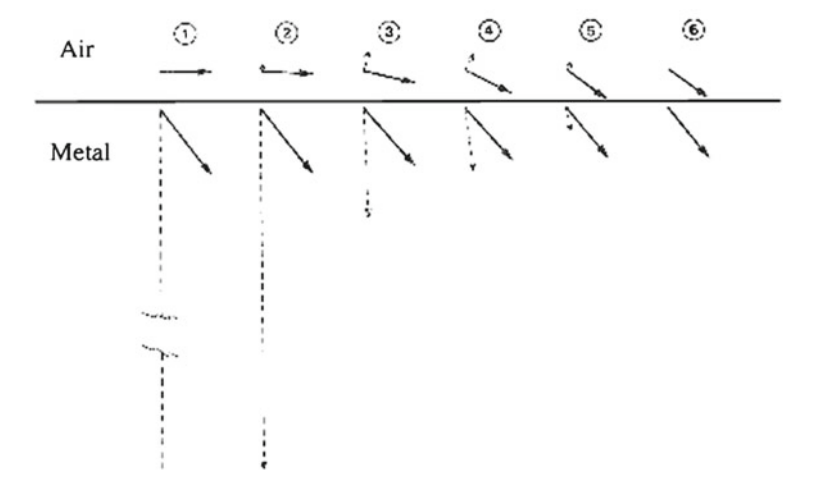


Fig. 2.9 Graph representation in air (top) and metal (bottom) of the normalized complex wavevectors  $\mathbf{u_r} + i\mathbf{u_i}$  corresponding to the six points of Fig. 2.7. The real part  $\mathbf{u_r}$  and the imaginary part  $\mathbf{u_i}$  are represented by *solid* and *dashed arrows*, respectively. The direction of propagation of the wave is given by  $\mathbf{u_r}$  while  $\mathbf{u_i}$  indicates the direction of maximum decrease. Reprinted by permission from Blackwell Publishing: [30]

conducting metal: the wave in air is a homogeneous plane wave propagating parallel to the interface, while in the metal  $\mathbf{u_i}$  is infinite, as it will be shown in the following. The evolution from point 1 to point 6 is essentially characterized in the metal by the decrease of  $\|\mathbf{u_i}\|$  and in the air by the transformation of the surface wave into an incident homogeneous plane wave.

#### **Excitation of a SPP**

The question which arises is to know how the SPP can be excited. It has been shown that it can be provoked by an electron beam on a metallic thin film [44]. Powell and Swan illuminated an aluminium thin film in normal incidence and observed peaks of absorption in the transmitted beam. One of these peaks was attributed to an excitation of a SPP. Clearly, the explanation of this phenomenon should be made in the frame of solid-state physics. However, electromagnetic theory can provide a heuristic interpretation of it. First, let us analyse the structure of the electric field, of the charges and of the currents of the SPP. From Eqs. (2.63) and (2.68) of Appendix 1,

in the metal, 
$$\mathbf{j_t} = i\omega\varepsilon_0 (1 - \varepsilon_2) \mathbf{E}$$
, (2.22)

in the dielectric, 
$$\mathbf{j_t} = i\omega\varepsilon_0 (1 - \varepsilon_1) \mathbf{E}$$
, (2.23)

where  $\mathbf{j_t}$  denotes the total current density, which includes both conduction current and the bound current inside the metal. The charge balance can be written in harmonic regime as:

$$\nabla \cdot \mathbf{j_t} = i\omega \rho_t, \tag{2.24}$$

with  $\rho_t$  being the volume density of total charges (including both free and bound charges). In both dielectric and metal,  $\Delta \cdot \mathbf{E} = 0$ , and since  $\mathbf{j_t}$  depend linearly on  $\mathbf{E}$ ,  $\rho_t$  vanishes: charges are located on the surface but for simplicity we will retain the same symbol  $\rho_t$  to denote the surface charge density (mathematically,  $\rho_t$  is the coefficient of a delta distribution located on the surface). Finally, the volume current density and the surface charge density can be derived from the electric field. Using Eq. (2.67), we deduce that:

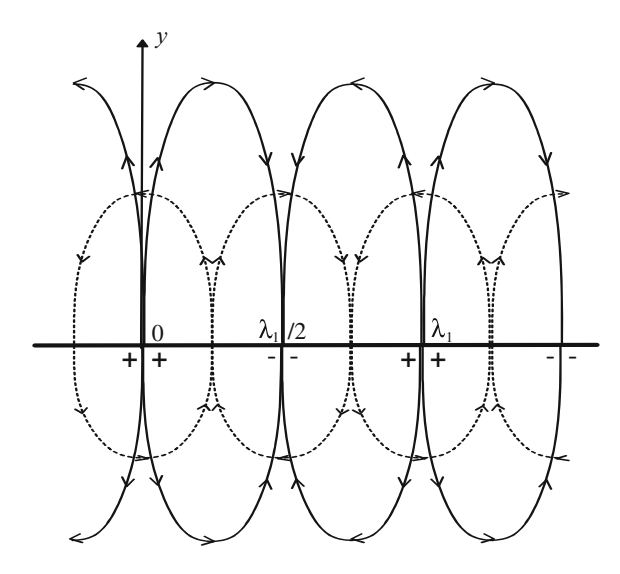
in the dielectric, 
$$\mathbf{E} = \frac{ik_1}{\omega\varepsilon_1\varepsilon_0} \nabla \times H\hat{\mathbf{z}} = \frac{k_1}{\omega\varepsilon_1\varepsilon_0} \left( -\beta\hat{\mathbf{x}} + \alpha\hat{\mathbf{y}} \right) \exp\left(ik_1\left(\alpha x + \beta y\right)\right)$$
, (2.25) in the metal,  $\mathbf{E} = \frac{ik_1}{\omega\varepsilon_2\varepsilon_0} \nabla \times H\hat{\mathbf{z}} = \frac{k_1}{\omega\varepsilon_2\varepsilon_0} \left( \gamma\hat{\mathbf{x}} + \alpha\hat{\mathbf{y}} \right) \exp\left(ik_1\left(\alpha x - \gamma y\right)\right)$ .

Equation (2.80) gives the total surface density of charges:

$$\rho_t = \varepsilon_0 \left( E_{y+} - E_{y-} \right) = \frac{\alpha k_1}{\omega} \left( \frac{1}{\varepsilon_1} - \frac{1}{\varepsilon_2} \right) \exp\left( i k_1 \alpha x \right). \tag{2.27}$$

In order to analyse the space distribution of the electric field, the volume current density and the surface charge density, we simplify the expressions of these quantities by assuming that  $\nu \simeq i\nu''$ , with  $\nu''$  real and  $\nu'' \gg 1$ ,  $\nu$ . Thus the relative index of metal is close to a purely imaginary number large in modulus, which is the case for the actual values of optical indices in the visible and near-infrared regions. From Eqs. (2.18) and (2.19), we find:

Fig. 2.10 The electric field and the total current density at t = 0 are represented by *solid* and *dashed lines*, respectively. The *signs* represent the total surface charge density



$$\varepsilon_2 \simeq -\nu''^2 \varepsilon_1$$
,  $\tilde{\alpha}^{\text{plane}} \simeq 1$ ,  $\tilde{\beta}^{\text{plane}} \simeq i/\nu''$ ,  $\tilde{\gamma}^{\text{plane}} \simeq i\nu''$ , (2.28)

and we can deduce that:

$$\rho_t \simeq \frac{k_1}{\omega \varepsilon_1} \left( 1 + \frac{1}{\nu''^2} \right) \exp\left(ik_1 x\right), \tag{2.29}$$

in the metal, 
$$\mathbf{E} \simeq \frac{-k_1}{\omega \nu'' \varepsilon_0} \left( i \hat{\mathbf{x}} + \frac{\hat{\mathbf{y}}}{\nu''} \right) \exp\left( i k_1 x \right) \exp\left( + k_1 \nu'' y \right),$$
 (2.30)

in the dielectric, 
$$\mathbf{E} \simeq \frac{-k_1}{\omega \nu'' \varepsilon_1 \varepsilon_0} \left( i \hat{\mathbf{x}} - \nu'' \hat{\mathbf{y}} \right) \exp\left( i k_1 x \right) \exp\left( -\frac{k_1}{\nu''} y \right)$$
. (2.31)

The volume current densities can be deduced from Eqs. (2.22), (2.23), (2.30) and (2.31).

Figure 2.10 shows the electric field lines (solid lines), the total current density (dashed lines) and the total surface charge density at t=0. Here, we abandon the use of complex amplitudes and the electric field is the real part of the product of its complex amplitude by  $\exp(-i\omega t)$ . It is worth noting from Eqs. (2.30) and (2.31) that the modulus of the fields decreases exponentially on both sides of the interface, the decrease being much larger in the metal than in the dielectric, while the phase remains constant in the range  $-\infty < y < +\infty$  as x is fixed. The electric field lines go from positive to negative surface charge densities. It can be noticed that the total volume current densities in the metal and in the air have opposite contributions to the total surface charge density, but the current density in the air is much smaller than that in the metal and can be neglected.

From Fig. 2.10, we can understand the mechanism of SPP propagation. Due to the current lines, charges are shifted from the region close to  $x = -\lambda_1/4$  (or  $x = 3\lambda_1/4$ ) towards the region close to  $x = +\lambda_1/4$  (or  $x = 5\lambda_1/4$ ). As a consequence, the charge in the vicinity of  $x = -\lambda_1/4$  (or  $x = 3\lambda_1/4$ ) becomes negative and that located around  $x = +\lambda_1/4$  (or  $x = 5\lambda_1/4$ ) becomes positive. The maximum charge density, located at the origin (or  $x = \lambda_1$ ), is shifted towards  $x = \lambda_1/4$  (or  $x = 5\lambda_1/4$ ), while the minimum charge density, located at  $x = -\lambda_1/2$  (or  $x = +\lambda_1/2$ ), is shifted to the right as well. As a consequence, the positive and negative charge densities propagate to the right, as well as the electric field and the volume charge density.

This result allows one to understand why an electron beam can excite a SPP. The electron beam creates local charges and electric fields on the metal surface, these charges and fields generate new charges and electric fields in the vicinity, and so on: as a result, SPPs propagate on both sides of the beam. Furthermore, Fig. 2.10 shows that the field penetrates more deeply in the dielectric than in the metal. More precisely, Eqs. (2.20) and (2.28) show that when the imaginary part of the index is increased, the attenuation of the field in the dielectric decreases, while that in the metal increases. At the limit, when this imaginary part goes to infinity (which corresponds to a perfect conductivity according to Eq. (2.65)), the attenuation does not exist anymore in the dielectric and the field does not penetrate at all in the metal. In that case,  $\alpha = 1$  and the field in the dielectric is given by:

$$H = \exp(ik_1x). \tag{2.32}$$

This field satisfies the Helmholtz equation and the boundary condition on the perfectly conducting metal since the electric field is parallel to the *y*-axis, thus its tangential component on the metal vanishes. On the other hand, such a field obviously cannot be classified as a surface wave. However, we will see that it becomes an actual surface wave as soon as the metal interface is corrugated, in such a way that it is not completely incorrect to claim that a SPP can propagate on a perfectly conducting metallic surface, even though in that case, the model of electron resonance and the name of SPP seem quite unrealistic.

Another way to excite a SPP on a flat metallic surface is to use a finite width of metal separating the dielectric material from vacuum (Fig. 2.11).

According to Eq. (2.18), and noticing that the relative index of metal with respect to vacuum is equal to  $\nu_2$ , the propagation constant  $k\tilde{\alpha}^{\text{plane}}$  at the metal-vacuum interface is given by:

$$k\tilde{\alpha}^{\text{plane}} = k\nu_2 / \sqrt{1 + \nu_2^2}, \qquad (2.33)$$

and in that case, for aluminium at 647 nm,

$$\tilde{\alpha}^{\text{plane}} = 1.009 + i \ 3.5 \ 10^{-3}.$$
 (2.34)

The real part of  $\tilde{\alpha}^{\text{plane}}$  is very close to unity, but  $k = k_1/\nu_1$  is smaller than  $k_1$ , in such a way that, if  $\nu_1$  if significantly greater than unity, the propagation constant

**Fig. 2.11** Excitation of a SPP at a metal–vacuum interface with a plane wave propagating in a dielectric

incident reflected

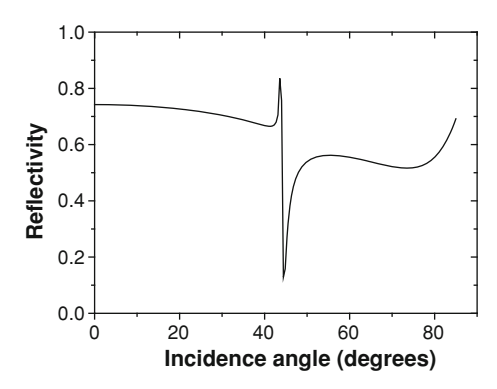
wave wave  $\theta$  dielectric  $(V_I)$  Wevanescent

wave

reflected

wave  $(V_I)$ 

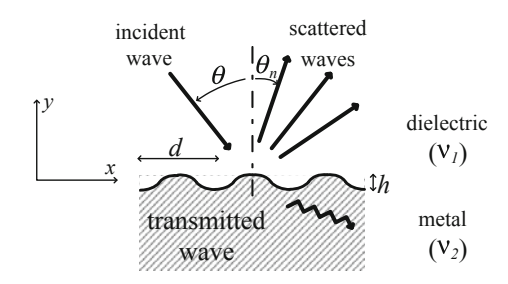
**Fig. 2.12** Reflectivity of the device depicted in Fig. 2.10



of the SPP becomes smaller than  $k_1$  and, provided that the width of metal is small (in practice, smaller than the skin depth) the SPP can be excited by a plane wave illuminating the thin film of metal from the dielectric side (Fig. 2.11). Let us give in Fig. 2.12 a numerical example of the consequences of this excitation using fused silica (index = 1.45) as a dielectric material and aluminium at 647 nm.

The reflectivity shows a resonance phenomenon at  $\theta=44.55^\circ$ . This incidence corresponds to a propagation constant of the incident field  $k_1 \sin{(\theta)} = k\nu_1 \sin{(\theta)} = 1.017k$ . Thus, assuming that the excitation occurs when the propagation constant of the incident field is equal to the real part of the propagation constant of the SPP, it turns out from Eq. (2.33) that Re  $\{\tilde{\alpha}^{\text{plane}}\}$  should be equal to 1.017, a value slightly different from the value of 1.009 given by Eq. (2.34). This discrepancy is not surprising. In our theoretical calculations, the propagation constant of the SPP has been calculated assuming an infinite width of metal, which is not the case in Fig. 2.11. It is worth noticing that the device shown in Fig. 2.11 is sometimes called "prism device" and has been widely used for both plane and modulated surfaces [35–43]. Indeed, if the light is generated by a light source located in vacuum, a plane air–dielectric interface parallel to the metal–dielectric interface (as in Fig. 2.11) cannot generate inside the

**Fig. 2.13** A metallic diffraction grating



dielectric a transmitted wave with propagation constant in x greater than k, which entails that the SPP at the metal–air interface (bottom of Fig. 2.11) cannot be excited.

Other possibilities to excite SPPs on a flat surface could be envisaged, but in fact, the most current way is to use a periodically modulated metal surface, i.e. a diffraction grating. The next section will be devoted to a detailed analysis of this possibility.

## 2.2.2 Case of the Diffraction Grating

#### **Scattering from a Diffraction Grating**

Figure 2.13 shows a metallic diffraction grating, i.e. a cylindrical periodic interface of period d and height h separating a metallic and a dielectric materials, invariant by translation with respect to the z-axis.

The grating is illuminated by a plane wave propagating in the xy plane at incidence  $\theta$ . Taking into account the results obtained for a flat interface, the study will be restricted to p-polarization, thus the incident magnetic field is parallel to the z-axis. In these conditions, it can be shown [29] from the elementary laws of electromagnetics and from theorems of existence and uniqueness of the solution of boundary-value problems that the total magnetic field  $\mathbf{H}(x, y) = H(x, y) \hat{\mathbf{z}}$  remains independent of z, parallel to the z-axis and that it is pseudo-periodic:

$$H(x+d, y) = H(x, y) \exp(ik_1\alpha d), \quad \alpha = \sin(\theta). \tag{2.35}$$

It follows from Eq. (2.35) that  $H(x, y) \exp(-ik_1\alpha x)$  is periodic. Expanding this function in Fourier series and introducing it in the Helmholtz equations (Eq. (2.72)), it can be easily shown that the magnetic field can be represented in the major part of space in the form of Rayleigh expansions [29, 45]. Denoting by  $y_{\text{max}}$  and  $y_{\text{min}}$  the ordinates of the top and of the bottom of the grooves, the Rayleigh expansions can be written:

if 
$$y > y_{\text{max}}$$
,  $H = \exp(ik_1\alpha x - ik_1\beta y) + \sum_{n=-\infty}^{+\infty} b_n \exp(ik_1\alpha_n x + ik_1\beta_n y)$ , (2.36)

if 
$$y < y_{\min}$$
,  $H = \sum_{n=-\infty}^{+\infty} c_n \exp(ik_1\alpha_n x - ik_1\gamma_n y)$ , (2.37)

$$\beta = \cos(\theta)$$
,  $\alpha_n = \alpha + n\lambda_1/d$ ,  $\beta_n = \sqrt{1 - \alpha_n^2}$ ,  $\gamma_n = \sqrt{\nu^2 - \alpha_n^2}$ , (2.38)

with  $b_n$  and  $c_n$  being complex coefficients called amplitudes of the plane waves scattered in the dielectric ( $y > y_{\text{max}}$ ) and in the metal ( $y < y_{\text{min}}$ ). The choice of the determination of the square roots contained in Eq. (2.38) will be the same as that given by Fig. 2.5 for  $\beta$  and  $\gamma$ . It is important to notice that in general, the Rayleigh expansions given above cannot represent the field inside the grooves. For example, the Rayleigh expansion given by Eq. (2.36) cannot in general represent the field in the region located between the interface and  $y = y_{\text{max}}$  [29, 45]. It must be remarked that the waves scattered in the dielectric region can be separated into two parts:

- a finite number of y-propagating waves corresponding to real values of  $\beta_n$ ,
- an infinite number of evanescent waves corresponding to imaginary values of  $\beta_n$ .

Whatever the value of  $\lambda/d$  may be, there exists at least one y-propagating wave, corresponding to n=0 (specularly reflected order).

Equations (2.36)–(2.38) permit us to understand why a plane wave illuminating the grating surface can excite a SPP. In contrast with a flat surface, a grating scatters waves having propagation constants in x equal to  $k_1\alpha_n = k_1\alpha + k_1n\lambda_1/d = k_1 (\alpha + 2\pi n/d)$ . Thus, the propagation constants of the scattered waves can take values outside the range  $(-k_1, +k_1)$  and the propagation constant of one of them can be close to the propagation constant in x of the SPP  $k_1\tilde{\alpha}^{\text{plane}} = k_1\nu/\sqrt{1+\nu^2}$  (see Eq. (2.18)). It can be predicted that the maximum excitation of the SPP occurs when one order  $n_e$  satisfies the equation:

$$\alpha_{n_e} = \pm \text{Re} \left\{ \tilde{\alpha}^{\text{plane}} \right\}. \tag{2.39}$$

Since Re  $\{\tilde{\alpha}^{\text{plane}}\}$  is slightly greater than unity in modulus, the order  $n_e$  must be evanescent, but close to the passing-off. It is worth noting that Eq. (2.39) assumes that the propagation constant of the SPP on a grating is equal to that on a flat surface. We will see that this is not correct and thus this equation must be considered as an approximation. Let us illustrate the excitation of SPPs on the example given at the bottom of Fig. 2.14, which shows the order -1 and total efficiencies of a holographic silver grating with a period of 1,205 nm illuminated by a p-polarized plane wave at a wavelength of 521 nm [21].

The use of Eq. (2.39) allows one to predict that a SPP is excited when

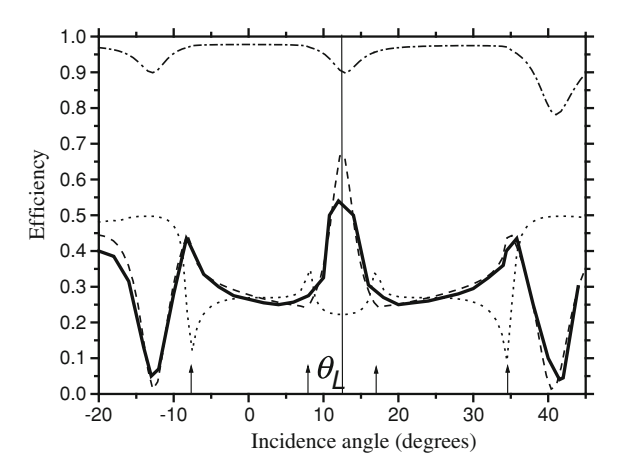


Fig. 2.14 Comparison between experimental data on a holographic silver grating (by courtesy of Hutley) and theoretical results for p-polarized light. The passing-off incidences are shown by *arrows* and the Littrow (Bragg) position by a *vertical line*. Solid line experimental data, dashed line theoretical results for the efficiency in the order -1 of a silver grating, dashed-dotted line theoretical results for the sum of efficiencies of scattered orders, dotted line theoretical results for the efficiency in the order -1 of a perfectly conducting grating

$$\alpha_{n_e} = \sin(\theta) + n_e \lambda_1 / d = \pm \text{Re} \left\{ \tilde{\alpha}^{\text{plane}} \right\},$$
(2.40)

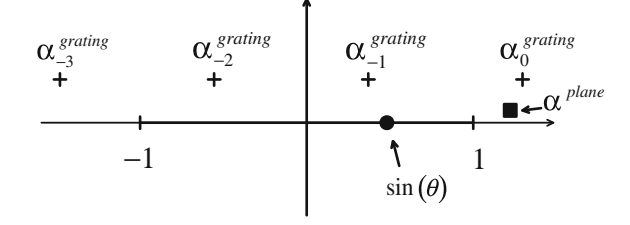
which reduces, after tedious calculations, to  $\sin(|\theta|) = |\text{Re}\left\{\tilde{\alpha}^{\text{plane}}\right\} - |n_e| \lambda_1/d|$ ,  $|\sin(\theta)| < 1$ . In that case, the index of silver is  $\nu_2 = \nu = 0.052 + i3.05$  and thus  $\tilde{\alpha}^{\text{plane}} = 1.06 + i2.2 \times 10^{-3}$ . Consequently, the solutions are given by  $|\theta| = 39^{\circ}$  for  $|n_e| = 1$ ,  $|\theta| = 11^{\circ}$  for  $|n_e| = 2$ ,  $|\theta| = 14^{\circ}$  for  $|n_e| = 3$ ,  $|\theta| = 42^{\circ}$  for  $|n_e| = 4$ . If we consider the bottoms of the drops of total efficiency caused by absorption in Fig. 2.14, we notice that the anomalies predicted for  $|\theta| = 39^{\circ}$  and  $|\theta| = 42^{\circ}$  cannot be separated, as well as those predicted for  $|\theta| = 11^{\circ}$  and  $|\theta| = 14^{\circ}$ , the values measured in Fig. 2.14 being  $\theta = \pm 14^{\circ}$  and  $\theta = 42^{\circ}$ , which are close to the values predicted by theory in the range of incidence  $(-20^{\circ}, 43^{\circ})$  represented in the figure.

Let us notice finally that a significant amount of energy (more than  $20\,\%$ ) can be absorbed in the anomalous regions in Fig. 2.14. The interpretation of the absorption phenomena is obvious: due to the resonant excitation of SPPs , the field inside the metal presents local enhancements which generate strong Joule effects. A study of absorption caused by SPPs can be found in [46].

#### SPP on a Grating

The study of SPPs on a grating can be achieved using the same lines as in the case of a flat surface. A SPP is a solution of a homogeneous problem, in which a scattered field exists without any incident field. From Eqs. (2.36) and (2.37), such a wave can

**Fig. 2.15** Normalized constants of propagation of the SPP on a grating in the complex plane



be written in the form:

if 
$$y > y_{\text{max}}$$
,  $H = \sum_{n=-\infty}^{+\infty} b_n \exp(ik_1\alpha_n x + ik_1\beta_n y)$ , (2.41)

if 
$$y < y_{\min}$$
,  $H = \sum_{n=-\infty}^{+\infty} c_n \exp(ik_1\alpha_n x - ik_1\gamma_n y)$ , (2.42)

$$\alpha_n = \alpha + n\lambda_1/d, \quad \beta_n = \sqrt{1 - \alpha_n^2}, \quad \gamma_n = \sqrt{\nu^2 - \alpha_n^2},$$
(2.43)

the choice of the determinations of  $\beta_n$  and  $\gamma_n$  being fixed by Fig. 2.5. Of course, the energy balance entails that the values of  $\alpha_n$  must be complex with a non-null imaginary part.

Thus, it turns out that the SPP can be represented by an infinity of plane waves having normalized propagation constants in x (constants of propagation divided by  $k_1$ ) spaced by multiples of  $\lambda_1/d$ . It must be noticed that the numbering of the parameters in Eqs. (2.41) and (2.42) is ambiguous since changing n into n+p (p constant integer) does not modify the sum of the series. In order to fix this determination, we can bear in mind that one of the terms of the series must tend to the SPP of the plane when the height h of the grating tends to zero. For example, if the profile is sinusoidal, we can go continuously from the grating  $y=h\cos(2\pi x/d)$  to the plane by decreasing h. By definition, the term of the series corresponding to the SPP of the flat surface is numbered by 0. Thus, denoting by  $\tilde{\alpha}_n^{\rm grating}$  the normalized constants of propagation, it can be written that:

$$\lim_{h\to 0} \left\{ \tilde{\alpha}_0^{\text{grating}} \right\} = \tilde{\alpha}^{\text{plane}}. \tag{2.44}$$

Figure 2.15 shows the locations of the normalized constants of propagation  $\tilde{\alpha}_n^{\text{grating}}$ . The different components of the SPP represented in Fig. 2.15 are very different in nature. For  $n \notin (-1, -2)$ ,  $\tilde{\alpha}_n^{\text{grating}}$  has a real part greater than unity in modulus, with a small imaginary part. Figure 2.16 shows the real and imaginary parts  $\beta'$  and  $\beta''$  of  $\beta = \sqrt{1 - \alpha^2}$  versus the real part  $\alpha'$  of  $\alpha = \alpha' + i\alpha''$ , for  $\alpha'' = 0$  and  $\alpha'' = 5 \cdot 10^{-2}$ , the determination of  $\beta$  being given by  $\beta' + i\beta'' > 0$ . Bearing in mind that the values

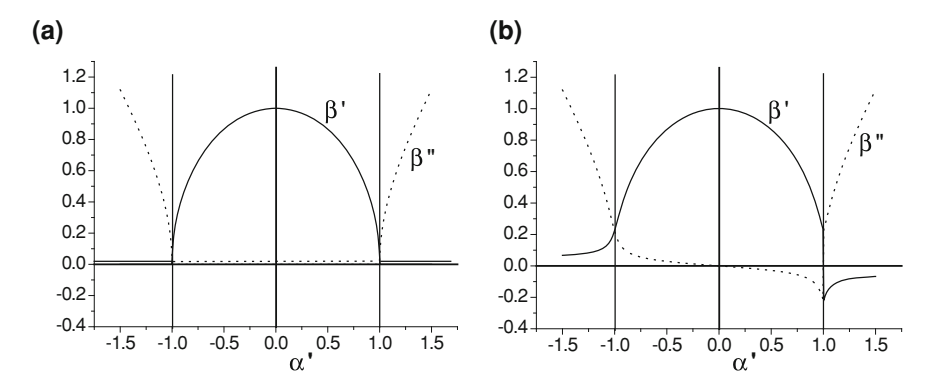


**Fig. 2.16** Real and imaginary parts of  $\beta = \beta' + i\beta'' = \sqrt{1 - \alpha^2}$  versus the real part of  $\alpha = \alpha' + i\alpha''$  with: **a**  $\alpha'' = 0$ , **b**  $\alpha'' = 5.10^{-2}$ 

of 
$$\tilde{\beta}_n^{\rm grating}$$
 deduce from those of  $\tilde{\alpha}_n^{\rm grating}$  by  $\tilde{\beta}_n^{\rm grating} = \sqrt{1-\left(\tilde{\alpha}_n^{\rm grating}\right)^2}$  with the

same determination as for  $\beta$ , it turns out that  $\tilde{\beta}_n^{\text{grating}}$  is close to the imaginary axis and thus, in the dielectric, this kind of wave is very close to an evanescent wave. In the following, this kind of wave will be called wave of evanescent type. Let us recall that the SPP of the flat surface was of evanescent type in the dielectric. The same remark applies to the metal of any order since the values of  $\tilde{\gamma}_n^{\text{grating}}$  and  $\tilde{\gamma}_n^{\text{plane}}$  are close to the imaginary axis (see Fig. 2.17), thus the field decreases exponentially in the metal. On the other hand, the waves corresponding to  $n \in (-1, -2)$  have a real part smaller than unity in modulus. Since the imaginary part is very small,  $\tilde{\beta}_n^{\text{grating}}$  is close to the real axis (Fig. 2.16) and the corresponding wave in the dielectric is close to a homogeneous plane wave propagating towards  $y = \infty$ . It will be called wave of y-propagating type. In that case,  $\tilde{\gamma}_n^{\text{grating}}$  remains close to the imaginary axis for any value of n, thus the field decreases exponentially in the metal. These properties allow us to predict that the imaginary part of  $\tilde{\alpha}_0^{\text{grating}}$  is larger than that of  $\tilde{\alpha}^{\text{plane}}$  since the waves of y-propagating type generate a supplementary loss of energy. Furthermore, this remark explains why a surface wave can propagate on a perfectly conducting grating. We have seen that the limit of the SPP of a flat perfectly conducting surface when the permittivity tends to  $-\infty$  is a plane wave with wave vector parallel to the x-axis. The field of such a wave does not decrease on the dielectric side and thus, this wave cannot be considered as a surface wave. If a periodic modulation is introduced and if there exists at least one y-propagating wave in the dielectric region, this propagating wave will transfer the energy at infinity and so, a loss occurs in the propagation. Due to this loss, the value of  $\tilde{\alpha}_0^{\text{grating}}$  is no more real and unitary, like  $\tilde{\alpha}^{\text{plane}}$ , but complex with a positive imaginary part.

Furthermore, it can be conjectured that the real part of  $\tilde{\alpha}_0^{\text{grating}}$  is greater than unity. A heuristic way to explain this property is to notice that a modulation entails an increase of the interface length between two points of the surface, thus reduces

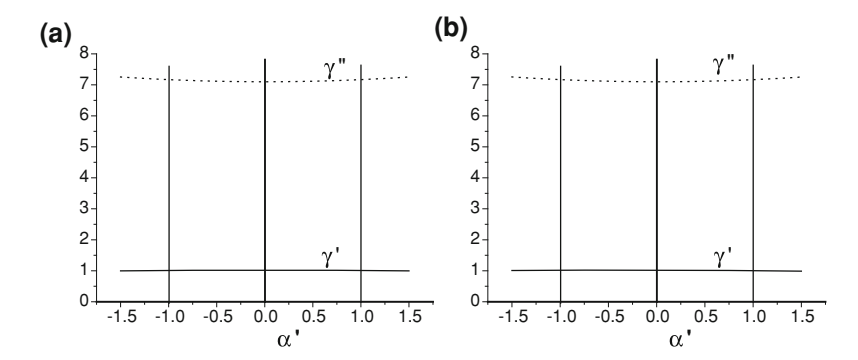


**Fig. 2.17** Real and imaginary parts of  $\gamma = \gamma' + i\gamma'' = \sqrt{\nu^2 - \alpha^2}$  versus the real part of  $\alpha = \alpha' + i\alpha''$  for  $\nu = 1.019 + i7.1$  (index of aluminium at 647 nm), with: **a**  $\alpha'' = 0$ , **b**  $\alpha'' = 5.10^{-2}$ 

the projection on the *x*-axis of the propagation speed of the SPP. So, the propagation constant, which is inversely proportional to the speed, is increased. Let us notice in addition that, in the opposite case, it would be possible to excite the SPP with a plane wave. It is straightforward to show that the value of  $\tilde{\beta}_0^{\text{grating}}$  corresponding to this value of  $\tilde{\alpha}_0^{\text{grating}}$  has a positive imaginary part and thus the field decreases in the dielectric.

### 2.3 Phenomenological Study of Wood Anomalies

Until now, we have analysed the scattering and guiding properties of gratings. The aim of this section is to show from the theory of analytic functions of the complex variable that the guiding properties, i.e. the possibility of SPP propagation, have strong consequences on the scattering properties, i.e. on the amplitudes of the waves generated by the grating when it is illuminated by a plane wave. These consequences will be evaluated quantitatively.

### 2.3.1 Pole of the Reflection and Transmission Coefficients

The SPP of a grating is obtained by setting the scattering coefficients  $b_n$  and  $c_n$  equal to infinity in Eqs. (2.36) and (2.37) in order to make the incident field negligible. Let us show that all the coefficients  $b_n$  and  $c_n$ , considered as functions of the normalized propagation constant  $\alpha$  of the incident wave, have an infinity of poles located at points given by:

$$\alpha = \tilde{\alpha}_n^{\text{grating}}.$$
 (2.45)

If the incident wave satisfies this equation, the normalized propagation constants  $\alpha_n$  of the field scattered by the grating identify with the normalized propagation constants  $\tilde{\alpha}_n^{\text{grating}}$  of the SPP, thus the field expressed by Eqs. (2.41) and (2.42) is the solution of the scattering problem, which shows that the amplitudes of the scattered waves are infinite with respect to the amplitude of the incident wave. This remark leads us to guess that the amplitudes of the scattered waves have a pole [47] when a SPP can propagate.

It seems that this remark is useless since  $\alpha=\sin\left(\theta\right)$  is real, while the  $\tilde{\alpha}_{n}^{\text{grating}}$  are complex (Fig. 2.15). However, if the real part of  $\tilde{\alpha}_{n}^{\text{grating}}$  is less than unity in modulus (like  $\tilde{\alpha}_{-1}^{\text{grating}}$  and  $\tilde{\alpha}_{-2}^{\text{grating}}$  in Fig. 2.15),  $\alpha$  can be close to  $\tilde{\alpha}_{n}^{\text{grating}}$ , and it can be conjectured that a resonance phenomenon will occur, provided that the imaginary part of the  $\tilde{\alpha}_{n}^{\text{grating}}$  is not too large. In other words, it can be considered that in real life,  $\alpha$  is real and the amplitudes  $b_{n}\left(\alpha\right)$  and  $c_{n}\left(\alpha\right)$  are complex functions of the real variable  $\alpha$ . However, mathematical theorems [47] state that such a function has one and only one analytic continuation in the complex plane of  $\alpha$ . In conclusion, all the  $\tilde{\alpha}_{n}^{\text{grating}}$  are poles of this continuation but using an actual plane wave, only some of them ( $\tilde{\alpha}_{-1}^{\text{grating}}$  and  $\tilde{\alpha}_{-2}^{\text{grating}}$  in Fig. 2.15) can be approached.

# 2.3.2 Zero of the Reflection Coefficient, Phenomenological Formula

Although the phenomenological approach can be generalized to more complicated cases, we now consider for simplicity that only one value of  $\tilde{\alpha}_n^{\rm grating}$  has a real part less than unity in modulus. Bearing in mind that  $\tilde{\alpha}_0^{\rm grating}$  is very close to unity for moderate values of the height h of the grating, Fig. 2.15 shows that n must be equal to -1 and that the real part of  $\tilde{\alpha}_{-1}^{\rm grating}$  must be negative. In these conditions, a resonance occurs when  $\alpha \simeq {\rm Re}\left\{\tilde{\alpha}_{-1}^{\rm grating}\right\}$ . In consequence, there exists only one non-evanescent reflected order since  $\alpha + n\lambda_1/d \simeq {\rm Re}\left\{\tilde{\alpha}_{-1}^{\rm grating} + n\lambda_1/d\right\} = {\rm Re}\left\{\tilde{\alpha}_n^{\rm grating}\right\}$  and by hypothesis, all the values of  ${\rm Re}\left\{\tilde{\alpha}_n^{\rm grating}\right\}$  are greater than unity in modulus, except  ${\rm Re}\left\{\tilde{\alpha}_{-1}^{\rm grating}\right\}$ . Thus we are led to the study of  $b_0\left(\alpha\right)$ , the amplitude of the reflected order 0. Mathematically, since  $\tilde{\alpha}_{-1}^{\rm grating}$  is a pole of the analytical continuation of  $b_0\left(\alpha\right)$ , it will be called  $\alpha^p$  in the following. Thus, it can be deduced that, when  $\alpha$  is close to  ${\rm Re}\left\{\alpha^p\right\}$ ,  $b_0\left(\alpha\right)$  can be expanded in a Laurent series [48], which can be written in the form:

$$b_0(\alpha) \simeq \frac{g_{-1}}{\alpha - \alpha^p} + g_0 + (\alpha - \alpha^p) u(\alpha), \qquad (2.46)$$

with  $g_{-1}$  and  $g_0$  being complex coefficients, and  $u(\alpha)$  an entire series of  $\alpha - \alpha^p$ . Neglecting the last term in the right-hand member of Eq. (2.46) yields:

$$b_0(\alpha) \simeq \frac{g_{-1}}{\alpha - \alpha^p} + g_0 \simeq \frac{g_{-1} + g_0(\alpha - \alpha^p)}{\alpha - \alpha^p}.$$
 (2.47)

Setting

$$\alpha^z = \alpha^p - \frac{g_{-1}}{g_0},\tag{2.48}$$

Eq. (2.47) can be written in the form:

$$b_0(\alpha) \simeq g_0 \frac{\alpha - \alpha^z}{\alpha - \alpha^p}.$$
 (2.49)

If the height of the grating tends to 0, there is no more resonance and then,  $g_{-1}$  tends to 0,  $g_0$  tends to the reflection coefficient r of a flat metallic plane, and since  $\tilde{\alpha}_0^{\rm grating}$  tends to  $\tilde{\alpha}_0^{\rm plane}$ :

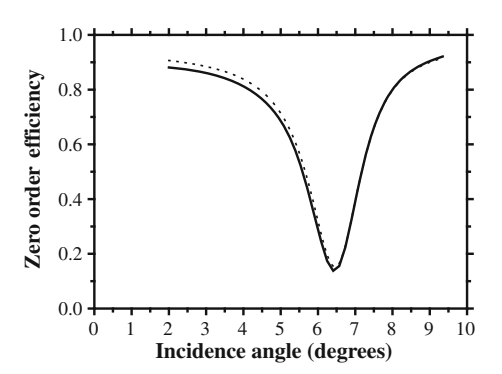
$$\lim_{h\to 0} \left\{ \alpha^z \right\} = \lim_{h\to 0} \left\{ \alpha^p \right\} = \tilde{\alpha}^{\text{plane}} - \frac{\lambda_1}{d}. \tag{2.50}$$

As a result, the effects of the pole and zero annihilate when h tends to zero, according to Eq. (2.49).

# 2.3.3 Verification of the Phenomenological Formula from Numerical Results

Now, let us show that the phenomenological formula allows one to predict with great precision the efficiency of a metallic grating in the region of anomaly. We consider a gold sinusoidal grating with period 555 nm and height 60 nm, illuminated by a p-polarized plane wave of wavelength 647 nm propagating in vacuum. We compare the efficiencies obtained from a computer code based on a rigorous integral theory of gratings [21, 29] and from the phenomenological formula. This formula requires the knowledge of the parameters  $g_0$ ,  $\alpha^z$  and  $\alpha^p$  contained in Eq. (2.49). We have given to  $g_0$  its limit value as the height of the grating tends to 0, i.e. the reflection coefficient of a gold plane. In order to calculate  $\alpha^z$  and  $\alpha^p$ , we have transformed the computer code based on a rigorous integral theory of gratings [11, 12]. First, this code has been extended to complex values of  $\alpha = \sin(\theta)$  in order to calculate the output  $b_0$  from the input  $\alpha$ . Then, this code has been used as a subroutine of a software able to find the zero of a complex function of a complex variable. This kind of software, based on very simple formulae like Newton's formula, requires an estimate of the location of the zero in order to initiate the iterative process. This estimate has been deduced from Eq. (2.50) . Thus we have searched for the zero of  $1/b_0$  for  $\alpha^p$  and of  $b_0$  for

Fig. 2.18 Comparison of the results deduced from the phenomenological formula (dashed line) with those deduced from the rigorous integral theory of gratings (solid line)



 $\alpha^z$ . The results are  $\alpha^p = -0.1135 + i0.0149$  and  $\alpha^z = -0.1126 - i0.00596$ . We have introduced these parameters in a formula deduced from Eq. (2.49) by taking the square modulus  $|b_0|^2$  of the amplitude in the order 0 (i.e. the efficiency in the order 0), the coefficient  $|g_0|^2$  being replaced by the reflectivity  $R = |r|^2$  of gold, equal to 0.953:

$$|b_0(\alpha)|^2 \simeq R \left| \frac{\alpha - \alpha^z}{\alpha - \alpha^p} \right|^2.$$
 (2.51)

Figure 2.18 shows a comparison between the efficiencies in the order 0 deduced from this phenomenological formula and from the rigorous integral theory versus the angle of incidence.

It must be noticed that from our data, the resonance should occur for negative incidences, but of course, the symmetry of the grating profile entails that the same resonance is obtained for positive incidences. The two curves are almost identical, except in the left side of the curve where discrepancies of the order of 3% appear. This is not surprising since a second resonance occurs for negative angles and of course, the effects of the corresponding pole and zero are not taken into account in the phenomenological formula. The obvious conclusion is that the phenomenological formula is a valuable tool for predicting the efficiency of gratings in the resonance region. It reduces the resonance phenomenon to the knowledge of two complex parameters.

Some elementary properties of the resonance curve can be easily deduced from this formula. Assuming that the real parts of the pole and zero are very close (which is in general the case), the minimum value  $e_m$  of the efficiency and the width w at half-height of the drop of efficiency are given by:

$$e_m = R \times \left| \frac{\operatorname{Im} \left\{ \alpha^z \right\}}{\operatorname{Im} \left\{ \alpha^p \right\}} \right|^2, \tag{2.52}$$

$$w = 2\operatorname{Im}\left\{\alpha^p\right\}. \tag{2.53}$$

Furthermore, it can be noticed from the phenomenological formula that the phase of  $b_0$  has violent variations at the vicinity of the resonance since the phase of both terms  $\alpha - \alpha^z$  and  $\alpha - \alpha^p$  in Eq. (2.49) is rapidly varying. If the pole and the zero are placed on the same side of the real axis, the total phase shift from one side of the resonance process to the other one is equal to zero, while in the opposite case, it reaches  $\pm 2\pi$ .

### 2.4 Total Absorption of Light by a Diffraction Grating

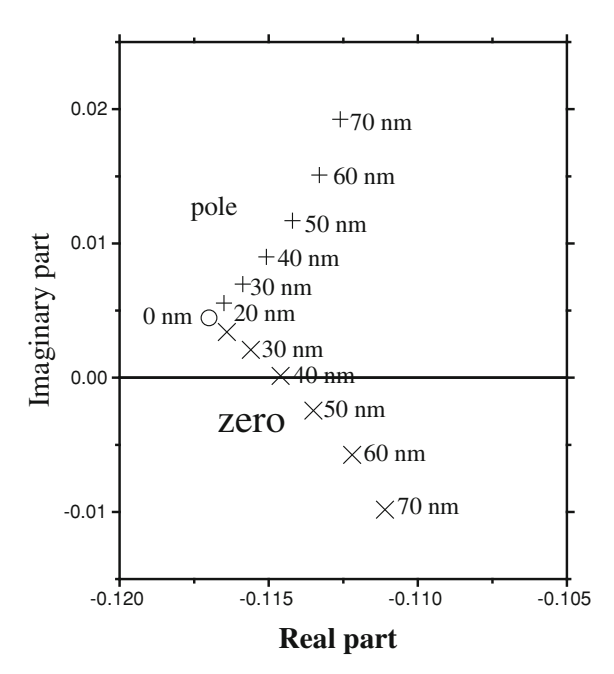
#### 2.4.1 Theoretical Demonstration

The existence of a total absorption of light by a grating, which cannot scatter more than a single y-propagating wave, can be demonstrated from many arguments. First, it can be shown from numerical results. Indeed, we have seen that for a flat surface the pole and the zero are located on the same side of the real axis, with a positive imaginary part. We know that the sign of the imaginary part of the pole holds, whatever the groove depth. Thus, if numerical calculations show that for a given groove depth, the zero has a negative imaginary part, it can be deduced from a topological argument that there exists a groove depth for which the zero crosses the real axis. Since it is so given in Fig. 2.18 (drawn using  $\alpha^z = -0.1126 - i0.00596$ ) for a gold sinusoidal grating, the total absorption must occur for a groove depth smaller than that of the grating of Fig. 2.18, as it will be seen in the following paragraph.

The existence of total absorption phenomenon can also be shown through a purely theoretical demonstration. It has been shown in Sect. 2.3.2 that for a perfectly conducting structure, the pole and zero at a given wavelength are complex conjugate, whatever the groove depth may be. Thus the zero is located below the real axis. On the other hand, for a flat, lossy metallic structure, the pole and zero are identical and located above the real axis. The perfect conductivity corresponds to a permittivity  $\varepsilon_2$  of the metal which is real, negative and infinite in modulus. Let us suppose that for a given groove depth of a sinusoidal grating, the permittivity of the metal is varied continuously from this negative and infinite value to the permittivity of an actual metal like gold. Then, let us tend the groove depth of the grating to 0. Since the zero goes from a point located below the real axis to a point located above the real axis, it must cross the real axis, at least if we assume the continuity of its trajectory. In fact, from several numerical analyses, it turns out that for a given shape (sinusoidal, triangular...) and a given period of the grating profile, with given metal and the angle of incidence, a phenomenon of total absorption occurs for p-polarized light for given wavelengths and groove depths, these two parameters depending on each other.

In Fig. 2.19, we have drawn the trajectory of the pole and zero of a sinusoidal gold grating when the groove depth is varied. The zero crosses the real axis for  $\alpha$  close to

Fig. 2.19 Trajectory of the pole  $\alpha^p$  and zero  $\alpha^z$  of  $b_0$  for a gold sinusoidal grating with period 555 nm, illuminated by a p-polarized plane wave with wavelength 647 nm, when the height h is increased. Reprinted from [50], with permission from Elsevier

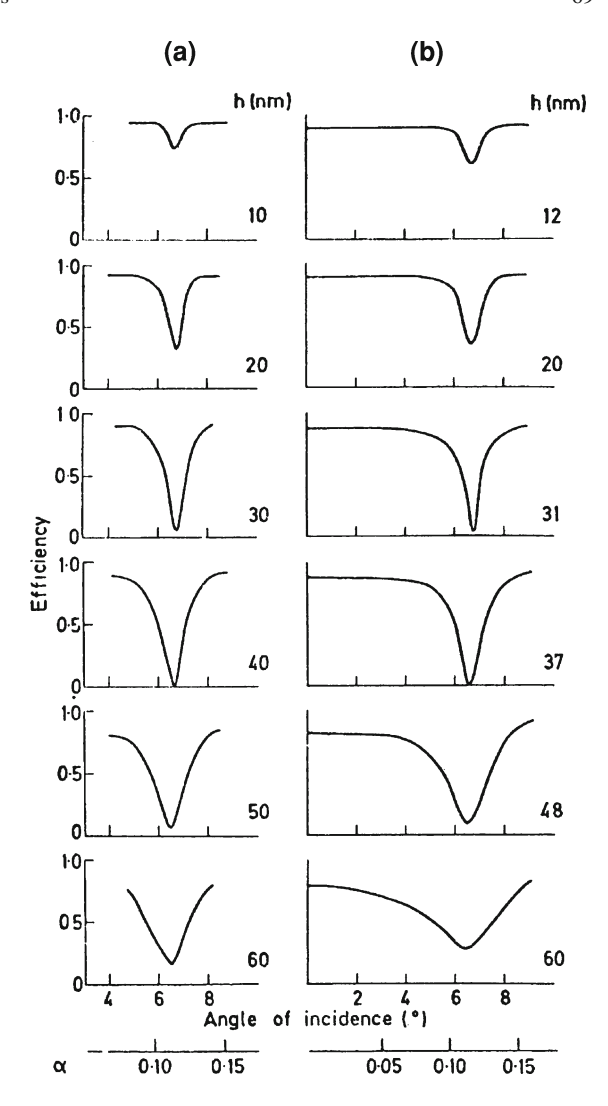


-0.115 ( $\theta \simeq -6.6^{\circ}$ ) for a groove depth equal to 40 nm, thus a total absorption must occur for these parameters.

### 2.4.2 Experimental Verification

The experimental verification of the phenomenon of total absorption discovered in [49] from theoretical results was given in [50]. It was performed on a holographic sinusoidal gold grating having the same pitch as in Fig. 2.19 illuminated by a krypton laser beam at the wavelength 647 nm. Due to a mishap during exposure, the groove depth varied from 13 nm on one side to 75 nm on the other. In order to study the reflectance as a function of the groove depth, it was necessary to simply select the appropriate region of the grating surface. The groove depth was measured using a profilometer fitted with a chisel-shaped stylus. The experimental results are shown in Fig. 2.20b, as well as the corresponding theoretical predictions obtained from the integral theory in Fig. 2.20a. The agreement between experimental and theoretical results is excellent. The minimum recorded reflectance of 0.3 % was at an angle of incidence of 6.6° and a groove depth of 37 nm, which are very close to the theoretical predictions. In the same paper, the authors obtained a total absorption for other wavelengths and were able, using a modified Mach-Zender interferometer, to show the change of  $\pi$  in the phase of the reflected wave as the incident beam crossed the region of the grating where  $\alpha^z$  becomes real.

**Fig. 2.20** Theoretical (**a**) and experimental (**b**) reflectance of a sinusoidal gold grating versus the angle of incidence for various groove depths *h*. Reprinted from [50], with permission from Elsevier



This result is quite remarkable and very surprising: a very gentle modulation in the surface of a gold mirror causes the reflectance to fall dramatically from over 90% to below 1%. Figure 2.20 also shows that the width of the reflectance drop is very small, of the order of  $1^\circ$ . The resonance remains very selective when other parameters (wavelength, groove depth) are changed. Similar results were published by Le Perchec et al. [51] for nanometric silver lamellar gratings.



**Fig. 2.21** Spectrum of a white light beam after reflection from a gold grating of Fig. 2.20 with groove height 37 nm with incidence 6.6°. Reprinted [50], with permission from Elsevier

#### 2.4.3 Some Applications

Figure 2.20 shows that the total absorption phenomenon can present a strong angular selectivity, typically less than  $1^{\circ}$ . The same selectivity can be found when, starting from total absorption, the wavelength is varied. Figure 2.21, reprinted from [50], shows the spectrum of the grating which corresponds to a total absorption in Fig. 2.20, illuminated with a collimated beam of white light from a tungsten lamp. The spectrum clearly shows a strong narrow absorption band in the red. Here, the grating absorbs in totality at 647 nm, but it is interesting to know that a nearly total absorption phenomenon holds for another wavelength when the angle of incidence is varied. Obviously, such a grating can be used as a rejection filter for eliminating a wavelength in a polychromatic light beam. A very selective absorption in incidence and frequency ranges can be used in metrology or to make selective filters like biosensors. It could prevent cross-talks between optical interconnects.

Let us describe the application to immunosensors. A direct immunosensor is an immunologically sensitized transducer that possesses the ability to observe antibody—antigen binding events in real time. An immunosensor can be made using the sensitivity of SPPs to changes in the dielectric permittivity of a dielectric-coated metallic grating [52]. It consisted of a gold or silver holographic diffraction grating on which 'sensitizing' immunological molecules were immobilized, realizing in some way a dielectric coating. The subsequent binding of complementary components (contained for example in human or animal serums) can be followed, in real time, by measuring changes in the reflectivity of the grating resulting from alterations in the conditions necessary for optimal SPP excitation.

Since Wood's anomalies entail strong local enhancements of the field on the grating surface, they are also used in Raman scattering [53] or second-harmonic generation [54].

On the other hand, it is interesting to realize a strong absorption in the wide ranges of angle of incidence or wavelength. Equation (2.53), deduced from the phenomenological formula, shows that the angular width of the absorption peak increases with the imaginary part of the pole. Furthermore, Fig. 2.19 clearly shows that this imaginary part strongly increases with the groove depth. As a consequence, it can be deduced that a wide-range strong absorption can be obtained with deep gratings. The SPPs of such gratings are sometimes termed "localized SPPs" since they are

very rapidly attenuated when they propagate. A nearly total absorption on a wide range of angles of incidence or wavelengths could lead to many practical applications, for example the realization of solar absorbers [55] or, as suggested by Teperik et al. [56], efficient photovoltaic cells, or light shielding of micro-photonic devices. As suggested by the Kirchhoff law, this kind of grating should constitute omnidirectional black-body emitters, possibly with the narrow a spectral range. The interested reader can find other possibilities to use SPPs in [57–73].

#### 2.5 Further Properties of Surface Plasmon Polaritons

# 2.5.1 Physical Interpretation and Fundamental Properties of the Zero of the Reflection Coefficient

It is possible to give a physical interpretation of the existence of a zero close to the pole. With this aim, let us consider the complex conjugate  $H^*$  of the expression of the SPP given by Eqs. (2.41) and (2.42). Such a field satisfies in the metal the Helmholtz equation

$$\nabla^2 H^* + k^2 \varepsilon_2^* H^* = 0, \tag{2.54}$$

while in the dielectric, the permittivity is real and thus the Helmholtz equation remains unchanged. In the following, we will call the structure so obtained as the adjoint structure. It is straightforward to show that  $H^*$  satisfies the boundary conditions on the interface and thus  $H^*$  is a solution of the elementary laws of electromagnetics in a structure made of a dielectric of permittivity  $\varepsilon_1$  and a material of permittivity  $\varepsilon_2^*$ . This permittivity corresponds to a material with gain [74]. However,  $H^*$  completely differs from a SPP since some waves included in  $H^*$  do not satisfy in the dielectric the radiation condition expressed by Eq. (2.16). Indeed, the complex conjugation changes the expression exp  $\left(ik_1\tilde{\alpha}_n^{\text{grating}} + ik_1\tilde{\beta}_n^{\text{grating}}\right)$  into  $\exp\left(-ik_1\left(\tilde{\alpha}_n^{\text{grating}}\right)^* - ik_1\left(\tilde{\beta}_n^{\text{grating}}\right)^*\right), \text{ which shows that } \tilde{\alpha}_n^{\text{grating}} \text{ becomes } \\ -\left(\tilde{\alpha}_n^{\text{grating}}\right)^* \text{ and } \tilde{\beta}_n^{\text{grating}} \text{ becomes } -\left(\tilde{\beta}_n^{\text{grating}}\right)^*. \text{ As a consequence, the real parts } \\ \text{of the propagation constants } -\left(\tilde{\alpha}_n^{\text{grating}}\right)^* \text{ of } H^* \text{ along the } x\text{-axis become the opposition} \\ \frac{1}{n} \left(\tilde{\beta}_n^{\text{grating}}\right)^* \left(\tilde{\beta}_n^{\text{grating}}\right)^* = \frac{1}{n} \left(\tilde{\beta}_n^{\text{grating}}\right)^* \left(\tilde{\beta}_n^{\text{grating}}\right)^* \\ \frac{1}{n} \left(\tilde{\beta}_n^{\text{grating}}\right)^* \left(\tilde{\beta}_n^{\text{grating}}\right)^* \left(\tilde{\beta}_n^{\text{grating}}\right)^* = \frac{1}{n} \left(\tilde{\beta}_n^{\text{grating}}\right)^* \left(\tilde{\beta}_n^{\text{grating}}\right)^* \\ \frac{1}{n} \left(\tilde{\beta}_n^{\text{grating}}\right)^* \left(\tilde{\beta}_n^{\text{grating}}\right)^* \left(\tilde{\beta}_n^{\text{grating}}\right)^* \left(\tilde{\beta}_n^{\text{grating}}\right)^* \\ \frac{1}{n} \left(\tilde{\beta}_n^{\text{grating}}\right)^* \left(\tilde{\beta}$ site of those of  $\tilde{\alpha}_n^{\rm grating}$ , while the imaginary part holds. This remark entails that the direction of propagation of  $H^*$  on the adjoint structure and of the SPP in the initial structure is opposite and that the amplitude is increased in the direction of propagation, a fact which is not surprising since the metal has been replaced by a material with gain. A simple way to restore a propagation towards  $x = +\infty$  is to change x into -x in the expression of  $H^*$ , which is the equivalent of changing  $-\left(\tilde{\alpha}_n^{\text{grating}}\right)^*$ 

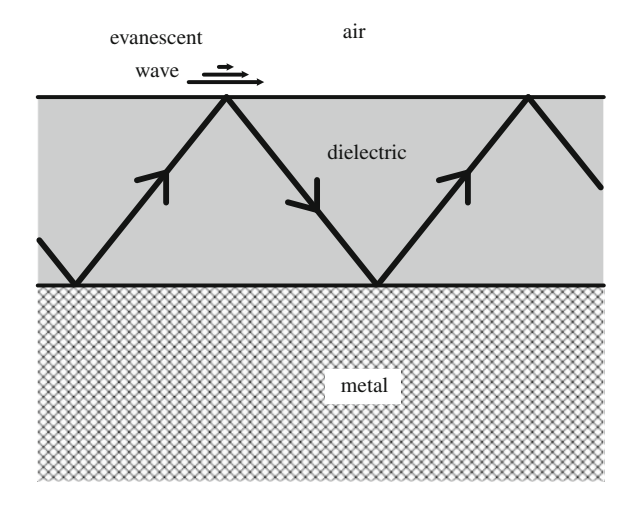
into  $+\left(\tilde{\alpha}_n^{\text{grating}}\right)^*$ . After this symmetry, the propagation constant along x of  $H^*$  and of the SPP of the initial structure are complex conjugate.

As regards the radiation condition on the dielectric side, two cases must be distinguished. If the nth component of the SPP is of the evanescent type,  $\tilde{\beta}_n^{\text{grating}}$  is very close to the imaginary axis, with a positive imaginary part. This positive imaginary part holds for  $-\left(\tilde{\beta}_n^{\text{grating}}\right)^*$  and thus the wave remains of the evanescent type and satisfies the radiation condition. On the other hand, for the waves of y-propagating type,  $\tilde{\beta}_n^{\text{grating}}$  and  $-\left(\tilde{\beta}_n^{\text{grating}}\right)^*$  are very close to the real axis and their real parts are opposite. Consequently, for the adjoint structure, the waves contained in  $H^*$  do not propagate towards  $y=+\infty$  anymore, but towards  $y=-\infty$ . Such a wave corresponds to an incident wave that propagates in the direction of the grating surface. In the metal, since the values of  $\tilde{\gamma}_n^{\text{grating}}$  are close to the imaginary axis, it is easy to show that the series of waves inside  $H^*$  still satisfy the radiation condition.

In conclusion, after a symmetry in x,  $H^*$  has a propagation constant along x which is the conjugate of that of the SPP on the initial structure. Moreover, all the waves included in  $H^*$  still satisfy the radiation condition, except those corresponding to y-propagating waves in the dielectric, which become incident instead of scattered. Assuming again that the only wave of propagating type in the dielectric is the order n=-1,  $H^*$  can be considered, after a symmetry along x, as the field scattered by an incident plane wave with propagation constants  $\left(\tilde{\alpha}_{-1}^{\text{grating}}\right)^*$  and  $-\left(\tilde{\beta}_n^{\text{grating}}\right)^*$  along the x- and y-axes. Furthermore, there is no scattered wave corresponding to n=-1, i.e. in the direction  $\left(\tilde{\alpha}_{-1}^{\text{grating}}\right)^*$ ,  $+\left(\tilde{\beta}_{-1}^{\text{grating}}\right)^*$ . It can be deduced that after symmetry with respect to the x-axis,  $H^*$  is the field corresponding to the zero of the adjoint structure, which is thus the conjugate of the pole of the initial structure. Following the same lines, it is easy to show that the zero of the initial structure is, after symmetry along x, the conjugate of the pole of the adjoint structure, i.e. the conjugate of the propagation constant of the SPP of the adjoint structure.

This property shows that there exists complete symmetry with respect to the real axis between the pole and zero of the initial structure and the pole and zero of the adjoint structure. Vital properties of the poles and zeros can be deduced. Let us notice first that the zero is an actual theoretical zero. It was not possible to state this important property from Eq. (2.47), which was obtained by neglecting the last term in Eq. (2.46). Furthermore, we have seen that it can be conjectured that the imaginary part of the pole of the initial structure should increase with the height of the grating, due to losses through propagating waves in the dielectric. For the adjoint structure, there is an exponential increase of the amplitude in the propagation. The propagating waves of the SPP of the adjoint structure will provoke the opposite effect. Since they entail losses of energy, the increase of the amplitude will be attenuated and may be cancelled. In that case, the propagating wave in the dielectric is an actual plane wave with real constants of propagation in x and y, which propagates towards  $y = +\infty$ : the grating, which is not illuminated by any incident wave, scatters this plane wave to infinity. Conversely, the zero of the initial structure is real: the grating, illuminated

**Fig. 2.22** Propagation of a guided wave in a dielectric film deposited on a metallic surface



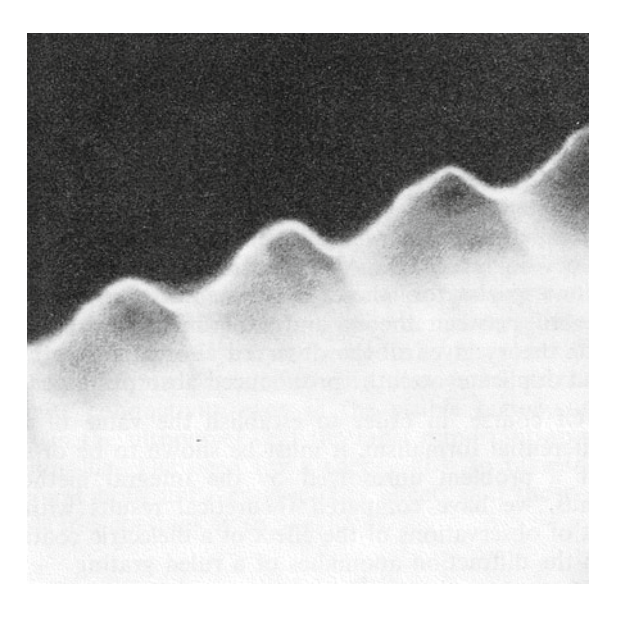
by a plane wave, does not scatter any plane wave. This is another way to theoretically predict the phenomenon of total absorption studied in the preceding section. Finally, for a perfectly conducting structure,  $\varepsilon_2$  is real, negative and infinite in modulus. In that case the initial and adjoint structures identify and so, the pole and zero of the initial structure are complex conjugate, as well as those of the adjoint structure.

# 2.5.2 Analogy with Guided Waves in Dielectric Films Deposited on Metallic Surfaces

It has been shown that the basic origin of the grating anomalies must be found in the excitation of a surface wave: the SPP. The consequence is that this kind of anomaly occurs only for p-polarized light. However, it should be noticed that other kinds of surface waves can propagate on a flat metallic surface, provided that the metal is covered by a plane dielectric coating, as shown in Fig. 2.22. The wave propagates in the dielectric film following a zigzag path, with a lossy metallic reflection on one side and a lossless total reflection on the other side, provided that the angle of incidence on the air exceeds the critical angle of total reflection. In that case, the field on the air side reduces to an evanescent wave and the propagation constant of the guided wave is greater than the wavenumber of the light in vacuum, like for a SPP. Thus this guided wave can play the same role as a SPP for generating a resonance phenomenon as soon as one of the interfaces (or both) is periodically modulated. The big difference with SPPs is that anomalies can occur for both polarizations.

Let us show an example of anomaly of a metallic, dielectric-coated grating for s-polarized light, taken from [28]. Figure 2.23 shows a scanning electron micrograph of the grating profile of a 1,264 lines/mm ruled aluminium grating (with triangular

Fig. 2.23 Electron micrograph of the profile of a ruled grating made in NPL. Reprinted by permission from IOP Publishing Ltd: [28] p. 90



groove) made in the NPL (National Physical Laboratory, Teddington, U.K.). The blaze angle of the grating (angle between the large facet and the mean plane of the profile) was equal to 23° and the included angle of the ruling diamond (angle between the two facets) was  $110^{\circ}$ . Two identical aluminium gratings were realized and one of them was covered with silicon monoxide with a thickness close to  $100 \, \mathrm{nm}$  (measured using multiple-beam interferometry). The efficiency in the order -1 was measured in Littrow mounting for both gratings. Let us recall that in the Littrow mount, the order -1 and the incident wave propagate in opposite directions. Using Eq. (2.1) with n=-1, it turns out that since  $\theta_{-1}=-\theta$ , the angle of incidence and the wavelength in vacuum satisfy the relation

$$\lambda/d = 2\sin\left(\theta\right). \tag{2.55}$$

The efficiency curves are shown in Fig. 2.24. Experimental measurements were realized in the NPL, while the theoretical results were obtained from the differential theory [28, 29].

For the uncoated grating, experimental and theoretical curves show a relatively featureless shape, the edge corresponding to a Rayleigh anomaly (passing-off of the orders -2 and +1). Both theory and experiment show that the coating introduces just after the Rayleigh anomaly a strong and sharp minimum, even though the theory gives an anomaly somewhat weaker than was observed. This discrepancy has been explained: the profile used in the calculations is perfectly triangular, which is not the case in Fig. 2.23, and calculations have shown that the strength and the width of the anomaly are very sensitive to small changes in profile form and coating thickness.

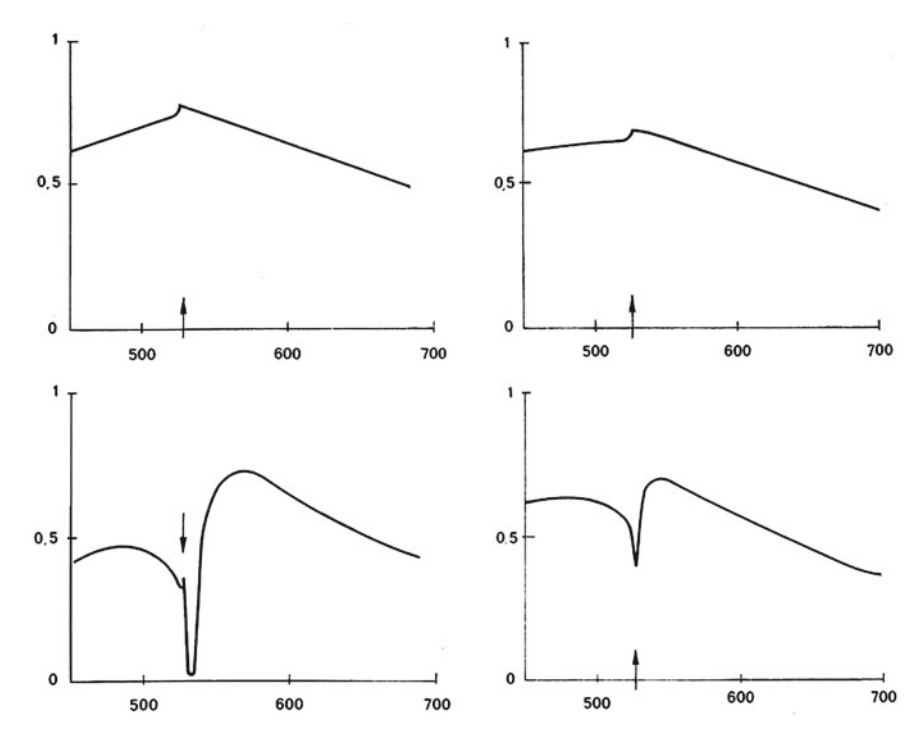


Fig. 2.24 Efficiency curves in Littrow mount and for s-polarized light of the 1,264 lines/mm, aluminium ruled grating of Fig. 2.23, with an uncoated profile (top) and a 100 nm-coating of silicon monoxide (bottom). Experimental values and theoretical ones are, respectively, given at *left* and at *right*. The wavelength scale is marked in nm and the *arrow* shows the location of the passing-off of orders +1 and -2. Reprinted by permission from IOP Publishing Ltd: [28] p. 91

A phenomenon of total absorption has been verified for s-polarized light with a 2,400 lines/mm 10°22′ blaze angle, aluminium grating covered with a 130 nm magnesium fluoride coating [75]. Total absorption was predicted by theory for a coating thickness of 152 nm, a wavelength of 492 nm and an angle of incidence equal to 7.5°. The measurements were performed with a 130 nm depth of magnesium fluoride, for a wavelength equal to 492 nm and at an angle of incidence close to 7°, the efficiency was found to drop sharply to just 5.5%. Other results on total absorption for s-polarized light can be found in [76]. The total absorption can be generalized to unpolarized light using crossed gratings [77, 78] or even using classical 2D gratings in conical (off-plane) mountings [79].

These examples show that guided waves generated by dielectric coatings on top of the metal can generate the same resonance phenomena as SPPs. This remark could be generalized to other domains of plasmonics.

#### 2.6 Conclusion

The study of Wood's anomalies and SPP resonances, initiated more than one century ago, is a typical example of the interest of converging analyses of experimentalists, theoreticians and specialists of phenomenology.

It is amazing to bear in mind that, initially, grating anomalies were considered as strong defects of gratings. The reason is that the gratings were mainly used in spectroscopy, where efficiency drops caused by anomalies around certain wavelengths considerably reduce the possibility of analysing a light spectrum in a wide range of wavelengths with good precision. Nowadays, non-spectroscopic applications of gratings have become a crucial field of optics and the practical applications of SPP anomalies have taken a strong importance in many fields of science and technology.

These modern applications of Wood's anomalies have been permitted by the progress of process of fabrication and of numerical tools, which allow one to optimize almost all kinds of diffraction gratings in all ranges of wavelength. It can be conjectured that the extraordinary features of the resonant excitation of SPPs will encourage the specialists of modern optics and nanophotonics to develop and to extend the field of applications of grating anomalies in the future.

#### **Appendix 1: Electromagnetic modelling in Two Dimensions**

We consider an interface  $\Sigma$  separating two homogeneous regions  $R_1$  and  $R_2$ . The Maxwell equations write:

$$\nabla \times \mathbf{E} = -\partial \mathbf{B}/\partial t, \tag{2.56}$$

$$\nabla \times \mathbf{H} = \mathbf{j}_c + \partial \mathbf{D} / \partial t, \tag{2.57}$$

where **E** and **H** are the electric and magnetic fields, **D** and **B** are the electric and magnetic inductions, and  $\mathbf{j}_c$  is the conduction current density. In the harmonic regime, the fields and currents have a sinusoidal behaviour in time. A function of space and time  $f(\mathbf{r}, t)$  with sinusoidal behaviour in time can be written as:

$$f(\mathbf{r},t) = a(\mathbf{r})\cos(\omega t - \varphi(\mathbf{r})), \qquad (2.58)$$

with a and  $\varphi$  being real functions of space called amplitude and phase,  $\omega$  being the frequency. Such a function is classically represented by its complex amplitude  $\tilde{f}$  ( $\mathbf{r}$ ) independent of time, and Eq. (2.58) is re-written in the form:

$$f(\mathbf{r}, t) = \operatorname{Re} \left\{ a(\mathbf{r}) \exp \left( -i\omega t + i\varphi(\mathbf{r}) \right) \right\} = \operatorname{Re} \left\{ a(\mathbf{r}) \exp \left( i\varphi(\mathbf{r}) \right) \exp(-i\omega t) \right\}.$$
(2.59)

The expression  $a(\mathbf{r}) \exp(i\varphi(\mathbf{r}))$  being called complex amplitude of f and denoted by  $\tilde{f}$ , Eq. (2.59) can be written:

$$f(\mathbf{r},t) = \operatorname{Re}\left\{\tilde{f}(\mathbf{r})\exp(-i\omega t)\right\}. \tag{2.60}$$

Thus the function f deduces from its complex amplitude  $\tilde{f}$  by multiplying by  $\exp{(-i\omega t)}$  then by taking the real part of the product. It is straightforward to show that the multiplication of  $f(\mathbf{r},t)$  by a real function  $u(\mathbf{r})$  results in a multiplication of the complex amplitude by the same function and conversely, and that the complex amplitude of  $\partial f/\partial t$  is equal to  $-i\omega \tilde{f}$ . Thus, Maxwell's equations can be written using the complex amplitudes of the field and, for simplicity, the complex amplitudes of the fields and current are denoted using the same names and symbols as the fields and current themselves, in such a way that harmonic Maxwell equations can be written:

$$\nabla \times \mathbf{E} = i\omega \mathbf{B},\tag{2.61}$$

$$\nabla \times \mathbf{H} = \mathbf{j}_c - i\omega \mathbf{D}. \tag{2.62}$$

In addition to Maxwell equations, constitutive relations allow one to express the electromagnetic properties of the materials. In contrast with Maxwell equations, they are not rigorous (except in vacuum). Assuming that a material is non-magnetic, homogeneous, isotropic and linear, these relations can be written:

$$\mathbf{B} = \mu_0 \mathbf{H}, \quad \mathbf{D} = \varepsilon_0 \varepsilon' \mathbf{E}, \quad \mathbf{j_c} = \sigma \mathbf{E},$$
 (2.63)

with  $\mu_0 = 4 \cdot \pi \cdot 10^{-7}$  being the permeability of vacuum and  $\varepsilon_0 = 1/\left(36\pi 10^9\right)$  being the permittivity of vacuum. The parameters  $\varepsilon'$  and  $\sigma$  denote the relative dielectric permittivity and the conductivity of the material respectively. Using the relations  $\mathbf{D} = \varepsilon_0 \mathbf{E} + \mathbf{P}, \quad \mathbf{P} = \varepsilon_0 \chi \mathbf{E}$ , with  $\mathbf{P}$  electric polarization density and  $\chi$  electric susceptibility, it turns out that  $\varepsilon' = 1 + \chi$ .

Introducing the constitutive relations in Maxwell equations yields:

$$\nabla \times \mathbf{E} = i\omega \mu_0 \mathbf{H},\tag{2.64}$$

$$\nabla \times \mathbf{H} = (\sigma - i\omega\varepsilon_0\varepsilon')\mathbf{E}. \tag{2.65}$$

Defining the complex permittivity:

$$\varepsilon = \varepsilon' + i\sigma/(\omega\varepsilon_0) = 1 + \chi + i\sigma/(\omega\varepsilon_0),$$
 (2.66)

Equation (2.65) takes a form symmetrical to Eq. (2.64):

$$\nabla \times \mathbf{H} = -i\omega \varepsilon_0 \varepsilon \mathbf{E}. \tag{2.67}$$

This equation can be expressed in the form:

$$\nabla \times \mathbf{H} = -i\omega\varepsilon_0 \mathbf{E} + \mathbf{j_t}$$
, with  $\mathbf{j_t} = \sigma \mathbf{E} - i\omega\varepsilon_0 \chi \mathbf{E} = i\omega\varepsilon_0 (1 - \varepsilon) \mathbf{E} = \mathbf{j_c} + \mathbf{j_b}$ , (2.68)

with  $\mathbf{j_t}$  total current density, including both the conduction current density  $\mathbf{j_c}$  and the bound current density  $\mathbf{j_b} = -i\omega\mathbf{P} = -i\omega\varepsilon_0\chi\mathbf{E}$  resulting from the electric polarization. The optical index of a material is given by  $\nu = \sqrt{\varepsilon}$ .

Let us notice that by taking the divergence of Eqs. (2.64) and (2.67) and using  $\nabla \cdot (\nabla \times \mathbf{V}) = 0$ , one can get the complementary couple of Maxwell equations in harmonic regime:

$$\nabla \cdot \mathbf{H} = 0, \quad \nabla \cdot (\varepsilon \mathbf{E}) = \nabla \cdot (\varepsilon' \mathbf{E}) = 0.$$
 (2.69)

By combining Eqs. (2.64) and (2.67), one can obtain partial derivative equations for each field inside a homogeneous region. Introducing the value of **H** given by Eq. (2.64) in Eq. (2.67), we obtain:

$$\nabla \times \nabla \times \mathbf{E} - k^2 \mathbf{E} = 0$$
, with  $k = \omega \sqrt{\varepsilon \varepsilon_0 \mu_0}$ . (2.70)

In a homogeneous region,  $\nabla \cdot (\varepsilon \mathbf{E}) = 0$  entails that  $\nabla \cdot \mathbf{E} = 0$  then using Eq. (2.69) and the vector relationship  $\nabla \times \nabla \times \mathbf{E} = \nabla (\nabla \cdot \mathbf{E}) - \nabla^2 \mathbf{E}$  we get:

$$\nabla \mathbf{E} + k^2 \mathbf{E} = 0, \tag{2.71}$$

and, following the same lines for the magnetic field:

$$\nabla \mathbf{H} + k^2 \mathbf{H} = 0. \tag{2.72}$$

It is worth noting that Maxwell equations (Eqs. (2.64) and (2.67)) are valid in the sense of distributions. In other words, they include the boundary conditions at the limit between two homogeneous materials. In order to express them in an explicit form, one can recall that the surface density of V included in  $\Delta \times V$  is equal to  $\mathbf{n} \times (V_+ - V_-)$ , with  $V_+ - V_-$  being the jump of V across the interface in the direction of  $\mathbf{n}$  [29]. It must be recalled that this surface term is the coefficient of a Delta distribution located on the surface. In Eqs. (2.64) and (2.67), the right-hand member contains the fields and thus they should not include distributive surface parts, thus the left-hand member satisfies the same property. We deduce that the tangential components of the electric and magnetic fields are continuous across an interface.

In the two-dimensional case, the interface is invariant by translation along the z-axis. One can distinguish the two fundamental cases of polarization: s-polarization with the electric field  $\mathbf{E} = E\hat{\mathbf{z}}$  and p-polarization with the magnetic field  $\mathbf{H} = H\hat{\mathbf{z}}$ . In both cases, the boundary-value problem becomes scalar. Projecting Eqs. (2.71) and (2.72) on the z-axis, we obtain:

$$\nabla^2 E + k^2 E = 0$$
 for s-polarized light and  $\nabla^2 H + k^2 H = 0$  for p-polarized light. (2.73)

Thus the electric and magnetic fields satisfy a scalar Helmholtz equation.

As regards the boundary conditions on the interface, the continuity of the tangential component of the fields entails the continuity of E for s-polarization and the continuity of H for p-polarization. Since the partial derivative equation is of

the second order, a second boundary condition is needed. For s-polarization, one can express the continuity of the tangential component of the magnetic field using Eq. (2.64). Bearing in mind the vector relation  $\nabla \times (E\hat{\mathbf{z}}) = \nabla E \times \hat{\mathbf{z}}$ , we obtain:

$$\mathbf{H} = \frac{1}{i\omega\mu_0} \nabla E \times \hat{\mathbf{z}}.\tag{2.74}$$

Furthermore, on each side of the interface with normal vector **n**, the continuity of the tangential component of the magnetic field entails the continuity of  $\mathbf{n} \times \mathbf{H}$ , and from Eq. (2.74), it turns out that

$$\mathbf{n} \times \mathbf{H} = \frac{1}{i\omega\mu_0} \mathbf{n} \times \left(\nabla E \times \hat{\mathbf{z}}\right) = \frac{1}{i\omega\mu_0} \nabla E \left(\mathbf{n} \cdot \hat{\mathbf{z}}\right) - \hat{\mathbf{z}} \left(\mathbf{n} \cdot \nabla E\right) = \frac{-1}{i\omega\mu_0} \hat{\mathbf{z}} \frac{\partial E}{\partial n}.$$
(2.75)

It follows that the normal derivative of the electric field  $\frac{\partial E}{\partial n}$  is continuous across the interface.

For p-polarization, the electric field can be expressed from Eq. (2.67):

$$\mathbf{E} = \frac{1}{-i\omega\varepsilon\varepsilon_0} \nabla \times (H\hat{\mathbf{z}}) = \frac{1}{-i\omega\varepsilon\varepsilon_0} \nabla H \times \hat{\mathbf{z}}, \tag{2.76}$$

and thus the continuity of  $\mathbf{n} \times \mathbf{E}$  leads to the continuity of  $\frac{1}{\varepsilon} \frac{\partial H}{\partial n}$ . This second boundary condition is slightly more complicated than that obtained for s-polarization, due to the fact that, in contrast with the permeability, the permittivity is not the same on the two sides of the interface. It can be noticed that this dissymmetry disappears for magnetic materials, for which  $\frac{1}{\mu}\frac{\partial E}{\partial n}$  is continuous across the interface. In conclusion, the boundary conditions across the interface can be written in 2D

problems:

E and 
$$\partial E/\partial n$$
 are continuous for s-polarized light, (2.77)

$$H$$
 and  $\frac{1}{\varepsilon} \frac{\partial H}{\partial n}$  are continuous for p-polarized light. (2.78)

The surface charge densities can be derived by taking the divergence of Eqs. (2.62) and (2.68). Bearing in mind that the surface density included in  $\Delta \cdot \mathbf{V}$  is equal to  $\mathbf{n} \cdot (\mathbf{V}_+ - \mathbf{V}_-)$ , with  $\mathbf{V}_+ - \mathbf{V}_-$  being the jump of  $\mathbf{V}$  in the direction of  $\mathbf{n}$  across the interface [29], it comes out that:

$$\rho_c = \mathbf{n} \cdot (\mathbf{D}_+ - \mathbf{D}_-) \tag{2.79}$$

$$\rho_t = \varepsilon_0 \mathbf{n} \cdot (\mathbf{E}_+ - \mathbf{E}_-) \,, \tag{2.80}$$

with  $\rho_c$  and  $\rho_t$  being the surface densities of free and total charges.

#### References

1. R.W. Wood, On a remarkable case of uneven distribution of light in a diffraction grating spectrum. Philos. Mag. 4, 396–402 (1902)

- Lord Rayleigh, Note on the remarkable case of diffraction spectra described by Prof. Wood. Philos. Mag. 14, 60–65 (1907)
- 3. Lord Rayleigh, On the dynamical theory of gratings. Proc. R. Soc. Lond. 79, 399–416 (1907)
- J. Strong, Effect of evaporated films on energy distribution in grating spectra. Phys. Rev. 49, 291–296 (1936)
- U. Fano, The theory of anomalous diffraction gratings and of quasi-stationary waves on metallic surfaces (Sommerfeld's waves). J. Opt. Soc. Am. 31, 213–222 (1941)
- A. Hessel, A.A. Oliner, A new theory of Wood's anomalies on optical gratings. Appl. Opt. 4, 1275–1297 (1965)
- 7. C.H. Palmer Jr., Parallel diffraction grating anomalies. J. Opt. Soc. Am. 42, 269–276 (1952)
- 8. C.H. Palmer Jr., Diffraction grating anomalies, II, coarse gratings. J. Opt. Soc. Am. **46**, 50–53 (1956)
- 9. J.E. Stewart, W.S. Gallaway, Diffraction anomalies in grating spectrophotometers. Appl. Opt. 1, 421–429 (1962)
- 10. D. Rudolph, G. Schmahl, Spektroscopische beugungsgitter hoher teilungsgenauigkeit erzeugt mit Hilfe von Laserlicht und photoresistschichten. Optik **30**, 475–487 (1970)
- D. Maystre, Sur la diffraction d'une onde plane par un réseau métallique de conductivité finie.
   Opt. Commun. 6, 50–54 (1972)
- D. Maystre, Sur la diffraction d'une onde plane électromagnétique par un réseau métallique. Opt. Commun. 8, 216–219 (1973)
- R. Petit, Etude numérique de la diffraction par un réseau. C. R. Acad. Sci. Paris 260, 4454–4457 (1965)
- R. Petit, Contribution à l'étude de la diffraction par un réseau métallique. Rev. Opt. 45, 249– 276 (1966)
- A. Wirgin, Considérations théoriques sur la diffraction par réflexion sur des surfaces, quasiment planes, applications à la diffraction par des réseaux, C. R. Acad. Sci. Paris 259, 1486– 1488 (1964)
- 16. A. Wirgin, Théorie électromagnétique de la diffraction d'une onde par une surface quasiment plane, Thèse d'Etat, Université de Paris, France, 1967
- J. Pavageau, J. Bousquet, Diffraction par un réseau conducteur nouvelle méthode de résolution.
   Opt. Acta 17, 469–478 (1970)
- R. Petit, D. Maystre, M. Nevière, Practical applications of the electromagnetic theory of gratings, Space Optics, in *Proceedings of the Ninth International Congress of Optics*, 1974, vol. 2, pp. 667–681
- J.L. Uretsky, The scattering of plane waves from periodic surfaces. Ann. Phys. 33, 400–427 (1965)
- D. Maystre, R.C. Mc Phedran, Le théorème de réciprocité pour les réseaux de conductivite finie: demonstration et applications. Opt. Commun. 12, 164–167 (1974)
- D. Maystre, Sur la diffraction et l'absorption par les réseaux utilisés dans l'infrarouge, le visible et l'ultraviolet; applications à la spectroscopie et au filtrage des ondes électromagnétiques, Thèse d'Etat, Université d'Aix-Marseille, 1974
- 22. R.C. McPhedran, M.D. Waterworth, Properties of diffraction grating anomalies. Opt. Acta **20**, 533–547 (1973)
- 23. M.C. Hutley, An experimental study of the anomalies of sinusoidal diffraction gratings. Opt. Acta 20, 607–624 (1973)
- M.C. Hutley, V.M. Bird, A detailed experimental study of the anomalies of a sinusoidal diffraction grating. Opt. Acta 20, 771–782 (1973)
- 25. R.C. McPhedran, D. Maystre, A detailed theoretical study of the anomalies of a sinusoidal diffraction grating. Opt. Acta 21, 413–421 (1974)

- R.C. McPhedran, D. Maystre, Theoretical study of the diffraction anomalies of holographic gratings. Nouv. Rev. Opt. 5, 241–248 (1974)
- 27. R.C. McPhedran, D. Maystre, Inadequacy of perfect reflectivity model for holographic gratings even in the visible region. J. Spectrosc. Soc. Jpn. 23 (suppl. Number 1) 13–20 (1974)
- M.C. Hutley, J.P. Verrill, R.C. McPhedran, M. Nevière, P. Vincent, Presentation and verification of a differential formulation for the diffraction by conducting gratings. Nouv. Rev. Opt. 6, 87–95 (1975)
- R. Petit (ed.), Electromagnetic Theory of Gratings. Topics in Current Physics (Springer, Berlin, 1980)
- 30. D. Maystre, General study of grating anomalies from electromagnetic surface modes, in *Electromagnetic Surface Modes*, ed. by A.D. Boardmanm (Wiley, New York, 1982)
- 31. R.H. Ritchie, Plasma losses by fast electrons in thin films. Phys. Rev. 106, 874–881 (1957)
- R.H. Ritchie, E.T. Arakawa, J.J. Cowan, R.N. Hamm, Surface-plasmon resonance effect in grating diffraction. Phys. Rev. Lett. 21, 1530–1533 (1968)
- J.J. Cowan, E.T. Arakawa, Dispersion of surface plasmons in dielectric-metal coating on concave diffraction gratings. Z. Phys. 235, 97–109 (1970)
- J.J. Cowan, E.T. Arakawa, Artificial polarization anomalies from holographic gratings. Opt. Commun. 21, 428–431 (1977)
- H. Raether, in Surface Plasmons on Smooth and Rough Surfaces and on Gratings. Springer Tracts in Modern Physics, vol. 111 (Springer, New York, 1988)
- I. Pockrand, Reflection of light from periodically corrugated silver films near the plasma frequency. Phys. Lett. 49A, 259–260 (1974)
- 37. I. Pockrand, Coupling of surface plasma oscillations in thin periodically corrugated silver films. Opt. Commun. 13, 311–313 (1975)
- 38. H. Raether, On the influence of roughness on the optical properties of surfaces: plasma resonance emission and the plasmon dispersion relation. Thin Solid Films **28**, 119–124 (1975)
- 39. R. Orlowski, H. Raether, The total reflection of light at smooth and rough silver films and surface plasmons. Surf. Sci. **54**, 303–308 (1975)
- I. Pockrand, H. Raether, Surface plasma-oscillations in silver films with wavy surface profiles—quantitative experimental study. Opt. Commun. 18, 395–399 (1976)
- I. Pockrand, Resonance anomalies in light intensity reflected at silver gratings with dielectric coatings. J. Phys. D Appl. Phys. 9, 2423–2432 (1976)
- 42. E. Kröger, E. Kretschmann, Surface plasmon and polariton dispersion at rough boundaries. Phys. Status Solid. B **76**, 515–523 (1976)
- I. Pockrand, H. Raether, Surface plasma oscillations at sinusoidal silver surfaces. Appl. Opt. 16, 1784–1786 (1977)
- C.J. Powell, J.B. Swan, Origin of the characteristic electron energy losses in aluminium. Phys. Rev. 115, 869–875 (1959)
- 45. D. Maystre, Rigorous vector theories of diffraction gratings, in *Progress in Optics*, vol. 21, ed. by E. Wolf (North-Holland, Amsterdam, 1984), pp. 1–67
- E. Popov, L. Tsonev, D. Maystre, Losses of plasmon surface wave on metallic grating. J. Mod. Opt. 37, 379–387 (1990)
- 47. E.C. Titchmarsh, *The Theory of Functions*, 2nd edn. (Oxford University Press, London, 1939)
- 48. P.M. Morse, H. Feshbach, Derivatives of analytic functions, in *Methods of Theoretical Physics*, Taylor and Laurent Series, Part I (McGraw-Hill, New York, 1953), pp. 374–398
- D. Maystre, R. Petit, Brewster incidence for metallic gratings. Opt. Commun. 17, 196–200 (1976)
- 50. M.C. Hutley, D. Maystre, The total absorption of light by a diffraction grating. Opt. Commun. **19**, 431–436 (1976)
- J. Le Perchec, P. Quemerais, A. Barbara, T. Lopez-Rios, Why metallic surfaces with grooves a few nanometers deep and wide may strongly absorb visible light. Phys. Rev. Lett. 100, 066408 (2008)
- D.C. Cullen, C.R. Lowe, A direct surface plasmon-polariton immunosensor: preliminary investigation of the non-specific adsorption of serum components to the sensor surface. Sens. Actuators B 1, 576–579 (1990)

82

 M. Nevière, R. Reinisch, Electromagnetic study of the surface-plasmon-resonance contribution to surface-enhanced Raman scattering. Phys. Rev. B 26, 5403–5408 (1982)

- R. Reinisch, M. Nevière, Electromagnetic theory of diffraction in nonlinear optics and surface enhanced nonlinear optical effects. Phys. Rev. 28, 1870–1885 (1983)
- 55. G.H. Derrick, R.C. McPhedran, D. Maystre, M. Nevière, Crossed gratings: a theory and its applications. Appl. Phys. **18**, 39–52 (1979)
- T.V. Teperik, F.J. García De Abajo, A.G. Borisov, M. Abdelsalam, P.N. Bartlett, Y. Sugawara,
   J.J. Baumberg, Omnidirectional absorption in nanostructured metal surface. Nat. Photonics
   2, 299–301 (2008)
- E.L. Wood, J.R. Sambles, N.P. Cotter, S.C. Kitson, Diffraction grating characterization using multiplewavelength excitation of surface-plasmon polaritons. J. Mod. Opt. 42, 1343–1349 (1995)
- 58. F. Pincemin, J.-J. Greffet, J.-J. Greffet, Propagation and localization of a surface plasmon polariton on a finite grating. J. Opt. Soc. Am. B 13, 1499–1509 (1996)
- W.L. Barnes, S.C. Kitson, T.W. Preist, J.R. Sambles, Photonic surfaces for surface-plasmon polaritons. J. Opt. Soc. Am. A 14, 1654–1661 (1997)
- T. López-Rios, D. Mendoza, F.J. Garcia-Vidal, J. Sánchez-Dehesa, B. Pannetier, Surface shape resonances in lamellar metallic gratings. Phys. Rev. Lett. 81, 665–668 (1998)
- F.J. Garcia-Vidal, J. Sánchez-Dehesa, A. Dechelette, E. Bustarret, T. López-Rios, T. Fournier,
   B. Pannetier, Localized surface plasmons in lamellar metallic gratings. J. Lightwave Technol.
   17, 2191–2195 (1999)
- W.-C. Tan, T.W. Preist, J.R. Sambles, N.P. Wanstall, Flat surface-plasmon-polariton bands and resonant optical absorption on short-pitch metal gratings. Phys. Rev. B 59, 12661–12666 (1999)
- 63. E.A. Smith, R.M. Corn, Surface plasmon resonance imaging as a tool to monitor biomolecular interactions in an array based format. Appl. Spectrosc. **57**, 320A–332A (2003)
- 64. R. Hooper, J.R. Sambles, Surface plasmon polaritons on narrow-ridged short-pitch metal gratings in the conical mount. J. Opt. Soc. Am. 20, 836–843 (2003)
- 65. S.F. Cheng, L.K. Chau, Colloidal gold modified optical fiber for chemical and biochemical sensing. Anal. Chem. **75**, 16–21 (2003)
- E. Hutter, J. Fendler, Exploitation of localized surface plasmon resonance. Adv. Mater. 16(19), 1685–1706 (2004)
- 67. S. Collin, F. Pardo, R. Teissier, J.L. Pelouard, Efficient light absorption in metal-semiconductor-metal nanostructures. Appl. Phys. Lett. **85**, 194–196 (2004)
- 68. K. Aslan, J.R. Lakowicz, C. Geddes, Plasmon light scattering in biology and medicine: new sensing approaches, visions and perspectives. Curr. Opin. Chem. Biol. 9, 538–544 (2005)
- 69. J.N. Gollub, D.R. Smith, D.C. Vier, T. Perram, J.J. Mock, Phys. Rev. B 71, 195402 (2005)
- 70. L.K. Chau, Y.F. Lin, S.F. Cheng, T.J. Lin, Fiber-optic chemical and biochemical probes based on localized surface plasmon resonance. Sens. Actuators B **113**, 100–105 (2006)
- E. Popov, N. Bonod, S. Enoch, Non-Bloch plasmonic stop-band in real-metal gratings. Opt. Express 10, 6241–6250 (2007)
- E. Popov, N. Bonod, S. Enoch, Comparison of plasmon surface waves on shallow and deep metallic 1D and 2D gratings. Opt. Express 15, 4224

  4237 (2007)
- 73. N. Bonod, E. Popov, L. Li, B. Chernov, Unidirectional excitation of surface plasmon by slanted grating. Opt. Express 18, 11427–11432 (2007)
- M. Guizar-Sicairos, J.C. Gutierrez-Vega, Propagation of Helmholtz-Gauss beams in absorbing and gain media. J. Opt. Soc. Am. 23, 1994–2001 (2006)
- E.G. Loewen, M. Nevière, Dielectric coated gratings—curious property. Appl. Opt. 16, 3009–3011 (1977)
- D. Maystre, M. Nevière, P. Vincent, General theory of anomalies and energy absorption by diffraction gratings and their relation with surface waves. Opt. Acta 25, 905–915 (1978)
- M. Nevière, D. Maystre, G.H. Derrick, R.C. McPhedran, M.C. Hutley, On the total absorption of unpolarized monochromatic light, in *Proceedings of I.C.O.XI Conference*, Madrid, Spain, 1978, pp. 609–612

- 78. E. Popov, D. Maystre, R.C. McPhedran, M. Nevière, M.C. Hutley, G.H. Derrick, Total absorption of unpolarized light by crossed gratings. Opt. Express 16, 6146–6155 (2008)
- N. Bonod, G. Tayeb, D. Maystre, S. Enoch, E. Popov, Total absorption of light by lamellar metallic gratings. Opt. Express 16, 15431–15438 (2008)

# Chapter 3

# A New Look at Grating Theories Through the Extraordinary Optical Transmission Phenomenon

Philippe Lalanne and Haitao Liu

**Abstract** The electromagnetic properties of subwavelength metallic surfaces are due to two kinds of elementary distinct waves: the famous surface plasmon polariton and the quasi-cylindrical wave, which are both scattered by the subwavelength indentations as they propagate on the metal. The ab initio microscopic description of the electromagnetic properties starting from the sole knowledge of the elementary waves launched in between the indentation has a long history in grating theories. We review the evolution of the ideas and the fundamental principles that govern these waves and their impacts. For the sake of illustration, the emblematic case of a metal surface perforated by a subwavelength-hole array, which exhibits remarkable transmission properties, is taken to illustrate our purpose.

#### 3.1 Introduction

Squeezing light into small volumes is an important and long-standing challenge in optics, with potential impact in many fields of nanosciences and nanotechnologies. The phenomenon of extraordinary optical transmission (EOT), whose first observation was published 12 years ago, is an emblematic phenomenon of light confinement.

The EOT was first observed in the near-infrared in subwavelength-hole arrays perforated in opaque gold and silver films [1]. Figure 3.1a presents a typical EOT

P. Lalanne (⊠)

Laboratoire Charles Fabry de l'Institut d'Optique, CNRS, Univ Paris-Sud Campus Polytechnique, 91127 Palaiseau cedex, France

e-mail: philippe.lalanne@institutoptique.fr

H. Liu

Key Laboratory of Opto-electronic Information Science and Technology, Ministry of Education, Institute of Modern Optics, Nankai University, 300071 Tianjin, China 86 P. Lalanne and H. Liu

transmission spectrum characterized by a Fano shape (red curve) with the presence of a minimum (blue arrow) followed by a peak (green arrow) at longer wavelengths. Although it corresponds to a transmission efficiency of a few percent, the peak has been called extraordinary transmission, simply because conventional theory for light transmission through a single subwavelength hole in a thin [2] or thick [3] perfectly conducting film predicts a transmission normalized to the hole area that is substantially less than unity.

Comparing experimental observations obtained with noble metals in the visible or near-infrared with theoretical results valid for perfectly conducting screen is not legitimate (see for instance the related discussion on spectroscopic gratings in chapters by Daniel Maystre), and rapidly experimentalists have compared the transmission of the array to that of a single hole perforated in the same film with the same diameter as that of the array. It is found that, on spectral averaging, the averaged transmissions are almost identical. However, for the peak wavelength, the transmission of the array is 40–100 [5] times larger than that of the isolated hole, depending on the hole diameter. It is nowadays known that this ratio increases as the hole diameter decreases.

Figure 3.1b shows computational results of the near-field, in the vicinity of the irradiated interface, for the resonance peak wavelength. The background image corresponds to the magnitude of the magnetic field component perpendicular to the picture. The magnetic field of the normally incident plane wave is parallel to this direction too. Superimposed on the image, we show the Poynting vector, represented by white arrows that indicate the direction and magnitude of the energy flow. At resonance, it appears that the surface acts as a light funnel that helps the holes to efficiently capture the incident energy beyond their geometrical apertures. This funneling effect alone is not new, as it was observed with frequency selective surfaces in microwave and millimeter-wave engineering for instance well before the EOT was first observed. What is new is the fact that the funneling is accompanied by an efficient transmission in a regime for which all the holes are much smaller than the wavelength and support only evanescent modes. It appears possible to efficiently confine light in a tiny volume, and apparently the surface waves excited around the holes help a lot.

The discovery of the EOT phenomenon sparked a huge volume of research trying to apply this phenomenon [6–8] and to unveil the underlying mechanisms.

How do we understand that for one specific wavelength, no light goes through, while for some others a slightly different one, a surprisingly high amount of light is transmitted through an aperture operating below cutoff? What are the surface waves that are locally excited between the holes and that are responsible for the funneling effect of Fig. 3.1b? Are they surface plasmon polaritons (SPPs) as suggested in [1]? In 1998 when the EOT was discovered, the theory of diffraction by metallic gratings, mainly developed for designing spectroscopic gratings, was mature and the research activity in the domain was mostly dedicated to increasing the efficiency of numerical methods, rather than deriving new concepts or revisiting the fundamentals, see Chaps. 1 and 2. Therefore one may wonder why the interpretation of the EOT has motivated so much effort.

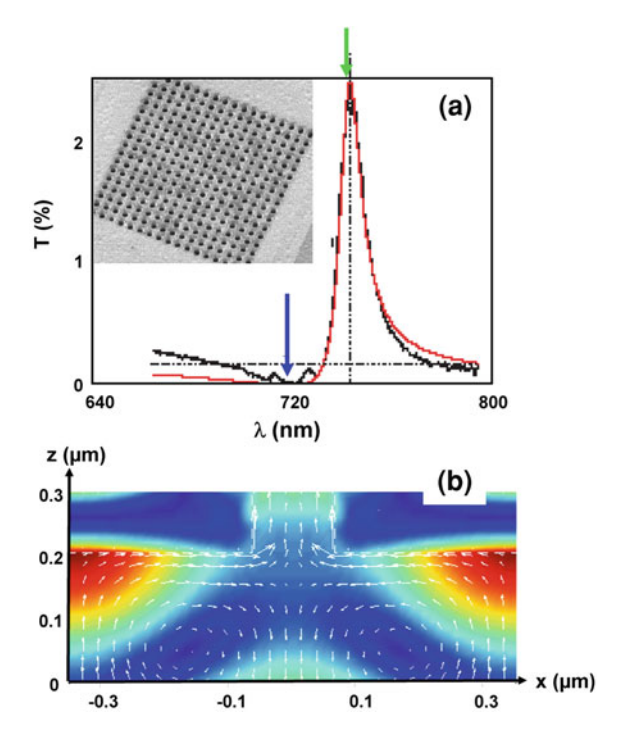


**Fig. 3.1** The EOT phenomenon. **a** Transmission data taken from [4] and obtained for a normally incident plane wave illuminating a 200 nm thick gold (Au) film perforated with a 700 nm-period square lattice of 70 nm radius holes (hole filling fraction 3%). The minimum and maximum transmissions are indicated by the blue and green arrows, respectively. (**b**) Magnetic near-field distribution (H<sub>y</sub>) and Poynting vector (*white arrows*) calculated for the resonance wavelength [*green arrow* in (**a**)] under illumination by a plane wave that is polarized along the *x*-axis and that is incident from the bottom with its wave vector parallel to the *z*-axis

In this chapter, we provide a comprehensive review of theoretical works aimed at providing a response to those questions. We are not exhaustive; we rather aim at providing guidelines, starting from the initial interpretation in [1] that attributed the EOT to the excitation of SPPs, and then analyzing the impact of grating theories [9] on our understanding of the EOT. We further discuss their limitations, before summarizing the main conclusions obtained by a microscopic model of the EOT [10].

# 3.2 The Initial Microscopic Interpretation of Wood's Anomaly

The EOT phenomenon, with its minima followed by a resonance peak, is essentially a Wood's anomaly. It is therefore important to start our discussion by considering the

P. Lalanne and H. Liu

pioneer works that have contributed to explaining the polarization-dependent Wood's anomalies discovered at the beginning of the twentieth century. In particular, we will consider Fano's work. In his seminal article published in 1941 (40 years after Wood's observation) [11], Fano first revisits the initial explanation proposed by Rayleigh [12] to explain Wood's anomalies in terms of the vectorial Huygens principle, recalling that the Rayleigh interpretation considers that (Fig. 3.2)

"each groove A of the grating acts as a center of diffusion of the incident light and hence scatters a spherical (probably Fano intended to say cylindrical) wave" and that "the part of the scattered wave travelling along the grating reaches the neighboring groove B in phase with the incident light."

This purely geometrical phase condition (Fig. 3.2) corresponds to the existence of a diffracted wave at grazing emergence, and can be written as  $k_0 = k_x + k_R$  (Rayleigh condition), where the free-space wave number  $k_0$  is matched to the parallel wave vector  $k_x$  of the incident plane wave through a wave vector  $k_R$  of the 1D reciprocal lattice associated to the grating.

To further explain why the anomaly in Wood's experiments is red-shifted from the Rayleigh condition and why it depends on the grating geometry, Fano retains a similar Huygens-type interpretation, but instead of considering a pure geometrical representation, he rather suggests that a surface mode with a parallel momentum greater than the free-space momentum be involved in the energy transport between adjacent grooves. It is retrospectively interesting and amazing to see how the SPP of the flat interface is intuitively introduced in Fano's work by considering Sommerfeld's waves (SPPs were discovered later on by Ritchie [13]) to explain the surface resonance of reflection gratings. Fano first considers the parallel propagation constants (called proper values in [11]) of the modes of a glass plate sandwiched between a metal and a vacuum and asks himself "Is there left any mode when the thickness of the glass layer vanishes?", before answering:

"One and only one proper value exists and this only if the wave is polarized with its magnetic vector parallel to the interface" ... "The proper value  $\chi$  is always slightly larger than the modulus  $k_0=1/\lambda$  of the momentum in vacuum" and "is no longer real and will be indicated by  $\chi+i\gamma$  where  $\gamma$  represents the damping". "The damping is always small for metals with large negative values of  $\varepsilon$ ; although heat production is proportional to the "conductivity"  $\sigma$ , increasing  $\sigma$  at constant  $\varepsilon$  has the effect of expelling the wave from the metal and of increasing the fraction of the time spent by the radiation outside the metal."

Fano's conclusion is clear: Wood anomaly takes its essence from a phenomenon, "which is analogous to the resonance of a mechanical oscillating system excited with its proper frequency", provided that the tangential parallel momentum of the incident wave augmented by a multiple of the grating wave-vector modulus "approaches the proper value". Denoting by  $k_{\rm SP}$  (surprisingly Fano does not give any analytical expression) the complex proper value and assuming that the grooves are infinitely small and thus neglecting multiple scattering (Fig. 3.2), the microscopic interpretation by Fano leads to the following phase-matching condition:

$$Re(k_{SP}) = k_x + k_R. \tag{3.1}$$

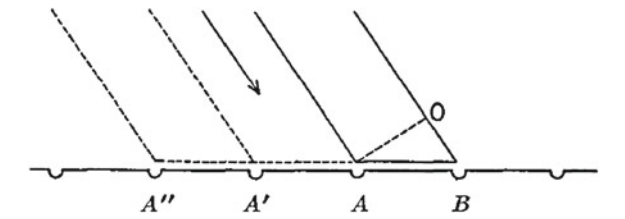


Fig. 3.2 Geometrical representation of Rayleigh's and Fano's anomaly conditions (from [11]). Rayleigh's condition requires that the part of the wave (scattered by groove A) traveling along the grating with the vacuum phase velocity reaches the neighboring groove B in phase with the incident wave and with the waves scattered by the grooves A', A''. . . This explains the so-called Rayleigh anomaly that occurs whenever a diffracted wave emerges at grazing incidence. What Fano proposes to explain the red-shifted Wood anomaly is to replace the free-space grazing wave of Rayleigh by a bounded mode (Fano calls this "superficial wave" in relation with the work performed by Sommerfeld on radio waves progressing on the surface of the earth) with a smaller phase velocity. This bounded mode is nothing else but the SPP of the flat metallic surface, which will be discovered 16 years after by Richie

This condition is very close to the Rayleigh condition, the difference lying in the fact that  $k_0$  is replaced by  $\operatorname{Re}(k_{\rm sp})$ . The theoretical works that followed Fano's one and that contributed to establishing the electromagnetic theory of gratings have mainly consisted in developing a theoretical and computational framework for quantitatively predicting the exact location and shape of grating anomalies through a study of the surface leaky mode of the interface dressed by periodic indentations. A pioneer article by Hessel and Oliner [14] has been followed by an impressive series of works summarized in [9, 15, 16] and in Chaps. 1 and 2 by Maystre, which contributed to the systematic development of a phenomenological study of grating anomalies through the poles (the surface leaky modes) and zeros of the scattering operator.

# 3.3 Why Question the Initial Plasmonic Interpretation?

An important observation of the initial report [1] of the EOT was the clear spectral dependence of the transmission minima and maxima on lattice period. The positions of the minima and maxima essentially exhibit a linear dependence on the lattice period and follow the phase-matching condition of Eq. (3.1). This observation immediately prompted the authors in [1] to suggest that SPPs are deeply involved in the EOT. In view of the previous considerations, the SPP interpretation of the EOT seems so convincing and so natural that it might even appear surprising that one may even question it. Trying to explain why the interpretation has been questioned is difficult; nevertheless, let us attempt to give some insights.

90 P. Lalanne and H. Liu

#### 3.3.1 Modern Grating Theory and Local Surface Waves

There is a large conceptual distance between our naïve (but intuitive) representation mainly used by experimentalists of the EOT phenomenon and the conceptual tools handled by the modern theory of the electromagnetic diffraction by gratings.

Immediately following the discovery, the EOT has sparked an intense activity aiming at designing new devices exploiting the phenomenon. Most often, the design relies on a microscopic model that is well suited and easy to handle in various situations. By microscopic model (the word was already employed in relation with Fano's interpretation of Wood's anomaly in the previous section), we intend to mean a representation in which the local elementary waves that are scattered by every individual hole (or groove) are at the core of the conceptual representation, like in the pioneer theoretical work by Lord Rayleigh for perfectly conducting gratings or in Fano's formalism. These waves are assumed to be initially launched on the surface by illuminated holes, to further interact with the adjacent holes before being eventually radiated back into free space. A famous example is the Bull-eye [17], a structure consisting of a through hole placed in the middle of a large array of blind holes. When designing the Bull-eye, researchers essentially look at optimizing the structure such that all the SPPs launched by the blind holes interfere constructively so that they maximally couple into the through hole. Elementary (microscopic) scattering coefficients such as the coupling coefficients between SPPs and modes in the blind or through holes are therefore at the heart of the conceptual representation. The latter are exactly those used by Rayleigh and Fano, when considering that each groove of the grating acts as a center of diffusion of the incident light and hence scatters a surface wave (a grazing plane wave for Rayleigh and an SPP for Fano) travelling on the grating surface, reaching the neighboring groove in phase with the incident light.

Unfortunately, with the exception of multiple scattering theories [18] developed in the 1950s for certain specific classes of gratings with relatively shallow groove depths, the microscopic representation has never been explicitly formalized in following works; the modern theory of grating diffraction [9, 14–16] mainly considers "macroscopic quantities" attached to the full periodicity, in particular the plane-wave (or Rayleigh) expansion in the uniform air half space below and above the grating. We can see that there is a large conceptual distance between the microscopic elementary waves that are locally launched by every individual groove or hole and the set of macroscopic plane waves that are scattered eventually at grazing incidence and that are used to numerically expand the field in air, a representation especially appropriate for analysing the far field waves.

# 3.3.2 Perfectly-Conducting Case

Initial theoretical works based on classical grating theories do not convincingly provide a comprehensive overview of the EOT and in particular cannot discuss what

is the actual nature of the elementary waves that are at work between the holes and that are responsible for the EOT.

The conceptual distance has embarrassed theoreticians who intended to discuss the role of SPPs in the EOT using classical grating theories in the early 2000s. Initial works have all considered modal methods, and have either numerically or analytically with approximations calculated the transmission spectra (initially mainly for slit arrays) for various geometrical parameters, such as the grating depth, the incident angle of the illuminating plane wave, the slit width... The results have shown that the transmission is weakly dependent on the metal conductivity and have predicted the EOT for various spectral ranges (visible, near-infrared...) [19-23], and even for perfectly conducting metals, a prediction that has been further confirmed by experimental results obtained at THz and microwave frequencies where metals are excellent conductors. At those low frequencies, there is strictly speaking no SPP but there exists an SPP-like mode with a pronounced photonic character (see discussion in Chaps. 2 and 3). This mode (it would be a plane wave for perfect metal) is highly delocalized in the air cladding (the normalized penetration depth  $\delta/\lambda$  in air scales as the metal refractive index,  $\delta/\lambda \propto |\varepsilon_m|^{1/2} \varepsilon_d$ ,  $\varepsilon_m$ , and  $\varepsilon_d$  being the relative permittivities of the metal and of the air, respectively), and it is difficult to accept that such nearly unbounded modes would be efficiently excited by subwavelength apertures. The fact that similar responses are observed in the visible and in the far-infrared is really puzzling and has been overlooked in the literature. For instance, trying to connect his work on the existence of a surface mode with Rayleigh's theoretical work [12] assuming perfect conductors, even Fano overlooked the difficulty [11],

"Increasing the conductivity of the metal makes the resonance phenomenon sharper and sharper because the damping  $\gamma$  vanishes; at the same time  $\chi$  approaches  $k_0$ . Rayleigh studied only the limiting case of a perfectly reflecting metal, in which the superficial wave is completely expelled from the metal and becomes a regular plane wave in vacuum grazing the surface of the metal."

As shown below, the transmission in the long wavelength regime is no longer due to the SPP-like mode, simply because this mode is expelled out of the metal far away in the dielectric cladding and cannot be excited with a dipole source localized on the surface [24].

In addition, other theoretical studies performed for composite (hypothetical) gratings whose horizontal surface is composed of a conductor with a conductivity (that may be changed at will) have reported that the phase-matching condition of Eq. (3.1), instead of predicting the position of transmission maxima, accurately predicts the exact location of the minima (blue arrow in Fig. 3.1a) and that the presence of a minimum can completely annihilate a transmission peak [23], thus concluding a negative role of SPP on the transmission through slit arrays. Since Eq. (3.1) is only approximate, one should not be surprised that it does not accurately predict the position of the maxima, but despite valuable efforts [25], why Eq. (3.1) predicts the exact location of deep (10<sup>-5</sup> theoretically) transmission minima remains difficult to figure out.

92 P. Lalanne and H. Liu

#### 3.3.3 The Quasi-Cylindrical Wave

Experimental results obtained for slit-hole doublets have evidenced that the field scattered on the surface in the vicinity of a subwavelength aperture is only partly composed of SPPs, even at visible frequencies [26].

In order to provide a definitive answer to the question of the involvement of SPP in the EOT, Lezec and his coworkers have performed a series of experiments, all aiming at measuring the near-field launched by sub- $\lambda$  indentations on a metallic surface. Curiously, before Lezec's works [26], this near-field, despite his importance, has not been considered in the optical literature.

However, the field scattered by sub- $\lambda$  antennas in the vicinity of metallic surfaces has been of long-standing interest in classical electromagnetism, in particular for long-distance radio transmission and for remote sensing. In 1907, Zenneck [27] was the first to analyze a solution to Maxwell's equations in the presence of a planar boundary between free space and a half-space conductor with a finite conductivity (the sea surface for instance) and to show that a bounded "surface mode", the analog of the SPP at optical frequencies in cylindrical coordinate, exists.

Always in the context of long-distance propagation, another more interesting and difficult question arises when considering a point source, such as an oscillating Hertzian vertical electric dipole, located over this conducting plane. Far from the source on the surface, does the field from such a dipole behave like the cylindrical Zenneck wave? This problem was analyzed in detail by Sommerfeld [28, 29], Norton [30, 31], and others. The conclusions were that the radiated field can be calculated as an integral along a contour in the complex plane and is composed of two contributions, the Zenneck mode (corresponding to the pole) and a "direct" wave (corresponding to branch integrals). In an intermediate region and near the surface, the field is well approximated by that of the cylindrical Zenneck wave; but then, as the distance increases further, the long-distance propagation is mainly due to a direct wave that is often referred to as the Norton wave. The latter, whose amplitude asymptotically decays as  $1/r^2$ , overcomes the exponentially-damped Zenneck mode at large distances. These issues are discussed in great detail in the review article by Collin [32] or in the book by Baños [33]. Although it shares many mathematical aspects with the Hertzian problem, the optical problem is rather different since a conductor like seawater does not reflect radio waves as a metal reflects light; its dielectric constant is not negative and therefore there is no total reflection by the conducting surface. More importantly, Lezec and his coworkers were not interested in any long-distance field behavior far away from the "antenna", but in short-distance interactions between indentations. In sub- $\lambda$  metallic surfaces, the distance between two neighboring indentations is of the order of the wavelength, or even smaller, and rarely exceeds  $\approx 10\lambda$ . The conclusions are rather different from the long-distance interaction regime.

The experimental data in [26], which were probably contaminated by an undesired adlayer on the silver film [34], have been interpreted in a confusing manner as shown in [34], but they had the merit to unambiguously reveal the existence and importance

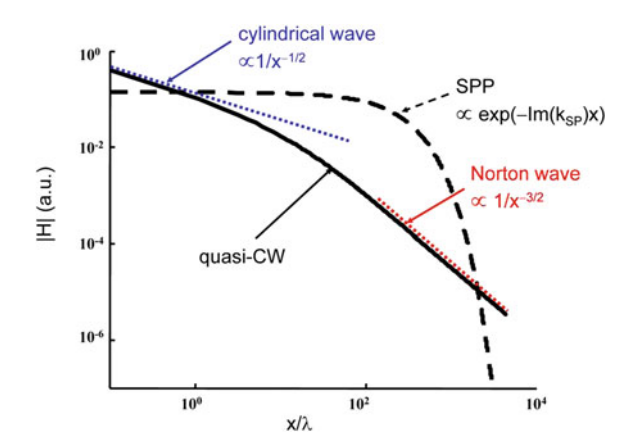


Fig. 3.3 Magnetic field radiated at  $\lambda=1~\mu m$  on an air/gold interface by a line source polarized vertically. The field is composed of an SPP (dashed curve) and of a quasi-CW contribution (solid curve). The latter takes two asymptotic forms. It is very intense and behaves as a cylindrical wave (dotted blue line) with a  $1/x^{1/2}$  decay rate at very small-distance propagation. At very long-distance propagation, it is very weak and decays as  $1/x^{3/2}$ . There the quasi-CW is the analog of the Norton wave (shown with the dotted red line) at optical frequencies

of a direct wave (different from the SPP) that rapidly drops in amplitude within the first few micrometers from the indentation. The properties of this wave have been rapidly studied in further theoretical [24, 34] and experimental [35] works. It has been shown that its amplitude is initially damping as  $x^{-1/2}$  (just as a cylindrical wave) in the vicinity of the indentation, then is dropping at a faster rate for intermediate distances  $\lambda < x < 10\lambda$ , before reaching an asymptotic regime behavior with a  $x^{-3/2}$  damping rate [24, 36, 37]) at large propagation distances.

Figure 3.3 illustrates the different contributions to the magnetic field radiated on an air/gold interface by a line source polarized vertically. The results hold for gold at  $\lambda=1~\mu m~(\varepsilon_m=-46.8+3.5i)$ . The dashed line is the SPP contribution, with an exponential damping  $\exp[-\mathrm{Im}(k_{\rm SP})x]$ , and the solid curve is the "direct" wave contribution. The latter dominates for small propagation distances and behaves as a cylindrical wave (dotted blue line); it can be shown that the initial crossing point between the SPP and the direct wave is located at  $x/\lambda=|\varepsilon_m|/(2\pi\varepsilon_d^{3/2})$  and increases with the metal conductivity [24]. At very large distance propagation, the direct-wave decay rate asymptotically tends to  $1/x^{3/2}$ . It is not unexpected; we find again the analog of the Norton wave for metals (shown with the *dotted red line*) at optical frequencies.

For intermediate distances of interest for sub- $\lambda$  metallic surfaces ( $x > 10\lambda$ ), the direct wave is very different from the Norton wave; it looks like a cylindrical wave, but with a slightly larger decay rate, and has been consistently called a quasicylindrical wave (quasi-CW) in the recent literature. The magnetic field (red curve) of the quasi-CW is illustrated in Fig. 3.4. The results have been obtained for gold at  $\lambda = 1 \,\mu\text{m}$ . Differently from the Norton wave, there is no asymptotic expansion

94 P. Lalanne and H. Liu

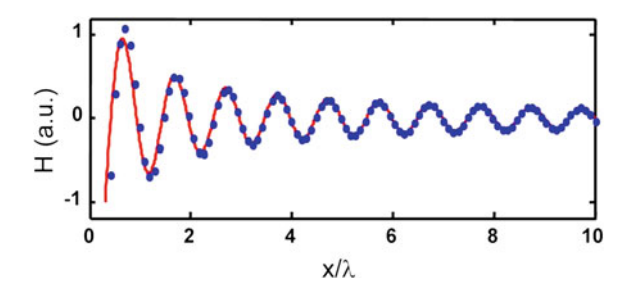


Fig. 3.4 Magnetic field of the quasi-CW radiated at  $\lambda = 1 \,\mu\text{m}$  on an air/gold interface by a line source polarized vertically and located on the surface at x = 0. The *red curve* is directly obtained by solving Maxwell's equations and the *blue dots* are obtained with an expression of the form  $(x/\lambda)^{-m} \exp(ik_0x)$ , with m = 0.8 and with  $k_0$  the free-space wave number

that accurately describes the property of the wave, however as shown by the blue dots, an expression of the form  $(x/\lambda)^{-m}\exp(ik_0x)$ , with m=0.8, can be considered as reasonably accurate. The fitted exponent m depends on the metal and dielectric permittivities; the general trend for noble metals is a decrease of m from  $m \approx 1$  in the visible part of the spectrum to 0.5 at thermal-infrared frequencies [24].

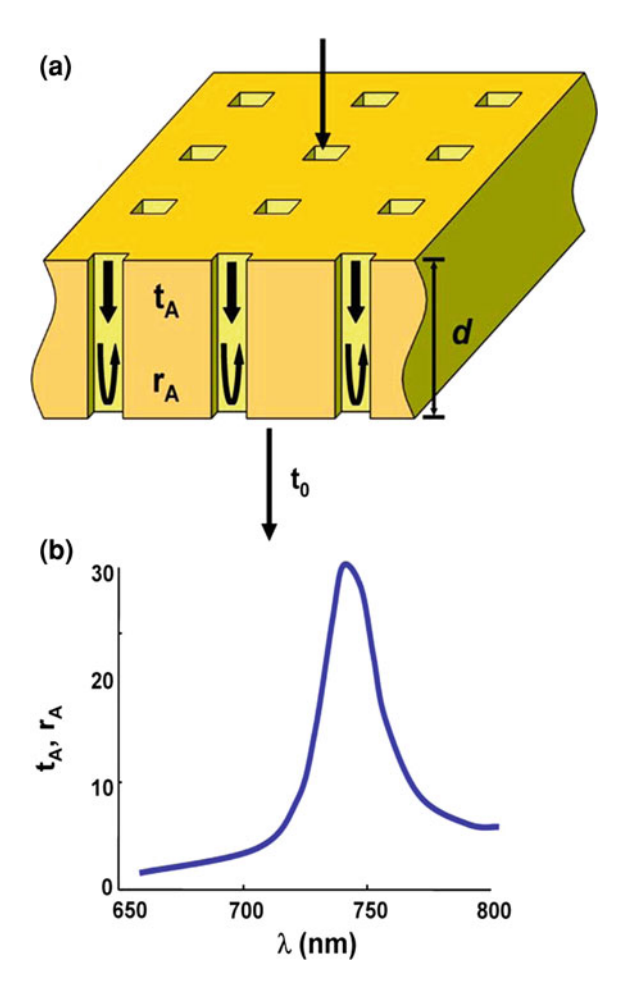
#### 3.4 Explaining the EOT with Grating Theories

For a detailed review of theoretical works on the EOT, the interested reader may refer to [38]. Hereafter, we briefly summarize a few selected contributions, which together provide a satisfactory overview of the concepts involved. The analysis is performed for a self-supported membrane in air for the sake of simplicity (the upper and lower grating interfaces are identical, see Fig. 3.5a). It essentially aims at explaining what is learnt from grating theories and what is not.

The first theoretical calculations [39] of the EOT were performed with the Rigorous Coupled Wave Analysis (RCWA), a modal method often used for analyzing the diffraction by gratings. The authors showed that the transmission is essentially driven by a single Bloch mode of the 2D hole array (the supermode formed by the coherent superposition of all the fundamental modes of every individual hole modes), and computed data closely matched with the initial observations. That first analysis was further refined by computing the poles and the zeros of the scattering operator relating the incident and scattered plane waves of the perforated membrane [39], and it was shown that the zero-order transmission coefficient  $t_0$  of the membrane can be well fitted with a phenomenological Fano line shape,

$$t_0 = c(\lambda - \lambda^Z)/(\lambda - \lambda^P), \tag{3.2}$$

Fig. 3.5 Tunneling effect interpretation (from [40]). a Self-supported geometry in air considered in this work for the sake of simplicity. The transmission coefficient of the membrane (between the incident plane wave and the (0,0)th-order transmitted plane wave) is denoted by  $t_0$ . Similarly we denote by  $t_A$ and  $r_A$  the transmission and reflection coefficients of the fundamental Bloch mode supported by the 2D hole array. The membrane thickness is denoted by d. b Sketch of the spectra of the scattering coefficients, which resonate for a wavelength that corresponds to the transmission peak in Fig. 3.1a (green arrow)



where c is a constant which does not depend on the wavelength, and  $\lambda^Z$  and  $\lambda^P$  are two complex numbers that were calculated numerically using the RCWA. Such a phenomenological expression (see Chaps. 1 and 2) is very accurate; the red curve in Fig. 3.1a shows an example of a fit with a Fano line shape.

Immediately following that first analysis, and exploiting the fact that the transmission is governed by a single Bloch mode of the 2D hole array, Martin-Moreno et al. [40] proposed a simplified modal analysis. Assuming that the light transport between the upper and lower interfaces is solely due to the fundamental evanescent Bloch mode of the hole array, they derive a Fabry–Perot-like formula for the transmission coefficient  $t_0$  of the membrane

$$t_0 = \frac{t_A^2 \exp(ik_0 nd)}{1 - r_A^2 \exp(i2k_0 nd)},$$
(3.3)

96 P. Lalanne and H. Liu

where  $t_A$  and  $r_A$  (Fig. 3.5a) are the transmission and reflection coefficients associated to the coupling of the incident plane wave with the fundamental hole-array Bloch mode and to the reflection of this mode on the bottom or top interface.

Because the holes are tiny, the fundamental Bloch mode of the 2D array is evanescent and its normalized propagation constant  $n = k_z/k_0$  is a complex number with a large imaginary part. Thus the exponential terms in Eq. (3.3) are small quantities: The energy transfer is essentially a tunneling effect. One of the main merits of the single-Bloch-mode approximation is to reveal that all the scattering coefficients associated to a single isolated interface (between a homogenous half-space and a metal substrate perforated by infinitely deep holes) have a Lorentzian shape (Fig. 3.5b) and may take values much larger than unity for wavelengths slightly larger than the period a. Mathematically, this implies that the scattering matrix associated to a single interface admits a complex pole, the surface leaky mode of the interface perforated by a 2D hole array. Note that this differs from the previous analysis leading to Eq. (3.2), where the pole and the zero are attached to the whole problem, composed of two interfaces.

What is happening mathematically is that for specific wavelengths and thickness d, the product of  $r_{\rm A}^2$  exp(i2k<sub>0</sub>nd) may be close to unity, so that the real part of the denominator in Eq.(3.3) vanishes. In other words, the tunneling (and therefore basically inefficient) transmission that couples the fields at both sides of the membrane is boosted by surface electromagnetic leaky modes that are resonantly excited at peak transmission. This resonant tunneling mechanism is widely accepted nowadays as playing a major role in the EOT. That physical picture was first derived by assuming surface-impedance boundary conditions in [40]. It has been further corroborated by more sophisticated calculations able to deal with the dielectric response of metals at optical frequencies [41]. The calculations show that, for thick enough membranes, the spectral locations of the transmission maxima are perfectly matched with the leaky mode wave vector  $k_{\rm LM}$  through a wave vector of the 2D reciprocal lattice,

$$Re(k_{LM}) = k_x + k_R. \tag{3.4}$$

The parameters in Eqs. (3.2) or (3.3) all rely on physical quantities that are macroscopic, in the sense that they are defined for the entire periodic structure. For instance, the pole in Eq. (3.2) corresponds to a leaky mode supported by the grating geometry. Similarly the scattering coefficients in Eq. (3.3), the  $t_A$  and  $r_A$ , are related to delocalized and pseudo-periodic quantities.

Although conceptually meaningful, the simplified Fabry–Perot model does not provide a self-consistent description of the EOT. In particular, the Fabry–Perot formula explains the resonance of the transmission  $t_0$  by the resonance of another scattering coefficient  $r_A$ . This is somewhat like shifting the problem: the real cause for the resonance is not explicitly handled. In reality, nothing is known about the actual waves that are launched in between the holes and that are responsible for the EOT. One has to admit that the electromagnetic theory of diffraction by gratings, although really mature by the end of the 1980s, does not allow a fine description of the EOT phenomenon and in particular of the role of SPPs. This is simply because the

theory is very general: only macroscopic or global quantities (such as plane waves or Bloch modes) are considered.

## 3.5 Microscopic SPP Theory

Indeed what is missing is a microscopic analysis, which explicitly considers the local excitation of surface waves in between the holes, their further scattering at nearby holes, their coupling to free space and to the holes themselves. Thinking that way, one would get a microscopic description of light scattered by metallic gratings, a sort of structuring of the initial picture developed by Rayleigh [12] and Fano [11].

At a microscopic level, the basic mechanism enabling the EOT is a coherent diffraction by all the individual holes acting as elementary scatterers. However, it is more convenient to consider isolated 1D arrays of holes (a periodic hole chain with periodicity a in the y-direction, see Fig. 3.5) perforated in a metal substrate as the elementary scatterers.

In order to determine the actual contribution of SPPs to the funneling effect of Fig. 3.1b, one may first build a microscopic pure-SPP model that relies on the assumption that the electromagnetic interaction among the chains is *only* mediated by the SPPs of the flat interfaces between the chains, other contributions due to the quasi-CW being neglected. Then by comparing the predictions of the model with fully vectorial computational results, one may directly determine the role of SPP in the EOT. This is exactly the approach developed in [10].

The elementary scattering events used in the pure-SPP model are shown in Fig. 3.6 for classical diffraction geometries (the *y*-component  $k_y$  of the in-plane wave-vector momentum is zero). Upon interaction with the chain, the SPP modes are partly excited, transmitted, reflected, or scattered into the chain mode and into a continuum of outgoing plane waves. The interaction defines four elementary SPP scattering coefficients. Two coefficients, see Fig. 3.6a, namely the SPP modal reflection and transmission coefficients,  $\rho_{SP}$  and  $\tau_{SP}$ , correspond to in-plane scattering. The other two,  $\alpha_{SP}$  and  $\beta_{SP}$ , correspond to the transformation of the SPPs into aperture modes or radiation waves, and vice versa, and they link the local field on the surface to the far field.

From these elementary SPP scattering coefficients, a coupled-mode model that provides closed-form expressions for the transmittance and reflectance coefficients of the fundamental Bloch mode,  $t_A$  and  $r_A$ , is readily derived [10]. For instance, the reflection coefficient  $r_A$  of the fundamental Bloch mode of the 2D hole array, a very important physical quantity of the EOT phenomenon, can be written

$$r_A = r + \frac{2\alpha_{\rm SP}^2}{u^{-1} - (\rho_{\rm SP} + \tau_{\rm SP})}.$$
 (3.5)

98 P. Lalanne and H. Liu

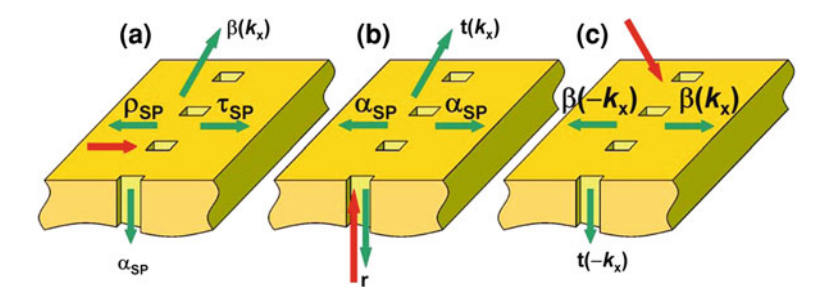


Fig. 3.6 SPP elementary scattering processes involved in the EOT. They are all associated to a single 1D hole chain under illumination by  $\bf a$  the SPP mode,  $\bf b$  the fundamental Bloch mode of the hole chain, and  $\bf c$  an incident TM-polarized (magnetic vector along the chain direction) plane wave impinging at an oblique incidence defined by its in-plane wave-vector component  $k_x$ . The red and green arrows refer to the incident and scattered modes, respectively. The processes in  $(\bf a)$ ,  $(\bf b)$ , and  $(\bf c)$  define six independent elementary scattering coefficients,  $\rho_{\rm SP}$  reflection coefficient of the SPP mode,  $\alpha_{\rm SP}$  (scattering coefficient from the SPP mode to the fundamental Bloch mode and vice versa according to the reciprocity theorem),  $\beta(k_x)$  (scattering coefficient from the SPP mode to the outgoing plane wave with an in-plane wave-vector component  $k_x$  and vice versa),  $t(k_x)$  (scattering coefficient from the fundamental Bloch mode to the plane wave and vice versa), and r (reflection coefficient of the fundamental Bloch mode)

In Eq. (3.5) that holds for normal incidence  $(k_x = 0)$ ,  $u = \exp(ik_{SP}a)$  is the phase delay accumulated by the SPP over a grating period and r is the reflection coefficient of the fundamental mode of the hole chain, see Fig. 3.6b.

It is crucial to realize that the SPP scattering coefficients involved in Eq. (3.5) are not related to the periodicity of the structure. All those coefficients are non-resonant. We are therefore at the heart of the EOT mechanism. Indeed, the essence of Eq. (3.5), and in particular of the denominator that results from a geometric summation over all chain contributions, is a multiple scattering process that involves the excitation of SPP modes by the incident field and further scatterings of the excited SPPs onto the infinite set of periodically spaced chains.

The pure SPP model (by the "pure-SPP model", we intend to emphasize that the electromagnetic interaction among the chains is only mediated by SPPs) shines new light on the resonance-assisted tunneling effect, by proposing an explicit mechanism of the resonance at the upper and lower interfaces of the metal membrane. From Eq. (3.5), the resonance originates from the presence of zeros in the multiple-scattering denominator  $u^{-1} - (\rho_{\rm SP} + \tau_{\rm SP})$ . The latter involves only the two elementary elastic scattering coefficients that are related to the scattering problem shown in Fig. 3.6a. As shown in [10] for tiny holes, the SPP scattering process of Fig. 3.6a is almost energy conservative. Actually  $|\rho_{\rm SP} + \tau_{\rm SP}| \approx |\tau_{\rm SP}|$  is very close to 1, and thus to  $|u^{-1}|$ , which is slightly larger than unity because of the small SPP damping through propagation over the subwavelength period. Thus the denominators of  $r_A$  (and of  $t_A$  [10]) can be made very close to zero, whenever the SPP scattering events of the hole chains constructively interfere for

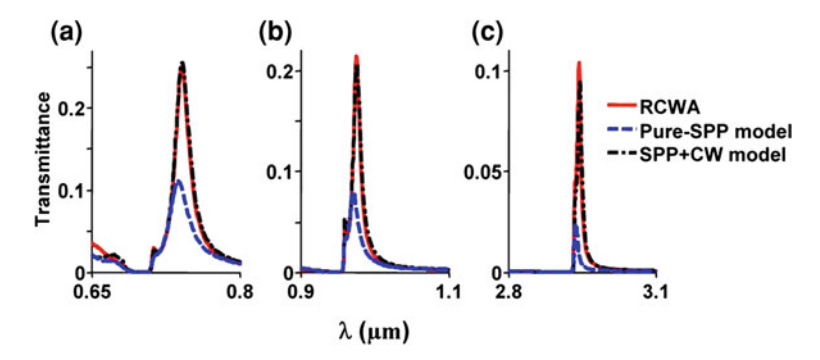


Fig. 3.7 The role of SPPs in the EOT. The *red-solid curves* represent fully-vectorial RCWA data and the blue-dashes are predictions obtained with the pure-SPP model. The *black dash-dot curves* (almost superimposed with the RCWA results) are obtained with a refined microscopic model [42] that takes into account SPPs and quasi-CWs. The data are collected for a gold membrane in air perforated by a periodic array of square holes illuminated by a normally incident plane wave, with the same parameters as in [10]: the hole side length is D = 0.28a (hole filling fraction 8%) and the membrane thickness is d = 0.21a, a being the grating pitch. Three spectral bands are covered, from visible to near-infrared frequencies:  $\mathbf{a} = 0.68 \,\mu\text{m}$ ,  $\mathbf{b} = 0.94 \,\mu\text{m}$ , and  $\mathbf{c} = 0.92 \,\mu\text{m}$ 

Re 
$$(k_{SP})$$
 + arg  $(\tau_{SP})/a = k_x + k_R$ . (3.6)

The phase-matching condition of Eq. (3.6) admits a very simple interpretation. At resonance, the phase shift  $k_x a$  between two plasmons generated by two adjacent hole chains equals the delay  $\text{Re}(k_{\text{SP}})a$  experienced by the plasmon propagating over a single period augmented by a weak retardation arg  $(\tau_{\text{SP}})$  acquired by the plasmon when flying over a single chain. This interpretation is consistent with our intuitive representation of a resonance surface Bloch mode built up from a coherent superposition of many elementary SPPs scattered by individual hole chains that sum up constructively (Fano's argument). For slit arrays, the physics is radically different. Even narrow slits support a propagative mode and SPPs efficiently scatter into this mode. The scattering problem in Fig. 3.6a is no longer energy conservative as the fundamental TEM<sub>0</sub> mode of the slit carries some energy. The modulus of  $\tau_{\text{SP}}$  becomes significantly smaller than one and the upper and lower interfaces no longer resonate.

#### 3.6 The Role of Surface Plasmons in the EOT

The question arises as how much the pure-SPP model may capture the EOT phenomenon. The answer is provided in Fig. 3.7, by comparing the pure-SPP model predictions with fully vectorial computational results obtained with the RCWA. The comparison is performed for three spectral intervals, from the visible ( $a = 0.68 \, \mu m$ ) to the near-infrared ( $a = 2.92 \, \mu m$ ).

100 P. Lalanne and H. Liu

The pure-SPP model quantitatively predicts all the salient features of the EOT, and especially the Fano-type spectral profile with the antiresonance transmission dip followed by the resonance peak. Importantly, there are also some discrepancies that are due to the model assumption of a pure-SPP electromagnetic interaction between the hole chains. As evidenced in Fig. 3.7, the SPPs account for only half of the total transmitted energy at peak transmittance at visible frequencies, and only one-fifth at longer wavelength in the near-infrared. The reason comes from the fact that the total nearby field scattered on the interface by hole chains (or more generally by subwavelength indentations) is not a pure-SPP mode; as discussed in Sect. 3.3, it additionally incorporates the quasi-CW, which creeps along the interface over several wavelength distances, with an initial amplitude damping approximately scaling as  $(1/x)^{1/2}$ . At visible frequencies, the quasi-CW-field decay rate is much faster than the SPP one, but at subwavelength distances  $(x/\lambda \approx 1)$  from the chain (like those encountered in the EOT), the two waves almost equally contribute to the total field. As the wavelength increases, the SPP propagates further and further, but it is also less and less efficiently excited. The quasi-CW excitation does not follow this scaling law; in fact, it can be shown that the quasi-CWs are equally excited at all energies [24, 34]. This well explains the general trend shown in Fig. 3.7: the SPP enrolment in the EOT becomes less and less important as the wavelength increases.

Recently, a refined microcopic model, which incorporates both the SPP and the quasi-CW, has been derived. This has been achieved by defining scattering coefficients for the quasi-CW, including cross-conversion from quasi-CW to SPP and vice-versa. The refined model [42] preserves the intuitive surface-wave progression picture of the pure-SPP model, but in addition it provides quantitative predictions, as shown by the dotted-dashed black curves in Fig. 3.7. The conceptual similarity between the pure-SPP model (aimed at evidencing the role of SPPs) and the improved model (aimed at obtaining accurate predictions) is readily found in the mathematics of the improved model: for instance, the improved expression for the reflection coefficient  $r_A$  reads as

$$r_A = r + \frac{2\alpha_{\rm SP}^2}{(h^{-1} + 1) - (\rho_{\rm SP} + \tau_{\rm SP})}. (3.7)$$

Equation (3.7) is very similar to Eq. (3.5), the only difference being the replacement of  $u^{-1}$  by a new term  $(h^{-1} + 1)$ , which encompasses the SPP  $u^{-1}$  term and an additional contribution corresponding to the interference of all the individual quasi-CWs scattered by every hole chains of the array [42]. In addition to provide a complete or accurate microscopic interpretation of EOT, the refined model may also be used as a semi-analytical design tool that is more efficient than the fully-vectorial numerical methods.

### 3.7 Conclusion

The Wood resonance anomaly is at the heart of the EOT phenomenon, as nicely explained by the resonance-assisted tunneling mechanism. Nevertheless, nearly 70 years after Fano's interpretation, an apparently "simple" grating diffraction phenomenon can surprisingly initiate intense research and a strong debate. The cause is the large conceptual distance that separates the mature tools (such as the polology) of classical grating theories and our intuition of the physics of subwavelength metallic surfaces. When people ask themselves what is the role of SPP in the EOT, they are back to the pioneer works by Rayleigh, Fano..., who established the foundation of modern grating theories using a microscopic analysis.

Indeed, the analysis of subwavelength metallic surfaces should be done with fully vectorial numerical tools. However, fully vectorial numerical methods, like those used in the main text to calculate the zero-order diffraction efficiency and the SPP scattering coefficients, are very limited. With the exception of periodic geometries (such as gratings), they require tremendous computational resources as soon as the number of indentations exceeds a few unities. And fully vectorial numerical methods are not advantageous in achieving physical intuition.

In addition to apparently closing the debate on the role of SPPs in the EOT (or more generally in metallic grating scattering problems), the microscopic model may also be viewed as a numerical tool. In its generalized version that includes the quasi-CWs, it offers highly accurate predictions (the deviation between the red and black curves in Fig. 3.7 is almost imperceptible) over a broad spectral range (below the plasma frequency of the metal). In addition, it is not restricted to the analysis of gratings. It may apply as well to the general case of metallic surfaces composed of an arbitrary set of N possibly different indentations located at arbitrary positions on the surface, provided that the indentations are sub- $\lambda$ . Since the numerical efforts required to calculate the microscopic scattering coefficients,  $\rho_{SP}$ ,  $\tau_{SP}$ ..., are really affordable because single scatterers are easily modelized with fully vectorial methods, the overall computational effort needed for the microscopic model remains modest [43].

Finally and perhaps more importantly, by promoting a surface-wave-progression picture, where SPPs and quasi-CWs are initially launched by some illuminated sub-  $\lambda$  indentations, then propagate on the surface, before being further scattered by nearby indentations, the model sticks to our physical intuition: the surface-wave progression is the conceptual tool that one uses for designing plasmonic devices.

**Acknowledgments** Haitao Liu acknowledges financial supports from the Natural Science Foundation of China (No. 10804057), from the Cultivation Fund of the Key Scientific and Technical Innovation Project, Ministry of Education of China (No. 708021), and from the Program for New Century Excellent Talents in University (No. NCET-08-0289). Jean Paul Hugonin and Pierre Chavel are acknowledged for fruitful discussions and for careful readings of the manuscript.

102 P. Lalanne and H. Liu

### References

T.W. Ebbesen, H.J. Lezec, H.F. Ghaemi, T. Thio, P.A. Wolff, Extraordinary optical transmission through sub-wavelength hole arrays. Nature 391, 667–669 (1998)

- 2. H. Bethe, Theory of diffraction by small holes. Phys. Rev. 66, 163–182 (1944)
- 3. A. Roberts, Electromagnetic theory of diffraction by a circular aperture in a thick, perfectly conducting screen. J. Opt. Soc. Am A 4, 1970–1983 (1987)
- 4. C. Genet, M.P. van Exter, J.P. Woerdman, Fano-type interpretation of red shifts and red tails in hole array transmission spectra. Opt. Commun. **225**, 331–336 (2003)
- F. Przybilla, A. Degiron, C. Genet, T.W. Ebbesen, F. de Leon-Perez, J. Bravo-Abad, F. Garcia-Vidal, L. Martin-Moreno, Efficiency and finite size effects in enhanced transmission through subwavelength apertures. Opt. Express 16, 9571–79 (2008)
- 6. C. Genet, T.W. Ebbesen, Light in tiny holes. Nature **445**, 39–46 (2007)
- J.V. Coe, J.M. Heer, S. Teeters-Kennedy, H. Tian, K.R. Rodriguez, Extraordinary transmission of metal films with arrays of subwavelength holes. Ann. Rev. Phys. Chem. 59, 179–202 (2008)
- 8. E. Ozbay, Plasmonics: merging photonics and electronics at nanoscale dimensions. Science **311**, 189–193 (2006)
- 9. R. Petit, *Electromagnetic Theory of Gratings* (Springer-Verlag, Berlin, 1980)
- H.T. Liu, P. Lalanne, Microscopic model for the extraordinary optical transmission. Nature 452, 728 731 (2008)
- U. Fano, The theory of anomalous diffraction gratings and of quasi-stationary waves on metallic surfaces (Sommerfeld's waves). J. Opt. Soc. Am. 31, 213–222 (1941)
- 12. Lord Rayleigh, On the dynamical theory of gratings. Proc. R. Soc. (London) **A79**, 399–416 (1907)
- 13. R.H. Ritchie, Plasma losses by fast electrons in thin films. Phys. Rev. 106, 874–881 (1957)
- A. Hessel, A.A. Oliner, A new theory of Wood's anomalies on optical gratings. Appl. Opt. 4, 1275–97 (1965)
- D. Maystre, General study of grating anomalies from electromagnetic surface modes. in Electromagnetic Surface Modes, ed. by A.D. Boardman, Chapter 17 (Wiley, New York, 1982)
- 16. E. Popov, Light diffraction by relief gratings. Prog. Opt. **31**, 141–187 (1993)
- 17. H.J. Lezec, A. Degiron, E. Devaux, R.A. Linke, L. Martin-Moreno, F.J. Garcia-Vidal, T.W. Ebbesen, Beaming light from a subwavelength aperture. Science **297**, 820–822 (2002)
- V. Twersky, On a multiple scattering theory of the finite grating and the Wood anomaly. J. Appl. Phys. 23, 1099–1118 (1952)
- J.J.A. Porto, F.J. Garcia-Vidal, J.B. Pendry, Transmission resonances on metallic gratings with very narrow slits. Phys. Rev. Lett. 83, 2845–2848 (1999)
- 20. P. Lalanne, J.P. Hugonin, S. Astilean, M. Palamaru, K.D. Möller, One-mode model and airy-like formulae for 1D metallic gratings. J. Opt. A: Pure Appl. Opt. 2, 48–51 (2000)
- S. Astilean, P. Lalanne, M. Palamaru, Light transmission through metallic channels much smaller than the wavelength. Opt. Commun. 175, 265–273 (2000)
- M.M.J. Treacy, Dynamical diffraction explanation of the anomalous transmission of light through metallic gratings. Phys. Rev. B 66, 195105 (2002)
- Q. Cao, P. Lalanne, Negative role of surface plasmons in the transmission of metallic gratings with very narrow slits. Phys. Rev. Lett. 88, 057403 (2002)
- P. Lalanne, J.P. Hugonin, H.T. Liu, B. Wang, A microscopic view of the electromagnetic properties of sub-metallic surfaces. Surf. Sci. Rep. 64, 453–469 (2009)
- D. Maystre, A.L. Fehrembach, E. Popov, Plasmonic antiresonance through subwavelength hole arrays. J. Opt. Soc. Am. A 28, 342–355 (2011)
- G. Gay, O. Alloschery, B. Viaris de Lesegno, C. O'Dwyer, J. Weiner, H.J. Lezec, The optical response of nanostructured surfaces and the composite diffracted evanescent wave model. Nat. Phys. 2, 262–267 (2006)
- 27. I. Zenneck, Propagation of plane electromagnetic waves along a plane conducting surface and its bearing on the theory of transmission in wireless telegraphy. Ann. Phys. **23**, 846–866 (1907)

- 28. A. Sommerfeld, The broadening of the waves and the wireless telegraph. Ann. der Physik 28, 665–36 (1909)
- A. Sommerfeld, The propagation of waves in wireless telegraphy. Ann. der Physik 81, 1135– 1153 (1926)
- 30. K.A. Norton, Propagation of radio waves over a plane earth. Nature **135**, 954–955 (1935)
- 31. K.A. Norton, The propagation of radio waves over the surface of the earth and in the upper atmosphere. Proc. IRE **24**, 1367–1387 (1936) and 1203–1236 (1937)
- 32. R.E. Collin, Hertzian dipole radiating over a lossy earth or sea: some early and late 20th-century controversies. IEEE Antennas Propag. Mag. 46, 64–79 (2004)
- 33. A. Baños, Dipole Radiation in the Presence of a Conducting Half-Space (Pergamon Press, Oxford, 1966)
- P. Lalanne, J.P. Hugonin, Interaction between optical nano-objects at metallo-dielectric interfaces. Nat. Phys. 2, 551–556 (2006)
- L. Aigouy, P. Lalanne, J.P. Hugonin, G. Julié, V. Mathet, M. Mortier, Near-field analysis of surface waves launched at nano-slit apertures. Phys. Rev. Lett. 98, 153902 (2007)
- W. Dai, C.M. Soukoulis, Theoretical analysis of the surface wave along a metal-dielectric interface. Phys. Rev. B 80, 155407 (2009)
- A.Y. Nikitin, S.G. Rodrigo, F.J. Garcia-Vidal, L. Martin-Moreno, In the diffraction shadow: Norton waves versus surface plasmon polaritons in the optical region. New J. Phys. 11, 123020 (2009)
- 38. F.J. Garcia-Vidal, L. Martin-Moreno, T.W. Ebbesen, L. Kuipers, Light passing through subwavelength apertures. Rev. Mod. Phys. **82**, 729–787 (2010)
- 39. E. Popov, M. Nevière, S. Enoch, R. Reinisch, Theory of light transmission through subwavelength periodic hole arrays. Phys. Rev. B **62**, 16100 (2000)
- L. Martin-Moreno, F.J. Garcia-Vidal, H.J. Lezec, K.M. Pellerin, T. Thio, J.B. Pendry, T.W. Ebbesen, Theory of extraordinary optical transmission through subwavelength hole arrays. Phys. Rev. Lett. 86, 1114–1117 (2001)
- P. Lalanne, J.C. Rodier, J.P. Hugonin, Surface plasmons of metallic surfaces perforated by nanohole arrays. J. Opt. A: Pure Appl. Opt 7, 422–426 (2005)
- H.T. Liu, P. Lalanne, A comprehensive microscopic model of the extraordinary optical transmission. J. Opt. Soc. Am. A 27, 2542–2550 (2010)
- X. Huang, M.L. Brongersma, Rapid computation of light scattering from aperiodic plasmonic structures. Phys. Rev. B 84, 245120 (2011)

# **Chapter 4 Introduction to Surface Plasmon Theory**

Jean-Jacques Greffet

**Abstract** This chapter is an introduction to the surface plasmon theory. We start with the solid-state point of view with emphasis on the concept of polariton and the limits of the Drude model. The concept of electromagnetic surface wave is then introduced in a general framework. Three particular cases are then discussed: the surface plasmon, the surface phonon polariton and the Sommerfeld surface wave. The key properties of surface plasmons for optics are discussed in general terms, with special emphasis on the concepts of field confinment and local density of states. The differences between the dispersion relations of surface waves in the presence of losses are analysed and their significance is explained. Finally, an equivalent of the Huygens–Fresnel principle is derived for the surface plasmon polaritons.

#### 4.1 Introduction

This chapter is part of a book devoted to the optics of surface plasmons. The term surface plasmon is used both for polarization oscillation of metallic nanoparticles and for waves propagating along a plane interface and exponentially decaying away from the interface. This chapter will mostly cover the latter case. From the point of view of electrodynamics, surface plasmons are a particular case of a surface wave, a topic that has been extensively covered in the early days of radiowave propagation along the earth [1–4]. From the point of view of optics, surface plasmons are modes of an interface. They have been extensively studied in the 1970s and 1980s. Several excellent monographs are available from this point of view [5–7] and more recent achievements are summarized in Refs. [8–10]. Finally, from the point of view of solid-state physics, a plasmon is a collective excitation of electrons. Excellent introductions can be found in well-known textbooks [11, 12] and in more advanced texts [13–15].

Institut d'Optique Université Paris-Sud, CNRS, RD 128, F-91127 Palaiseau Cedex, France e-mail: jean-jacques.greffet@institutoptique.fr

J.-J. Greffet (⋈)

The goal of this chapter is to provide an introduction to the three different points of view and to serve as a lecture guide. In the first section, we will show how the plasma frequency can be seen as the natural oscillation frequency of electrons in a thin film. This (solid-state) point of view will be generalized to bulk plasmons in an electron gas in the second section using a hydrodynamic model. This analysis will serve the purpose of explaining the concept of polariton: an electromagnetic wave coupled to a polarization excitation in the material. We will then adopt the macroscopic electrodynamics point of view and derive the dispersion relation of a surface wave. In this approach, the material properties are accounted for by using a dielectric constant without any microscopic model. We will discuss the similarities and differences between different types of surface waves (lateral waves, Zenneck modes, Sommerfeld modes, quasicylindrical waves) without invoking any specific model of the dielectric constant. Hence, this discussion will be equally valid for radio waves or optical waves, for metals or dielectrics. We will then focus on the case of surface plasmon polaritons. To this aim, it is often convenient to use the Drude model but it is also critical to be aware of its limitations. This will be summarized in Sect. 4.5. Surface phonon polaritons and radio surface waves will be introduced in the following sections. In Sect. 4.8, we will outline the key properties that make surface plasmons so unique. The aim of this section is to identify fundamental properties of surface plasmons that may help us to decide when surface plasmons can be useful for optics applications. The subtle issue of the dispersion relation of surface plasmons on lossy materials will be analysed in Sect. 4.9. Finally, surface plasmon optics will be the subject of the last section. It will be shown how the propagation of surface plasmons along a flat interface can be modelled using a Fourier optics framework

## **4.2 Surface and Particle Electron Oscillation Modes:** Introductory Examples

To start, we consider a thin metallic film. The metal is described by a simple model: we assume that there are n free and independent electrons per unit volume. The crystal lattice is modelled by a uniform positively charged background. This is the so-called jellium model. The purpose of this section is to illustrate the essence of a plasmon: it is an oscillatory collective mode of the electrons. To proceed, we assume that classical mechanics can be used.

Let us now assume that a positive static homogeneous electric field  $E_{\rm ext}\hat{\bf x}$  is applied normally to the film along the x-axis (see Fig. 4.1). A force  $-eE_{\rm ext}\hat{\bf x}$  is exerted on the electrons so that they will be displaced by x (with x < 0). A negative static surface charge nex will appear on the left interface and a positive surface charge on the right side. These surface charges produce a static field that cancels the external field in the metal. Let us now assume that the external electrostatic field is turned off at time t=0. The electrons in the film will be accelerated by the electric field generated by the surface charges. When they return to their initial position, they have acquired a

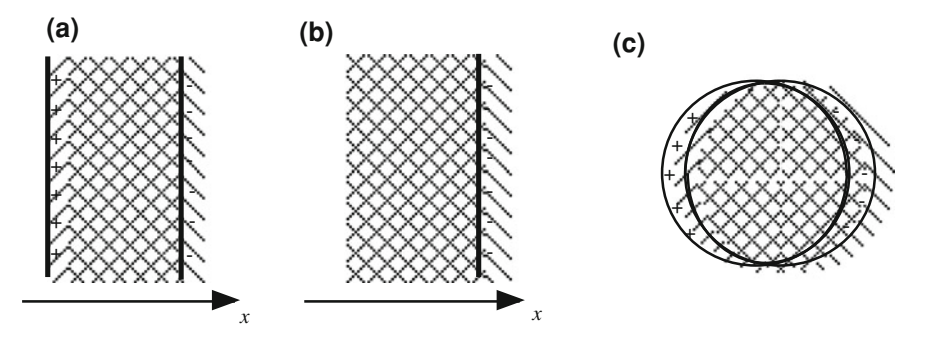


Fig. 4.1 Oscillation of the electron gas for a a thin film, b a metal-vacuum interface, and c a nanosphere

momentum so that they keep moving along the positive *x*-axis and therefore generate an electric field of opposite sign. This process will be repeated and will produce an oscillation. It is easy to quantitatively describe this phenomenon by using Newton's law applied to a single electron:

$$m\frac{\mathrm{d}^2x}{\mathrm{d}t^2} = -eE_x,\tag{4.1}$$

where we have neglected the magnetic force. Using Gauss's theorem, it can be shown that the field generated by a sheet carrying a surface charge nex is  $(nex/2\epsilon_0)\mathbf{u}$  where  $\mathbf{u}$  is an outward unit vector. It follows that the field generated by the surface charge nex for a displacement x is found to be  $E_x = 2nex/2\epsilon_0$  where the factor 2 accounts for the presence of two interfaces. It follows from Newton's equation that the movement of one electron is given by:

$$\frac{\mathrm{d}^2 x}{\mathrm{d}t^2} + \frac{ne^2}{m\epsilon_0} x = 0. \tag{4.2}$$

This simple argument allows us to introduce in a simple way the plasma frequency  $\omega_p$ :

$$\omega_p^2 = \frac{ne^2}{m\epsilon_0} \tag{4.3}$$

that appears to be the frequency of the collective oscillation of the electrons in the bulk of the film. To summarize, the oscillation is produced by an electric field due to all the electrons. This is why it is called a collective oscillation. With this simple argument, we have captured the essence of the plasmon: it is the natural collective oscillation of the electrons characterized by the plasma frequency.

We now consider the case of a single interface. In other words, we consider that the thickness of the film goes to infinity so that the force is only due to the charge density of one interface. It follows that the electric field is due to only one interface

instead of two and takes the value  $nex/2\epsilon_0$ . The oscillation frequency is therefore  $\omega_p/\sqrt{2}$ .

We finally consider the case of a nanosphere. For a sphere much smaller than the wavelength, retardation effects can be neglected so that we can use the electrostatic form of the field generated by a uniform polarization field  $P_x$  of the particle  $E_x = -P_x/3\epsilon_0$  [16]. Inserting this form of the electric field in Eq. (4.1) yields:

$$m\frac{\mathrm{d}^2x}{\mathrm{d}t^2} = -e\frac{-P_x}{3\epsilon_0}. (4.4)$$

The polarization  $P_x$  is due to the displacement of the electrons so that we have  $P_x = -nex$ . Upon inserting this expression in Eq. (4.4), we find:

$$\frac{\mathrm{d}^2 x}{\mathrm{d}t^2} + \frac{ne^2}{3m\epsilon_0}x = 0. \tag{4.5}$$

so that the resonance frequency of the plasmon in a nanosphere is given by  $\omega_p/\sqrt{3}$ . The modes of a sphere will be further discussed in the chapter written by J. Aizpurua and R. Hillenbrand . In this chapter, we will focus on surface modes that can propagate along a flat interface while decaying exponentially on both sides of the interface. Here, we simply make a comment on terminology. It turns out that both nanosphere modes and modes propagating along an interface are called surface modes although they are different.

### 4.3 Bulk Plasmon

## 4.3.1 Hydrodynamic Model: The Concept of Polariton

We now consider a more general analysis of the concept of plasmon. We do not consider a specific geometry. Instead, we look for a general equation describing a charge density wave in an infinite homogeneous electron gas. Our primary objective in this section is to illustrate the concept of polariton in the particular case of a plasmon. The key idea that will be introduced here is that when an electromagnetic wave propagates in a material medium, the field polarizes the medium and therefore excites a mechanical movement of the charges. It follows that field and charges are coupled. This coupled excitation is called a polariton. In the case of a metal, the field can couple to a longitudinal charge density wave that can be viewed as an acoustic wave in the electron gas. The resulting polariton is called a plasmon polariton. In an ionic crystal like NaCl for instance, an electromagnetic field can excite the mechanical motion of the ions (a phonon) and therefore generate a polarization oscillation. This is called a phonon polariton. Finally, the coupling between the field and an electronhole pair (an exciton) is called exciton polariton. The purpose of this section is to

provide a simple explicit model of this coupling in the case of a metal within the jellium model introduced above. We will use a hydrodynamic model to derive the equation of the charge density wave. To begin, we write Euler's equation, the mass conservation and Gauss–Maxwell equation:

$$nm \left[ \frac{\partial \mathbf{v}}{\partial t} + \mathbf{v} \cdot \nabla \mathbf{v} \right] = -ne\mathbf{E} - \nabla P_e,$$

$$\nabla \cdot (n\mathbf{v}) = -\frac{\partial n}{\partial t}$$

$$\nabla \cdot \mathbf{E} = \frac{n - n_0}{\epsilon_0} (-e),$$
(4.6)

where  $P_e$  is the electronic pressure and n(x,t) is the number of electrons per unit volume. We finally introduce the compressibility of the electron gas  $\partial P_e/\partial n = mv_F^2/3$  where  $v_F$  is the Fermi velocity [12]. When looking for a small amplitude perturbation  $n_1(x,t) = n(x,t) - n_0$  and  $P_{e1} = P_e - P_{e0}$  where  $x_0$  indicates the equilibrium value of x, the non-linear term  $\mathbf{v} \cdot \nabla \mathbf{v}$  can be neglected. Let us comment on this set of equations. For a neutral gas, the electric force  $-ne\mathbf{E}$  in Euler's equation would be suppressed. One would then find the usual propagation equation for acoustic waves. Here, after linearizing, we find a set of two coupled linear equations:

$$\nabla^{2} n_{1} - \frac{3}{v_{F}^{2}} \frac{\partial^{2} n_{1}}{\partial t^{2}} = -\frac{3n_{0}e}{mv_{F}^{2}} \nabla \cdot \mathbf{E}$$

$$\nabla \cdot \mathbf{E} = \frac{n_{1}}{\epsilon_{0}} (-e). \tag{4.7}$$

This system clearly exhibits the coupling between the acoustic wave and the electric field. It is seen that the electron density satisfies a propagation equation with a source term given by the divergence of the electric field. Similarly, the equation describing the longitudinal component of the electric field is driven by the electron density modulation  $n-n_0$ . The resulting coupled oscillation is called a polariton. The key idea here is that the acoustic and the electromagnetic fields are no longer modes of the system. The mode of the system is a coupled mode called polariton. It can be viewed as an object which is half a photon and half a phonon.

It is now a simple matter to eliminate the electric field and find the propagation equation for the electron density wave that accounts for both the pressure force and the electric force. When searching for a solution of the form  $\exp(ikx - i\omega t)$ , we find the dispersion relation:

$$\omega^2 = \omega_p^2 + \frac{v_F^2}{3}k^2. \tag{4.8}$$

It turns out that the electric force yields the  $\omega_p^2$  contribution, which is much larger than the pressure contribution  $v_F^2 k^2$  for wavevectors in the optical regime (i.e.  $k \ll \omega/v_F$ ).

It follows that in the optical regime, the dependence of  $\omega$  on the wavector can be neglected.

To summarize this section, it has been shown that the plasmon appears to be an acoustic wave in an electron gas. As the particles are charged, an additional electric force has to be accounted for. It turns out that this electric force yields the dominant contribution so that the waves are essentially spatially non-dispersive. Note also that with this approach, it clearly appears that the electric field is parallel to the wavevector as it is due to the charge density gradient.

## 4.3.2 Bulk Plasmon: Electromagnetic Model

When studying the propagation of waves in a vacuum, we always focus on transverse waves as longitudinal solutions do not exist. This is no longer the case in a material medium. Plasmons are longitudinal solutions of Maxwell equations. In the previous section, we have studied the propagation of coupled mechanical and electromagnetic waves using a hydrodynamic model of a metal. We have found that the electromagnetic solution has an electric field, which is parallel to the wavevector. From a more general perspective, this solution is a longitudinal solution, namely a solution that satisfies  $\nabla \times \mathbf{E} = 0$ . Such a solution is therefore fully described by the equation  $\nabla \cdot \mathbf{D} = 0$ . In this section, we examine the existence of a longitudinal solution of Maxwell equations without invoking a specific model of the medium. If we assume that the medium is linear, homogeneous and isotropic, we can introduce a dielectric constant. The most general linear form includes a dependence on the frequency and the wavevector  $\epsilon(\mathbf{k}, \omega)$ :

$$\mathbf{D}(\mathbf{k}, \omega) = \epsilon(\mathbf{k}, \omega) \mathbf{E}(\mathbf{k}, \omega). \tag{4.9}$$

The dependence of  $\epsilon(\mathbf{k},\omega)$  on  $\omega$  is called dispersion and the dependence on  $\mathbf{k}$  is called spatial dispersion. This dependence on the wavevector leads to a non-local relation between the electric field and the vector  $\mathbf{D}$  in direct space so that spatial dispersion and non-local dielectric constant are two aspects of the same property:

$$\mathbf{D}(\mathbf{r},\omega) = \int \frac{\mathrm{d}\mathbf{k}}{8\pi^3} \epsilon(\mathbf{k},\omega) \mathbf{E}(\mathbf{k},\omega) \exp(i\mathbf{k}\cdot\mathbf{r}) = \int \epsilon(\mathbf{r} - \mathbf{r}',\omega) \mathbf{E}(\mathbf{r}',\omega) \mathrm{d}\mathbf{r}'. \quad (4.10)$$

The equation  $\nabla \cdot \mathbf{D} = 0$  can be cast in the form:

$$\nabla \cdot \mathbf{D} = \nabla \cdot \int \frac{d\mathbf{k}}{8\pi^3} \frac{d\omega}{2\pi} \epsilon(\mathbf{k}, \omega) \mathbf{E}(\mathbf{k}, \omega) \exp(i\mathbf{k} \cdot \mathbf{r} - i\omega t)$$

$$= \int \frac{d\mathbf{k}}{8\pi^3} \frac{d\omega}{2\pi} \epsilon(\mathbf{k}, \omega) [i\mathbf{k} \cdot \mathbf{E}(\mathbf{k}, \omega)] \exp(i\mathbf{k} \cdot \mathbf{r} - i\omega t) = 0. \tag{4.11}$$

If we seek a non-zero longitudinal electric field, then  $\mathbf{k} \cdot \mathbf{E}(\mathbf{k}, \omega) \neq 0$  so that  $\epsilon(\mathbf{k}, \omega) = 0$ . A local medium has a dielectric constant that does not depend on  $\mathbf{k}$  so that the dispersion relation of the longitudinal solution is given by  $\epsilon(\omega) = 0$ .

For the particular case of a non-lossy Drude model,  $\epsilon(\omega) = \epsilon_0 (1 - \omega_p^2/\omega^2)$  so that we find  $\omega = \omega_p$  in agreement with the local approximation of Eq. (4.8). The discrepancy with the previous section illustrates the fact that the Drude model is an approximation that does not account for the **k**-dependence of the dielectric constant. This is usually an excellent approximation as we have discussed above. Yet, it is necessary to be aware that the Drude model is valid, provided that  $k \ll \omega_p/v_F$ . Models accounting for the k-dependence of the dielectric constant (i.e. non-local models) are discussed in Refs. [12–14, 17].

### 4.4 Surface Electromagnetic Wave

So far, we have introduced the concept of polariton and the particular case of a bulk plasmon polariton. Let us emphasize that we have only discussed waves propagating in a bulk medium. Moreover, we have studied longitudinal electromagnetic modes. We now consider waves propagating along an interface which are transverse. The aim of this section is to search for a solution confined close to the interface. More precisely, we look for a solution that decays exponentially away from the interface. At this stage, we do not make any particular assumption regarding the specific properties of the medium. Hence, the surface wave dispersion relation that we will find can be applied to any material (e.g. metals, dielectrics) and any frequency range (e.g. radio waves, IR, visible). The only assumption made in what follows is that the media are local and isotropic. Hence, they are characterized by a complex frequency-dependent dielectric constant  $\epsilon_r$  and a complex frequency-dependent permeability  $\mu_r$ . We denote the upper medium (z > 0) with the index 1 and the lower medium (z < 0) with the index 2 as indicated in Fig. 4.2. We denote **k** the wavevector and denote ( $\alpha$ ,  $\beta$ ,  $\gamma$ ) its Cartesian components and k its modulus.

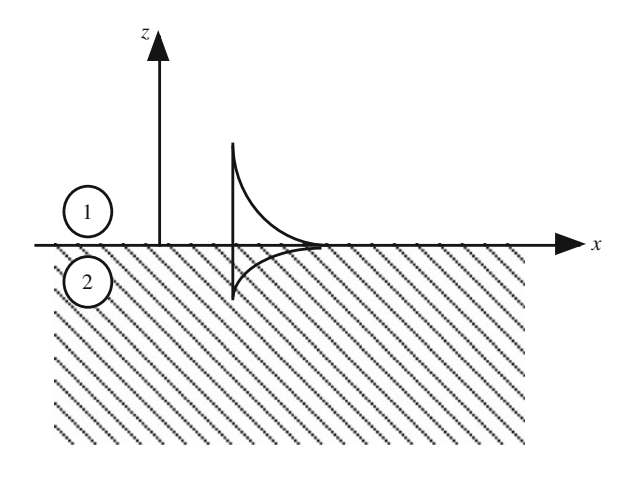
## 4.4.1 Dispersion Relation for the Non-Magnetic Case

The electric field obeys the Helmholtz equation in both media:

$$\nabla^2 \mathbf{E}_i + \mu_i \epsilon_i \frac{\omega^2}{c^2} \mathbf{E}_i = 0, \tag{4.12}$$

with i = 1, 2. For a p-polarized solution (also called TM for transverse magnetic), we seek a solution of the form:

**Fig. 4.2** Schematic representation of the exponential decay along *z* of the amplitude in media *I* (dielectric) and 2 (metal) of a surface wave propagating along the *x*-axis



$$z > 0 \quad E_{x1} = E_0 \exp[i\alpha x + i\gamma_1 z]$$
  

$$z < 0 \quad E_{x2} = E_0 \exp[i\alpha x - i\gamma_2 z]$$
(4.13)

that satisfies the continuity condition along the interface. Here,

$$\gamma_1 = [\mu_1 \epsilon_1 \omega^2 / c^2 - \alpha^2]^{1/2} \tag{4.14}$$

with  $Im(\gamma_1) > 0$  and

$$\gamma_2 = [\mu_2 \epsilon_2 \omega^2 / c^2 - \alpha^2]^{1/2} \tag{4.15}$$

with  $Im(\gamma_2) > 0$  so that the waves decay exponentially far from the interface. We look for transverse waves so that, by definition,  $\nabla \cdot \mathbf{E} = 0$ . In Fourier space, this relation becomes  $\mathbf{k} \cdot \mathbf{E} = 0$  where  $\mathbf{k} = (\alpha, 0, \gamma)$ . We stress that this equation does not have the usual geometrical meaning of two perpendicular real vectors because  $\mathbf{k}$  is complex. In other words, transverse (i.e. $\nabla \cdot \mathbf{E} = 0$ ) should not be confused with perpendicular. It follows that:

$$z > 0 \quad E_{z1} = -\frac{kE_0}{\gamma_1} \exp[i\alpha x + i\gamma_1 z]$$

$$z < 0 \quad E_{z2} = \frac{kE_0}{\gamma_2} \exp[i\alpha x - i\gamma_2 z]. \tag{4.16}$$

If we now enforce the continuity condition of the z-component of  $\epsilon \mathbf{E}$  at the interface, we obtain:

$$\epsilon_1 \gamma_2 = -\epsilon_2 \gamma_1. \tag{4.17}$$

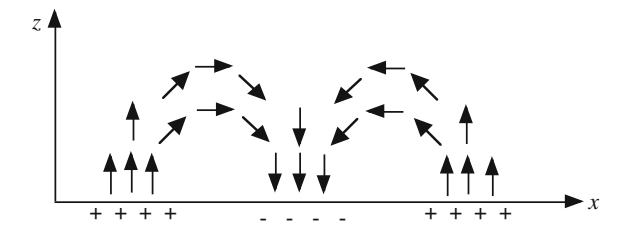


**Fig. 4.3** Polarization of the surface plasmon polariton. The figure illustrates the surface charge density wave. It follows that the electric field has a normal component at the interface that oscillates. The figure shows that the continuity of the field in the vacuum requires a curvature of the field lines. The electric field is thus elliptically polarized in the plane (x, z)

These equations are the dispersion relations of the surface wave. To obtain a more explicit form, we take the square of both terms. Note that we lose the sign at this point so that we will need to check that the final solution satisfies the original dispersion relation. For TM-polarization, the solution for  $\alpha$  is denoted as  $K_{SP}(\omega)$  and is given by:

$$K_{SP}^2(\omega) = \frac{\omega^2}{c^2} \frac{\epsilon_1 \epsilon_2}{\epsilon_1 + \epsilon_2}.$$
 (4.18)

A similar calculation for the magnetic case in s-polarization yields:

$$\mu_1 \gamma_2 = -\mu_2 \gamma_1. \tag{4.19}$$

## 4.4.2 Polarization of the Surface Wave

We have seen that the electric field of a surface wave propagating along the x-axis has two components along the x and the z axes. Moreover, the z-component of the electric field is complex. Hence, the electric field has an elliptic polarization in the (x, z) plane. This peculiar polarization can be understood from the following remark. The existence of a z-component of the electric field entails the presence of a surface charge  $P_{z2} - P_{z1}$  along the interface. Hence, the surface wave can be viewed as a surface charge density wave propagating along the x-axis as depicted in Fig. 4.3. Since in the vacuum above the interface the field lines must be continuous, there must be an x-component of the field to close the line fields (see Fig. 4.3).

It is worth emphasizing a difference between the current density and the surface charge associated with the surface plasmon. Although the current density  $\mathbf{j} = -i\omega\mathbf{P} = -i\omega\epsilon_0(\epsilon_2 - 1)\mathbf{E}$  penetrates in the metal over the skin depth, the surface charge does not penetrate in the metal as  $\nabla \cdot \mathbf{P} = \epsilon_0(\epsilon_2 - \epsilon_1)\nabla \cdot \mathbf{E} = 0$  below the interface. The contribution to the surface charge is a pure surface term given by  $P_{z2} - P_{z1}$ . For a metal-vacuum interface, it is simply given by  $P_{z2}$ . From a physical

	, , , , , , , , , , , , , , , , , , , ,			
$\lambda_i \; (\mu  \mathrm{m})$	0.633	1	10	36
$\delta_x$	9.8	91.6	38,880	504,243
$\delta_{z1}$	0.165	0.51	57.3	702.67
$\delta_{z2}$	0.014	0.012	0.011	0.013

**Table 4.1** Decay length for a surface plasmon propagating along a gold/vacuum interface

Data taken from Etchegoin et al. at 633 nm and 1 µm [19], from Ordal et al. [20] for 10 and 34 µm

point of view, a surface charge must have some finite extension along the *z*-axis. One has to account for non-local effects to introduce the relevant length scale. It is the Thomas–Fermi length scale, which is of the order of tenths of nm.

### 4.4.3 Length Scales of a Surface Wave

There are three different lengths characteristic of a surface wave. It is seen from Eq. (4.18) that the wavevector is complex if there are losses. The imaginary part of  $K_{SPP}$  accounts for the decay of the surface wave upon propagation along the interface. A characteristic decay length can be defined by  $\delta_x = 1/Im(K_{SPP})$ . As the wave does not radiate, the decay is entirely due to losses in the media. In other words, the surface wave energy is converted into heat. There are two other characteristic lengths accounting for the exponential decay of the surface wave away from the interface. They are given by  $\delta_{zi} = 1/Im(\gamma_i)$  in medium i. They are found by inserting Eq. (4.18) into Eqs. (4.14, 4.15):

$$\frac{1}{\delta_{zi}} = Im[\gamma_i] = \frac{\omega}{c} Im \left[ \frac{\epsilon_i^2}{\epsilon_1 + \epsilon_2} \right]^{1/2}$$
 (4.20)

Typical orders of magnitude for metals are given in Table 4.1. It is clearly seen that the surface plasmon has a decay length along the x-axis of the order of a few micrometers in the visible range, but considerably larger in the infrared. Regarding the spatial extension of the wave in the metal (medium 2), it is seen that the decay length is almost constant. It is mainly given by the skin depth in the metal and is of the order of 12 nm. By contrast, the extension of the surface wave given by  $\delta_{z1}$  in medium 1 changes dramatically. It varies between 165 nm in the visible and 700  $\mu$ m in the IR. Hence, it is seen that the surface wave is not confined close to the interface in the IR. Since most of the energy of the mode is in the vacuum, Joule losses are negligible so that the decay length upon propagation is drastically reduced.

We finally note that the confinment in a dielectric is due to the fact that  $\alpha^2 > \epsilon_1 \omega^2/c^2$ . We note in particular that for very large wavevectors  $\alpha$ ,  $\delta_{zi} = 1/Im(\gamma_i) \approx 1/\alpha$ , so that large vectors are strongly confined.

### 4.4.4 Link with Resonances of the Reflection Factor

An alternative approach to find the dispersion relation consists in looking for the poles of the Fresnel reflection factor. The reason for looking at the Fresnel factors is simple. Since we can write  $E_r^{s,p} = r_{s,p} E_{inc}^{s,p}$ , it is seen that the reflection factor  $r_{s,p}$  can be considered to be a linear response factor to the incident field  $E_{inc}^{s,p}$  viewed as an external excitation. As for any linear system, a resonant response is the signature of the excitation of a mode of the system. Hence, writing that the denominator of  $r_{s,p}$  is zero yields the pole, which is the signature of a mode of the interface. It can be checked that  $\epsilon_1 \gamma_2 + \epsilon_2 \gamma_1$  is indeed the denominator of the Fresnel reflection factor for p-polarization for a non-magnetic material. We can now generalize the approach to a magnetic material for both polarizations. The Fresnel reflection factors can be cast in the form:

$$r_s = \frac{\mu_2 \gamma_1 - \mu_1 \gamma_2}{\mu_2 \gamma_1 + \mu_1 \gamma_2}; \quad r_p = \frac{\mu_1 \epsilon_2 \gamma_1 - \mu_2 \epsilon_1 \gamma_2}{\mu_1 \epsilon_2 \gamma_1 + \mu_2 \epsilon_1 \gamma_2}.$$
 (4.21)

It follows that the corresponding dispersion relation can be written as follows:

$$\mu_2 \gamma_1 + \mu_1 \gamma_2 = 0; \quad \mu_1 \epsilon_2 \gamma_1 + \mu_2 \epsilon_1 \gamma_2.$$
 (4.22)

It is seen that a surface wave can be obtained in the case of a magnetic material in s-polarization if the permeabilities  $\mu_i$  have opposite signs. It is also of interest to note that the zeros and the poles of the reflection factor are given by very similar equations. We will come back to this point in the section on surface plasmons. This approach is of particular interest when dealing with more complex systems such as multilayers. It does account for guided modes, interface modes and the coupling between these modes.

A technical remark might be useful here. The reader may be familiar with a presentation of the Fresnel reflection factor using the incident angle  $\theta_i$  as a variable instead of the parallel component of the wavevector k. For the case of a propagating incident wave in a lossless dielectric medium with refractive index  $n_1$ , it is essentially a matter of taste to use k or  $n_1(\omega/c)\sin\theta_i$ . If we seek the zero of the denominator, we need to use a real value of k, which is larger than  $n_1\omega/c$ . A question then arises: is such a large k physical? If yes, how can we generate a large surface wavevector?

## 4.4.5 Generation of a Surface Wave

When using the Fourier representation of a field, a real wavector k is used. It is known that in a vacuum, the wavevector has a modulus  $\omega/c$  so that it might seem that large values of k are not possible. It might be useful at this point to write the Fourier expansion of a scalar spherical wave propagating with phase velocity c known as Weyl's expansion:

$$\frac{\exp(ikr)}{r} = 2i\pi \int_{-\infty}^{\infty} \frac{d\alpha}{2\pi} \int_{-\infty}^{\infty} \frac{d\beta}{2\pi} \frac{1}{\gamma} \exp[i(\alpha x + \beta y + \gamma |z|)], \tag{4.23}$$

where  $\gamma = [\omega^2/c^2 - \alpha^2 - \beta^2]^{1/2}$  and  $Im(\gamma) > 0$ . This mathematical identity clearly exhibits the fact that a spherical scalar wave produced by a point-like source contains arbitrarily large values of  $\alpha$  and  $\beta$ . Due to the dispersion relation  $\alpha^2 + \beta^2 + \gamma^2 = \omega^2/c^2$ , it is seen that  $\gamma$  is imaginary for  $\alpha^2 + \beta^2 > \omega^2/c^2$ . Hence, the field produced by a point-like source contains evanescent waves that always decay away from the source as indicated by the absolute value |z|. Placing a point-like source above an interface amounts to illuminate this interface with decaying evanescent waves. There are other techniques to generate evanescent waves, i.e. to generate large wavevectors.

- (1) One can use a metal film with a thickness smaller than the skin depth separating two dielectric media with different dielectric constants  $n_1$  and  $n_2 > n_1$ . Here, the key idea is to take advantage of a large refractive index to increase the modulus of the wavevector. By illuminating from the side of the high refractive index medium, it is possible to excite through the film with a plane wave with wavevector  $\alpha = n_2\omega/c\sin(\theta_i)$  and excite the surface wave on the other side by taking adavantage of the fact that the incidence angle can be chosen so that  $\alpha > n_1\omega/c$ .
- (2) A grating with period d can be used so that the nth order of the grating has a wavevector  $\alpha_n = n_1 \omega/c \sin \theta_i + n2\pi/d$  that can be equal to  $k_{SD}$ .

### 4.5 Surface Plasmon Polariton

In this section, we will consider the specific case of surface waves propagating at the interface between a metal and a dielectric. These surface waves are called surface plasmon polaritons. Some authors [6, 8] call surface plasmons the electrostatic limit (or large wavevector limit) of the surface plasmon polariton as introduced in the previous section. However, most authors use the term "surface plasmon" as a generic term without making this distinction.

## 4.5.1 Dielectric Constant of a Metal

#### Drude model

We start the discussion by introducing the Drude model of the dielectric constant for a metal described by an electron gas. The relative dielectric constant can be cast in the form:

$$\epsilon_r(\omega) = 1 - \frac{\omega_p^2}{\omega^2 + i\gamma(\omega)\omega}.$$
 (4.24)

This relation clearly shows that there is a strong frequency dependence (i.e. dispersion) of the dielectric constant. Since the Fourier transform of a product is a convolution product, the relation  $\mathbf{D}(\mathbf{r}, \omega) = \epsilon_0 \epsilon_r(\omega) \mathbf{E}(\mathbf{r}, \omega)$  becomes in time domain:

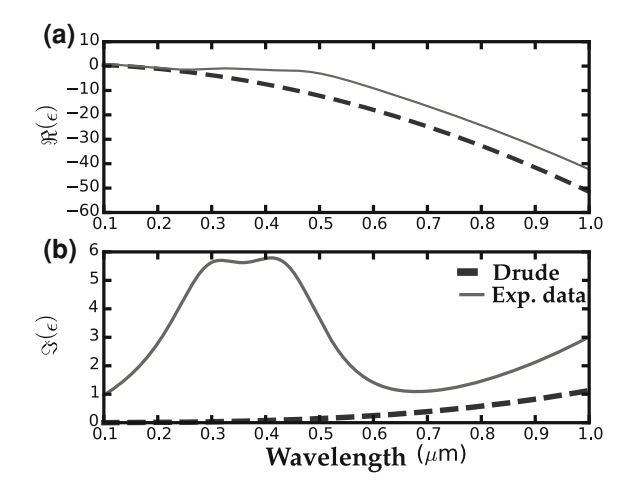
$$\mathbf{D}(\mathbf{r},t) = \int_{-\infty}^{t} \epsilon_0 \epsilon_r(t-t') \mathbf{E}(\mathbf{r},t') dt'.$$
 (4.25)

Two time scales are included in the model. On the one hand, the plasma frequency is the mode frequency of the charge density oscillation. The plasma frequency lies in the near ultraviolet for most metals. A second time scale appears in this formula, namely the relaxation time  $\tau(\omega) = 1/\gamma(\omega)$ . The relaxation time describes the relaxation processes for excited electrons. A major source of confusion is that in most references, the dependence of the relaxation coefficient on the frequency  $\omega$  is omitted. Care must be taken as the relaxation of an electron with an energy of a few eV has little in common with the relaxation of an electron with an energy of few meV. The decay processes are completely different. It follows that it is not correct to insert in the model of optical properties the value of  $\gamma$  derived from the conductivity at zero frequency. In particular, it is known that  $\gamma$  at zero frequency decays when the temperature decays. However, this is not a valid conclusion in the optics regime. Indeed, even at low temperature, the electron-electron interaction remains an efficient relaxation channel and is almost not dependent on the electron temperature. In addition, electrons can emit phonons. These two mechanisms are still possible at low temperature. One of the practical conclusions of this paragraph is that metal losses cannot be significantly reduced when reducing the temperature. The reader will find more information on electron losses in Refs. [21–26]. Finally, we mention that the relaxation time is typically of the order of 10 fs for noble metals and visible excitations.

#### **Beyond the Drude model**

Although the Drude model can be a very useful tool, it is important to keep in mind that its accuracy is much better in the IR than in the visible range. The reason is that the Drude model accounts for the contribution of the free electrons in the conduction band. When the frequency increases, photons can excite electrons in electronic bands of lower energies (usually a d-band) so that new absorption channels are available. This introduces serious deviations from the Drude model. This can be accounted for by developing fits of the measured dielectric constant as reported in several references [19, 27–29]. It is of course essential to use these realistic models when studying plasmons using time-domain calculations. Figure 4.4 illustrates the large difference in the optical part of the spectrum between a Drude model obtained by

Fig. 4.4 Comparison of experimental data and a Drude fit of the dielectric constant for gold **a** real part of the dielectric constant **b** imaginary part of the complex dielectric constant



fitting experimental data and a more detailed fit of the data reported by Johnson and Christy for gold [30]. The absorption band observed in the imaginary part of the dielectric constant between  $0.3\,\mu m$  and  $0.4\,\mu m$  is due to absorption by d-band electrons.

Another limitation of the Drude model is that it does not account for non-locality also called spatial dispersion. Spatial dispersion means that the dielectric constant depends on the wavector. In direct space, the polarization at point r depends not only on the value of the electric field at this point but also in its vicinity, hence the name non-locality [18]. The dielectric constant has two length scales corresponding to two different phenomena. The first effect is the screening of the field at an interface. Classical local electromagnetism assumes that the normal component is divided by  $\epsilon_r$  at the interface between a vacuum and a metal. The microscopic phenomenon responsible for this effect is the screening of the field by the electrons. It requires a certain length to take place. This screening length is the so-called Thomas–Fermi length for metals. For electrolytes, the corresponding screening length is called Debye-Huckel length. This phenomenon corresponds to longitudinal fields. We now consider the second length scale that appears in non-local models of the optical response of metals. This length scale is the length travelled by an electron at velocity  $v_F$  during an optical cycle. When this length scale is much smaller than the wavelength, the optical properties are not affected. By contrast, for wavectors  $k > \omega_p/v_F$ , non-local corrections are expected. This can be understood from the hydrodynamic model introduced in Sect. 4.3.1. It is seen from that model that the term  $v_E^2 k^2$  becomes dominant for large values of k. This condition also corresponds to a threshold for energy absorption. It can be understood in two different ways. The first picture is due to Landau and has been introduced to explain the absorption in plasmas. When the electron velocity  $v_F$  is equal to the phase velocity  $\omega/k$  of the field, the electron velocity and the field are always in phase so that the energy transfer is very efficient. This is the so-called Landau damping mechanism.

Another point of view is to consider that the absorption of a plasmon allows generating an electron hole-pair. There is a threshold value of k due to momentum conservation. Let us consider an interaction between an electron with initial momentum  $\hbar q$  and initial energy  $\hbar^2 q^2/2m$  with a surface plasmon with energy  $\hbar \omega$  and momentum  $\hbar k$ . The electron is close to the Fermi surface so that  $\hbar q = m v_F$ . The interaction must conserve the energy and the momentum so that we have

$$\hbar\omega = \frac{\hbar^2}{2m} \left[ (\mathbf{q} + d\mathbf{q})^2 - \mathbf{q}^2 \right] \approx \frac{\hbar^2 q dq}{m} \approx \hbar v_F dq,$$

$$\hbar \mathbf{k} = \hbar d\mathbf{q}$$
(4.26)

where we have given a rough estimate of  $\hbar\omega$ . Eliminating dq between the two equations, it is seen that for  $k\approx \omega/v_F$ , the interaction satisfies energy and momentum conservation. For usual electromagnetic excitations, this process is forbidden as the electromagnetic wavevector  $k\approx \omega/c$  is too small. Yet, surface plasmons may have large wavevectors and therefore this process can take place. We note here that this process can also take place when a dipole is close to a metal interface at a distance d smaller than  $v_F/\omega$  as its near-field contains large wavevectors. In summary, for values of k larger than  $\omega/v_F$ , the plasmon is damped as it can relax by generating an electron-hole pair. Clearly, this process introduces a cut-off spatial frequency for the surface plasmons. More information on the non-local description of the optical properties of solids can be found in Refs. [12–14, 17]. For noble metals, the typical Thomas–Fermi screening length is of the order of 0.1 nm and the typical Landau damping length scale is of the order of 1 nm.

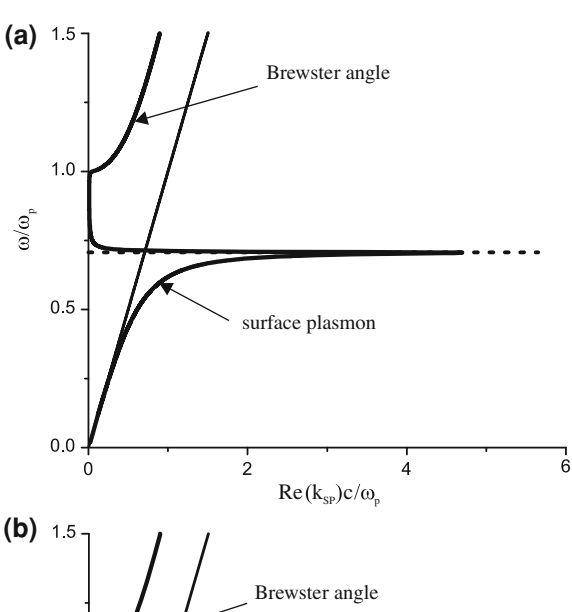
## 4.5.2 Dispersion Relation of a SPP

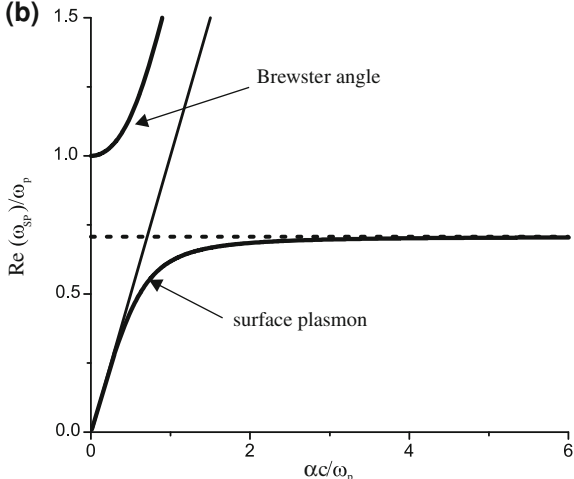
#### **Non-Lossy Drude Metal**

In this section, we discuss the dispersion relation of a surface plasmon using the discussion on the Drude model. As already stated, this is a crude model for noble metals when the frequency approaches the plasma frequency. We nevertheless use it for the sake of simplicity to discuss a few key issues. Although losses play a very important role, we start by neglecting them in order to base our introductory discussion on the simplest analytical formulas. However, we emphasize that the results obtained are only a rough approximation of the actual properties. We consider that the upper medium is a dielectric with a real dielectric constant  $\epsilon_1$  and the lower medium is a metal described by a non-lossy ( $\gamma = 0$ ) Drude model.

Inserting the Drude form of the dielectric constant in the dispersion relation given by Eq. (4.18), we obtain:

Fig. 4.5 Dispersion relation of a surface plasmon propagating along an interface separating a lossy metal described by the Drude model from a vacuum. The implicit dispersion relation can be solved searching for a real frequency and a complex wavevector or vice versa. Two different dispersion relations are obtained. a Frequency versus real part of the complex value of  $k_{SD}$ , **b** real part of the complex frequency versus the real wavevector  $\alpha$ .





$$k_{sp} = \frac{n_1 \omega}{c} \left[ \frac{\omega^2 - \omega_p^2}{(1 + \epsilon_1)\omega^2 - \omega_p^2} \right]^{1/2}.$$
 (4.27)

It is seen in this formula that the dispersion relation has an asymptote for a frequency  $\omega_p/\sqrt{1+\epsilon_1}$  (see Fig. 4.5). When plotting this equation, a second branch is obtained for frequencies larger than  $\omega_p$ . This branch is not a surface wave. Indeed, for  $\omega>\omega_p$ , the metal dielectric constant is a positive real number so that the metal is a dielectric from the optical point of view. In this regime, the waves can propagate although the refractive index is smaller than 1, indicating that the phase velocity is larger than c. The meaning of this branch of the dispersion relation is clear if one remembers that we did neglect the sign when solving the dispersion relation  $\epsilon_1\gamma_2+\epsilon_2\gamma_1=0$ .

As  $\omega$  becomes larger than  $\omega_p$ , the sign of the dielectric constant changes. In this range of frequency, the Eq. (4.18) is simply the solution of  $\epsilon_1 \gamma_2 - \epsilon_2 \gamma_1 = 0$  or, in other words, the zero of the reflection factor known as the Brewster angle.

### Surface Wave on a Lossy Drude Metal. Is it a Surface Plasmon?

In this section, we do not neglect losses. From Eq. (4.18), it is seen that for a real value of the frequency  $\omega$ , we find a complex value of the wavevector. Alternatively, it is possible to search for a solution of the equation with complex  $\omega$  and real  $\alpha$ . Both possibilities are equally valid. When plotting the real part of  $\omega$  as a function of the real part of  $\alpha$ , we find different dispersion relations as illustrated in Fig. 4.5 depending on the choice. This raises the question of the interpretation of the physical content of each dispersion relation. We shall come back to this subtle issue in Chap. 9.

We now compare the case of low frequencies with the case of optical frequencies. The question that is raised here is the nature of the surface wave for different frequencies. We start by analysing the Drude model in the low- and high-frequency regimes. It is easily seen that we can approximate the dielectric constant by:

$$\begin{split} \omega \gg \gamma(\omega), \quad \epsilon(\omega) \approx 1 - \frac{\omega_p^2}{\omega^2} \\ \omega \ll \gamma(\omega), \quad \epsilon(\omega) \approx 1 + i \frac{\omega_p^2}{\omega \gamma} = 1 + \frac{i \sigma}{\omega \epsilon_0}, \end{split} \tag{4.28}$$

where  $\sigma = ne^2/m\gamma$  is the DC conductivity. This form is enlightening as it shows that the optical properties of the metal are dominated by the plasmon response in the optical regime, whereas such properties are dominated by the drag force in the low-frequency regime. In the former case, the dielectric constant is almost a negative real number, whereas in the latter case, it is almost a pure imaginary number. It follows that the plasmonic (oscillatory) character of the surface wave is only meaningful in the regime  $\omega \gg \gamma$ . Indeed, if we rewrite the equations of motion of the electrons including the friction term as in Eq. (4.2), we find:

$$-\omega^2 x = i\omega\gamma x - \frac{ne^2}{m\epsilon_0}x. \tag{4.29}$$

For large frequencies or small frequencies, we have different approximate expressions:

$$\omega \gg \gamma(\omega), -\omega^2 x + \frac{ne^2}{m\epsilon_0} x = 0$$
  
$$\omega \ll \gamma(\omega), -i\omega\gamma x + \frac{ne^2}{m\epsilon_0} x = 0.$$
 (4.30)

It is clearly seen that the oscillation regime, which is the essence of a plasmon, corresponds only to the case  $\omega\gg\gamma$ . Instead, for small frequencies, the electronic response of the medium is dominated by the viscous term. Since the typical value of  $\gamma$  is  $10^{14}$  Hz, we note that a surface wave is hardly a surface plasmon for frequencies in the IR or smaller. On the other hand, the plasmonic behaviour (i.e. oscillatory behaviour) dominates the metal response in the case of femtosecond pulses. In summary, whereas from a macroscopic point of view, there is only one well-defined surface wave for any frequency, it turns out that from a microscopic point of view, the underlying behaviour of the electrons is very different in the low- and large-frequency regimes. Beyond this remark on semantics, this distinction is important as the detailed form of the dispersion relation is different for low frequencies and large frequencies as we examine in more detail below.

## Dispersion Relation of Surface Waves in the Radio-Frequency Range

Let us analyse in more detail the nature of the surface waves propagating along a conductive surface at low frequencies. We can give a more explicit form of the dispersion relation (4.18) in this regime. At radiofrequencies, the dielectric constant of a metal can be cast in the form:  $\epsilon = 1 + \frac{i\sigma}{\omega\epsilon_0} \approx \frac{i\sigma}{\omega\epsilon_0}$  so that the modulus of the dielectric constant is much larger than 1. A Taylor expansion of the wavevector of the surface wave can thus be written in the form:

$$k_{SP} = \frac{\omega}{c} \left[ \frac{1}{1 + \frac{1}{\epsilon}} \right]^{1/2} \approx \frac{\omega}{c} \left( 1 + \frac{i\omega\epsilon_0}{2\sigma} \right). \tag{4.31}$$

It is seen that in the limit of the perfect conductor,  $\sigma$  becomes infinite so that the wavevector becomes  $k = \omega/c$ . This entails that the wave is almost not confined close to the interface. Here, we recover the concept of surface wave used in the context of radio waves propagating along perfectly conducting wires or impinging on perfectly conducting structures. Note in particular that in this limit, there is no more damping as the wavevector becomes real. Let us now check that (4.31) is a valid solution of the equation  $\epsilon_1 \gamma_2 + \epsilon_2 \gamma_1$ . In the radio regime, the analysis is very different from the case of the surface plasmon in the optical regime. We consider the case of an interface separating a metal (medium 2) from a vacuum (medium 1) and we use the notation  $\epsilon = |\epsilon| \exp(i\phi_{\epsilon})$ .

$$\gamma_2 \approx \frac{\omega}{c} [\epsilon]^{1/2} \approx \frac{\omega}{c} |\epsilon|^{1/2} \exp(i\phi_{\epsilon}/2)$$

$$\gamma_1 \approx \frac{\omega}{c} \left[ \frac{1}{\epsilon} \right]^{1/2} \approx -\frac{\omega}{c} \left[ \frac{1}{|\epsilon|} \right]^{1/2} \exp(-i\phi_{\epsilon}/2). \tag{4.32}$$

The choice of determination of the square root is imposed by the condition  $Im(\gamma) > 0$  so that we had to include a sign minus for  $\gamma_1$ . It clearly appears then that the condition  $\epsilon \gamma_1 + \gamma_2 = 0$  is satisfied.

To summarize, inserting the Drude model in the dispersion relation of a surface wave yields two limits: the surface plasmon for  $\omega > \gamma(\omega)$  and the surface wave with  $k = \omega/c$  for  $\omega << \gamma$ . The latter is the so-called Sommerfeld or Zenneck mode. Note that when dealing with THz waves, the nature of the wave is closer to a radio surface wave than to a surface plasmon.

#### 4.5.3 Electrostatic Limit

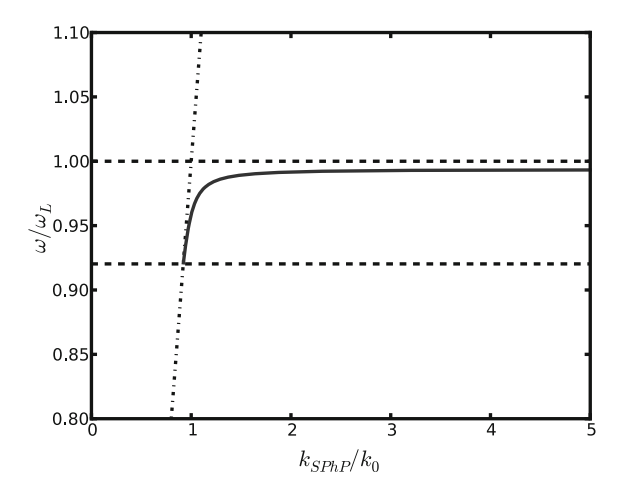
In this section, we extend the previous discussion to the non-retarded limit. Let us consider a dipole source oscillating at a frequency  $\omega = 2\pi c/\lambda$  at a distance d above the interface such that  $d \ll \lambda$ . As the distance is much smaller than the wavelength, the interaction between the source and the interface can be described within the electrostatic approximation. Here, we mean that the spatial structure of the field in the near-field of a small object can be computed by solving an electrostatic problem. To justify this statement, it suffices to examine the structure of the field radiated by an oscillating dipole. It is clearly seen that the leading terms are the terms varying as  $1/r^3$ . These terms yield a time-dependent electric field, which has the spatial structure of the field produced by an electrostatic dipole. In other words, the short distance approximation of the Green tensor is the electrostatic Green tensor. It follows that the interface can be modelled by introducing an image charge. The standard electrostatic formalism [16] allows one to introduce an electrostatic reflection factor given by  $\frac{\epsilon-1}{\epsilon+1}$ . Using a non-lossy Drude model (see next section), this yields a resonance for  $\epsilon + 1 = 0$  and hence for  $\omega = \omega_p / \sqrt{2}$  in agreement with the qualitative argument given in the first section. This frequency can also be derived by searching a mode of Laplace equation for the scalar potential for a system with one interface separating two homogeneous media [8].

### **4.6 Surface Phonon Polaritons**

#### 4.6.1 Lorentz Model

In the case of a metal and a frequency in the range  $[\gamma, \omega_p]$ , we have seen that the dielectric constant is negative. In this regime, the surface wave has the character of a surface plasmon. There are other situations such that the dielectric constant becomes negative. In agreement with the Kramers–Kronig relations, they always correspond to frequencies close to resonant excitation of the medium. In the infrared, crystals can absorb light due to the coupling to the optical phonons. There is a frequency range called reststrahlen band where the dielectric constant is negative. A simple

Fig. 4.6 Dispersion relation of a surface phonon polariton propagating along a GaAs/vacuum interface with dielectric constant given by a non-lossy Lorentz model  $\epsilon(\omega) = \epsilon_\infty \frac{\omega_L^2 - \omega^2}{\omega_T^2 - \omega^2}$ . The wavevector axis has been normalized by  $\omega_L/c$  and the frequency axis by  $\omega_L$ .  $\omega_L = 292.1 \, \mathrm{cm}^{-1}$ ,  $\omega_T = 267.8 \, \mathrm{cm}^{-1}$ ,  $\epsilon_\infty = 11$ 



model allows to show that the dielectric constant can be cast in the form:

$$\epsilon(\omega) = \epsilon_{\infty} \frac{\omega_L^2 - \omega^2 - i\Gamma\omega}{\omega_T^2 - \omega^2 - i\Gamma\omega}$$
(4.33)

where  $\omega_L$  is the longitudinal frequency and  $\omega_T$  is the transverse optical frequency. These frequencies are due to the presence of optical phonons. Like for electrons, a longitudinal solution exists at  $\omega_L$ . It corresponds to a charge density wave. Here, it is a polarization charge density. A detailed discussion can be found in the books by Ziman [13] or Ashcroft and Mermin [12] for example.

There are some differences with the plasmon case. The dielectric constant is negative only in the range  $[\omega_T, \omega_L]$ . This range corresponds to a wavelength range of the order of  $1\,\mu$ m typically. The central frequency is typically between 10 and 40  $\mu$ m. Hence, the surface phonon polariton can exist only in the mid-infrared or near THz. A very important similarity of the surface phonon polariton with the surface plasmon is the existence of a horizontal asymptote in the dispersion relation. This indicates the presence of a peak in the local density of states close to the interface as will be discussed later [31, 32]. Figure 4.6 is an example of a dispersion relation of a surface phonon polariton. It corresponds to the case of a wave propagating at the interface between GaAs and a vacuum.

## 4.7 A Potpourri of Surfaces Waves: Sommerfeld or Zenneck Modes, Quasicylindrical or Lateral Wave

In the previous sections, we have introduced the surface waves as solutions of Maxwell equations in the presence of interfaces. We have seen that there are several cases where a solution can be found for both s- and p-polarizations. Surface waves

often receive different names depending on the frequency range (visible, radio waves) or type of waves (electromagnetics, seismology, acoustics). It turns out that the topic of surface waves is much broader than the topic of surface plasmons. Electromagnetic surface waves have been studied in the context of radiowave propagation well before surface plasmons were discovered. Surface waves have also been studied in different contexts. The purpose of this section is not to give a detailed discussion, but instead to introduce the terminology and to serve as a lecture guide.

## 4.7.1 Historical Perspective

The concept of surface wave has been introduced by Zenneck at the begining of the nineteenth century. His motivation was to identify the mechanism of long-range propagation of radio waves. The basic idea was that a surface wave decays as 1/rinstead of  $1/r^2$  in 3D. It finally turned out that the correct explanation is the presence of the ionosphere so that the space between the earth and the ionosphere acts as a waveguide. The concept of surface wave was further studied by Sommerfeld when he derived a rigorous solution of the field generated by a dipole above a flat interface separating two homogeneous media. In Sommerfeld's derivation, the surface mode is defined as the contribution of the pole of the reflection factor to the field produced by a dipole above an interface. This definition agrees with our remark on the previous section linking the surface wave with the pole of the reflection factor. This surface wave is often named after Zenneck or Sommerfeld. The much debated existence of a surface wave in the radio literature is due to the fact that the field has a complex structure. It should be stressed that there is perfect consensus on the integral form of the field radiated by a dipole above an interface. Yet, such an integral is not useful for practical applications. Several authors have therefore derived approximate analytical expressions valid in different cases. It is only when it comes to the interpretation of the different contributions that there is a debate. The reader will find a detailed account of these works in the books by Brekhovskikh [1], Banos [2], Felsen [3], King [4] and a recent review paper by Collin [34]. To make a long story short, let us summarize the situation as follows. The field radiated by a dipole can be decomposed into a sum of plane waves. In the presence of an interface, each plane wave is transmitted and reflected. The total field is hence the field radiated by the source plus a sum of plane waves weighted by the corresponding Fresnel factors. When performing the integral over all reflected plane waves, one can extract the pole contribution due to the pole of the reflection factors. This contribution yields the surface waves. There is a second contribution that appears when using analytical techniques to evaluate asymptotically the integral in the complex plane: it is the contribution along the branch cuts in the complex plane. We give a very brief account of this wave in the following section.

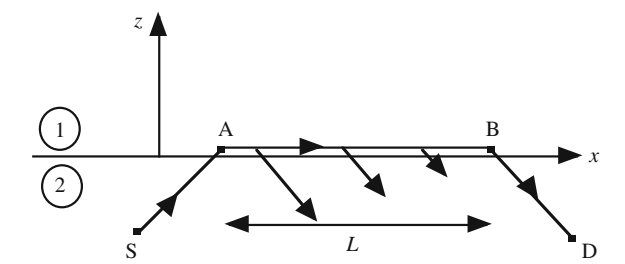


**Fig. 4.7** Illustration of the lateral wave. The wave propagates from the source to the interface at the critical angle. After refraction, it propagates along the interface as a plane wave and reenters the medium continuously. This contribution becomes dominant when the medium is lossy so that direct propagation in the medium is rapidly damped

#### Lateral Wave

The second noteworthy contribution is called lateral wave in the radiowave and seismology community. It has been investigated only recently [35] in the optics community and was called quasicylindrical wave [36, 38] or Norton wave [39]. An extensive discussion of this wave in the context of propagation of radio waves along the earth was written by King [4]. In this section, we briefly describe a physical picture of the origin of the lateral wave. Let us consider a source located at z = -d in a material medium with refractive index n. The lateral wave is the wave corresponding to propagation from the source to the interface at the critical angle followed by a refraction at the interface and propagation by a plane wave parallel to the interface in the medium z > 0 (see Fig. 4.7). When the medium at z < 0 is absorbing and the medium z > 0 is not absorbing, this is the most efficient mechanism for propagation over large distances as most of the energy is in the nonabsorbing medium. When excited by a line, this two-dimensional wave decays as  $1/L^{3/2}$  where L is the distance of propagation along the interface. Instead, the surface wave has an exponential decay.

The lateral wave is very well known in seismology. An excellent account of surface waves in elastic media can be found in the textbook by Aki and Richards [40]. In the context of radiowaves, it has received a lot of attention in the 1960s and 1970s. The reader will find a detailed account in the works quoted above [1–4, 34]. Of particular interest in optics are Refs. [35, 36, 38, 39] where it has been shown that these waves cannot be neglected in many cases when studying propagation and scattering along metallic surfaces including the resonant transmission phenomenon [37].

In what follows, we focus on key properties of surface plasmons related to (i) the local density of states, (ii) the spatial confinment and (iii) the fast temporal response. Regarding these three aspects, surface plasmons are very different from lateral waves. These properties are intimately linked to the underlying electronic character of the surface plasmon polariton.

### 4.8 Key Properties of SPP

Plasmonics has become a very active area of research due the large number of applications. However, all these applications rely on a small number of key properties. The purpose of this chapter is to discuss these key properties of surface plasmons in simple and general terms. We will first analyse the importance of having a dispersion relation with very large wavevectors. We will discuss the implications in terms of field confinment and the implications in terms of local density of states. Finally, we will discuss the spectral width of surface plasmon excitation and its significance in terms of ultrafast response.

## 4.8.1 Confinment of the Field

A large number of applications of surface plasmons rely on the possibility of producing highly confined fields and/or to produce or observe light at a length scale smaller than the wavelength in a vacuum. The purpose of this section is to review the basic properties of surface plasmons underlying these applications. Let us first consider the case of surface plasmons propagating along flat interfaces. It is necessary to distinguish between confinment of the field along the normal of the interface and confinment in the plane of the interface. We have already given some orders of magnitude of the field confinment away from the interface in Table 4.1. We now discuss the potential of surface waves for in-plane confinment.

#### **Lateral Confinment**

The losses introduce a limitation to the extent of the surface waves along the interface. The decay length is given by  $1/Im(k_{\rm SP})$ . This value depends significantly on the losses of the material. A typical order of magnitude for noble metals and visible frequencies is a few micrometers. We note that this length is considerably reduced for frequencies close to the asymptote of the dispersion relation. The main reason is connected to our previous discussion. A photon-like surface plasmon is poorly localized close to the interface and has most of its energy in the dielectric above the metal where there are no losses. By contrast, a plasmon-like surface plasmon has a large part of its energy in the metal so that it is very sensitive to the losses. It is a general rule that modes with most of the field energy in the dielectric have a longer propagation length. In practice, another mechanism can reduce the propagation length. It is due to radiative leakage of energy (often called radiative losses) due either to scattering by random roughness or by diffraction by a periodic structure such as a grating.

We have discussed the larger length scale of a surface plasmon along the interface. We now address the issue of the smallest length scale. Let us remind what is the origin of the confinment limit in a vacuum when dealing with a monochromatic field at frequency  $\omega$ . Due to the dispersion relation in a vacuum, the wavector modulus is given by  $k=\omega/c$ . Let us assume that we consider an electromagnetic field in the vacuum far from any boundary. The field can then be decomposed into a sum of planes waves with real wavectors. A property of Fourier transform gives  $\Delta x \Delta \alpha \geq 2\pi$  where  $\alpha$  is the x-component of the wavector. If we deal with a field in a vacuum far from any surface or object, the modulus of the wavevector is given by  $\omega/c$  so that the smallest possible size of the field along the x-axis is given by  $2\pi/\alpha_{max} = \lambda$ . Hence, the field cannot vary rapidly as it would, close to a tip for example.

By contrast, it was seen in Fig. 4.5b that the maximum wavector given by the plasmon dispersion relation may be much larger than  $\omega/c$ . This seems to pave the way to a strong confinment of the field. There have been some attempts to take advantage of this strong localization of the field. It has been proposed by Pendry that this property can be used to realize a superlens [41] with a simple thin film supporting surface plasmons. The experimental implementation has been reported by two groups in the visible using silver [42] and in the infrared using SiC [43]. Another proposal for superresolution based on the use of surface plasmons was put forward in Ref. [44]. The key idea was to take advantage of the large wavevectors that are seen on the dispersion relation (with the choice of a real wavevector and a complex frequency). A debate followed that proposal [45, 46]. However, in practice, it is not possible to fully take advantage of this property of surface plasmons because losses play an important role. We shall show in Sect. 4.9 that the relevant dispersion relation that must be used for discussing confinment of the field is the dispersion relation shown in Fig. 4.5a. It is seen that the wavector modulus is limited due to the so-called backbending of the dispersion relation. This entails that the surface plasmons always have an intrinsic limitation in terms of resolution. This is a rather severe limitation as in many cases, the maximum value of the wavector is hardly larger than  $2\omega/c$ . Let us stress that so far, the resolution obtained in different experimental results [42, 43] appears to be indeed limited by the losses.

However, surface plasmons are often used to produce highly localized spots that go well beyond these limitations. In all the practical examples, the origin of the localization of the fields lies in the spatial structure of the material. In most cases, one uses nanometric particles or nanostructures such as nanowires, nanoholes or indentations in a metallic substrate. Examples include the first implementation of nearfield optical microscopes [47, 48], the strong confinment obtained using nanoholes [49] and the use of tips as nanosources [50, 51]. One might then ask what is the role of plasmons in that case? A simple answer can be obtained by analysing the fields produced by a subwavelength spherical particle of dielectric constant  $\epsilon$  and radius a (see the chapter by J. Aizpurua). If  $a \ll \lambda$ , the non-retarded approximation is valid so that the spatial structure of the field can be found using an electrostatic approximation. The scattered field is given by the field of a dipole for a distance r > a. The field decays as  $1/r^3$  for r > a so that the confinment is only limited by a. This confinment is due to the geometry and not to the plasmon, it is independent of the material properties. Yet, the amplitude of the field depends on the material properties at the particular frequency considered. For instance, when dealing with a spherical nanoparticle with radius a, its polarizability  $\alpha_p$  can be written as:

$$\alpha_p = 4\pi a^3 \frac{\epsilon(\omega) - 1}{\epsilon(\omega) + 2}.\tag{4.34}$$

In the previous equation, it is clearly seen that the only limitation to the confinment is the fact that the amplitude of the dipole tends to zero with a. However, if the frequency is such that  $\epsilon(\omega)+2$  is almost zero, a resonance is excited as it will be discussed in more detail in Sect. 4.8.3. Within the Drude model, this condition is satisfied for  $\omega=\omega_p/\sqrt{3}$ . Thus, it is seen that a surface plasmon resonance of a particle is useful for light confinment indirectly: its role is to compensate for the small value of the dipole moment of a small object.

In the above example, we have seen that the form of the electric field close to a particle can be factorized in two terms. The dependence on space variables is the electrostatic form of the dipolar field, the frequency dependence is given by the polarizability. Only the latter has a resonant behaviour which is the signature of the plasmon resonance.

This concept of confinment by geometry coupled to resonance enhancement has been put forward by Li, Stockman and Bergman who proposed to use a chain of nanoparticles to realize an efficient nanolens [52].

Finally, we mention another possibility for confining the field. Metal/dielectric/metal (MDM) structures can support surface modes which are plasmonic even if the dielectric is only a few nanometers thick so that these modes are highly localized in the gap [53]. Remarkable guiding properties have been demonstrated using channel surface polaritons which essentially rely on this type of structure [54]. Other applications of the confinment in MDM structures include applications for light emission in the weak coupling regime [55] and achieving strong light-matter coupling [56]. These are intimately related to the concept of local density of states that we now introduce.

## 4.8.2 Surface Plasmons Contribution to the Local Density of States

The lifetime of an atom can typically be reduced by orders of magnitude when it is located close to an interface. This has been first demonstrated experimentally by Drexhage [57]. Excellent discussions can be found in Refs. [17, 58, 59]. Similarly, the electromagnetic energy density at thermodynamic equilibrium can be increased by orders of magnitude close to an interface [31, 60]. Both phenomena depend on the density of electromagnetic states. The changes by orders of magnitude are the clear signature of a change of the physical phenomena that determine the local density of states. In both cases, the contribution of surface waves plays a key role. The purpose of this section is to briefly review the concept of Local Density Of States (LDOS)

and to show how the surface waves may drastically modify it. We will briefly discuss applications to light emission assisted by surface waves. We will also show that the influence of surface plasmons on the LDOS plays a key role in the Casimir force, a pure quantum electrodynamics phenomenon.

## **Elementary Introduction to the Density** of Electromagnetic States

Before starting the discussion, we make a remark on semantics regarding the meaning of state, mode and eigenfunction. The word "state" is usually used in the context of quantum mechanics or statistical physics, whereas the word "mode" is often used in the context of wave theory. Both words deal with eigenfunctions of linear operators so that the terms are often interchanged. The term density of states is used for  $g(\omega)$  such that  $g(\omega)d\omega$  is the number of states (modes) with frequency in the interval  $[\omega, \omega + d\omega]$ . To begin, we briefly remind how to derive the density of electromagnetic states or, in other words, how to count the number of different solutions (plane waves) of Maxwell equations in a vacuum. We will then analyse how the presence of surface waves modifies the situation. It is useful to introduce a virtual cubic box of size L and to look for fields satisfying periodic boundary conditions. Indeed, this allows one to discretize the solutions and therefore to count them. From the periodic boundary condition, it follows that the wavevector components are of the form  $\alpha = n2\pi/L$ ,  $\beta = m2\pi/L$ ,  $\gamma = l2\pi/L$  where n, m, l are integers. In k-space, the volume occupied by a state is therefore  $(2\pi/L)^3$  so that the number of states in the volume element  $d\alpha d\beta d\gamma$  is  $2L^3 d\alpha d\beta d\gamma/(2\pi)^3$  where the factor 2 accounts for the two possible polarizations of each state. The density of states in k-space per unit volume is thus given by  $1/4\pi^3$ . We can now easily find the number of states with a given frequency  $\omega = ck$ . They occupy the volume  $4\pi k^2 dk$  in k-space. Using the dispersion relation  $k = \omega/c$ , we find the number of states per unit volume in the range  $\omega$ ,  $\omega + d\omega$ :

$$g_v(\omega)d\omega = \frac{\omega^2}{\pi^2 c^3} d\omega, \qquad (4.35)$$

where we have introduced the density of states per unit volume  $g_v(\omega)$  in a vacuum. We now illustrate the importance of this concept using three examples. Let us first count how many states  $N(\omega)$  are available between 0 and  $\omega$  in a volume V:

$$N(\omega) = V \int_{0}^{\omega} g_{v}(\omega') d\omega' = V \frac{\omega^{3}}{3\pi^{2}c^{3}} = \frac{8\pi}{3} \frac{V}{\lambda^{3}}.$$
 (4.36)

The simple rule to remember is that the number of states with frequency smaller than  $\omega$  is roughly given by the volume divided by  $(\lambda/2)^3$ . The second example is the form of the energy of the blackbody radiation. Each mode has a quantum of energy  $\hbar\omega$  and the mean excitation number is given by Bose–Einstein statistics

 $n_{BE}(\omega) = 1/[\exp(\hbar\omega/k_BT) - 1]$ . The product of these two terms by the density of states yields the Blackbody density of energy at temperature T:

$$u(\omega, T) = \frac{\hbar\omega^3}{\pi^2 c^3} \frac{1}{\exp(\hbar\omega/k_B T) - 1}.$$
 (4.37)

We now show how the local density of states plays a key role in the lifetime of a two-level system. From the Fermi golden rule, it is known that the lifetime is proportional to the number of final states. When studying the rate of radiative relaxation, the radiative decay rate is therefore proportional to the number of electromagnetic states at the corresponding frequency. This can be seen by comparing the stimulated and spontaneous emission rates given by the Einstein coefficients. Their ratio is given by:

$$\frac{A_{21}}{B_{21}\hbar\omega} = \frac{\omega^2}{\pi^2 c^3},\tag{4.38}$$

which is nothing but the vacuum density of states. For stimulated emission, only the mode of the incident photon has to be considered, whereas for spontaneous emission, one has to sum over all possible electromagnetic states. Hence, the spontaneous emission coefficient is proportional to the LDOS. Let us finally point out a slight difference in the definition of local density of states depending on the application: evaluating the equilibrium energy or evaluating spontaneous emission. A two-level system that is coupled to the electromagnetic field through an electric dipole moment can couple only to the component of the electric field parallel to the electric dipole. The relevant form of the local density of states is thus called projected-LDOS as only one component of the field matters. In a vacuum, this is simply a factor 3 difference as the field is isotropic. In more complex situations, the LDOS can be different for different polarizations. It is well known for instance that the lifetime of a molecule close to an interface depends on the orientation of its dipole moment.

To summarize, the concept of density of states plays a key role when looking at the radiative decay of a two-level system and when looking at the thermodynamic properties of electromagnetic radiation. In what follows, we shall analyse how the presence of surface plasmons drastically modifies the density of states. We will give a hint of the physical reason behind this phenomenon and derive from it an upper limit of the number of states.

#### **Electron and Phonon Density of States**

We have pointed out that surface plasmons are polaritons. In other words, they are half photons, half electrons. Since electrons are also described by waves, the same technique can be used to analyse the density of states. The density of states in k-space is also given by  $1/4\pi^3$  for electrons. Here, we have accounted for the degeneracy due to the spin 1/2 of the electron. The total number of states in a crystal of volume V with N atoms is given by 2N for a s band. Similarly, the total number of phonon

states is given by 3N because this is simply the total number of degrees of freedom of the atoms. Hence, the number of states per unit volume is roughly N/V, which is the inverse of the volume  $a^3$  of a unit cell of the crystal. If we now compare the number of states available for light in a vacuum  $((2/\lambda)^3 \approx 10-19\text{m}^{-3})$  and for condensed matter excitations  $(1/a^3 \approx 10-30\text{m}^{-3})$ , we find a difference of 11 orders of magnitude.

This crude estimate shows what is the key to the efficiency of plasmons or optical phonons in increasing the energy density or in reducing the lifetime of quantum emitters. The density of states of polaritons benefits from the large number of states of condensed matter excitations (electrons or phonons). However, many of these modes do not contribute to surface waves. A better estimate of the number of surface plasmons can be obtained by working with the dispersion relation and introducing a cut-off at  $\omega/v_F$  as we will discuss below.

## Increasing the Density of States: Surface Waves, Slow Light and Microcavities

Let us make a pause in the discussion of surface wave density of states and make a comment regarding the increased density of states in a waveguide with slow velocity. It is known that slow velocity systems can be used to increase the density of states. The mechanism is depicted in Fig. 4.8. As the dispersion relation becomes flat close to the band edge, the number of states (represented by dots) with a frequency in the interval  $\Delta\omega$  increases. This behaviour is known as van Hove singularity. A major advantage of photonic crystals is that there are almost no losses in dielectric media. Since the density of states diverges (the group velocity becomes zero), these systems seem to be the perfect solution to engineer the optical properties of quantum emitters. Yet, it is important to emphasize that the number of states available when using a waveguide is always finite. A plasmonic system can provide a local density of states which is orders of magnitude larger than what can be achieved with a slow waveguide. In order to understand this apparent paradox, let us first remind about the derivation of the density of states for a one-dimensional system. We consider a waveguide branch characterized by a dispersion relation  $k_z(\omega)$  for a mode propagating along the z-axis in a periodic waveguide with period a. In order to count the number of modes, we again consider that the system has a finite length L and we introduce the so-called Born von Karman (or periodic) boundary conditions stipulating that the system is periodic with period L along z. It follows that  $k_z = p 2\pi/L$ . The number of modes in the interval  $d\omega$  corresponding to an interval  $dk_z$  is given by

$$g(\omega)d\omega = \frac{L}{2\pi}dk_z = \frac{L}{2\pi}\frac{dk_z}{d\omega}d\omega. \tag{4.39}$$

It is seen that the density of states diverges as the group velocity goes to zero. However, one should keep in mind that *this divergence is integrable* so that the number of states in a finite interval  $[\omega_1, \omega_2]$  always remains finite.

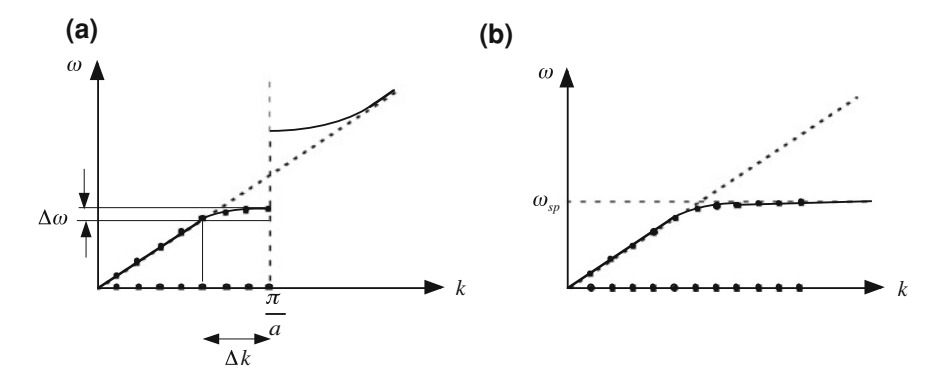


Fig. 4.8 Increasing the density of states. States are characterized by k and  $\omega$ . They correspond to a point located on the dispersion relation. In k-space, the density of states per unit length is constant and takes the value  $1/2\pi$ . **a** shows that in  $\omega$  space, the density of states increases close to the gap edge, **b** shows that the increase close to the asymptote is considerably larger as the asymptote is not limited along the k-axis

This is clearly seen in Fig. 4.8 where we represent schematically the dispersion relation of a guided wave close to a band edge and the dispersion relation of a surface plasmon. It is seen that the modes are simply redistributed close to the band edge so that this only concerns a finite number of modes although mathematically the density of states diverges. An upper value of the number of modes involved is clearly the size of the Brillouin zone  $2\pi/a$  divided by the interval between two modes  $2\pi/L$ . We find L/a. The period of a photonic crystal is of the order of the wavelength so that we obtain an estimate of an upper bound of the number of modes in a photonic crystal given by  $L/\lambda$ . This is orders of magnitude less than the number of modes available with surface waves at resonance.

We now discuss briefly another possibility for increasing the density of states originally proposed by Purcell. The idea is to use a cavity with a single mode. The number of states per unit volume is thus 1/V where V is the cavity volume. Taking into account the finite value of the quality factor of the cavity, we obtain for a Lorentzian resonance a density of states:

$$g(\omega) = \frac{1}{V} \frac{\gamma}{2\pi} \frac{1}{(\omega - \omega_0)^2 + \gamma^2/4}.$$
 (4.40)

At resonance, the density of states is thus given by:

$$g(\omega_0) = \frac{2}{\pi V \gamma}. (4.41)$$

The Purcell factor is the local density of states in the cavity normalized by the density of states in a vacuum<sup>1</sup>:

$$F_p = \frac{2}{\pi V \gamma} \frac{3\pi^2 c^3}{\omega^2} = \frac{3}{4\pi^2} Q \frac{\lambda^3}{V},\tag{4.42}$$

where  $Q = \omega_0/\gamma$ . This derivation is based on a poorly defined volume. A more accurate description should account for the polarization of the mode field as well as its space dependence. Indeed, the field in a cavity is not uniform so that the coupling between a mode and an emitter will strongly depend on the exact location of the emitter. A more detailed analysis can be found in Refs. [66–68].

#### **Local Density of States Due to Surface Waves**

We first start the discussion of the role of surface waves on the local density of states with a qualitative discussion based on the dispersion relation. We then present a more quantitative analysis. It is seen in Fig. 4.8 that the number of states provided by a surface plasmon at resonance is infinite as the dispersion relation seems flat and unbounded. This is not correct and is a consequence of the model of the dielectric constant that does not account for the non-locality. A non-local dielectric constant introduces a cut-off [17] in the dispersion relation given by  $v_F \omega_{SP}/\sqrt{2}$  where  $v_F$  is the Fermi velocity as already discussed. We can now easily compare the density of states due to surface plasmons to the vacuum density of states. A rough estimate of the number of surface plasmons per unit area is given by dividing the area of a disk with a radius  $\pi k_{SP \text{ max}}^2$  by the area per state  $1/4\pi^2$ :

$$\frac{\pi k_{SP,\text{max}}^2}{4\pi^2} \approx \frac{\omega_{SP}^2}{4\pi v_F^2},\tag{4.43}$$

which is clearly much larger than what we found for dielectrics where the order of magnitude is  $1/\lambda^2 \approx \omega^2/c^2$ . We remind that  $c/v_F$  is typically on the order of 300.

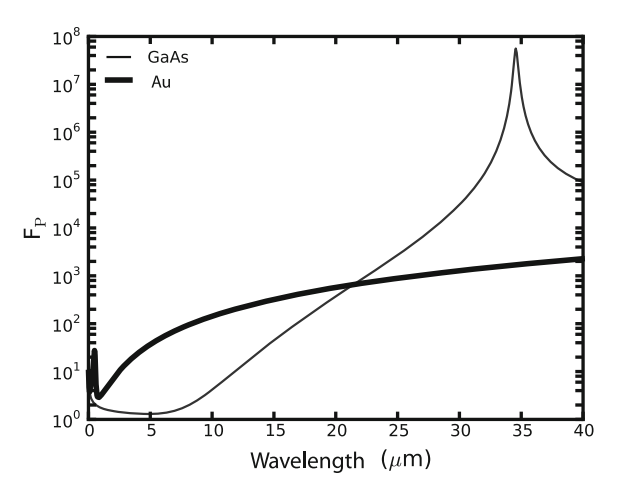
We now turn to a quantitative analysis of the local density of states due to surface waves. An explicit form can be derived from the imaginary part of the Green tensor. The reader will find a detailed analysis in Ref. [32]. Of particular interest is the asymptotic expression of the local density of states at a distance z from the interface such that  $z \ll \lambda$ .

$$\frac{g(z,\omega)}{g_v(\omega)} = \frac{Im[\epsilon]}{|\epsilon+1|^2} \frac{1}{4(k_0 z)^3},$$
(4.44)

where  $g_v(\omega)$  stands for the vacuum density of states. The surface plasmon resonant contribution is clearly given by the term  $1/|\epsilon+1|^2$ . Figure 4.9 illustrates the contri-

<sup>&</sup>lt;sup>1</sup> In the context of Fermi golden rule, a factor 1/3 is introduced in order to account for the fact that a given dipole can couple to only one component of the electric field.

Fig. 4.9 Local density of states at a distance of 10 nm above an interface separating a vacuum from gold or GaAs



bution of this term to the LDOS at a distance of 10 nm of a gold surface and a GaAs surface.

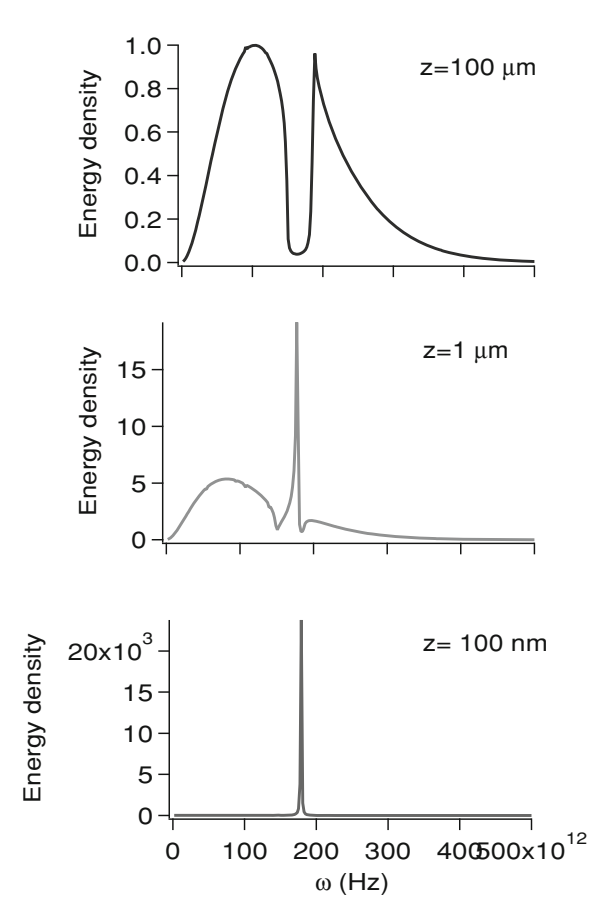
In both cases, the presence of the surface wave results in a peak in the LDOS. It clearly appears that the role of the surface phonon polariton is orders of magnitude more important than the surface plasmon.

#### Local Density of States and Energy Transfer at Nanoscale

Another remarkable consequence of the increase of the density of states due to surface waves is the increase of energy density at equilibrium. Since the modes are thermally excited at equilibrium, there is a large energy density close to the interface. Figure 4.10 illustrates the evolution of the energy spectral density at different distances from an interface separating SiC from a vacuum. Two features appear clearly in this figure: (i) the energy density normalized by the energy density of a blackbody is increased by several orders of magnitude and (ii) the spectrum becomes quasimonochromatic. The existence of surface waves thermally excited has been observed experimentally by de Wilde et al. [61] who were able to obtain near-field images of samples without external illumination. We note that in the near-field, the spectrum becomes quasimonochromatic indicating that the field is partially temporally coherent. The coherence time is essentially the decay time of the surface phonon polariton as discussed in Refs. [31, 33].

As a consequence of this increase of energy density close to the interface, the heat transfer between two half-spaces separated by a distance smaller than the wavelength increases. This heat transfer mechanism can be viewed as mediated by the surface phonon polaritons. Since the number of surface waves increases dramatically at small distance, the heat flux through a vacuum gap can be enhanced by orders of magnitude. This effect due to surface waves was predicted in Refs. [62, 63] and measured recently

Fig. 4.10 Electromagnetic energy density at equilibrium at 300 K as a function of distance from an interface vacuum/SiC. The energy density is normalized by the maximum blackbody value at 300 K



[64, 60]. The heat transfer through the gap due to this surface phonon interaction can be viewed as a phonon tunelling phenomenon. It can also be described in a form similar to the Landauer conductance. It has been shown recently [65] that each mode characterized by  $(\alpha, \beta, \omega)$  yields a contribution to the radiative heat conductance proportional to the thermal quantum of conductance  $\pi^2 k_B^2 T/3h$  and a transmission factor where  $k_B$  is Boltzmann's constant and h is Planck's constant.

# Local Density of States and Light Emission Assisted by Surface Waves

In the introduction of this section, we have cited the pioneering experiment by Drexhage showing that the lifetime of an emitter can be drastically reduced close to an interface. When the distance is below 5 nm, the energy goes into heat in the substrate and surface plasmons do not provide a significant contribution to this mechanism.

However, if the distance is larger than approximately 10 nm, most of the energy goes into the surface plasmon for appropriate frequencies. In the case of a flat surface, this energy is then converted into heat. However, if e.g. a grating is ruled on the surface, the energy can be radiated. In that case, the surface works as an antenna: the energy of the source is efficiently coupled into the surface (due to the large LDOS) and then efficiently radiated by the surface (due to the grating). This idea has been put forward in the context of light-emitting diodes [69, 70]. The influence of the surface plasmon resonance on the single molecule fluorescence assisted by a resonant particle has been investigated theoretically [71, 72]. Quantum wells' light emission assisted by surface plasmons has been demonstrated more recently [73]. A remarkable demonstration of optical nanoantennas at the level of a single emitter has been reported using metallic nanospheres. An emitter located at a distance of the order of 10 nm excites efficiently the surface plasmon of the particle. By properly choosing the radius of the particle, it is possible to increase the ratio of power emitted versus the power absorbed in the particle so that the nanosphere becomes an efficient nanoantenna. Two experiments have clearly demonstrated how metallic nanospheres can be used as efficient nanoantennas to increase molecules' fluorescence [74, 75]. More recently, several metallic structures have been proposed as antennas to control the angular emission and also increase the emission rate [55, 76, 77].

#### **Local Density of States and Casimir Force**

Another consequence of the contribution of surface plasmon to the LDOS is the Casimir force between two metallic parallel plates. Casimir force is a pure quantum electrodynamics effect that manifests itself at macroscopic scale. Casimir predicted [78] that there is an attractive force between two parallel perfectly conducting surfaces at 0 K separated by a gap of width d. Since then, his remarkable prediction has been measured experimentally with great accuracy [79–81]. However, when comparing the measurements with the data, the assumption of a perfect conducor cannot be used any longer [82]. A careful analysis shows that the surface plasmons are responsible for the forces actually observed [83–85]. We give here a brief qualitative discussion of this effect. We refer the reader to references [83] for a further discussion. The gap behaves as a waveguide with a set of modes. From the quantum electrodynamics point of view, each mode  $(k, \omega)$  has a zero point energy at 0 K given by  $\hbar\omega$ . It follows that the total energy is given by  $\sum_n \hbar \omega_n$  where the sum is over all modes of the gap. Since the number of modes in the gap decreases when the width d decreases, the energy also decreases. Hence, the electromagnetic energy plays the role of an attractive potential. In the original derivation of Casimir, modes of a planar waveguide with perfectly conducting surfaces were used. When accounting properly for the optical properties of metals, it turns out that the density of states is dominated by the surface plasmon contribution.

# 4.8.3 Broad Spectrum and Fast Response

When comparing plasmonic resonators with dielectric resonators, the presence of losses in the metal is often put forward. The quality factor of the resonator depends on the dielectric constant of the material. To illustrate this idea, we consider the polarizability of a small sphere. Close to the sphere resonance, we can expand the dielectric constant. We use the notation  $\epsilon(\omega) = \epsilon_R(\omega) + i\epsilon_I(\omega)$  and assume that  $\epsilon_R(\omega_0) = -2$ .

$$\epsilon(\omega) \approx \epsilon_R(\omega_0) + \frac{\mathrm{d}\epsilon_R}{\mathrm{d}\omega}(\omega - \omega_0) + i\epsilon_I(\omega_0)$$

$$\approx -2 + \left(\frac{\mathrm{d}\epsilon_R}{\mathrm{d}\omega}\right)_{\omega_0} [\omega - \omega_0 + i\Gamma], \tag{4.45}$$

where  $\Gamma = \epsilon_I(\omega_0)/[\mathrm{d}\epsilon_R/\mathrm{d}\omega]$ . The polarizability can be approximated by a Lorentzian profile:

$$\alpha(\omega) = 4\pi a^3 \frac{\epsilon(\omega) - 1}{\epsilon(\omega) + 2} \approx \frac{12\pi a^3}{\left(\frac{\mathrm{d}\epsilon_R}{\mathrm{d}\omega}\right)} \frac{1 - i\epsilon_I(\omega_0)/3}{\omega_0 - \omega - i\Gamma}$$
(4.46)

We have already seen that metallic losses in the optical frequency regime are due to electron—electron interaction and to electron—phonon interaction. These processes have a low dependence on temperature so that they cannot be suppressed. Hence, these losses are a specific property of a plasmonic resonator. They result in two properties of surface plasmons. The quality factor of the resonance depends on the imaginary part of the dielectric constant at the resonance frequency. A typical quality factor for plasmons is between 10 and 100. Accordingly, the relaxation time of the system in the visible is of the order of a few femtoseconds. A small quality factor can be viewed as a drawback in terms of Purcell effect for instance. On the other hand, a resonator with a large bandwidth can be very interesting. In particular, it allows one to perform a coherent control of pulses on extremely short time scales. This particular property is the basis of a large number of recent contributions [86, 87]. Another important application is the possibility of designing a nanoantenna with a broad bandwidth [55].

Finally, we should emphasize that the relaxation time of a plasmonic resonance does also depend on the geometry of the structure. To illustrate this idea, we discuss the example of the so-called long-range and short-range surface plasmons on symmetric thin metallic films in a dielectric first investigated by Sarid [88]. In order to understand why the geometry influences the relaxation time of a plasmonic mode, it is sufficient to realize that the field of the long-range surface plasmon energy is mostly in the non-lossy dielectric, whereas the short-range surface plasmon is more confined in the metal where losses take place. This has also been widely discussed in the context of shell structures [89]. In both cases, the coupling between two modes

depends on the thickness of the metal film and allows to control the resonance frequencies.

#### 4.9 Surface Plasmon Polaritons on Lossy Materials

As already mentionned, the dispersion relation given by (4.18) cannot be solved by using a real frequency and a real wavevector when the dielectric constant is complex. Yet, a solution can be found when using either a complex  $\alpha$  and a real  $\omega$  or vice versa. These two choices lead to different shapes of the dispersion relation as seen in Fig. 4.5. One dispersion relation has an asymptote for very large values of  $\alpha$ , while the other has limited values of  $\alpha$  and presents a backbending. We have discussed the key properties of surface plasmon with emphasis on the lateral confinment (e.g. necessary for a super lens) and on the large LDOS (e.g. necessary for nanoantennas). Since the existence of a horizontal asymptote plays a key role both for the transverse confinment of the field (large k values of surface plasmons are needed) and for the LDOS (flat dispersion curve), it is important to establish a prescription on which choice should be made when looking for a dispersion relation. In this section, we discuss the origin and physical content of these two dispersion relations summarizing Ref. [90] where further details can be found.

# 4.9.1 First Interpretation

The existence of two different forms of the dispersion relation was first pointed out by Alexander [91]. It was first thought that the dispersion relation with a backbending was an unphysical mathematical curiosity. Yet, Arakawa [92] remarked that when plotting the position of the dips in a reflectivity experiment where the angle of incidence is varied at fixed frequency, the dispersion relation presents a backbending branch. Instead, when plotting the points obtained from a spectrum at fixed angle, one finds the dispersion relation without backbending. This approach gives a practical prescription for the analysis of attenuated total reflection (ATR) experiments. We can go beyond this simple observation and note that when measuring a reflectivity spectrum at fixed angle, the experiment contains the following ingredients: a real incident wavevector, a reflectivity spectrum showing a resonance at a given (real) frequency with a width that accounts for the imaginary part of the frequency. Similarly, a reflectivity measurement done at fixed frequency for different angles displays a resonance peak at a given (real) wavevector with a width that accounts for the imaginary part of the wavevector.

Nevertheless, this discussion is not a general prescription that can be used to discuss all possible issues. To illustrate this point, we consider two questions regarding important properties of surface plasmons: confinment of the fields and large density of states. What can we learn from the dispersion relation regarding these questions?

The dispersion relation with a backbending predicts a cut-off spatial frequency  $k_{co}$ : it follows that the LDOS has an upper bound and that the maximum confinment of the field is also limited by  $1/k_{co}$ . By contrast, the dispersion relation without backbending predicts a divergence of the LDOS at the frequency corresponding to the asymptote of the dispersion relation. It also predicts no limit to the possible resolution. It is thus clear that a general discussion on the applicability of the different dispersion relations is needed.

# 4.9.2 Representation of the Fields

In order to analyse the meaning of the dispersion relation and to clarify this issue, it is necessary to investigate the meaning of the choice of a real or complex wavector. In what follows, we emphasize that the relevant quantity is not a field with real or complex wavevector, but the field which depends on time and position. Introducing complex or real wavevectors amounts to introduce a particular representation of the field. A standard and convenient representation is the Fourier transform of the field with respect to both time and position. The resulting modes have real frequencies and real wavevectors. We note that a Fourier transform can always be introduced for a square integrable function in time and space. Any field that carries a finite energy is square integrable in time and space so that we can use a Fourier representation.

When looking at the field excited by any distribution of sources in the presence of an interface, it is possible to extract the pole contribution to the integral. Following Sommerfeld's prescription, this contribution of the pole of the Fresnel reflection or transmission factor to the integral is the surface wave. The contribution of the pole can be evaluated analytically using the residue theorem. This first analytic integration can be done either over frequencies or over the wavevector. Since the pole is complex, the analytic integration yields either a complex wavevector or a complex frequency depending on the choice. When following this program, we find two different representations of the surface plasmon field equally valid since the final value of the integral does not depend on the way chosen to perform the evaluation. One representation uses surface modes with real frequency and complex wavevector, whereas the other uses complex frequencies and real wavevectors. We skip all details and give the result of the integration reported in Ref. [90] hereafter.

#### Field Representation with a Real Wavevector

The field can be cast in the form of a linear superposition of modes with real wavevector **K** and complex frequency  $\omega_{SP}$ . We denote **K** the projection of the wavevector parallel to the interface **K** =  $(\alpha, \beta, 0)$ :

$$\mathbf{E}_{SP} = 2\Re \left[ \int \frac{\mathrm{d}^2 \mathbf{K}}{(2\pi)^2} E(\mathbf{K}, t) \left( \hat{\mathbf{K}} - \frac{K}{\gamma_m} \mathbf{n}_m \right) e^{i(\mathbf{K} \cdot \mathbf{r} + \gamma_m |z| - \omega_{SP} t)} \right], \tag{4.47}$$

where  $\mathbf{n}_m = -\hat{\mathbf{z}}$  if z < 0 and  $\hat{\mathbf{z}}$  if z > 0, and  $\hat{\mathbf{K}} = \mathbf{K}/K$ . The surface plasmon field takes a form that looks as a mode superposition, *except that the amplitude*  $E(\mathbf{K}, t)$  depends on the time t. Indeed, when describing a stationary field using modes that have an exponential decay, the amplitude is necessarily time dependent. In order to obtain a superposition of modes with fixed amplitudes, it is necessary to assume that all sources are extinguished after time t = 0 so that we observe the field after it has been excited. In that case, the decay of the mode is well described by the imaginary part of  $\omega_{SP}$ . Equation (4.47) is thus well suited for fields excited by pulses. Note that the polarization of each mode is specified by the complex vector  $\hat{\mathbf{K}} - \frac{K}{\gamma_m} \mathbf{n}_m$ , whose component along the z-axis depends on the medium from which the field is evaluated.

#### Field Representation with a Real Frequency

A different representation of the field can be derived using modes characterized by a real frequency  $\omega$  and a real  $\beta$ . The *x*-component of the wavector is complex and is given by

$$K_{x,SP} = [k_{SP}^2 - \beta^2]^{1/2}. (4.48)$$

The z-component of the wavector is given by the usual form  $\gamma = [\epsilon_m \omega^2/c^2 - k_{SP}^2]^{1/2}$ . With these notations, the field can be cast in the form:

$$\mathbf{E} = \int \frac{\mathrm{d}\omega}{2\pi} \int \frac{\mathrm{d}\beta}{2\pi} \left[ E_{>}(\beta, \omega, x) \left( \hat{\mathbf{K}}^{+} - \frac{K_{SP}}{\gamma_{m}} \mathbf{n}_{m} \right) e^{i(K_{x,SP}x + \beta y + \gamma_{m}|z| - \omega t)} + E_{<}(\beta, \omega, x) \left( \hat{\mathbf{K}}^{-} - \frac{K_{SP}}{\gamma_{m}} \mathbf{n}_{m} \right) e^{i(-K_{x,SP}x + \beta y + \gamma_{m}|z| - \omega t)} \right]$$
(4.49)

where  $\hat{\mathbf{K}}^+ = (K_{x,SP}\hat{\mathbf{x}} + \beta\hat{\mathbf{y}})/K_{SP}$  and  $\hat{\mathbf{K}}^- = (-K_{x,SP}\hat{\mathbf{x}} + \beta\hat{\mathbf{y}})/K_{SP}$ . Note that the *modes amplitudes depend on x*. A proper mode representation should use only fixed amplitudes. This is possible if all the sources lie in the x < 0 region and the region of interest is the x > 0 region. It can be shown in that case that the surface plasmon field can be cast in the form:

$$\mathbf{E} = \int \frac{\mathrm{d}\omega}{2\pi} \int \frac{\mathrm{d}\beta}{2\pi} \left( \hat{\mathbf{K}} - \frac{K_{SP}}{\gamma_m} \mathbf{n}_m \right) E_{>}(\beta, \omega) e^{i(\mathbf{K} \cdot \mathbf{r} + \gamma_m |z| - \omega t)}. \tag{4.50}$$

where  $\mathbf{K} = K_{x,SP}\hat{\mathbf{x}} + \beta\hat{\mathbf{y}}$  is complex and  $\hat{\mathbf{K}} = \mathbf{K}/K_{SP}$ . We conclude that stationary monochromatic fields excited by sources confined in a bounded domain are well described out of this domain by a representation that uses complex wavevectors and real frequencies.

#### Complex $\omega$ or Complex K? A Simple Prescription

To summarize, we have shown that the surface plasmon field can be represented using modes that have either a complex frequency or a complex wavevector. However, these modes amplitudes may still depend on either time or space in the more general case. However, there are two cases where these modes with a complex wavevector or complex frequency can be used with amplitudes which are constant. The first case is the representation of a field excited by a pulse for times after the end of the excitation. Then a representation with modes having a complex frequency is possible. The second case is a field excited by a stationary but localized source. Then a representation using complex wavevectors is possible. To each situation corresponds a specific dispersion relation. This simple analysis yields a simple prescription to choose the proper dispersion relation. Note that in the case of pulses limited in space, both representations can be used.

# 4.9.3 Implications for LDOS

Let us now discuss the Local Density of States (LDOS). We have already pointed out the connection between the dispersion relation and the LDOS in Sect. 4.8.2. In particular, we have seen that the density of states diverges when the group velocity goes to zero. A quick look at Fig. 4.5 shows that different dispersion relations seem to predict different LDOS. While Fig. 4.5b predicts a very large peak at  $\omega_{sp}/\sqrt{2}$  due to the asymptote (zero group velocity) and no states above this frequency, Fig. 4.5a predicts a smaller peak and a non-zero LDOS between  $\omega_{SP}/\sqrt{2}$  and  $\omega_{SP}$ . There must be a unique answer as the LDOS determines the energy density at equilibrium and the lifetime of emitters which are well-defined physical quantities. Again, we see that a prescription is needed to choose the right dispersion relation.

A standard procedure to derive the DOS in the reciprocal space is based on the periodic boundary conditions. Assuming a surface of side L, the wavevector takes the form  $\mathbf{K} = n_x \frac{2\pi}{L} \hat{\mathbf{x}} + n_y \frac{2\pi}{L} \hat{\mathbf{y}}$ . When performing this analysis, both  $K_x$  and  $K_y$  are real. Thus the relevant representation uses real wavevectors and complex frequencies. The corresponding dispersion relation has no backbending and therefore presents a singularity. This is in agreement with another approach of the LDOS based on the use of the Green's tensor that predicts an asymptotic behaviour proportional to  $1/(z^3|\epsilon+1|^2)$  [32, 33]. Of course, this divergence is nonphysical. It is related to the modelling of the medium using a continuous description of the metal without accounting for the non-locality.

# 4.9.4 Implications for Superresolution and Strong Confinment

Let us first discuss the issue of resolution when imaging with a surface plasmon driven at frequency  $\omega$  by an external source. If the dispersion curve with the asymptotic behaviour is chosen, there seems to be no diffraction limit (if we neglect the

cut-off due to Landau damping) and only the amplitude decay of surface plasmon due to Ohmic losses in the metal limits the resolution. The effect of the backbending of surface plasmon dispersion discussed in Ref. [46] limits the surface plasmon wavelength  $2\pi/\Re(k_{SP})$  and therefore, the resolution. Clearly, both dispersion relations do not lead to the same conclusion and a prescription to choose one or the other is needed. Let us consider a situation where a surface plasmon is excited locally by a stationary monochromatic field. From Sect. 4.9.2, we know that it is valid to use a representation with fixed amplitudes using modes with complex wavevectors and real frequencies. This implies that the dispersion relation with real frequency (with backbending) is relevant. Hence, there is a cut-off spatial frequency. Indeed, as  $K_x$ may be complex, the propagation term  $\exp(iK_xx)$  introduces damping. In the case of a lossy medium, damping may be due to losses. However, even for a non-lossy medium  $(k_{SP} \text{ is real})$ ,  $K_x = (k_{SP}^2 - \beta^2)^{1/2}$  can be imaginary. This occurs when  $\beta$ exceeds the value  $K_{SP}$ . This situation is the 2D analogue of the evanescent waves with wavevector K larger than  $\omega/c$  that cannot propagate in a vacuum. Clearly,  $k_{SP}$ is a cut-off frequency and the propagation term  $\exp(iK_xx)$  works as a low-pass filter that prevents the propagation of fields associated with spatial frequencies larger than  $k_{SP}$ . When dealing with lossy media, it is the real part of  $k_{SP}$  that specifies the cut-off spatial frequency. It is seen in Fig. 4.5 that this real part is limited by the backbending of the dispersion relation.

In summary, when discussing *imaging with stationary monochromatic surface* plasmons, the relevant representation is based on modes with a complex wavector and a real frequency given by Eq. (4.50). This corresponds to a dispersion relation with a backbending. It follows that the resolution is limited by the cut-off spatial frequency given by the maximum value of  $\Re(k_{SP})$ .

# 4.10 Fourier Optics for SPP

In this section, we study the propagation of surface plasmon polaritons along a flat interface. Several experiments demonstrating propagation, interferences and diffraction by surface plasmons have been reported in the literature [93–97]. In usual optics, these phenomena are well described in the framework of optical physics, which is based on the Huygens–Fresnel principle. In this section, we derive an analogue of this principle for surface plasmons following Ref. [98]. We consider the propagation of a monochromatic surface plasmon field along a planar surface z=0 in the direction of positive x. We assume that the field is known at x=0 and we seek an expression of the field for x>0. If a Huygens–Fresnel-type approach can be used, we expect to be able to assume that each point along the line x=0 acts as a secondary source that radiates a cylindrical wave.

# 4.10.1 General Representation

The general representations of the field given in Sect. 4.9.2 provide the adequate formalism to deal with these phenomena. In particular, Eq. (4.50) is a rigorous form of the surface plasmon field valid in a region with no sources. Let us stress that this representation is valid for a complex wavevector **K** and a real frequency  $\omega$  so that this representation is necessarily associated with a dispersion relation with backbending. We emphasize that this representation is well suited to discuss propagation for  $x > x_0$  of a surface plasmon field known along a line  $x = x_0$ . It is seen in Eq. (4.50) that propagation over a distance d amounts to multiply the amplitude of each mode by a factor  $\exp(ik_{x,SP}d)$ . In general, this involves modifying both the phase and the amplitude of the mode. Thus, it allows us to discuss any surface wave diffraction problem. Hereafter, the time dependence  $\exp(-i\omega t)$  will be omitted for brevity. From Eq. (4.50), we have:

$$\mathbf{E}^{SP}(x,y) = \int \frac{d\beta}{2\pi} \, \mathbf{E}^{SP}(\beta) e^{i\sqrt{k_{SP}^2 - \beta^2} x + i\beta y}.$$
 (4.51)

This expansion is analogous to the angular plane wave representation of fields in a vacuum. It is valid for x>0 in a source free region. Note that we have omitted the z-dependence of the field given by  $\exp(i\sqrt{\epsilon_1\omega^2/c^2-k_{SP}^2}\ z)$  in the upper medium and by  $\exp(-i\sqrt{\epsilon_2\omega^2/c^2-k_{SP}^2}\ z)$  in the metal. Indeed, the decay along the z-axis depends on the frequency but not on  $\beta$ .

A first simplification arises when reducing the problem to a scalar problem. Indeed, it turns out that the x- and y-components of the electric field can be derived from the form of the z-component of the electric field. This is a straightforward consequence of div  $\mathbf{E}=0$  so that  $\mathbf{K}\cdot\mathbf{E}+k_zE_z=0$ . The electric field components are thus given by:

$$E_x(\beta) = \sqrt{k_{SP}^2 - \beta^2} \frac{k_z}{k_{SP}^2} E_z^{SP}(\beta)$$

$$E_y(\beta) = k_y \frac{k_z}{k_{SP}^2} E_z^{SP}(\beta)$$

$$E_z^{SP}(\beta), \qquad (4.52)$$

where  $k_z = \sqrt{\epsilon_1 \omega^2/c^2 - k_{SP}^2}$  is the z-component of the wavevector in dielectric environment.

# 4.10.2 Huygens-Fresnel Principle

We now proceed to derive a vectorial form of the Huygens principle with no approximation. Note in particular that the result will account for polarization and near-field effects. We observe that the integral in Eq. (4.51) is the Fourier transform of the product of two functions of  $\beta$ . For example, for the *z*-component, we have:

$$E_z^{SP}(x,y) = \int \frac{\mathrm{d}\beta}{2\pi} \left[ E_z^{SP}(\beta) \right] \left[ e^{i\sqrt{k_{SP}^2 - \beta^2} x} \right] e^{i\beta y}. \tag{4.53}$$

The integral can thus be written as a convolution product of the Fourier transforms of  $E_z^{SP}(\beta)$  and  $\exp(i\sqrt{k_{SP}^2-\beta^2}x)$ . Making use of the integral representation of the Hankel function, we obtain:

$$\int d\beta \left[ e^{i\sqrt{k_{SP}^2 - \beta^2}x} \right] e^{i\beta y} = -i\pi \frac{\partial}{\partial x} H_0^{(1)}(k_{SP}\rho)$$

where  $\rho = \sqrt{x^2 + y^2}$ . Equation (4.53) can thus be cast in the form:

$$E_z^{SP}(x, y) = \frac{-i}{2} \int dy' \ E_z^{SP}(x = 0, y') i \frac{\partial}{\partial x} H_0^{(1)}(k_{SP}\rho).$$
 (4.54)

Similarly, we find:

$$E_x^{SP}(x, y) = \frac{-1}{2} \int dy' \ E_z^{SP}(x = 0, y') \frac{k_z}{k_{SP}^2} \frac{\partial^2}{\partial x^2} H_0^{(1)}(k_{SP}\rho), \tag{4.55}$$

and:

$$E_y^{SP}(x, y) = \frac{-1}{2} \int dy' \ E_z^{SP}(x = 0, y') \frac{k_z}{k_{SP}^2} \frac{\partial^2}{\partial x \partial y} H_0^{(1)}(k_{SP}\rho). \tag{4.56}$$

Equation (4.54) can be viewed as a vectorial Huygens–Fresnel principle for surface plasmons. Indeed, the surface plasmon field at (x, y) appears to result from the interferences of surface plasmons emitted by secondary sources located at (x = 0, y') with an amplitude  $E_z^{SP}(x = 0, y')$ . In order to see more clearly the link with Huygens–Fresnel principle, we use the asymptotic form of the Hankel function, valid for distances larger than the wavelength. We obtain:

$$E_z^{SP}(x, y) = -\frac{i}{\sqrt{\lambda_{SP}}} \int dy' \cos\theta \ E_z^{SP}(x = 0, y') \frac{e^{ik_{SP}\rho}}{\sqrt{\rho}} e^{i\pi/4},$$
 (4.57)

where  $\lambda_{SP} = 2\pi/k_{SP}$  is the surface plasmon wavelength and  $\theta = \arccos(x/\rho)$ . Here, the propagator is a damped cylindrical wave  $e^{ik_{SP}\rho}/\sqrt{\rho}$  instead of the

spherical wave  $e^{ikr}/r$  in the case of light propagation in a 3D vacuum. We recover in this asymptotic regime a surface plasmon form that has been conjectured previously [99, 96]. However, let us emphasize two differences between the scalar approximation and the propagator given by Eq. (4.54). Firstly, Eq. (4.54) is valid for any distance and includes near-field terms. Secondly, Eqs. (4.55) and (4.56) show that the x- and y-components of the electric field can be derived from the z-component. More specifically, the parallel components of the field are given by  $E_x = \frac{k_z}{k_{SP}^2} \frac{\partial E_z}{\partial x}$ ,

$$E_y = \frac{k_z}{k_{SP}^2} \frac{\partial E_z}{\partial y}.$$

#### 4.11 Conclusion

After more than 50 years, surface plasmons are still a very active research area. There has been a remarkable increase of novel results in the last ten years, mostly due to the simultaneous progress in observation and fabrication techniques. Observation techniques are reviewed in a separate chapter. They have made tremendous progress since the first near-field microscopy image [100] of a surface plasmon. The progress of nanofabrication makes possible the control of nanostructures that can take full advantage of the potential of surface plasmons. It is the purpose of this introductory chapter to highlight the polaritonic aspect of surface plasmons, or in other words, its dual electronic and electromagnetic nature. Surface plasmons are becoming a very important tool for the control of optical fields at the nanoscale. I believe that it is important to be aware of the underlying microscopic nature of surface plasmons in order to fully appreciate their potential and limitations.

#### References

- 1. L.M. Brekhovskikh, Waves in layered media (Academic Press, New York, 1960)
- A. Banos, Dipole radiation in the presence of a conducting half-space (IEEE Press, Piscataway, 1994)
- L. Felsen, N. Marcuvitz, Radiation and scattering of waves (Oxford University Press, NY, 1996)
- 4. R.W.P. King, M. Owens, T.T. Wu, Lateral electromagnetic waves (Springer Verlag, NY, 1992)
- 5. A.D. Boardman(ed.), Electromagnetic surface modes (Wiley, New York, 1982)
- 6. V.M. Agranovich, D.L. Mills (eds.), Surface Polaritons (North-Holland, Amsterdam, 1982)
- 7. H. Raether, Surface Plasmons (Springer-Verlag, Berlin, 1988)
- 8. A.V. Zayats, I.I. Smolyaninov, A.A. Maradudin, Phys. Rep. 408, 131 (2005)
- 9. W.L. Barnes, A. Dereux, T.W. Ebbesen, Nature **424**, 824 (2003)
- J.A. Schuller, E.S. Barnard, W. Cai, Y.C. Jun, J.S. White, M.L. Brongersma, Nat. Mater. 9, 193 (2010)
- 11. C. Kittel, Solid State Physics (John Wiley, New York, 1987)
- 12. N.W. Ashcroft, N.D. Mermin, Solid State Physics (Holt-Saunders, New York, 1976)
- 13. J.M. Ziman, Principles of the theory of solids (Cambridge University Press, London, 1964)

- 14. D. Pines, Elementary excitations in solids: lectures on phonons, electrons and plasmons (W.A. Benjamin, London, 1964)
- 15. C. Kittel, Quantum Theory of Solids (Wiley, New York, 1987)
- 16. J.D. Jackson, Classical Electrodynamics, 3rd edn. (Wiley, New York, 1999)
- 17. G.W. Ford, W.H. Weber, Phys. Rep. 113, 195 (1984)
- L.D. Landau, L.P. Pitaevskii, E.M. Lifshitz, Electrodynamics of continuous media (Elsevier, Amsterdam, 2004)
- 19. P.G. Etchegoin, E.C. Le Ru, M. Meyer, J. Chem. Phys. 125, 164705 (2006)
- 20. M. Ordal et al., Appl. Opt. 24, 4493 (1985)
- 21. N. Del Fatti, Ph.D Dissertation, Ecole Polytechnique, 1999
- 22. M. Kaveh, N. Wiser, Adv.in Phys. 33, 257 (1984)
- 23. C. Yi Tsai, C. Yao Tsai, C.H. Chen, T.L. Sung, T.Y. Wu, F.P. Shih, IEEE J. Quantum. Electron. **34**, 552 (1998)
- 24. P.B. Allen, Phys. Rev. B 3, 305 (1971)
- 25. J.B. Smith, H. Ehrenreich, Phys. Rev. B 25, 923 (1982)
- 26. R.N. Gurzhi, M. Ya Azbel', H.P. Lin, Sov. Phys. Solid State 5, 554 (1963)
- A. Vial, A.S. Grimault, D. Macias, D. Barchiesi, M. Lamy de la Chapelle, Phys. Rev. B 71, 085416 (2005)
- 28. T. Laroche, C. Girard, Appl. Phys. Lett. 89, 233119 (2006)
- 29. F. Hao, P. Nordlander, Chem. Phys. Lett. 446, 115 (2007)
- 30. P.B.Johnson, R.W.Christy, Phys. Rev. B **6**, 4370 (1972)
- 31. A.V. Shchegrov, K. Joulain, R. Carminati, J.J. Greffet, Phys. Rev. Lett. 85, 1548 (2000)
- 32. K. Joulain, R. Carminati, J.P. Mulet, J.J. Greffet, Phys. Rev. B 68, 245405 (2003)
- 33. K. Joulain, J.P. Mulet, F. Marquier, R. Carminati, JJ Greffet. Surf. Sci. Rep. 57, 59 (2005)
- 34. R.E. Collin, IEEE Trans. Antennas Propag. Mag. 46, 64 (2004)
- 35. P. Lalanne, J.P. Hugonin, Nat. Phys. 2, 551 (2006)
- 36. P. Lalanne, J.P. Hugonin, H.T. Liu, B. Wang, Sur. Sci. Rep. 64, 453 (2009)
- 37. H. Liu, P. Lalanne, Nature **452**, 728 (2008)
- 38. W. Dai, C.M. Soukoulis, Phys. Rev. B 80, 155407 (2009)
- A. Yu Nikitin, S.G. Rodrigo, F.J. Garcia-Vidal, L. Martin-Moreno, New J. Phys. 11, 123020 (2009)
- 40. K. Aki, P.G. Richards, Quantitative Seismology (University Science Books, Sausalito, 2002)
- 41. J.B. Pendry, Phys. Rev. Lett. 85, 3966 (2000)
- 42. N. Fang, H. Lee, C. Sun and X. Zhang. Science 308, 534 (2005)
- 43. T. Taubner, D. Korobkin, Y. Urzhumov, G. Shvets, R. Hillenbrand, Science 313, 1595 (2006)
- 44. I.I. Smolyaninov, C.C. Davis, A.V. Zayats, New J. Phys. 7, 175(1)–175(7) (2005)
- 45. I.I. Smolyaninov, C.C. Davis, J. Elliot, A.V. Zayats, Phys. Rev. Lett. 98, 209704 (2007)
- 46. A. Drezet, A. Hohenau, J.R. Krenn, Phys. Rev. Lett. 98, 209703 (2007)
- 47. D.W. Pohl, W. Denk, M. Lanz, Appl. Phys. Lett. 44, 651 (1984)
- 48. A. Lewis, M. Isaacson, A. Harootunian, A. Murray, Ultramicroscopy 13, 227 (1984)
- H.J. Lezec, A. Degiron, E. Devaux, R.A. Linke, L. MArtin-Poreno, F.J. Garcia-Vidal, T.W. Ebbesen, Science 297, 820 (2002)
- 50. J. Wessel, J. Opt. Soc. Am. B 2, 1538 (1985)
- 51. A. Madrazo, R. Carminati, M. Nieto-Vesperinas, J.J. Greffet, J. Opt. Soc. Am. A 15, 109 (1998)
- 52. K. Li, M.I. Stockman, D.J. Bergman, Phys. Rev. Lett. 91, 227402 (2003)
- 53. Y.C. Jun, R.D. Kekatpure, J.S. White, M.L. Brongersma, Phys. Rev. B 78, 153 111 (2008)
- 54. S.I. Bozhevolnyi, V.S. Vokov, E. Devaux, JY Laluet and T. Ebbesen, Nature 440, 508 (2006)
- 55. R. Esteban, T. Teperik, JJ Greffet. Phys. Rev. Lett. 104, 026802 (2010)
- Y. Todorov, A.M. Andrews, R. Colombelli, S. de Liberato, C. Ciuti, P. Klang, G. Strasser, C. Sirtori, Phys. Rev. Lett. 105, 196402 (2010)
- 57. K.H. Drexhage, in Progress in Optics (Ed. E. Wolf, North Holland, Amsterdam, 1974)
- 58. R.R. Chance, A. Prock, R. Silbey, Adv. Chem. Phys. 37, 1 (1978)
- 59. W.L. Barnes, J. Mod. Opt. 45, 661 (1998)

 E. Rousseau, A. Siria, G. Jourdan, S. Volz, F. Comin, J. Chevrier, JJ Greffet. Nat. Photonics 3, 514 (2006)

- 61. Y. de Wilde, F. Formanek, R. Carminati, B. Gralak, PA Lemoine, K. Joulain, JP Mulet, Y. Chen, JJ Greffet. Nature 444, 740 (2006)
- J.P. Mulet, K. Joulain, R. Carminati, J.J. Greffet, Nanoscale Microscale Thermophys. Eng. 6, 209 (2002)
- 63. J.P. Mulet, K. Joulain, R. Carminati, J.J. Greffet, Appl. Phys. Lett. 78, 2931 (2001)
- 64. S. Shen, A. Narayanaswamy, G. Chen, Nano Lett. 9, 2909 (2009)
- 65. S.A. Biehs, E. Rousseau, JJ Greffet. Phys. Rev. Lett. **105**, 234301 (2010)
- 66. J.M. Gérard, B. Gayral, J. Lightwave Technol. 17, 2089 (1999)
- 67. J.J. Greffet, M. Laroche, F. Marquier. Phys. Rev. Lett. 105, 117701 (2010)
- 68. S. Haroche, in Proceedings of the Les Houches Summer School Fundamentals Systems in Quantum Optics, Elsevier Science Publishers, Amsterdam, 1992, ed. by J. Dalibard
- 69. A. Kock, E. Gornik, M. Hauser, W. Beistingl, Appl. Phys. Lett. **57**, 2327 (1990)
- 70. D.K. Gifford, D.G. Hall, Appl. Phys. Lett. 81, 4315 (2002)
- 71. J. Azoulay, A. Débarre, A. Richard, P. Tchénio, Europhys. Lett. 51, 374 (2000)
- 72. M. Thomas, JJ Greffet, R. Carminati, JR Arias-Gonzalez. Appl. Phys. Lett. 85, 3863 (2004)
- K. Okamoto, I. Niki, A. Shvartser, Y Narukawa, T. Mukai, A. Scherer. Nat. Mater. 3, 601 (2004)
- 74. S. Kuhn, Ulf Hakanson, L. Rogobete, V. Sandoghdar. Phys. Rev. Lett. 97, 017402 (2006)
- 75. P. Anger, P. Bharadwaj, L. Novotny, Phys. Rev. Lett. 96, 113002 (2006)
- A. Curto, G. Volpe, T.H. Taminiau, M.P. Freuzer, R. Quidant, N.F. van Hulst, Science 329, 930 (2010)
- 77. T.H. Taminiau, F.D. Stefani, F.B. Segerink, N.F. van Hulst, Nat. Photonics 2, 234 (2008)
- 78. H.B.G. Casimir, Proc. Koninkl. Ned. Akad. Wetenschap. 51, 793 (1948)
- 79. S.K. Lamoreaux, Phys.rev.Lett. **78**, 5 (1997)
- 80. R.S. Decca, D. Lopez, E Fishbach, DE Krause. Phys. Rev. Lett. 91, 050402 (2003)
- 81. G. Jourdan, A. Lambrecht, F. Comin, J. Chevrier, Europhys. Lett. 85, 31001 (2009)
- 82. C. Genet, A. Lambrecht, S. Reynaud, Phys. Rev.A 62, 012110 (2000)
- 83. C. Henkel, K. Joulain, J.P Mulet, J.J Greffet, Phys. Rev.A 69, 023808 (2004)
- 84. F. Intravaia, A. Lambrecht, Phys. Rev. Lett. 94, 110404 (2005)
- 85. F. Intravaia, C. Henkel, A. Lambrecht, Phys. Rev. A 76, 033820 (2007)
- 86. M.I. Stockman, S.V. Faleev, D.J. Bergman, Phys. Rev. Lett. 88, 067402 (2002)
- 87. M. Aeschlimann et al., Nature **446**, 301 (2007)
- 88. D. Sarid, Phys. Rev. Lett. 47, 1927 (1981)
- 89. E. Prodan, C. Radloff, N.J. Halas, P. Nordlander, Science 302, 419 (2003)
- 90. A. Archambault, T. Teperik, F. Marquier, J.J. Greffet, Phys. Rev. B 79, 195414 (2009)
- 91. R.W. Alexander, G.S. Kovener, R.J. Bell, Phys. Rev. Lett. 32, 154 (1974)
- 92. E.T. Arakawa, M.W. Williams, R.N. Hamm, R.H. Ritchie, Phys. Rev. Lett. 31, 1127 (1973)
- 93. L. Feng, K.A. Tetz, B. Slutsky, V. Lomakin, Y. Fainman Appl, Phys. Lett. 91, 081101 (2007)
- Z. Liu, J.M. Steele, W. Srituravanich, Y. Pikus, C. Sun, X. Zhang, Nano Lett. 5, 1726–1729 (2005)
- L. Yin, V.K. Vlasko-Vlasov, J. Pearson, J.M. Hiller, J. Hua, U. Welp, D.E. Brown, C.W. Kimball, Nano Lett. 5, 1399–1402 (2005)
- 96. A.J. Huber, B. Deutsch, L. Novotny, R. Hillenbrand, Appl. Phys. Lett. 92, 203104 (2008)
- 97. R. Zia, M.L. Brongersma, Nat. Nanotechnol. 2, 426–429 (2007)
- 98. T.V. Teperik, A. Archambault, F. Marquier, J.J. Greffet, Opt. Express 17, 17483 (2009)
- 99. I.I. Smolyaninov, D.L. Mazzoni, J. Mait, C.C. Davis, Phys. Rev. B 56, 1601 (1997)
- 100. P. Dawson, F. de Fornel, J.P. Goudonnet, Phys. Rev. Lett. **72**, 2927 (1994)

# Part II Surface Plasmons Localized on Metallic Particles

# Chapter 5 Localized Surface Plasmons: Basics and Applications in Field-Enhanced Spectroscopy

Javier Aizpurua and Rainer Hillenbrand

Abstract The oscillation of the surface charge density in metallic nanoparticles, commonly named localized surface plasmons (LSPs), is a result of the collective oscillation of the conduction electrons under the constraints imposed by the physical boundaries of the nanoparticle geometry. In this chapter, a review on the basic properties of LSPs, acting as effective optical nanoantennas, is presented. The optical response in the simplest nanoparticle, a metallic sphere, serves as a guide to understand concepts such as dipolar approximation, multipolar modes, effects of retardation, and shape-effects in the optical response of metallic nanoparticles. Special emphasis is paid to the coupling of metallic nanostructures as a standard approach to design optical nanoantennas, where aspects such as the tuning of the spectral response and the magnitude of the field enhancement are described in simple terms. The role of metallic nanostructures as optical antennas assisting in field-enhanced spectroscopy is also detailed in the context of surface-enhanced Raman scattering and surface-enhanced infrared absorption (SEIRA). Other spectral and sensing techniques are briefly discussed for completeness.

The optical properties of metallic nanoparticles are determined by the excitation of electromagnetic surface modes, also called localized surface plasmons (LSPs) [1]. These modes belong to resonant oscillations of the surface charge density at the boundaries of the metal nanoparticle. In contrast to the surface modes propagating

J. Aizpurua

Center for Materials Physics CSIC-UPV/EHU and Donostia International Physics Center DIPC, Paseo Manuel Lardizabal 5, 20018 Donostia-San Sebastián, Spain e-mail: aizpurua@ehu.es

R. Hillenbrand

CIC nanoGUNE Consolider, Avda. Tolosa 76, 20018 Donostia-San Sebastián, Spain

e-mail: r.hillenbrand@nanogune.eu

R. Hillenbrand

IKERBASQUE, Basque Foundation for Science, 48011 Bilbao, Spain

along metal—dielectric interfaces, as those detailed in previous chapters, localized plasmon modes are stationary oscillations of the surface charge density at optical frequencies along the metal boundaries of a metallic particle. The optical properties of LSP modes have made these excitations very attractive from a scientific and technological point of view. Localized surface plasmons are the basis to generate subwavelength-enhanced electromagnetic fields that can govern, control, and improve physical processes such as molecular fluorescence [2], vibrational spectroscopy [3], photovoltaics [4], energy transfer [5], molecular sensing [6], nanoscale optical signal interconnection [7], photoemission [8], nanoscale microscopy [9], among others. We describe in the first section of this chapter the basic properties of localized surface plasmon modes to understand the key factors governing the optical response in finite metallic nanostructures. In the second sections we will focus on the role of these surface plasmons to turn single metal nanostructures into effective spectroscopic nanoantennas.

#### 5.1 Localized Plasmons and Optical Antennas

# 5.1.1 Surface Plasmon Polaritons Versus Localized Surface Plasmon Polaritons

In previous chapters, surface plasmon polaritons (SPPs) have been described in detail. In brief, SPPs are surface charge density waves that propagate at a metal-dielectric interface with a typical dispersion curve as the one presented by the dashed blue line in Fig. 5.1a. Light cannot couple directly to plasmon excitations of a flat, semiinfinite metal surface since energy and momentum cannot be conserved simultaneously. This momentum mismatch can be observed in Fig. 5.1 where the light line is plotted as a black-solid line. It is probably because of this intrinsic difficulty of SPPs to be excited by light that surface plasmons were predicted in the context of the interaction of charges with thin metallic films in 1957 by R. Ritchie [10]. In that case, the excitation of plasmons by fast electrons is possible due to the momentum transfer k from the electrons that involves their velocity v as  $k \approx \omega/v$ , with  $\omega$  the energy loss experienced by the electrons. Nevertheless, SPPs can also be excited by light. There are several possibilities to provide the additional momentum, so that the surface plasmon can couple to incident light. One of the options consists in modifying the planar metal surface by means of indentations or gratings [11] that can provide "lattice" momentum to ensure momentum conservation. Experimental implementations of this situation have been commonly used not only to launch plasmons in surfaces but also to scatter SPPs from an interface in order to detect them [12].

In a metallic nanoparticle, opposite to the propagating SPPs in a flat surface, the closed geometrical boundaries can sustain a localized oscillation of the surface charge density (see schematics to the right-hand side of Fig. 5.1). This localized excitation is commonly referred to as LSP. The optical response of the LSP in a metallic particle

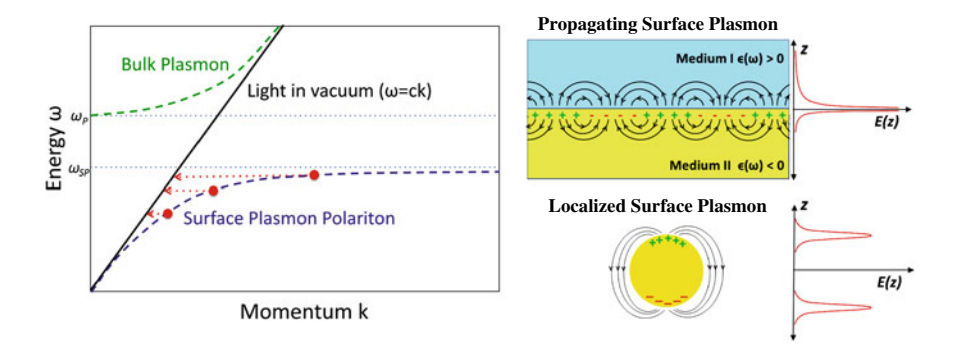


**Fig. 5.1** Left Dispersion curve of the bulk plasmon (green-dashed line) and surface plasmon polariton (blue-dashed line). The curve of light in vacuum is displayed as a solid black line. Red dots and red-dashed lines denote schematically a certain momentum provision that allows for effective coupling to light. Right Top, schematics of the surface charge density of a propagating surface plasmon polariton. Bottom, schematics of the surface charge density of a LSP. In the latter, the closure of the boundaries due to the geometry produces a stationary surface charge density oscillation that allows for intense coupling of LSP and light

can be described through the particle polarizability  $\alpha$  that relates the incoming electric field  $E_0$  with the electric dipole moment  $p=\alpha E_0$ . Generally, the polarizability of a metallic object is a frequency-dependent magnitude that depends on the dielectric function  $\varepsilon(\omega)$  of the metal and on the surrounding medium, as well as on the particle geometry. A localized surface plasmon resonance is associated with a pole of the polarizability  $\alpha$  of the metal nanoparticle as a function of frequency (wavelength). The explicit form of this polarizability will be discussed in simple cases such as spheres and spheroids in the next sections. For small nanoparticles made of noble metals such as gold and silver, the LSP resonances fall typically in the visible range of the spectrum.

The electromagnetic coupling of light to the LSP resonances can be understood alternatively in the context of simultaneous conservation of energy and momentum, as delineated above. In a metallic nanoparticle, the finite geometry acts as a source of momentum, generating a stationary surface charge density wave that is localized at the particle. For a particle of generic size a, the momentum provision  $\Delta k$  by the geometrical boundaries can be roughly approximated as  $\Delta k = n \frac{2\pi}{a}$  where n is an integer. In this case, a discrete set of LSP modes of order n that couple effectively to light are possible. In Fig. 5.1, the effect of this momentum provision allowing coupling to light is schematically depicted by red-dashed lines. In analogy to other ranges of the electromagnetic spectrum, these localized electromagnetic surface modes are commonly referred to as optical antenna resonances. The finite geometry of the metal nanoparticles essentially determines their optical properties. It does not only allow for coupling to external light, but it also provides a means to tune the energies of the plasmon excitations and to localize and enhance optical fields in the vicinity of the particles. All these aspects of metal nanoparticles make them key building blocks in nano-optics.

# 5.1.2 The Simplest Optical Nanoantenna: A Metallic Nanoparticle

We define an optical antenna as a structure that converts effectively electromagnetic radiation from the far-field into the near-field and vice versa [13]. A spherical metallic nanoparticle can be considered to be the simplest optical antenna. We will therefore focus on this geometry to understand the basic concepts in optical nanoantennas.

The description of the scattering and absorption by a nanoparticle is essentially given by the scattering and absorption cross-sections that relate the energy that is sent back to the far-field and the energy that is dissipated within the nanoparticle, respectively. When we relate the scattered power  $I_{\rm scat}$  and the absorbed power  $I_{\rm abs}$  to the incident power  $I_{\rm inc}$ , we obtain the scattering cross-section  $C_{\rm scat} = \frac{I_{\rm scat}}{I_{\rm inc}}$  and the absorption cross-section  $C_{\rm abs} = \frac{I_{\rm abs}}{I_{\rm inc}}$ . For spherical particles with radius a smaller than the incoming wavelength  $\lambda$ , retardation does not play a role and we find [14]:

$$C_{\text{scat}} = \frac{8\pi}{3} k^4 a^6 \left| \frac{\varepsilon_{\text{sph}} - \varepsilon_{\text{med}}}{\varepsilon_{\text{sph}} + 2\varepsilon_{\text{med}}} \right| = \frac{k^4}{6\pi} |\alpha_{\text{sph}}|^2 \Rightarrow C_{\text{scat}} \propto \frac{a^6}{\lambda^4}$$
 (5.1)

$$C_{\rm abs} = 4\pi k a^3 {\rm Im} \left\{ \frac{\varepsilon_{\rm sph} - \varepsilon_{\rm med}}{\varepsilon_{\rm sph} + 2\varepsilon_{\rm med}} \right\} = k {\rm Im} \{\alpha_{\rm sph}\} \Rightarrow C_{\rm abs} \propto \frac{a^3}{\lambda},$$
 (5.2)

where  $\alpha_{\rm sph}$  is the dipolar polarizability of a spherical particle of radius a in the quasistatic approach:

$$\alpha_{\rm sph} = 4\pi\varepsilon_o a^3 \frac{\varepsilon_{\rm sph} - \varepsilon_{\rm med}}{\varepsilon_{\rm sph} + 2\varepsilon_{\rm med}},\tag{5.3}$$

with  $\varepsilon_{\rm sph}$  the dielectric function of the sphere and  $\varepsilon_{\rm med}$  the dielectric function of the surrounding medium. k is the wavevector that is related to the frequency  $\omega$  and the speed of light in vacuum c as  $k=\omega/c$ . If the dielectric value of  $\varepsilon_{\rm sph}$  is constant and with negligible imaginary part of the dielectric function  $\varepsilon''$ , the scattering cross-section shows a rather flat spectral response and almost zero absorption. When the sphere is made of a metal characterized by a plasma frequency  $\omega_p$ , as introduced previously in Chap. 2 (see, for example, Eq. (2.24)), a good approximate model to describe the dielectric response  $\varepsilon_{\rm sph}$  in the optical range is given by the Drude model:

$$\varepsilon_{\rm sph} = \varepsilon_{\rm metal} = 1 - \frac{\omega_p^2}{\omega(\omega + i\gamma)},$$
 (5.4)

where  $\gamma$  describes the damping of the electrons, caused mainly by the electron-phonon scattering in the metal.

The optical properties of the nanoparticle are given by the polarizability in Eq. (5.3). As pointed out in the previous section, a pole in the polarizability determines a maximum in scattering and absorption (when losses are small). In the particular case of a small sphere, as derived from Eq. (5.3), the expression that determines the

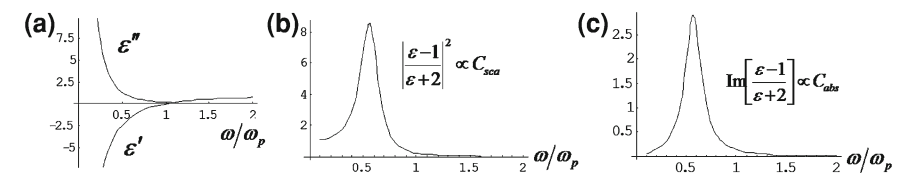


Fig. 5.2 a Real  $\varepsilon'$  and imaginary  $\varepsilon''$  of a Drude-like dielectric function as a function of frequency normalized to the plasma frequency  $\omega_p$ . The energy region with negative real-value response is the ideal situation to sustain surface plasmons. **b** Modulus of the response function in a small spherical metallic particle  $\frac{\varepsilon_{\rm sph}+2\varepsilon_{\rm med}}{\varepsilon_{\rm sph}+2\varepsilon_{\rm med}}$  showing the spherical surface plasmon dipolar resonance for a Drude-like sphere surrounded by vacuum. The scattering cross-section is proportional to the square of this magnitude. **c** Imaginary part of the same response function as in **b**. The absorption cross-section is proportional to this magnitude. A damping of  $0.2\omega_p$  has been used in both cases. The resonances are not maximum at the same frequency exactly, but for small damping, both are located close to the dipolar surface plasmon frequency  $\omega_{\rm res} = \omega_p/\sqrt{3}$ 

optical properties of the nanoparticle is the so-called optical response  $\frac{\varepsilon_{\rm sph} - \varepsilon_{\rm med}}{\varepsilon_{\rm sph} + 2\varepsilon_{\rm med}}$ . When the Drude-like dielectric function (see Fig. 5.2a) is introduced in Eqs. (5.1) and (5.2), the spherical nanoparticle shows resonant behavior for both cross-sections (see Fig. 5.2b, c). The resonance position appears at the frequency  $\omega_{\rm res}$  that fulfills  $\varepsilon_{\rm sph} + 2\varepsilon_{\rm med} = 0$ . If we assume now that the surrounding medium is vaccum ( $\varepsilon_{\rm med} = 1$ ), the resonance frequency  $\omega_{\rm res}$  is found at a frequency  $\omega_{\rm res} = \frac{\omega_p}{\sqrt{3}}$ . This is the frequency of the spherical dipolar surface plasmon.

The interest in the dipolar surface plasmon of small particles is twofold: on the one hand, the electromagnetic near-field associated with the plasmon excitation is strongly localized on the scale of the nanoparticle size, typically on the nanometer scale, allowing for an effective squeezing down of the oscillations of the electromagnetic field to subwavelength dimensions. On the other hand, the LSP resonances produce a considerable increase of the local fields around the particles ranging from 5 to 500 times enhancement in amplitude. This is the basis of many field-enhanced spectroscopy techniques, photovoltaics, medical applications, and optical antenna effects.

It is convenient to distinguish two regions around the particles where we have localized fields (near-field) and propagating fields (far-field). We can express the electric field  $\mathbf{E}(\mathbf{r})$  of a dipole characterized by its dipolar momentum  $\mathbf{p}$  located at the origin of coordinates, as a canonical example of an emitter:

$$\mathbf{E}(\mathbf{r}) = \frac{1}{4\pi\varepsilon_o} \frac{e^{ikr}}{r} \left\{ k^2 [(\mathbf{n} \times \mathbf{p}) \times \mathbf{n}] + \frac{1}{r} \left( \frac{1}{r} - ik \right) [3\mathbf{n}(\mathbf{n} \cdot \mathbf{p}) - \mathbf{p}] \right\} e^{-i\omega t}. (5.5)$$

If the dipolar momentum  $\mathbf{p}$  is assumed to be the electric dipole given by the static polarizability of a sphere  $\alpha_{sph}$  (related to the incident field  $\mathbf{E_0}$ ) as introduced above, it is possible to obtain the field produced by the sphere as a response to the incident field in both regions of interest.

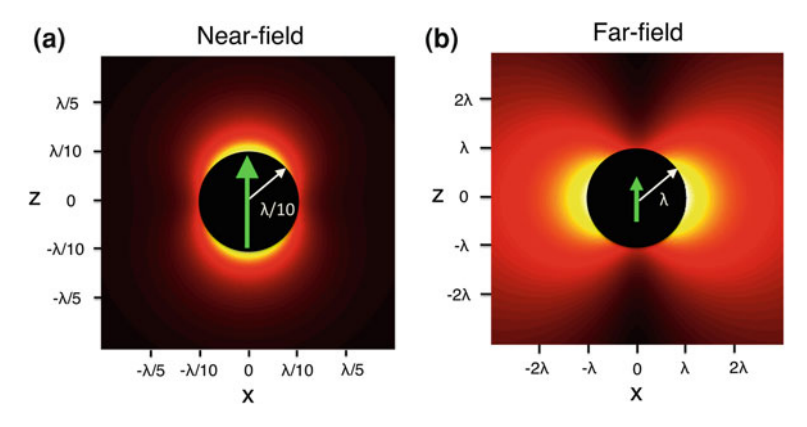


Fig. 5.3 a Modulus of the amplitude of the near-field around a plasmonic dipole  $(r \ll \lambda)$ . b Modulus of the far-field radiation pattern emitted from a plasmonic dipole  $(r \gg \lambda)$ 

In the near-field zone, where  $kr \ll 1$ , the field in Eq. (5.5) can be asymptotically expressed as:

$$\mathbf{E}(\mathbf{r}) = \frac{1}{4\pi\varepsilon_0} \frac{3\mathbf{n}(\mathbf{n} \cdot \mathbf{p}) - \mathbf{p}}{r^3} e^{-i\omega t}.$$
 (5.6)

This near-field distribution of a nanoscale metallic particle is represented in Fig. 5.3a [15] normalized to the incident field. From this figure, it is straightforward to conclude that a metallic particle acts as an effective optical antenna, converting propagating electromagnetic energy (far-field) into strongly localized near-fields. This is possible due to the excitation of the LSPs, expressed through the polarizability of the sphere involving the metallic response  $\varepsilon_{\rm sph}$ . The nanoscale localization of the electromagnetic fields by LSPs is a key factor for the impact of these excitations in nano-optics. Due to this high degree of localization, nanoscale fields allow for sensing [16], nanoscale imaging [9], controlling [17], and manipulating the optical signal [18], for example. On the other hand, in the far-field or radiation zone, where  $kr \gg 1$ , the field in Eq. (5.5) can be asymptotically expressed as:

$$\mathbf{E}(\mathbf{r}) = \frac{(\mathbf{n} \times \mathbf{p}) \times \mathbf{n}}{r} \frac{k^2}{4\pi\varepsilon_o} e^{i(kr - \omega t)}.$$
 (5.7)

The far-field radiation scattered by the dipolar surface plasmon (see Fig. 5.3b) exhibits the typical radiation pattern of the emission of a dipolar radioantenna. Notice that the far-field produced by a small metallic particle can be described by a point dipole located at the center of the particle, as observed in the figure. The optical scattering of nanoscale antennas shows properties of gain, directionality, and emissivity extensively studied in electrical engineering for other electromagnetic spectral ranges. The properties of the LSPs will therefore govern the actual properties of the nanoscale optical antenna.

# 5.1.3 Higher-Order Modes

The dipolar LSP resonance is the simplest low-energy resonance that one can find in a metallic nanoparticle. In a spherical particle, more complex surface charge density oscillations can be supported by the particle. When the oscillations of the surface charge density associated with the LSPs show several nodes, the resonances are referred to as high-order resonance modes, or multipolar modes that can be understood as stationary surface charge density waves over the surface. A l-order mode is characterized by the presence of l nodes in the surface charge density oscillation along the surface. In the quasistatic approximation, where the particles are considerably smaller than the wavelength of the incoming light, the Helmholtz equation is replaced by the Laplace equation where the incoming field can be considered constant. By solving the Laplace equation with the use of an expansion in spherical harmonics of order l, it is easily found that the l-polar modes of a spherical metallic particle are given by [19]:

$$\omega_l = \sqrt{\frac{l}{2l+1}}\omega_p. \tag{5.8}$$

Here, it is assumed that the dielectric response of the metal can be described by the Drude model in Eq. (5.4), while the surrounding medium is vacuum.

An example of higher-order surface plasmon modes is illustrated in Fig. 5.4. We discuss elongated nanoparticles (nanorods) exhibiting higher-order surface modes more clearly. These modes are the solution of the Laplace equation for rotationally invariant particle geometries such as rods or ellipsoids (we select m=0 modes, with m the index expressing the azymuthal symmetry following  $\cos(m \phi)$ ). Cross-sections of the time-oscillating, stationary surface charge densities of the first five higher-order modes, l=0 to l=5, are displayed, as well as the l=9 and l=19 modes.

Very interesting aspects of LSPs can be derived by considering the symmetry of the surface charge density. In the case of simple nanorods/elongated particles, for example, it is possible to find modes with net dipole moment (l=1, l=3, l=5, l=9, l=19 in Fig. 5.4), as well as modes with a zero net dipole moment (l=0, l=2, l=4 in Fig. 5.4). A plane wave polarized along the long (symmetry) axis of the particles can excite only modes with a net dipole moment. Modes with a zero net dipole moment cannot be excited. We also see in Fig. 5.4 that the lowest energy mode (l=0) requires a finite net charge. Illumination with electromagnetic radiation thus cannot excite this mode.

A very efficient way to excite higher-order modes in metallic nanoparticles can be implemented with the use of the external electric field produced by a fast electron beam traveling at relativistic velocity ( $\approx$  100–200 keV energy) in the proximity of a nanoparticle. When the electrons pass near the particle, the electrons excites LSPs and therefore the electron beam loses the corresponding amount of energy. By measuring the energy loss  $\Delta E$  experienced by the electron beam in electron energy loss

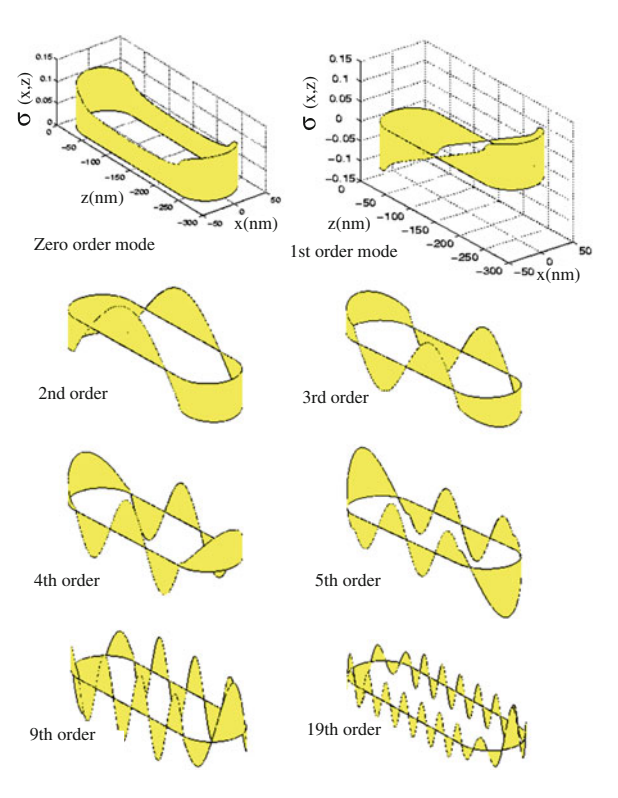


Fig. 5.4 Cross-section of elongated particle nanorods in the (x, z) plane with the corresponding surface charge density  $\sigma_{(x,z)}$  of the higher l-order surface modes plotted along the elongated surface of the particles. The surface modes are the eigenvalues of the Laplace equation for a particle with azimuthal invariance (rotational invariance); therefore, these modes are characterized by the azimuthal number m=0

spectroscopy (EELS), it is possible to obtain spectral features of the LSPs excited in the metal particle [21, 22].

The energy loss probability  $P_{\omega}$  of the electron beam when passing a spherical nanoparticle can be expressed as [23]:

$$P(\omega) = \frac{4q^2}{\pi v^2 a^2} \sum_{l=0}^{\infty} \sum_{m=0}^{l} A_{lm} \left(\frac{\omega a}{v}\right)^{2l} K_m^2 \left(\frac{\omega b}{v}\right) Im[\alpha_l(\omega)], \tag{5.9}$$

where  $\alpha_l(\omega)$  is the l-order polarizability of the nanoparticle associated with the l-order mode,  $\alpha_l(\omega) = \frac{\varepsilon(\omega)_{\rm sph}-1}{\varepsilon(\omega)_{\rm sph}+(l+1)/l}a^3$ .  $P(\omega)$  depends basically on the radius of the particle a, the impact parameter of the electron beam b (distance between the particle center and the electron beam), and the velocity of the electrons v. Figure 5.5 shows the spectrum of energy losses  $P_{\omega}$  for an electron beam passing very close to the particle surface (b roughly > a). In such a case, the electron beam excites very

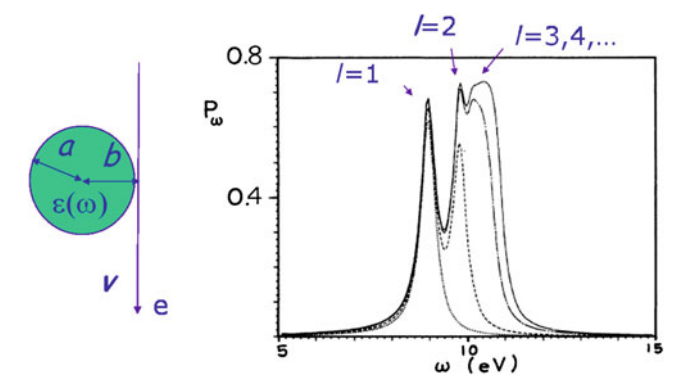


**Fig. 5.5** Electron energy loss probability per unit energy for a  $50 \,\text{keV}$  electron moving at grazing incidence on an aluminum sphere of radius  $a = 10 \,\text{nm}$ . Adapted from Ref. [23] with permission from APS

efficiently high-order multipolar modes, yielding several peaks in the energy loss spectrum with modes labeled as l = 1, 2, ...

Excitation of higher-order modes in extreme subwavelength scale spheres is nearly impossible by conventional optical spectroscopy, because the plane wave illumination provides a homogeneous electric field across the particle, thus essentially exciting the dipole mode. The excitation of higher multipoles such as the quadrupole or octupole modes is negligible for small spheres with  $a \ll \lambda$ . Nevertheless, if the particles are large enough, higher-order modes can be efficiently excited [24].

The example brought up in this section shows that alternative external probes other than optical planewaves such as electrons can also couple and excite efficiently non-standard surface plasmon modes. Other external sources of surface plasmon excitation can be found in electrostatic fields [25] or in the field produced by tunneling electrons in a cavity [26] where the properties of the plasmons excited depend on the characteristics of the external fields and the environment.

#### 5.1.4 Retardation

The quasistatic approximation can be well applied for nanoparticles that are much smaller than the wavelength of light, as the incoming optical fields are nearly constant across the particle (see schematics in Fig. 5.6a). When the size of the particles increases, the quasistatic approach is no longer valid, and a full solution of Maxwell's equations (through solving Helmholtz equation) is necessary to correctly obtain the spectral position and intensity of the resonances. The solution of the modes in a spherical geometry can be traced back to Mie [27] where retardation in the electromagnetic interaction is considered. In the so-called Mie theory, solutions of scattering and absorption are obtained by an expansion of the fields in spherical harmonics.

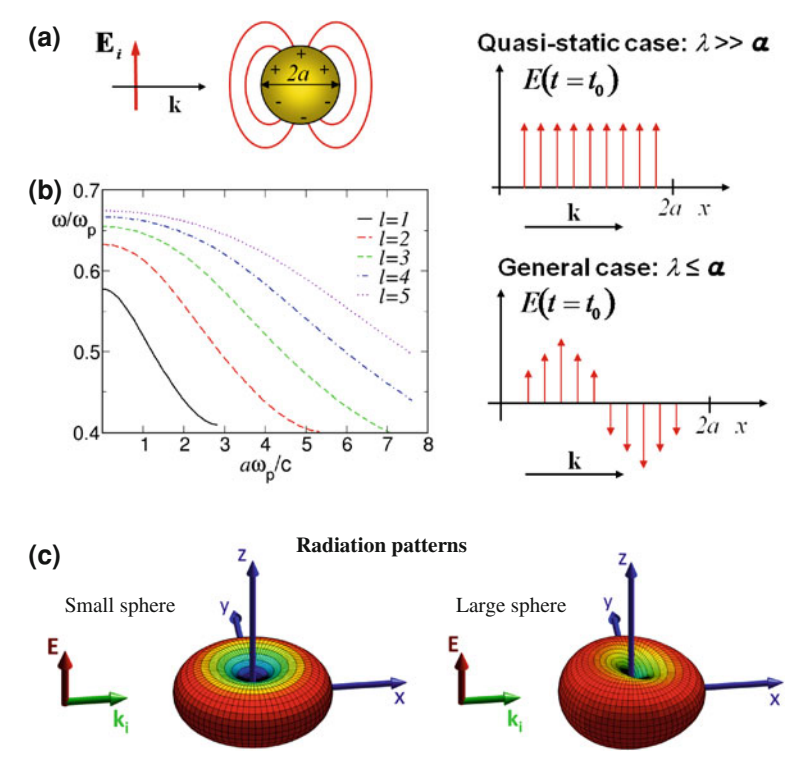


Fig. 5.6 a Schematics of the assumption made in the quasistatic approach in terms of the particle size and incoming wavelength. The general case does not impose the constraint that the particle size a needs to be smaller than the wavelength  $\lambda$ . **b** Frequency of the multipolar spherical surface plasmon modes as a function of the particle radius a, as obtained from the scattering coefficients of a metallic sphere in a full electrodynamical description within the Mie theory. **c** Radiation patterns for the dipolar spherical plasmonic mode in the case of a gold particle of radius  $a=10\,\mathrm{nm}$  (lefthand side) and a particle of radius  $a=200\,\mathrm{nm}$  (right-hand side). The distorted dipolar pattern is observed for large particles

Both scattering and absorption show maxima at certain resonance frequencies whose spectral positions depend on the size of the particles. The solutions of the electromagnetic modes for a metallic nanoparticle in vacuum characterized by a Drude-like optical response are displayed in Fig. 5.6b. In the limit of very small particles ( $a \rightarrow 0$ ), a set of l-modes appear consistent with the non-retarded solutions of Laplace equation presented in Eq. (5.8). As the radius of the particle a increases, each mode l shifts to lower frequencies (red-shift). In addition to the redshift of the resonance frequencies  $\omega_l$ , the scattering and absorption cross sections are broadened because of radiation losses. Furthermore, the far-field radiation pattern changes with increasing size. In Fig. 5.6c, radiation patterns at the lowest resonance frequency are displayed for a small (left) and a large (right) particle. The small particle shows a perfectly dipolar pattern radiating over all directions, whereas the large particle scatters more

strongly in the forward direction [14]. All these effects show that a full electrodynamical solution of the scattering of metallic nanoparticles is crucial for a correct description of the LSP spectral position and the scattering properties.

# 5.1.5 Influence of Particle Shape in Plasmon Response

The resonance condition for the optical response of a metallic nanoparticle is given by the maximum of its polarizability  $\alpha$ , as detailed in the previous section. For shapes differing from simple spheres, the polarizability becomes anisotropic, exhibiting different optical responses along the different directions. In such a case, it is necessary to define the polarizability as a tensor that addresses the optical response along several directions. For the case of ellipsoidal particles elongated along one symmetry axis z, we obtain within the electrostatic approximation the following polarizabilities along the different symmetry axes x, y, z:

$$\alpha_{x,y,z} = \frac{4}{3}\pi L_x L_y L_z \frac{\varepsilon_{\text{ell}} - \varepsilon_{\text{med}}}{\varepsilon_{\text{med}} + P_{x,y,z}(\varepsilon_{\text{ell}} - \varepsilon_{\text{med}})}.$$
 (5.10)

Here,  $P_{x,y,z}$  are the depolarization factors in the direction of the x, y, and z axes,  $L_x$ ,  $L_y$ , and  $L_z$  are the semilengths of the ellipsoid along the respective axis.  $\varepsilon_{\rm ell}$  is the dielectric function of the material of the ellipsoid and  $\varepsilon_{\rm med}$  that of the surrounding medium. If the short semi-axes are equal,  $L_x = L_y$ , the particle is a spheroid rather than an ellipsoid, yielding  $P_x = P_y$ .

The depolarization factors  $P_{x,y,z}$  are determined by the ellipticity e of the ellipsoid:

$$P_z = \frac{1 - e^2}{e^2} \left[ \frac{1}{2e} \ln \left( \frac{1 + e}{1 - e} \right) - 1 \right]$$
 (5.11)

$$P_x = P_y = \frac{1 - P_z}{2}. ag{5.12}$$

with

$$e = \sqrt{1 - (L_x/L_z)^2}. (5.13)$$

For a spheroid, two different solutions of the dipolar LSP are possible: one associated with the long axis polarizability and the other one with the short axis polarizability, respectively.

The anisotropy of the optical response of a metallic spheroid is illustrated in Fig. 5.7, showing far-field spectra (a) and near-field distribution (b, c) of a silver spheroid when illuminated with polarization along and perpendicular to the long axis, respectively. A long wavelength resonance is present in the spectrum when light is polarized along the long axis. This LSP is commonly named as longitudinal LSP. The resonance associated with the short axis appears at shorter wavelength

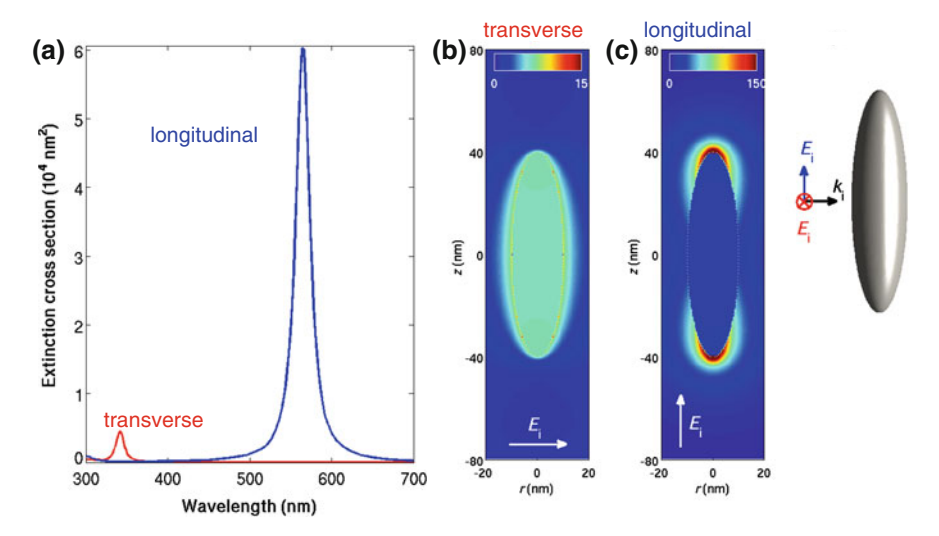


**Fig. 5.7** a Extinction cross-section for longitudinally polarized light and transversally polarized light illuminating a silver ellipsoid. Longitudinal and transverse LSPs are excited. **b** Near-field distribution of the transverse LSP in the proximity of the ellipsoid at the resonant wavelength  $\lambda = 342$  nm. **c** Near-field distribution of the longitudinal LSP at the resonant wavelength  $\lambda = 565$  nm

and is commonly named as transversal LSP. The near-field distribution of both the transverse and longitudinal LSPs can be observed in Fig. 5.7b, c. For the longitudinal resonance, we find a large field concentration at the ellipsoid extremities because of the large polarizability and sharp edges. A much weaker field enhancement is found for the short axis resonance. The ellipticity, i.e. the aspect ratio  $(L_x/L_z)$ , thus provides a means to tune the frequency (wavelength) of both the longitudinal and transverse LSPs [28]. We note that the longitudinal resonances of spheroids are commonly referred to as linear optical antenna resonances.

A variety of metallic nanoparticle shapes together with their corresponding optical properties can be found in the literature [29]. Chemical synthesis and lithographic methods have made it possible to produce different metallic particle geometries and configurations [30–33]. Besides the standard, canonical shapes such as spheres and spheroids, it is possible to produce nanocubes, nanoshells, nanorings, nanocups, nanorice, nanostars, among others. Obviously, an increase in the complexity of the particle geometry requires to go beyond analytical models to calculate their optical response. To that end, different computational methods have been implemented to solve exactly Maxwell's equations in arbitrarily shaped particles. Among the most common methods are the dipole–dipole approximation (DDA) [34], finite difference in time domain (FDTD) techniques [35], or boundary element methods (BEM) [36]. A major goal of numerical simulations is to understand and engineer the local field enhancement, which is essential for spectroscopy and microscopy applications.

Current efforts concentrate on engineering the particle shape in order to optimize the field enhancement for spectroscopy applications. Another aspect of interest is the tunability of the LSP response. The modification of the particle shape modifies the spectral position of the plasmonic resonance, thus providing a tool to tune the optical response at the nanoscale. Several effects, strongly dependent on the particle shape, play a role in determining the actual LSP resonance frequency and the field enhancement. We summarize some of these effects:

- *Elongation*. Elongated particles yield strong anisotropy in the optical response and can be extremely valuable to localize the field at the ends of the elongation and tune the response through the aspect ratio. This is the case in nanorods and ellipsoids, as shown in Fig. 5.7.
- *Curvature*. Plasmons are also sensitive to the lightning rod effect produced by rapid electric potential variations in the proximity of a curved surface. As the radius of curvature of a surface becomes smaller, the strong localization of the surface charge density provides a very intense field. Some of the particles that present this feature are tappered rods, tips, or nanostars, for example.
- Asymmetry. The generation of nanoparticles that break symmetry has turned out
  to be valuable to obtain sharper lineshapes in the optical spectrum (Fano-like
  shapes) [37] and to manipulate the polarization of the incoming light. The use of
  non-centrosymmetric particles, such as L- and U-shaped particles and spirals, are
  among some examples.
- *Intracoupling*. The use of particles that present inner and outer walls, arms, or edges that provide a source of Coulomb coupling is very effective for spectral tuning of the optical response. Within this spirit, nanoshells or nanorings where the interaction takes place between inner and outer walls of the nanoparticles provide a direct source to tune the optical response.

In Table 5.1, a selection of nanostructures is itemized, outlining some particular optical property that makes them interesting in the context of plasmon optics.

# 5.1.6 Field Enhancement by Plasmon Coupling

Another powerful tool to control LSPs relies on the near-field coupling between nanoparticles. The localized modes of each single particle couple to each other via Coulomb interaction, giving rise to new hybridized modes [56] that are shifted with respect to the single particle resonance [57]. The simplest case of such a situation is the coupling of two closely spaced spherical particles in the dipole approximation (see schematics in Fig.5.8a). In this case, we can assign to the coupled particles an effective polarizability  $\alpha_{\rm eff}$ , which is a function of the particles polarizabilities  $\alpha_1$  and  $\alpha_2$ , and the distance between the dipoles r. We distinguish two cases: longitudinally aligned dipoles and transversally aligned dipoles. Their respective effective polarizabilities  $\alpha_{\rm eff}^{\rm long}$  and  $\alpha_{\rm eff}^{\rm trans}$  are given by [58]:

Nanoparticle	Material	Reference	Properties
Nanosphere	Gold	[38]	Isotropic scattering, moderate enhancement.  Interesting for quantitative optical characterization of single particle
Nanospheroid	Gold	[28]	Anisotropic scattering and enhancement. Transverse and longitudinal modes
Nanorod	Gold	[39, 40]	Longitudinal and transverse resonances. Linear behavior with rod length. Modification of plasmon decaying rates
Nanodisk	Gold	[41]	Substrates to optimize biosensing. Useful as constituents for patch antennas
Nanoshell	Gold	[42]	Tunability due to shell thickness
Nanoring	Gold	[43]	Tunability due to ring thickness
Nanorice	Gold	[44]	Intense resonances, large field enhancements.  Combines rod and shell properties
Nanocube	Silver	[45]	Appropriate for plasmon sensing
Nanostar	Gold	[46]	Intense hot spots at the nanostar tips
Nanoegg	Gold	[47]	Tunability, asymmetric system, Fano spectral profiles
Nanocup	Gold	[48]	Capability to bend light
Nanospiral	Gold	[49]	Complex response
Nanocrescent	Gold	[50]	Tunable narrow resonances in the mid-infrared with good figures of merit for sensing
Nanotriangle	Silver	[51]	Strong scattering in the red. Modes associated to the triangle edges
Nanoprism	Gold	[52]	Presence of sharp edges. Breaking of symmetry
Nanohole	Gold	[53, 54]	Inverse symmetry. Babinet's principle. Similar trends for complementary electric and magnetic fields
L-shaped	Gold	[55]	No center of inversion symmetry. Strong dependence on polarization. Presence of bulk-like plasmons

Table 5.1 Selected plasmonic nanostructures and their optical properties

Some relevant optical properties associated with the structures are pointed out. The references selected are not necessarily the only ones nor the first ones to address the particular geometry. They are pointed out here as a practical guide to obtain more information on a particular nanoparticle geometry

$$\alpha_{\text{eff}}^{\text{long}} = \frac{\alpha_1 + \alpha_2 + \frac{\alpha_1 \alpha_2}{\pi r^3}}{1 - \frac{\alpha_1 \alpha_2}{4\pi^2 r^6}}$$
(5.14)

and

$$\alpha_{\text{eff}}^{\text{trans}} = \frac{\alpha_1 + \alpha_2 - \frac{\alpha_1 \alpha_2}{2\pi r^3}}{1 - \frac{\alpha_1 \alpha_2}{16\pi^2 2 \cdot 6}}.$$
 (5.15)

The basic trend of the longitudinal coupling can be observed in Fig. 5.8b. With decreasing dipole separation r, the spectral response shifts to lower frequencies (redshift), accompanied by a slight increase in the magnitude of effective polarizability. Contrary to longitudinally coupled dipoles, transversally coupled dipoles exhibit a blueshift when the separation r is reduced.

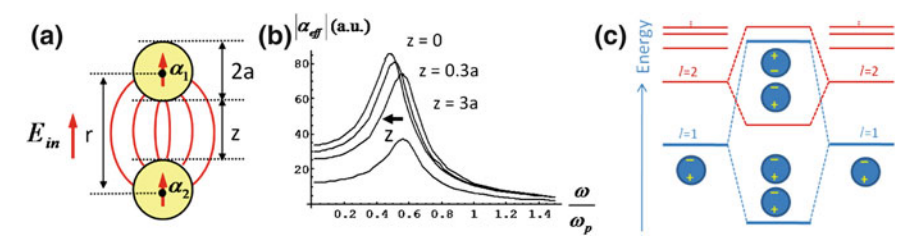


**Fig. 5.8** a Schematics of the longitudinal coupling of two particles characterized by their dielectric dipoles. **b** Modulus of the effective polarizability corresponding to the longitudinal coupling in **a** as derived from Eq. (5.14). A Drude-like response has been considered and the dipoles are located at a separation distance r. **c** Schematics of the hybridization of the l=1 and l=2 modes of single metallic nanoparticles. As the particles come together, new "bonding" (lower energy) and "antibonding" (higher energy) modes, which are solutions of the coupled system, are created

The spectral redshift of the resonance when the particles come closer together has been experimentally addressed [59, 60]. In Fig. 5.9a, the resonance shift of metallic dimers is shown as a function of the separation distance between the particles [61]. In close proximity, the particles form a gap where the surface charge densities of each particle interact strongly. This near-field interaction across the gap sustains a strongly localized symmetric surface plasmon mode, also called bonding dimer plasmon (BDP) which presents lower energy and comes from the hybridization of the single dipolar surface plasmons from each particle [62]. A schematic of the energetics of these hybrydized modes can be observed in Fig. 5.8c. The formation of the hybridized bonding surface plasmon produces large field enhancement at the particles gap, commonly named as hot spot. A similar coupling can also be found with other particle shapes such as triangles, forming a so-called bowtie antenna [63, 64]. Figure 5.9b shows the field enhancement in the gap of a bowtie antenna as a function of separation distance. As the two triangle particles come closer, a dramatic increase of the field enhancement is produced, associated with the formation of a bonding surface plasmon. The calculated near-field distribution is displayed in Fig. 5.9c, showing that the local fields at the gap are enhanced by a factor of about 100 times compared to the incident field amplitude. Employing near-field microscopy, it is possible to map the strongly localized fields [9, 65–67]. In Fig. 5.9d, an example of such a near-field map is provided. It shows the topography, experimental, and calculated near-field distribution of bowtie aperture, clearly visualizing the hot spot generated by the nanogap in the center of the aperture. Hot spots in nanoscale gaps can strongly enhance Raman and infrared spectroscopy, as we will detail in Sect. 5.2.

A very interesting regime occurs when metallic nanoparticles nearly touch each other. When the particles are separated by a certain distance, the interaction established between both particles leads to the formation of the BDP [62, 68], described above. The physical situation at the gap can also be understood in terms of circuit theory [69] as a capacitive coupling between the metal particles. As the particles come to close proximity and touch each other, a conductive connection between both particles is achieved, establishing a charge transfer plasmon [17, 70] that sustains

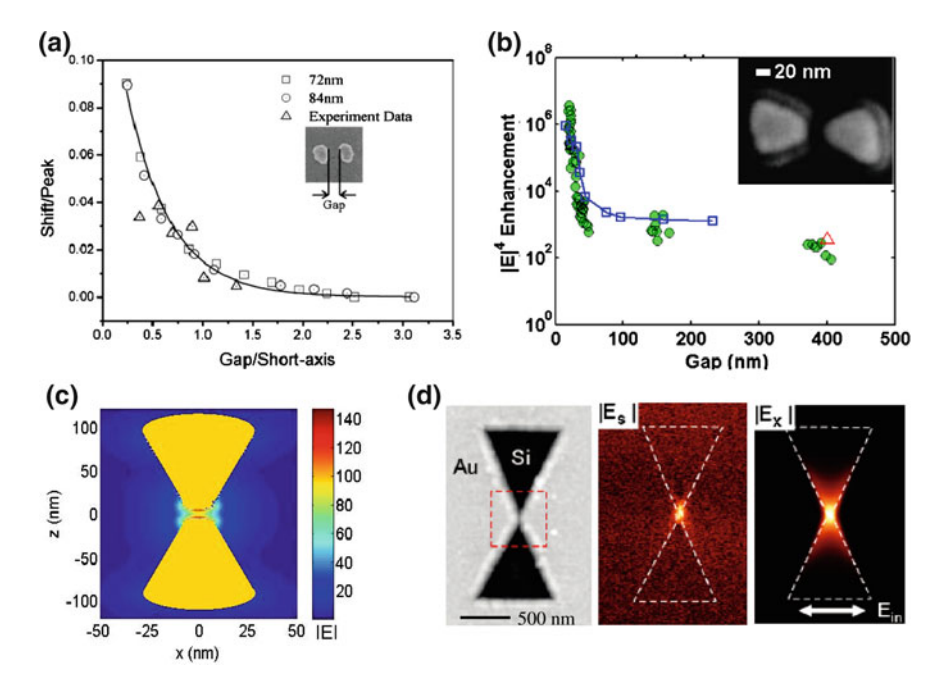


**Fig. 5.9** a Spectral shift of the antenna gap resonance as a function of separation distance of the gap. Adapted from Ref. [61] with permission from ACS. **b** Experimental field enhancement to the fourth power in a bowtie antenna as a function of the separation distance of the antenna gap. Adapted from Ref. [64] with permission from APS. **c** Calculation of the field amplitude enhancement in the proximity of a gold bowtie conical antenna. The coupling of the two structures originates enhanced fields at the gap. **d** Near-field at a metallic cavity for an inverse bowtie antenna. The measured signal  $E_S$  and the calculated in-plane local field  $E_X$  are shown. Adapted from Ref. [67] with permission from ACS

a longer wavelength mode with net charge at each particle. This can be understood within the circuit theory as an inductive coupling [69] between the two particles. The manipulation of the dielectric properties of the cavity to control the response of a nanoantenna (coupled metal nanoparticles) is the optical analog to the manipulation of the gap impedance to tune radiowave antennas.

# 5.1.7 Optical Antennas: From Radiowaves to Visible Light

As we have described in the previous sections, the spectral position of the LSPs depends on the material, the geometry, the environment, and the coupling with nearby structures. All these factors determine both the near-field distribution as well as the far-field scattering, including efficiency and directionality of the scattered light. Many of these aspects are similar to conventional antennas operating in the radiowave

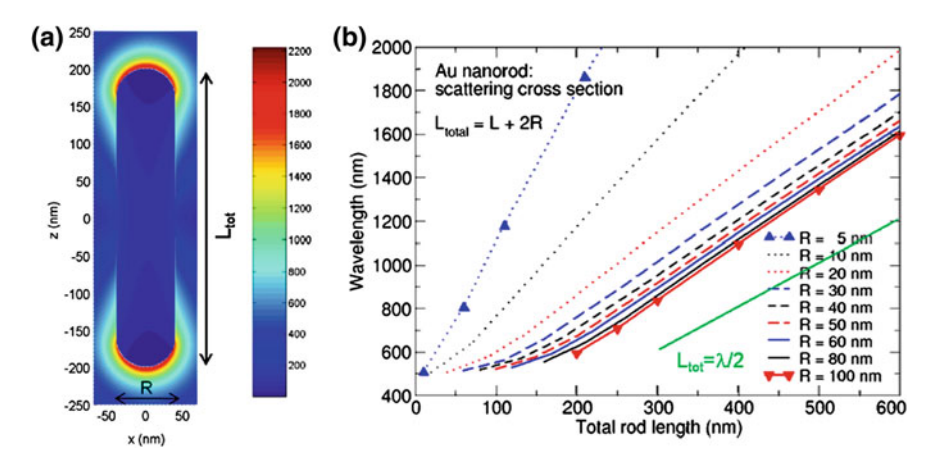


Fig. 5.10 a Calculated near-field distribution of a gold nanorod at its resonance frequency. The rod has a total length  $L_{\rm tot}=400\,{\rm nm}$  and radius  $R=25\,{\rm nm}$ . b Spectral position of the dipolar resonance in gold nanorods as a function of total length  $L_{\rm tot}$  and radius R. In the optical range of the spectrum, these antennas behave like linear dipole antennas of length  $\lambda_{\rm eff}/2$  where  $\lambda_{\rm eff}$  is the effective wavelength of the surface plasmon propagating on the rod  $\lambda_{\rm LSP}$ . The resonance position of a nanorod consisting of an ideal metal is displayed by a green line  $(L=\lambda_{\rm eff}/2=\lambda/2)$ 

spectral range, where the wavelength is several orders of magnitude larger than that of light, reaching several meters. It is thus of interest to apply radiofrequency (RF) antenna concepts for the design of optical antennas. As we will see below, RF concepts cannot be simply scaled to the visible spectral range because of the excitation of surface plasmon polaritons, which are not present at RFs.

Considering the definition of an antenna as a device that converts propagating electromagnetic energy into strongly localized and enhanced near-fields, metallic particles are the counterpartner of radiowave antennas in the optical range of the electromagnetic spectrum [71]. Both radiowave and optical antennas show resonant frequencies (or wavelengths) that perform this conversion from the far-field to the near-field with large efficiency. Nevertheless, a striking difference needs to be pointed out. The resonance frequencies of a radiowave antenna rely purely on the geometry of the supporting structure. Optical antenna resonances, however, occur due to the excitation of surface plasmons, which present shorter wavelength than the free space illumination wavelength and are strongly damped [72, 73]. Thus optical antennas exhibit stronger damping than RF antennas and the antenna length needs to be substantially shorter than the illumination wavelength. This effect can be observed in Fig. 5.10b where the spectral position of the dipolar antenna resonance is plotted as a function of the antenna length for different widths of the metallic rods. A clear departure of an ideal RF antenna resonance ( $L \approx \lambda/2$ ) can be observed for all antenna widths due to the excitation of the surface plasmons (near-field distribution shown in Fig. 5.10a).

Among the different optical antenna designs, we describe some examples successfully implemented recently. Linear dipole antennas consist of a single metallic nanowire of length  $L = \lambda_{LSP}/2$  where  $\lambda_{LSP}$  is the surface plasmon polariton wavelength. As  $\lambda_{LSP} < \lambda$ , the relative antenna length is significantly shorter than for a RF antenna of length  $L = \lambda/2$ . Such an antenna yields a strong dipolar like emission. It is one of the first examples where a RF antenna design has been scaled down to the optical regime.  $\lambda/4$  antennas or ground antennas have also been implemented producing omnidirectional emission of fluorescence molecules located in their proximity [74]. Another standard design from radiowave frequencies is a Yagi-Uda antenna. It consists of parallel linear dipole antennas of slightly different lengths, yielding large directionality in the scattering properties of electromagnetic radiation. Optical Yagi-Uda antennas have been also scaled down to optical frequencies [75]. One last example of this analogy are parabolic antennas, with an optical analog implemented recently as metallic nanocups [48] to bend light according to the direction of the nanocup. In all these examples of design, the resonance position cannot be simply scaled down. The penetration of the field associated with the surface plasmons can modify the antenna resonance frequencies, thus the most straightforward way to calculate the antenna resonances in complex designs and nanostructures as the ones pointed out above relies on numerical calculations to solve Maxwell's equations. Nevertheless, scaling laws that consider the plasmonic response through effective wavelengths have been found to successfully obtain the optical antenna modes [76].

# 5.2 Field-Enhanced Vibrational Spectroscopy

The vibrational energy of molecular groups is typically of a few tenths of meV and thus falls in the infrared range of the electromagnetic spectrum. The energy spectrum is highly specific to chemical bonds, thus a vibrational fingerprint of a substance can be used for chemical identification. Two important techniques that obtain spectral information on these vibrational fingerprints are Raman and infrared spectroscopy. In Raman spectroscopy, visible light is typically used for sample illumination. Due to the interaction between photons and molecular vibrations, inelastic light scattering occurs, producing an energy shift (stokes and anti-stokes shifts) between the incoming and outgoing radiation. An inherent problem to Raman spectroscopy is that the scattering cross-sections are very low ( $\approx 10^{-28}$  cm<sup>2</sup>/molecule), thus preventing single molecule spectroscopy. Infrared spectroscopy, on the other hand, relies on the direct excitation of molecular vibrations. In typical transmission and reflection measurements, the extinction spectrum of a substance is measured. Extinction cross-sections are of the order of  $\approx 10^{-18}$  cm<sup>2</sup>/molecule. These weak cross-sections can be enhanced when molecules are adsorbed on metal structures, due to the local field enhancement produced in the proximity of metallic surfaces [77–79]. The enhancement of the Raman scattering and IR absorption can thus be related to the local field enhancement generated by surface plasmon polaritons or by antenna resonances. When such enhancement mechanisms are employed, these spectroscopy techniques are named surface-enhanced Raman spectroscopy (SERS) and surface-enhanced infrared absorption (SEIRA). These techniques are also referred to as field-enhanced spectroscopies.

# 5.2.1 Concept

The concept of surface- or field-enhanced spectroscopy relies on the enhancement of optical fields in the proximity of metallic surfaces or nanoparticles which enhances the Raman and IR absorption signals. The initial implementation of surface-enhanced spectroscopy was based on rough metallic surfaces generating intense local fields at gaps and protusions. Because of their high local field and strong localization, they are typically called hot spots. This concept has been sophisticated in the last years with the use of metallic nanostructures acting as optical antennas that support LSPs and thus enhance significantly local fields at specific LSP resonance frequencies. The field enhancement can be as high as about 100 times the incoming amplitude, thus increasing the Raman scattering cross section by 6–10 orders of magnitude, which enables one to detect Raman scattering from only a few or even single molecules [80, 81]. The basic idea of both SERS and SEIRA is to locate the molecular groups on top of the electromagnetic hot spots produced by the LSP or the antenna, as schematically displayed in Fig. 5.11. By doing so, the visible (SERS) or IR radiation (SEIRA) are enhanced, improving the spectroscopic signals.

#### 5.2.2 SERS

In a typical Raman scattering process, an incoming photon of frequency  $\omega_{\rm vis}$  suffers inelastic scattering. It loses part of his energy due to the excitation of a molecular vibration of frequency  $\omega_{\rm vib}$ . The inelastically scattered Raman photon has a smaller energy ( $\hbar\omega_R = \hbar\omega_{\rm vis} - \hbar\omega_{\rm vib}$ ), thus it is shifted to lower frequencies  $\omega_R$  (Stokes shift). The Stokes and anti-Stokes shifts (gain of energy from a vibrational excitation) are the spectral information that allows for identification of molecular bonds. Both processes is depicted in the schematics of Fig. 5.12. The scattering cross-section depends directly on the local field  $E_{\rm loc}$ , which is the near-field  $E_{NF}$  at the position of the molecules. The local field acts on the molecules in a twofold manner. First, the enhancement f of the incoming radiation yields a larger field illuminating the molecules,  $f = |E_{\rm loc}(\omega_{\rm vis})/E_o|$ . Second, the enhancement of the scattered radiation yields another enhancement factor at the Raman frequency,  $f = |E_{\rm loc}(\omega_R)/E_o|$ . Both enhancements influence the final scattered signal (see Fig. 5.11), thus the Raman scattering cross-section is elastically enhanced by a factor M which is given by [82]:

$$M = |E_{loc}(\omega_{vis})/E_o|^2 |E_{loc}(\omega_R)/E_o|^2.$$
 (5.16)

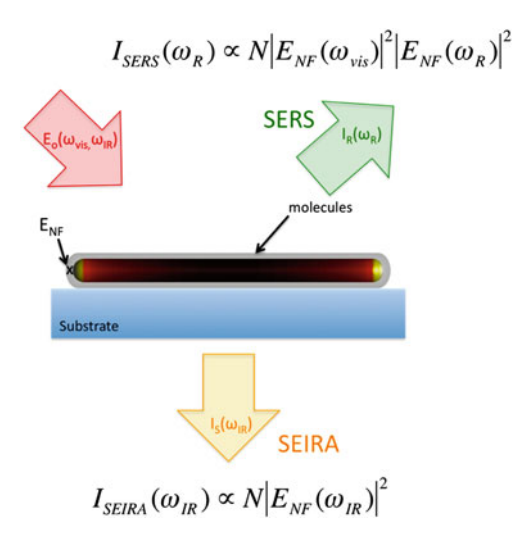
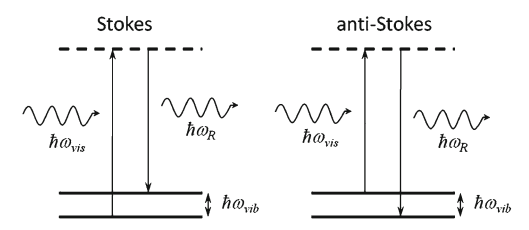


Fig. 5.11 Schematics of the concept of field-enhanced spectroscopy in two of the most commonly used spectroscopies: surface-enhanced Raman spectroscopy (SERS) and surface-enhanced infrared absorption (SEIRA). Amounts of molecules are deposited near a metallic structure that acts as an optical or infrared antenna thus enhancing the inelastic scattering, and the absorption signals from the molecular groups. While SERS relies on the inelastic scattering of visible and near-infrared light to obtain signal of the vibrational fingerprints from the frequency shifts between incoming and outgoing radiation, SEIRA relies on the direct absorption of infrared light at the frequencies of the molecular vibrations. Both techniques are complementary and present differences in the spectra due to the different selection rules to excite vibrations

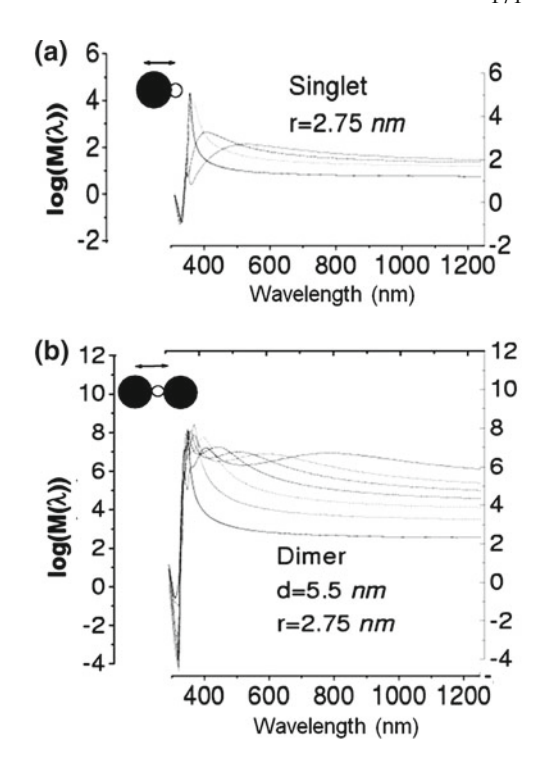


**Fig. 5.12** Schematics of a Stokes process (*left*) and an anti-Stokes process (*right*). A photon of energy  $\hbar\omega_{\rm vis}$  generates (Stokes) or loses (anti-Stokes) a vibrational mode of energy  $\hbar\omega_{\rm vib}$ , and the outgoing photon results with a smaller or a larger energy  $\hbar\omega_R$  respectively

The frequency of a vibration is typically much smaller than the frequency of visible light ( $\omega_{\rm vib} \ll \omega_{\rm vis}$ ). Thus, the Raman enhancement factor can be expressed approximately by the fourth power of the local field enhancement:

$$M \approx |E_{\text{loc}}(\omega_{\text{vis}})/E_o|^4 \approx f^4.$$
 (5.17)

Fig. 5.13 SERS enhancement factor for two canonical metallic nanoparticle structures at a distance r=2.75 nm from the particles surface. **a** A single silver sphere for different radii of the particle ranging from a=10 to a=70 nm. **b** A silver dimer with a separation d=5 nm for the same sizes of the particles as in **a**. The polarization of light is marked in the inset



The scaling of M with the fourth power of the local field enhancement f is one of the reasons why SERS has become such a powerful tool in molecular spectroscopy. The sensitivity is dramatically enhanced, enabling even single molecule studies.

In the previous sections, the capacity of LSPs to localize and enhance the fields in the proximity of metallic nanoparticles has been described (see, for example, the local field produced in a cavity in Fig. 5.9). Metallic nanoparticles and nanostructures sustaining LSPs are therefore natural building blocks to act as optical nanoantennas in SERS. Particularly, sharp edges and cavities in between particles generate electromagnetic "hot spots" that have been proven to be very effective to increase the Raman signal, reporting single molecule detection [3].

Figure 5.13 shows an example of SERS employing LSPs in metal nanoparticles. We compare the enhancement factor M obtained with a single silver sphere with that in a silver particle dimer. We assume a molecule to be located at a distance  $r=2.75\,\mathrm{nm}$  to the particle. In the case of the dimer, this position corresponds to the center of the gap formed between the two spheres. Figure 5.13a shows M for a single sphere as a function of wavelength for different particle radii. A clear dipolar plasmon resonance can be observed, showing a redshift as the particle size increases. The Raman factor  $\mathrm{Log}(M)$  reaches typical values of about 5 at resonance, and about M=2 off resonance where the field enhancement is due to the lightning rod effect exclusively. This corresponds to local field amplitude enhancements of the order of

f=15 and f=3 respectively. When a second particle is located close to the first one, the plasmon coupling gives rise to a new even more localized bonding surface plasmon that produces a much larger field enhancement (see Fig. 5.13b). Even though the actual values vary with the ratio between separation distance and size (larger particles produce a redshift) standard values of up to M=8 can be easily achieved for realistic separation distances. This means field amplitude enhancements of up to 100 in the gap.

Additional enhancement factors needed for single spectroscopy are usually associated with chemical enhancements due to charge transfer in the chemisorption of the molecules to the surfaces. Chemical effects are complex and go beyond the electromagnetic enhancement described in this chapter, but they usually provide an additional enhancement factor of the order of 100. Insights into the chemical enhancement in SERS can be found in Ref. [83] and unified treatments of both types of enhancement mechanisms [84]. Other limitations of the simple fourth power model presented here are connected with the influence of the actual frequency shift in the evaluation of the enhancement of the incoming and outgoing radiation and with the polarization of the incoming and outgoing light that can provide additional selection rules driving the molecular vibrations [85]. All these additional effects need to be considered in a proper description of SERS enhancement.

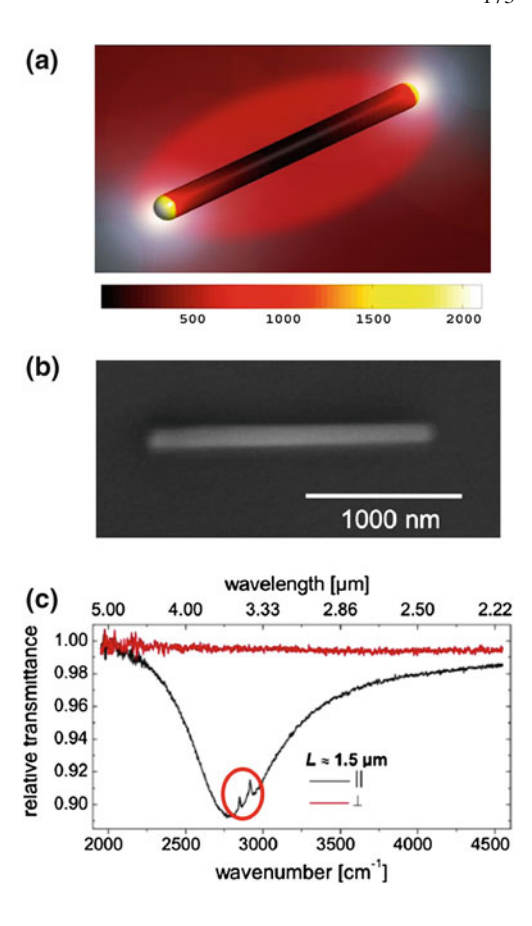
## **5.2.3 SEIRA**

A complementary spectroscopic technique to SERS relies on the direct excitation of molecular vibrations with use of infrared light [86]. This spectroscopic technique is commonly addressed as Surface-Enhanced Infrared Spectroscopy (SEIRA), even though the spectral information is usually obtained in transmission mode, as schematically displayed in Fig. 5.11, therefore the information obtained involves both absorption and scattering processes.

The effective extinction cross-section in SEIRA configurations is sensitively smaller than the effective scattering cross-section, even though single molecule IR absorption cross-section is larger than single molecule Raman scattering cross-section. This is because IR absorption scales with  $f^2$  while Raman scattering scales with  $f^4$ .

To obtain intense signal in SEIRA, a considerable field enhancement needs to be achieved. One of the approaches uses antennas resonating directly at IR frequencies. Thus, such antennas have dimensions of about half the wavelength, i.e. a few micrometers. An example is a gold nanowire of length  $L=\lambda/2$  acting as a linear dipole antenna [87] (Fig. 5.14b). Strong field enhancement (hot spots) occurs at the wire extremities (Fig. 5.14a), yielding strongly enhanced IR spectra from a few molecules adsorbed on the antenna surface. This effect can be observed in Fig. 5.14c where a broadband IR antenna resonance is clearly visible when the polarization of the incoming light is parallel to the antenna's long axis (black solid line). Near the resonance, two narrow spectral lines (marked by a red circle) are seen. They corre-

**Fig. 5.14 a** Local field intensity at a 1.341 μm long infrared antenna. **b** Single gold IR antenna deposited on a CaF substrate. **c** Absorption spectroscopy of octodecanothiol groups deposited on top of a single gold IR nanoantenna. The signal of the molecular groups is outlined in a red circle. Adapted from Ref. [87]



spond to the vibrational fingerprints of a few thousand molecules deposited on the antenna. Rotating the polarization of the incident line, no antenna resonance occurs (red line) and no vibrational fingerprints can be observed. This experiment shows the importance of the antenna resonance to overcome detection limits in IR spectroscopy. Notice that the spectral lines of the molecules appear as peaks rather than dips due to the electromagnetic interference between the local field of the antenna and the field of the molecular vibrations. This effect is analogous to the quantum mechanical Fano effect. Antenna-assisted SEIRA can be optimized with the use of more complex and advanced antenna structures [88–93].

# 5.2.4 Localized Plasmons in Other Applications

The potential for application of the field localization and enhancement of LSPs is not limited to field-enhanced spectroscopies. A variety of physical, biological, and

chemical processes can be enhanced or mediated by LSPs. Among others, we can mention the action of plasmons to boost the performance in photovoltaics [4], or the antenna effect that metallic structures can impose on the emission, directivity, and decaying rates of molecular fluorescence [2, 18, 94]. Standard plasmon sensing can also take advantage of plasmons localized in metallic particles that usually show larger figures of merit. Energy transfer in biological environments is another aspect where LSPs can play an important role. Metallic interconnections to deal with polaritonic signals can be a practical interface in optoelectronic devices. In medicine, LSPs have become more than a promise to diagnose and treat certain types of cancer [6]. In all these fields, the nature and properties of localized surface plasmons are the key factors governing the performance of the optical response. The reader will find further details of this aspect in R. Quidant's chapter.

## References

- 1. B.E. Sernelius, Surface Modes in Physics (Wiley-VCH, Berlin, 2001)
- 2. P. Anger, P. Bharadwaj, L. Novotny, Phys. Rev. Lett. 96, 113002 (2006)
- 3. H. Xu, E.J. Bjerneld, M. Käll, L. Börjesson, Phys. Rev. Lett. 83, 4357 (1999)
- 4. H.A. Atwater, A. Polman, Nat. Mater. 9, 205 (2010)
- 5. P. Andrew, W.L. Barnes, Science **306**, 1002 (2004)
- 6. S. Lal, S. link, N. J. Halas, Nat. Photnics 1, 641 (2007)
- 7. S. Bozhevolny, *Plasmonic Nanoguides and Circuits* (Pan Stanford, Singapore, 2010)
- 8. M. Aeschlimann, M. Bauer, D. Bayer, T. Brixner, F.J. Garcia de Abajo, W. Pfeiffer, M. Rohmer, C. Spindler, F. Steeb, Nature **446**, 301 (2007)
- R. Hillenbradn, F. Keilmann, P. Hanarp, D.S. Sutherland, J. Aizpurua, Appl. Phys. Lett. 83, 368 (2003)
- 10. R. Ritchie, Phys. Rev. 106, 874 (1957)
- 11. H. Raether, Surface Plasmons on Smooth and Rough Surfaces and on Gratings (Springer, Berlin, 1988)
- F. López-Tejeira, S.G. Rodrigo, L. Martín-Moreno, F.J. García-Vidal, E. Devaux, T.W. Ebbesen, J.R. Krenn, I.P. Radko, S.I. Bozhevolny, M.U. González, J.C. Weeber, A. Dereux, Nat. Phys. 3, 324 (2007)
- 13. P. Bharadwaj, B. Deutsch, L. Novotny, Adv. Opt. Photonics 1, 438 (2009)
- 14. C.F. Bohren, D.R. Huffman, Absorption and Scattering of Light by Small Particles (Wiley, New York, 1998)
- L. Novotny, B. Hecht, *Principles of Nano-Optics* (Cambridge University Press, Cambridge, 2006)
- 16. E.M. Larsson, J. Alegret, M. Käll, D.S. Sutherland, Nano Lett. 7, 1256 (1957)
- M. Schnell, A. Garcia-Etxarri, A.J. Huber, K. Crozier, J. Aizpurua, R. Hillenbrand, Nat. Photonics 3, 287 (2009)
- 18. T.H. Taminiau, F.D. Stefani, F.B. Segerink, N.F. Van Hulst, Nat. Photonics 2, 234 (2008)
- 19. M. Pelton, J. Aizpurua, G.W. Bryant, Laser Photon Rev. 2, 136 (2008)
- 20. O. Muskens, D. Christofilos, N. Del Fatti, F. Valee, J. Opt. A Pure Appl. Opt. 8, S264 (2006)
- 21. P.E. Batson, Phys. Rev. Lett. 49, 936 (1982)
- J. Nelayah, M. Kociak, O. Stéphan, F.J. García de Abajo, M. Tencé, L. Henrard, D. Taverna,
   I. Pastoriza-Santos, L.M. Liz-Marzán, C. Colliex, Nat. Phys. 3, 348 (2007)
- 23. T.L. Ferrel, P.M. Echenique, Phys. Rev. Lett. **55**, 1526 (1985)
- 24. J. Dorfmüller, R. Vogelgesang, R. Thomas Weitz, C. Rockstuhl, C. Etrich, T. Pertsch, F. Lederer, K. Kern, Nano Lett. 9, 2372 (2009)

- 25. R.J. Walters, R.V.A. van Loon, I. Brunets, J. Schmitz, A. Polman, Nat. Mater. 9, 21 (2009)
- 26. R. Berndt, J.K. Gimzewski, P. Johansson, Phys. Rev. Lett. 67, 3796 (1991)
- 27. G. Mie, Ann. Phys. 342, 881 (1908)
- 28. S. Link, M.A. El-Sayed, J. Phys. Chem. B 103, 8410 (1999)
- 29. K.L. Kelly, E. Coronado, L.L. Zhao, G.C. Schatz, J. Phys. Chem. B 107, 668 (2003)
- 30. S.J. Oldenburg, R.D. Averitt, S.L. Westcott, N.J. Halas, Chem. Phys. Lett. 288, 243 (1998)
- 31. C.L. Haynes, R.P. Van Duyne, J. Phys. Chem. B. 105, 5599 (2001)
- 32. L.M. Liz-Marzán, Mater. Today 7, 26 (2004)
- 33. C.J. Murphy et al., J. Phys. Chem. B **109**, 13857 (2005)
- 34. E.M. Purcell, C.R. Pennypacker, Astrophys. J. 186, 705 (1973)
- 35. E.K. Miller, J. Electromagn. Waves Appl. 8, 1125 (1994)
- 36. F.J. García de Abajo, A. Howie, Phys. Rev. B 65, 115418 (2002)
- H. Wang, Y. Wu, B. Lassiter, C.L. Nehl, J.H. Hafner, P. Nordlander, N.J. Halas, PNAS 103, 10856 (2006)
- 38. O.L. Muskens, N. Del Fatti, J.R. Hutzinger, P. Billaud, M. Broyer, Appl. Phys. Lett. 88, 063109 (2006)
- J.R. Krenn, G. Schider, W. Rechberger, B. Lamprecht, A. Leitner, F.R. Aussenegg, J.C. Weeber, App. Phys. Lett. 77, 3379 (2000)
- C. Sönnichsen, T. Franzl, T. Wilk, G. von Plessen, J. Feldmann, Phys. Rev. Lett. 88, 077402 (2002)
- 41. P. Hanarp, M. Käll, D.S. Sutherland, J. Phys. Chem. B 107, 5768 (2003)
- 42. S.J. Oldenburg, S.L. Westcott, R.D. Averitt, N.J. Halas, J. Chem. Phys. 111, 4729 (1999)
- 43. J. Aizpurua, P. Hanarp, D.S. Sutherland, M. Kall, G.W. Bryant, F.J. Garcia de Abajo, Phys. Rev. Lett. 90, 057401 (2003)
- 44. H. Wang, D.W. Brandl, F. le, P. Nordlander, N. J. Halas. Nano Lett. 6, 827 (2006)
- L.J. Sherry, S.-H. Chang, G.C. Schatz, R.P. Van Duyne, B.J. Wiley, Y. Xia, Nano Lett. 5, 2034 (2005)
- 46. C.L. Nehl, H. Liao, J.H. Hafner, Nano Lett. 6, 683 (2006)
- 47. M.W. Knight, N.J. Halas, New J. Phys. 10, 105006 (2008)
- 48. N.A. Mirin, N.J. Halas, Nano Lett. 9, 1255 (2009)
- 49. J.I. Ziegler, R.F. Haglund Jr., Nano Lett. 10, (2010)
- 50. R. Bukasov, J.S. Shumaker-Parry, Nano Lett. 7, 1113 (2007)
- 51. R. Jin, Y. Cao, C.A. Mirkin, K.L. Kelly, G.C. Schatz, J.G. Zheng, Science 294, 1901 (2001)
- 52. V. Myroshnychenko et al., Chem. Soc. Rev. 37, 1792 (2008)
- T. Rindzevicius, Y. Alaverdyan, B. Sepulveda, T. Pakizeh, M. Käll, R. Hillenbrand, J. Aizpurua,
   F.J. García de Abajo, J. Phys. Chem. C. 111, 1207 (2007)
- H. Rigneault, J. Capouladel, J. Dintinger, J. Wenger, N. Bonod, E. Popov, T. W. Ebbesen,
   P-F. Lenne. Phys. Rev. Lett. 95, 117401 (2005)
- 55. M. Sukharev, J. Sung, K.G. Spears, T. Seideman, Phys. Rev. B 76, 184302 (2007)
- 56. E. Prodan, C. Radloff, N.J. Halas, P. Nordlander, Science. 302, 419 (2003)
- 57. W. Rechenberger et al., Opt. Commun. 220, 137 (2003)
- 58. L. Silberstein et al., Philos. Mag. **33**, 521 (1917)
- 59. T. Atay, J.-H. Song, A.V. Nurmikko, Nano Lett. 4, 1627 (2004)
- J.B. Lassiter, J. Aizpurua, L.I. Hernandez, D.W. Brandl, I. Romero, S. Lal, J.H. Hafner, P. Nordlander, N.J. Halas, Nano Lett. 8, 1212 (2008)
- 61. K.-H. Su, Q.-H. Wei, X. Zhang, Nano Lett. 3, 1087 (2003)
- 62. P. Nordlander, C. Oubre, E. Prodan, K. Li, M.I. Stockman, Nano Lett. 04, 899 (2004)
- 63. D.P. Fromm, A. Sundaramurthy, P.J. Schuck, G. Kino, W.E. Moerner, Nano Lett. 4, 957 (2004)
- P.J. Schuck, D.P. Fromm, A. Sundaramurthy, G.S. Kino, W.E. Moerner, Phys. Rev. Lett. 94, 017402 (2005)
- 65. R. Hillenbrand, F. Keilmann, App. Phys. B 73, 239 (2001)
- 66. E. Cubukcu, E.A. Kort, K.B. Crozier, F. Capasso, Appl. Phys. Lett. 89, 093120 (2006)
- M. Schnell, A. Garcia-Etxarri, J. Alkorta, J. Aizpurua, R. Hillenbrand, Nano Lett. 10, 3524 (2010)

- 68. I. Romero, J. Aizpurua, G.W. Bryant, F.J. García de Abajo, Opt. Express 14, 9988 (2006)
- 69. A. Alu, N. Engheta, Nat. Photonics 2, 226 (2008)
- O. Pérez-González, N. Zabala, A.G. Borisov, N.J. Halas, P. Nordlander, J. Aizpurua, Nano Lett. 10, 3090 (2010)
- 71. P. Mühlschlegel, H.-J. Eisler, O.J.F. Martin, B. Hecht, D.W. Pohl, Science 308, 1607 (2005)
- 72. J. Aizpurua, G.W. Bryant, L.J. Richter, F.J. García de Abajo, Phys. Rev. B 71, 235420 (2005)
- 73. G.W. Bryant, F.J. García de Abajo, J. Aizpurua, Nano Lett. 8, 631 (2007)
- T.H. Taminiau, R.J. Moerland, F.B. Segerink, L. Kuipers, N.F. van Hulst, Nano Lett. 7, 28 (2007)
- 75. A.G. Curto, G. Volpe, T.H. Taminiau, M.P. Kreuzer, R. Quidant, N.F. van Hulst, Science 329, 930 (2010)
- 76. L. Novotny, Phys. Rev. Lett. 98, 266802 (2007)
- 77. M. Moskovits, Rev. Mod. Phys. **57**, 783 (1985)
- 78. K. Kneipp, M. Moskovits, H. Kneipp (eds.), Surface-enhanced Raman Scattering; Physics and Applications (Springer, Heidelberg, 2006)
- 79. R. Aroca, Surface-Enhanced Vibrational Spectroscopy (Wiley, Hoboken, 2006)
- 80. S.M. Nie, S.R. Emory, Science **275**, 1102 (1997)
- K. Kneipp, Y. Wang, H. Kneipp, L.T. Perelman, I. Itzkan, R.R. Dasari, M.S. Feld, Phys. Rev. Lett. 78, 1667 (1997)
- 82. H. Xu, J. Aizpurua, M. Käll, P. Apell, Phys. Rev. E 62, 4318 (2000)
- 83. A. Otto, J. Raman Spectrosc. 36, 497 (2005)
- 84. P. Johansson, H. Xu, M. Kll, Phys. Rev. B 72, 035427 (2005)
- E.C. Le Ru, J. grand, N. Felidj, J. Aubard, G. Levi, A. Hohenau, J.R. Krenn, E. Blackie, P.G. Etchegoin, J. Phys. chem. C 112, 8117 (2008)
- 86. R.F. Aroca, D.J. Ross, C. Domingo, Appl. Spectrosc. 58, 324A (2004)
- 87. F. Neubrech, A. Pucci, T.W. Cornelius, S. Karim, A. Garcia-Etxarri, J. Aizpurua, Phys. Rev. Lett. 101, 157403 (2008)
- 88. T.R. Jensen et al., J. Phys. Chem. B **104**, 10549 (2000)
- 89. R. Ruppin, R. Englman, Rep. Prog. Phys. 33, 149 (1970)
- 90. M.S. Anderson, Appl. Phys. Lett. 83, 2964 (2003)
- 91. V. Giannini, A. Berrier, S.A. Maier, J.A. Sánchez-Gil, J. Gómez-Rivas, Opt. Express 18, 2797 (2010)
- 92. F. Le, D.W. Brandl, Y.A. Urzhumov, H. Wang, J. Kundu, N. J. halas, J. Aizpurua, P. Nordlander. ACS Nano 2, 707 (2008)
- 93. M. Brehm, T. Taubner, R. Hillenbrand, F. Keilmann, Nano Lett. 6, 1307 (2006)
- 94. S. Kühn, U. Hakanson, L. Rogobete, V. Sandoghdar, Phys. Rev. Lett. 97, 017402 (2006)

# Chapter 6 Plasmons on Separated Particles: Homogenization and Applications

Ross McPhedran

Abstract In this chapter, we discuss localized plasmons in optical systems containing metallic particles, clusters of metallic particles, or periodic arrays of metallic particles, separated in all cases by a background dielectric material or matrix. We begin with a brief discussion of the equations governing electromagnetic propagation in structured or composite systems containing metal particles in a matrix. A full electromagnetic solution for a periodic array of particles or a finite cluster of them is possible, but much can be learned from treatments in the quasistatic approximation, where properties of the particles are subsumed in effective dielectric permittivities and magnetic permeabilities, and these are used in Maxwells' equations for a homogeneous material to calculate reflection and transmission properties. The two most important equations used to calculate effective dielectric permittivities and magnetic permeabilities are the Maxwell-Garnett formula and Bruggeman's effective medium formulae. We compare these in Sect. 6.3, and look at applications in Sect. 6.4 to the field of selective absorbers for photothermal and photovoltaic energy applications. In the next section, we go on to consider collections of particles and their resonant properties, which can be exploited to deliver strong local concentrations of electromagnetic fields. These are used in Sects. 6.6 and 6.7 to discuss cloaking using plasmonic resonance, and spasers, devices which can overcome through amplification the propagation losses associated with plasmons.

## 6.1 Introduction

In this chapter, we will continue the discussion of localized plasmons in optical systems containing metallic particles, clusters of metallic particles, or periodic arrays of metallic particles, separated in all cases by a background dielectric material or

R. McPhedran (⋈)

CUDOS and IPOS, School of Physics, University of Sydney, Sydney 2006, Australia e-mail: ross@physics.usyd.edu.au

matrix. We have already seen that structured systems containing metallic particles can provide strongly enhanced local fields, useful in contemporary applications like creating efficient nanoantennas and molecular sensing. However, this field has a long history: loading a material like glass with metal particles has a profound effect on the colour of the transmitted light, a fact which was known in Ancient Rome. Indeed, the famous Lycurgus cup [1] of the fourth century AD was made of soda glass containing at the 1% level colloidal nanoparticles of around 50–100 nm in diameter, made of a silver–gold alloy. These nanoparticles make the cup dichroic: in reflection it looks like jade, with an opaque greenish-yellow tone, but in transmission it acquires a translucent ruby colour. Thus, the power of metal particles to control the reflection, transmission and absorption of light has been known for thousands of years, and, as we shall see, continues to be exploited in a growing number of ways in today's technologies.

We begin with a brief discussion of the equations governing electromagnetic propagation in structured or composite systems containing metal particles in a matrix. A full electromagnetic solution for a periodic array of particles or a finite cluster of them is possible (while often difficult), but we shall see that much can be learned from treatments in the quasistatic approximation, where properties of the particles are subsumed in effective dielectric permittivities and magnetic permeabilities, and these are used in Maxwells' equations for a homogeneous material to calculate reflection and transmission properties. The quasistatic treatment is useful in regions where fields change rapidly with distance, on the scale of the wavelength, and much is known about particular solutions and general constraints on solutions. The two most important equations used to calculate effective dielectric permittivities and magnetic permeabilities are the Maxwell-Garnett formula and Bruggeman's effective medium formulae. We compare these in Sect. 6.3, and look at applications in Sect. 6.4 to the field of selective absorbers for photothermal and photovoltaic energy applications. In the next section, we go on to consider collections of particles and their resonant properties, which can be exploited to deliver strong local concentrations of electromagnetic fields. These are used in Sects. 6.6 and 6.7 to discuss cloaking using plasmonic resonance, and spasers, devices which can overcome through amplification the propagation losses associated with plasmons.

# **6.2** Electromagnetic Waves in Structured Systems

We consider electromagnetic waves propagating in a medium where the dielectric permittivity  $\epsilon(\mathbf{x})$  and the magnetic permeability  $\mu(\mathbf{x})$  are functions of the position vector  $\mathbf{x}$ . We will be interested primarily in cases where the functions change discontinuously as we move from one material to the other, and in particular in the *cermet* topology, where there are isolated metallic particles in a continuous ceramic or dielectric matrix. The particles may be spherical or distorted spheres in shape, or cylinders, either circular or distorted circles in cross-section. In the former case,

we need to consider full three-dimensional propagation equations, while in the latter case it may be sufficient to use Maxwell's equations in two dimensions.

The propagation of electromagnetic waves with angular frequency  $\omega$  may be described by the Helmholtz equation, say for the electric field  $\mathbf{E}(\mathbf{x})$ :

$$\nabla^2 \mathbf{E}(\mathbf{x}) + \frac{\epsilon(\mathbf{x})\mu(\mathbf{x})\omega^2}{c^2} \mathbf{E}(\mathbf{x}) = 0, \tag{6.1}$$

with a similar equation applying to the magnetic field  $\mathbf{H}(\mathbf{x})$ . The boundary conditions applying at interface boundaries are continuity of the tangential components of the electric and magnetic fields, as discussed in Chaps. 1 and 2.

From the form of the Eq. (6.1), we can see that the solution is well approximated by the solution of Laplace's equation if the first term dominates the second. This will occur if a length scale for the variation of the fields is much smaller than the wavelength. For example, in the region close to a source, there is an inner or inductive region governed by Laplace's equation, where electric and magnetic fields are decoupled. This gives way to a coupling region, and is surrounded by a radiation zone, where electric and magnetic fields are coupled, with their cross product giving the energy flow outwards. Similarly, near a tight focus, there will be a static region, and in regions where electromagnetic fields are concentrated this may again occur. In families of resonant modes, higher members with fields rapidly changing in space again will be well approximated by static solutions.

There are then various approaches to calculating electromagnetic field distributions in structured systems. Sophisticated numerical procedures based on the finite element or finite difference time domain methods can be used in conjunction with powerful computers to give field maps and important derived quantities. For periodic geometries with scatterers of simple form, like spheres or circular cylinders, semi-analytic methods may be used, where the known solution of the single-scatterer problem is used as the building block of the periodic solution. For example, Stefanou, Yannopapas and Modinos [2] have built a method based on Mie scattering from a single sphere [3] and the well-known Korringa-Kohn-Rostoker method from solidstate physics [4, 5], which can solve problems associated with layers or lattices of spheres. Another approach is to use the quasistatic procedure, and rely on the extensive literature on effective dielectric permittivities and similar transport properties in structured media for equivalent properties which may be used to construct in simple fashion the fields in a homogeneous material. This approach is described in Chap. 11 of the comprehensive survey by Milton [6], which is also an excellent source for the literature on effective properties for composite materials.

One way of validating the quasistatic approach is to take a semi-analytic method, and use it to study the waves existing in a periodic structure for wavelengths which increase steadily in comparison with the structure spacing [7–9]. In this way, it has been established that the quasistatic method can be applied in general when the wavelength  $\lambda$  is sufficiently large compared with the typical scale size d, where the criterion is often written

$$\frac{\lambda}{d} \ge 5. \tag{6.2}$$

This criterion should be used with caution, since if the particles are metallic, the wavelength inside them can be much smaller in magnitude than in free space, so that the quasistatic treatment may only achieve accuracy at longer wavelengths than one might expect from (6.2).

#### **6.3** Effective Permittivities and Permeabilities

Brief histories of some of the important formulae, which give effective permeabilities and permittivities of structured materials, are given in Chap. 10 of the book by Milton [6] and in the seminal review article of Landauer [10]. The Maxwell-Garnett formula is useful for composites with the cermet topology. Its history goes back as far as the work of Faraday in 1837, and notable contributions are associated with the names of Clausius and Mossotti, Maxwell, Lorentz, Lorenz and Maxwell-Garnett. The last was in fact the son of Maxwell's lecture demonstrator, and his first three names stem from his father's admired employer. The history of formulae of this type is somewhat entangled, so the same equation may bear different names in different accounts of this important topic. It should be noted that the same mathematical framework applies without change to a number of different physical situations, so that the formulae quoted here for effective permittivities and permeabilities also apply to electrical conductivity, thermal conductivity, diffusivity, fluid permeability and the shear matrix of anti-plane elasticity. It should also be understood that the derivations of some of the useful results given below are long and quite technical. Thus, many readers will be content to take the results as given, and use them in modelling to test their effectiveness; those others who wish to understand full technical details can refer to the original references, or to Milton's book [6].

The generic version of such relations may be called the Clausius–Mossotti formula, and applies to a dilute distribution of inclusions in a matrix. We suppose we are in three dimensions, and there are N inclusions per unit volume, each occupying a volume V. The most important parameter characterizing the distribution of inclusions is the volume fraction f, which is the volume NV occupied by the particles per unit volume of the system. We suppose the response of the inclusions to an applied electric field to be given by the *polarizability*  $\alpha$ , such that the dipole moment induced by a unit applied field is  $\alpha$ . If the dielectric permittivity of the matrix is  $\epsilon_1$ , then the effective dielectric permittivity of the dilute composite system is

$$\epsilon_{\text{eff}} \simeq \epsilon_1 \mathbf{I} + f \frac{\alpha}{V}.$$
 (6.3)

This could be the expression for the permittivity tensor if  $\alpha$  were a tensor quantity depending on the direction of the applied field, in which case **I** would be the diagonal

tensor, or it could be the expression for a scalar quantity if  $\alpha$  were independent of applied field direction, in which case **I** would be unity. If we deal with a two-dimensional problem, the formula applies with V replaced by an area A.

The Maxwell-Garnett, or Maxwell, or Lorentz–Lorenz formula, follows from the Clausius–Mossotti formula (6.3) if the polarizability takes the value corresponding to a particle of a particular shape, placed far enough from its neighbours so that it interacts with them only though dipole terms. For example, in three dimensions, we consider the most important case: that of an isolated sphere. Letting  $B_1$  denote the dipole moment induced in the sphere by the local field of strength  $E_0$  oriented along the Ox axis, from which the angle  $\theta$  is measured, the electrostatic potential in the external neighbourhood of the sphere is

$$V_{\text{ext}} = E_0 r \cos \theta - \frac{B_1 \cos \theta}{4\pi \epsilon_1 r^2},\tag{6.4}$$

where r denotes radial distance from the centre of the sphere. The potential distribution inside the sphere involves a dipole coefficient  $C_1$ :

$$V_{\rm int} = C_1 r \cos \theta. \tag{6.5}$$

These potentials have to satisfy the following boundary conditions at r = a:

$$V_{\rm ext} = V_{\rm int}, \epsilon_1 \frac{\partial V_{\rm ext}}{\partial r} = \epsilon_2 \frac{\partial V_{\rm int}}{\partial r}.$$
 (6.6)

These boundary conditions give

$$E_0 - \frac{B_1}{4\pi\epsilon_1 a^3} = C_1, \ \epsilon_1 \left[ E_0 + 2\frac{B_1}{4\pi\epsilon_1 a^3} \right] = \epsilon_2 C_1,$$
 (6.7)

which may be solved to yield

$$\frac{B_1}{E_0} = \alpha = 4\pi a^3 \epsilon_1 \left(\frac{\epsilon_2 - \epsilon_1}{\epsilon_2 + 2\epsilon_1}\right). \tag{6.8}$$

Substituting (6.8) into the Clausius–Mossotti equation (6.3), we obtain

$$\epsilon_{\text{eff}} = \epsilon_1 \left[ 1 + 3f \left( \frac{\epsilon_2 - \epsilon_1}{\epsilon_2 + 2\epsilon_1} \right) \right].$$
(6.9)

This expression is the dipole model correct to first order in the volume fraction f. A slightly more elaborate treatment gives a result correct to order  $f^2$ , the Maxwell-Garnett equation for spherical particles:

$$\epsilon_{\text{eff}} = \epsilon_1 \left[ 1 + \frac{3f(\epsilon_2 - \epsilon_1)}{3\epsilon_1 + (1 - f)(\epsilon_2 - \epsilon_1)} \right]. \tag{6.10}$$

It is worth emphasizing that the formula (6.10) is not symmetric in  $\epsilon_2$  and  $\epsilon_1$ : the assumption is made that the former corresponds to isolated particles with volume fraction f placed in a continuous matrix with dielectric permittivity  $\epsilon_1$ .

We can find the value of the ratio  $\epsilon_2/\epsilon_1$  at which the effective permittivity becomes infinite from (6.10). This is

$$\left(\frac{\epsilon_2}{\epsilon_1}\right)_{\infty} = -\left(\frac{2+f}{1-f}\right). \tag{6.11}$$

This equation gives the *permittivity ratio for the excitation of localized surface plasmons* in dilute systems of spherical particles. It requires the ratio to be real, negative and below -2. The corresponding ratio at which the effective permittivity goes to zero is given by

$$\left(\frac{\epsilon_2}{\epsilon_1}\right)_0 = -\left(\frac{2-2f}{1+2f}\right),\tag{6.12}$$

a result which requires the effective permittivity to lie between -2 and 0.

We illustrate the resonant nature of the response given by the Maxwell-Garnett formula in Fig. 6.1. This shows the effective permittivity as a function of wavelength for a cermet containing a 10% volume fraction of silver spheres in a silica matrix. The complex refractive index data used for silver were taken from measured data of Johnson and Christy [11]. The pole of  $\epsilon_{\rm eff}$  from (6.11) would occur at  $\epsilon_2/\epsilon_1=-2.33$ , and the zero at -1.5. In practice, of course, silver does not ever have this ratio which is exactly negative and real, so  $\epsilon_{\rm eff}$  becomes large in magnitude near the pole and small in magnitude near the zero. We also show in Fig. 6.1 the absorptance in TE and TM polarizations of a 0.5  $\mu$ m thick layer of this composite in air, for a 30° angle of incidence. The absorptance is similar for the two polarizations, and is high at short wavelengths where the film is optically thick. It varies rapidly in two regions: around 0.3  $\mu$ m where the optical properties of silver change rapidly, and around 0.4  $\mu$ m where the Maxwell-Garnett resonance occurs.

If the volume fraction of the inclusions becomes large, the interactions between them become more complicated, as higher and higher order multipoles become comparable in strength with dipoles. This means that, instead of having only the dipole resonance available to enhance plasmonic optical responses, multiple resonances can be exploited. This effect was investigated by Rayleigh [12], in a classic 1892 paper discussing lattices of spheres in three dimensions, or of cylinders in two dimensions, which was taken up and extended by Doyle [13] and by McPhedran, McKenzie and Derrick [14, 15]. The Rayleigh treatment may be expressed in a generic form as a matrix equation:

$$(\mathbf{M} + \mathbf{S})\mathbf{B} = \mathbf{E}_{\text{appl}}. (6.13)$$

Here, electrostatic fields are written in terms of multipole expansions, with each term specified by integers l and m. The multipole coefficients are placed in the

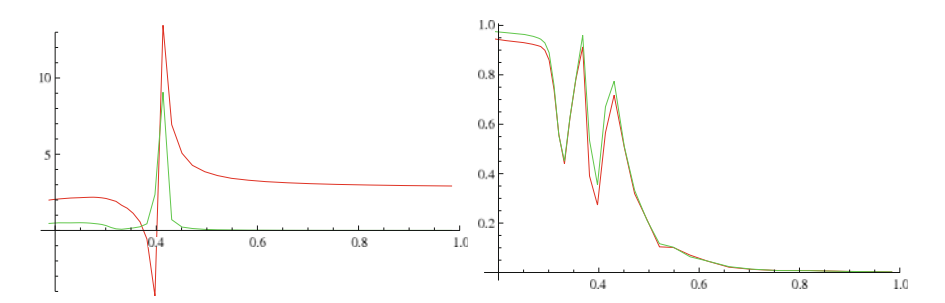


Fig. 6.1 Left  $\epsilon_{\rm eff}$  as a function of wavelength (in  $\mu$ ) for a composite containing silver spheres with a volume fraction of 10% in a silica matrix. Right absorptance as a function of wavelength for a 0.50  $\mu$ m thick layer of the composite in air, for an angle of incidence of 30°. In both cases, the red curve is for TE polarization, and the green curve for TM polarization

vector  $\mathbf{B}$ , with those for the applied field in the vector  $\mathbf{E}_{appl}$ . The matrix  $\mathbf{M}$  results from the application of boundary conditions at the particle surface surface, as is exemplified in Eqs. (6.16–6.18). The matrix  $\mathbf{S}$  is filled with lattice sums, which depend only on the geometry of the lattice, and whose evaluation is discussed in e.g., Refs. [12–15].

The dependence on radial distance for multipole terms with first index l is  $1/r^{(l+1)}$  for multipoles with their source at r=0, and  $r^l$  for multipoles with their sources inside spheres with centres not at the origin. The dependence on spherical polar angles  $(\theta, \phi)$  is given by the same functions  $Y_{lm}(\theta, \phi)$  which occur in the theory of Mie scattering of electromagnetic waves by a sphere [16], and in the solution of the Schrödinger equation for the hydrogen atom. The dipole term is given by  $Y_{1,0}$ , which is just a constant times  $\cos \theta$ , and so gives the terms included in the potential expansions in Eqs. (6.4–6.5). The potential outside the inclusion is written in the form

$$V_{\text{ext}} = \sum_{l=1}^{\infty} \sum_{m=-l}^{l} (A_{lm} r^l + B_{lm} r^{-l-1}) Y_{lm}(\theta, \phi), \tag{6.14}$$

while inside the inclusion it is

$$V_{\text{int}} = \sum_{l=1}^{\infty} \sum_{m=-l}^{l} C_{lm} r^{l} Y_{lm}(\theta, \phi).$$
 (6.15)

The periodicity of the problem means the coefficients  $A_{lm}$ ,  $B_{lm}$  and  $C_{lm}$  are the same for each sphere in the lattice.

The boundary conditions at the surface of a sphere of radius a give the connection between the  $A_{lm}$ ,  $B_{lm}$  and  $C_{lm}$ . The condition that the potential be continuous is:

$$A_{lm}a^{l} + \frac{B_{lm}}{a^{l+1}} = C_{lm}a^{l}, (6.16)$$

while the second condition gives the continuity of the normal component of the displacement field:

$$\epsilon_1 \left[ A_{lm} a^l - \frac{B_{lm}}{a^{l+1}} \right] = \epsilon_2 C_{lm} a^l. \tag{6.17}$$

The two boundary conditions may be combined to eliminate  $C_{lm}$  and express  $A_{lm}$  in terms of  $B_{lm}$ :

$$A_{lm} = \frac{B_{lm}}{a^{2l+1}} \frac{\epsilon_2 + \epsilon_1 (l+1)/l}{\epsilon_1 - \epsilon_2} = \frac{B_{lm}}{T_l a^{2l+1}}.$$
 (6.18)

To complete the solution, we need extra equations from which the multipole coefficients  $B_{lm}$  may be obtained from the applied field. Those extra equations come from the Rayleigh identity, which expresses the part of  $V_{ext}$  which is not singular at the origin, i.e., the terms involving the  $A_{lm}$ , in terms of the contributions from sources on all the other spheres in the lattice, together with a contribution from the applied field. The terms coming from other spheres in the lattice are re-expressed in terms of the coordinates  $(r, \theta, \phi)$  of the sphere at the origin using the addition theorem for spherical harmonics (see, for example, [17]). The result is a matrix system of equations which always takes the form (6.13), regardless of the lattice we deal with, and for cylindrical as well as spherical inclusions.

The matrix  $\mathbf{M}$  in (6.13) is diagonal, with the terms multiplying  $B_{lm}$  in (6.18) along the diagonal. The second matrix  $\mathbf{S}$  is filled with *lattice sums*, which incorporate information about the way inclusions are placed in the matrix. The right-hand side of (6.13) contains the multipole coefficients representing the applied field. Note that the matrix equation (6.13) could be used to treat inclusions of arbitrary shape, as long as the boundary condition equation (6.18) was appropriately altered. The two matrices  $\mathbf{M}$  and  $\mathbf{S}$  independently represent the two aspects of the problem: the properties of the inclusions ("what's there") and the way they are arranged ("what's where").

Equation (6.13) may be solved numerically, or low-order truncations may be found in analytic form. For the simple cubic lattice, the volume fraction for unit spacing of spheres is  $f = 4\pi a^3/3$ , and the volume fraction at which the spheres touch is  $f_c = \pi/6$ . An analytic expression taking into account the multipole coefficients  $B_{1,0}$ ,  $B_{3,0}$ ,  $B_{5,0}$  and  $B_{7,0}$  is

$$\epsilon_{\text{eff}} = 1 - \frac{3f}{D},\tag{6.19}$$

where

$$D = T_1^{-1} + f - b_1 T_5 f^{14/3} - c_1 T_7 f^6 - a_1 f^{10/3} \frac{\left[1 - c_2 T_5 f^{11/3} + c_3 T_5^2 f^{22/3}\right]}{\left[T_3^{-1} + b_2 f^{7/3} - c_4 T_5 f^6\right]}$$
(6.20)

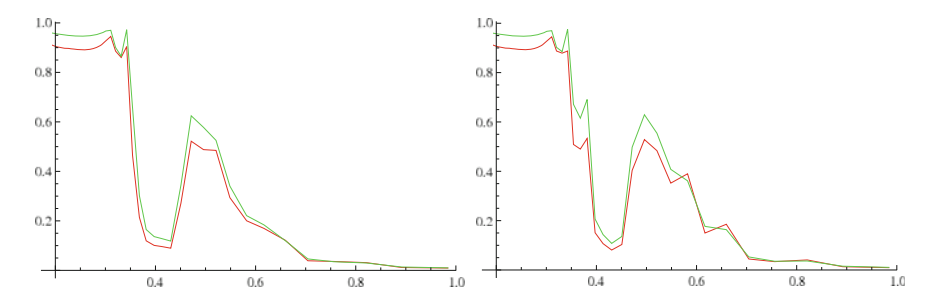


**Fig. 6.2** Absorptance as a function of wavelength for a 0.50  $\mu$ m thick layer placed in air of a composite containing 30% of silver spheres in silica, for an angle of incidence of 30°. In both cases, the *red curve* is for TE polarization, and the *green curve* for TM polarization. At *left*, the results of the Maxwell-Garnett formula, at *right*, those of the fourth-order Rayleigh formula

and  $a_1 = 1.3045$ ,  $b_1 = 0.01479$ ,  $b_2 = 0.4054$ ,  $c_1 = 0.1259$ ,  $c_2 = 0.5289$ ,  $c_3 = 0.06993$  and  $c_4 = 6.1673$ . Of course, (6.19) reduces to the Maxwell-Garnett equation (6.10) if  $a_1, b_1, b_2, c_1, c_2, c_3$  and  $c_4$  are replaced by zero.

In Fig. 6.2, we compare the results given by the Maxwell-Garnett formula and the fourth-order Rayleigh formula for the same situation as in Fig. 6.1, but with the volume fraction of spheres increased from 10 to 30%. This increase moves the absorption peak towards longer wavelengths, while the Rayleigh formula can be seen to give a more complex absorptance peak, due to the higher number of plasmon resonances contained in (6.19, 6.20) than in (6.10).

The exact solution of the system of Eq. (6.13) would have an infinite set of resonances. Bergman [18] has shown that  $\epsilon_{\text{eff}}$  can be determined if the electrostatic resonances of the system are known.

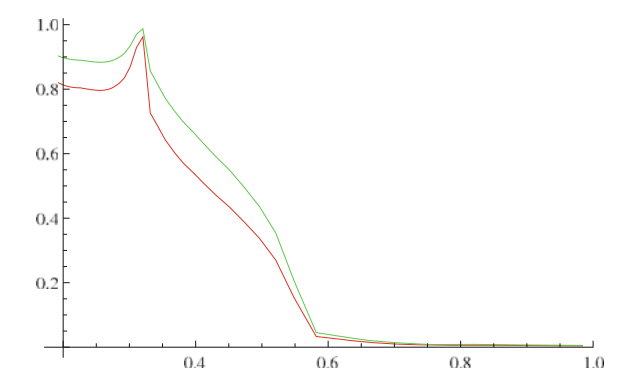
A second major class of theories of effective properties is that of effective medium models. These are widely encountered in solid-state physics, under the name of the Coherent Potential Approximation. They are useful for optical systems involving two or more materials, in which there is no well-identified continuous or matrix phase in which the other materials occur as isolated particles (e.g., they could apply well to alloy systems). An early influential example is the symmetric effective medium theory of Bruggeman [19], which differs from the Maxwell-Garnett class of theories in that the two media constituting the composite material are placed on an equal footing, unlike the cermet model of inclusions in a matrix. The theory leads to the following simple formula:

$$\epsilon_{\text{eff}} = \frac{1}{4} \left[ \gamma \pm (\gamma^2 + 8\epsilon_1 \epsilon_2)^{1/2} \right], \tag{6.21}$$

with

$$\gamma = (3f_1 - 1)\epsilon_1 + (3f_2 - 1)\epsilon_2, \tag{6.22}$$

**Fig. 6.3** Absorptance as a function of wavelength according to the symmetric Bruggeman formula for a 0.50 μm thick layer placed in air of a composite containing 40% of silver spheres in silica, for an angle of incidence of 30°. The *red curve* is for TE polarization, and the *green curve* for TM polarization



where  $f_1$  and  $f_2$  are the volume fractions of components 1 and 2, and  $f_1 + f_2 = 1$ . In (6.21), the plus or minus sign should be chosen to yield a positive imaginary part for  $\epsilon_{\text{eff}}$ .

In Fig. 6.3, we see that the symmetric effective medium model does not give plasmonic resonances of the type evident in Fig. 6.2. Essentially, surface plasmons cannot be formed since the geometry corresponds to an intimate mixture of the two components, without the well-defined boundaries of the cermet geometry.

We turn now to the two-dimensional case, where the composite is composed of cylinders aligned along the z axis, with area fraction f. For an applied electric field aligned along the z axis, the effective dielectric permittivity is given by the linear mixing formula, independent of the cylinder cross-sectional shape:

$$\epsilon_{\text{eff},z} = f \epsilon_2 + (1 - f)\epsilon_1. \tag{6.23}$$

This choice of applied field then does not give plasmonic resonances.

For the applied field lying in the xy plane, the problem of calculating the effective dielectric permittivity is linked with the theory of analytic functions of a complex variable, since the electrostatic potential obeys Laplace's equation, in keeping with analytic functions. This correspondence allows one to prove a beautiful result connecting  $\epsilon_{\rm eff}$  in two different problems:

Applied electric field along the x axis, and media with dielectric permittivities  $\epsilon_1$  and  $\epsilon_2$  occupying a particular arrangement;

Applied electric field along the y axis, and media with dielectric permittivities  $\epsilon_1$  and  $\epsilon_2$  interchanged spatially. The connection between the two situations is Keller's theorem [20]

$$\epsilon_{\text{eff},x}(\epsilon_1, \epsilon_2)\epsilon_{\text{eff},y}(\epsilon_2, \epsilon_1) = \epsilon_1 \epsilon_2.$$
 (6.24)

The geometry underlying this result is illustrated for a particular case in Fig. 6.4.

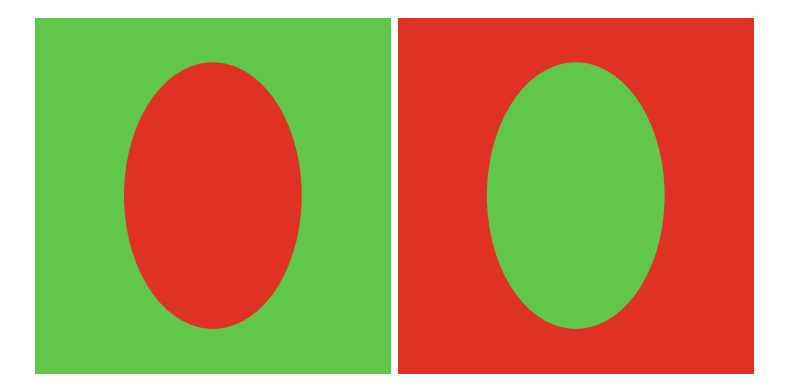


Fig. 6.4 At *left* and *right*, we show unit cells of two-phase composites with the *red region* having permittivity  $\epsilon_1$  and the *green region* having permittivity  $\epsilon_2$ , with the applied external electric field across the page at *left*, and up the page at *right*. The effective dielectric permeabilities of the two systems are connected by (6.24)

Dykhne [21] realized that if the geometry of the composite was unaffected by the interchange of the two components, and  $\epsilon_{\rm eff}$  was unaltered by the rotation of the applied field through 90°, then (6.24) gives

$$\epsilon_{\text{eff},x}(\epsilon_1, \epsilon_2) = \epsilon_{\text{eff},y}(\epsilon_2, \epsilon_1) = \sqrt{\epsilon_1 \epsilon_2}.$$
 (6.25)

This result applies for example to a checkerboard made of materials with alternating permittivities.

The Maxwell-Garnett equation for a square array of circular cylinders is

$$\epsilon_{\text{eff}} = \epsilon_1 \left[ 1 + \frac{2f(\epsilon_2 - \epsilon_1)}{\epsilon_1(1+f) + \epsilon_2(1-f)} \right]. \tag{6.26}$$

It will be noticed that this equation satisfies Keller's theorem exactly. This property also applies to the low-order Rayleigh formulae for arrays of cylinders [22]. In their derivation, the relation between multipole coefficients (6.18) becomes

$$A_l = \frac{B_l}{a^{2l}} \frac{\epsilon_2 + \epsilon_1}{\epsilon_1 - \epsilon_2} = \frac{B_l}{Ta^{2l}}.$$
 (6.27)

The fact that the quantity T now does not depend on the multipole order l means that for cylinders the plasmonic resonances of arbitrary order occur simultaneously, as distinct to the situation for spheres, where the values of  $\epsilon_2/\epsilon_1$  at resonance depend on the value of l. The higher-order Rayleigh formula we give for the square array of circular cylinders takes into account the multipole coefficients  $B_1$ ,  $B_3$ ,  $B_5$  and  $B_7$ , and is

$$\epsilon_{\text{eff}} = \epsilon_1 \left\{ 1 - \frac{2f}{\left[ T + f - \frac{0.305827f^4T}{T^2 - 1.402958f^8} - \frac{0.013362f^8}{T} \right]} \right\}.$$
 (6.28)

The most general framework within which to evaluate effective properties of composite systems is provided by the Bergman–Milton bounds [23, 24]. These depend on the dimensionality of the composite (something which may not be entirely obvious in thin film systems) and can incorporate a wide variety of known information about the composite. As more information is supplied, the bounds get tighter and tighter. Conversely, as one approaches the region of the negative real axis in the complex permittivity plane, the bounds get looser and looser; this is to be expected since poles of the effective permittivity are located on the negative real axis, and the effective permittivity becomes very sensitive to the composite structure in the neighbourhoods of such poles. The bounds may be used in an inverse way to go from measured permittivities of a composite back to knowledge of structural information (such as the volume fraction) [25, 26].

#### 6.4 Plasmon Resonances in Particle Clusters

We have so far discussed the plasmon resonances of single particles, infinite systems of particles in the dipole or effective medium approximation, and of periodic systems of particles. Intermediate between these cases is that of clusters containing a finite number of particles. As we shall see, interesting effects arise in finite systems, and in some cases analytic models can be constructed illustrating the coupling effects on the plasmonic resonances. When these are strong, the plasmons become "not-so-localized" entities, lying between the plasmons of isolated particles and those on continuous metallic surfaces in their properties.

The simplest system to be discussed is that of a pair of particles. Keller [27] analysed the current flowing between two perfectly conducting spheres with radius  $r_0$  and separated by a gap h, in a medium of conductivity  $\sigma_0$ . For  $r_0/h$  large, Keller estimated the effective resistance of the gap as

$$R_g \simeq \frac{1}{\pi \sigma_2 r_0 \log(r_0/h)}. (6.29)$$

For arrays of spheres, this translates into an effective dielectric permittivity formula [15, 27]

$$\epsilon_{\text{eff}} \simeq \epsilon_1 [\alpha - \beta \log(f_c - f)],$$
(6.30)

where  $\alpha$  and  $\beta$  are constants depending on the geometry of the array, in particular the number of nearest neighbours to any sphere, and  $f_c$  is the critical volume fraction at which the spheres touch. For the simple cubic lattice,  $\alpha = 0$ ,  $\beta = \pi/2$  and  $f_c = \pi/6$ . For the body-centred cubic lattice,  $\alpha = -0.55$ ,  $\beta = 2.73$  and  $f_c = \pi\sqrt{3}/8$ . For the

face-centred cubic lattice,  $\beta=4.43$  and  $f_c=\pi\sqrt{2}/6$ . For the case of the random packing of identical spheres under gravity studied by Bernal [28], the constants are  $\alpha=0.054$ ,  $\beta=2.0$  and  $f_c=0.63$ . For touching spheres, Batchelor and O'Brien [29] and McKenzie et al. [14, 15] give the effective dielectric permittivity in the asymptotic region as

$$\epsilon_{\text{eff}} = \gamma \epsilon_1 \log(\epsilon_2/\epsilon_1),$$
(6.31)

where for the simple cubic lattice,  $\gamma = \pi$ , for the body-centred cubic lattice  $\gamma = 5.44$  and for the face-centred cubic lattice,  $\gamma = 8.90$ . Formulae such as these are of use in designing plasmonic metamaterials using metallic nanoparticles [30], and also microstructures for enhancing local field strengths.

For a pair of circular cylinders, each of radius a and with unit centre–centre separation, there exists an asymptotic expression for the resistance which applies whether the cylinders have finite or infinite conductivity, or whether the gap between them (h) is small or exactly zero [31]:

$$R_g = \frac{2s\log(c) + 1 - 2s[\gamma + \psi(s+1)]}{\pi(c-1)}.$$
(6.32)

Here  $\psi$  is the logarithmic gamma function,  $\gamma$  is Euler's constant, while c becomes large for small gaps:

$$c = \frac{2a+h}{\sqrt{h(4a+h)}} \approx \sqrt{a/h},\tag{6.33}$$

and s becomes large for large conductivity ratios:

$$s = \frac{\log[(\sigma_1/\sigma_2 - 1)(\sigma_1/\sigma_2 + 1)]}{\log[(c - 1)/(c + 1)]} \approx c\sigma_2/\sigma_1.$$
 (6.34)

An interesting structural variation on the pair of particles has been considered by Alu and Engheta [32]: a spherical particle with its upper and lower halves composed of two different materials and used in the quasistatic regime. The potential distributions are given for the case where the two halves are in plasmonic resonance and illustrate the extreme anisotropy delivered by this design. For the electric field pointing up, the particle behaves as if it were made of a perfect electrical conductor, with its surface being an equipotential. For the electric field rotated through 90°, the equipotential lines shown in Fig. 6.5 cut the sphere surface at right angles, just as if the sphere were filled with a perfect magnetic conductor (its effective permittivity being zero).

The examples quoted in this section illustrate just a few cases from a literature which is already large and growing rapidly. However, they are sufficient to show the reader that, with sophisticated techniques available to manufacture microstructures and design tools to predict their properties, our ability to exploit plasmonic resonances of particle systems will continue to deliver surprising and important results.

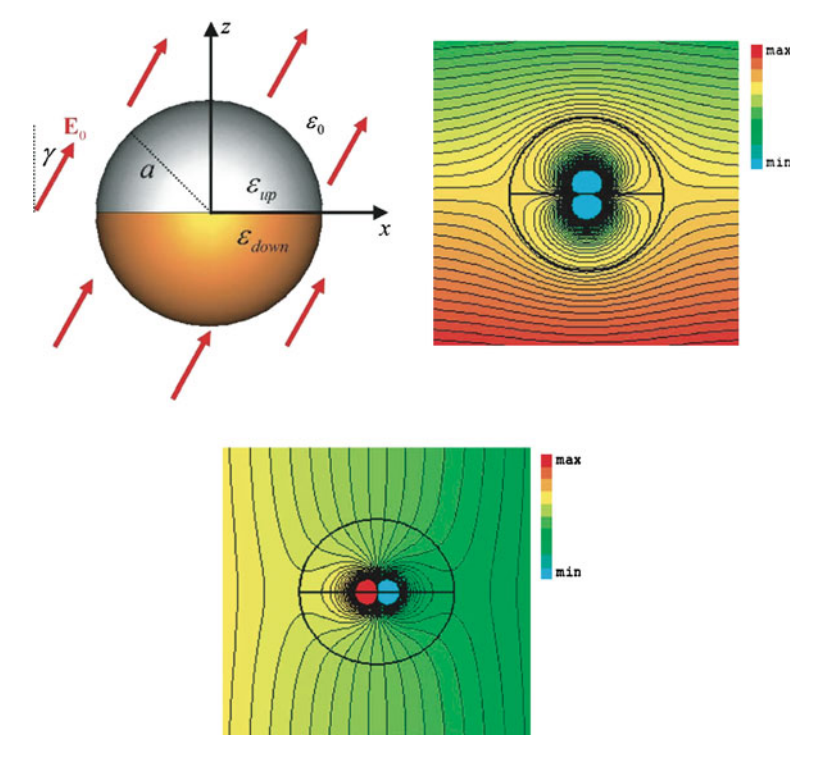


**Fig. 6.5** Left the sphere with hemispheres having two different permittivities, placed in an external electric field  $\mathbf{E}_0$ . Right the electric potential distribution when relative permittivities of the upper and lower hemispheres are 16 and -16, respectively, with  $\mathbf{E}_0$  pointing up. Below as for the previous case, but with  $\mathbf{E}_0$  pointing right (From [32])

# **6.5** Application of Plasmonic Resonances in Solar Energy Absorbers

There is currently a surge in interest in the development of renewable energy technologies. Among the most promising of these in terms of widespread availability and prospective impact is the use of incoming solar energy to generate both heat and electricity. We will show here how the control of plasmonic effects is leading to efficiency and utility gains for both photothermal and photovoltaic energy production.

The conversion of the incoming solar flux into heat is a mature technology, which is widely commercialized in both developed and developing nations. In general, there are two ways in which this conversion is carried out- using flat plate collectors to heat water for home use and using large dishes, or mirror clusters to concentrate the flux and to generate higher temperatures for industrial applications. However, evacuated tubular collectors [33] can provide solutions for both domestic heat delivery  $(50-80\,^{\circ}\text{C})$  and for the medium temperature industrial market  $(150-300\,^{\circ}\text{C})$ . They

can also perform better in conditions of diffuse illumination or low ambient temperatures than flat plate collectors.

The requirements to be satisfied by collectors capable of delivering heat in the medium temperature range are

- losses of energy from the collector by convection and conduction should be minimized:
- the collector should absorb incoming energy with high efficiency in the range of appreciable solar terrestrial flux (0.4–1.5 μm);
- the collector should lose as little heat as possible by radiation in the near infrared (beyond 1.5 μm);
- the collector should have a long lifetime (in excess of 20 years) at the operating temperature.
- the collector should be capable of large-area production at an economic cost-level.

These requirements can be satisfied by evacuated tubular collectors of the type shown in Fig. 6.6. Energy losses by convection and conduction are minimized by placing the solar-absorbing surface inside a vacuum tube, and placing the absorbing surface on a metal substrate which can deliver heat effectively by conduction to a heat transfer medium in good thermal conduct with the surface. (The heat transfer medium may be superheated steam, or a high-boiling-point liquid which flows in heat extraction pipes.) Lifetime and production issues can be solved with an appropriate choice of refractory materials and film deposition technologies.

The remaining issues of good solar absorptance and low infrared emissivity can be solved using an appropriate design for the solar-selective surface. This is required to have as low a reflectance as possible in the wavelength region up to 1.5 µm, and as high a reflectance as possible in the region beyond 1.5 µm. (By Kirchoff's law of radiation, a high reflectance guarantees a low emissivity.) An appropriate design for such a surface is to use graded cermet films: the cermet should have a dielectricrich structure on the vacuum side to ensure low reflectance of the incident radiation, and then the volume fraction of metallic inclusions should gradually increase to ensure wide-band absorption through a rich spectrum of plasmonic resonances, and low reflectance at the interface with the substrate metal [34, 35]. The performance reported by Zhang, Yin and Mills [35] for molybdenum-alumina cermet systems is an absorptance of 0.955 and an emittance of 0.032 at room temperature, with a modelled emittance at 350 °C of 0.08. The good combination of high absorptance and low emittance is achieved by a design which can deliver a sharp transition between low reflecting and high reflecting regions, as seen in Fig. 6.6. Such systems are certainly capable of delivering energy over a good lifetime for industrial applications (such as generating steam in a preheating capacity for power stations, and for sterilizing food in processing plants).

Turning now to photovoltaic cells, this emerging technology is confronting the challenge of substantially reducing the cost of modules. First-generation silicon PV cells have been developed to the stage where they offer good efficiency and acceptable lifetimes. To bring down cell cost, second-generation cells are being developed which use the expensive material of highly purified silicon in thin film rather than

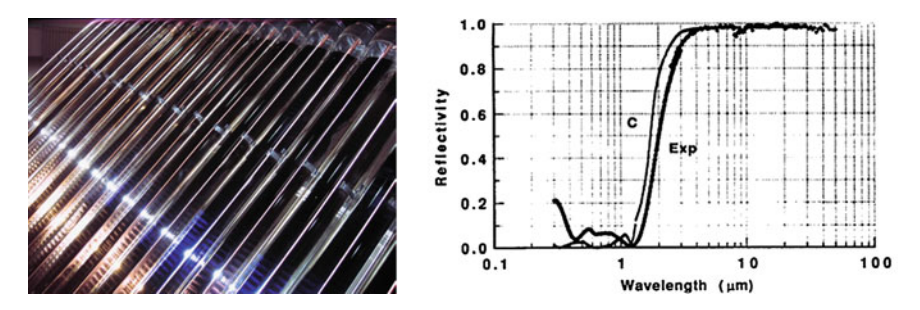


**Fig. 6.6** *Left* an evacuated tubular solar collector module. (From [33]) *Right* the calculated (C) and experimental (Exp) reflectance curves of a Cu-SiO<sub>2</sub> cermet (From [36])

wafer form. The challenge with the thin film cells is to deliver good absorption and photocurrent generation in the much smaller thickness geometry. There is rapidly growing interest in the exploitation of particle plasmonic effects as part of the answer to this challenge [37]. The basic idea is to use scattering of incoming waves by plasmonic particles to increase the optical path length within the cell, so as to compensate for the reduced thickness. Of course, the design has to be optimized, to ensure that the metallic particles do not overly absorb light, or scatter photo-induced holes and electrons, so preventing them from contributing to the current generated by the cell.

The tuning of the balance between scattering and absorption is governed by the scattering and absorption cross-sections. For small particles in the quasistatic limit, these are given by [38] (see also Eqs. (3.1) and (3.2) of Chap. 3)

$$C_{\text{abs}} = \frac{2\pi}{\lambda} \Im \alpha, \tag{6.35}$$

and

$$C_{\text{sca}} = \frac{1}{6\pi} \left(\frac{2\pi}{\lambda}\right)^4 |\alpha|^2,\tag{6.36}$$

where  $\alpha$  is the polarizability of the particles. For a small spherical particle of volume V and relative permittivity  $\epsilon$  in vacuum, it is given by the electrostatic expression (6.8)

$$\alpha = 3V\left(\frac{\epsilon - 1}{\epsilon + 2}\right). \tag{6.37}$$

The balance between scattering and absorption is quantified by the scattering efficiency  $Q_{\text{sca}} = C_{\text{sca}}/(C_{\text{sca}} + C_{\text{abs}})$ .

To increase the scattering efficiency, it is better to use larger rather than smaller particles. The scattering resonance peak occurs at a wavelength determined by the particle material and the matrix material in which it is embedded. Alloys can be used

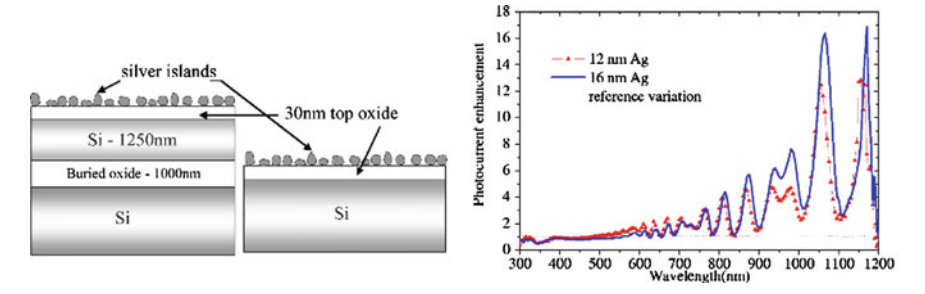


**Fig. 6.7** Left two silicon cell designs- one silicon-on-insulator with  $1.25 \,\mu\text{m}$  active Si and the other a wafer-based  $300 \,\mu\text{m}$  planar Si cell. Right photocurrent enhancement from the  $1.25 \,\mu\text{m}$  thick cell for two different mass thicknesses of silver particles, relative to the cell without silver particles (From [37])

(as in the Lycurgus cup) to shift the resonant wavelength, and the shape of the particle is another factor.

The system designs shown in Fig. 6.7 feature silver particles on a thin oxide layer, which serves as a waveguide to increase the photon propagation distance laterally. Ideally, the scattering by the particles should be into the range of angles which will couple to waveguide modes. The work of Pillai et al. [37] was aimed at enhancing absorption of light and photocurrent generation near the band edge of silicon. One can see how effective their design was in the right part of Fig. 6.7, where a 16-fold increase in photocurrent is demonstrated at the wavelength of 1.050 µm.

# 6.6 Coated Cylinders and Plasmonic Cloaking

We return to the discussion of Sect. 7.4, and in particular to the Rayleigh treatment of solid cylinders. Suppose the cylinders are now coated and are placed in a matrix with unit relative permittivity. We take the coated cylinder to be specified by radii  $r_c$  and  $r_s$  of its core and shell regions, respectively, and take the relative permittivities of these to be  $\epsilon_c$  and  $\epsilon_s$ . The analysis follows that of Sect. 7.3, except that potential expansions in cylindrical harmonics are needed for the matrix, the shell and the core regions. The electrostatic continuity conditions enable the cylindrical harmonic coefficients in the core and shell regions to be eliminated. The result of some protracted algebra [39] is that the multipole coefficients of the electrostatic potential in the external region are connected by

$$A_{l} = \frac{r_{c}^{2l}(\epsilon_{s} - \epsilon_{c})(1 - \epsilon_{s}) + r_{s}^{2l}(\epsilon_{s} + \epsilon_{c})(1 + \epsilon_{s})}{r_{c}^{2l}(\epsilon_{s} - \epsilon_{c})(1 + \epsilon_{s}) + r_{s}^{2l}(\epsilon_{s} + \epsilon_{c})(1 - \epsilon_{s})} \frac{B_{l}}{r_{s}^{2l}}.$$

$$(6.38)$$

We examine what the formula (6.38) gives when the plasmonic resonance condition is satisfied on both boundaries of the shell. Firstly, if a shell-core resonance

occurs,  $\epsilon_s = -\epsilon_c$ , and we find

$$A_l = \frac{(1+\epsilon_c)}{(1-\epsilon_c)} \frac{B_l}{r_s^{2l}}.$$
(6.39)

This is exactly the relationship (6.27), but for a solid cylinder with radius  $r_s$  and relative permittivity  $\epsilon_c$ : the shell-core resonance magnifies the core, making the cylinder appear as if it had radius  $r_s$ . Secondly, if a shell-matrix resonance occurs,  $\epsilon_s = -1$ , and (6.38) gives

$$A_{l} = \frac{(1 + \epsilon_{c})}{(1 - \epsilon_{c})} \frac{B_{l}}{(r_{s}^{2}/r_{c})^{2l}}.$$
(6.40)

The shell-matrix resonance makes the coated cylinder appear as if it were solid, with relative permittivity  $\epsilon_c$  and radius  $r_s^2/r_c$ .

Although it was not realized to be the case by the authors of [39], the curious phenomena they termed partial resonance [40] implicit in the resonant equivalences between coated cylinders and solid cylinders embody the seeds of two of the most important discoveries of recent years in photonics: the perfect imaging by a flat slab of negative index material of Pendry [41], and cloaking of objects from electromagnetic waves [42, 43].

If it is desired to render an object undetectable by electromagnetic probes, one strategy is to devise a shield to be placed round the object, so that the electromagnetic waves pass round the shield like water sliding round a rock, and then reunite leaving no trace of a disturbance, much as the stream quickly hides any traces of its encounter with the rock. In order to achieve this, techniques from general relativity are applied [42, 43] to design shields which incorporate spatially-varying, anisotropic materials, designed to guide light round a central cavity.

A second strategy is based on plasmonic interactions between light and the particle to be detected, either using designs of the particle to lower its detectability or placing a coated cylinder nearby which reacts to the probe beam and cancels its effect on polarizable particles within a cloaking zone.

Alu and Engheta [44] consider small spherical particles with a plasmonic or metamaterial coating, and analyse the required properties of the coating to minimize its scattering cross-section, using the Mie theory to describe the interaction [16]. The full formula for the scattering cross-section involves a sum over TE and TM amplitudes  $c_n^{\rm TE}$  and  $c_n^{\rm TM}$  of spherical harmonics of order n:

$$Q_s = \frac{2\pi}{k_0^2} \sum_{n=1}^{\infty} (2n+1)(|c_n^{\text{TE}}|^2 + |c_n^{\text{TM}}|^2).$$
 (6.41)

Alu and Engheta show that this cross-section may be minimized for a ratio of shell to core radii  $\gamma$  lying close to critical lines in the complex plane, see Fig. 6.8. These critical lines correspond to those identified in [39] for the case of coated cylinders,

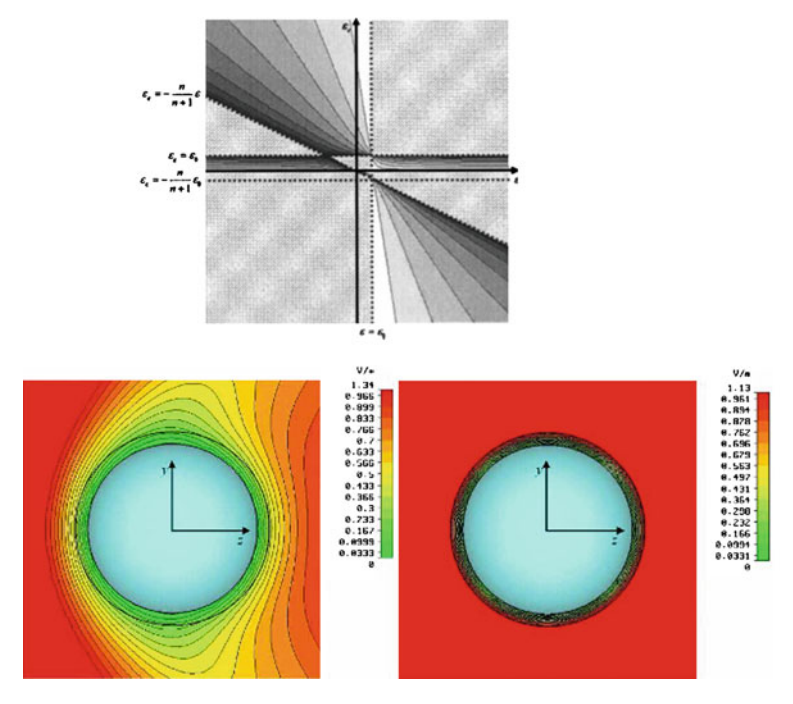
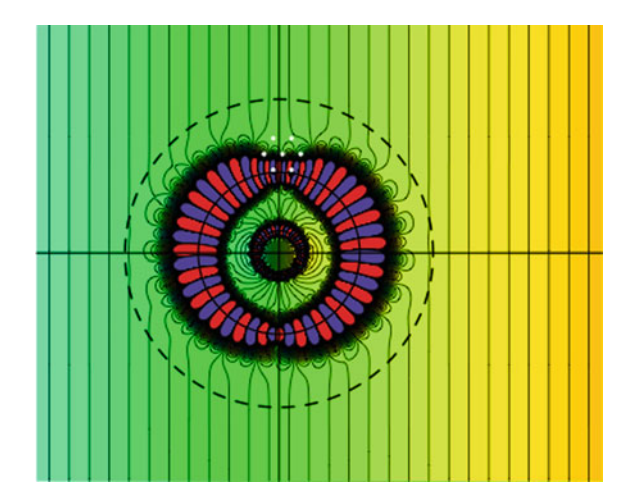


**Fig. 6.8** *Above* the critical lines in the shell/core permittivity plane for is scattering by a coated sphere. *Darker regions* give reduced scattering. *Below* the amplitude of the electric field distribution at *left* for an uncoated sphere, and at *right* for a sphere with a coating which almost entirely eliminates scattering. The core has a radius of 0.2 wavelengths, while the shell material has relative permittivity of 0.1 and relative permeability of 5.1 (From [44] and [45])

with the difference that the order n of the spherical multipoles occurs in the threedimensional shell-core resonance condition  $\epsilon_s = -n\epsilon_c/(n+1)$ . Alu and Engheta [44] give the interpretation that the reduced scattering occurs because the polarization fields in the shell and core act in opposed directions. For an experimental verification of this type of cloaking, see [46].

At the beginning of this section, we mentioned that quasistatic resonance could also be used to achieve cloaking. This has been analysed in detail in [47] and illustrated with figures and animations in [48]. The situation studied in the latter paper consists of a set of polarizable dipoles placed in a uniform static field. They approach a coated cylinder, whose core permittivity matches that of the region outside the shell, and whose shell has a relative permittivity close to -1. This means that both shell-core and shell-matrix plasmonic resonances can occur, with the former tending to occur first. If the radii of shell and core are, respectively,  $r_s$  and  $r_c$ , then the coated cylinder creates a cloaking region of radius  $r_{\#} = \sqrt{r_s^3/r_c}$  around itself. Once the polarizable dipoles approach this region, the shell-core resonance begins, and acts in such a way as to counteract the applied field near the polarizable dipoles. As the dipoles enter the radius  $r_{\#}$ , the shell-matrix resonance also strengthens, and the dipole moment of the polarizable dipoles rapidly falls to zero i.e., they become

Fig. 6.9 A cluster of seven polarizable dipoles is deep in the cloaking region, bounded by the *dashed circle*, created by a coated cylinder with  $\epsilon_s = -1 + 10^{-12}i$ . There is a horizontally aligned uniform applied field, and *equipotential lines* of the total field are shown (From [48])



cloaked. As the dipoles move in the cloaked region, the resonant field patterns on the matrix-shell and shell-core boundaries move to keep themselves aligned with respect to the cluster of dipoles they are cloaking. As the dipoles leave the cloaking region, the resonances weaken and the cloaking effect disappears (Fig. 6.9).

Note that in this style of cloaking, both the cloaking body and the cloaked object are hidden. This is a desirable feature in cloaking designs, but is not always achieved.

# 6.7 The Spaser: Cutting our Losses

As we have seen, plasmonic structures involving metals can deliver high electromagnetic field concentrations, resonant effects which can be used to construct sensors and cloak objects, compact waveguides, better absorbers for solar energy and many other useful effects. However, a constraining factor in many potential applications comes from the high losses which can accompany the concentrated fields. These losses could be overcome if a "spaser device" could be developed, which could be used to create high intensity surface plasmons, or pump them to overcome losses. The spaser could transform plasmonics, in the same way the laser transformed optics in the 1960s and thereafter. It would also be a crucial development in the field of metamaterials, enabling low loss devices for the visible and near-infrared spectral regions to be constructed incorporating metals.

Progress towards the development of a spaser commenced with a theoretical paper by Bergman and Stockman [49]. These authors studied the eigenmodes of structures consisting of V-shapes in silver, with embedded emitters such as quantum dots. The emitters could add energy into the plasmon eigenmodes, whose strength would grow with the field concentration effect produced by the tapering of the V-shape. Stockman [50] further analysed the spaser, pointing out its potential as an ultrafast nano-amplifier, with gain in excess of 50 and switching time below 100 fs.

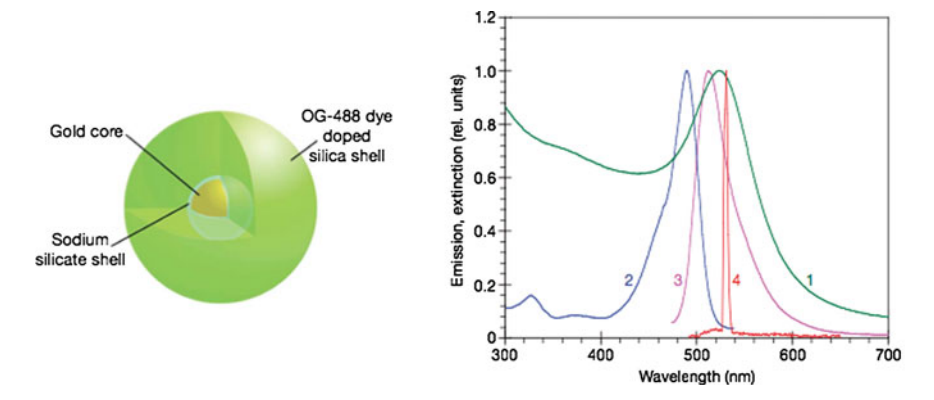


**Fig. 6.10** *Left* a nanoparticle having a gold core and a silicate shell, impregnated with the dye Oregon Green, which provides for gain. *Right* Normalized extinction (1), excitation (2), spontaneous emission (3) and stimulated emission (4) of the nanoparticles (From [51])

Two recent papers have made the spaser concept into a reality. Noginov et al. [51] demonstrated spaser action in a system containing gold nanoparticles with a silicate shell, with the latter containing a dye facilitating pumping of the dipole plasmonic mode of the nanoparticles (see Fig. 6.10). The pumping was at a wavelength of 488 nm, with the emission at 521 nm. Spaser action is evident from the spectral narrowing of the stimulated emission spectrum compared with the spontaneous emission spectrum, and an abrupt transition from dominance by the latter to the former at the pumping threshold for the spaser.

The second experimental spaser design was developed by Oulton et al. [52]. This used a CdS semiconductor nanowire separated from a silver substrate by a thin  $MgF_2$  spacer layer (see Fig. 6.11). The stimulated emission from the CdS is channelled and tightly confined in a 5 nm waveguide lying between the nanowire and the substrate. The mode is one hundred times smaller than the diffraction limit.

Progress in this exciting field is rapid. The initial devices just described succeeded in demonstrating gain, i.e. reduction of plasmon losses by metallic absorption, but not the entire elimination of loss. At the international conference Metamaterials 2010 held in Karlsruhe, Germany, Vladimir Shalaev reported that his group at Purdue University had succeeded in reversing the sign of plasmonic loss (i.e. inducing gain which exceeded metallic absorption loss) in a wavelength band from 720 to 740 nm. The structure consisted of a two-layer fishnet metamaterial in silver, capable of exhibiting a negative refractive index, but having substantial plasmonic absorption. This was surrounded on each side by layers of epoxy impregnated with a laser dye, which could be pumped. The optical design generated enhanced local fields in the gain layers, and this was reported to be a key feature enabling the pumping to be sufficiently effective to overcome loss.

While devices using laser dyes are useful in proving the principle of plasmonic loss compensation, the dyes generally lose efficiency quickly due to photo-bleaching.

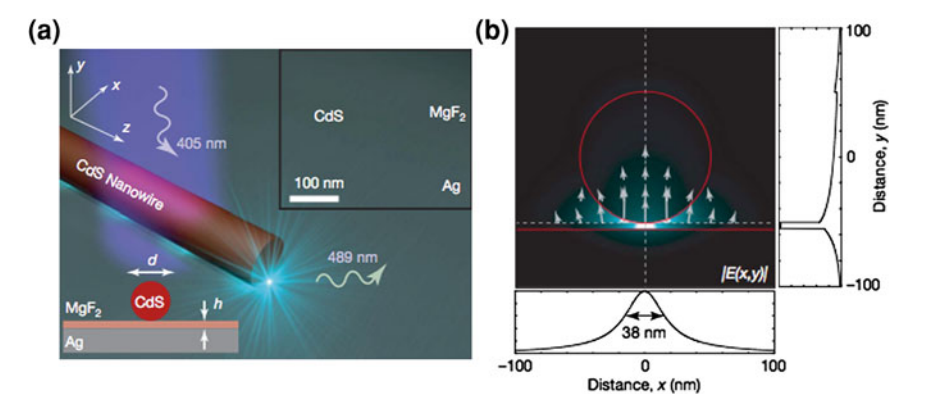


**Fig. 6.11** Left a CdS nanowire is pumped at 405 nm. Its emission is coupled into a 5 nm MgF<sub>2</sub> waveguide between the particle and a silver substrate. Right the stimulated electric field intensity |E(x, y)| at a wavelength of 489 nm (From [52])

This means that a gain element not suffering from photo-bleaching will have to be developed for applications requiring long lifetimes. It seems that this will most likely be achieved using quantum dot emitters, which are under development for this and other applications in photonics.

## 6.8 Envoi

We have seen that the field of plasmonics has a long history, dating back to the time when that which was Caesar's may have been rendered unto him in a cup containing gold nanoparticles. The field continued to be used through the age of medieval church building, with the magnificent stained glass windows owing their colour to skilful use of embedded metal particles. At the dawn of the atomic era, one of the first models of atoms was the idea of Faraday that they could be viewed as tiny polarizable metallic particles, and their properties probed with electromagnetic waves. The field has continued to grow through the laser and microfabrication eras. Today, we can combine nanofabrication tools with computer simulations and electromagnetic analysis, to design exciting new devices. At the beginning of the spaser era, plasmonics has a golden future!

#### References

- I. Freestone, N. Meeks, M. Sax, C. Higgitt, The Lycurgus Cup—a Roman nanotechnology. http://www.goldbulletin.org/assets/file/goldbulletin/downloads/Lycurgus\_4\_40.pdf
- N. Stefanou, V. Yannopapas, A. Modinos, MULTEM2: a new version of a program for transmission and band-structure calculations of photonic crystals. Comput. Phys. Commun. 132, 189196 (2000)

- 3. G. Mie, Beitrge zur Optik trber Medien, speziell kolloidaler Metallsungen, Leipzig. Ann. Phys. **330**, 37745 (1908)
- 4. J. Korringa, On the calculation of the energy of a bloch wave in a metal. Physica 13, 392 (1947)
- W. Kohn, N. Rostoker, Solution of the Schrodinger equation in periodic lattices with application to metallic lithium. Phys. Rev. 94, 1111 (1954)
- 6. G.W. Milton, *The Theory of Composites* (Cambridge University Press, Cambridge, 2002)
- W. Lamb, D.M. Wood, N.W. Ashcroft, Long-wavelength Electromagnetic Propagation in Heterogeneous Media. Phys. Rev. B 21, 2248–2266 (1980)
- 8. R.C. McPhedran, L.C. Botten, M.S. Craig, M. Neviere, D. Maystre, Lossy lamellar gratings in the quasistatic limit. Opt. Acta 29, 289–312 (1982)
- R.C. McPhedran, C.G. Poulton, N.A. Nicorovici, A.B. Movchan, Low frequency corrections to the static effective dielectric constant of a two-dimensional composite material. Proc. R. Soc. Lond. A 415, 185–1896 (1996)
- R. Landauer, *Electrical Conductivity in Inhomogeneous Media*, ed. by J.C. Garland,
   D.B. Tanner. Electrical Transport and Optical Properties of Inhomogeneous Media (American Institute of Physics Conference Proceedings Series, New York, 1978), pp. 2–43
- P.B. Johnson, R.W. Christy, Optical constants of the noble metals. Phys. Rev. B 6, 4370–4379 (1972)
- 12. L. Rayleigh, On the influence of obstacles arranged in rectangular order upon the properties of a medium. Phil. Mag. **34**, 481–502 (1892)
- W.T. Doyle, The Clausius-Mossotti problem for cubic arrays of spheres. J. Appl. Phys. 49, 795–797 (1978)
- R.C. McPhedran, D.R. McKenzie, The conductivity of lattices of spheres. I. The simple cubic lattice, Proc. R. Soc. A 359, 45–63 (1978)
- D.R. McKenzie, R.C. McPhedan, G.H. Derrick, The conductivity of lattices of spheres. II. The body-centred and face-centred cubic lattices, Proc. R. Soc. A 362, 211–232(1978)
- 16. M. Born, E. Wolf, *Principles of Optics* (Pergamon Press, Oxford, 1980)
- B.U. Felderhof, R.B. Jones, Addition theorems for spherical wave solutions of the vector Helmholtz equation. J. Math. Phys. 28, 836–839 (1987)
- D.J. Bergman, The dielectric constant of a simple cubic lattice of identical spheres. J. Phys. C: Solid State Phys. 12, 4947–4960 (1979)
- D.A.G. Bruggeman, Berechnung verschiedener physikalischer Konstanten von heterogen Substanzen. I. Dielektrizitätskontanten und Leitfähigkeiten der Mischkörper aus isotropen Substanzen. Ann. Phys. 24, 636–679 (1935)
- J.B. Keller, A theorem on the conductivity of a composite medium. J. Math. Phys. 5, 548–549 (1964)
- A.M. Dykhne, Conductivity of a two-dimensional two-phase system. Sov. Phys. JETP 32, 63–65 (1971)
- W.T. Perrins, D.R. McKenzie, R.C. McPhedran, Transport properties of regular arrays of cylinders. Proc. Roy. S. Lond. A 369, 207–225 (1979)
- D.J. Bergman, Exactly solvable microscopic geometries and rigorous bounds for the complex dielectric constant of a two-component composite material. Phys. Rev. Lett. 44, 1285–1287 (1980)
- G.W. Milton, Bounds on the complex dielectric constant of a composite material. Appl. Phys. Lett. 37, 300–302 (1980)
- R.C. McPhedran, D.R. McKenzie, G.W. Milton, Extraction of structural information from measured transport properties of composites. Appl. Phys. A 29, 19–27 (1982)
- E. Cherkaeva, K. Golden, Inverse bounds for microstructural parameters of composite media derived from complex permittivity measurements. Waves Random Media 8, 437

  –450 (1998)
- 27. J.B. Keller, Conductivity of a medium containing a dense array of perfectly conducting spheres or cylinders or nonconducting cylinders. J. Appl. Phys. **34**, 991–993 (1963)
- J.D. Bernal, Radial distribution of random close packing of equal spheres. Proc. R. Soc. A 280, 299–322 (1962)

 G.K. Batchelor, R.W. O'Brien, Thermal or electrical conduction through a granular material. Proc. R. Soc. Lond. 355, 313–333 (1977)

- I.J. Romero, F.C. Garcia d'Abajo, Anisotropy and particle-size effects in nanostructured plasmonic metmamaterials. Opt. Express 17, 22012–22022 (2009)
- R.C. McPhedran, L. Poladian, G.W. Milton, Asymptotic studies of closely spaced, highly conducting cylinders. Proc. R. Soc. A 415, 185–196 (1988)
- 32. A. Alu and N. Engheta, Optical nanoswitch: an engineered plasmonic nanoparticle with extreme parameters and giant anisotropy, N. J. Phys. **11**(0130226), 14 (2009)
- 33. X. Jiang, Metal glass vacuum tube solar collectors are approaching lower-medium temperature heat application. Opt. Express 18, A112–A117 (2010)
- 34. D.R. McKenzie, Gold, silver, chromium, and copper cermet selective surfaces for evacuated solar collectors. Appl. Phys. Lett. **34**, 25–28 (1979)
- Q.-C. Zhang, Y. Yin, D.R. Mills, High efficiency Mo-Al<sub>2</sub>O<sub>3</sub> cermet selective surfaces for high-temperature applications. Sol. Energy Mater. Sol. Cells 40, 43–53 (1996)
- Q.-C. Zhang, D.R. Mills, Very low-emittance solar selective surfaces using new film structures,
   J. Appl. Phys. 72, 3013–3021 (1992)
- 37. S. Pillai, K.R. Catchpole, T. Trupke, M.A. Green, Surface plasmon enhanced silicon solar cells. J. Appl. Phys. **101**(093105), 1–8 (2007)
- 38. C.F. Bohren, D.R. Huffman, Absorption and Scattering of Light by Small Particles (Wiley-Interscience, New York, 1983)
- N.A. Nicorovici, R.C. McPhedran, G.W. Milton, Transport properties of a three-phase composite material: the square array of coated cylinders. Proc. R. Soc. Lond. A 442, 599–620 (1993)
- N.A. Nicorovici, R.C. McPhedran, G.W. Milton, Optical and dielectric properties of partially resonant composites. Phys. Rev. B 49, 8479–8482 (1994)
- 41. J.B. Pendry, negative refraction makes a perfect lens. Phys. Rev. Lett. 85, 3966–3969 (2000)
- J.B. Pendry, D. Schurig, D.R. Smith, Controlling electromagnetic fields. Science 312, 1780–1782 (2006)
- 43. U. Leonhardt, Optical conformal mapping. Science **312**, 1777–1780 (2006)
- 44. A. Alu, N. Engheta, Achieving transparency with plasmonic and metamaterial coatings. Phys. Rev. E 72, 016623 (2005)
- 45. A. Alu, N. Engheta, Plasmonic materials in transparency and cloaking problems: mechanism, robustness, and physical insight. Opt. Express 15, 3318–3332 (2007)
- 46. B. Edwards, A. Alu, M.G. Silveirinha, N. Engheta, Experimental verification of plasmonic cloaking at microwave frequencies with metamaterials. Phys. Rev. Lett. 103, 153901, 4 (2009)
- 47. G.W. Milton, N.A.P. Nicorovici, On the cloaking effects associated with anomalous localized resonance. Proc. R. Soc. Lond. A **462**, 3027–3059 (2006)
- 48. N.-A.P. Nicorovici, G.W. Milton, R.C. McPhedran, L.C. Botten, Quasistatic cloaking of two-dimensional polarizable discrete systems by anomalous resonance. Opt. Express, 15, 6314–6323 (2007)
- D.J. Bergman, M.I. Stockman, Surface plasmon amplification by stimulated emission of radiation: quantum generation of coherent surface plasmons in nanosystems, Phys. Rev. Lett. 90, 027402, 4 (2003)
- M.I. Stockman, The spaser as a nanoscale quantum generator and ultrafast amplifier. J. Opt. 12, 024004, 13 (2010)
- M.A. Noginov, G. Zhu, A.M. Belgrave, R. Bakker, V.M. Shalaev, E.E. Narimanov, S. Stout, E. Herz, T. Suteewong, U. Wiesner, Demonstration of a spaser-based nanolaser. Nature 460, 1110–1112 (2009)
- R.F. Oulton, V.J. Sorger, T. Zentgraf, R.-M. Ma, C. Gladden, L. Dai, G. Bartal, X. Zhang, Plasmon lasers at deep sub-wavelength scale. Nature 461, 629–632 (2009)

# Chapter 7 Plasmon Nano-Optics: Designing Novel Nano-Tools for Biology and Medicine

Romain Quidant

**Abstract** Light plays a growing role in health science especially with the recent developments of new optical techniques that enable imaging biological processes down to the molecular scale and monitor dynamically physiological mechanisms in patients. In parallel, recent groundbreaking advances in nanotechnologies have opened new perspectives in medicine, for instance in creating new therapies or designing novel compact and highly sensitive diagnostic platforms. In this chapter, the aim is to discuss recent research that sits at the convergence of photonics, nanotechnology, and health. This research is based on the extraordinary optical properties of metallic nanoparticles (MNP) supporting Localized Surface Plasmon (LSP) (see Chap. 4). We discuss how plasmonic MNP can be used as nano-sources of either light or heat for biological and medical applications.

# 7.1 Optical and Thermal Properties of Plasmonic Metallic Nanoparticles

It was shown in Chap. 5 (Sect. 5.1.2) that LSP resonances in MNP are associated with resonances of both the absorption and scattering cross-sections. In practice, coupling light to the LSP resonance of a MNP leads to two combined effects. On the one hand, the absorbed light concentrates at the particle surface and its scattering to the far field is enhanced. On the other hand, the remaining part of the energy is dissipated into heat, creating an increase of the metal temperature. While optical and thermal properties of MNP are intrinsically correlated, the aim of this section is to

R. Quidant (⋈)

ICFO-Institut de Ciencies Fotoniques, Mediterranean Technology Park, 08860 Castelldefels, Barcelona, Spain

e-mail: romain.quidant@icfo.es

ICREA-Institucio Catalana de Recerca i Estudis Avançats (ICREA), 08015 Barcelona, Spain

202 R. Quidant

show that MNP can be engineered to act specifically as efficient point-like sources of either light or heat.

## 7.1.1 Nanoscale Light Concentration in MNP

While confinement and enhancement of light field is intrinsic to LSP modes in MNP, it strongly depends on the particle geometry and illumination parameters. For instance, geometries with sharp corners such as triangular [1], rice-like [2], or star-like [3] can lead to a much stronger concentration of the electromagnetic field at the apex of their tips as compared to spherical particles. Nevertheless, a more accurate control of light confinement in plasmonic nanostructures can be achieved in ensembles of electromagnetically coupled particles. In particular, a strong field concentration is achieved in the so-called dimer geometry (also known as optical gap antenna) consisting of two adjacent MNP separated by a nanometer-sized dielectric gap. Upon illumination linearly polarized along the particle alignment, a strong gradient of surface charges is created across the gap, leading to a concentration of light in between the two particles [4–6]. For illustration, we show in Fig. 7.1 the distribution of the electric field intensity in the equatorial plane of a dimer formed by two gold cylinders lying upon a glass substrate and separated by a 10 nm air gap. A direct comparison with an isolated cylinder (inset of Fig. 7.1) enables one to appreciate the dramatic field intensity enhancement within the gap region. Both the magnitude and confinement of the so-called hot spot increase as the gap becomes smaller and the near-field coupling becomes stronger [7, 8].

Independently of the gap size, the geometry of the particles has a considerable influence on the optical properties of the antenna, both on its spectroscopy and on the distribution of the local field. For instance, using triangular particles or rods instead of cylinders tends to broaden the resonance bandwidth and increase the ratio between the field within the gap and at the outer edges [9].

The dimer geometry has been used in a wide range of experiments to enhance the interaction of light with tiny amounts of matter, down to the single molecule level [10, 11]. Further on in this chapter, we will show how its properties can be exploited within the context of biosciences for molecular sensing and optical trapping.

#### 7.1.2 Nanoscale Heat Generation in MNP

Generally speaking, the ability of a bulk material to heat up upon laser illumination is mostly dictated by its structural properties and in particular by the imaginary part of its dielectric function at the illumination wavelength. Conversely, heating in plasmonic metallic nanoparticles is a process that, in addition, directly depends on their optical response as reflected in the expression of the heat source density q(r):

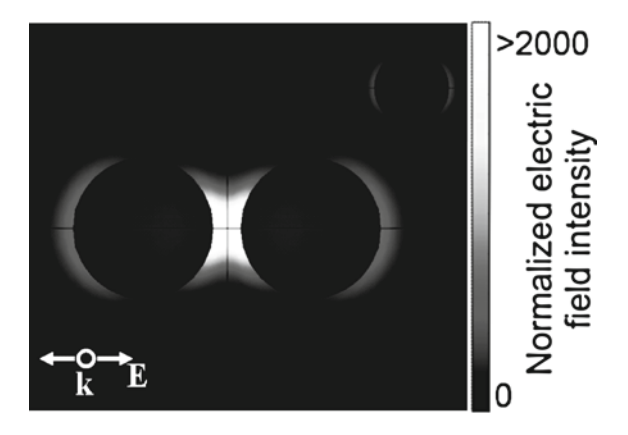


**Fig. 7.1** Plasmonic dimer formed by two gold cylinders (50 nm diameter and 20 nm height) separated by a 10-nm air gap. Normalized electric field intensity distribution computed (in the equatorial plane of the particles) at the plasmon resonance (659 nm) upon a plane wave illumination (normal incidence) linearly polarized across the particle alignment. The normalization is done with respect to the incident intensity. For reference, the near-field distribution for a single gold disk at resonance is shown in the inset

$$q(\mathbf{r}) = n^2 \omega / 2\Im(\epsilon(\omega)) |\mathbf{E}(\mathbf{r})|^2, \tag{7.1}$$

where n and  $\epsilon(\omega)$  stand for the refractive index of the surrounding medium and the dielectric function of the metal at the light frequency  $\omega$ , respectively. One can clearly see that the quantity of generated heat is governed by the electric field intensity  $\Im(\epsilon)|E(r)|^2$  within the metal. Consequently, the drastic influence of particle geometry on the plasmon mode distribution offers some degree of control for designing efficient nano heat-sources, remotely controllable by laser illumination.

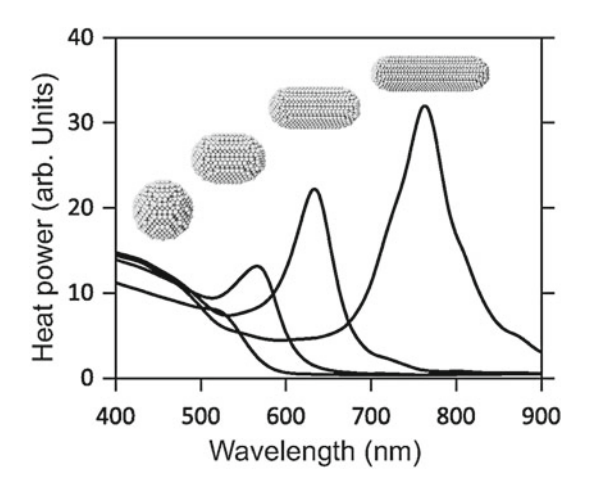
# Influence of the MNP Morphology

Recently, the Green Dyadic Method (GDM) [12, 13] has been used to quantify the influence of the geometry of a gold MNP on its heating efficiency. The GDM makes it possible to map the spatial distribution of the heat power density inside the nanoparticles, providing further insight into the influence of the particle shape and the illumination conditions on the origin of heat. Figure 7.2 displays calculations of heating power (q(r)) integrated over the particle volume) spectra for different geometries of gold nanoparticles surrounded by water and illuminated by a plane wave. We fix the intensity of the incoming light at  $1 \text{ mW} \mu \text{m}^{-2} = 10^5 \text{ W} \text{ cm}^{-2}$  according to the typical value found in the literature for biological applications.

To illustrate the influence of the particle geometry, the heat generation of a sphere progressively elongating into a rod-like structure at a constant volume  $(4\pi r_{\rm eff}/3$ , where  $r_{\rm eff}=25\,{\rm nm})$  is shown in Sect. 7.2. The successive nanorods

204 R. Quidant

**Fig. 7.2** Calculated spectra of the heat generated in four different colloidal gold nanoparticles of the same volume

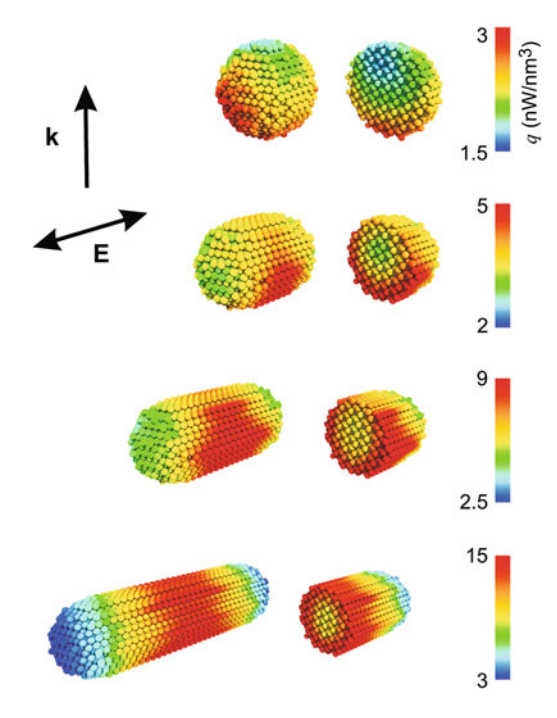


aspect ratios are 1:1 (sphere), 1.4:1, 2:1, and 3:1. Two major features arise from the calculations. First, the LSP resonance markedly depends on the nanoparticle shape. A redshift is indeed expected for nanorods compared with spheres. Beyond the resonance redshift, a substantial increase in the heating efficiency, by a factor of 5 from the sphere to the 3:1 nanorod, is observed.

The GDM can be efficiently employed to understand this feature. Figure 7.3 represents the distribution of the heat power density q(r) around and across each of the geometries. Interestingly, for a sphere excited at the LSP resonance, the heat generation arises mainly from the outer part of the particles facing the incoming light. Consequently, the major part of the nanoparticle sees a weak electric field intensity and thus does not contribute to heating. However, for elongated nanorods, the field can further penetrate the inner part of the particle thus making the whole metal volume more efficiently involved in the heating process. It should be underlined that the heat generation mainly arises from the central part of the nanorods because the extremities undergo charge accumulation that leads to a weaker electric field inside the structure.

Depending on the foreseen application, efficient nano heat-sources can be fabricated from the simulated design by using either colloid synthesis (bottom-up) or e-beam lithography (top-down). While both approaches offer an accurate control over the size and geometry, colloid synthesis enables obtaining nanoparticles in solution featuring sharp crystalline edges, whereas e-beam lithography is well suited to fabricate arranged ensembles of particles or complex architectures lying onto a substrate. Beyond the fabrication of plasmonic heat nano-sources, a suitable thermal microscopy technique is required to test their photothermal response.

**Fig. 7.3** 3D mapping of the heat power density computed for the four nanoparticles of Fig. 7.2 at their respective plasmon resonance. The *k* and *E* vectors give the illumination conditions



#### **Temperature Mapping of Plasmonic Heat Nano-Sources**

Along with the need of understanding thermal processes at the micro-and nanoscale, several techniques aiming at high-resolution temperature mapping have been proposed. Scanning Thermal Microscopy (SThM) uses a composite sharp tip to directly probe the temperature of the sample surface [14]. Although it allows a spatial resolution higher than 100 nm, this technique is only suited for surface science investigations and is known to remain slow and invasive. More recently, a collection of optical-based temperature probing techniques have been proposed based on the temperature dependence of either Raman spectra [15, 16], fluorescence intensity/spectra/time correlation [17–19] or infrared spectra. However, none of these techniques combines reliability, fast readout rate, and high-resolution making them inadequate for temperature imaging in nanotechnology.

To address this need, a novel technique has recently been developed to locally probe the stationary temperature  $T_a$  of the medium surrounding nano heat-sources including those formed by plasmonic nanostructures [20]. It is based on the measurement of the Fluorescence Polarization Anisotropy (FPA) of free fluorophores in solution located at the vicinity of the plasmonic structures. A local temperature increase makes the nearby fluorescent molecules rotate faster during their fluorescence lifetime, reducing the degree of polarization of the emitted fluorescence [21]. In other words, due to Brownian rotational dynamics, molecules tend to lose the

206 R. Quidant

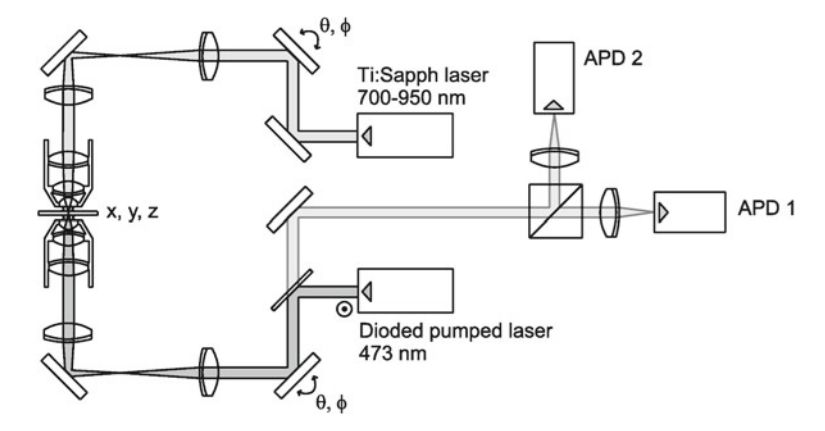


**Fig. 7.4** Description of the FPA-based thermal imaging setup. The dual illumination enables to both excite the fluorescence of the fluorophores (*blue laser*) and heat up the plasmonic nanostructure (NIR laser). The FPA is acquired by simultaneously measuring the fluorescence intensity along both in-plane polarization directions

memory of the initial polarization during their fluorescence lifetime. Once the calibration giving the relation between FPA and temperature is known, the temperature map can be extracted in real time from the measurement of FPA.

Figure 7.4 shows the thermal microscope setup used for measuring the photothermal properties of plasmonic heat nano-sources. It includes two illumination paths: a blue laser beam (473 nm) to excite the fluorescent molecules and an infrared (700–950 nm) laser beam to heat up the plasmonic nanostructures. Using two fast steering mirrors, both laser beams can be individually positioned and raster scanned. The sample is mounted on a piezo-stage that can be raster scanned as well. All these degrees of freedom allow one to assess different physical quantities by scanning either the blue beam, the infrared beam or the sample.

In this experiment, the plasmonic nanostructures lie upon a glass substrate and are embedded in a 30  $\mu$ m thick layer of a glycerol–water mixture containing fluorescein molecules ( $c=1.4\times10^{-4}$  M). A glass coverslip is placed on top of the solution layer to avoid water exchange with the surrounding air, which could affect the glycerol–water ratio and hence the fluid viscosity. The viscosity of glycerol decreases by more than one order of magnitude from 20 to 50 °C, which makes FPA measurements in glycerol highly temperature sensitive. Fluorescein is a xanthene-type chromophore, characterized by a high photostability and a fluorescence quantum efficiency close to 100 %. Fluorescein in pure glycerol exhibits a rotational correlation time  $\tau_R$  of around 150 ns at 20 °C, while its fluorescence lifetime  $\tau_F$  is about 4 ns. Consequently, a (4:1) glycerol–water mixture is used to reduce the viscosity from 1400 to 60 mPas and the rotational correlation time to  $\tau_R=6$  ns. This results in a much stronger variation of the polarization anisotropy between 20 and 50 °C, our window of interest.

To obtain the steady-state temperature map  $T_a(r)$ , the metal structure of interest is illuminated by an extended (unfocused) IR light through the top objective, the

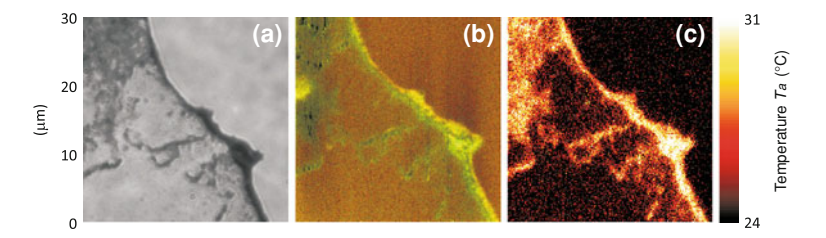


Fig. 7.5 Temperature mapping near dispersed gold nanorods: a Optical image  $(30 \times 30 \ \mu m)$  of dispersed and agglomerated nanorods (NRs). b Fluorescence polarization anisotropy of the fluorescein molecules surrounding the gold nanorods and sensing the temperature variations. c Temperature map calculated from image (b)

sample stage is fixed, and the bottom blue beam is raster scanned throughout the sample. Figure 7.5a displays a CCD picture of the edge of a drop of a solution of gold nanorods  $(50 \times 12 \text{ nm})$  individually resonant at around 765 nm after evaporation. For the FPA measurements, we chose an area showing large variations of the gold NR concentration in a single image, from agglomerated (dark region) to more dispersed (bottom-left region). The upper-right part of the picture corresponds to the region outside of the drop. In Fig. 7.5b, both fluorescence polarization maps are overlapped using a color convention in which green and red colors correspond to parallel and orthogonal fluorescence polarizations, respectively. The associated temperature map is displayed in Fig. 7.5c. No temperature variation is observed outside the drop edge (upper right part) as expected since this region contains no NR. As expected, the temperature increase is higher where the NRs are agglomerated. A deeper analysis of the data shows a spatial resolution of about 250 nm and a typical temperature accuracy of 0.1 °C. In a biological environment, the viscosity is likely to be much lower than the glycerol-water mixture preventing the use of fluorescein because of the too fast molecular Brownian dynamics. However, it remains possible to match the fluorescence lifetime and the rotational correlation time in aqueous medium by using larger fluorophores a few nanometers in size such as fluorescent proteins. This should enable us to easily apply this thermal microscopy to a biological medium as well.

Beyond measuring the steady-state temperature, one can extend the technique to assess the heat source density q(r) inside the structures of interest [22]. In that case, both the blue beam and the IR beams are focused and spatially overlapped while the stage is scanned. In such a configuration, local heating and FPA probing are performed simultaneously at each scanned location. Figure 7.6 displays the data from the two operational modes on a gold nanowire (2  $\mu$ m long, 200 nm wide, and 30 nm high) fabricated by e-beam lithography on a glass substrate. Figure 7.6a shows the experimental measurement of the steady-state temperature distribution  $T_a(r)$  around the gold structure, while Fig. 7.6b, c displays the associated distribution of the heat source density q(r) for both parallel and perpendicular polarizations. These results reveal drastically different behaviors between heat generation (thermal hot spots) and light concentration (optical hot spots) in plasmonic nanostructures:

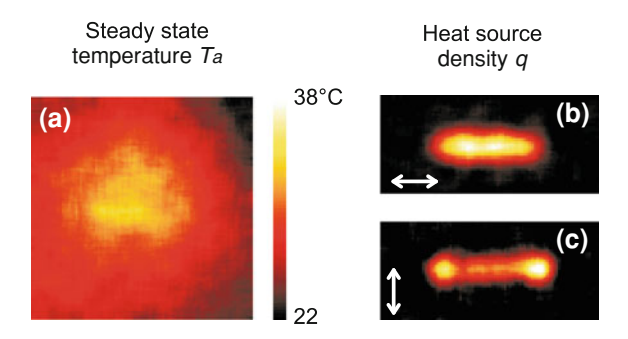


Fig. 7.6 Illustration of the two operation modes of the FPA-based thermal microscopy: **a** Steady-state temperature profile measured around a gold nanowire lying upon a glass substrate (the wire is 2  $\mu$ m long, 200 nm wide, and 35 nm thick). **b**, **c** Experimental measurements of the associated heat source density for **b** an illumination linearly polarized parallel and **c** perpendicular to the nanowire axis. The laser wavelength is 725 nm and the illuminance around 40 mW  $\mu$ m<sup>-2</sup>

for a transverse polarization of the incident light (perpendicular to the nanowire long axis) (Fig. 7.6c), the heat arises mainly at the extremities, while the optical near-field enhancement is expected at these locations precisely for the other polarization. An intuitive way of understanding this difference relies on a simple model based on surface charges. While optical hot spots are usually created at the metal surface due to charge accumulation for instance at edges or gaps, thermal hot spots arise from currents of charges into the metal.

### 7.2 MNP as Nano Light-Sources: Application to Biosensing and Optical Trapping

This section aims at illustrating how the optical properties of plasmonic nanostructures can be exploited to implement different kinds of interesting functionalities ranging from biosensing and trapping for bio-analysis and diagnostic to photothermal cancer therapy.

#### 7.2.1 Enhanced Sensitivity LSP-Based Biosensing

Since surface plasmon modes are bound to the metal surface, their dispersion is naturally strongly sensitive to any perturbation introduced at or nearby the interface such as those caused by a local change of the refractive index. This dependence on the shallow dielectric function that explicitly appears in formulas (18) of Chap. 3 and (3) of Chap. 4 for both extended and localized surface plasmon, respectively, is the foundation of the use of surface plasmons for optical sensing. Plasmon sensors

based on extended flat metal films have been widely studied [23] and have led to several commercial devices that are broadly used as tabletop systems by chemists and biologists in the detection of biomolecules and study of they specific binding. The so-called SPR sensors usually monitor changes in the resonance condition associated to the modification of the surrounding refractive index. They have been applied to many different contexts including unraveling biological mechanism, drug design, virology, etc. Like SPP at extended flat metal films, LSP supported by MNP can be used for sensing [24–26]. In this case, the typical sensing experiment consists in monitoring the frequency shift in the LSP resonance.

The three main attractive features of LSP sensors are:

- The possibility to directly couple free space light to LSP modes without needing any bulk glass prism that strongly limits integration.
- A priori, each individual MNP can act as a sensor offering possibilities for integrating a large number of sensing sites on a chip for parallel measurements.
   In practice though, the use of a single MNP is not compatible with simple detection schemes. Nevertheless, substantial signal-to-noise ratio can be achieved with a moderate number of MNP, maintaining an overall smaller size as compared to typical SPR pads.
- As for the sensitivity to a given change of the surrounding refractive index, the pros and cons of each configuration depend on the kind of application that is considered. The SPR configuration is more sensitive to bulk changes, i.e. a homogeneous change of refraction index over the whole dielectric superstrate in contact with the metal film. This is typically the case for liquid and gas sensing. In counterpart, the LSP sensors have the potential to be more sensitive to shallow changes of refractive index as those induced by the binding of small molecules at the metal surface [27]. This can be easily understood when considering that the sensitivity of an optical sensor is directly related to the spatial overlap between the optical mode and the volume occupied by the target molecules. Indeed, MNP offer much more flexibility than films to tailor the spatial distribution of the mode and therefore of the sensing volume. In particular, exploiting the electromagnetic coupling between adjacent MNP enables one to squeeze the plasmonic mode to a size that is commensurable with the molecular target (cf Sect. 7.1.1).

The concept of engineering the plasmon mode of MNP for improved plasmonic sensing was first suggested in 2004, in a theoretical proposal by Enoch and collaborators [28]. The proposed configuration consists of a periodic ensemble of plasmonic dimers formed by two adjacent gold cylinders separated by a nanometer-sized air gap. Using the Fourier modal method (FMM) [29], the resonance shift induced by a thin dielectric layer covering the metal, aiming at mimicking bound molecules, was calculated as a function of the geometrical parameters of the plasmonic nanostructures. The results showed that an array of gold dimers is about five times more sensitive as compared to an array of isolated particles. Similar calculations performed more recently by using another numerical method have confirmed the enhanced sensitivity of gold dimers [30].

210 R. Quidant

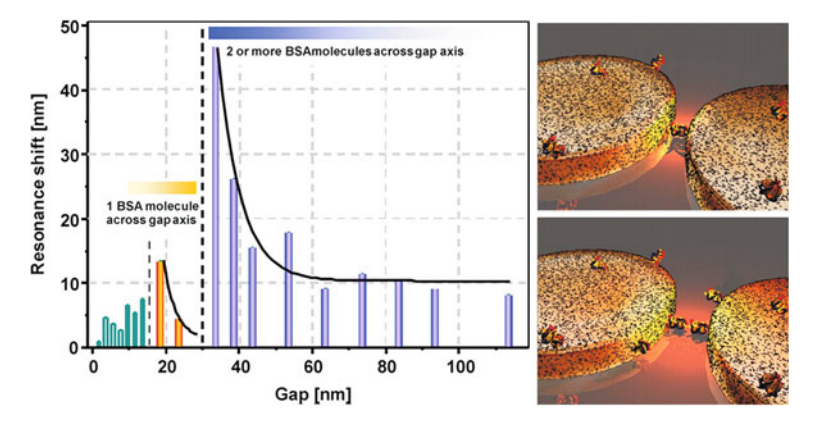


Fig. 7.7 Evolution with the gap size of the resonance shift resulting from the binding of BSA

Based on these numerical predictions, arrays of dimers with different gap sizes were fabricated by e-beam lithography on a glass substrate [31]. In order to maximize the level of reproducibility in the gap size all over each of the arrays, the conventional positive resist process combined with lift-off, usually used in plasmonics, was substituted by an alternative process based on negative resist combined with reactive ion etching. Using this process, arrays of gold cylinder dimers with gaps as small as 10 nm were successfully fabricated (see this chapter). The sensing properties of the fabricated structures were tested by measuring the extinction resonance shifts after binding Bovine Serum Albumin (BSA) to a self-assembled monolayer of mercaptoundecanoic acid (MUA). The experimental data are summarized in Fig. 7.7 in which the resonance shift is plotted as a function of the gap size. Two different regimes can be identified. For gap sizes greater than 60 nm, the resonance shift is small (about 10 nm) and nearly constant. Under these conditions, the weak near-field coupling between the adjacent particles forming the gap makes the dimers behave similarly to isolated particles. A drastically different regime is observed while decreasing the gap size from 60 nm to contact. The shift increases exponentially until reaching a maximum at about 30 nm. For this gap size, the sensitivity to the BSA binding is about five times larger than with isolated particles, in good agreement with the predictions of reference [28]. Further decrease of the gap leads to a dramatic drop of the shift followed by a second maximum. In order to understand this discrete evolution, one needs to consider the geometry and the binding properties of the BSA molecule. BSA is an elongated 14 nm molecule that tends to bind perpendicularly to the MUA layer. The maximum resonance shift thus corresponds to a gap size for which two BSA molecules bound across the gap fill in the whole sensing volume. For slightly shorter gaps (of about 25 nm), only one molecule can fit across the gap decreasing the spatial overlap with the dimer mode and subsequently leading to a large drop of the resonance shift. Further decreasing the gap size leads to a second maximum corresponding to a single molecule filling in the gap.

Exploiting this same concept of plasmon mode engineering, several other approaches have been considered to increase the sensitivity of LSP-based plasmonic sensors [32–34]. References [32, 33] propose the use of coupled plasmonic geometries with low symmetry to exploit the optical equivalent to Electromagnetically Induced Transparency (EIT) in atom physics. Along the same strategy, Liu and coworkers have recently used EIT in a planar metamaterial to achieve narrow resonance linewidths featuring enhanced sensitivity to the surrounding refractive index [33].

#### 7.2.2 Plasmon-Based Optical Trapping

The ability of plasmonic nanostructures to concentrate optical fields in true nanometer scale volumes is very attractive to enhance the interaction of light with small quantities of matter down to the molecular level. Among the main use of plasmon field enhancement in biomedical applications, let us mention Surface-Enhanced Raman Scattering (SERS) in which the very low efficiency of Raman emission can be dramatically enhanced, making it possible to detect the signature from a few to single molecules (see Chap. 5). In this section, we describe a different application in which enhanced plasmonic fields are used to develop a novel generation of integrated optical tweezers (OT) for optical trapping of tiny objects at a surface.

The momentum transfer of photons to matter is at the origin of optical forces that are for instance known to be partially responsible for the tail of comets. In first approximation, the total force experienced by a tiny object (much smaller than the incident wavelength) illuminated by a focused laser beam can be split into two different contributions. The scattering force (or radiation pressure) is a repulsive force pointing along the incident wave vector  $k_0$ . Conversely, the gradient force, arising from the gradient of the electromagnetic field intensity profile, is an attractive force that tends to pull the object toward the regions with the highest light intensity. Conventional three-dimensional (3D) OT are based on the competition between these two forces. In practice, focusing a high-quality laser beam through a high numerical aperture objective easily provides the conditions under which the restoring forces along the longitudinal and transverse directions overcome radiation pressure and Brownian motion respectively.

OT have become a powerful noninvasive manipulation technique that has found a wide range of applications especially in biology. Exploiting the ultra-gentle grip of OT has for instance allowed to study the interaction between molecules, as between myosin and actin. In such an experiment, double tweezers are used to trap two micrometer beads connected by an actin filament. The filament is brought in proximity to a third bead with attached myosin molecules [35]. OT also enable one to directly manipulate single cells and study intracellular mechanisms when combined for instance with Raman spectroscopy [36].

Since the pioneer works by Ashkin [37], more than 30 years of very active research have contributed in considerably increasing the performances of OT. Henceforth

with this technique, it is possible to rotate and manipulate dynamically in 3D several micrometer specimens [38]. Despite these performances, conventional OT face two main limitations. First, tight focusing with a bulky high NA objective is incompatible with the integration of optical trapping at the surface of a chip. Second, the trapping efficiency of convention 3D OT decreases very quickly with the size of the trapped object, due to the drop in the magnitude of the gradient forces (scaling with the third power of its radius) combined with the increase of Brownian motion. In practice, compensating the decrease in the trapped object size requires (i) to squeeze the size of the optical trap down to dimensions commensurable with the object volume and (ii) to increase the depth of the potential well by increasing the local intensity experienced by the object. Extending optical trapping to the nanometer scale would for instance enable one to directly manipulate single tiny biological specimens or even molecules, without needing to bind them to micrometer beads.

At the end of the 1990s, several theoretical proposals suggested exploiting concepts of nano-optics to create nanometer-sized optical traps. Novotny et al. [39] on one side and Martin et al. [40] on the other side first proposed to use the strong field enhancement and confinement created at the extremity of a sharp metallic tip. Nearly, at the same time, Kawata et al. came up with the idea of using the light transmitted through a nano-aperture in an opaque metallic film [41]. Inspired by these works, it was proposed in 2005 to pattern the surface of a transparent substrate with micro- and nanosized plasmonic structures with the aim of creating a near-field optical potential landscape able to trap small objects at predefined locations of the surface [42]. In this configuration, each plasmonic nanostructure acts as a nano-lens creating a sub- $\lambda$  concentration of the optical field from an extended unfocused illumination. This is particularly attractive in terms of integration since it naturally leads to a 2D trapping platform in which a large number of objects can be trapped in parallel from a single laser beam. In counter part, the use of a fixed plasmonic pattern a priori prevents moving the trapped objects over the surface.

Experimental research on SP-based trapping was triggered by two pioneer studies of the enhanced force field at a flat gold/water interface supporting a SPP. Garcés-Chávez and coworkers first reported on the SP-induced self-assembly of a large number of micrometer dielectric beads at the metal surface [43]. The same year, Volpe et al. used Photonic Force Microscopy to probe the SP force field and evaluate the enhancement of the force magnitude to a factor of about 50 [44].

While a homogeneous metallic film illuminated upon an unfocused laser beam features a homogeneous optical force field, stable trapping at a predefined location of the surface requires patterning the metal to create a confined trapping well. The first generation of SP traps consisted of micrometer gold disks illuminated in the Kretschmann configuration. Efficient parallel trapping of polystyrene (PS) microbeads was demonstrated with incident laser intensities about two orders of magnitude smaller than those required by conventional 3D OT for trapping the same beads [45] (see Fig. 7.8). Interestingly, it was also shown that, unlike 3D tweezers, SP traps can be operated to be selective to the size of the specimen, opening new perspectives in cell sorting [46]. More recent developments have shown the compatibility

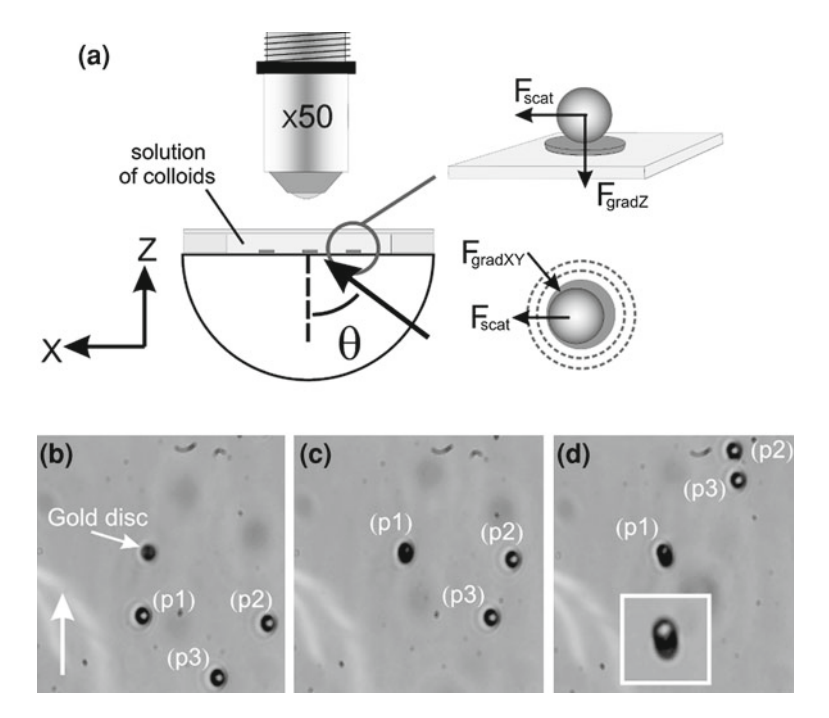


**Fig. 7.8** a Sketch of the optical configuration. **b–d** Chronological frame sequence recorded for an incidence angle  $\theta=68^\circ$  and p-polarization showing the trapping of a 4.88  $\mu$ m PS bead at a 4.8  $\mu$ m gold pad. (P1), (P2), and (P3) locate three different beads, while the vertical arrow points along the incident in-plane k-vector. A close-up of the trapped bead (P1) is shown in the inset of (**d**)

of SP traps at gold pads for the trapping of living yeast cells within a microfluidic environment [47].

As mentioned before, trapping a nanosized object requires: (i) first, increasing the trap confinement in order to maintain the object into a volume commensurable with its size; in the case of a nanometer object, this requires confining light down to the nanoscale; (ii) second, increasing the depth of the potential to overcome Brownian motion by boosting the local intensity within the trap.

#### **Nano-Optical Trapping with Optical Antennas**

A good candidate, to simultaneously fulfill both above-mentioned requirements, is the optical gap antenna that enables efficiently concentrating light within the gap region (see Sect. 7.1.1). In this direction, metal dimers have been recently shown to assist conventional 3D OT in further confining Rayleigh objects near an interface [48]. As a step forward, one can fully exploit the hot spots generated around plasmonic antennas to implement on-a-chip autonomous integrated optical nanotweezers. For this purpose, gap antenna formed by two adjacent 500 nm gold bars (120 nm wide

214 R. Quidant

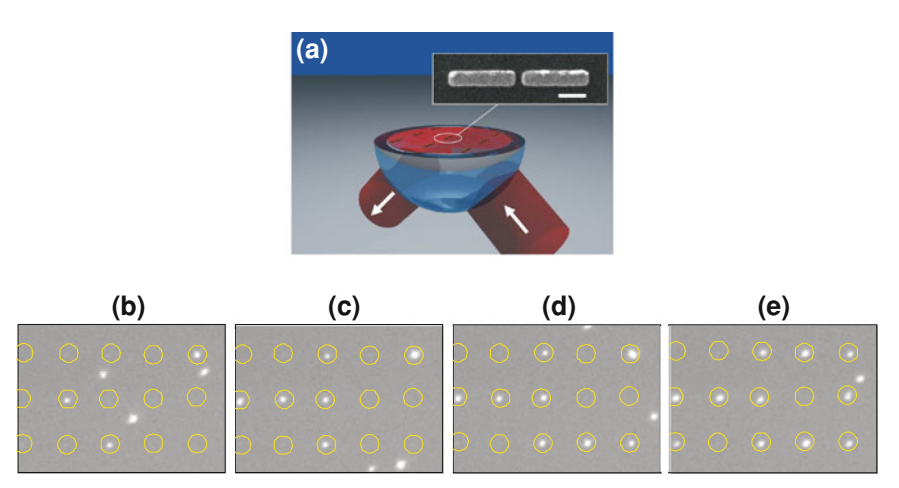


**Fig. 7.9** Optical antenna trapping: **a** Optical configuration, **b**–**e** time sequence of fluorescent images showing a parallel trapping of 200 nm fluorescent polystyrene beads in an aqueous solution. Each circle locates the position of individual antennas. The illumination is performed under total internal reflection through a glass prism using an 800 nm laser line, linearly polarized along the antenna's long axis. The incident intensity is  $10^7 \, \text{W m}^{-2}$ 

and 50 nm high) separated by a 30 nm gap was designed. For these dimensions, the antenna features a  $3\lambda/2$  resonance at 730 nm, which shifts to 800 nm when covered with water. An array of such antennas was fabricated on a glass substrate and illuminated under total internal reflection by a slightly focused laser beam, linearly polarized along the antenna long axis. The average beam diameter and power were fixed at  $100~\mu m$  and 300~mW, respectively, corresponding to an incident intensity of about  $10^7~W~m^{-2}$ .

The trapping properties of the antennas were first studied by exposing them to a diluted solution of 200 nm PS beads doped with fluorescent molecules. Figure 7.9 shows a time sequence of fluorescent images recorded over a portion of the antenna array. Here, the pronounced Brownian motion of the beads is exploited to load the trap and only one minute is necessary for most of the antennas to capture a bead [49]. In order to evaluate the operation bandwidth of the nanotweezers, further experiments in which the incident wavelength of the laser was scanned from 750 to 850 nm in steps of 10 nm were performed. The trapping efficiency  $\eta$  of the antennas is defined as the fraction of antennas (out of 15) that simultaneously trap a bead. Under longitudinal polarization,  $\eta$  features a resonant behavior with a maximum centered around 800 nm in good correspondence with the antennas resonance when immersed in water. Conversely, a rather constant low trapping ability is observed under transversal polarization, because the antennas do not feature any transversal resonance in this spectral window.

At this stage, in order to test the applicability of antenna trapping to biological specimens, further experiments with E-coli bacteria were performed. E-coli are rod-shaped cells typically 2 µm long (at the initial stage of their growth) and about

half-a-micrometer in diameter with an effective refraction index of about 1.38. Substituting the aqueous solution PS bead by a solution of E-coli bacteria in LB broth media, an efficient parallel trapping of single bacteria on adjacent antennas was observed. Remarkably, beyond being trapped, the bacteria systematically aligned along the antenna's long axis. It is believed that their elongated geometry enables them to exploit all trapping sites along the antenna bars as confirmed by the torque calculation (Fig. 7.10g), thus making the aligned configuration the most stable one. Beyond this demonstration of efficient trapping and in order to evaluate the actual applicability of this method in true biological studies, one should be concerned about any damage that could have been caused to the trapped bacteria. For this purpose, additional measurements over several hours were performed. The results presented in Fig. 7.10 illustrate how the bacteria exposed to the antennas local fields keep on growing and dividing while being trapped. Their average division time, measured to be about 1 h, does not differ from the division time of other bacteria located away from the antennas and out of the illumination area. Moreover, since the actual optical intensity experienced by the bacteria in the trapping sites ( $\sim 10^8 \, \mathrm{W \, m^{-2}}$  accounting for the local intensity enhancement) was found to be at least 10 times lower than the noninvasive intensity reported in the literature using a more harmful wavelength, no serious damage is expected to be inflicted by trapping. Further testing on the cell activity would require more elaborated methods such as the one used in [50].

#### **Self-Induced Back Action Trapping**

While an approach based on antennas is satisfactory for dielectric objects down to 200 nm, going to objects with even smaller polarizabilities (smaller than 100 nm), brings us to a practical limitation that is in fact intrinsic to the physics of optical trapping. Indeed, halving the object size requires about one order of magnitude increase in the local field intensity. Consequently, one is quickly faced to limit the specimen size beyond which the increase of the local intensity exceeds its damage threshold. This is even more critical when dealing with biological specimens that are particularly sensitive to laser heating. In order to address this fundamental issue, an alternative approach to conventional trapping in which the trapped object plays an active role in the trapping mechanism has recently been proposed. The so-called Self-Induced Back Action (SIBA) trapping configuration enables drastically reducing, as compared to conventional trapping, the minimum local intensity required for trapping, thus opening new opportunities toward the noninvasive manipulation of nanometer objects, including bio-specimens.

SIBA trapping has first been demonstrated using a tiny hole in a gold film [51]. The dimension of the aperture was chosen such that its transmission cut-off was blue detuned with respect to the trapping wavelength at 1064 nm. Under these conditions, the aperture acts as an efficient sensor whose transmission varies as a function of the specimen position. Having a larger refractive index than water, a particle occupying the aperture makes it appear larger, which allows for more transmission above the usual cut-off wavelength. In order to illustrate the general concept of SIBA trapping,

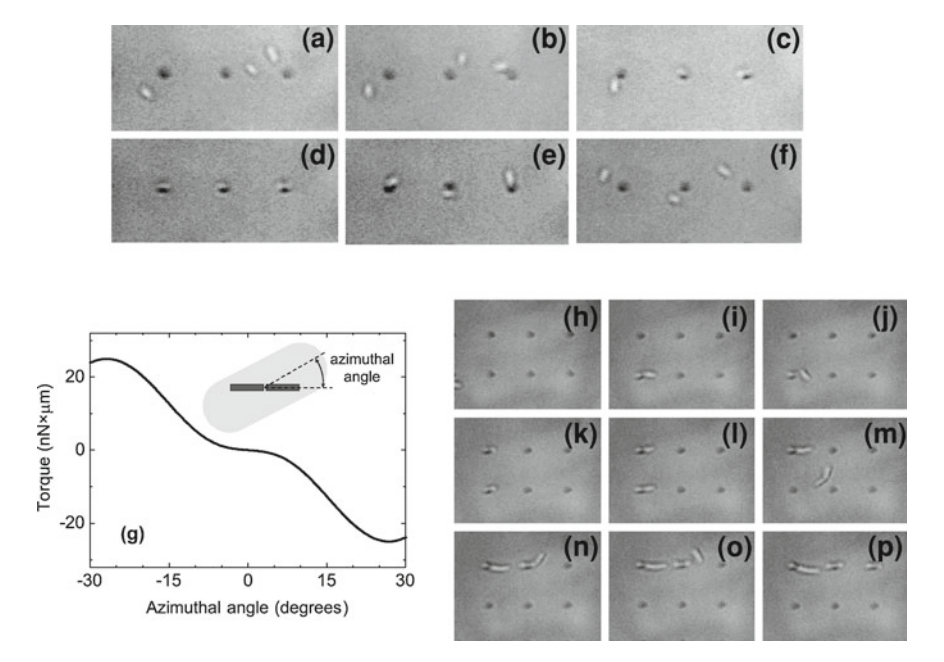


**Fig. 7.10** a–f Successive frames showing simultaneous trapping of E-coli bacteria. The incident laser (800 nm) has been switched off just before recording the frame (e). g Calculated torque acting on the bacteria as a function of their angle relative to the rod axis. h–p Another sequence of trapping recorded over two hours, showing how the trapped bacteria keep on growing and dividing

let us consider the equilibrium point for the particle at the opening of the aperture. The transmission drops when the particle is moved away from the aperture, with a corresponding drop in the rate of photon momentum traveling through the aperture. This momentum change leads to a force in the opposite direction that will act on the particle; the balancing force will be directed toward the aperture, thereby pulling the particle back to the equilibrium position. Conversely, if the particle moves further into the aperture the transmission will increase and the restoring force will push the particle out. FDTD simulations show for instance that the active role of a PS 50 nm particle in the trapping efficiency reduces the intensity requirement by an order of magnitude as compared to conventional trapping.

Figure 7.11 shows the time evolution of the aperture transmission when exposed to a diluted solution of 100-nm PS beads. The higher value of the transmission corresponds to the time when a particle occupies the aperture. Stable trapping over an acquisition time of 5 min is observed (see Fig. 7.11b) for a relatively small incident power of 1 mW, corresponding to a maximum intensity in the focus center of about 1 mW  $\mu m^{-2}$ . The experiment was repeated with 50 nm PS spheres showing stable trapping during several seconds upon an incident laser power of only 1.9 mW (see Fig. 7.11c).

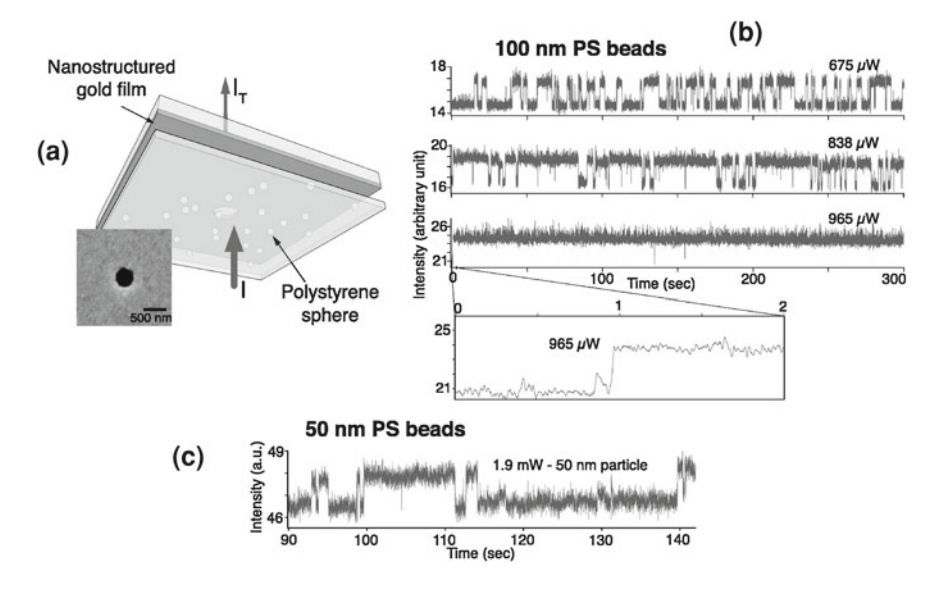


**Fig. 7.11** Experimental trapping of 100- and 50-nm PS particles in a metallic nano-aperture: **a** Sketch of the experimental configuration. **b** Experimental time evolution of the intensity transmitted through a 310 nm aperture using different incident laser power when exposed to a solution of 100-nm PS particles. Abrupt increases are from a particle trapped in the aperture. **c** Experimental time evolution of the transmitted intensity showing the trapping of a 50-nm particle upon 1.9 mW laser illumination

While the SIBA trapping has been successfully demonstrated using a nanohole in a metallic film, it is a very general concept that could be extended to other geometries in which the trapped object significantly enhances the local field within the trap.

#### Toward an Integrated Plasmonic Platform for Bio-Analysis

SP-based molecular sensing and trapping are versatile nano-tools that could be of a potentially strongly benefit to the so-called concept of lab-on-a-chip (LOC). LOCs are devices that integrate one or several laboratory functions on a compact chip. They operate with microfluidics that enables the handling of extremely small fluid volumes down to less than picoliters.

The main advantages of LOCs are:

- Low fluid volumes, consumption (less waste, lower reagents costs, and less required sample volumes for diagnostics)
- Faster analysis and response times due to short diffusion distances, fast heating, high surface-to-volume ratios
- Massive parallelization due to compactness, which allows high-throughput analysis

218 R. Quidant

• Lower fabrication costs, allowing cost-effective disposable chips, fabricated in mass production

• Safer platform for chemical, radioactive, or biological studies because of integration of functionality, smaller fluid volumes, and stored energies

Although the application of LOCs is still in its infancy, there is a growing interest of companies and applied research groups in using them in different fields such as analysis (e.g. chemical analysis, environmental monitoring, medical diagnostics, and cytometry). To advance into further application developments, research in LOC systems is expected to extend not only toward downscaling of fluid handling structures but also through a marriage with nanotechnology. Here, nano-optics and in particular plasmon nano-optics could be strongly beneficial by integrating plasmonic nano-tools, such as sensors and tweezers, as a way to perform an optical inspection of a biological sample from the molecular to the cell level. Within the context of biomolecule detection for medical diagnosis, plasmonic sensors based on gold MNP integrated into a microfluidic environment could play a decisive role by combining compactness with ultra-high sensitivity, offering key advantages over conventional SPR technology. Additionally, SP-based optical trapping opens new opportunities within the frame of flow cytometry for circulating cancer cell tracking through selectively trapping combined with optical inspection for instance by SERS.

## 7.3 MNP as Nano Heat-Sources for Photothermal Cancer Therapy

We have seen in Sect. 7.1.2 how MNP can be engineered to become efficient heat nanosources remotely controllable by laser illumination. In this section, we discuss the application of plasmonic gold nanoparticles to photothermal cancer therapy (PCT). The general idea behind PCT is to specifically bind photo-heaters to cancer cells (not to healthy cells) and to use laser illumination to heat them up until they get killed.

For most types of cancers, standard treatments consist of:

- Surgical removal that is limited to large, accessible tumors.
- Chemotherapy that suffers from dramatic side effects including depression of the immune system and organ damage.
- Radiotherapy that is strongly invasive to healthy tissues along the radiation path.

Alternatively, laser hyperthermia (photothermal therapy) that uses light-induced heating for tumor ablation is a much milder solution that overcomes all the drawbacks of conventional approaches. In that case indeed, irreversible heating only occurs where the particles are agglomerated (within cancer cells) without damaging surrounding healthy tissues that are exposed to the laser. On the one hand, organic photoabsorbers such as indocyanine green have been used for PCT, but they suffer from a small absorption cross-section that limits their heating ability upon moderate

laser illumination. On the other hand, inorganic absorbers like iron oxide require concentrations that can become toxic. The main advantages of gold nanoparticles over other absorbers are their potentially high ability to heat up upon reduced laser irradiation, their low toxicity, and the relatively simple surface chemistry that enables specific targeting of cancer cells.

#### **7.3.1** *Toxicity*

Considering that nearly anything can be toxic beyond a certain dose, one should wonder about the level of toxicity of gold nanoparticles at the concentrations at which they might be used in PCT, typically of the order of 100 per cell. While under these conditions, gold in itself can be considered as harmless, potential toxicity can arise from the surface reagents used in the nanoparticle growth.

Depending on the growth recipe, particles can end up with different surface modifiers including citrate, cysteine, glucose, biotin, and cetyltrimethylammonium bromide (CTAB). CTAB is the structure-directing agent that is used to control gold nanorod shape that forms a tightly bound cationic bilayer on gold nanoparticles. It was found that free CTAB (which may result from an incomplete purification of gold nanorods or desorption from the bound bilayer) was toxic for cells at  $\sim \! 10 \, \text{nM}$  concentrations [54]. Hence, a proper purification of gold nanorods is crucial for any in vivo work. A more sophisticated and safer approach consists in using the ligand exchange to substitute CTAB with a nontoxic molecule such as poly(ethylene glycol) (PEG) [52, 53]. Readers interested in further details about toxicity can for instance be directed to specific review articles [54, 55].

## 7.3.2 Cancer Cell Targeting and Latest Advances in Hyperthermia

Another crucial aspect toward the use of metallic nanoparticles in PCT is to achieve their specific binding to cancer cells (and not to healthy cells). This is usually achieved by using antibody-conjugated nanoparticles that specifically bind to cancer markers overexpressed at the surface and inside the cells.

Plasmon-based photothermal destruction of SK-BR-3 cancer cells was first demonstrated in vitro and in vivo by Halas and colleagues using thiolated-PEG-passivated gold nanoshells with a 110-nm-diameter core and a 10 nm-thick shell resulting in a peak absorbance at 820 nm. The achieved temperature increase upon 820-nm laser diode irradiation was of 37.4  $\pm$  6.6 °C at a depth of 2.5 mm beneath the dermal surface, which is well above the temperature at which irreversible tissue damage occurs (about 45 °C) [56]. Laser intensity used was one order of magnitude weaker than those needed for the Indocyanine green dye. Maximal depth of treatment

220 R. Quidant

was 6 mm, but it could reach 1 cm or even more in related studies. Slightly later, the same authors used gold nanoshells conjugated with antibodies to HER2, a protein overexpressed in breast cancer cells, to destroy breast cancer cells in vitro [57]. Gold nanorods conjugated to anti-EGFR antibody were used as a contrast agent to image malignant HOC and HSC that overexpress EGFR proteins using simple dark field imaging [58]. They also found that upon exposure to continuous red laser at 800nm, malignant cells were killed with half the laser intensity needed for nonmalignant cells.

Since these pioneer works, lots of efforts have been put worldwide into improving the efficiency of hyperthermia. Researchers have been considering different geometries of particles, illumination conditions as well as conjugation strategies to increase the specificity of particle binding to cancer cells. In recent years, the company Nanospectra [59] has been conducting some clinical tests on head and neck cancers using gold nanoshells.

#### 7.4 Conclusion

We have discussed how the optical and thermal properties of plasmonic nanostructures can be exploited to develop novel nano-tools with attractive applications to healthcare, from diagnosis to treatment. We have first shown that there is room for an accurate control of light and heat accumulated at the nanoparticle, upon laser illumination. On the one hand, intense and confined plasmonic fields can be engineered to detect the binding of low concentrations of small molecules or to trap in a noninvasive way tiny objects at a predefined location of a surface. Plasmon-based sensing and trapping are foreseen to become important ingredients in the development of future lab-on-chip devices for advanced healthcare diagnosis, from the molecular to the cell level. On the other hand, metallic nanoparticles can act as efficient point-like heat-sources for lesser invasive cancer therapy.

Beyond the selected topics treated in this chapter, there are many other examples in which plasmonic nanoparticles can be of benefit to biosciences and medicine. One can for instance mention the use of gold nanoparticles as a contrast agent in bioimaging [60–64] and thermal-assisted drug delivery [65, 66].

#### References

- 1. J. Kottmann, O. Martin, D. Smith, S. Schultz, Opt. Express 6, 213 (2000)
- 2. H. Wang, D.W. Brandl, F. Le, P. Nordlander, N.J. Halas, Nano Lett. 6, 827 (2006)
- L. Rodriguez-Lorenzo, R.A. Ivarez-Puebla, I. Pastoriza-Santos, S. Mazzucco, O. Stphan, M. Kociak, L.M. Liz-Marzan, F.J. Garca de Abajo. J. Am. Chem. Soc. 131, 4616 (2009)
- 4. J. Kottmann, O. Martin, Opt. Express **8**, 655 (2001)
- 5. I. Romero, J. Aizpurua, G.W. Bryant, F.J. Garca De Abajo, Opt. Express 14, 9988 (2006)
- 6. P. Mühlschlegel, H.-J. Eisler, O.J.F. Martin, B. Hecht, D.W. Pohl, Science 308, 1607 (2006)

- P.J. Schuck, D.P. Fromm, A. Sundaramurthy, G.S. Kino, W.E. Moerner, Phys. Rev. Lett. 94, 017402 (2005)
- 8. W. Rechberger, A. Hohenau, A. Leitner, J.R. Krenn, B. Lamprecht, F.R. Aussenegg, Optics Commun. 220, 137 (2003)
- 9. H. Fischer, O.J.F. Martin, Opt. Express 16, 9144 (2008)
- 10. J.N. Farahani, D.W. Pohl, H.-J. Eisler, B. Hecht, Phys. Rev. Lett. 95, 017402 (2005)
- 11. O.L. Muskens, V. Giannini, J.A. Sánchez-Gil, J. Gómez Rivas, Nano Lett. 7, 2871 (2007)
- 12. O.J.F. Martin, C. Girard, A. Dereux, Phys. Rev. Lett. 74, 526 (1995)
- 13. C. Girard, E. Dujardin, G. Baffou, R. Quidant, New J. Phy. 10, 105016 (2008)
- 14. H.M. Pollockand, A. Hammiche, J. Phys. D-Appl. Phys. 34, R23 (2001)
- J.W. Pomeroy, M. Kuball, D.J. Wallis, A.M. Keir, K.P. Hilton, R.S. Balmer, M.J. Uren, T. Martin, P.J. Heard, Appl. Phys. Lett. 87, 103508 (2005)
- 16. K.K. Liu, K.L. Davis, M.D. Morris, Anal. Chem. **66**, 3744 (1994)
- 17. P. Low, B. Kim, N. Takama, C. Bergaud, Small 4, 908 (2008)
- 18. G.A. Robinson, R.P. Lucht, M. Laurendeau, Appl. Opt. 47, 2852 (2008)
- B. Samson, L. Aigouy, P. Low, C. Bergaud, B.J. Kim, M. Mortier, Appl. Phys. Lett. 92, 023101 (2008)
- 20. G. Baffou, M.P. Kreuzer, F. Kulzer, R. Quidant, Optics Express 17, 3291 (2009)
- B. Valeur, Molecular Fluorescence: Principles and Applications (Wiley-VCH, New York, 2002)
- 22. G. Baffou, C. Girard, R. Quidant, Phys. Rev. Lett. 104, 136805 (2010)
- 23. J. Homola, S.S. Yee, G. Gauglitz, Sens. Actuators B 54, 3 (1999)
- G. Raschke, S. Kowarik, T. Franzl, C. Sonnichsen, T.A. Klar, J. Feldmann, A. Nichtl, K. Kurzinger, Nano. Lett. 3, 935 (2003)
- 25. E.M. Larsson, J. Alegret, M. Kall, D.S. Sutherland, Nano Lett. 7, 1256 (2007)
- 26. M.P. Jonsson, P. Jonsson, A.B. Dahlin, F. Hook, Nano Lett. 7, 3462 (2007)
- S. Chen, M. Svedendahl, M. Käll, L. Gunnarsson, A. Dmitriev, Nanotechnology 20, 434015 (2009)
- 28. S. Enoch, R. Quidant, G. Badenes, Opt. Express 12, 3422 (2004)
- 29. L. Li, J. Opt. Soc. Am. A 14, 2758 (1997)
- 30. P.K. Jain, M.A. El-Sayed, Nano Lett. 8, 4347–4352 (2008)
- 31. S. Acimovics, M.P. Kreuzer, M.U. Gonzlez, R. Quidant, ACS Nano 3, 1231 (2009)
- 32. N. Verellen, Y. Sonnefraud, H. Sobhani, F. Hao, V. V. Moshchalkov, P. Van Dorpe, P. Nordlander, S. Maier, Nano Lett. 9, 1663 (2009)
- N. Liu, T. Weiss, M. Mesch, L. Langguth, U. Eigenthaler, M. Hirscher, C. Snnichsen, H. Giessen, Nano Lett. 10, 1103 (2010)
- A.B. Evlyukhin, S.I. Bozhevolnyi, A. Pors, M.G. Nielsen, I.P. Radko, M. Willatzen, O. Albrektsen, Nano Lett. 10, 4571 (2010)
- 35. J.T. Finer, R.M. Simmons, J.A. Spudich, Nature 368, 113 (1994)
- 36. C. Creely, G. Volpe, G. Singh, M. Soler, D. Petrov, Opt. Express 13, 6105 (2005)
- 37. A. Ashkin, J.M. Dziedzic, J.E. Bjorkholm, S. Chu, Opt. Lett. 11, 288 (1986)
- 38. D. Grier, Nature **424**, 810 (2003)
- 39. L. Novotny, R.X. Bian, X.S. Xie, Phys. Rev. Lett. 79, 645 (1997)
- 40. O.J.F. Martin, C. Girard, Appl. Phys. Lett. **70**, 705 (1997)
- 41. K. Okamoto, S. Kawata, Phys. Rev. Lett. 83, 4534 (1999)
- 42. R. Quidant, D.V. Petrov, G. Badenes, Opt. Lett. 30, 1009 (2005)
- 43. V. Garcés-Chávez, R. Quidant, P.J. Reece, G. Badenes, L. Torner, K. Dholakia, Phys. Rev. B 73, 085417 (2006)
- 44. G. Volpe, R. Quidant, G. Badenes, D. Petrov, Phys. Rev. Lett. 96, 238101 (2006)
- 45. M. Righini, A.S. Zelenina, C. Girard, R. Quidant, Nat. Phys. 3, 477 (2007)
- 46. M. Righini, G. Volpe, C. Girard, D. Petrov, R. Quidant, Phys. Rev. Lett. 100, 186804 (2008)
- 47. L. Huang, S.J. Maerkl, O.J. Martin, Opt. Express 17, 6018 (2009)
- 48. A.N. Grigorenko, N.W. Roberts, M.R. Dickinson, Y. Zhang, Nat. Photonics 2, 365 (2008)

222 R. Quidant

 M. Righini, P. Ghenuche, S. Cherukulappurath, V. Myroshnychenko, F.J. Garca de Abajo, R. Quidant, Nano Lett. 9, 3387 (2009)

- 50. M.B. Rasmussen, Appl. Environ. Microbiol. 174, 2441 (2008)
- 51. M.L. Juan, R. Gordon, Y. Pang, F. Eftekhari, R. Quidant, Nat. Phys. 5, 915 (2009)
- 52. S. Pierrat, I. Zins, A. Breivogel, C. Sonnichsen, Nano Lett. 7, 259 (2007)
- H. Liao, J.H. Hafner, Chem. Mater. 17, 4636 (2005)
   E.E Connor, J. Mwamuka, A. Gole, J.C. Murphy, M.D. Wyatt, Small 1, 325 (2005)
- 55. N. Lewinski, V. Colvin, R. Drezek, Small 4, 26 (2008)
- L.R. Hirsch, R.J. Stafford, J.A. Bankson, S.R. Sershen, B. Rivera, R.E. Price, J.D. Hazle, N.J. Halas, Proc. Natl. Acad. Sci. U. S. A. 100, 13549 (2003)
- 57. C. Loo, A. Lowery, N.J. Halas, J. West, R. Drezeck, Nano Lett. 5, 709 (2005)
- 58. X.H. Huang, I.H. El-Sayed, W. Qian, M.A. El-Sayed, J. Am. Chem. Soc. 128, 2115 (2006)
- 59. Nanospectra, http://www.nanospectra.com/index.html
- 60. I.H. El-Sayed, X. Huang, M.A. El-Sayed, Nano Lett. 5, 829 (2005)
- 61. S. Kumar, N. Harrison, R. Richards-Kortum, K. Sokolov, Nano Lett. 7, 1338 (2007)
- 62. J. Aaron, K. Travis, N. Harrison, K. Sokolov, Nano Lett. 9, 3612 (2009)
- 63. B. Wang, E. Yantsen, T. Larson, A.B. Karpiouk, S. Sethuraman, J.L. Su, K. Sokolov, S.Y. Emelianov, Nano Lett. 9, 2212 (2009)
- S. Mallidi, T. Larson, J. Tam, P.P. Joshi, A. Karpiouk, K. Sokolov, S. Emelianov, Nano Lett. 9, 2825 (2009)
- M.R. Choi, K.J. Stanton-Maxey, J.K. Stanley, C.S. Levin, R. Bardhan, D. Akin, S. Badve, J. Sturgis, J.P. Robinson, R. Bashir, N.J. Halas, S.E. Clare, Nano Lett. 7, 3759 (2007)
- 66. R. Huschka, O. Neumann, A. Barhoumi, N.J. Halas, Nano Lett. 10, 4117 (2010)

# Part III Imaging and Nanofabrication

## **Chapter 8 Imaging Surface Plasmons**

Alexandre Bouhelier, Gérard Colas des Francs and Jonathan Grandidier

**Abstract** Controlling surface plasmons is at the heart of plasmonics. Advances in this field are to a large extent triggered by our ability to visualize surface plasmons in their different forms. In this chapter, we provide a review of the different techniques capable of imaging and visualizing surface plasmons. We have divided these techniques in three distinct families: proximal probe techniques, far-field microscopies, and electron imaging. We review here their principal characteristics, advantages, and limitations and illustrate the discussion with images taken from the literature.

#### 8.1 Introduction

Let us start by placing the context of this chapter from a historical perspective. Without repeating D. Maystre in his account of the history of surface plasmon, it is interesting to note that the middle of the 1990s corresponded to a decline of the scientific interest concerning surface plasmons. A rapid survey of the literature shows a steady decrease in the number of published papers until approximately 1995. This decline is fairly well explained by the fact that the field was in a mature stage of understanding and the applications were scarce. The famous references written by Raether in 1980 and 1988 [1, 2] and the book of Kreibig and Vollmer in 1995 [3] are attesting the degree of comprehension about surface plasmons at that time. An important remark to make is that inside these books, nowhere will the reader *see* a plasmon. Yet, after reading, the reader will have a profound knowledge of what is a surface plasmon and what are its principal characteristics and properties. It is remarkable to note that the majority of this understanding is essentially derived from a limited series of indirect measurements revealing the peculiar nature of surface

A. Bouhelier (⊠) · G. Colas des Francs · J. Grandidier Laboratoire Interdisciplinaire Carnot de Bourgogne CNRS UMR 5209, Université de Bourgogne, 21078 Dijon, France e-mail: alexandre.bouhelier@u-bourgogne.fr plasmons. These measurements are the attenuated total internal reflectivity curve [4, 5], electron energy-loss and extinction spectroscopies [3, 6]. Without going through an exhaustive list of surface plasmon characteristics deduced from these experiments, let us mention the extreme sensitivity of the plasmon to interfaces, the determination of the dispersion curve across a large range of wavevectors ( $\mu$ m<sup>-1</sup> to Å<sup>-1</sup>) and interfaces, the estimation of the lifetime of the surface plasmon and its different decaying channels, the spectral position of the plasmon resonances as a function of shape, materials, polarization, dielectric environment...

So, what is the added value of actually seeing a surface plasmon? What are the new physical properties revealed by imaging those waves that are not accessible by the techniques exposed above? One word might provide a hint to answer these questions and this word is *control*. It is because we visualized a plasmon on a bare gold film that we started to develop planar structures to alter and modify its propagation [7–9]. It is because we probed the spatial extent of confined fields that we are able to control near-field interactions [10–13], and it is because we imaged snapshot of the plasmon temporal evolution that we managed to control local surface plasmon dynamics [14–16]. These are a few examples of the new concepts triggered by recent advances of surface plasmon imaging.

This chapter will review the different techniques implemented to image surface plasmons supported by metal structures. We will cover the visualization of propagating surface plasmons in bare and decorated metal films as well as the microscopy of localized surface plasmons, characteristic of confined geometries. We will introduce essentially three families capable of imaging surface plasmons. Each family uses a distinct intrinsic plasmon property introducing therefore a series of pro and contra depending upon the system under observation and the type of information collected. Despite this distinction, all these techniques comply with a mandatory requirement to visualize a running plasmon: the excitation area must be smaller than the spatial extension of surface plasmon.

Because surface plasmons are confined at an interface, techniques based upon proximal probes are therefore a prime imaging tool to access the surface plasmon intensity distribution. They are traditionally used to observe the propagation of surface plasmons in a structured metal film. However, advanced near-field techniques are nowadays being developed to also visualize surface plasmons on nanoparticles with profusion of details. These near-field techniques constitute the first family of imaging tools that will be described and illustrated with examples taken from the literature.

To the difference with near-field techniques, the second family of tools does not require a local probing to optically image surface plasmons. These approaches rely on specific radiative properties of surface plasmons to either directly map the plasmon distribution or to image a response modulated by the presence of the plasmon. Here again, the discussion will be supported by a series of vivid examples.

In the first two imaging families, the observable is always the photon and for the vast majority of cases, the plasmon is the result of an electromagnetic stimulus. However, a surface plasmon is by definition a polariton, which is a photon coupled to an electron. The last family of imaging tools that will be discussed uses this dual nature by spatially interrogating either the photon or the electron. We will conclude this chapter by providing the reader a discussion about the advantages and drawbacks of these methods compared to purely optical approaches.

#### 8.2 Optical Near-Field Imaging

#### 8.2.1 Near-Field Imaging of Propagative Surface Plasmons

In 1994, the *American Physical Society* published in its leading journal *Physical Review Letters*, an article co-authored by Paul Dawson from Queen's University of Belfast, Fréderique de Fornel and Jean-Pierre Goudonnet from Université de Bourgogne in Dijon, France [17]. The authors entitled their publication "Imaging Surface Plasmon Propagation and Edge Interaction Using a Photon Scanning Tunneling Microscope". With this article, a surface plasmon became visible under the tip of a scanning near-field optical microscope. The intensity distribution of the plasmon, its propagation and interaction were directly imaged for the first time.

Scanning near-field optical microscopy [18, 19] belongs to the family of proximal probe microscopes such as scanning tunneling microscopy (STM) and atomic force microscopy (AFM). In these techniques, high resolution is achieved by minimizing the sensing volume between a probe and an object. The probe usually takes the form of a tip where only the very apex is responsible for the interaction. The angular representation of the field in a plane  $z = z_0$  near an arbitrary object can be written as:

$$E(x, y, z_o) = \int_{-\infty}^{+\infty} \int_{-\infty}^{+\infty} A(k_x, k_y) \exp i \left( k_x x + k_y y + z_o \sqrt{k_o^2 - k_x^2 - k_y^2} \right) dk_x dk_y,$$
(8.1)

where  $A(k_x, k_y)$  represents the complex amplitude of the field and  $k_o = \omega/c$  is the vacuum wavevector. Equation (8.1) is the sum of plane waves and evanescent waves propagating in different spatial directions. Wavevectors  $k_x$  and  $k_y$  smaller than  $k_o$  constitute homogeneous plane waves that propagate in free space. Wavevectors satisfying this condition have low spatial frequencies. The integration in Eq. (8.1) runs also over  $k_x$  and  $k_y$  values that are larger than  $\omega/c$ . Consequently, the field components become evanescent. The electric field of evanescent waves propagates in the x, y plane, but is exponentially attenuated in the z-direction. These fields are associated with high spatial frequencies (fine details of an object). In order to achieve superresolution, the variations of the field in the immediate vicinity of the object have to be collected. The collection of evanescent waves is the basis of scanning near-field optical microscopy.

This technique is very well suited to collect surface plasmon field because of its evanescent nature [20]. The dispersion relation for a metal/air interface writes:  $k_{zi} = \sqrt{\varepsilon_i (\omega/c)^2 - k_x^2}$ , where  $\varepsilon$  is the dielectric function of the medium i (metal or air) [2]. For surface plasmon excitation,  $k_x$  must be greater than  $\omega/c$ . Consequently,

228 A. Bouhelier et al.

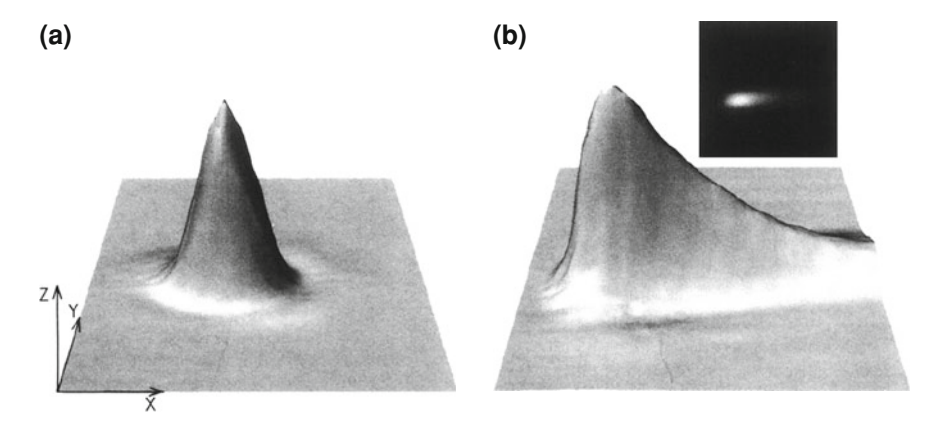


Fig. 8.1 Three-dimensional rendering of the intensity distribution at the silver/air interface of focused laser beam undergoing total internal reflection. a TE-polarization. b TM-polarization. The exponential tail in b is the signature of the propagating surface plasmon. Inset: two-dimensional view of the image. Scan size is  $40 \times 40 \,\mu m$ . Reprinted with permission from [17]. Copyright 1994, The American Physical Society

the wavevectors  $k_{zi}$  in the metal and in the air are imaginary: the field amplitude of the surface plasmon decreases exponentially from the interface.

The basic units forming a near-field microscope are very similar to other scanning probe techniques. They consist of a near-field probe confining an optical interaction to dimensions smaller than the wavelength, a scanning stage permitting to raster scan the sample or the tip laterally, a photodetector to collect the response of the optical probe-sample interactions, and finally an acquisition software to reconstruct an optical image [21–23]. One of the requirements to achieve high-resolution imaging is that the tip sample distance should be controlled with sub-nanometer precision to warrant optimum near-field probing of the surface plasmon field. Shear-force regulation based on quartz tuning fork is extensively used nowadays [24].

Figure 8.1 shows a three-dimensional rendering of the light intensity collected by a near-field probe scanned above a focused laser spot undergoing total internal reflection at a glass/Ag interface. The images are extracted from Dawson's publication [17]. Figure 8.1a illustrates the light distribution for a TE-polarization. For this excitation condition, no plasmons can be excited and the image displays the Gaussian distribution of the laser beam. For a TM-polarization, however, the intensity distribution of Fig. 8.1b reveals an exponentially decaying tail on the right-hand side. This tail is the signature of a running surface plasmon at the silver/air interface propagating several tens of micrometers.

Note that the extension of the surface plasmon is becoming visible in the image because the excitation area is smaller than the lateral decay of the plasmon intensity (focused laser beam). As already alluded to before, this is a prerequisite to visualize running plasmons.

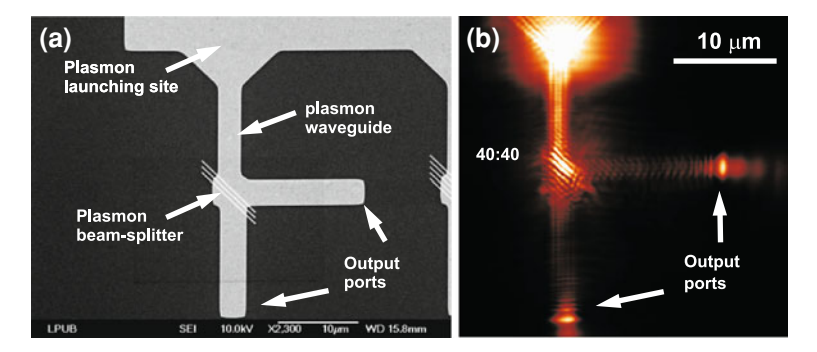


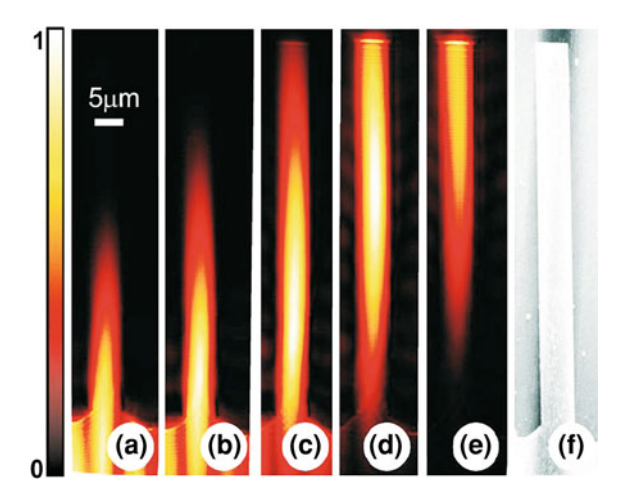
**Fig. 8.2** a Scanning electron micrograph of a structured metal (Au) film comprising of a launching plasmon pad, a surface plasmon waveguide, a grating beam-splitter, and two output ports. **b** Nearfield image of the plasmon intensity interaction with the different elements. The plasmon is diffracted by the termination of the two output ports. Residual out-of-plane scattering is visible at the location of the beam splitter. Reprinted with permission from [29]. Copyright 2005, The American Institute of Physics

The image of Fig. 8.1b contains a wealth of information that are not easily accessible by the "historical" measurements, in particular details on the surface plasmon propagation. The decaying length is readily accessible by this imaging technique as well as the interaction of surface plasmons by edges and defects in the silver film [7, 25]. This visualization of the plasmon decay definitively sparkles the idea that by structuring the silver film, the surface plasmon propagation can be manipulated in two-dimensions by micro-elements.

An example of such degree of manipulation through an engineering of the metal film is illustrated in Fig. 8.2. Electron-beam lithography was used here to fabricate a series of surface plasmon control elements including a launching pad, a waveguide taking the form of a metal stripe, a beam splitter consisting of a Bragg-like structure, and two additional orthogonal waveguides serving as output couplers (Fig. 8.2a). Using near-field optical microscopy, the manner with which the surface plasmon is developing through these elements is revealed. The near-field image of Fig. 8.2b elucidates the role of the funnel element (taper) used to couple the plasmon inside the stripe waveguide, emphasizes the existence of the different modes inside the stripe [9, 26–28], and allows to measure the splitting ratio of the Bragg reflector [29].

Another example of the imaging benefits brought by near-field optical microscopy is the ability of the technique to track in time and space surface plasmon field [30]. To do so, a heterodyne detection is employed by incorporating the signal path into an interferometer to retrieve amplitude and phase information about the plasmon field [31]. By combining this detection scheme with time-resolved femtosecond pulsed excitation, the surface plasmon wavepacket was visualized at different positions in time as it propagates inside a stripe waveguide [32]. The frames of Fig. 8.3 illustrate the propagation of a surface plasmon pulse inside a gold stripe (Fig. 8.3e). The pulse duration is 120 fs. The time difference between individual sequences, adjusted by an optical delay line, is 48 fs. The series of images taken at different time stamps allows

Fig. 8.3 a–e Near-field images of the surface plasmon wavepacket (amplitude). Each frame is delayed by 48 fs. f Topography of the Au stripe serving as a plasmon waveguiding structure. Reprinted with permission from [32]. Copyright 2008, American Institute of Physics



one to follow the surface plasmon as it leaves the launching site (Fig. 8.3a, bottom part of the picture), how it evolves in the waveguide (Fig. 8.3c), and finally how it is backscattered by the end of the structure (Fig. 8.3e, standing wave at the top of the waveguide). This remarkable visualizing apparatus is not only capable of imaging amplitude and phase of a surface plasmon field but also probes its ultrafast dynamics.

The examples shown above concerned the imaging of SPPs excited by total internal reflection that are leaky in the substrate by nature (see also Sect. 8.4). Obviously, bound modes can also be imaged by near-field techniques [33]. In that case, propagative bound SPPs are excited by momentum transfer on a defect or a grating. The mode propagation can then be investigated in the near field by raster scanning a local optical probe as above.

#### 8.2.2 Near-Field Imaging of Localized Surface Plasmons

Near-field techniques described in the previous section are also a prime tool to image surface plasmon in confined geometry, e.g. metal nanoparticles. Different approaches were developed to reveal the localized nature of this excitation. They are all based upon high-quality optical probe to achieve the lateral resolution needed (<50 nm). For a complete account, the reader is referred to a comprehensive review written by Wiederrecht [34].

Without going into a lengthy discussion about the experimental details characterizing all the possible variations of a near-field optical microscope [35], let us distinguish two main stream techniques that are generally used for surface plasmon imaging. The first approach relies on a near-field contrast obtained by transmission measurements whereby the light emitted by a sub-wavelength aperture is scanned over the sample of interest: the intensity transmitted through the sample, e.g. a nanoparticle, is

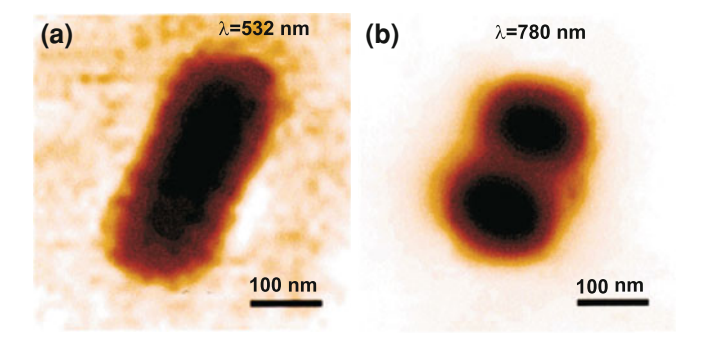


**Fig. 8.4 a** and **b** Near-field transmission images of gold nanorods taken at wavelengths of 532 and 780 nm, respectively. These two wavelengths approximately correspond to the transverse and longitudinal resonances of the nanorod. Reprinted with permission from [36]. Copyright 2004, American Chemical Society

recorded for each position of the tip. An example of near-field imaging of a plasmon field is shown in the transmission images of Fig. 8.4. The images are extracted from the work of Imura and coworkers [36]. The object is an isolated nanorod that was chemically synthesized and deposited on a glass substrate. The images were obtained by scanning a near-field aperture for two excitation wavelengths corresponding to the transverse and longitudinal resonances, respectively. The contrast in the images is understood in terms of local density of electromagnetic states [37]. Figure 8.4b, for instance, shows the surface plasmon oscillations with a node at the center of the rod and two maxima at the extremities when the nanorod is excited at its longitudinal resonance. For longer nanorods, the number of oscillations gradually increases from a dipole-like behavior to cavity-like resonators [10, 11, 36, 38, 39].

The second imaging approach is based on a local scattering of the electromagnetic field by a sharp tip. Because the tip can be made of homogeneous material without any aperture, e.g. gold, tungsten, or  $SiO_2$ , this technique is commonly referred to as apertureless near-field optical microscopy [41]. The tip acts as a scatterer by converting an evanescent component from a plasmon bound at a surface into a propagative wave that can be far-field detected [40, 42, 43]. To illustrate this conversion, Fig. 8.5 shows two near-field images of the surface of a gold film at percolation obtained for excitation wavelengths of 714 and 738 nm, respectively [40]. Semi-continuous metal films are notorious for producing randomly distributed regions of large field enhancement, generally used for surface-enhanced spectroscopies. The extreme localization of surface plasmons at metal clusters is responsible for this effect. Wavelength-dependent localizations are visible in Fig. 8.5 where the intensity of the near-field information was collected and demodulated at the vibration frequency of a vertically oscillating tip (tapping mode).

As discovered through the few examples illustrated above, near-field techniques are a method of choice for imaging surface plasmons with high lateral resolution because of their capability of accessing bound electromagnetic fields. It is also fully

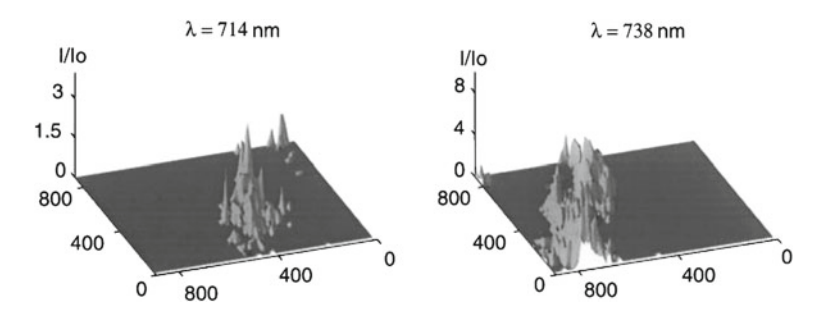


**Fig. 8.5** Near-field images of the intensity distribution at the surface of a percolated semi-continuous gold film. The localization of surface plasmons is responsible for the stochastic distribution of the intensity. The images were taken at two different wavelengths (lateral units are in nm). Reprinted with permission from [40]. Copyright 1999, American Physical Society

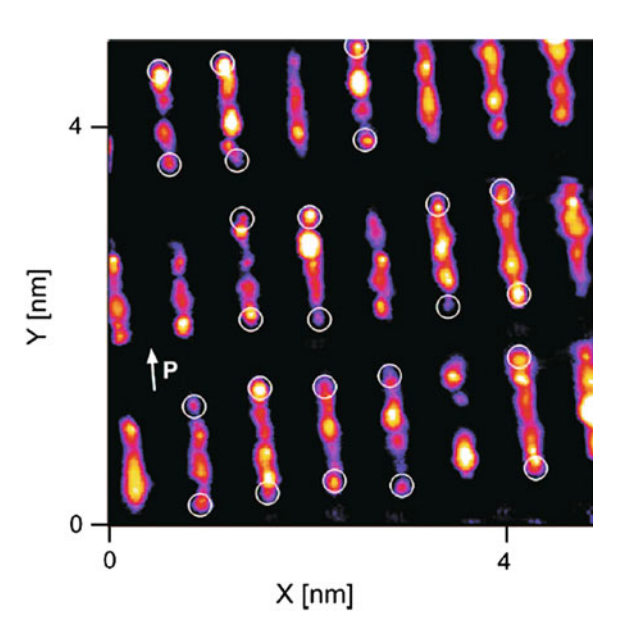
suited to investigate time-resolved dynamic and spectroscopic properties of surface plasmons. Because near-field techniques come in a variety of configurations, it is flexible with sample requirements. However, and it is a long-standing issue, near-field microscopy is strongly dependent on the quality of the near-field probe and is therefore directly impacting the reproducibility of a measurement. Finally, the approach can be considered as perturbative: the size of the probe is usually comparable to the size of the plasmonic nanostructures being imaged forming thus a coupled system.

#### 8.3 Photochemical Mapping

Harnessing light-matter interaction occurring at length scale much smaller than the wavelength has fostered advances in high-resolution optical lithography. The use of evanescent waves allowed patterning with sub-diffraction-limited resolution with ultrathin photoresists [44]. Inspired by these advances, it was soon realized that a local photopolymerization could serve as a replica of the near-field intensity bound to a nanostructure. This technique is not a direct imaging tool *per se* because the visualization relies on a second-order effect: typically a measure of a surface deformation by atomic force microscopy.

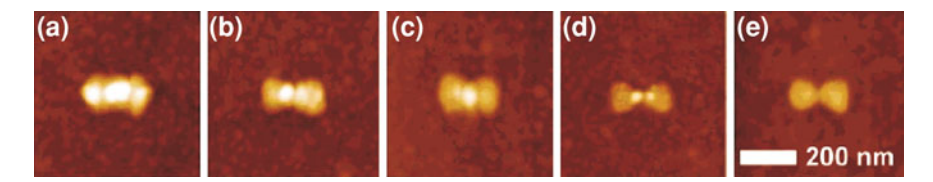
Several sensitive formulations were employed to mold or image confined fields, notably on metallic surfaces. One approach uses azo-dye molecules grafted on the backbone of a long polymer chain, typically poly(methyl methacrylate). This chromophore is known to be responsible for polymer mass transport through multiple *cis-trans* photo-induced isomerizations. Interestingly, the migration of the grafted polymer was found to be dependent on the orientation of the local electric field. For in-plane polarizations, the polymer moves laterally away from field maxima, while for an out-of-plane polarization the mass transport produces nanoscale protrusions [45, 46]. This is an important characteristic as it permits a complete vectorial

Fig. 8.6 Topographic images of the photo-induced surface deformation of 75 nm thick DR1MA/MMA layer deposited on silver nanorods. The topography reveals the location of localized surface plasmons associated with surface roughness. Reprinted with permission from [49]. Copyright 2009, American Chemical Society



description of the near-field that would be difficult to obtain with other techniques [47]. Using photo-initiated diffusion of the dye and its associated topography, surface plasmon dipolar responses and more complex field patterns were unambiguously imaged [48]. An example of the potential of the technique is illustrated in Fig. 8.6 where a photosensitive solution was coated on top of long silver nanowires [49]. Because the wires were fabricated by electron-beam lithography, their polycrystalline nature and associated surface roughness generated localized surface plasmons similar to the ones discussed previously in Fig. 8.5. After laser irradiation, the topography of the rods was imaged by atomic force microscopy. The white circles emphasize the formation of a protrusion at the extremities of a series of nanorods. The authors attributed this surface deformation to the presence of a longitudinally oriented enhanced electrical field. One should also note that protrusions are also visible on the length of the nanorods and are explained by roughness-induced plasmon localization and subsequent molecular accumulation.

Other type of photosensitive formulations were developed to specifically reveal the confined and enhanced surface plasmon field. This was demonstrated on strongly interacting resonant antennas [50] using two-photon polymerization. An example is shown in Fig. 8.7 [50]. Bowtie optical antennas with controlled gaps were fabricated by electron-beam lithography. The authors coated their antennas with a 75-nm-thick SU-8 resist layer. A 800-nm wavelength femto-second laser was chosen as the excitation source to promote two-photon absorption of the resist and subsequent cross-linking as well as a reasonable on-resonant excitation of the bowties. The frames were measured after a development procedure revealing only the areas where significant



**Fig. 8.7** Topography of a series of bowtie antennas after non-linear photopolymerization and resist development. The exposure was **a** 225  $\mu$ W, **b** 106  $\mu$ W, **c** 54  $\mu$ W, and **d** 27  $\mu$ W. **e** is an unexposed bowtie. Reprinted with permission from [50]. Copyright 2006, American Chemical Society

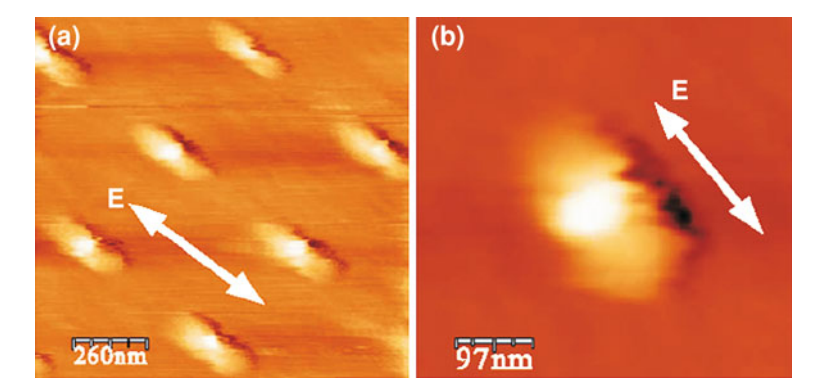


**Fig. 8.8** AFM images of a series of silver nanoparticles recorded after illumination of a self-developing photopolymer. The dipolar surface plasmon field triggered a local photopolymerization taking the form of two-side polymer lobe oriented with the electric field. Reprinted with permission from [51]. Copyright 2007, American Physical Society

non-linear absorption took place. The images demonstrate a polymerized area near the gap of the bowties corresponding to the primary region of field enhancement.

Similar approaches were used by employing a polymerization mechanism characterized by a threshold. In these systems, the polymerization is triggered by the formation of free radicals above a given incident energy [51]. The enhanced electromagnetic field associated with surface plasmon excitation can therefore locally initiate a nanoscale photopolymerization. A rinse-off procedure is then performed to remove the regions exposed below the threshold energy. A subsequent AFM analysis of the topography reveals the spatial extent of the polymerized areas corresponding to the footprint of the surface plasmon field. This is illustrated in Fig. 8.8 where the dipolar response of individual silver nanoparticles created side lobes of the polymer oriented along the polarization [51].

In principle, photochemical mapping of surface plasmon may approach molecular resolution. Another important aspect is that with specific molecules (Azo-dyes), the method is sensitive to the orientation of the electric field. This permits not only to map the region of high field intensity typical with surface plasmons, but also to control molecular diffusion with these systems. The limit of photochemical imaging is the restricted wavelength range that can be used. The conformational change and the

photopolymerization occur at the absorption maximum of the photoresists that are usually centered in the blue-red part of the visible spectrum. This imaging technique is therefore best employed for small nanoparticles. Finally, because it is a second-order measurement (topography), the interpretation of the results requires complex numerical modeling taking into account diffusion effects [52] and the presence of inhibitors.

#### 8.4 Leakage Radiation Microscopy

In this section, we present a mechanism whereby surface plasmons are detected and imaged. The technique uses the fact that surface plasmons traveling on a thin metal film are not completely evanescent as they lose a significant portion of their energy inside the substrate. This technique is referred to as leakage radiation microscopy. Reference [54] presents a review devoted to this approach and its applications to SPP imaging. Excitation of surface plasmon and detection of its leakage radiation were described as soon as 1976 [55]. However, it only relied on the angular emission of the leaky modes into the substrate giving access to the plasmon wavenumber, without direct observation of the SPP propagation. To the best of our knowledge, this pioneering work was not followed until 1996. Indeed, profiting from the local excitation of a near-field optical microscope, Hecht et al. investigated SPP propagation in both direct (image) and reciprocal (Fourier) planes [53] as presented in Fig. 8.9. In this example, the tiny aperture of a near-field probe acts as a local excitation source for surface plasmon excitation due to the large momentum spread brought by the size of the aperture. The energy lost by the plasmon in the substrate is collected via a high numerical aperture objective. The mode propagation is directly observed in the image plane and follows the expected 2D surface wave shape  $I(\rho,\phi) \propto \frac{e^{-\rho/L_{\rm SPP}}}{\rho} \cos^2 \phi$ with a propagation length  $L_{\rm SPP}=8\pm 2\,\mu{\rm m}$ . The excited plasmon decouples into the substrate at angle  $\theta_{SPP} = 44.3^{\circ}$  as directly visualized in the Fourier plane of Fig. 8.9c (corresponding to the SPP wavenumber  $k_{\text{SPP}} = nk_0 \sin \theta_{\text{SPP}} = 5.7 \,\mu\text{m}^{-1}$ ).

This has been followed by numerous works devoted to the direct imaging of SPP in various configurations [8, 56–63]. Some examples will be given below, after a brief introduction to leakage radiation microscopy. Particular attention will be given to describe the signal recorded in the image and Fourier planes.

#### 8.4.1 Leaky Mode Properties

#### **Guided Modes**

As an example, let us focus on plasmonic and photonic modes supported by the four-layer system: glass-metal-dielectric-air, presented in Fig. 8.10a. The main

A. Bouhelier et al.

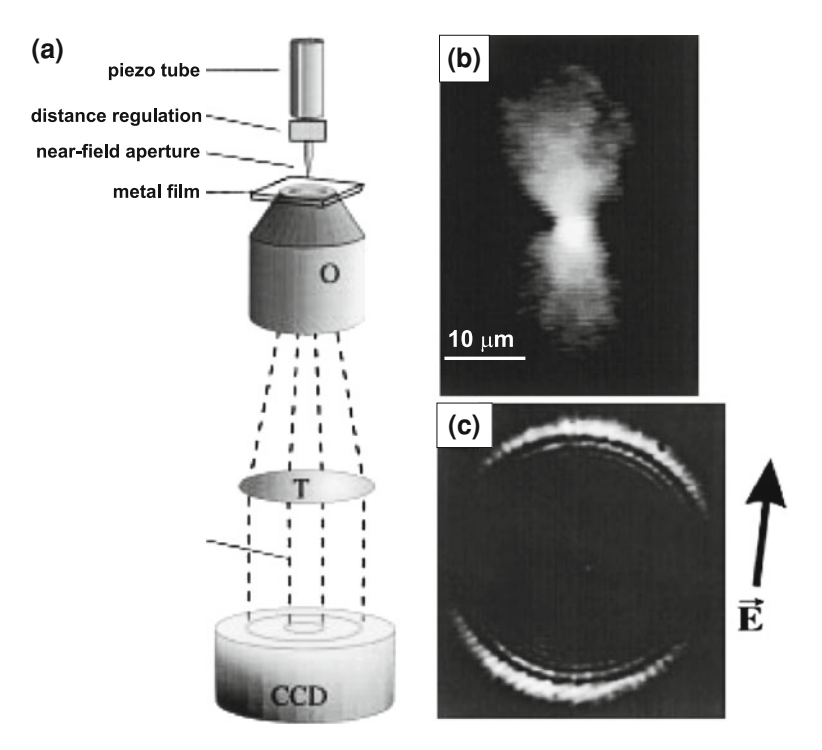


**Fig. 8.9** a Scanning Near field Optical Microscope (SNOM) setup for imaging the surface plasmon in the image plane (b) and Fourier plane (c). The SPP is locally excited using a near-field optical probe. Reprinted with permission from [53]. Copyright 1996, American Physical Society

properties of propagative surface plasmon-polaritons can be deduced by this 1D model. Moreover, 2D waveguide can be approximated by a combination of two 1D planar waveguides by applying the effective index model so that the discussion below is easily generalized to more complex configurations [64–67].

For simplicity, we fix the gold thickness to d=50 nm, the wavelength in vacuum is  $\lambda=\frac{2\pi c}{\omega}=1.55\,\mu\mathrm{m}$  (telecom C band), and the polymer thickness (PMMA for polymethylmethacrylate) to t=300 nm. The influence of the gold thickness will be discussed especially in relation with leakage radiation microscopy. The surface plasmon-polariton mode is TM polarized. It writes  $E=E_p(z)e^{i(k_xx-\omega t)}$ , where  $E_p$  is the component in the incident plane and  $k_x$  is the propagation constant. Figure 8.10b describes the considered system and defines the used notations.

In each layer  $m \in \{1, 2, 3, 4\}$ , the wavevector writes  $\mathbf{k}_m = (k_x, k_y = 0, w_m = \sqrt{\varepsilon_m k_0^2 - k_x^2})$  and the electric field  $\mathbf{E}_m = \mathbf{E}_m^+ + \mathbf{E}_m^-$  has the form (the dependence on  $e^{-i\omega t}$  is omitted):

$$E_m = e_m^+ e^{i(k_x x + w_m z)} + e_m^- e^{i(k_x x - w_m z)}$$
(8.2)

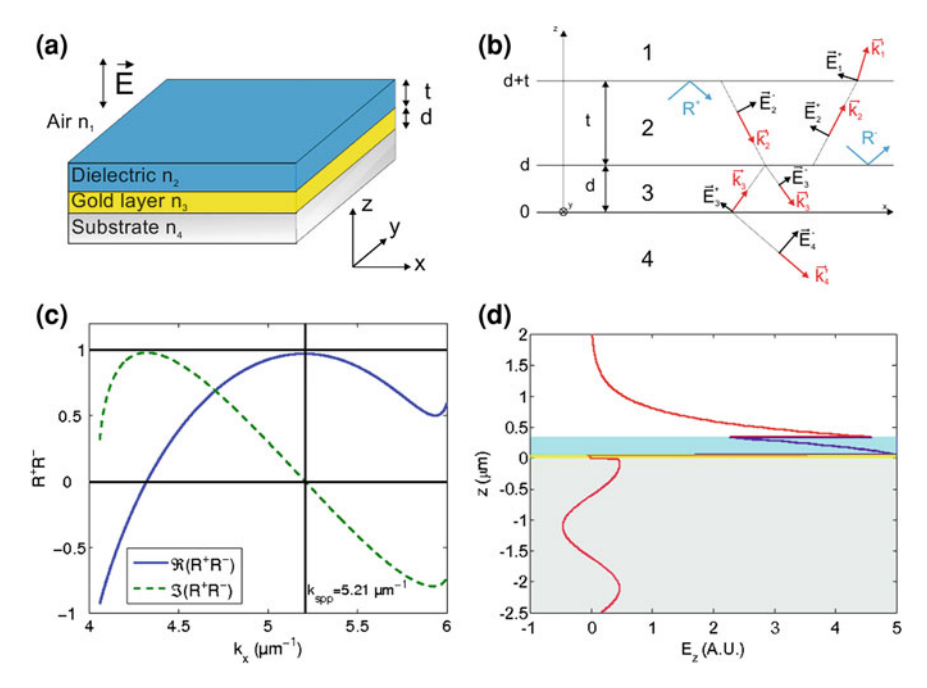


**Fig. 8.10** a Representation of a multilayer system glass-gold-dielectric-air. The two extreme layers are semi-infinite. The metal and dielectric layers have thicknesses d and t, respectively. The refractive indices at  $\lambda=1.55\,\mu\mathrm{m}$  are  $n_4=1.5,\,n_3=0.55+i11.5,\,n_2=1.49$  (corresponding to PMMA resist), and  $n_1=1$ . **b** Representative scheme and used notations. **c** Representation of the real and imaginary parts of  $R^+R^-$  as a function of  $k_x$  when  $d=50\,\mathrm{nm},\,t=300\,\mathrm{nm}$ , and  $\lambda=1.55\,\mu\mathrm{m}$ . **d** Mode electric field amplitude along the multilayer system. Adapted from [69]

with  $\boldsymbol{e}_m^+$  associated to an ascending wave and  $\boldsymbol{e}_m^-$  to a descending wave.

The resonance condition is easily assessed from the reflection coefficients  $R^+ = e_2^-/e_2^+$  at the PMMA-air and  $R^- = e_2^+/e_2^-$  at the PMMA-gold interface (see Fig. 8.10b). The medium (2) supports a non-zero electric field if and only if [68]:

$$R^+R^- = 1. (8.3)$$

Figure 8.10c shows the real part and the imaginary part of  $R^+R^-$  as a function of  $k_x$ . The system supports a mode for  $k_x = k_{\rm SPP} = 5.21\,\mu{\rm m}^{-1}$  because  $\Re(R^+R^-) = 1$  and  $\Im(R^+R^-) = 0$ .  $k_{\rm SPP}$  is the propagation constant of the mode supported by this system. We define equivalently the *effective index* of the mode  $\Re(N_{\rm eff}^*) = k_{\rm SPP}/k_0$ . Here,  $\Re(N_{\rm eff}^*) = 1.285$ .

Importantly, as  $1 < N_{\text{eff}}^* < n_4$  with  $n_4 = 1.5$ , this mode is *radiative* in the substrate but evanescent in the superstrate (air), as it clearly appears in Fig. 8.10d. It is a so called leaky mode.

Although this simple description gives access to the guided modes propagation constant, it does not allow one to estimate the mode propagation constant.

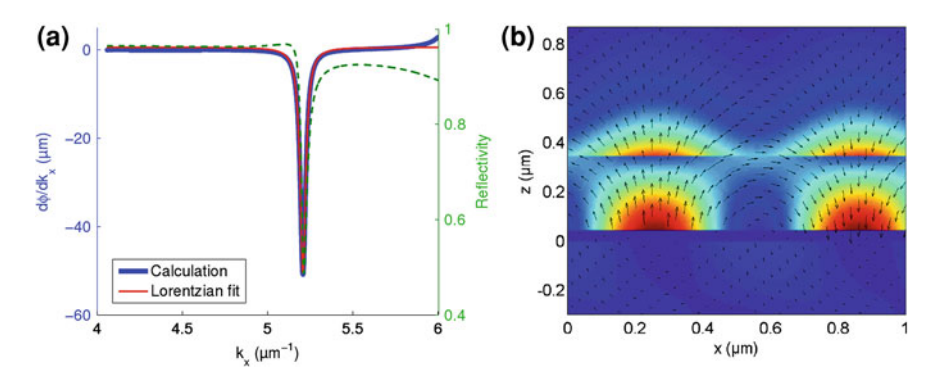


**Fig. 8.11** a Representation of the phase denominator derivative of the reflection coefficient  $\frac{d\phi}{dk_x}$  as a function of  $k_x$  (*continuous line*). The reflectivity is also represented (*dashed line*). **b** Mode intensity profile

Parenthetically, this shows that the SPP propagation is fairly described by the internal reflections of a ray [65]. More accurate description, including propagation length, is achieved by the reflection pole method (RPM) [65, 70].

RPM relies on the location of singularities of the reflectivity R instead of the direct calculation of R. This method is presented in detail in Ref. [70] and in the chapter by D. Maystre of the present book. We simply indicate the essentials in the following. The multilayer reflection coefficient is obtained using the transfer matrix formalism. Since a guided mode corresponds to the reflection coefficient singularity, resonance condition is precisely deduced from the pole of the coefficient. Indeed, it can be shown that a pole is accurately located working on the phase  $\phi$  of the denominator of that reflection coefficient. Practically, the derivative  $\frac{d\phi}{dk_x}$ , with respect to the wavenumber, follows a Lorentzian profile centered at the mode propagation constant  $k_{\text{SPP}}$  and with a full width at half maximum (FWHM)  $\Delta k = 1/L_{SPP}$ . In addition to precisely locating the mode propagation constant, this method also provides an accurate value for its propagation length. Finally, we recover the very general physical property that a supported mode presents a Lorentzian profile [71]. We will recover this property in different observables associated to the guided mode and will show that it is of great interest to interpret leakage radiation micrographs [54]. Figure 8.11a represents  $\frac{d\phi}{dk}$ . A Lorentzian fit gives  $k_{SPP} = 5.208 \,\mu\text{m}^{-1}$  and  $L_{SPP} = 24.70 \,\mu\text{m}$ . In this figure, we also traced the reflectivity R. It follows a similar behavior near the resonance as discussed later on [2].

#### Loss Mechanisms

Two types of losses are responsible for the low plasmon propagation lengths [2, 57] as schematically represented in Fig. 8.12: namely (i) intrinsic losses with the rate per unit length  $\Gamma_i$  connected with the mode dissipation in the metal and

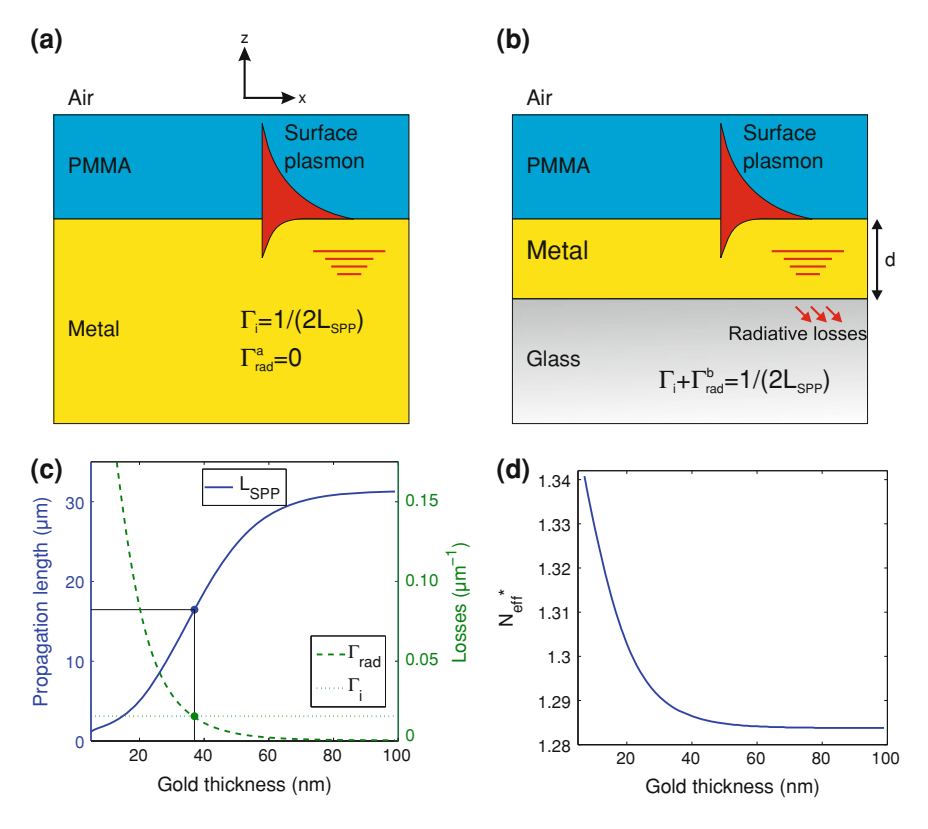


**Fig. 8.12** a Representation of a three-layer system metal-dielectric-air that does not support any radiative losses. **b** Representation of a four-layer system glass-metal-dielectric-air that supports radiative losses ( $\Gamma_{\rm rad}$ ) and intrinsic losses ( $\Gamma_i$ ). **c** Variation of the losses rates and propagation length as a function of the gold thickness. **d** Variation of the effective index as a function of the gold thickness. The wavelength is  $\lambda = 1.55 \, \mu \rm m$  and the PMMA thickness is  $t = 300 \, \rm nm$ 

(ii) radiative losses, with the rate  $\Gamma_{\text{rad}}$ , connected with leakage into the substrate. The mode propagation length is given by:

$$L_{\rm SPP} = \frac{1}{2(\Gamma_{\rm rad} + \Gamma_i)},\tag{8.4}$$

where  $\Gamma_i$  can be estimated considering a semi-infinite gold film in Fig. 8.12a, and using the RPM. This assumes that the intrinsic losses do not depend on the gold film thickness [2]. Radiative losses rate is then obtained as  $\Gamma_{\rm rad}(d) = 1/2L_{\rm SPP}(d) - \Gamma_i$  (Fig. 8.12b). In Fig. 8.12c, we represent the evolution of these losses as well as the propagation length as a function of the gold thickness. The radiative losses decrease with the gold thickness and are almost null above 70 nm of gold. The critical thickness for which  $\Gamma_i = \Gamma_{\rm rad}(d \approx 40\,{\rm nm}$  in Fig. 8.12c) will be discussed later.

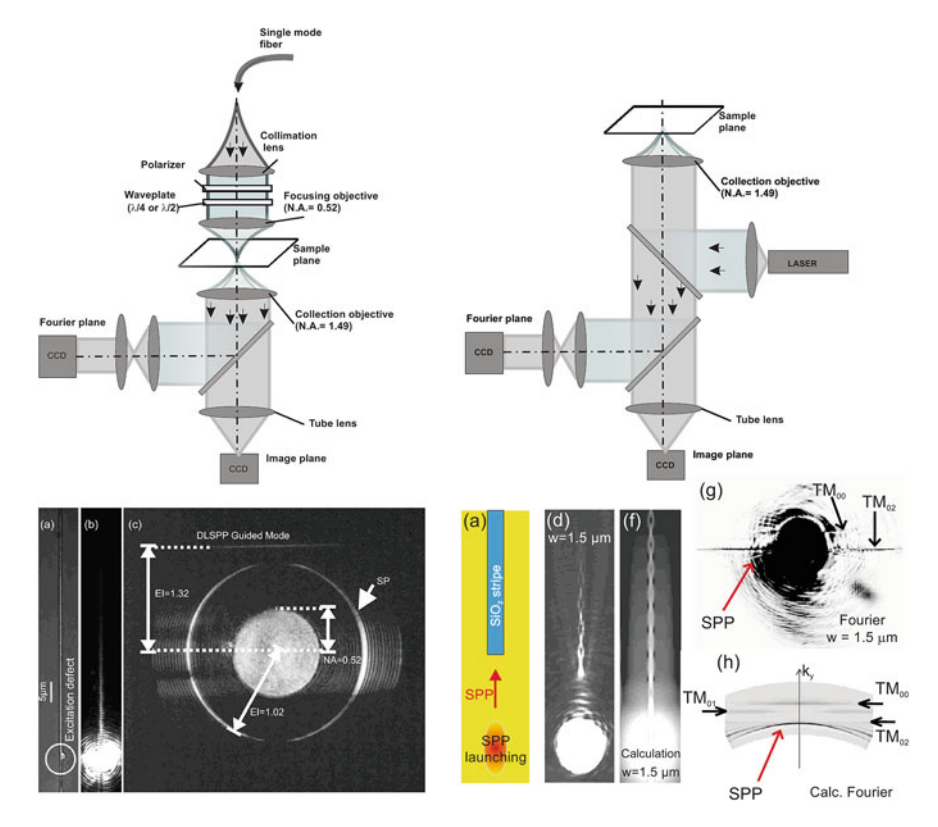


**Fig. 8.13** Leakage radiation microscopes setup in *left* diascopic and *right* episcopic configuration. In diascopic configurations (*left column*), the propagating SPP is excited by momentum transfer via scattering on a defect (*white circle* in **a**). The mode propagation is analyzed in both the image (**b**) and Fourier (**c**) planes. In episcopic configuration (*right column*), the SPP is directly excited by total internal reflection and recorded in image (**d**) and Fourier (**g**) planes. **f** and **h** represent the corresponding numerical simulations. SPPs propagate along plasmonic waveguide made of dielectric ridge deposited on a gold film, in monomodal or multimodal conditions. Reprinted with permission from [62]. Copyright 2008, American Physical Society

#### 8.4.2 Leakage Radiation Microscopy

Various leakage radiation microscope setups exist that can be arbitrarily classified depending on the illumination process. First experiments relied on plasmon excitation by momentum transfer in the near field using scattering on a small defect (surface rugosity [55] or lithographied nanostructures [60]) or the local probe of an optical near field microscope (Fig. 8.9) [8, 53]. The top panel of Fig. 8.13 presents two variants of leakage radiation microscope setup. In the diascopic configuration (left), the SPP is excited from the top by scattering on a defect. The mode leaking into the substrate (proportional to  $\Gamma_{\rm rad}$ ) is detected in the far field [8, 53, 54, 72].

The advantage of leakage radiation microscopy technique is its simplicity and versatility. However, it relies on the radiative losses of the mode, implying thus the use of thin metallic films in order to increase the available signal at the expense of propagation length.

Leakage radiation microscopy gives an information on the electromagnetic field intensity of the surface plasmon and its associated wavevectors content by correctly visualizing the image plane or the Fourier plane, respectively [54, 60, 73]. Examples of this combination are demonstrated in the lower panels of Fig. 8.13. Here, plasmonic waveguides constituted of a polymer section fabricated on a gold layer are considered (Fig. 8.13a). The TM-polarized magnetic field writes  $\mathbf{H}_{\mathrm{SPP}}(x, y, z) = H_{\mathrm{SPP}}(y, z)e^{ik_{\mathrm{SPP}}x}e^{-x/(2L_{\mathrm{SPP}})}\mathbf{e}_{\mathbf{y}}$ . The intensity recorded in the direct plane is qualitatively:

$$I(x, y) \propto |\mathbf{H}_{SPP}(x, y, z_0)|^2 = |H_{SPP}(y, z_0)|^2 e^{-x/L_{SPP}},$$
 (8.5)

where  $z_0$  is the focus point of the detection objective. The mode propagation constant is therefore directly measured from the intensity exponential decay. The leakage image of Fig. 8.13b shows how the surface plasmon mode is guided by the polymer waveguide. The bright spot at the bottom of the image is the location of excitation (diascopic illumination) and the surface plasmon develops as an exponentially attenuated streak from the bottom to the top of the image.

In the Fourier plane, the recorded signal is approximated to (tilde stands for the Fourier transform):

$$I(k_x, k_y) \propto |\tilde{\mathbf{H}}_{SPP}(k_x, k_y, z_0)|^2 = \frac{|\tilde{H}_{SPP}(k_x, z_0)|^2}{(k_y - k_{SPP})^2 + (1/2_{L_{SPP}})^2}.$$
 (8.6)

In Fig. 8.13c, the Fourier image presents a horizontal line, with a *constant* wavevector component along the waveguide axis at  $k_y = k_{\rm SPP}$  corresponding to the propagation constant of the mode (effective index  $\Re(N_{\rm eff}^*) = k_{\rm SPP}/k_0 = 1.32$ ). Note that the mode profile in k space follows a Lorentzian profile as it will be shown in the next paragraph. The semi-continuous circles at effective index  $\Re(N_{\rm eff}^*) = 1.02$  correspond to the film SPP mode propagating isotropically at the metal surface.

It is also possible to excite the plasmon in Kretschmann-like configuration as schematically shown in the right panel of Fig. 8.13. Here a high numerical aperture objective is used to provide the resonant wavevectors contained inside a weakly focused beam and the optical support to detect plasmon's leakage [57, 72]. Note that in this case, the optimal contrast in the Fourier plane is obtained for metal thickness such that  $\Gamma_{\text{rad}} = \Gamma_i$ . Indeed, the detected signal is nothing else than the reflectivity R. R also follows a Lorentzian profile near the SPP excitation incident angle [2]:

$$R = 1 - \frac{4\Gamma_i \Gamma_{\text{rad}}}{(k_x - k_{\text{SPP}})^2 + (\Gamma_i + \Gamma_{\text{rad}})^2},$$
(8.7)

so that R = 0 for  $\Gamma_{\text{rad}} = \Gamma_i$  (see also Fig. 8.12). This null reflectivity originates from destructive interference between the incident field and the mode leakage [2].

For comparison purposes, Fig. 8.13d shows an image of a surface plasmon excited with this scheme and propagating inside a multimodal waveguide confirmed by the presence of a beating between several modes visible in the recorded image and in agreement with numerical simulation (Fig. 8.13f). All the supported leaky modes are discriminated in the Fourier plane of Fig. 8.13g and h since they appear at different propagation constants. In addition, the Fourier signal presents negative contrast inside the incident spot (according to reflectivity decreasing near the resonance), whereas it presents positive contrast outside this spot since no interference with the excitation beam occurs in this k space region [62].

LRM was subsequently applied to many in-plane plasmonic passive components such as beam splitters, plasmonic lenses and dioptres [72], gratings, Bragg mirrors [58, 60], and waveguides [62, 67, 74]. In particular, LRM images were compared to near-field optical measurement and showed good agreement in the cases considered [72, 74]. LRM appears thus in this context as a complementary far-field optical method to near-field techniques.

Figure 8.14 shows another example of the versatility of this imaging tool applied to SPP Bragg mirror [58, 60, 61]. The mode propagation is directly observed in the image plane (Fig. 8.14a) and follows the expected intensity distribution  $I(\rho,\phi) \propto \frac{e^{-\rho/L_{\rm SPP}}}{\rho} \cos^2\phi$  already observed in Fig. 8.9. The propagation constant is determined in the Fourier plane (Fig. 8.14b) since the mode profile follows a Lorentzian shape, centered on the propagation constant  $k_{\rm SPP} \approx 8\,\mu{\rm m}^{-1}$  and with a full-width at half-maximum FWHM  $\Delta k = 1/L_{\rm SPP}$  as expected. The SPP reflection on a Bragg mirror is visible in both the image and Fourier planes. Finally, an extended grating, similar to the Bragg mirror used in Fig. 8.14a–d,is investigated in Fig. 8.14e and f. The opening of a gap is clearly visible in the Fourier plane. A plasmon propagating with a wavevector within this forbidden gap will be reflected by the grating as observed in the image [58, 61].

## 8.4.3 Leakage Radiation Microscopy of Surface Plasmon Coupled Emission

Finally, we would like to mention surface plasmon coupled emission developed by Lakowicz and coworkers recently [59, 75–78]. In this case, SPPs are excited by fluorescent molecules dispersed on the metallic film or plasmonic wave guide. The high momentum of the dipolar fluorescent emitters allows to excite all the supported modes. It can then be profitably associated to leakage radiation microscopy to investigate mode propagation [63, 79] or can serve as an imaging contrast. We will briefly come back to that point in Sect. 8.5. Since the excited emitters are non-radiatively coupled to the SPP, this coupling can be regarded as *spontaneous* emission of surface plasmon-polariton. An example is given in the inset of Fig. 8.15. A plasmonic waveguide is doped with lead-sulfide (PbS) quantum dots (QDs) optically pumped at  $\lambda = 532$  nm and emitting in the near infrared. Signals are recorded around the emission wavelength. The Fourier plane was taken for a global excitation of the doped

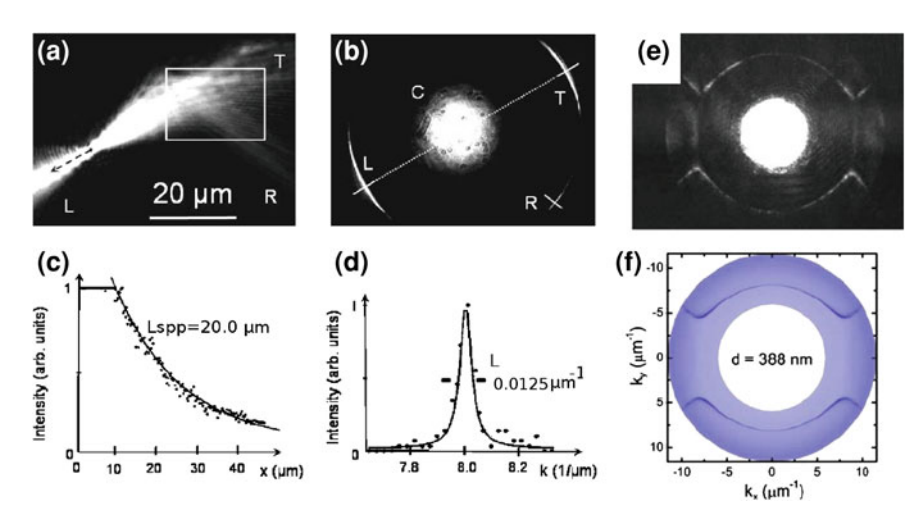


Fig. 8.14 Leakage radiation micrograph in the image (a) and Fourier (b) planes. The SPP is launched on a 50 nm gold film by focusing a laser beam ( $\lambda_0 = 800 \, \mathrm{nm}$ ) on a lithographied defect and developed symmetrically on both sides (L and T) of the defect. The plasmon is partially reflected toward R by a mirror grating located in T. c, d Cross-cut in the image and Fourier planes, respectively. Solid lines represent an exponential or Lorentzian fit. e, f Measured (e) and calculated (f) Fourier images for SPP supported by an extended ( $100 \times 100 \, \mu \mathrm{m}$ ) grating. Reprinted with permission from [60, 61]. Copyright 2006, American Insitute of Physics. Copyright 2007, American Optical Society

waveguide and clearly reveals the  $TM_{00}$  SPP mode guided along the waveguide as well as  $TM_0$  and  $TE_0$  planar film modes supported in the large tapered region [79]. The direct image was measured for a focused excitation of the QDs. The two traces propagating away from the excitation zone are associated to the guided SPP mode.

Moreover, the excited emitters can act as a gain medium for a SPP signal propagating in this medium, since then *stimulated* emission of SPP could occur. Figure 8.15 displays a recent experiment that demonstrated gain assisted propagation characterized by leakage radiation microscopy. The propagation length presents a typical threshold effect as a function of pump irradiance. The mode effective index FWHM  $\Delta n_{\rm eff}$  is narrowed. This narrowing reveals both (i) propagation length increase since  $\Delta n_{\rm eff} \propto 1/L_{\rm SPP}$  and (ii) QDs emission narrowing due to stimulated emission [79, 80].

The advantage of leakage radiation microscopy relies on its simplicity and easy way to image either in the direct or in Fourier plane giving access to both mode propagation constant and length of waveguided SPP modes. Multimodal systems are also accurately investigated. To sum up, the main advantage of this technique is its simplicity of implementation. It is adapted for a rapid investigation of plasmon propagation in various devices, with *direct* measure of the *complex* mode effective index. The drawbacks are the limited spatial resolution (diffraction) and the restriction to leaky plasmons.

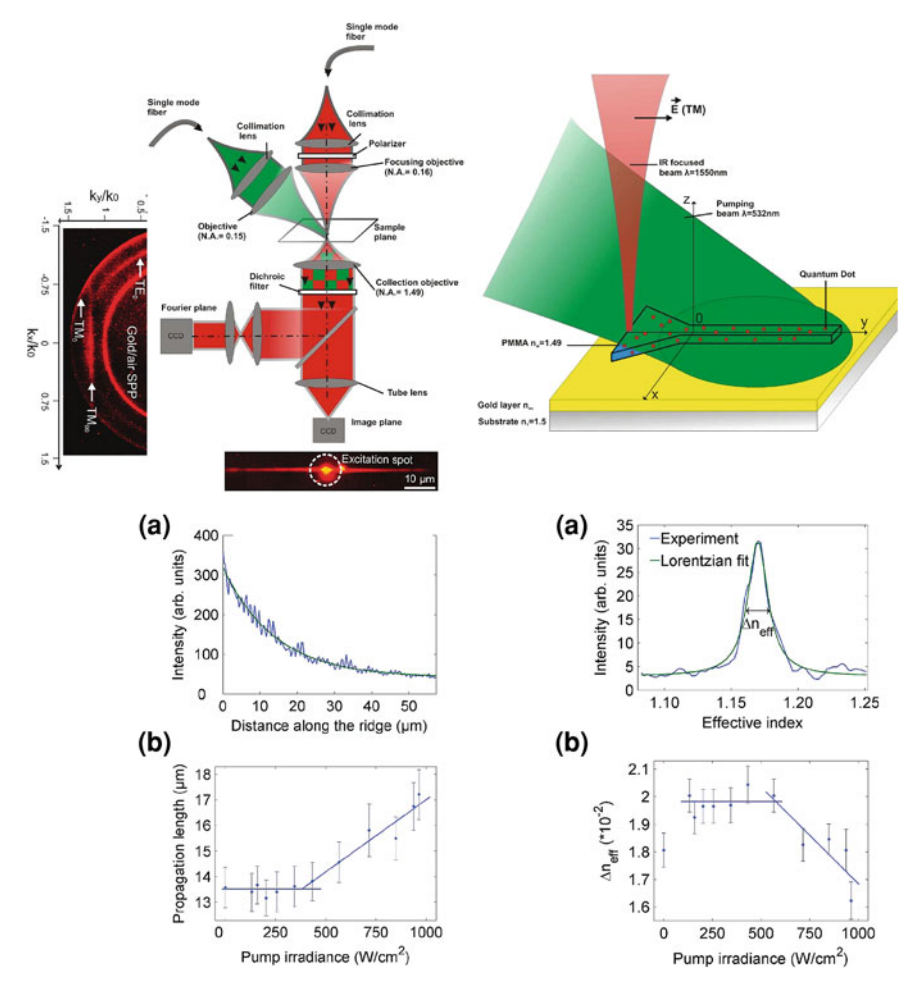
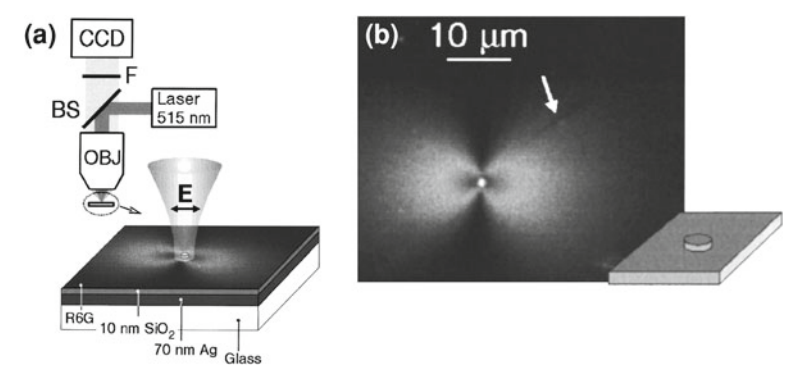


Fig. 8.15 **a** and **b** Schematic description of gain-assisted propagation in plasmonic waveguide investigated by leakage radiation microscopy of surface plasmon emission. The SPP signal is excited in the near-infrared ( $\lambda=1.55\,\mu\text{m}$ ). QDs doping the waveguide are optically pumped at  $\lambda=532\,\text{nm}$  and emit in the near infrared. Insets show the images recorded for an infrared emission in the Fourier and image planes for QDs optically pumped at  $\lambda=532\,\text{nm}$ , in the absence of SPP signal. **c** and **d** Propagation length without and with QDs optical pumping, respectively. **e** and **f** Effective index FWHM without pump and as a function of incident pump irradiance, respectively. Reprinted with permission from [79]. Copyright 2009, American Chemical Society

#### **8.5** Fluorescent Probes

In this section, we describe how surface plasmon fields can be imaged in real time by detecting the fluorescence of a molecular film close to the plasmon carrying metal surface. This method was nicely demonstrated by Ditlbacher and coworkers [81]



**Fig. 8.16** a Schematic of the experimental setup used to image the surface plasmon distribution by fluorescence emission. **b** Intensity distribution of the surface plasmon imaged by the fluorescence signal emitted by a layer of reporter molecules. Reprinted with permission from [81]. Copyright 2002, American Institute of Physics

as illustrated in Fig. 8.16. The basic principle of this imaging technique resides on the high coupling probability between a dipole placed close to an interface (e.g. a fluorescent dye) and a surface plasmon. In the example shown, Rhodamine 6G molecules were deposited by vacuum sublimation on a 10 nm thick  $SiO_2$  layer covering a silver film to prevent quenching. A surface plasmon was excited by focusing a laser matching the absorption of the molecule onto a man-made defect acting as a point source. The fluorescence response of the molecular layer was then imaged by a microscope objective and detected by a CCD camera. The intensity distribution follows again a  $\cos^2 \phi$  characteristics of a point-like excitation. This type of distribution has already been observed for a near-field excitation obtained by leakage radiation microscopy (Figs. 8.9 and 8.14).

The advantages of fluorescent microscopy are the benefit of a local probe with a large choice of chromophores or QDs (SPP matching wavelength). As already mentioned in the previous section, this type of imaging is compatible with direct space and reciprocal space investigations (Fourier plane). However, only qualitative information can be extracted as the emission wavelength is usually quite broad and the spatial resolution remains limited by the diffraction. The technique is also plagued by the poor long-term stability of the fluorescent species (photo-bleaching, blinking, etc.)

## 8.6 Dark-Field Microscopy

Dark-field optical microscopy refers to a technique that discriminates the contribution of the light used to illuminate a specimen from the light scattered by the specimen. Applied to the purpose of this chapter, dark-field optical microscopy is a straightforward technique for imaging localized surface plasmon on nanoparticles.

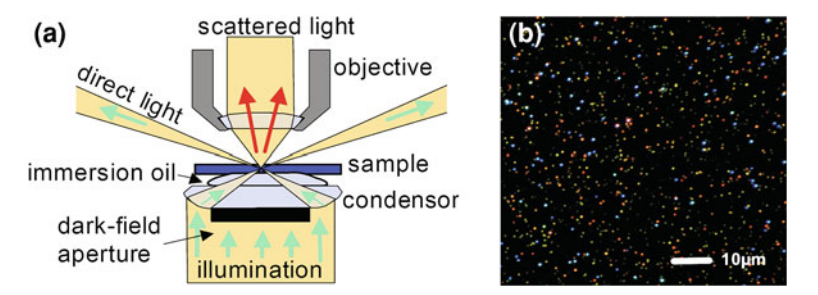


**Fig. 8.17** a Schematic of the setup used for dark-field transmission microscopy. Large-angle illumination of the specimen (e.g. nanoparticles) results from a beam stop placed on the condenser. The objective is collecting only the scattered rays. **b** True-color dark-field image of light scattered by isolated metal nanoparticles dried on a glass substrate. The different colors result from the spectral positions of the plasmon resonances. Reprinted with permission from the Ph.D. dissertation of C. Sönnichsen, Münich (2001) [82]

Even at resonance, metallic nanoparticles are characterized by a relatively low extinction cross-section, typically of the order of  $1 \times 10^{-15}$  cm<sup>2</sup>. This is equivalent to saying that one photon in every 10<sup>15</sup> will be scattered or absorbed by a nanoparticle. Dark-field microscopy is seeking after this weak interaction process buried among an overwhelming background of unperturbed photons. The basic units forming a dark-field microscope are depicted in Fig. 8.17a for a transparent sample [82]. The specimen is illuminated with a dark-field condenser. This type of condenser differs from standard wide-field ones by the fact that the central region of the lens is physically masked by an aperture. The specimen is therefore illuminated with annulus of light with large incident angles (incoming green arrows). For oil-immersion dark-field condenser, the useful numerical aperture (NA) lies above 1 (evanescent illumination). For dry condenser, the N.A. is typically comprised between 0.85 and 0.95. The principle of the technique is to collect the scattered light with an objective having a N.A. smaller than the dark-field condenser, typically N.A. = 0.65 (outgoing red arrows). Without any sample to scatter incoming photons, the transmitted light is not collected by the objective (outgoing green arrows) and the background remains dark.

Figure 8.17b shows the imaging potential of dark-field microscopy [82]. In this image, gold and silver nanoparticles were randomly deposited on a glass substrate. Under dark-field illumination, the nanoparticles are scattering centers and become visible. The color associated with each nanoparticle reflects the spectral position of their surface plasmon resonance: blue for silver spheres, green to yellow for gold, and red for small aggregates. This shape-induced color variation is perhaps better illustrated by Fig. 8.18a and b. The top row shows a series of electron-beam fabricated metal nanoparticles with controlled size and shape. The bottom row are the corresponding dark-field images [83]. The short axis of the nanorods exhibits a surface plasmon resonance located in the blue side of the visible spectrum, while the largest triangular particle resonates in the red.

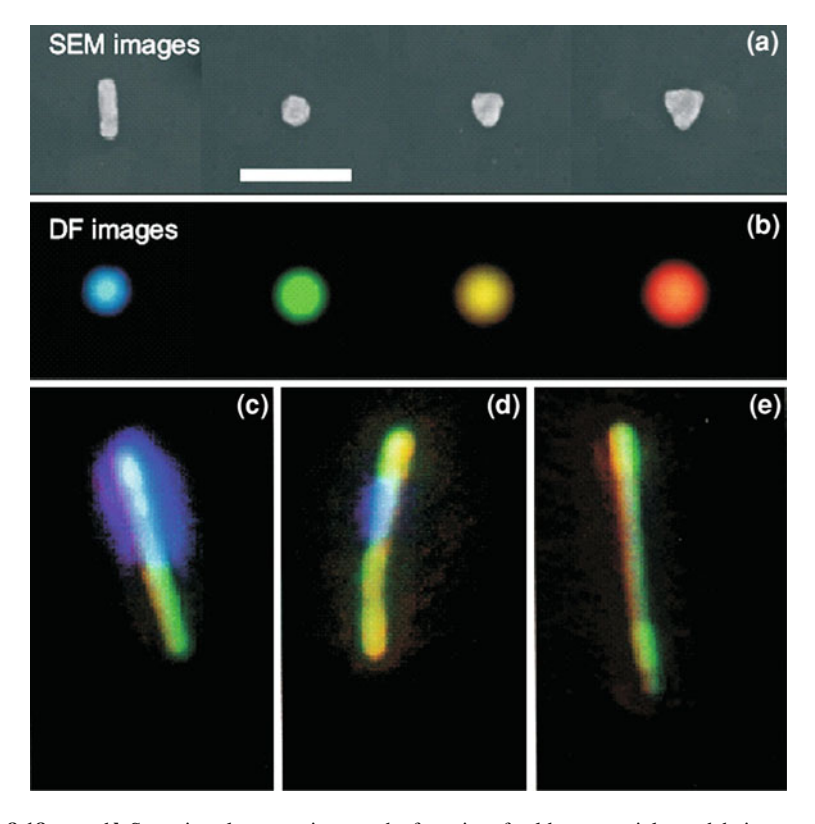


**Fig. 8.18** a and **b** Scanning electron micrograph of a series of gold nanoparticles and their respective dark-field images. *Scale bar*: 300 nm. Reprinted with permission from [83]. Copyright 2007, John Wiley and Sons. **c–e** Dark-field images of composite nanowires constituted of silver (*blue*), gold (*green*), and nickel (*brownish*) segments. The nanowires are approximately 5 μm long. Reprinted with permission from [84]. Copyright 2002, American Chemical Society

Another example of dark-field surface plasmon imaging is shown in Fig. 8.18c–e. The frames are true-color images of composite nanowires [84] illuminated with a white-light illumination polarized along their short axis. These wires are formed by adding segments of different metals here gold, silver, and nickel. Even though the wires have a very thin section (ca. 30 nm), the scattering strength associated with the surface plasmon resonances allows to distinguish individual segments constituting a single nanowire. For instance, in Fig. 8.18c, the blue portion corresponds to a silver segment and the green one to a gold segment. The images of Fig. 8.18d and e depict a wire where a silver section, respectively, a nickel section, is sandwiched between two gold segments.

Through the few examples briefly illustrated above, dark-field microscopy is a relatively simple approach that can be used to image localized surface plasmons. Because most spectrographs have imaging capabilities, spectral and spatial characteristics of surface plasmons in confined geometries are accessible for ensemble measurements (arrays) as well as at a single particle level. However, this type of microscopy lacks the spatial resolution that can be reached by near-field techniques since it is plagued by the diffraction limit. The technique is also restricted to large particles with dimensions typically larger than 50 nm. For smaller particles, the extinction cross-section is dominated by absorption and scattering becomes negligible. Another limitation of this type of microscopy is that the result obtained is equivocal: a silver nanorod excited along its main axis may exhibit a similar response than a small cluster or an irregular large gold particle or a triangular-shaped nanostructure. Without prior knowledge of the sample investigated (electron microscopy, AFM) [85], it is very difficult to provide a conclusive answer about the shape and the type of plasmonic structure imaged with dark-field microscopy.

## 8.7 Confocal Laser Microscopy

The principle of confocal microscopy resides in the use of a diffraction-limited point-like illumination and a pinhole placed at the conjugated image plane. To the difference with dark-field microscopy described above where the complete field of view is illuminated, a tightly focused laser beam, *i.e.* the point source, is raster scanned in space and the specimen's response is recorded for each pixel to reconstruct a complete three-dimensional image of the specimen. Out-of-focus contribution is spatially filtered out by the pinhole. In the context of surface plasmon imaging, a three-dimensional map and the pinhole are usually not required since the height of the plasmonic nanostructures is very well located axially (glass/air interface) and is much smaller than the axial resolution of the microscope ( $\sim \lambda$ ). From the few particularities highlighted above, it is clear that this imaging technique is better suited to investigate localized surface plasmons than propagating surface waves.

Several confocal techniques were developed to access the plasmon response of nanoparticles. The reader is referred to an article written by Van Dijk, Lippitz, and Orrit [86] to find a comprehensive review describing far-field measurements at the single particle level. Because plasmonic particles are usually smaller than the resolution capability, the images obtained do not directly inform about the spatial extent of the surface plasmon. However, at the surface plasmon resonance, scattering and absorption efficiencies are modified and can be measured by confocal techniques.

The extinction of a tightly focused laser beam by a 20-nm gold particle approaches  $10^{-3}$  [87]. By spatially modulating the position of the nanoparticle inside the laser spot and detecting the differential transmission  $\Delta T/T$  with a lock-in amplifier, Arbouet and coworkers were able to quantify the absorption cross-sections of particles as small as 5 nm [87, 88]. Small particles were also identified and their plasmon resonances measured by combining a coherent white-light continuum excitation with an interferometric detection of the backscattered signal [89]. The reflection of the continuum at the interface interferes with the component scattered by a metal nanoparticle to render a size-dependent contrast of the confocal images: large particles (>30 nm) appear brighter than the background because scattering

dominates, while for smaller particles the response is purely absorptive and a dark contrast is observed.

Because the process of absorption is dissipative, the energy accumulated by an illuminated metal particle is converted into heat by thermalization of the hot electrons. The particle then cools down by exchanging heat with its environment modifying thus the local refractive index n. Photothermal imaging takes advantage of  $\delta n/\delta T$  by detecting the resulting phase shift in a dual-beam interferometer [90]. The first beam, resonant with the surface plasmon resonance, deposits energy on a nanoparticle, while a second beam probes the temperature-dependent local refractive index. Using photothermal imaging, the homogeneous linewidth of surface plasmon resonance can be determined by probing the intrinsic response at the single particle level [91].

For particle size in which the scattering cross-section still dominates the extinction cross-section, an efficient spatial filtering of the illumination wave-vector permits one to measure the differential scattering cross-section of resonant metal nanoparticles [92]. This can be achieved by detecting a portion of the frustrated evanescent spectrum scattered by the object in the so-called forbidden light angular region [93–95]. Figure 8.19a illustrates the contrast obtained with this method. In these images, the bright spots correspond to the intensity scattered by coupled dimers for a polarization aligned with the main axis of the dimer (top scan) and perpendicular to it (bottom scan). The distance separating the dimers is decreasing from left to right down to touching dimers (arrows). For a polarization along the dimer, the three-dimensional rendering shows that the scattered intensity steadily increases to suddenly drop for the contacted particles, whereas the intensity stays at the same level for the orthogonal polarization. The contrast is understood as follows. When the surface plasmon wavelength matches that of the excitation, resonant scattering occurs. When it is out of resonance (arrows in the top scan), the scattering cross-section is drastically reduced and very weak signal is detected [92]. Figure 8.19b shows the angular distribution of the signal responsible for the contrast in Fig. 8.19a. The incident polarization is marked by an arrow. The image was obtained by placing a CCD camera in the Fourier plane of the microscope. The intensity is distributed with an annulus bound by the N.A. of the detecting objective, here 1.45 and forms a two-lobe pattern. This pattern is similar to the well-known dipolar pattern as illustrated in the calculation of Fig. 8.19c.

Another contrast mechanism was recently developed relying on the non-linear response of gold nanoparticles. Upon ultrafast near infrared excitation, a two-photon interband absorption can be promoted between the electronic states of the nanoparticle giving rise to a photo-induced luminescence [96]. The luminescence is assigned to the radiative recombination of Fermi-level electrons and sp- or d-band holes [97, 98] and is modulated by the excitation of surface plasmons [99, 100]. Because of its non-linear character, two-photon induced photoluminescence strongly depends on the field intensity at the surface of the nanoparticle and has been employed to investigate the capabilities of nanoparticles to locally enhanced electromagnetic fields [101]. An example of such imaging is shown in Fig. 8.20 for individual nanorods and coupled dimers. Figure 8.20a and b shows the polarization dependence of the photoluminescence signal of an isolated gold nanorod (insets) excited by a

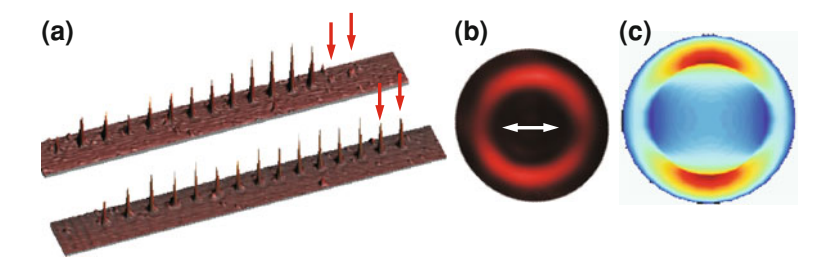


**Fig. 8.19** a and b Confocal maps of the partial differential scattering cross-sections of gold dimers with different gaps for two orthogonal polarizations. Touching dimers (*arrows*) are off-resonance with a 633 nm excitation for a polarization along their longitudinal axis and weakly on-resonant for a crossed polarization. **c** Scattering diagram of a Au nanoparticle showing a dipolar response. The polarization of the incoming field is marked by the arrow. **d** Calculated emission diagram of in-plane dipole placed at a glass/air interface. Reprinted with permission from [92]. Copyright 2008, American Physical Society

femtosecond pulsed Ti:Saph laser centered at 785 nm [100]. Because of the increased confinement of the charges at the two extremities of a nanorod (electromagnetic singularities), the magnitude of the longitudinal surface plasmon is typically much larger than its transverse counterpart and larger field enhancements are thus attained. The consequence is that for a polarization aligned with the nanorod's longitudinal axis, the photoluminescence signal is strong, while for the orthogonal polarization the image is dominated by a residual background. Figure 8.20c and d illustrates another example where the photoluminescence provides a valuable imaging tool. As mentioned above, photoluminescence is strong at the extremities of a nanorod, and for rod lengths greater than the resolution limit of the confocal microscope, they concentrate the response as shown in Fig. 8.20c. For interacting dimer constituted of two bars, Fig. 8.20d, the largest photoluminescence signal occurs at the gap area where an interstitial enhancement is generated [102].

Because of the different contrast mechanisms available, confocal microscopy remains a prime imaging tool to investigate surface plasmon resonances. Since the heart of the technique is a diffraction-limited focal spot, it is generally applied to localized surface plasmons occurring in confined systems. Of course, the main limitation is the spatial resolution and cannot compete with the proximal probe technique. However, precisely because it does not require a local probe, it is generally considered as a non-perturbative measurement (at least for optical power below the damage threshold [100]). Confocal imaging is also suited to extract spectroscopic response of resonant metal nanoparticle [87, 89, 92, 102, 103] and can be very sensitive to the field magnitude when using non-linear phenomenon.

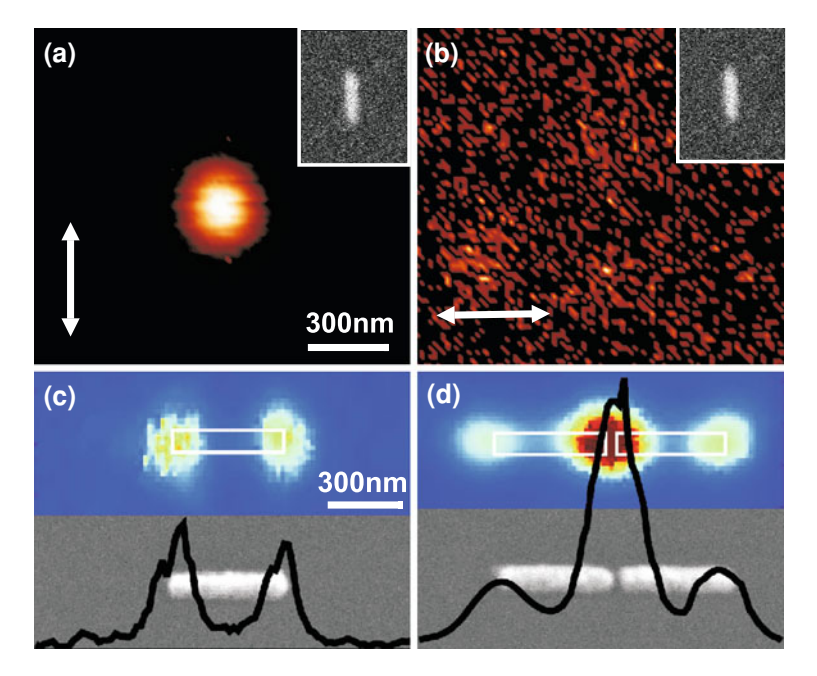


Fig. 8.20 a and b Confocal maps of the two-photon-induced luminescence (TPL) generated by a single gold  $30 \times 100$  nm nanorod for two polarizations. Because charge confinement is the largest at the extremities, only the longitudinal polarization gives rise to a measurable signal. c and d TPL confocal images obtained for a 500-nm gold bar and a dimer formed by two bars. Coupling between the two bars leads to a strong TPL signal located at the interstice. Reprinted with permission from [100] and [102]. Copyright 2005 and 2008, American Physical Society

## **8.8 SPP Imaging with Electrons**

Surface plasmon-polaritons are associated to high momentum, leading to their strong confinement. Since electron de Broglie wavelength can be extremely short, electron-beam wavevector can be easily matched to SPP momentum [1]. Indeed, first demonstration of SPP sustained by metallic film was done using electron excitation [104, 105]. Obviously, the extremely small electron wavelength ensures high resolution, so that electron microscopy is an important alternative to near-field optical microscopy to image SPP. We briefly review here SPP imaging by electron microscopy. The interested reader would find extensive discussions on general principles and applications of transmission electron microscopy (TEM) in the text-book written by Williams and Carter [106], and electron energy loss spectroscopy (EELS) in a recent review by Egerton [107]. We also advise to read the very recent review by Garcia de Abajo on "Optical excitations in electron microscopy" closely related to our subject, but more general [108].

A. Bouhelier et al.

#### 8.8.1 Electron-Matter Interaction

Quantitatively, let us consider an electron of mass  $m_e$  accelerated through a potential difference V up to velocity v. Its classical kinetic energy obeys  $E_K = m_e v^2/2$  = eV so that the accelerated electron (non relativistic) momentum can be written as  $p = m_e v = (2m_e \text{eV})^{1/2}$ . The de Broglie wavelength associated with this electron is then expressed as:

$$\lambda_e = \frac{h}{p} = \frac{h}{(2m_e \text{eV})^{1/2}}.$$
 (8.8)

For instance, a 50-eV energetic electron beam is associated with a wavelength  $\lambda_e=0.17$  nm. This is of the same order of value as the interatomic distance in solid state. Therefore, such an energetic electron beam will be diffracted by the atomic plane, giving important information on the crystallographic structure of a sample. This is the base of the so-called low energetic electron diffraction (LEED). Moreover, these low-energy electrons have a low penetration depth (about 1 nm). Therefore, it is of interest for characterizing low-dimensional plasmons (1D and 2D plasmons) [109, 110]. Differently, we are interested here in surface plasmon-polaritons that could expand on several tens of nanometers into the metal. We therefore consider fast electrons that penetrate into the sample. In this case, relativistic effect cannot be neglected anymore. The kinetic energy of the accelerated electron, initially at rest, is then  $E_K=E-m_ec^2=\sqrt{(m_ec^2)^2+(pc)^2}-m_ec^2=$ eV and the electron wavelength obeys:

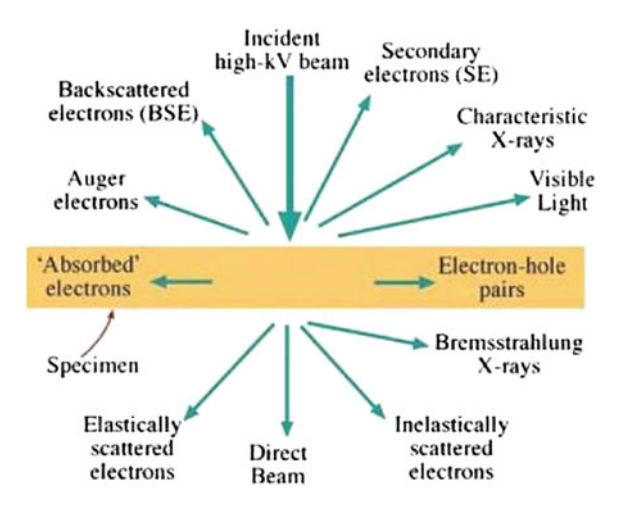
$$\lambda_e = \frac{h}{p} = \frac{h}{[2m_e \text{eV} + \text{eV}/(2m_e c^2)]^{1/2}}.$$
 (8.9)

An electron under 200 kV accelerating voltage has a wavelength of  $\lambda_e=2.5$  pm. These fast electrons can completely cross thin sample leading to transmission electron microscopy (TEM) presenting high resolution.

In addition, as negatively charged particles, electrons strongly interact with atomic nucleus and atomic electrons through electrostatic Coulomb forces. Since the nuclear mass is largely higher than the electron mass, atomic nucleus-incident electron interaction involves almost no energy exchange so that it is practically described by elastic collision. Oppositely, the electron-electron interactions between atomic cloud and incident beam give rise to inelastic scattering. Importantly, these two processes can be profitably considered to simultaneously image the sample (elastic scattering) and excite quasi-particle in the sample thanks to energy transfer (inelastic scattering).

Finally, the particle or wave description of electrons is a simple way to grasp the ability of electron microscopy to simultaneously image sample with extremely high resolution due to the electron small wavelength and bring some information on the sample through measurement of energy transfer of inelastically scattered electron particles [106]. We briefly summarize below the main properties of the electron-sample interaction.

Fig. 8.21 List of main excitation processes involved in a thin film excited by a fast electron beam. Reprinted with permission from [106]. Copyright 2009, Springer



#### **Elastic Scattering**

Elastic scattering mainly describes the incident electron interaction with the atomic nucleus. The scattering angle of the electron therefore mainly depends on the properties of the atomic nucleus. The angular width of the elastic scattering distribution is approximately  $\theta_0 \approx Z^{1/3}/(k_0a_0)$  where Z is the atomic number,  $k_e = 2\pi/\lambda_e$  is the electron wavenumber, and  $a_0 = 0.05\,\mathrm{nm}$  is the first Bohr radius.  $\theta_0$  is typically of several tenths of mrads for 100-keV incident electrons. The probability that an electron is scattered at large angles ( $\theta \gg \theta_0$ ) is proportional to  $Z^{4/3}$ . This means that chemical imaging can be done by detecting electrons scattered at high angles (High Angular Dark-Field Microscopy, HADF).

#### **Inelastic Scattering**

We now consider energy exchange between the incident electrons and the electrons of sample atoms. Figure 8.21 gathers the main excitations responsible for energy loss of the incident electron beam. Depending on the process (volume and surface plasmon, cathodoluminescence, electron-hole pair, secondary electron emission, ...), energy loss  $\Delta E$  from a few electron volts up to hundreds of electron-volts arises. Importantly, inelastic scattering involves small angles. Indeed, the inelastic scattering angular distribution half-width is typically a few tenths of mrad for 10 eV energy loss. This scattering angle is due to momentum transfer  $\mathbf{p} = \hbar \mathbf{k}_s$  during the interaction and opens the possibility to perform electron energy-loss spectroscopy (EELS). EELS can be done at small angles, giving access to e.g. excited surface plasmon-polariton properties (mode energy and momentum) simultaneously to precise localization of the incident beam localization thanks to e.g. HADF [111, 112].

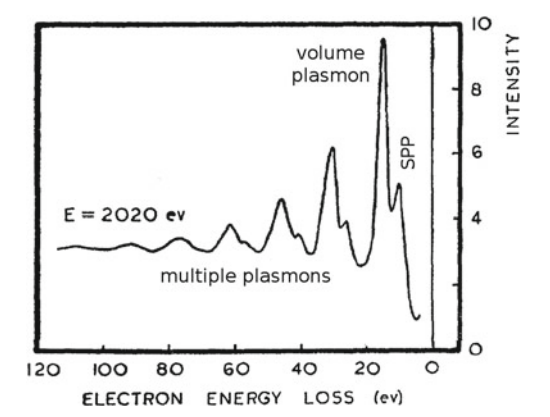


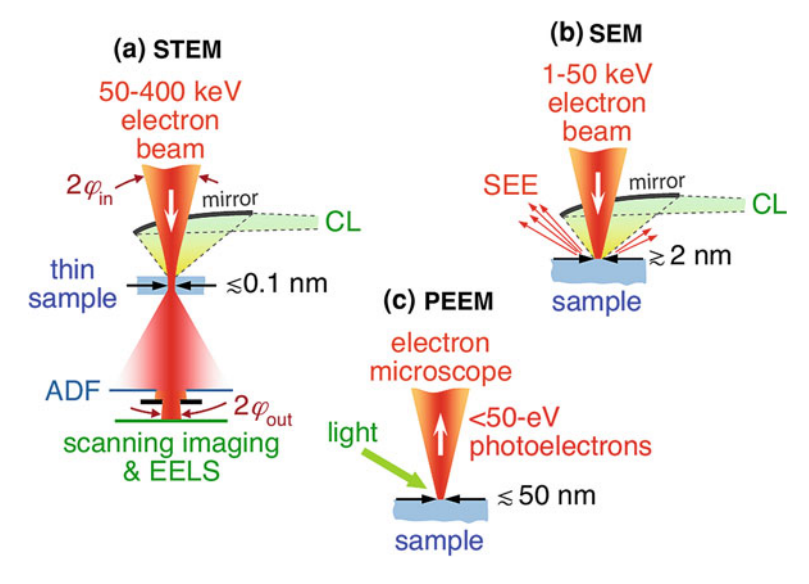
Fig. 8.22 Electron energy-loss spectrum measured on a 10-nm aluminum foil excited with a 2.02-keV electron beam. The zero loss peak (not shown) intensity was adjusted to 25. Volume and surface plasmon peak appear at  $\hbar\omega_p=15.3\,\mathrm{eV}$  and  $\hbar\omega_s=10.3\,\mathrm{eV}$  losses, respectively. Secondary peaks correspond to multiple plasmon excitation. The ratio between surface and volume plasmons energy agrees with  $\hbar\omega_s/\hbar\omega_p=1/\sqrt{2}$ . Reprinted permission from [105]. Copyright 1959, American Physical Society

Figure 8.22 presents a typical EELS spectra of a 10-nm aluminum film. This was the first experimental observation of the surface plasmon [105] previously theoretically proposed by Ritchie [104]. The surface plasmon peak is located between the volume plasmon and zero loss peaks, so that it can be difficult to observe and could require dedicated post-processing treatment.

#### Instrumentation

Figure 8.23 schematically represents the main types of electron microscopes of interest for SPP imaging. The principal characteristics are listed below.

- The electron source is often a thermionic electron gun where electrons are emitted from a heated tungsten filament and then accelerated under high voltage. Such types of electron guns are relatively cheap and do not require high vacuum. However, they provide an energy width of about 1 eV. Cold-field emission gun (CFEG), where electron emission is induced by a very strong electric field on the tungsten filament offers a better energy resolution; typically of 0.5 eV. The incident electron beam is then shaped with magnetic lens (collimated beam or focused beam for TEM and scanning TEM, respectively).
- Interaction with the sample. This point was briefly discussed above. TEM can
  be applied to a thin sample only (about 100 nm). In case of scanning electron
  microscopy (SEM), thick films can be investigated since secondary electrons emitted above the sample can be used to image the object.



**Fig. 8.23** A brief overview of the electron microscopes of interest for SPP imaging. The main specifications (incident electron energy, spatial and energy resolution) are indicated in the figure. Reprinted with permission from [108]. Copyright 2010, American Physical Society

• Signal recording. Electron microscopy of SPPs relies on recording both spectroscopic and spatial information on the sample. The better spatial resolution is achieved in a STEM configuration where it could be down to 0.1 nm. The energy resolution is limited by the electron source width and the function of transfer of the TEM. Optimized energy-loss resolution is around 0.1 eV that is at least 10 nm and up to 100 nm in wavelength resolution in the visible range or near infra-red domain of interest here. In case of cathodoluminescence, the spectroscopic width is only limited by the emitted light so that it can be extremely reduced, keeping excellent spatial resolution by imaging the secondary electrons (typically several nms).

## 8.8.2 Spatially Resolved Electron Energy-Loss Spectroscopy

In his original paper of 1957, Ritchie theoretically discussed SPP excitation effects on EELS spectra [104], in order to explain unexpected peaks observed in previous experiments. He demonstrated that the plasma confinement leads to the apparition of two types of losses peaks, in addition to the volume plasmon peak expected at  $\hbar\omega_p$  for a bulk plasma. In the presence of a metallic film, the additional peak arises at  $\hbar\omega_p/\sqrt{2}$  corresponding to the now well-known single interface (quasi-static) surface

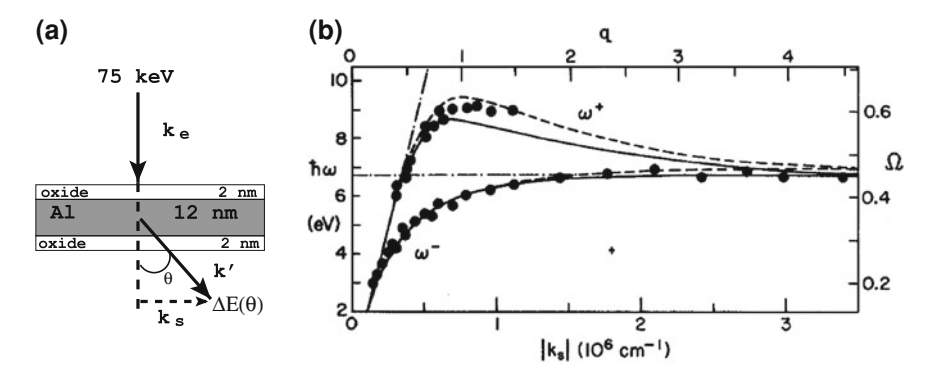


**Fig. 8.24** Dispersion relation measured by Pettit et al. for a 16-nm (oxidized) aluminum film. a Schematic representation of the TEM-EELS principle method. b Aluminum dispersion curve built from experimental data (points) or calculated (*lines*). *Solid* and *dashed lines* refer to α-allotropic and amorphous forms of the aluminum oxide respectively. Reprinted with permission from [113]. Copyright 1975, American Physical Society

plasmon-polariton mode, whereas spherical particles should lead to an absorption peak at  $\hbar\omega_D/\sqrt{3}$ , corresponding to the dipolar plasmon mode resonance.

#### **Delocalized Plasmon**

Two years later, Powell and Swan achieved a direct experimental evidence of the existence of SPP (see Fig. 8.22) [105]. These primary works were quickly followed by systematic investigations of SPP by TEM-EELS. Figure 8.24a schematically represents the TEM-EELS configuration used by Pettit and coworkers to experimentally reproduce a thin aluminum film dispersion curve. A fast incident electron beam excites surface plasmon mode. Energy losses measured as a function of the scattering angle fully characterize the excited SPP (Fig. 8.24b). Due to the large electron wavenumber, an almost whole dispersion curve is described. Note also that both the symmetric and antisymmetric branches are easily accessed by this method.

#### Localized Plasmon: STEM-EELS and EFTEM

For nanoparticles, the only parameter is the mode resonance energy. First investigations were done in the so-called aloof configuration where the incident electron beam does not cross the nanoparticle but rather flies in close proximity, avoiding to damage the sample. Moreover, this aloof configuration allows one to detect surface mode without strong contribution from the volume plasmon [114]. Additional information is however achieved by resolving electron energy losses as a function of position. Then, the localized mode is directly imaged by recording the signal at given energy loss as a function of the incident beam position. It is important here to be

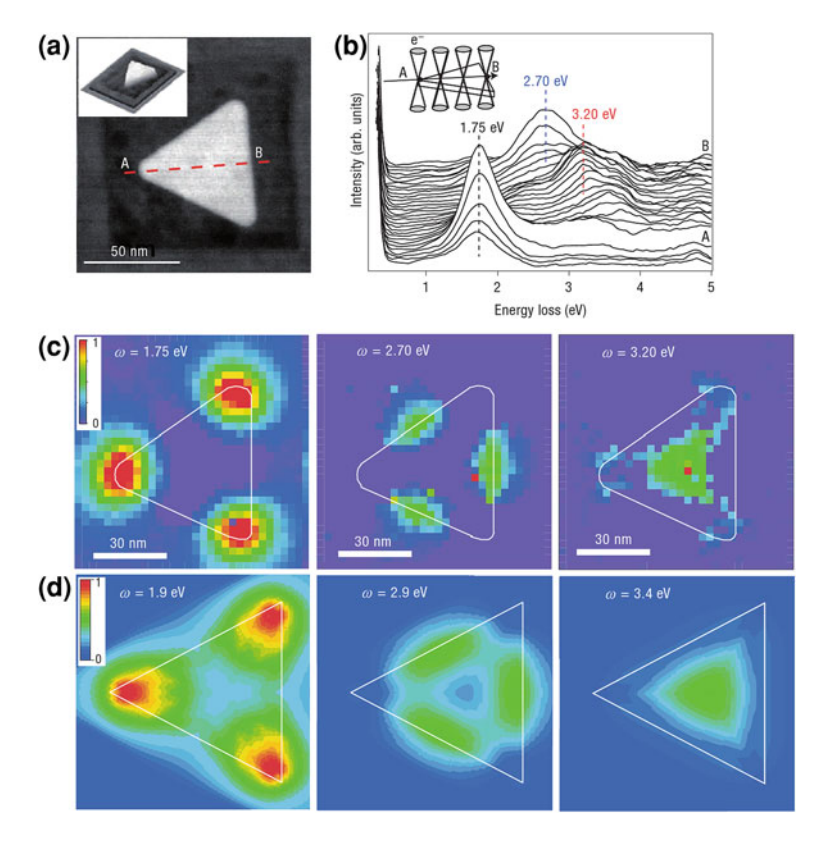


**Fig. 8.25 a** HADF image of a 30-nm length silver triangle. **b** Position-dependent electron energyloss spectra. **c** STEM images recorded at three resonant energies revealing the localized plasmon profile (a Gaussian fitting has been applied). **d** Calculated mode profiles. Reprinted with permission from [115]. Copyright 2007, Nature group

able to register simultaneously both the sample morphology and electron energy-loss spectra so that losses are precisely correlated to the sample shape. Several strategies were adopted there. First experimental maps of localized plasmon were acquired by energy-filtered TEM (EFTEM) [114]. Colliex and coworkers recently improved the resolution accuracy by registering the probe position using high angle dark-field microscopy in a scanning TEM (STEM) [115] (see Fig. 8.25). STEM-EELS combines high spatial resolution with the ability to excite high-order modes, poorly coupled to light so that it gives access to the SPP mode unachievable by optical excitation [116]. Unfortunately, this imposes to register a full spectrum for each image pixel so that it requests heavy memory size and image post-processing. Thanks to strong improvement on EFTEM equipment specifications (both on energy and resolution accuracy), a renewal of interest recently appeared for this method instead of STEM-EELS in order to gain in acquisition time and memory request [117, 118].

A. Bouhelier et al.

#### **Images Interpretation**

Although EELS is a well-understood signal, we would like to mention here an original interpretation recently proposed by García de Abajo and Kociak that makes the links with near-field optical measurement [119]. Let us consider an incident fast electron moving with velocity  $\mathbf{v} = v\mathbf{e_z}$  along the trajectory  $\mathbf{r}_e(t) = (\mathbf{r}_e^{//}, z)$ . The associated charge and current densities follow  $\rho(\mathbf{r}, t) = -e\delta(\mathbf{r} - \mathbf{r}_e(t))$  and  $\mathbf{j}(\mathbf{r}, t) = -ev\delta(\mathbf{r} - \mathbf{r}_e(t))$ , that induces an electromagnetic field (**E**, **B**) according to Maxwell equations. This induced near field can be evaluated by well developed numerical methods where the object is generally described by a classical dielectric constant [120, 121]. Electron energy loss originates from the work exerted back on the swift electron by the induced field [122]:

$$\Delta E(\mathbf{r}_e) = -\int dW = -\int_{-\infty}^{\infty} dt \int d\mathbf{r} \mathbf{E}(\mathbf{r}, t) \cdot \mathbf{j}(\mathbf{r}, t)$$
(8.10)

$$= e \int_{-\infty}^{\infty} dt \mathbf{E}[\mathbf{r}_{e}(t), t] \cdot \mathbf{v} = e \int_{0}^{\infty} d\omega \hbar \omega \Gamma(\mathbf{r}_{e}, \omega), \quad (8.11)$$

with 
$$\Gamma(\mathbf{r}_e, \omega) = \frac{e}{\pi \hbar \omega} \int dt Re[e^{-i\omega t} \mathbf{E}(\mathbf{r}_e(t), \omega) \cdot \mathbf{v}].$$
 (8.12)

 $\Gamma(\mathbf{r}_e,\omega)$  is the spectrally resolved energy loss [119]. This classically derived expression accurately reproduces the measured EELS data. Nevertheless, optical properties of the object's are hidden in the object dielectric constant. Recently, García de Abajo and Kociak recast this expression in order to let the local density of electromagnetic states (LDOS) appear. Optical LDOS  $\rho(\mathbf{r},\omega)$  is the electromagnetic analog of electronic local density of states and is a key quantity to interpret near-field optical images [123–127]. Due to the vectorial nature of the electromagnetic field, partial LDOS are generally defined such that  $\rho(\mathbf{r},\omega)=\rho_x(\mathbf{r},\omega)+\rho_y(\mathbf{r},\omega)+\rho_z(\mathbf{r},\omega)$  where for instance  $\rho_z(\mathbf{r},\omega)$  only retains the z-component of the electric field associated with the supported mode [128].

In case of 2D systems with their invariant axis superimposed with the electron trajectory, García de Abajo and Kociak obtained that loss probability per unit length follows:

$$\frac{\Gamma(\mathbf{r}_e^{\prime\prime},\omega)}{L} = \frac{2\pi e^2}{\hbar\omega}\tilde{\rho}_z(\mathbf{r}_e^{\prime\prime},q=\omega/v,\omega),\tag{8.13}$$

where the quantity  $\tilde{\rho}_z(\mathbf{r}_e^{//},q,\omega)$  is linked to optical LDOS by  $\rho_z(\mathbf{r}_e,\omega)=\int \mathrm{d}q \tilde{\rho}_z$   $(\mathbf{r}_e^{//},q,\omega)$ . Expression (8.13) shows that spatially and spectrally resolved electron energy-loss spectroscopy probes optical LDOS at given energy  $\hbar\omega$  and momentum  $q=\omega/v$ . This expression has been generalized to arbitrary 3D geometry. Finally, numerical simulations indicate that optical LDOS  $\rho_z(\mathbf{r}_e,\omega)$  (instead  $\tilde{\rho}_z(\mathbf{r}_e^{//},q,\omega)$ )

calculated in the near-field of the object gives a fair agreement with the measured STEM-EELS images (see also Fig. 8.25) [119]. This makes an important bridge between optical and electronic imaging of SPP. A detailed discussion of EELS signal interpretation in terms of optical LDOS can be found in Refs. [108, 119, 129, 130].

### 8.8.3 Cathodoluminescence Microscopy

Cathodoluminescence results from light emission when matter is excited with a high-energy electron beam. It was originally observed in the mid-nineteenth century, in a cathode ray tube as the electron beam collides the glass tube walls giving its name to this phenomenon. The most common applications were the cathodic screens during the second half of the twentieth century. Additionally, as every luminescence technique, it is extensively applied in material characterization. When used in combination with SEM, cathodoluminescence offers an unprecedented optical resolution. Therefore, it is very well appropriate for SPP imaging. In that case, the electron beam (1-50 keV) leads to a local excitation of the sample, followed by an extremely localized light emission coupled to supported surface plasmons. As a swift electron crosses the metallic structures, an effective dipole, resulting from the incident electron charge-image charge, is created. This elementary optical (dipolar) excitation emits light (transition radiation) and couples to surface plasmon-polariton. Other cathodoluminescence mechanisms, such as Cerenkov radiation, could occur in the presence of a dielectric substrate but are not considered here as they do not concern SPP [108, 131].

#### **Localized Plasmon**

In their original work, Yamamoto and coworkers imaged the sample thanks to secondary electron emission, whereas they registered the EELS spectra for each incident position, revealing thereby nanoparticle dipolar and quadrupolar modes (Fig. 8.26) [132].

#### **Delocalized Plasmon**

Apart from the important point of source localization, cathodoluminescence SPP imaging is very similar to near-field optics imaging in illumination mode. The surface plasmon is locally excited with an incident electron source (instead of a localized optical source) and radiative signal is detected. This means that the non-radiative plasmon has to be decoupled using e.g. a grating or a high index prism to be detected. Figure 8.27 presents a recent experiment where a film plasmon is locally excited with a fast electron and the emitted light is decoupled towards far-field optics detector with a grating. The signal recorded as a function of the distance

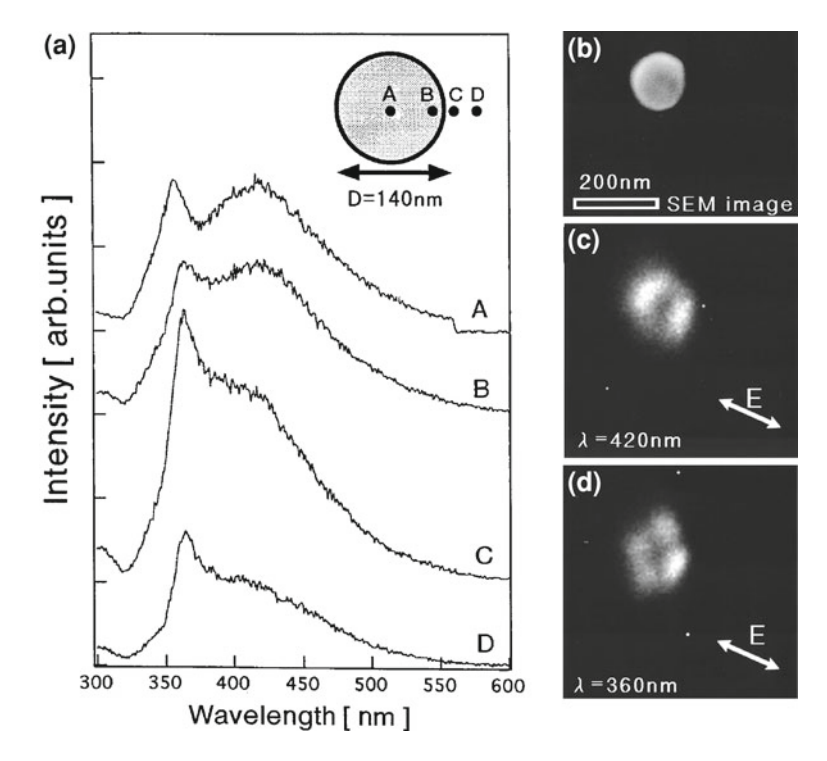


**Fig. 8.26 a** Cathodoluminescence spectra taken for various incident 200-keV electron-beam positions on a 140-nm diameter silver sphere. **b** Secondary electron emission images (SEM) of the sample. **c** and **d** Cathodoluminescence image along the indicated polarization filtered at  $\lambda = 420$  nm (dipolar mode) and  $\lambda = 360$  nm (quadrupolar mode), respectively. Reprinted with permission from [132]. Copyright 2001, American Physical Society

between the incident electron beam and the grating, presents interference oscillations as well as an intensity envelop exponentially decaying giving a direct measurement of the surface plasmon propagation constant, in strong equivalence with SNOM measurement. Obviously, uncomparable resolution is achieved thanks to cathodoluminescence since the electron excitation perfectly models an optical point like dipolar excitation (Fig. 8.27b).

However, the cathodoluminescence signal is also well modeled by the local density of electromagnetic states [133] in direct analogy with SNOM imaging [134] since both of them can be modeled with an optical dipolar excitation. For instance, LDOS measurements done on metallic nanorods by either Scanning Near-Field Optical Microscopy [36] (see Fig. 8.4) or cathodoluminescence microscopy (Fig. 8.28) [135] are interestingly compared. Let us insist here again that the strong improvement on the mode mapping resolution using electronic excitation instead of optical source is a breakthrough toward accurate investigation of e.g. optical antennas [136].

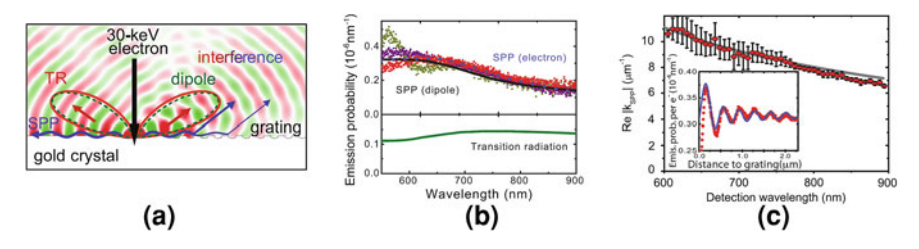


**Fig. 8.27** Cathodoluminescence microscopy on a gold film. **a** 30 keV electron coupling to transition radiation and SPP. The *red lobes* represent the transition radiation angular emission. *Dashed green lobes* represent a vertical dipole angular emission in the presence of the gold film. **b** SPP and transition radiation emission probability calculated for a 30-keV incident electron or vertical dipole excitation. This demonstrates the validity of the optical point-like dipole to model the cathodoluminescence signal. **c** Measured cathodoluminescence as a function of the distance between the incident electron beam and the decoupler grating. The inset shows a fit using LDOS (*blue line*). Reprinted with permission from [133]. Copyright 2009, American Physical Society

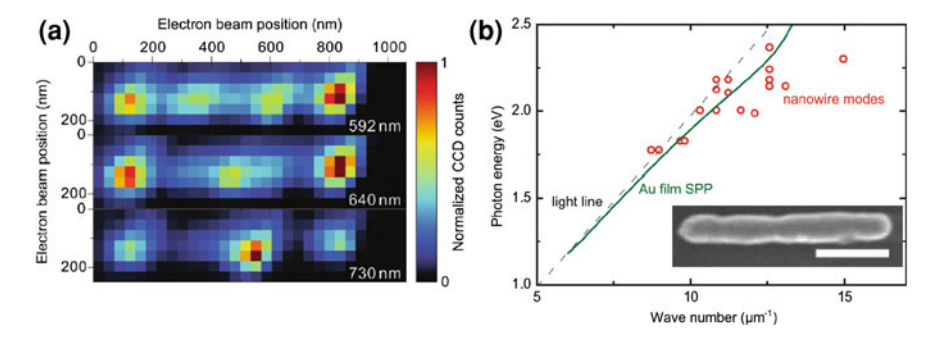


**Fig. 8.28** a Cathodoluminescence images of a 725-nm gold nanowire recorded for three wavelengths. **b** Nanowire dispersion curve dispersion (*red circles*) deduced from the interference patterns measured in **a**. The inset shows the scanning electron micrograph of the gold nanowire (*scale bar* 250 nm). Reprinted with permission from [135]. Copyright 2007, American Chemical Society

## 8.8.4 Photoemission Electron Microscopy

The work functions of gold and silver are in the range 4–5 eV (corresponding to wavelengths 250–310 nm). Therefore, conventional mercury vapor lamp (UV line emission at 253 nm) can be used to extract electrons from the metallic sample. Then, the photoemitted electrons are locally resolved with an electron microscope revealing the surface plasmon mode structure with the electron microscope resolution (see for instance Figs. 8.29 and 8.30) [137]. Note that two-photon or three-photon induced photoemission electron processes are also used in order to profit from the ultra-fast laser technology in the visible or near infrared range. Then, photoemission electron microscopy (PEEM) signal varies as the square or the cube of the incident light intensity.

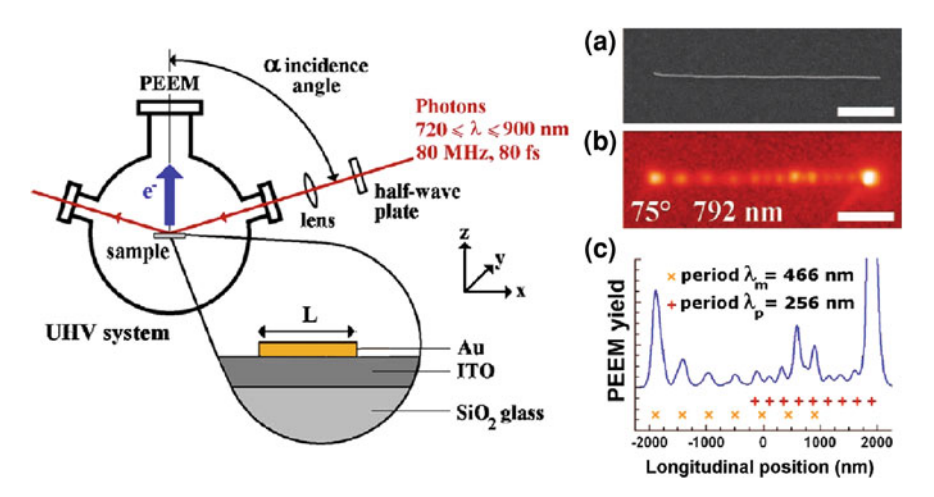


**Fig. 8.29** Left Schematic representation of the PEEM experimental setup. Right **a** SEM picture, **b**, **c** PEEM map **b** and cross-section **c** of a 4  $\mu$ m long gold nanowire. The interference pattern originates from the beating between incident pump light and propagative plasmon along the nanowire, in agreement with excitation of the guided nanowire plasmon mode of effective wavelength  $\lambda_{\rm SPP} = 335$  nm and propagation length (3.3  $\pm$  0.5)  $\mu$ m. Incident light is p-polarized,  $\lambda = 792$  nm, P = 110 MW.cm<sup>-2</sup>. The angle between the incident excitation light and the detected photoemitted electrons is  $\alpha = 75^{\circ}$ . Reprinted with permission from [138, 139]. Copyright 2007, American Institute of Physics, Copyright 2008, American Chemical Society

#### **Time-Resolved PEEM**

By combining the time resolution of laser spectroscopy with the excellent resolution of electron microscopy, time resolved photoemission electron microscopy offers unprecedented tools for SPP investigation [14, 140]. To this aim, the incident pulse light plays the role of both pump and probe. Indeed, the beating between the incident pulse and the generated plasmon induces a stationary wave that can be imaged thanks to the photoemitted electrons. By tuning the delay between the pump pulse launching the plasmon and next pulse (probe), the plasmon propagation dynamic is imaged as shown in Fig. 8.30.

## 8.8.5 Photon-Induced Electron Microscopy: Highly Resolved Electron Energy-Loss/Gain Spectroscopy Imaging

As the last technique for imaging surface plasmons, we would like to mention the very recent progress achieved with photon -induced electron microscopy (PINEM) [141, 142]. Zewail and coworkers experimentally demonstrated that electron energy spectroscopy on an optically excited nanoparticle (carbon nanotube or silver nanowire) presents loss or gain at multiple energies of the excitation optical beam

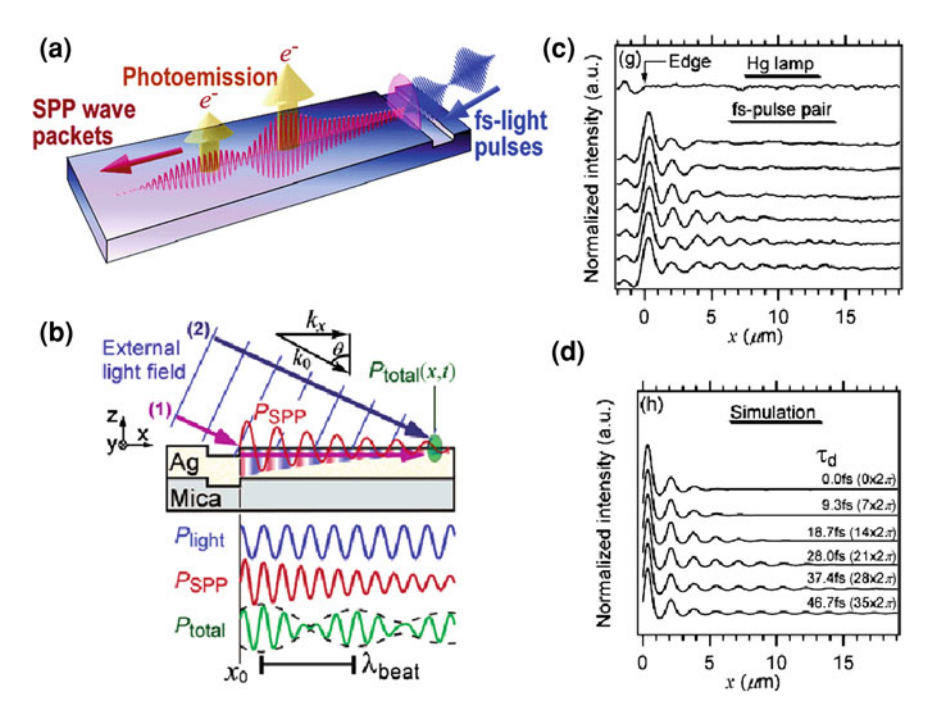


**Fig. 8.30** a Artist's view of time resolved PEEM investigation of SPP on a silver film. **b** Pulsed light incident on a trench to launch a SPP. **c** Time-resolved PEEM profiles and their simulation (**d**). Reprinted with permission from [14]. Copyright 2007, American Chemical Society

(Fig. 8.31). Particularly, the evanescent optical field created in the near-field of the nanostructure brings gain to the incident electron by momentum transfer from light to electron via the evanescent field. Additionally, Zewail et al. used optical (220 fs) and electron pulses (achieved by exciting a photocathode source with a femtosecond laser source) so that they were able to investigate the dynamic of the evanescent field. Although both carbon nanotubes and silver nanowires have a metallic behavior, the dynamic of the SPP was not imaged since their lifetimes were too short [142, 143].

However, PINEM should find extremely useful applications to investigate SPP. Noteworthy, continuous optical excitation is also of interest here. In that case, one measures electron energy *loss or gain* spectra. Interestingly enough, electron-energy gain spectroscopy (EEGS) gives similar information about cathodoluminescence,but with strong improvement of the signal-to-noise ratio [144]. In addition, the energy resolution is then only limited by the width of the optical pump, making a strong breakthrough compared to electron microscopy energy resolution [144].

Electron microscopy of SPP gives access to unprecedented mode imaging resolution. Technically, this imposes to work in vacuum. Also, one should keep in mind that only conductive samples can be investigated with these techniques. The use of a conductive layer (as ITO) qualitatively modifies the resonance property of

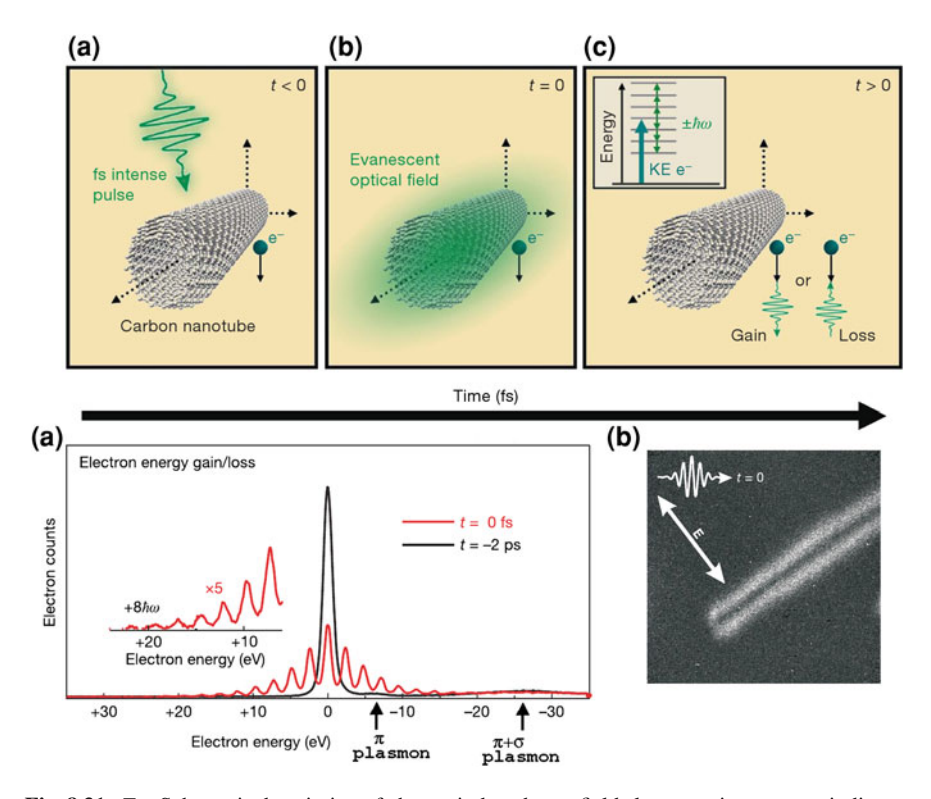


Fig. 8.31 Top Schematic description of photon-induced near-field electron microscopy. t indicates the delay between the incident electron and the optical pulse. Bottom a Electron-energy (loss or gain) spectrum for a 200-keV incident electron packet arriving before (black curve) or in coincidence with (red curve) the optical femtosecond pulse. Apart from the zero loss peak, only  $\pi$  and  $\pi + \sigma$  volume plasmon peaks are visible at 6 and 25 eV, respectively, on the EELS spectrum (black curve). For t=0, electron energy loss and gain clearly appear at a multiple of incident optical pulse energy (red curve,  $\hbar\omega=2.4$  eV). b Gain energy-filtered image (the optical pulse polarizations is indicated). Reprinted with permission from [141]. Copyright 2009, Nature group

the investigated structure. Importantly, electron microscopy involves small electron wavelength, allowing up to subnanometric resolution, and high electron momentum, that could match SPP large wavevector. Consequently, non-radiative (e.g. bound surface modes) or poorly radiative (e.g. multipolar particle modes) can be directly imaged in an electron microscope. However, this is at the price of energy resolution that is rather low. As we briefly discussed, this limitation could be overcome by combining the electron microscopy spatial resolution with the optical spectroscopy narrow linewidth. Finally, several works have recently demonstrated that SPP dynamic imaging can be achieved by associating electron microscope resolution with ultrafast optical pulse. This opens the door to dynamical control of surface plasmon-polaritons and is a key for active plasmonic.

#### References

- H. Raether, Excitation of Plasmons and Interband Transitions by Electrons, Springer Tracts in Modern Physics, vol. 88 (Springer, Berlin, 1980)
- H. Raether, Surface Plasmons on Smooth and Rough Surfaces and on Gratings, Springer Tracts in Modern Physics, vol. 111 (Springer, New York, 1988)
- 3. U. Kreibig, M. Vollmer, Optical properties of metal clusters (Springer, Berlin, 1995)
- 4. E. Kretschmann, H. Raether, Z. Naturforsch. 23a, 2135 (1968)
- 5. A. Otto, Z. Angew. Phys. 27, 207 (1968)
- 6. M. Rocca, Surf. Sci. Rep. 22, 1 (1995)
- 7. S. Bozhevolnyi, F. Pudin, Phys. Rev. Lett. 78, 2923 (1997)
- 8. A. Bouhelier, T. Huser, H. Tamaru, H.J. Güntherodt, D.W. Pohl, F.I. Baida, D.V. Labeke, Phys. Rev. B 63, 155404 (2001)
- J.C. Weeber, J.R. Krenn, A. Dereux, B. Lamprecht, Y. Lacroute, J.P. Goudonnet, Phys. Rev. B 64, 045411 (2001)
- 10. R. Hillenbrand, F. Keilmann, Appl. Phys. B Lasers Optics **73**, 239 (2001)
- 11. A. Bouhelier, M. Beversluis, L. Novotny, Appl. Phys. Lett. 82, 4596 (2003)
- 12. T.H. Taminiau, F.D. Stefani, F.B. Segerink, N.F. van Hulst, Nat. Phot. 2, 234 (2008)
- 13. M. Schnell, A. Garcia-Etxarri, A.J. Huber, K. Crozier, J. Aizpurua, R. Hillenbrand, Nat. Photo. 3, 287 (2009)
- 14. A. Kubo, N. Pontius, H. Petek, Nano Lett. **7**, 470 (2007)
- 15. M. Stockmann, M. Kling, U. Kleineberg, F. Krausz, Nat. Phot. 1, 539 (2007)
- M. Aeschlimann, M. Bauer, D. Bayer, T. Brixner, F.J.G. de Abajo, W. Pfeiffer, M. Rohmer, C. Spindler, F. Steeb, Nature 446, 301 (2007)
- 17. P. Dawson, F. de Fornel, J.P. Goudonnet, Phys. Rev. Lett. 72, 2927 (1994)
- 18. D. Pohl, Phil. Trans. R. Soc. Lond. A **362**, 701 (2004)
- L. Novotny, Progress in Optics. in *The History of Near-field Optics* (Elsevier, Amsterdam, 2007), pp. 137–184.
- O. Marti, H. Bielefeldt, B. Hecht, S. Herminghaus, P. Leiderer, J. Mlynek, Opt. Comm. 96, 225 (1993)
- 21. M.A. Paesler, P.J. Moyer, Near-Field Optics: Theory, Instrumentation, and Applications (Wiley, New York, 1996)
- L. Novotny, B. Hecht, *Principles of Nano-Optics* (Cambridge University Press, Cambridge, 2006)
- I. Horcas, R. Fernández, J.M. Gómez-Rodríguez, J. Colchero, J.M. Gómez-Rodríguez, A.M. Baro, Rev. Sci. Instr. 78, 013705 (2007)
- 24. K. Karrai, D.R. Grober, Appl. Phys. Lett. **66**, 1842 (1995)
- 25. S.I. Bozhevolnyi, Phys. Rev. B 54, 8177–8185 (1996)
- B. Lamprecht, J.R. Krenn, G. Schider, H. Ditlbacher, M. Salerno, N. Felidj, A. Leitner, F.R. Aussenegg, J. Weeber, App. Phys. Lett. 79, 51 (2001)
- 27. J.C. Weeber, Y. Lacroute, A. Dereux, Phys. Rev. B 68, 115401 (2003)
- 28. R. Zia, A. Chandran, M.L. Brongersma, Opt. Lett. **30**, 1473–1475 (2005)
- 29. J.C. Weeber, M.U. González, A.L. Baudrion, A. Dereux, Appl. Phys. Lett. 87, 221101 (2005)
- 30. M. Sandtke, L. Kuipers, Nat. Phot. 1, 573 (2007)
- 31. R. Hillenbrand, F. Keilmann, Phys. Rev. Lett. 85, 3029 (2000)
- 32. M. Sandtke, R.J.P. Engelen, H. Schoenmaker, I. Attema, H. Dekker, I. Cerjak, J.P. Korterik, F.B. Segerink, L. Kuipers, Rev. Sci. Instr. 79, 013704 (2008)
- 33. E. Verhagen, M. Spasenovic, A. Polman, L. Kuipers, Phys. Rev. Lett. 102, 203904 (2009)
- 34. G.P. Wiederrecht, Eur. Phys. J. Appl. Phys. 28, 3 (2004)
- 35. A. Bouhelier, A. Hartschuh, L. Novotny, Microscopy for Nanotechnology. in *Near-Field Optical Microscopy in the Nanosciences* (Springer, Berlin, 2004)
- 36. K. Imura, T. Nagahara, H. Okamoto, J. Phys. Chem. B 108, 16344 (2004)
- 37. A. Dereux, C. Girard, J.-Cl. Weeber, J. Chem. Phys. **112**, 7775 (2000)

A. Bouhelier et al.

 R. Hillenbrand, F. Keilmann, P. Hanarp, D.S. Sutherland, J. Aizpurua, Appl. Phys. Lett. 83, 368 (2003)

- J. Dorfmüller, R. Vogelgesang, R. Weitz, C. Rockstuhl, C. Etrich, T. Pertsch, F. Lederer, K. Kern, Nano Lett. 9, 2372 (2009)
- S. Grésillon, L. Aigouy, A.C. Boccara, J.C. Rivoal, X. Quelin, C. Desmarest, P. Gadenne,
   V.A. Shubin, A.K. Sarychev, V.M. Shalaev, Phys. Rev. Lett. 82, 4520 (1999)
- 41. F. Keilmann, R. Hillenbrand, Nano-Optics and Near-Field Optical Microscopy. in *Near-Field Nanoscopy by Elastic Light Scattering from a Tip* (ArtechHouse, Boston, 2009), pp. 235–265
- 42. U. Fischer, D. Pohl, Phys. Rev. Lett. 62, 458 (1989)
- 43. Y.D. Wilde, F. Formanek, R. Carminati, B. Gralak, P.A. Lemoine, K. Joulain, J.P. Mulet, Y. Chen, J.J. Greffet, Nature **444**, 740 (2006)
- 44. M.M. Alkaisi, R.J. Blaikie, S.J. McNab, Adv. Mat. 13, 877 (2001)
- 45. Y. Gilbert, R. Bachelot, P. Royer, A. Bouhelier, G.P. Wiederrecht, L. Novotny, Opt. Lett. 31, 613 (2006)
- 46. T. Grosjean, D. Courjon, Opt. Exp. 14, 2203 (2006)
- 47. C. Hubert, R. Bachelot, J. Plain, S. Kostcheev, G. Lerondel, M. Juan, P. Royer, S. Zou, G.C. Schatz, G.P. Wiederrecht, S.K. Gray, J. Phys. Chem. C 112, 4111 (2008)
- C. Hubert, A. Rumyantseva, G. Lerondel, J. Grand, S. Kostcheev, L. Billot, A. Vial, R. Bachelot, P. Royer, S. Chang, S.K. Gray, G.P. Wiederrecht, G.C. Schatz, Nano Lett. 5, 615 (2005)
- M.L. Juan, J. Plain, R. Bachelot, A. Vial, P. Royer, S.K. Gray, J.M. Montgomer, G.P. Wiederrecht, J. Phys. Chem. A 113, 4647–4651 (2009)
- A. Sundaramurthy, P.J. Schuck, N.R. Conley, D.P. Fromm, G.S. Kino, W.E. Moerner, Nano Lett. 6, 355 (2006)
- H. Ibn El Ahrach, R. Bachelot, A. Vial, G. Lerondel, J. Plain, P. Royer, O. Soppera, Phys. Rev. Lett. 98, 107402 (2007)
- M.L. Juan, J. Plain, R. Bachelot, P. Royer, S.K. Gray, G.P. Wiederrecht, ACS Nano 3, 1573 (2009)
- 53. B. Hecht, H. Bielefeldt, L. Novotny, Y. Inouye, D.W. Pohl, Phys. Rev. Lett. 77, 1889 (1996)
- A. Drezet, A. Hohenau, D. Koller, A. Stepanov, H. Ditlbacher, B. Steinberger, F.R. Aussenegg,
   A. Leitner, J.R. Krenn, Mat. Sci. Eng. B 149, 220 (2008)
- 55. H. Simon, J. Guha, Opt. Comm. 18, 391 (1976)
- 56. H. Kano, D. Nomura, H. Shibuya, App. Opt. 43, 2409 (2004)
- 57. A. Bouhelier, G.P. Wiederrecht, Opt. Lett. 30, 884 (2005)
- 58. A. Giannattasio, W.L. Barnes, Opt. Exp. **13**, 428 (2005)
- I. Gryczynski, J. Malicka, W. Jiang, H. Fischer, W.C.W. Chan, Z. Gryczynski, W. Grudzinski, J.R. Lakowicz, J. Phys. Chem. B 109, 1088 (2005)
- A. Drezet, A. Hohenau, A.L. Stepanov, H. Ditlbacher, B. Steinberger, N. Galler, F.R. Aussenegg, A. Leitner, J.R. Krenn, App. Phys. Lett. 89, 091117 (2006)
- M.U. Gonzàlez, A.L. Stepanov, J.C. Weeber, A. Hohenau, A. Dereux, R. Quidant, J.R. Krenn, Opt. Lett. 32, 2704 (2007)
- J. Grandidier, S. Massenot, G. Colas des Francs, A. Bouhelier, J.C. Weeber, L. Markey,
   A. Dereux, J. Renger, M.U. González, R. Quidant, Phys. Rev. B 78, 245419 (2008)
- J. Grandidier, G. Colas des Francs, S. Massenot, A. Bouhelier, J.C. Weeber, L. Markey, A. Dereux, J. Micros. 239, 167 (2010)
- 64. D. Marcuse, Theory of Dielectric Optical Waveguides (Academic Press, Boston, 1991)
- 65. R. Zia, M.S. Schuller, M.L. Brongersma, Phys. Rev. B **71**, 165431 (2005)
- 66. T. Holmgaard, S.I. Bozhevolnyi, Phys. Rev. B **75**, 245405 (2007)
- J. Grandidier, G. Colas des Francs, L. Markey, A. Bouhelier, S. Massenot, J.C. Weeber, A. Dereux, Appl. Phys. Lett. 96, 063105 (2010)
- 68. J.A. Kong, Electromagnetic Wave Theory (Wiley, New York, 1986)
- 69. J. Grandidier, Guide plasmonique polymère-métal: Composants passifs et actifs pour la photonique intégrée. Ph.D. thesis, Université de Bourgogne (2009)
- 70. E. Anemogiannis, E.N. Glytsis, T.K. Gaylord, J. Light. Tech. 17, 929 (1999)

- G. Colas des Francs, J. Grandidier, S. Massenot, A. Bouhelier, J. Weeber, A. Dereux, Phys. Rev. B 80, 115419 (2009)
- A. Hohenau, J.R. Krenn, A. Stepanov, A. Drezet, H. Ditlbacher, B. Steinberger, A. Leitner, F. Aussenegg, Opt. Lett. 30, 893 (2005)
- 73. J.W. Goodman, Introduction to Fourier Optics (McGraw-Hill Publishing, New York, 1988)
- B. Steinberger, A. Hohenau, H. Ditlbacher, A.L. Stepanov, A. Drezet, F.R. Aussenegg, A. Leitner, J.R. Krenn, Appl. Phys. Lett. 88, 94104 (2006)
- 75. I. Gryczynski, J. Malicka, Z. Gryczynski, J.R. Lakowicz, Anal. Biochem. 324, 170 (2005)
- 76. I. Gryczynski, J. Malicka, Z. Gryczynski, J.R. Lakowicz, J. Phys. Chem. B 108, 12568 (2004)
- 77. J.R. Lakowicz, Anal. Biochem. **337**, 171 (2005)
- 78. J. Zhang, Z. Gryczynski, J.R. Lakowicz, Chem. Phys. Lett. **393**, 483 (2004)
- J. Grandidier, G. Colas des Francs, S. Massenot, A. Bouhelier, L. Markey, J. Weeber, C. Finot, A. Dereux, Nano Lett. 9, 2935 (2009)
- A. Krishnan, S.P. Frisbie, L. Grave de Peralta, A.A. Bernussi, App. Phys. Lett. 96, 111104 (3 pages) (2010)
- H. Ditlbacher, J.R. Krenn, N. Felidj, B. Lamprecht, G. Schider, M. Salerno, A. Leitner, F.R. Aussenegg, Appl. Phys. Lett. 80, 404 (2002)
- C. Sönnichsen, Plasmons in metal nanostructures. Ph.D. thesis, Ludwig-Maximilians-Universität München (2001)
- 83. A. Murray, W. Barnes, Adv. Mat. 19, 3771 (2007)
- 84. J.J. Mock, S.J. Oldenburg, D.R. Smith, D.A. Schultz, S. Schultz, Nano Lett. 2, 465 (2002)
- S. Yang, H. Kobori, C.L. He, M.H. Lin, H.Y. Chen, C. Li, M. Kanehara, T. Teranishi, S. Gwo, Nano Lett. 10, 632–637 (2010)
- 86. M.A.V. Dijk, M. Lippitz, M. Orrit, Acc. Chem. Res. 38, 594 (2005)
- A. Arbouet, D. Christofilos, N.D. Fatti, F. Vallée, J.R. Huntzinger, L. Arnaud, P. Billaud, M. Broyer, Phys. Rev. Lett. 93, 127401 (2004)
- 88. O.L. Muskens, N.D. Fatti, F. Vallée, J.R. Huntzinger, P. Billaud, M. Broyer, App. Phys. Lett. 88, 063109 (2006)
- 89. K. Lindfors, T. Kalkbrenner, P. Stoller, V. Sandoghdar, Phys. Rev. Lett. 93, 037401 (2004)
- 90. D. Boyer, P. Tamarat, A. Maali, B. Lounis, M. Orrit, Science 297, 1160 (2002)
- 91. S. Berciaud, L. Cognet, P. Tamarat, B. Lounis, Nano Lett. 5, 515 (2005)
- 92. C. Huang, A. Bouhelier, G. Colas des Francs, A. Bruyant, A. Guenot, J.C. Weeber, A. Dereux, Phys. Rev. B 78, 155407 (2008)
- 93. W. Lukosz, R.E. Kunz, J. Opt. Soc. Am. 67, 1615 (1977)
- 94. L. Novotny, J.J. Opt, Soc. Am. 14, 91 (1997)
- 95. H.F. Arnoldus, J.T. Foley, Opt. Lett. 28, 1299 (2003)
- 96. G.T. Boyd, Z.H. Yu, Y.R. Shen, Phys. Rev. B 33, 7923 (1986)
- J.P. Wilcoxon, J.E. Martin, F. Parsapour, B. Wiedenman, D.F. Kelley, J. Chem. Phys. 108, 9137 (1998)
- 98. M.R. Beversluis, A. Bouhelier, L. Novotny, Phys. Rev. B 68, 115433 (2003)
- 99. E. Dulkeith, T. Niedereichholz, T.A. Klar, J. Feldmann, G. von Plessen, D.I. Gittins, K.S. Mayya, F. Caruso, Phys. Rev. B **70**, 205424 (2004)
- A. Bouhelier, R. Bachelot, G. Lerondel, S. Kostcheev, P. Royer, G.P. Wiederrecht, Phys. Rev. Lett. 95, 267405 (2005)
- 101. P. Mühlschlegel, H.J. Eisler, O.J.F. Martin, B. Hecht, D.W. Pohl, Science 308, 1607 (2005)
- P. Ghenuche, S. Cherukulappurath, T.H. Taminiau, N.F. van Hulst, R. Quidant, Phys. Rev. Lett. 101, 116805 (2008)
- W. Zhang, H. Fischer, T. Schmid, R. Zenobi, O.J.F. Martin, J. Phys. Chem. C 113, 14672–14675 (2009)
- 104. R.H. Ritchie, Phys. Rev. 106, 874 (1957)
- 105. C. Powell, J. Swan, Phys. Rev. 115, 869 (1959)
- 106. D.B. Williams, C.B. Carter, Transmission Electron Microscopy: A Textbook for Materials Science (Springer, New York, 2009)
- 107. R. Egerton, Rep. Prog. Phys. **72**, 016502 (2009)

A. Bouhelier et al.

- 108. F.J. García de Abajo, Rev. Mod. Phys. 82, 209 (2010)
- 109. T. Nagao, T. Hildebrandt, M. Henzler, S. Hasegawa, Science 493, 680 (2001)
- 110. T. Nagao, S. Yaginuma, T. Inaoka, T. Sakurai, Phys. Rev. Lett. 97, 116802 (2006)
- 111. K. Kimoto, T. Asaka, T. Nagai, M. Saito, Y. Matsui, K. Ishizuka, Nature 450, 702 (2007)
- 112. C. Colliex, Nature **450**, 622 (2007)
- 113. R. Pettit, J. Silcox, R. Vincent, Phys. Rev. B 11, 3116 (1975)
- 114. D. Ugarte, C. Colliex, P. Trebbia, Phys. Rev. B 45, 4332 (1992)
- J. Nelayah, M. Kociak, O. Stephan, F.J. García de Abajo, M. Tence, L. Henrard, D. Taverna,
   I. Pastoriza-Santos, L.M. Liz-Marzàn, C. Colliex, Nat. Phys. 3, 348 (2007)
- M.W. Chu, V. Myroshnychenko, C.H. Chen, J.P. Deng, C.Y. Mou, F.J. García de Abajo, Nano Lett. 9, 399 (2009)
- 117. B. Schaffer, U. Hohesnester, A. Trügler, F. Hofer, Phys. Rev. B 79, 041401(R) (2009)
- J. Nelayah, L. Gu, C. Koch, I. Pastoriza-Santos, L. Liz-Marzàn, P. van Aken, Opt. Lett. 34, 1003 (2009)
- 119. F. García de Abajo, M. Kociak, Phys. Rev. Lett. **100**, 106804 (2008)
- 120. F.J. García de Abajo, J. Aizpurua, Phys. Rev. B **56**, 15873 (1997)
- 121. C. Girard, Rep. Prog. Phys. 68, 1883 (2005)
- 122. J. Jackson, Classical Electrodynamics, 3rd edn. (Wiley, Hoboken, 1998)
- G. Colas des Francs, C. Girard, J.C. Weeber, C. Chicanne, T. David, A. Dereux, D. Peyrade, Phys. Rev. Lett. 86, 4950 (2001)
- 124. G. Colas des Francs, C. Girard, J.C. Weeber, A. Dereux, Chem. Phys. Lett. 345, 512 (2001)
- 125. G. Lévêque, G. Colas des Francs, C. Girard, J.C. Weeber, C. Meier, C. Robilliard, R. Mathevet, J. Weiner, Phys. Rev. E **65**, 36701 (2002)
- 126. K. Joulain, R. Carminati, J.-P. Mullet, J.-J. Greffet, Phys. Rev. B 68, 245405 (2003)
- 127. C. Girard, O. Martin, G. Lévêque, G. Colas des Francs, A. Dereux, Chem. Phys. Lett. 404, 44 (2005)
- 128. G. Colas des Francs, C. Girard, A. Dereux, J. Chem. Phys. 117, 4659 (2002)
- 129. U. Hohenester, H. Ditlbacher, J.R. Krenn, Phys. Rev. Lett. 103, 106801 (2009)
- 130. J.J. Cha, Z. Yu, E. Smith, M. Couillard, S. Fan, D.A. Muller, Phys. Rev. B 81, 113102 (2010)
- 131. C. Chen, J. Silcox, R. Vincent, Phys. Rev. B 12, 64 (1975)
- 132. N. Yamamoto, K. Araya, F.J. García de Abajo, Phys. Rev. B **64**, 205419 (2001)
- M. Kuttge, E.J.R. Vesseur, A.F. Koenderink, H.J. Lezec, H.A. Atwater, F.J. García de Abajo, A. Polman, Phys. Rev. B 79, 113405 (2009)
- 134. C. Chicanne, T. David, R. Quidant, J.C. Weeber, Y. Lacroute, E. Bourillot, A. Dereux, G. Colas des Francs, C. Girard, Phys. Rev. Lett. 88, 97402 (2002)
- 135. E.J.R. Vesseur, R. de Waele, M. Kuttge, A. Polman, Nano Lett. 7, 2843 (2007)
- R. Gómez-Medina, N. Yamamoto, M. Nakano, F.J. García de Abajo, New J. Phys. 10, 105009 (2008)
- M. Cinchetti, A. Gloskovskii, S.A. Nepjiko, G. Schonhense, H. Rochholz, M. Kreiter, Phys. Rev. Lett. 95, 047601 (2005)
- L. Douillard, F. Charra, C. Fiorini, P. Adam, R. Bachelot, S. Kostcheev, G. Lerondel, M. Lamy de la Chapelle, P. Royer, J. Appl. Phys. 101, 083518 (2007)
- L. Douillard, F. Charra, Z. Korczak, R. Bachelot, S. Kostcheev, G. Lerondel, P.M. Adam, P. Royer, Nano Lett. 8, 935 (2008)
- 140. A. Kubo, K. Onda, H.P.Z. Sun, Y.S. Jung, H.K. Kim, Nano Lett. 5, 1123 (2005)
- 141. B. Barwick, D.J. Flannigan, A.H. Zewail, Nature **462**, 902 (2009)
- 142. F.J. García de Abajo, A. Asenjo-Garcia, M. Kociak, Nano Lett. 10, 1859 (2010)
- 143. F.J. García de Abajo, Nature **462**, 861 (2009)
- 144. F. García de Abajo, M. Kociak, New J. Phys. **10**, 073035 (2008)

# Chapter 9 Nanofabrication for Plasmonics

Gilles Lérondel, Sergei Kostcheev and Jérôme Plain

Abstract Within the last 15 years, the scientific interest for individual or assembly of metallic nanostructures of well-defined size, geometry, and distribution has constantly increased. This paper aims at giving a comprehensive overview of the different nanofabrication techniques used in plasmonics including focused electronand ion-beam lithography as well as the major associated challenges and issues. Alternative techniques, such as interference lithography and self-assembly techniques, are also discussed including material-related issues. The paper is divided into four parts emphasizing on metallic structures fabrication on planar surface, metallic structures fabrication on nonplanar surfaces, metallic structure surface functionalization and hybrid nanostructures fabrication. Finally, alternative techniques and forthcoming issues, such as material quality, nanostructuring on large scale, and plasmonic integration, are also addressed.

#### 9.1 Introduction

The development of microelectronics and associated fabrication techniques such as electron-beam lithography (EBL) has allowed in recent years a tremendous progress in the control of light interaction with metallic nanoparticles or nanostructured thin film and the associated elementary excitation namely plasmon polaritons leading to the field of plasmonics. As demonstrated first for electrons, then for photons in

G. Lérondel (⋈) · S. Kostcheev · J. Plain

LNIO and CNRS UMR6279-STMR, Université de technologie de Troyes,

Troyes, France

e-mail: gilles.lerondel@utt.fr

S. Kostcheev

e-mail: sergei.kostcheev@utt.fr

J. Plain

e-mail: jerome.plain@utt.fr

G. Lérondel et al.

photonic crystals, and now for plasmon polaritons, nanostructuring is a key factor. As far as nanostructuring is concerned, there currently exist two routes namely physical and chemical approaches. A third one will consist in combining both of them. It is interesting to note here that the chemical approach also includes biological species or linkers.

Because integrated circuit (IC) techniques have become available only very recently, alternative techniques were initially proposed to obtain nanostructured metallic thin films in a controllable way. As for photon confinement, the first structuring technique ever proposed was the rugosification. Figure 9.1 shows the evolution of the nanostructuration techniques as far as metallic structured layers are concerned. The initial works were actually driven by enhanced Raman spectroscopy reported as early as in 1974 on electrochemically roughened electrodes [1]. As soon as the effect was ascribed to the surface [2], numerous efforts became devoted to the development of techniques allowing for surface engineering starting from the nanosphere lithography in 1995 [3] and later, electron-beam lithography (EBL) [4]. While EBL allows for a full control of the shape, size, and distribution of the metallic nanostructures, nanosphere lithography presents the advantage to be large-scale compatible, cost effective and easy to implement which in the field of sensing are definitely important aspects.

This paper aims at giving an overview of the various nanofabrication techniques and approaches used in plasmonics. After introducing the various lithographic and related techniques including surface functionalization, examples of metallic structures on planar and nonplanar surfaces will be presented. Alternative architectures relying on surface chemistry and hybrid metallic structures will also be illustrated. Finally, forthcoming issues, such as large-scale nanostructuring and plasmonic integration, will be discussed.

Since we concentrate on the integration of metallic nanostructures, the chemical synthesis of metallic structures in colloidal solutions will not be addressed in this paper. It is however important to mention here that the chemical route has given rise to astonishing accomplishments and especially structures that are hardly realizable using the top–down approach, e.g. core-shell nanorices, nanoboxes and cages, nanotubes, decahedrons to only name a few. For a review on the topic, please see [6].

## 9.2 Methods of Nanofabrication and Related Techniques

Nanofabrication is usually associated to a lithographic process. By a lithographic process, one means defining a pattern that can be either defined by using a so-called writing tool or by self-assembly of particles. To some extent, a crystal can be considered as the ultimate self-assembled structure in terms of size, precision, and regularity. The writing can be either indirect or direct depending on if a mask is used for transferring the pattern or not.

Before presenting the various lithographic techniques used in plasmonics, we will briefly discuss the resolution issue that has driven the development of lithographic

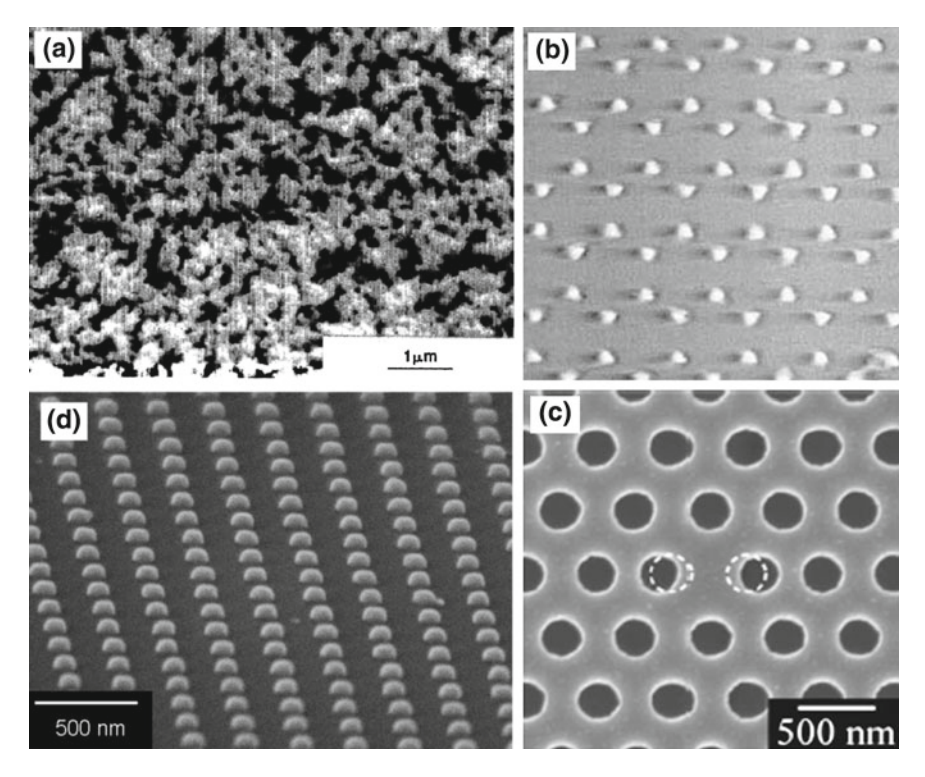


**Fig. 9.1** Evolution in time of the structuration techniques starting from **a** the rugosified surface [1], **b** localized deposition of metallic nanostructures using nanosphere lithography [3], and **c** more recently localized deposition using electron-beam lithography combined with the lift-off technique. For comparison **d** an example of a state-of-the-art photonic crystal tapered microcavity is shown [5]

processes over the year keeping in mind that with feature sizes below 100 nm, plasmonic structures require state-of-the-art nanolithographic processes.

## 9.2.1 Lithography: Evolution and Resolution Issue

The main lithographic process is the mask-assisted photolithography that has been the major tool in the development of microelectronics. The Very Large-Scale Integration (VLSI) concept has forced one to constantly decrease the feature size in order to increase the number of transistors on a chip. The principle of photolithography is shown in Fig. 9.2. A photon source usually monochromatic is used to insolate a photosensitive-coated film through a mask that is projected on the sample to expose. The sample is moved stepwise in order to allow multi-exposures at the wafer scale.

Because photolithography is based on the projection of a mask via lenses, it is diffraction limited. For a feature size smaller than the wavelength,  $\lambda$ , of the source,

272 G. Lérondel et al.

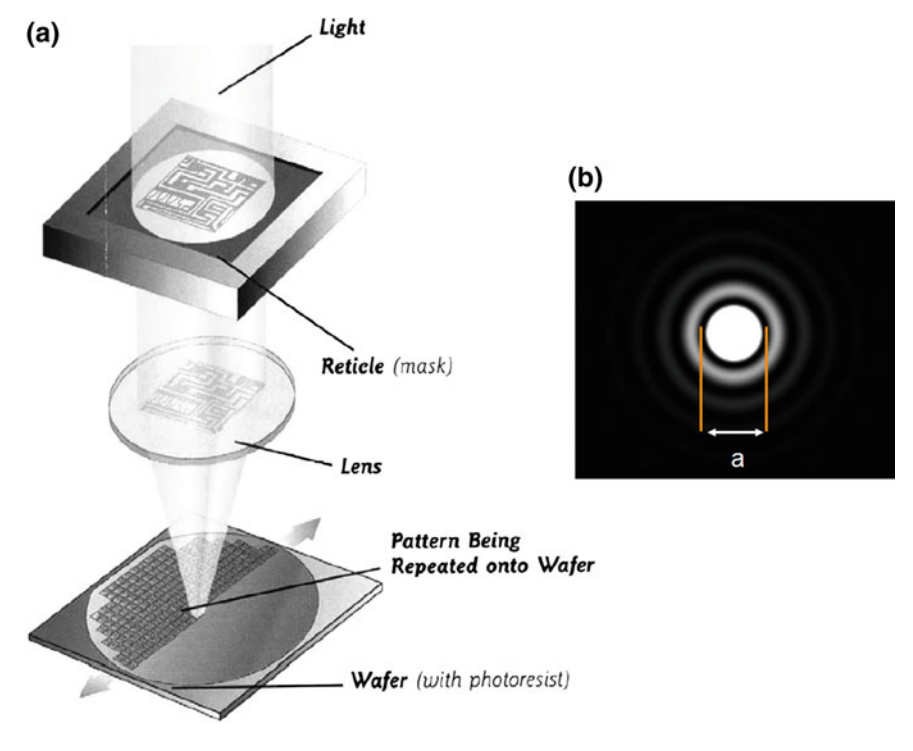


**Fig. 9.2** Principle of mask-assisted photolithography and typical airy pattern illustrating minimum feature achievable using a projection-type lithography

the illumination pattern will no longer be limited by the mask, but by the numerical aperture and  $\lambda$  according to the famous Airy formula:

$$a = 1.22 \frac{\lambda}{NA},\tag{9.1}$$

with NA being the numerical aperture of the lens ( $n\sin\theta$  with  $\theta$  the projection angle and n the refractive index of the surrounding medium). This very simple formula can be used to illustrate the evolution in time of the lithographic techniques.

To decrease the feature size i.e. increase the resolution, there are three possibilities.

The first one is to reduce the wavelength. Firstly demonstrated in the visible, the wavelength of light sources used in photolithography has been decreased over the years to reach the deep UV; first 248 nm, then 193 nm, and more recently 157 nm (F2 laser).

The second possibility is to increase the numerical aperture by working in a medium or through a material with a refractive index larger than 1. This led to the immersion lithography.

The third possibility is to overcome the diffraction limit by working in the near-field leading to the so-called near field lithography, which includes the plasmon-assisted lithography as recently proposed [7, 8].

Coming back to Eq. (9.1), one finds that the resolution limit assuming a numerical aperture of 1 is given by  $\lambda/2$  i.e. roughly 150 nm (UV source) which is larger than a typical plasmonic particle resonant in the visible. Therefore, these techniques do not seem to be appropriate for plasmonic structures. The limit in microelectronics is currently 45 nm. This is achieved using 193 nm lithography combined with immersion lithography, double-patterning, and phase-shifting techniques. As a consequence, the cost of the writing tool has exponentially increased these recent years to be of the order of \$10M.

Following the idea of reducing the wavelength, X-ray lithography is definitely the most promising technique [9]. With a typical wavelength of 13.4 nm, it is perfectly compatible with sub-100 nm lithography. There are however two major issues that are currently limiting the use of X-ray lithography. The first one is the nature of the X rays that prevent working in transmission. To obtain an efficient reflective surface, a multilayered coating is necessary with typical periodicity smaller than 10 nm. Such multilayered coatings are difficult to obtain on a large scale. The second limitation is the source efficiency.

To summarize this part, while mask-assisted photolithography has been widely used in microelectronics, it may not be considered as fully appropriate for plasmonics. Standard equipment are diffraction limited leading to a resolution of half a micron. The cost of deep UV equipments combined with immersion lithography prevents their use at academic level. It is also worth mentioning that a mask is necessary. Down to 1 micron, the masks for photolithography are fabricated using laser writing while for a submicron scale, the EBL is used.

The next section will actually be devoted to EBL and we will explain why this technique can be seen as a universal lithographic method and therefore suitable for plasmonics.

## 9.2.2 Electron-Beam Lithography

Instead of photons, it was proposed in 1936 to use accelerated electrons to do microscopy. Indeed, the wavelength associated with 100 keV electrons can be as small as 3.9 pm (without relativistic correction), which is much smaller than the atomic scale and therefore according to Eq. (9.1), the diffraction limit should no longer be an issue and the atoms should become visible using electron microscopy. It is nowadays common to observe at atomic scale in transmission microscopy using very thin samples.

The same electron beam can be used to expose an electron-sensitive resist leading to electron-beam lithography as first reported in 1960 with the writing of 50-nm features into colloidon thin films [10]. If the accelerated electron wavelength can be as small as 3.9 pm, the diffraction limit is usually larger because of the aperture

angle, which is only of the order of a few degrees. This value is a trade-off between the diffraction and spherical aberrations which, respectively, scale as  $\theta^3$  and  $\theta^{-1}$ . At the end, the typical size (full-width at half-maximum) of the beam will be of the order of a few nanometers down to less than 1 nm for the very best equipment. The beam size is fixed by the current probe (number of electrons per unit time) and the aberrations, which give a resolution limit for the electron-beam lithography of about 1 nm.

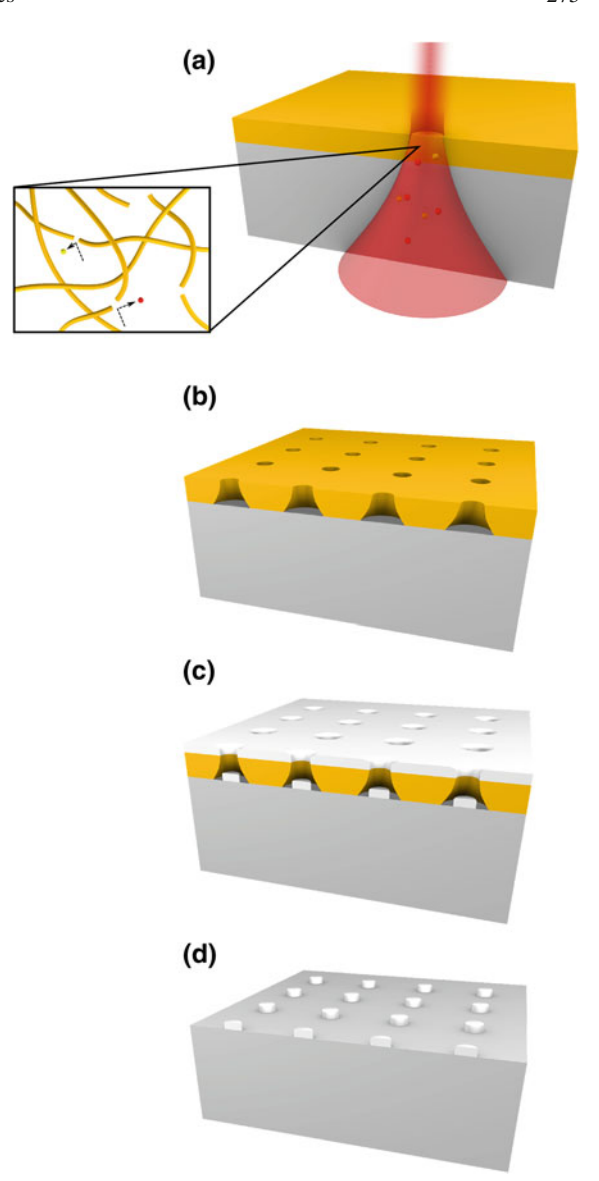
Figure 9.3 illustrates the main steps of electron-beam lithography combined with the lift-off technique. The first step Fig. 9.3a consists in exposing the positive resist using the vector scan of the beam, which is deflected to allow for intermittent writing. This exposure mode allows to "write" down any pattern shape. The pattern is usually defined using a computer-aided design (CAD) software. While the beam is scanned the electrons interact with the resist, usually a polymer, and release their energy that is used to break polymeric chains as illustrated by the inset. After exposure Fig. 9.3b, the resist is developed in a selective solvent. As an example the solution of methyl isobutane ketone (MIBK) in IPA is used for the poly(methylmethacrylate) (PMMA) resist. Smaller chains in the exposed area lead to a material of higher solubility and therefore to a faster dissolution rate of the corresponding area.

At this stage, the pattern can be transferred using an etching process, although the selectivity of PMMA, for example, compared to semiconductors or metals is rather poor. Another possibility lies in using the lift-off process which consists in metallizing the entire sample. This process will only be made possible if a so-called inverted profile is obtained as shown in Fig. 9.3b). One needs a discontinuity between the metal deposited onto the substrate and the resist (Fig. 9.3c). In addition to the undercut or inverted profile, a minimum ratio of 1:3 for the metal:resist thickness is used to prevent any contact. Finally, the unwanted metal areas are lifted up by dipping the sample in a solvent in order to dissolve the remaining resist (Fig. 9.3d). Another important aspect as far as the lift-off is concerned is the adhesion of the metallic layer to the substrate. An ultrasonic bath can be used to further increase the dissolution speed of the resist during lift-off. This is however, only possible if the adhesion of the metallic layer to the substrate is sufficient. Noble metals deposited on glass will actually require the deposition of a thin adhesion layer of Cr or Ti. The lift-off process as well as the optical effect of adhesion will be discussed further in the paper.

In case of nonconductive substrates however, like glass, an additional process will be needed. It consists in metallizing the resist with typically, a 10-nm thick Al layer. This layer prevents the charging of the resist. The very thin layer will be removed by chemical etching before developing the resist. Alternatively one can use substrates that are coated with a transparent conductive oxide layer, like ITO (indium tin oxide) for example.

When starting with EBL, typical test patterns, lines, and dots are used. These test patterns are essential to verify the instrument parameters (focus and stigmatism) and the exposure conditions (acceleration voltage and dose). Figure 9.4 shows various test pattern examples. Figure 9.4a shows a cross-section of PMMA lines after development. The effect of overdose at the substrate–PMMA interface, due to both

Fig. 9.3 Electron-beam lithography for the local deposition of metals. a Electron-beam (red in illustration) exposure of the resist (yellow in illustration) leading to polymeric chain breaking. b Inverted resist profile after development. The profile shape is due to overexposure at the resist—substrate interface. c Metal coating (white in illustration) and d The remaining structures after the stripping of the resist in a solvent



forward and backward scattering, is evidenced at the bottom of the line where the gap is slightly larger. Such a profile is enough to obtain a clear contour after the lift-off. Examples of patterns locally deposited by the lift-off are shown in Fig. 9.4b. While the edges are clear, a slight undulation can be observed, which is most probably due to the electromagnetic noise during exposure. This effect is further evidenced in Fig. 9.4c where elongated dots were obtained explosing lines with different spacings. A size variation can be cleared observed. The observation has been done after

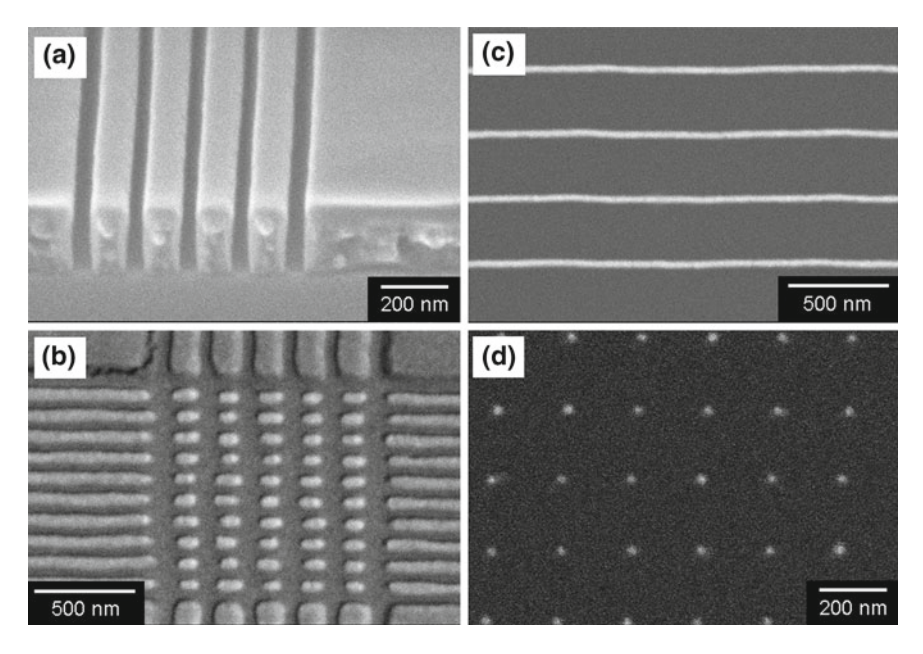


**Fig. 9.4** Test pattern 1: lines and dots. SEM pictures of lines obtained before (a) (cross-sectional view) and after lift-off (b) and dots obtained by line crossing (c) or single dot exposures (d). Patterns (a) to (c) have been obtained on Si, whereas pattern (d) has been obtained on glass (BSE image)

the metallization (Au) before the removal of the resist. Finally, the Fig. 9.4c shows nanometric dots obtained on glass by a single shot exposure. This technique allows for the minimum dot size. The use of backscattered electrons is here required to observe the metallic dots deposited on glass. The resolution is however not enough to observe the edge of the dots whose size can be estimated to be less than 30 nm. We achieved here the resolution limits of both the instrument and lithographic process. Exposure conditions include 30 kV of acceleration voltage and 10 pA of probe current (tungsten filament) and a 150-nm-thick PMMA layer (950 K). Typical line and dot exposure doses on glass are 1.3–2 nC/cm and 6 pC/dot, respectively.

An example of a third important pattern after dots and lines is shown in Fig. 9.5. Segmented wheel patterns are very useful to check (a posteriori) the stigmatism adjustment of the writing beam. Both figures show a wheel pattern obtained after lift-off on silicon. In the top figure, one clearly sees that segments are missing at 45°. This is due to an ellipsoidal shape of the beam with the longest axis at 45°. The surface dose is therefore lower at 45° and PMMA is not totally exposed. The remaining PMMA will give rise to a complete lift-off of the metallic layer. The figure below shows a pattern obtained after stigmatism correction. Individual segments as evidenced by the white arrow can be observed in all directions.

In the field of plasmonics, we are also interested in nanometric features such as metallic nanogaps or sharp nanostructures. This brings us to the resolution limit

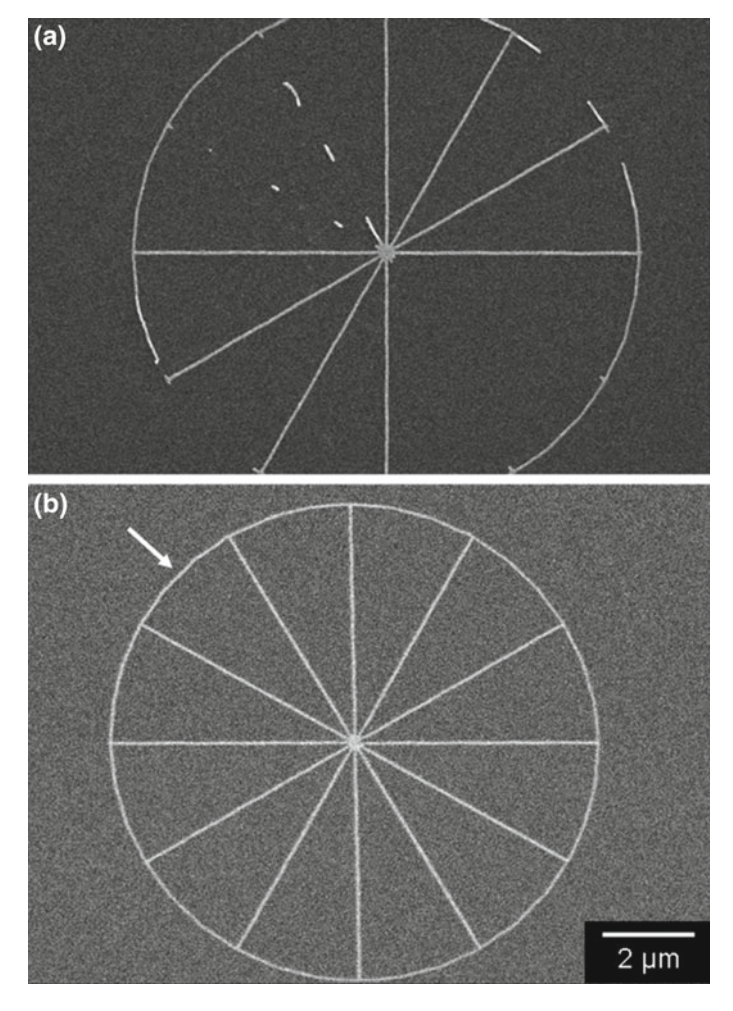


**Fig. 9.5** a Segmented wheel as a test pattern for stigmatism adjustment. If the stigmatism is not well adjusted the dose in the x and y directions is different, leading to partial exposure. **b** Example of structures obtained after stigmatism correction. The segment as indicated by the arrow should be visible in any direction

achievable through electron-beam lithography. A key parameter is the interaction volume of the primary and backscattered electrons in the resist. As far as the interaction volume broadening is concerned, the effect of secondary electrons can be considered as negligible for a distance over 10 nm [11]. In order to control the interaction area, two parameters are of importance: the energy of the primary electron and the thickness of the resist. For an acceleration voltage larger than 50 kV and a resist thickness below 100 nm, forward scattering in the resist can be neglected [12]. Figure 9.6 qualitatively illustrates the mechanism of electron scattering in a resist.

The resist is exposed by both the forward and backscattered electrons. As a function of the acceleration voltage, the lateral scattering of the forward and backward scattered electrons will, respectively, decrease and increase. In other words, larger acceleration voltage allows for smaller and higher density features. Values are given for 20 kV and a one-micron-thick PMMA layer. It is worth noting that for a thin film of resist, the backscattered and secondary electrons' density will strongly depend on the substrate. As already mentioned, while secondary electrons will affect the effective dose, the induced spreading is negligible for a feature size over typically 10 nm.

Electron-beam lithography resolution using PMMA has been thoroughly addressed in a recent paper by Vieu et al. [13]. They show that the resolution can be pushed below 10 nm for isolated structures and that the intrinsic resolution limit of the writing process in the resist can be as small as 3–5 nm at high energy (200 kV). The practical resolution is limited by the development of the resist and pattern transfer. Figure 9.7 shows one of the most impressive results obtained by Vieu et al. The SEM pictures show an array of 7-nm-width gold lines obtained by lift-off of an extremely thin evaporated gold film (2 nm). The PMMA layer was 140-nm thick, exposed with a line dose of 4 nC/cm. The lines appear uniform in size. The enlarged view figure (b) reveals that the line width corresponds to the grain size of the thin film, suggesting that atomic diffusion on the surface was triggered by the line width of the PMMA pattern. These monogranular metallic lines can be seen as the smallest realizable plasmonic chains reaching the granularity limit of the gold evaporated thin film. These results show that sub-10-nm resolution can be achieved with PMMA and that as far as plasmonics is concerned, there is room for reducing further the feature size. It is worth mentioning here that by using alternative processes like direct sublimation or radiation damage lithography, sub-1-nm resolution was already demonstrated in 1988 [11].

## 9.2.3 Complementary and Alternative Lithographic Techniques

In this section, we will resent alternative or complementary lithographic techniques for plasmonics.

#### **Ion-Beam Lithography**

A technique related to electron lithography is the focused ion-beam lithography or commonly called FIB. The FIB is based on the use of accelerated ions instead of electrons. If the wavelength of accelerated ions can be similar to that of accelerated electrons and therefore an atomic resolution is expected in the ideal case, the major difference lies in the mass of the ions that allows very efficient momentum transfer and therefore physical etching of a material (almost any kind of material). As a consequence, when the accelerated ions are tightly focused, a material can be

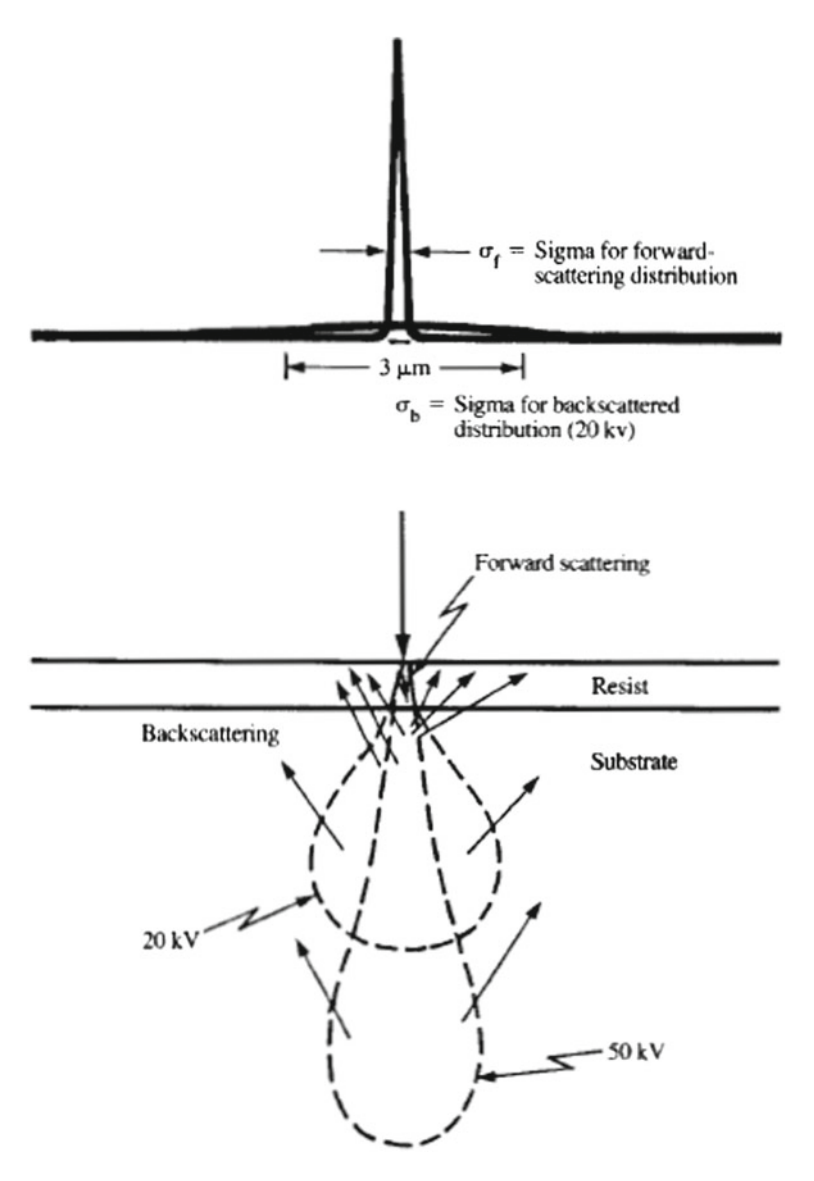


**Fig. 9.6** Schematic view of the electron scattering process at the air/resist/substrate interface [11]. Because of backscattered electrons, the dose is higher at the resist/substrate interface

locally removed. It is worth noting that the ion physical etching has been known for a long time. Let us cite, for example, the preparation of TEM slides by ion milling.  $Ga^+$  ions are usually used. Since the mid-1980s, FIB has been developed to become a major nanofabrication tool. Structures as small as 6 nm have been written using  $50\,\mathrm{kV}$   $Ga^+$  ions with a two-lens system (magnetic lenses) as in an electron micro-

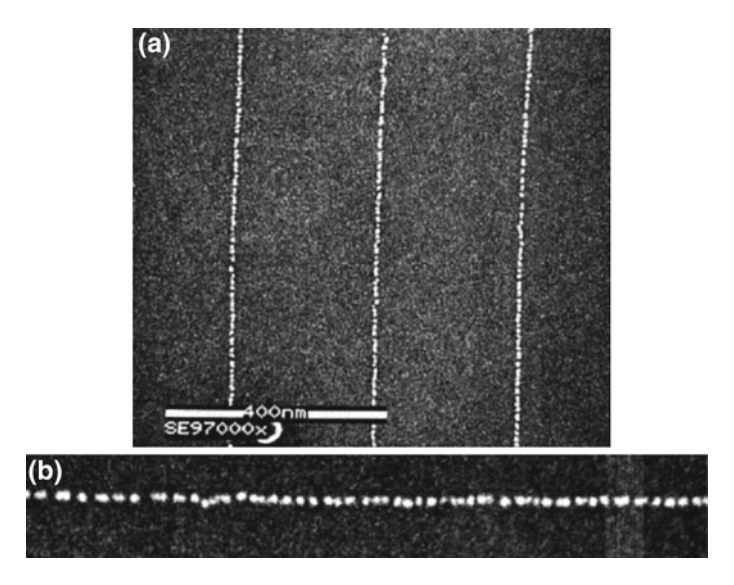


**Fig. 9.7** Sub-10-nm metallic lines obtained by lift-off of a granular gold extremely thin film (2 nm) from [13]

scope [14]. This technique has been intensively used in plasmonics especially to fabricate perforated metallic thin films [15]. Indeed, FIB is a complementary technique with electron-beam lithography combined with lift-off. FIB is well adapted for discontinuous patterns such as hole or gaps. Despite its own advantages, FIB is less popular than electron beam lithography because it requires a dedicated equipment. A related aspect is that while FIB can also be used for the observation at low energy, besides relatively limited resolution, it may also contaminate the sample. Therefore, dual-beam systems have been developed where the electron beam can be used for observation and the ion beam for writing. This kind of dual system has made possible the fabrication of nanoantenna at the extremity of scanning near-field microscope (SNOM) tips. Fabrication of nanostructures on nonplanar substrates will be the subject of a dedicated subsection. Finally sub-5 nm resolution is achievable using FIB and membranes. Sub-5 nm arrays of holes have been obtained in SiC membrane [16]. While metallic membrane fabrication is an issue itself, the same technique offers great potential for extremely tiny hole or gap arrays fabrication and related applications like sensing.

#### **Immersion Lithography**

Following (9.1), another way to further decrease the diffraction limit of conventional optical lithography is to use immersion lithography. This has been demonstrated in imaging using immersion lenses. In microelectronics, immersion lithography has been used to push further down the resolution of 193 nm lithography and achieve

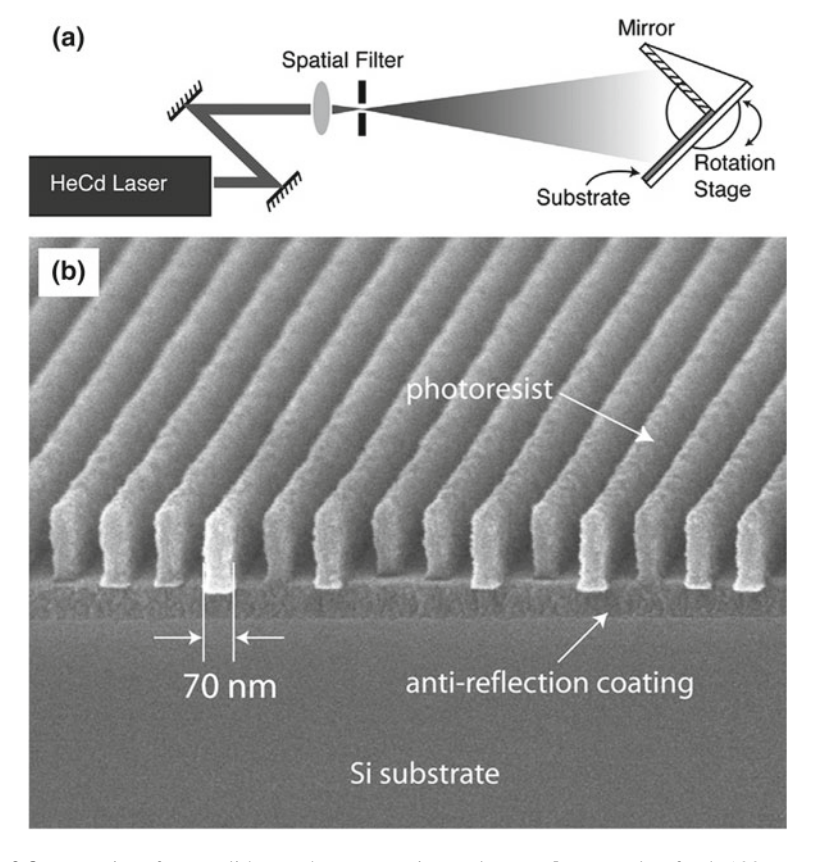


Fig. 9.8 Laser interference lithography. a Experimental setup. b Example of sub-100-nm pitch grating. From [17]

the 45-nm node. As already mentioned, the cost of the equipment prevents its use by the scientific community.

#### Laser Interference Lithography

Laser interference lithography is a rather simple technique. While only periodic or quasiperiodic structures can be realized, the technique is of low cost, large-scale compatible, and allows for sub-100-nm structures to be fabricated. Figure 9.8 shows an example of 70-nm wide line pattern Fig. 9.8b in a photoresist obtained with the Lloyd configuration as illustrated in Fig. 9.8a [17].

More recently, 50-nm period gratings have been obtained by the so-called multilevel interference lithography where each grating level is patterned with a phase shift with respect to a reference grating [18]. This process could be used for the fabrication of more complex periodic structures or commensurable metallic gratings [19]. Despite its advantages and achievable feature size, this technique has merely been applied to plasmonic structures (cf. Sect. 11).

#### Nanosphere Lithography

As an alternative technique, one should also mention the nanosphere lithography (NSL) that was first proposed in 1995 [3] and has then been intensively used, especially for Surface-Enhanced Raman Scattering (SERS) studies [2]. Self-assembled nanospheres on a surface can be used as templates in various ways such as corrugated metallic layers after a uniform coating or template for lift-off after dissolution. In the latter case, the spheres interstices have been found to form a perfect template for sharp edges' metallic structures. As already mentioned, NSL is a high-throughput technique, cost effective and large-scale compatible. For highlights of representative research accomplishments in the NSL-derived fabrication techniques, the reader may refer to [20].

#### Scanning Near-Field-Based Lithography

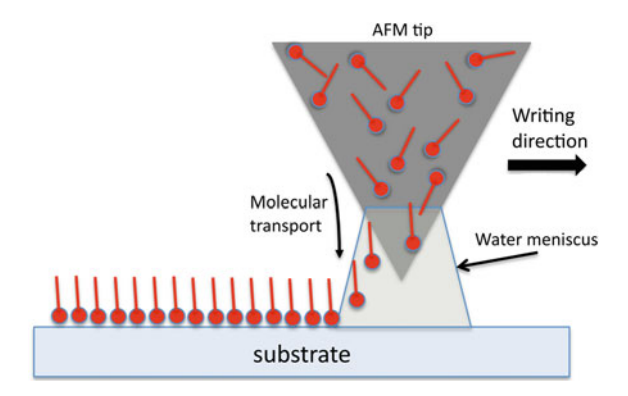
A way to get rid of the diffraction limit is to go behind this limit using near-field optical lithography. Near-field optical lithography has been first demonstrated using SNOM (Scanning Near-field Optical Microscope) with an aperture probe and has then been extended to the scattering tips, making this technique possible with a standard atomic force microscope (see for a review [21]). Alternatively, near-field probes, such as Scanning Tunneling Microscope (STM) or Atomic Force Microscope (AFM), can also be used to induce a physical interaction. While metallic nanostructures have often been used to demonstrate these techniques, none of them has been used to fabricate metallic structures. One of the most promising techniques as far as plasmonics is concerned, is the dip pen lithography [22], which could be combined with surface chemistry to locally link metallic particles to a substrate. As shown in Fig. 9.9, the dip pen lithography is based on molecular transport.

One of the advantages of AFM-based lithography is that it works in ambient atmosphere. Recent progress in combining interferometric stages with near-field microscopes such as AFM or SNOM may also help to achieve large-scale near-field probe-based nanostructuring [23, 24]. A relative high throughput is also achievable using parallel writing.

## 9.2.4 Lift-off

The lift-off technique combined with EBL is definitely well suited for metal local deposition. It is easier to implement than the standard mask transfer technique using

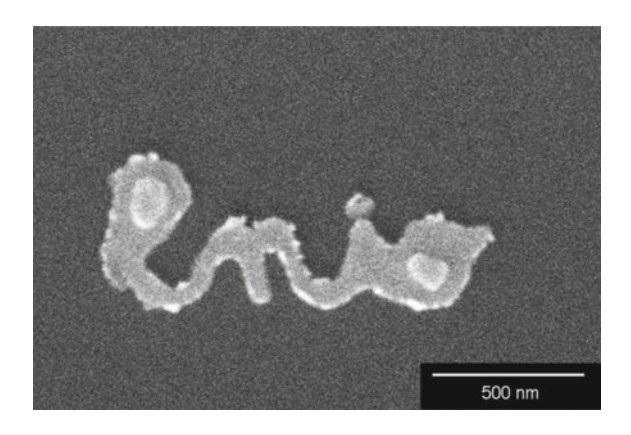
Fig. 9.9 Dip pen lithography



wet and especially dry etching. The mask transfer technique is used for semiconductors or more generally materials showing high crystallinity. Such materials are less suitable for the lift-off process, as they are usually deposited at high temperature using the nondirectional deposition technique. Indeed, two conditions must be fullfilled for the lift-off process. One is to use a directional deposition technique and the second one is an undercut profile as illustrated in Fig. 9.3b. Regarding the first aspect, metals, which can be deposited by thermal or electron beam evaporation on low (ambient) temperature surfaces, are well suited for the lift-off. As far as the undercut profile is concerned, the method depends on the typical size. For microscopic features down to 100 nm, a bilayer of resist with a thin top layer of low sensitivity and an underlying layer of high sensitivity is used. While the bilayer allows for the perfect "mushroom" profile to be obtained, it requires rather thick resist layers and therefore the resolution is limited. For thin structures such as plasmonic structures typically of the order of 50 nm, a monolayer is sufficient to obtain an undercut profile using electron-beam lithography. For thin layers, the dose is higher at the substrate interface due to the backscattered electrons as illustrated in Fig. 9.6. While this effect limits the density of nanostructures, it allows for an undercut profile to be obtained. The shape of the profile will however be very sensitive to the dose.

Figure 9.10 shows an unsuccessful example of lift-off with rough edges. Contrary to the pattern shown in Fig. 9.1c where the nanoparticles have clear contours, rough edges are the results of metal scratching occurring during the resist dissolution. An additional interesting feature is the "O" and "l" letter patterns where the metal has remained. The resist in these areas cannot be dissolved and this is because of the thickness of the resist, which was too thin in this case (50 nm) compared with the metallic layer thickness. Another example of well-defined contour structures is the pattern obtained by nanosphere lithography. Allowing for the shadowing effect, spherical particles are well adapted for the lift-off.

Fig. 9.10 Unsuccessful example of lift-off (electron beam evaporated Au on Si through a 50-nm-thick PMMA layer)



### 9.2.5 Direct Writing

Direct writing techniques allow for the fastest prototyping as they are compatible with a one-step structuration. Such techniques are however strongly dependent on the material to be nanostructured, unless the process is mainly physical as in the case of ion-beam etching (IBE). Focused ion-beam etching is definitely one of the best examples of a direct writing technique and has been extensively used in plasmonics (see Sect. 9.2 for examples of structures). Alternatively again, electrons can be used to locally deposit or etch materials leading to electron-beam-induced deposition (EBID) or electron-beam-induced etching (EBIE). EBID or EBIE in SEM chambers has been used for direct (carbon) nanowire fabrication [25] or photomask repair [26]. Figure 9.11 illustrates the EBID process.

Despite their very high-resolution potential [11], these techniques, apart from the FIB technique, have almost not been used for plasmonics. One of the limitations could lie in the available gas precursors and the partial pressure necessary as recently discussed in a theoretical paper for the fabrication of high-resolution radially symmetric nanostructures [27]. Laser ablation (thermal or chemical) using either intense IR lasers or UV lasers can also be classified as a direct writing technique. Being diffraction limited, the use of this technique for plasmonics is again limited. Subwavelength resolution has however been achieved for microstructures using a nonlinear process like two-photon absorption (see for a review on the topics [28]). Based on polymeric materials, two-photon photolithography cannot be considered as a direct writing technique, unless charged resists are used as very recently demonstrated with a gold-precursor-doped photoresist [29]. In this paper, a polymeric line of 200 nm and periodic arrays of chiral elements have been reported. As shown for photonic crystals, the ability of two-photon lithography for 3D direct writing is of a great potential for metamaterials working in the IR or NIR. Self-organization can also be considered as a direct writing technique for plasmonics when metallic objects or materials are considered. Self-organization of metallic nanoparticles has however been demonstrated only recently. One of the limitations lies in the small

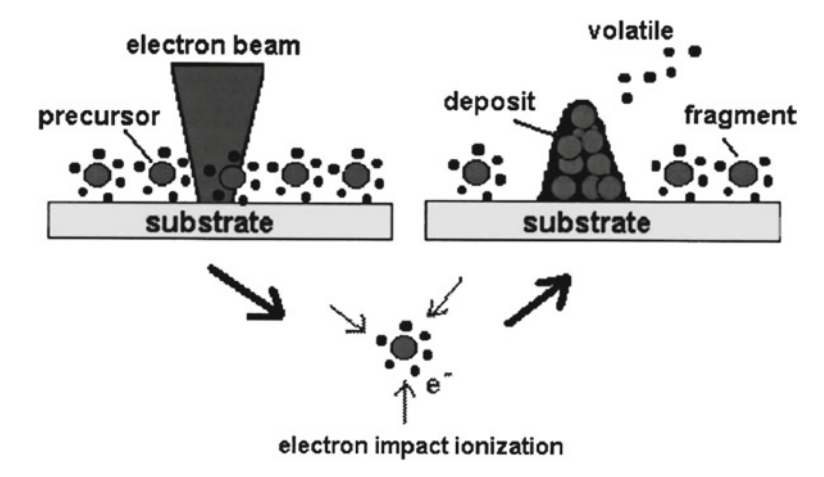


**Fig. 9.11** Illustration of the EBID process. Absorbed molecules brought to the substrate by a precusor gas are dissociated by the electron beam. From [25]

size of the particles that requires surface chemistry. This aspect will not be treated in this subsection, but in the next one dealing with surface functionalization.

## 9.2.6 Surface Functionalization

#### Why Surface Functionalization?

The surface modification using self-assembled monolayer (SAM) or physisorption of polymers is a very useful tool for numerous reasons. As claimed by nanotechnologists, the properties of numerous nanosystems are new and relevant for applications because the number of atoms at the interface is higher than the number of atoms in the bulk at the nanoscale [30]. Thus, by controlling the nature of the surface, it is possible to tune the properties of the nanosystem, as for example, plasmon-based nanosensors [31]. Moreover, even if the SAM (or an organic layer in general) induces a change in the properties, it could also be seen as a brick in a more complex nanoarchitecture [32] or it could act as a stabilizer for the nanostructure [33]. In terms of surface functionalization, two cases must be separated. First, the functionalization of typical substrates used in nanooptics (glass or Si in case of integration) and second, the functionalization of the plasmonic structures themselves (Au, Ag, or noble metals in general).

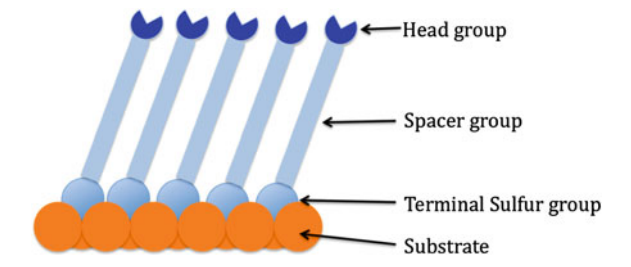


**Fig. 9.12** Schematic representation of a thiol molecule. The sulfur group links the molecule to the gold surface. The spacer group separates the sulfur group from the head group. The head group can be designed to provide virtually any surface chemistry, binding capacity, or property

**Table 9.1** Some head group examples useful for applications

Application	Common head group
Non-fouling surfaces	$PEG_n$ or mannose
Cell supports	Peptides
Specific binding receptors	Biotin, NTA, peptide, carbohydrates
Molecular electronics	$CH_3$ , SH
Microarrays	DNA, Peptides, $PEG_n$
Surface reactions	Azide, COOH, NH <sub>2</sub> , OH, SH

#### **Self-Assembled Monolayer**

Materials can spontaneously assemble on the surface under the effect of driving forces. The molecules able to form a self-assembled monolayer (SAM) are generally formed by three groups as shown in Fig. 9.12 in the case of a thiol molecule.

The first group is a reactive group, which will react with the substrate to form a covalent bond. The second one is the spacer group (generally an alkane chain). This group is used to separate the head group from the surface. Finally, the head group allows giving to the surface the specific chemical function. For example, a  $CH_3$  (resp. OH) terminated molecule will show a contact angle with water of about  $110^{\circ}$  (resp.  $\leq 20^{\circ}$ ). The chemical nature of the head group will depend on the final application, specific binding, or chemical reactions... Different head groups are commercially available with different properties. Some examples are listed in Table 9.1.

#### **Organosilicon Molecules on Oxides**

Surface functionalization of oxide layer ( $SiO_2$  for example) is principally obtained by the grafting of organosilicon derivatives. The general structure of the organosilicon (or silane) molecules is  $X_3 - Si - R - F$ . The X groups are reactive groups like hydroxy, chlorine, methoxy, and ethoxy. The R - F group is generally an alkyl chain

(R) terminated by a specific function (F). This function will determine the substrate properties. SAMs of organosilicon or silanes (alkylchlorosilane, alkylalkoxysilane, or alkylaminosilane. . .) require a hydroxylated substrate to be formed. In this case, the self-assembly is obtained through the formation of polysiloxane. This polysiloxane is then connected to the substrate via the formation of Si - O - Si covalent bonds. The well-admitted scenario for the covalent bonding is divided in two steps. The first one relies on a hydrolysis of the silane molecule by  $H_2O$  molecules absorbed on the substrate as shown by Eq. (9.2).

$$R - SiX_3 + H_2O \rightarrow R - SiX_2OH + HX \tag{9.2}$$

The second step is a condensation of the silanol group of the hydrolyzed molecule with the silanol group onto the substrate as shown by Eq. (9.3).

$$R - SiX_2OH + HO - Si \rightarrow Si - O - SiX_2 - R + H_2O$$
 (9.3)

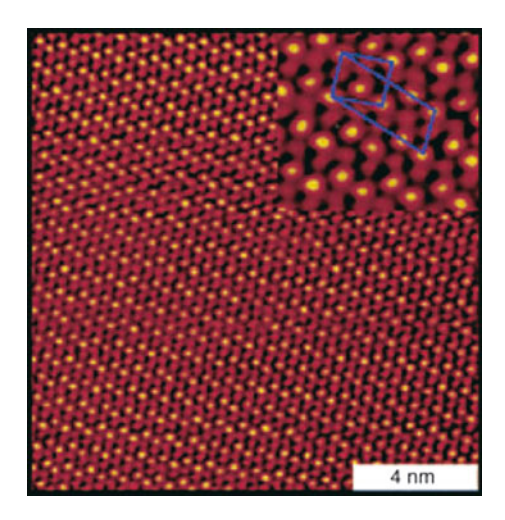
The final structure of the SAM depends on numerous parameters like the length of the spacer group, the head group nature and the temperature [34]. High-quality SAMs of silanes are very challenging to obtain. The main issue is the difficulty to control the amount of water present on the substrate [34].

#### Thiol Molecules on Gold (111)

Surface functionalization of noble metal (for example, gold or silver) is usually obtained through the spontaneous binding of a thiol group (R-SH), also called the mercapto- group to the metal. Not only thiol but disulfide molecules ( $R_1 - S - S - R_2$ ) are able to bind spontaneously onto gold (or silver). This results in a 2D crystalline layer on the metal surface as shown in Fig. 9.13. The typical thiol molecule is schematically represented in Fig. 9.12. As shown in Fig. 9.12, three groups generally form a thiol molecule. The first one is the terminal sulfur group (-SH), which links the molecule to the metal surface (S-Au, for example). The S-Au bond is a quasi-covalent bond characterized by a bonding energy of about 45 kcal/mol [33] (the binding energy of C-C is about 80 kcal/mol), which induces a very stable layer.

Practically, the formation of a thiol (or disulfide) monolayer is very simple. If the thiol molecules are volatile, they will bind spontaneously on any gold substrate in a closed reactor. Note that heating can easily vaporize a liquid thiol. Alternatively, by dissolving thiol in a suitable solvent (ethanol, for example) at a concentration of about 1 mM, it will be possible to induce the formation of a SAM on a gold substrate by immersion during 1 to 24h. Finally, in both cases, i.e. gas-phase or liquid-phase deposition, the substrate is rinsed with an adequate solvent to remove the physisorbed molecules.

Fig. 9.13 Scanning tunneling microscopy image of a self-assembled monolayer of decanethiol on gold. Adapted from [35]



#### **Physisorption of Polymers**

In contrast with the cases of chemisorptions presented above (SAM), macromolecules like polymer will physisorb irreversibly to the surface. The reason is directly correlated with the number of bonds between the polymer chain and the surface. Single bond energy is about  $k_BT$ , but the sum of all the bonds together will represent a strong binding energy.

Even if polymers are often used to give a particular function to a substrate (for example, PMMA/QDs will allow the luminescence of a substrate [36]), we will emphasize on polyelectrolytes, which are charged polymers that are particularly well studied and understood [37]. Moreover, polyelectrolytes are used as a brick in the nanofabrication to assemble different materials without specific chemical modification. Polyelectrolytes are positively charged (polycations) polymers or negatively charged (polyanions) polymers. The charges are linked to dissociation of a specific group on the polymer chain (for example  $NH_3Cl$  will dissociate to  $NH_3^++Cl^-$ ). The total charge will depend on the number of dissociated groups in the polymer chain. The polyelectrolytes are generally deposited in solution in an aqueous medium. The final morphology of the deposited film will depend on numerous parameters such as pH and salt concentration (see [37] for more details). In nanofabrication, the technique used with charged species is called layer-by-layer (lbl) deposition. The deposition is obtained through a simple dip-coating process. First, the substrate is immersed for a given time t (typically a few minutes) in a solution of polyanions (resp. polycations), then the substrate is washed and immersed again during the same time t in a solution of polycations (resp. polyanions) and washed [38]. The process is then repeated until the number of desired bilayers (polyanion/polycation) has been achieved. The complete process is schematized in Fig. 9.14.

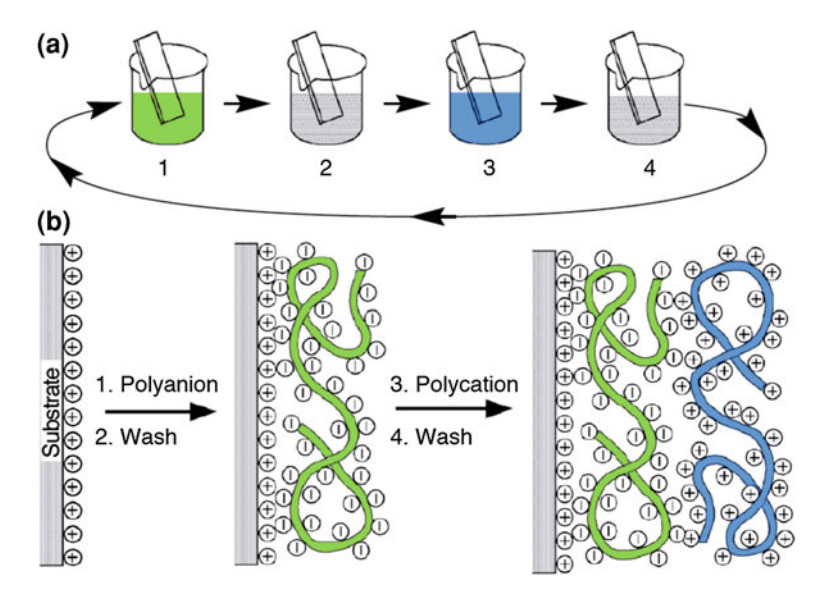


**Fig. 9.14 a** Schematic of the film deposition process using slides and beakers. Steps 1 and 3 represent the adsorption of a polyanion and polycation, respectively, and steps 2 and 4 are washing steps. **b** Simplified molecular picture of the first two-adsorption steps, depicting film deposition starting with a positively charged substrate. From [38]

#### 9.3 Structures Fabrication

Two challenges are particularly relevant for nanotechnology and more precisely for nanooptics and plasmonics. The first one is the fabrication of new structures presenting unique features induced by the size reduction down to the nanoscale. For example, a plasmonic antenna, which is composed of metal nanoparticles, allows one to efficiently outcouple (direct) the emission of quantum dots as demonstrated by the group of N. van Hulst [39].

The second one is the nanostructuration of large areas, typically from hundred of  $\mu m^2$  to several cm². For example, metamaterials are composed of nanostructures replicated on wide areas and thus present new macroscopic optical properties as negative refraction [40] or extraordinary transmission [15]. In this part, we will present examples of plasmonic nanostructures obtained by the techniques presented in the previous sections.

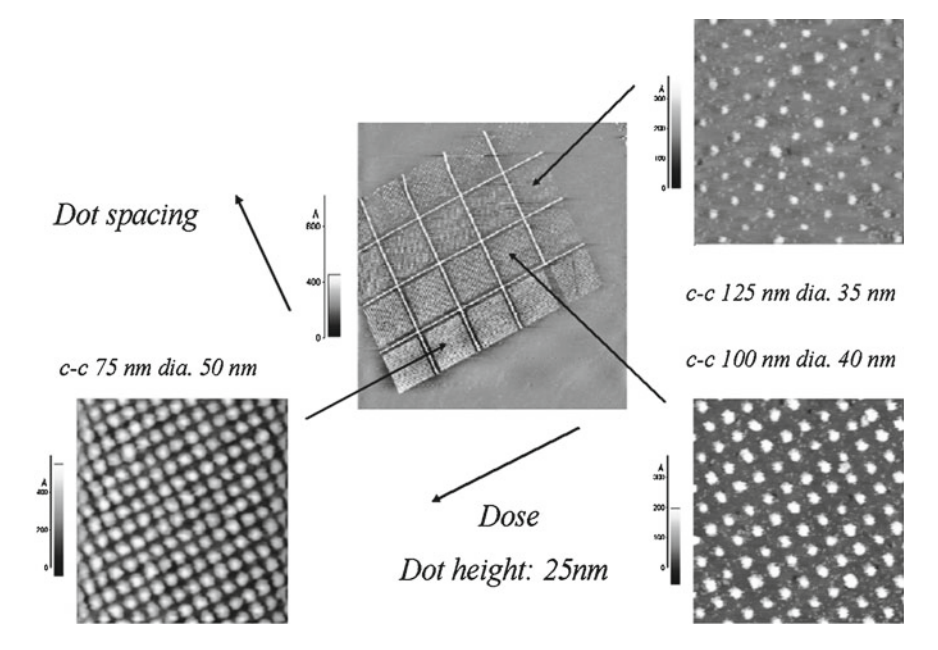


Fig. 9.15 Illustration of a systematic study of particle resonance using a single sample with dose and spacing gradual changes. Central and side images are, respectively, 30 and 1  $\mu$ m wide

### 9.3.1 Metallic Nanostructuring on Planar Surfaces

#### **Lithographic Structures**

Lithographic techniques like electron-beam or ion-beam lithography allows the entire control for designing metallic nanostructures. In addition, they allow for so-called fast prototyping using patches leading to the concept of one sample—one study. We aim in this section at illustrating through examples, the full potential of electron- and ion-beam-based lithography for plasmonics starting with the lift-off technique.

#### Size and Spacing Control

A typical example of the interest of a lithographic sample for plasmonics is the study of particles' optical response as a function of the particle size and spacing.

Figure 9.15 shows the AFM images of a SERS substrate obtained with a single shot exposure and constant increase of the dose, diameter, and spacing effects have been probed. It is noteworthy to mention that a tip correction has been here applied to deduce the size of the particles from the AFM profiles.

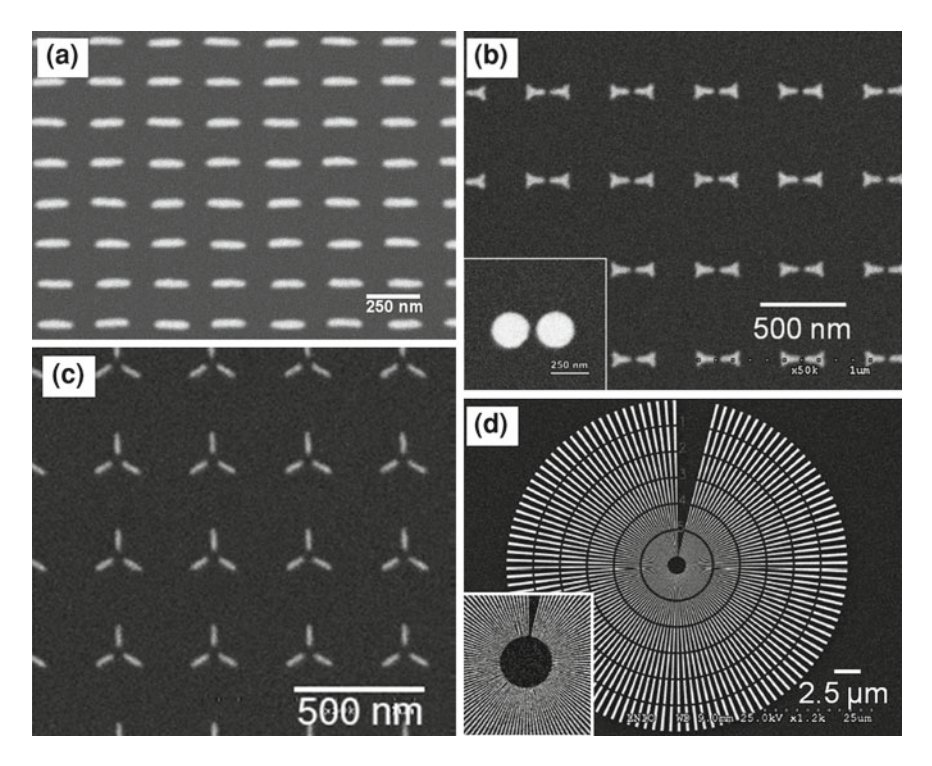
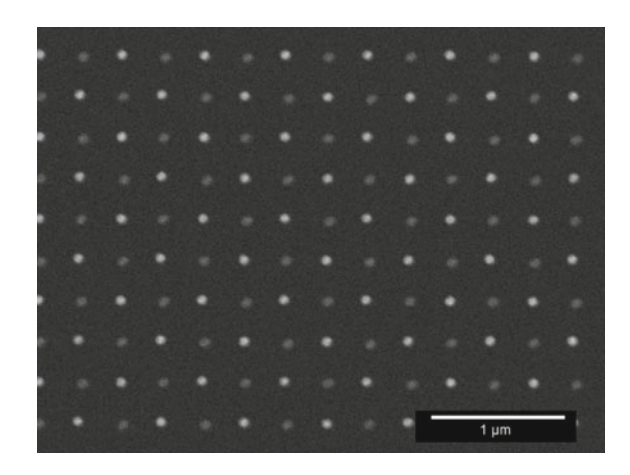


Fig. 9.16 Illustration of plasmonic structures shape control: a ellipsoid, b dimers (spheres and bow-ties), c trimers, and d multiscale concentric structures

#### **Shape Control**

As already mentioned besides the size and the spacing, resonances of plasmonic particles are also shape and assembly dependent. Figure 9.16 shows various shapes and assemblies achievable using electron-beam lithography. As long as structures are isolated, the proximity effect will be negligible and reproducible structures can be fabricated. For dense structuring like the asian-umbrella structure, a dose variation is necessary to compensate the proximity effect. The latter structure shows the possibility to fabricate multiscale patterns. As far as dimers are concerned, the major issue is the control of the gap between the two particles. In the case of spheres, this could be achieved by the dose control as evidenced by the image. Together with the shape, the sharpness of plasmonic structures is also an issue especially for "tip" structures like bow-tie antenna. Figure 9.16d shows rounded edges which are due to the beam size.

**Fig. 9.17** Silver–gold binary array



#### **Binary Array**

Another interesting aspect, which has not been really explored yet, is the possibility of mixing different materials. Figure 9.17 shows a double array of gold and silver metallic nanoparticles obtained using a one-step alignment [41]. Such binary structures could be of interest to fabricate double-resonant SERS substrates or to widen the absorption spectrum for efficient energy conversion.

#### Plasmonic Structures on Transparent Conductive Oxide

Glass coated with transparent conductive oxide like Indium Tin Oxide (ITO) is an alternative substrate for plasmonics. As already mentioned, the presence of an ITO layer will influence the optical response especially in the case of localized surface plasmon modes. Therefore, a resist metallization is usually preferable (cf. section on EBL). Figure 9.18a shows a 4  $\mu$ m long single nanowire realized on ITO substrate on purpose. This sample was actually fabricated to be probed by the recently introduced PEEM technique. PEEM standing for photoemission electron microscopy requires a conductive substrate. Photoelectrons emitted by the sample are accelerated and imaged on a 2D sensor allowing subdiffraction imaging. Plasmon interferences are clearly observed here, as evidenced by the PEEM image (cf. Fig. 9.18b) and the associated intensity profile (Fig. 9.18c).

#### **Corrugated Structures**

As already proposed using nanosphere lithography or even earlier with rough surface coating, the easiest way for obtaining a structured metallic thin film is to coat a corrugated surface. Using electron-beam lithography, well-defined corrugations can

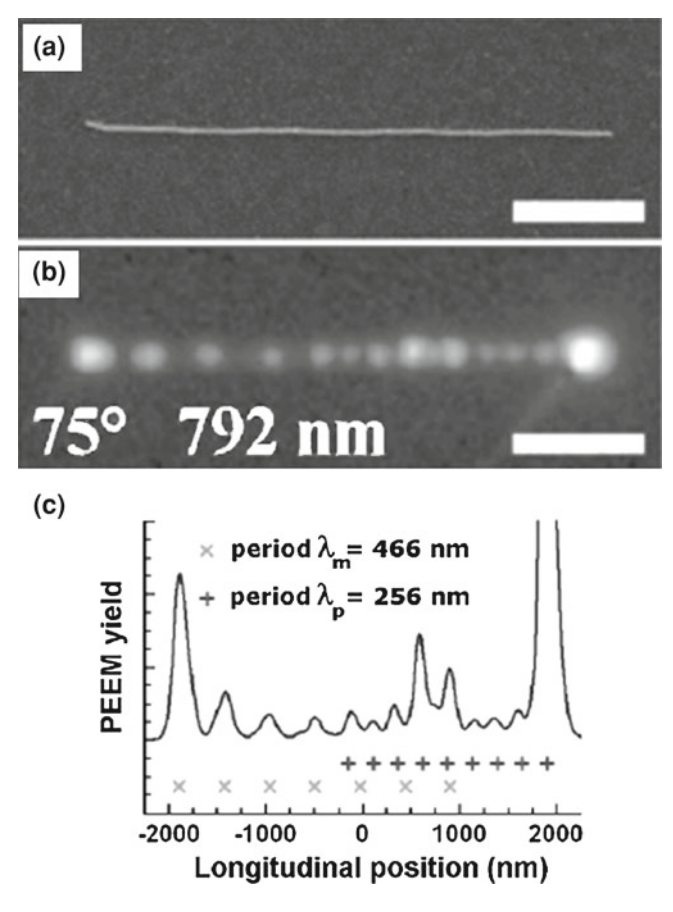
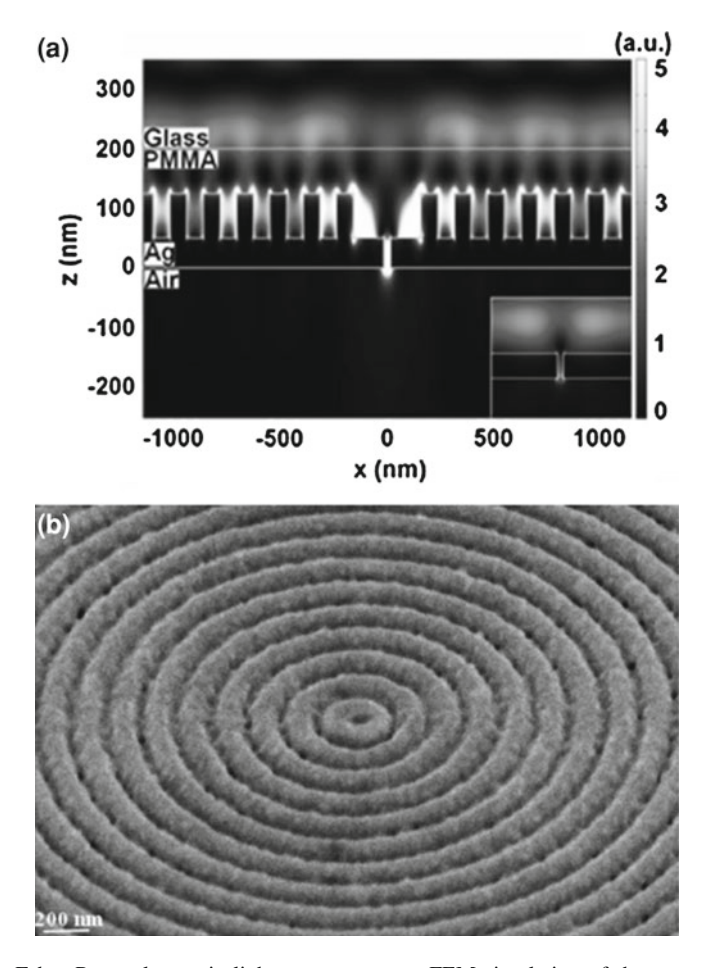


Fig. 9.18 Single gold plasmonic nanowire as probed by PEEM: a SEM image, b PEEM image, and c Intensity profile. Scale bars are  $1 \mu m \log$ . From [42]

be obtained. Figure 9.19 shows a Fabry–Perot plasmonic light concentrator fabricated by combining electron- and ion-beam lithographies. The circular pattern has been obtained by partially exposing a PMMA 150-nm thin film which after development has been then coated with a 50-nm silver film. The nanoaperture has been drilled by FIB using a dual-beam system. The major difficulty in fabricating such a structure lies in the centering of the aperture for which SEM observation prior to the focused ion milling is necessary. The layered structure can be guessed from the simulated image 9.19a.

#### **Dielectric Structuring on Metal**

While plasmonic structures are usually obtained by the local deposition of metal using the lift-off technique, an alternative technique can be used, which consists in



**Fig. 9.19** Fabry-Perot plasmonic light concentrator. **a** FEM simulation of the resonant optical structure as compared with a single nanoaperture (30 nm) of equivalent size. **b** SEM image of the structure realized by combining EBL for the concentric corrugation and FIB for the nanoaperture. Adapted from [43]

depositing a dielectric material on top of a metal. Indeed, surface plasmon modes are very sensitive to the metal/dielectric interface. Therefore, one could think of controlling the polaritons' propagation by locally modifying the interface condition. This is evidenced in Fig. 9.20 extracted from [44]. Plasmonic prims or lenses can be fabricated using dielectric elements. These elements have been fabricated using electron-beam lithography combined with the lift-off technique, but using  $SiO_2$ .

Alternatively one may think of fabricating structures supporting long-range plasmon polaritons. The advantage of this structuration technique is that it allows for symmetric (low loss) structures to be easily fabricated. These hybrid structures are of special interest at telecommunication wavelengths.

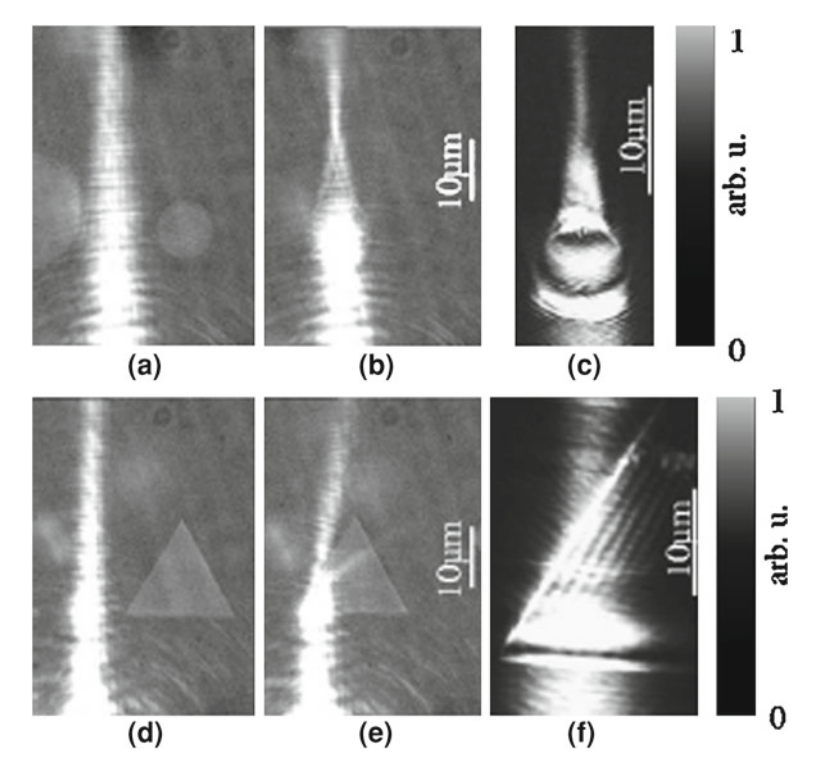


**Fig. 9.20** Dielectric  $(SiO_2)$  optical elements on a thin metallic film. **a** and **d** unaffected plasmon polarition beams. **b** and **e** focused and refracted beams, respectively. **c** and **f** zoomed images of the **b** and **e** images, respectively showing plasmon polaritions interferences. From [44]

#### **Metallic Nanogaps**

Metallic nanogaps are of great interest for amplifying signal (SERS or SEIRA) or nonlinear interaction (see the chapter written by Aizpurua and Hillenbrandt). Therefore, many efforts have been devoted to the fabrication of metallic nanogaps and especially reproducible nanogaps. EBL or FIB will lead to gaps usually larger than 10 nm, unless high-resolution equipment is used (cf. section on "EBL"). Alternative techniques have been proposed such as "gap filling" by electrochemical deposition [45]. Gaps as small as 9 nm have been obtained with this technique. Another approach lies in using planar thin film technology which has led to a 3-nm-thick MIM (Metal-Insulator-Metal) optical cavity with a squeezing of light of 82 % of the free-space wavelength (970 nm) [46].

Finally, a completely different approach has been recently proposed, which consists in using DNA strands to link nanoparticles and fabricate in solution metallic nanolenses [47]. Extremely small gaps can be obtained (0.5–5 nm) by this technique. Examples of such dimers are shown in Fig. 9.21. Current efforts focus on the inte-

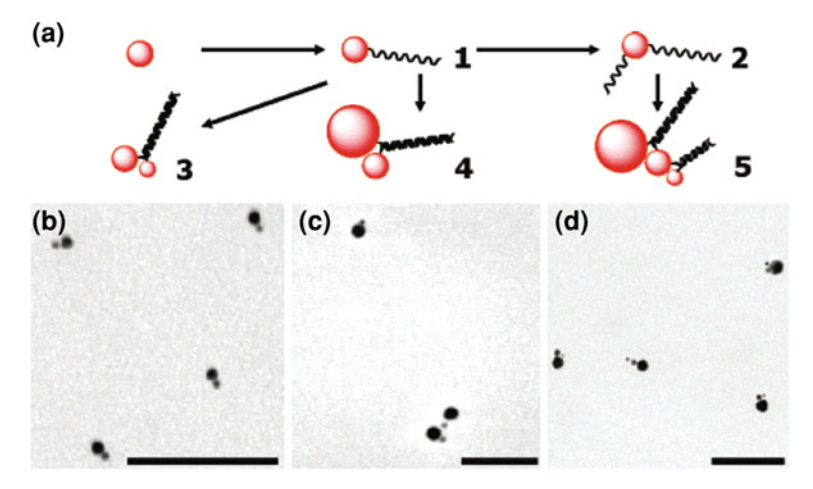


Fig. 9.21 Plasmon-based nanolenses obtained using DNA strands (scale bar is 100 nm). From [47]

gration of such DNA-linked dimers. This leads us to the next section devoted to the self-assembly approach.

#### From Colloids to Nanostructures

The easiest way to organize metal nanoparticles onto a substrate is most probably to involve the self-assembly process and corresponding driving force. Various driving forces can be used. The most simple case is the use of solvent evaporation combined with a repulsive force between nanoparticles (see Fig. 9.22a) [48]. This approach allows organizing nanoparticles on large areas with a good control on the organization (Fig. 9.22b). By comparison, extinction spectra from isolated particles (SEM image in Fig. 9.22c) and arrays (SEM image in Fig. 9.22b) are presented on Fig. 9.22d. The difference is the broad and intense plasmon band situated in the NIR for the arrays. Finally, the authors take advantage of the structure fabricated and more particularly of the sub-10 nm gaps between the particles to considerably enhance the Raman signal of molecules onto their substrate. The enhancement factor obtained by SERS is clearly shown in Fig. 9.22e for different Raman modes of p-mercaptoaniline and different excitation wavelengths using these nanostructured substrates.

A second approach allows us to obtain a better control of the 2D arrangement of the nanoparticles on the substrate as shown in Fig. 9.24g. This approach relies on the chemical patterning of the surface [32, 49] using two different SAMs. Using a hybrid approach combining top—down (lithography) and bottom—up (SAM) techniques, it is possible to organize metal nanoparticles onto a substrate. The first step is to define a pattern in a negative resist using a lithography technique: optical lithography [50], electron-beam lithography [49], or nanosphere lithography [51]. The second step is to functionalize the nanoholes created in the resist with a first SAM. The function

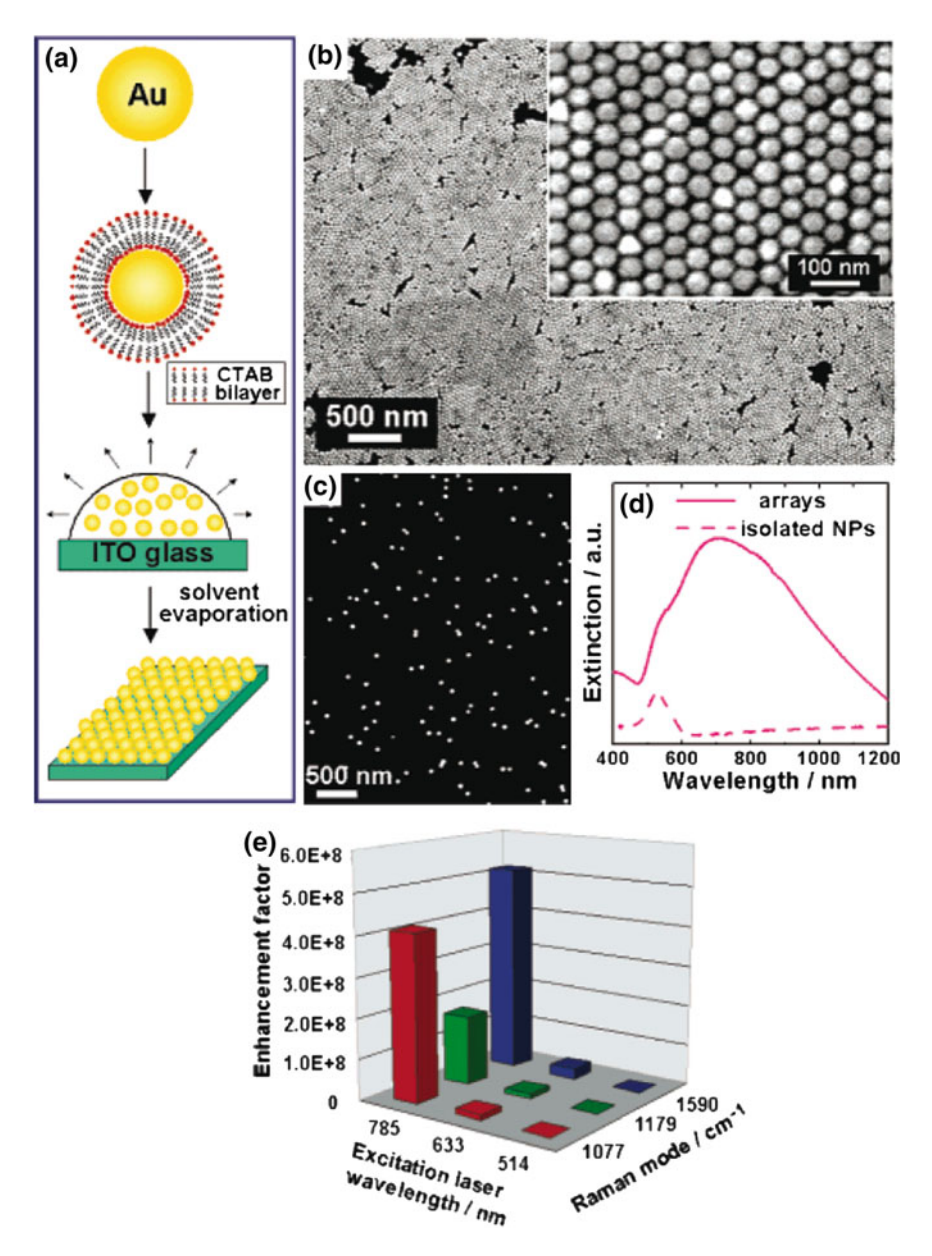


**Fig. 9.22** a Schematic illustration of the fabrication of sub-10-nm gap Au NP arrays. **b** SEM image of the arrays. **c** SEM image of monolayer of isolated Au NPs on ITO glass. **d** Visible and near-infrared (Vis-NIR) extinction spectrum of the monolayer of isolated Au NPs and arrays. **e** Empirical SERS enhancement factors obtained on the basis of different Raman modes under different laser excitations. Adapted from [48]

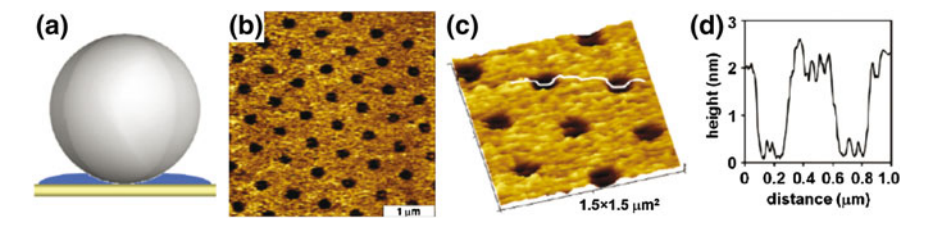


Fig. 9.23 Nanopatterns prepared using 500-nm latex balls as a mask. a Interstitial areas between spheres are covered with water when the mask is dried briefly; **b** topography of a porous OTS film on mica (0001) formed by briefly drying latex masks; **c** zoomed image of B; and **d** corresponding line profile. From [51]

carried by the SAM will allow a specific interaction with the metal nanoparticles. For example, it could be a thiol function for a quasi-covalent binding on gold or an amine group for an electrostatic interaction with the citrate groups stabilizing the metal nanoparticles in most cases [52]. After removing the resist, a second step of functionalization by SAM is fabricated. In that case, a function repelling the metal nanoparticles is used in order to drive the nanoparticles at the desired positions. For example, an alkane-terminated silane is used [51]. Finally, a rinsing step is used to remove all the nonbonded nanoparticles. Such an approach has been demonstrated for metal nanoparticles by the group of Prof. Garno [51]. Their approach is described below. First, nanosphere lithography is used in order to define a pattern and the first step of functionalization is made by gas-phase deposition as shown in Fig. 9.23 and in Fig. 9.24a-c. A second step of functionalization is then used to finish the pattern (see Fig. 9.24d–f) and the gold nanoparticles are deposited on the patterned substrate. The result is presented in Fig. 9.24g-i. By means of UV-visible spectrophotometry, clear differences are reported between the gold nanoparticle solution and the gold nanoparticles organized onto the substrate [51].

Another simple approach reported in the literature is lithography free and relies on employing the stick—slip motion of a water meniscus [53]. First, a monolayer of metal colloid is deposited on water. This film is then transferred noncontinuously onto a substrate in order to create lines of colloids as shown in Fig. 9.25. To fabricate the transfer and to avoid the deposition of a continuous film, various criteria must be met. First, the particle—substrate interaction must be favored over the interparticle interaction at the contact line. Second, the wettability of the substrate must be carefully controlled to avoid the deposition of a continuous film. Finally, a discontinuous deposition technique must be employed to avoid the continuous deposition of the lines.

The authors present an application of those lines of colloids to create a 3D (isolated) plasmonic array as shown in Fig. 9.26. They use the colloid particles as the local catalyst to grow silicon nanowires thus creating a silicon array with gold nanoparticles at the top of the wires.

Another way to create a 3D plasmonic nanostructure is to use polymers between the substrate and nanoparticles. Such an approach will be described below. For this

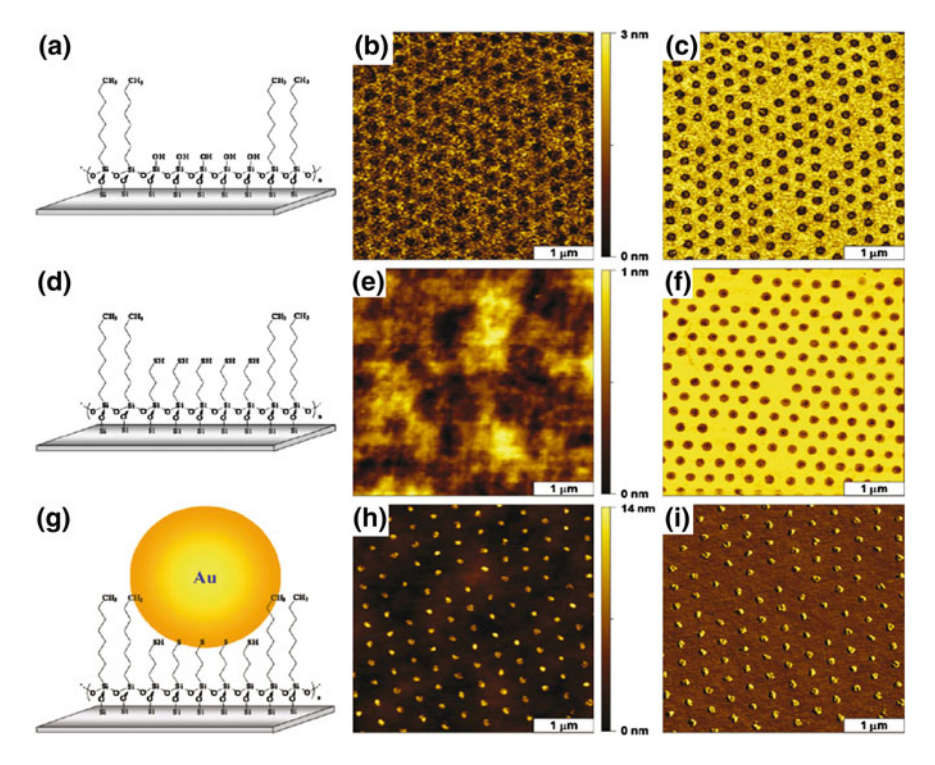


**Fig. 9.24** Sequence of chemical steps for selective attachment of gold nanoparticles on nanopatterns of organosilanes produced on a polished silicon wafer. **a** Nanopatterns of OTS produced by nanosphere lithography; **b** and **c** topography and corresponding lateral force image of an OTS film with pore structures produced with 300-nm latex balls; **d** after depositing MPTMS onto uncovered pore areas within OTS; **e** and **f** topography and corresponding lateral force image of a surface nanopatterned with OTS and MPTMS; **g** gold nanoparticles attached selectively to areas with MPTMS; **h** and **i** topography and corresponding lateral force image of arrays of gold nanoparticle clusters. From [51]

example, monolayers of charged metal colloids are stacked between layers of an amphiphilic copolymer schematically shown in Fig. 9.27a. In that case, the copolymer layer is deposited by the Langmuir–Blodgett (LB) technique [54]. An amphiphilic copolymer is deposited at the water/air interface. The hydrophilic part of the copolymer will be in contact with water and the hydrophobic part will be in contact with air. The nanolayer of cationic copolymer is then transferred to the substrate by dipping. Then, the substrate is immersed in metal nanoparticles solution (i.e. colloids stabilized by citrate groups in aqueous solution) and finally rinsed in water. The process can be repeated to increase the number of deposited bilayers (copolymer + metal nanoparticles) as schematically shown in Fig. 9.27b. Different nanostructures obtained by this strategy are presented in Fig. 9.27c. It clearly appears that the final color of the nanostructured film directly depends on the number of layers (Fig. 9.27c).

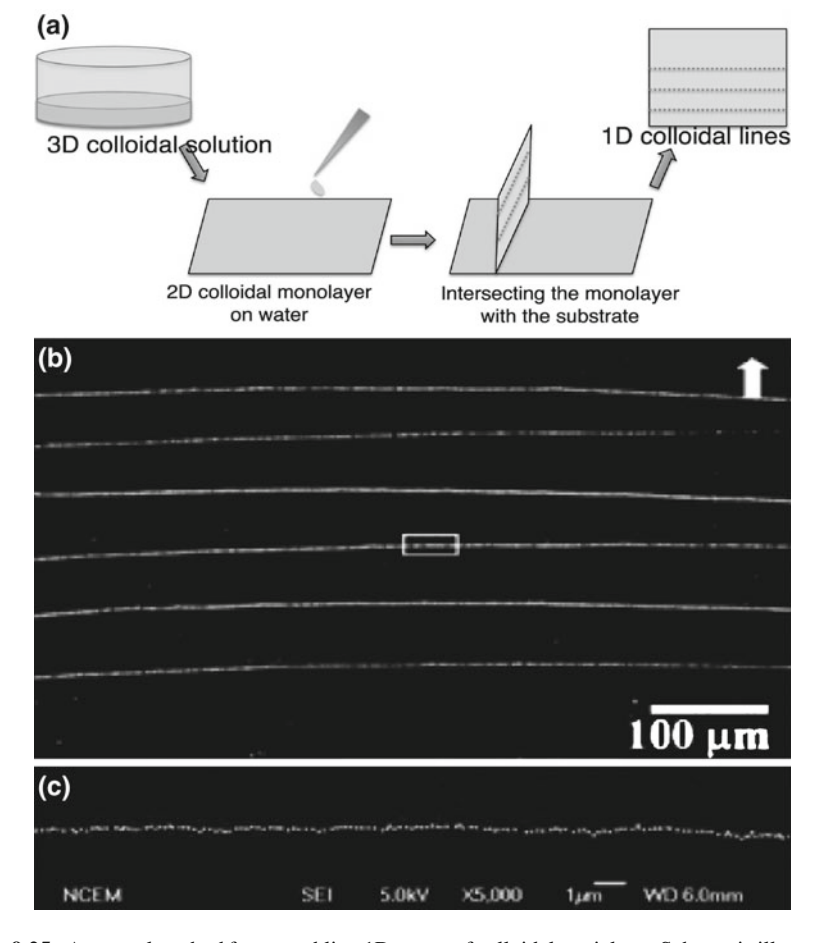


**Fig. 9.25** A general method for assembling 1D arrays of colloidal particles. **a** Schematic illustration showing colloidal particle dispersions with sequentially reduced dimensionality. First, a 3D colloidal solution is spread onto a water surface, forming a 2D particle monolayer. An immersed substrate intersects the monolayer and creates a contact line. Under proper conditions, parallel 1D arrays of particles can be deposited on the substrate upon lifting through a stick–slip motion of the contact line. A typical optical microscopy image of the prepared Ag single nanocube (diameter of about 50 nm) lines on a Si substrate is shown in (**b**). The curvature of the lines replicates that of the water meniscus. The typical line width is about 1 nanoparticle as revealed by the scanning electron microscopy image in (**c**). From [53]

## 9.3.2 Metallic Structures Fabrication on a NonPlanar Surface

Derived from planar technology, nanolithography is usually not well suited for structures on a nonplanar surface. The problem of a nonplanar surface lies in the sensitivity of the different lithography techniques to the height of the sample. Nonplanar surfaces will lead to in- and outfocus areas. This may not be an issue as long as one

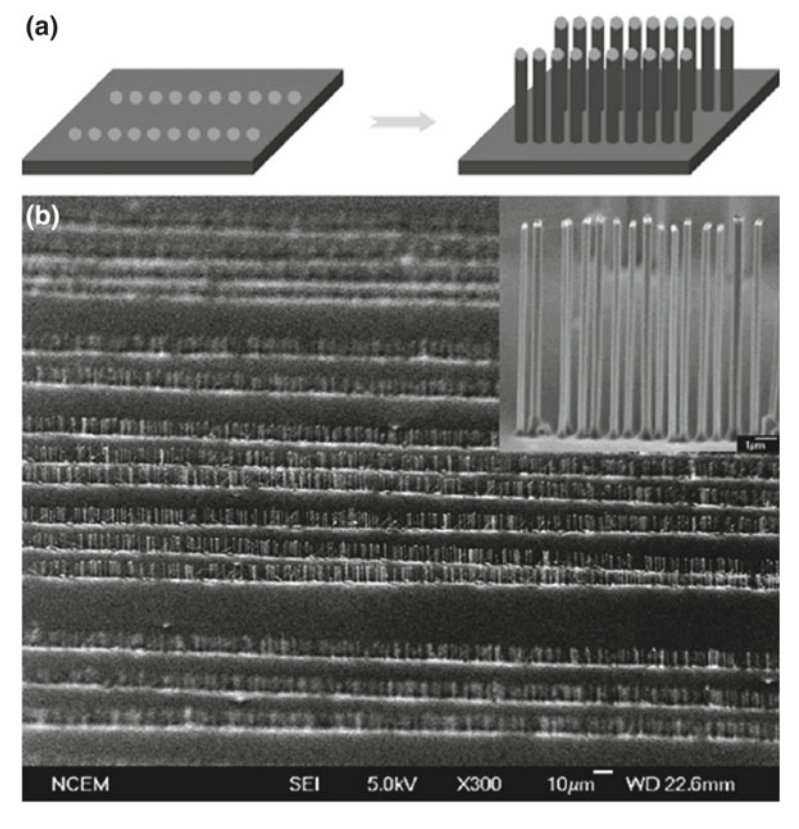


**Fig. 9.26** a 1D arrays of Si nanorods can be grown on the Au single nanoparticle lines, replicating the pattern of the Au nanoparticles. Part (b) and its inset are SEM images showing an overview and a close-up of the Si nanowire array, respectively. From [53]

is interested in localized structuration. Indeed as shown in Fig. 9.28, nanostructures have been fabricated at the very end of SNOM tips, for example [55], using a dual-beam system combining ion-beam lithography and electron-beam microscopy. The main issue here will be to have the ion and electron beams focused on the same area, i.e. within the beam diameter typically smaller than 10 nm. The SEM picture shown in Fig. 9.28 illustrates well the ion-beam milling process (cf. subsection FIB lithography), which is very similar to sculpting where matter is first removed at micron scale before being removed at nanoscale. This step is necessary to avoid any redeposition of the material.

A similar type of structures has also been demonstrated on a few optoelectronic devices in order to obtain electrically driven optical nanosources. Figure 9.29 shows one of the very first results obtained where a nanoantenna has been drilled on the edge of a laser diode [56]. As simulated, one will expect the emission from the active region to be concentrated in the nanoantenna gap. Indeed, as probed by apertureless SNOM,

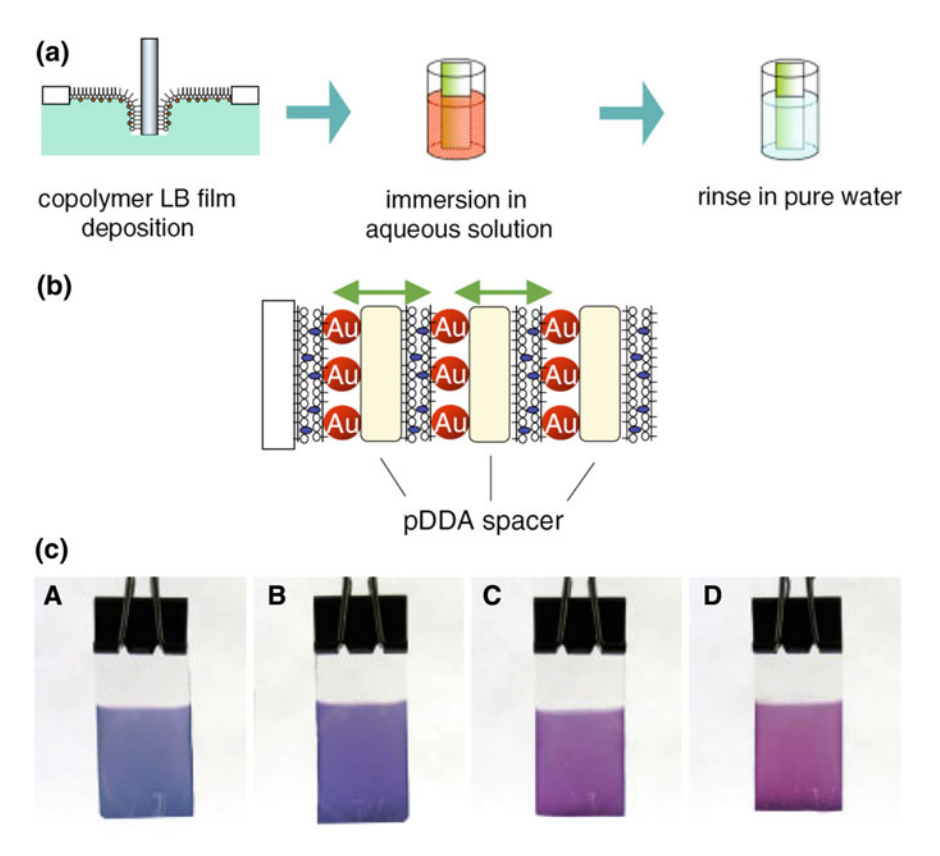


**Fig. 9.27** a Schematic illustration of the preparation process of hybrid polymer nanoassemblies. **b** Schematic representation of the Au/copolymer architecture. **c** Photographs of gold nanoparticle multilayers with different numbers of pDDA layers after their respective third deposition cycles. The numbers of pDDA spacer layers include (A) 0, (B) 4, (C) 8, and (D) 24. From [54]

the near-field pattern shows a polarization and wavelength-dependent maximum at the center of the nanoantenna.

Even if a multistep process can be used with subsequent planarization as discussed later, this is a rather heavy, time-consuming process where precise alignment will be needed. This is not compatible with low cost and easy fabrication. An alternative and original approach will consist in combining surface functionalization as previously described with meso- or micro-structuring. The approach consists in shaping the substrate in order to obtain a 3D plasmonic nanostructure with enhanced optical properties [57]. The approach is schematically represented in Fig. 9.30a–h. In this example, a SAM terminated by an amine group is used to functionalize the glass substrate. Then, a dense layer of metal colloids stabilized by citrate groups is grafted onto the substrate. Then, the substrate is etched through a patterned resist obtained by optical lithography. Finally, a structured substrate under the form of an array of

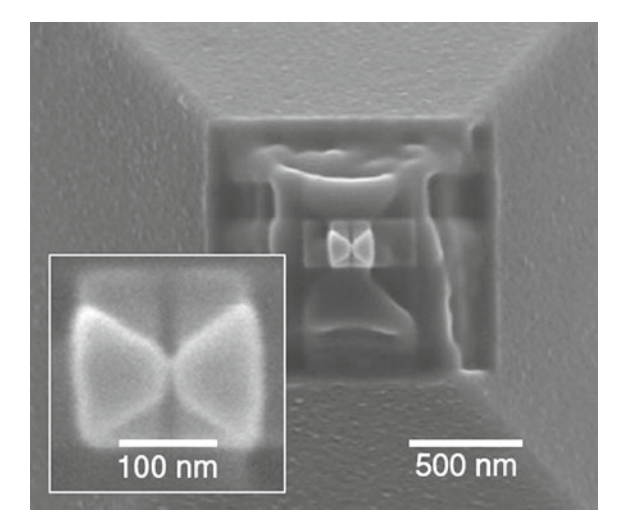
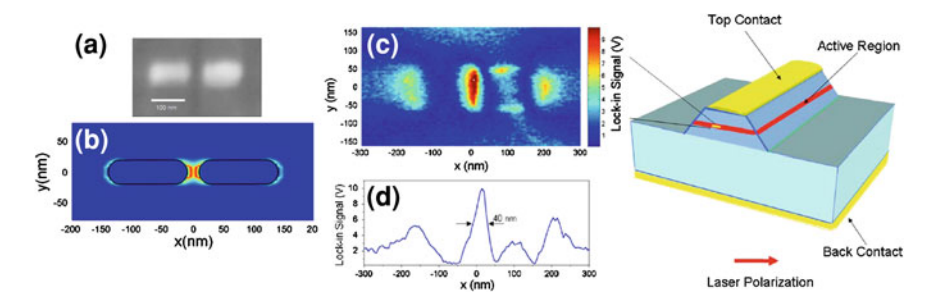


Fig. 9.28 Integration of a nanoantenna on a SNOM tip from [55]



**Fig. 9.29** Integration of a nanoantenna on an optoelectronic device. From left to the right, SEM image of the nanoantenna, calculated optical response, measured optical response as probed by SNOM, intensity profile. Right schematic view of the electrically driven optical nanosource. Adapted from [56]

glass tips is obtained as shown in Fig. 9.30i–k. Each tip acts as a lens to focalize the light at its apex where 1–3 metal colloidal particles are grafted as clearly evidenced by Fig. 9.30j.

## 9.3.3 Metallic Structure Surface Functionalization

The functionalization of noble metal nanoparticles primarily relies on the thiol-based molecules. As explained above (see Sect. 9.2.6), a thiol group binds spontaneously onto gold (or silver). Depending on the final application, the head group of the thiol molecule will be adjusted. A few examples will be detailed below. The first applica-

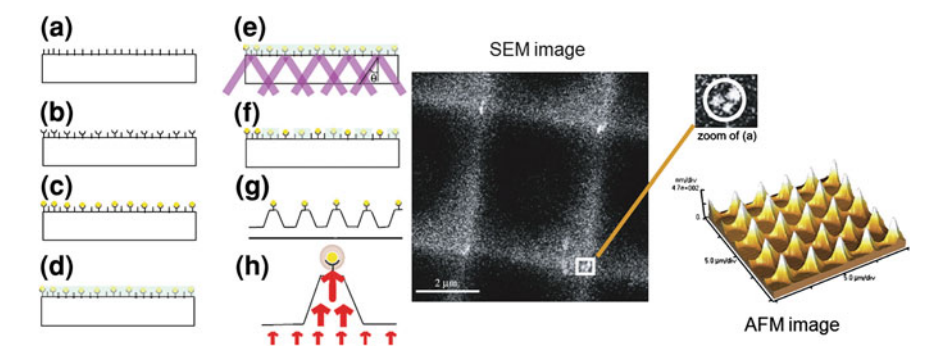


**Fig. 9.30** Fabrication steps of integrated plasmonic glass nanotips **a**–**c** functionalization; **d**–**f** realization of the holographic grating; **g** and **h** chemical etching and final result. Left, SEM image of the integrated plasmonic glass nanotips with, on the top of each tip, only a few gold nanospheres as evidenced by the zoom. *Bottom left*, AFM image of glass nanotips array. From [57]

tion of functionalization of metal is the lock–key system for detecting the streptavidin molecule or antibiotin molecule (key) with the biotin one (lock). In such a case, the metal nanoparticle is functionalized with 11-mercaptoundecanoic acid (MUA). Then, an amine–biotin molecule is grafted to MUA using an EDC crosslinker: 1-Ethyl-3-(3-dimethylaminopropyl) carbodiimide [58]. Finally, streptavidin or antibiotin will react specifically with biotin. The complete process is schematically represented in Fig. 9.31a–d. Moreover, the corresponding measured shifts are shown in Fig. 9.31e. A second approach is the use of thiolated DNA molecule to functionalize gold nanoparticles [47, 59]. In such case, a thiolated DNA strand is grafted onto a gold nanoparticle. Then the complementary strand is grafted on the first one to attach another gold nanoparticle. Such approach is used in a more complex process, which is schematically explained in Fig. 9.32.

## 9.3.4 Hybrid Nanostructures Fabrication

Emerging nanostructures include hybrid nanostructures, which are constituted of at least two different materials (metal/polymer [52, 60] or metal/semiconductor [39] or metal/polymer/semiconductor [61]). These hybrid nanostructures show new properties as polarization dependent plasmon resonance [60], fluorescence enhancement [61], or directional emission [39].

The first example relies on the localized photopolymerization induced by the local increase of the incident field around a metallic resonant nanoparticle. The process is schematically shown in Fig. 9.33a—e. First, the bare nanoparticle (Fig. 9.33a) is covered by the photopolymerizable solution (Fig. 9.33b). Then, the system is illuminated with an incident power lower than the dose threshold  $D_{th}$  (Fig. 9.33c). As shown in Fig. 9.33f, there is a threshold energy to overpass in order to trigger the

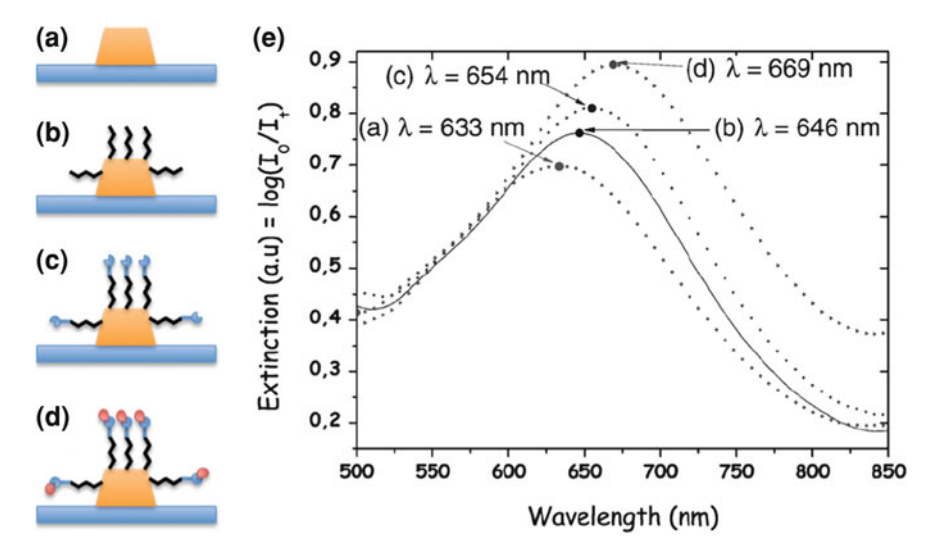


**Fig. 9.31** Schematic representation of the different functionalization steps of gold nanoparticle (a). (b) Grafting of MUA followed by the grafting of the amine—biotin (lock) onto the MUA using the EDC crosslinker (c). Finally, the key (streptavidin or antibiotin) reacts with the lock (biotin) (d). (e) Corresponding measured extinction spectra after each step. From [58]

polymerization process. This threshold dose is principally due to the presence of oxygen which acts as a radical killer [60]. Thus, using an incident power lower than the threshold of polymerization, induces no polymerization in the far field. Contrarily, in the near field of the nanoparticle, due to the localized plasmon resonance, the threshold will be overpassed and the polymerization will be induced (Fig. 9.33c,d). Finally, the nonreacting solution is removed by a rinsing step (Fig. 9.33e, g, and h). This approach allows one to fabricate hybrid nanoparticles with a tunable plasmon resonance due to symmetry breaking. Indeed, the two polymer lobes created around the metal nanoparticle will induce a second plasmon mode (i.e. one along the short axis and another one along the long axis). Thus, it will be possible to continuously tune the plasmon resonance of the created hybrid nanostructure by changing the incident polarization [60].

The second example not shown here combines top—down approach (two-step e-beam lithography) with surface functionalization in order to graft the semiconducting quantum dots (QD) only at one end of a metallic nanoparticle [39]. Such an approach allows to localize the emitters at a high electric mode density position.

Finally, the third approach is schematically shown in Fig. 9.34a—e. In such a case, gold nanoparticles (GNP) were fabricated by electron-beam lithography technique and lift-off offering thus the possibility to precisely control size, shape, and interdistance of the metal nanostructures. The QD—GNP distance is controlled through a layer-by-layer deposition of polyelectrolytes. Polyelectrolyte multilayers were deposited by alternate dipping of the substrate in aqueous solutions of

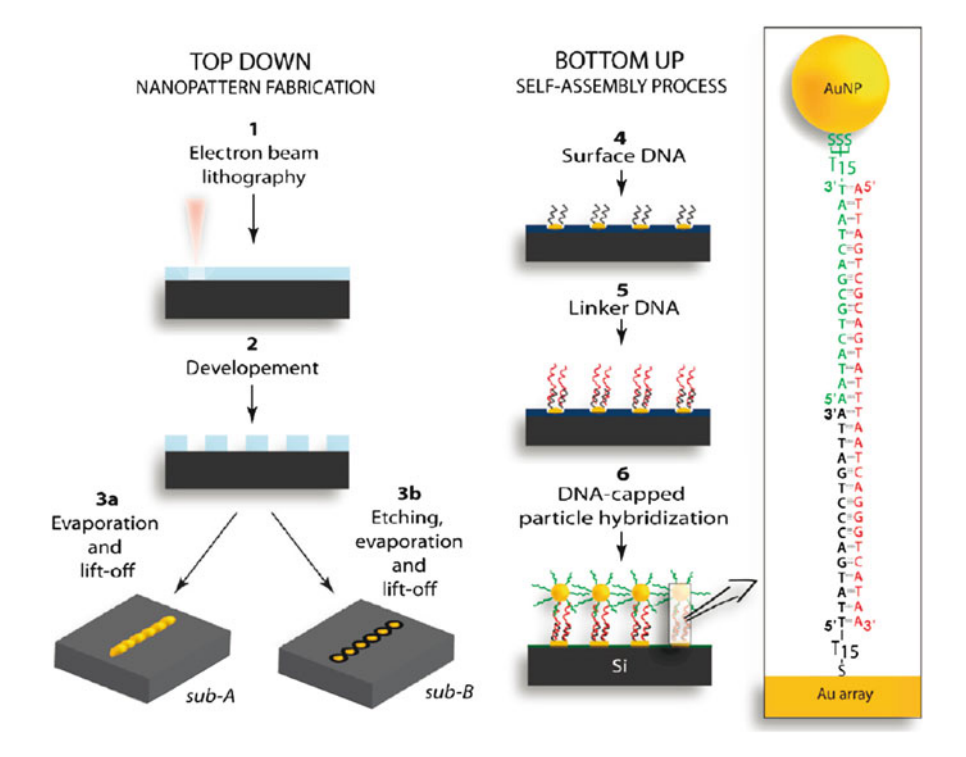


**Fig. 9.32** Schematic representation of a combination of top-down nanopattern fabrication and bottom-up gold nanoparticle self-assembly process (Not to Scale). (1) Nanopattern generation into PMMA by means of EBL; (2) stripping; (3) etching (sub-B only), chromium and gold evaporation, and PMMA lift-off, yielding sub-A with elevated feature and sub-B with negative surface features as schematically illustrated; (4) gold nanopattern arrays functionalization with thiol-terminated surface DNA; (5) linker DNA hybridized with the surface DNA; and finally (6) hybridization of the AuNP–DNA conjugates. The inset shows an illustration of the DNA interaction that drives the self-assembly. The linker DNA (*red* in illustration) links the particle to the nanopatterned surface thanks to two different 15 base-pair segments: one complementary to the surface DNA (*black* in illustration) and the other complementary to the particle DNA (*blue* in illustration, sticky-end). Adapted from [59]

PDDA (poly(diallyldimethylammonium chloride) and PSS (poly(styrenesulfonate)). Finally, a thin layer of QD-doped PMMA (10 nm thick) is spin coated onto the sample. By controlling the interdistance between the QDs and the GNP, it is possible to modulate the QD emission as shown in Fig. 9.34f.

## 9.4 Alternative Techniques and Emerging Issues

In this section, we will address various alternative techniques and emerging issues related to the application of plasmonics such as large-scale nanostructuring and integration.

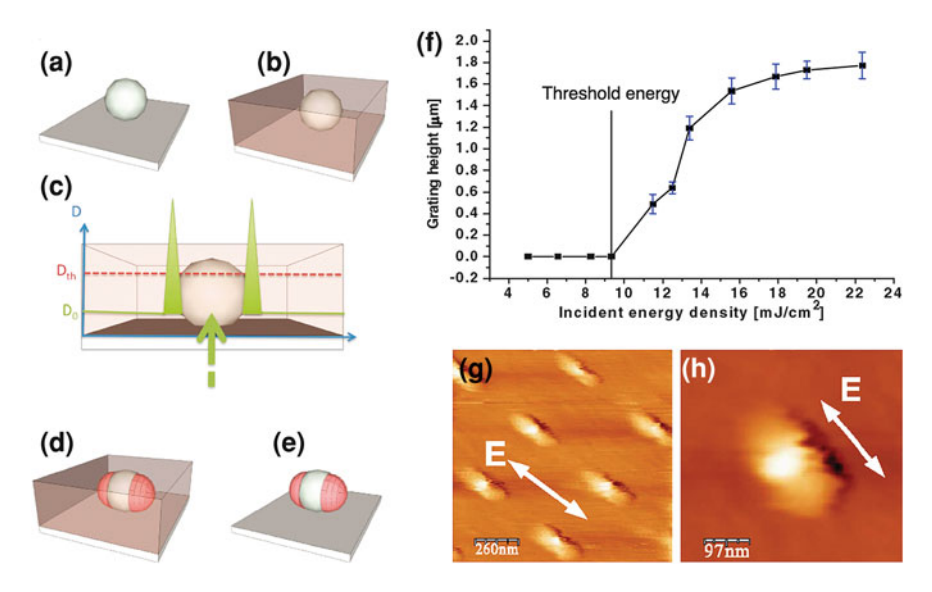


**Fig. 9.33** Scheme of the approach. **a** AgNP deposited on a functionalized glass substrate. **b** Deposition of the photopolymerizable formulation. **c**, **d** Plasmon-enhanced near-field photopolymerization of PPF leading to two wings corresponding to the dipolar LSP resonance. **e** The resulting hybrid nanoparticle revealed by the rinsing procedure. **f** Grating height as a function of incident energy density allowing one to define the threshold of polymerization. **g** and **h** AFM images recorded after irradiation and developing of the silver nanoparticles arrays covered with the photopolymerizable formulation. From [52] and [60]

# 9.4.1 Localized Photochemical Combined Synthesis and Patterning

A new approach has been recently developed by Jradi et al. [62]. This method relies on the photogeneration of silver nanoparticles. Starting from a solution of photosensitizer and silver cations, the absorbed light will induce the generation of radicals, which will reduce the silver cations to form silver nanoparticles. Thus, it is very easy to pattern silver nanoparticles using this method combined with the different optical-based lithography techniques. In this example, the growth of metal nanoparticles at the very end of a single mode optical fiber is demonstrated.

#### 9.4.2 Material Issues

There are two material issues emerging in the field of plasmonics. The first one is related to the adhesion of metals on oxide substrate and the second one concerns the material intrinsic losses. A third one will be the material compatibility with standard already existing processes and especially Complementary metal—oxide—

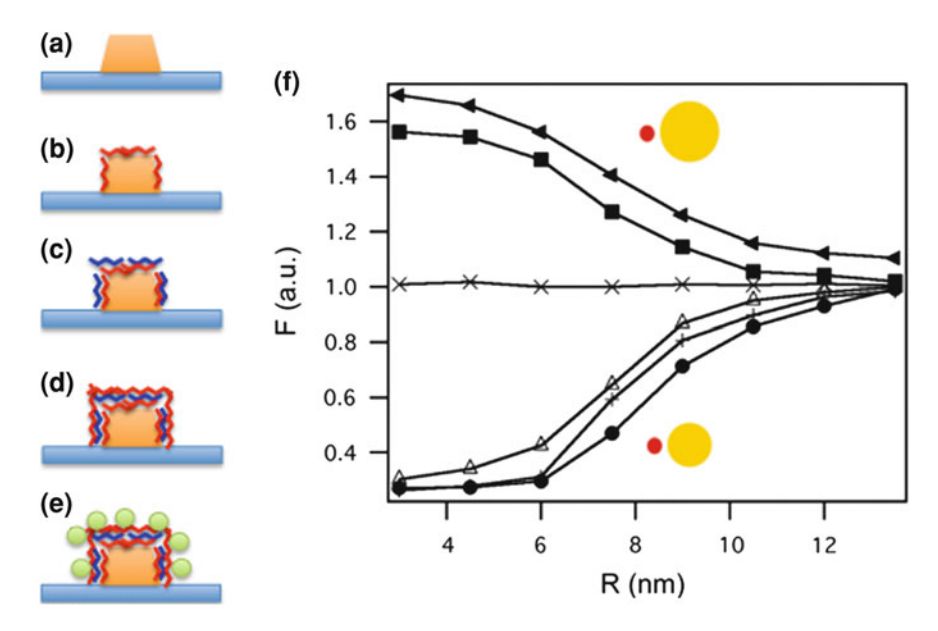


**Fig. 9.34** a—e Schematic representation of the different steps allowing one to control the interdistance between the gold nanoparticle and the QDs. The interdistance is tuned by successive dipping in polycations and polyanions solutions. **f** Fluorescence enhancement measured on gold nanoparticles of different sizes (from 80 to 160 nm in diameter) as a function of the interdistance. From [61]

semiconductor (CMOS) process in the case of silicon integration (cf. Sect. 9.4.4 on Plasmonic integration).

Chromium is usually used to promote adhesion on the glass substrate of gold and silver. This has been confirmed by adhesion force measurement using an AFM tip interacting with the gold surface [63]. The mechanism could be the formation of a chromium oxide at the substrate interface. While a Cr thin layer gives satisfactory results as an adhesion promoter, it appears that it also strongly affects the optical properties of the overlaying metallic structures. Figure 9.36 simulates the effect of Cr adhesion layer on particle resonance [64]. FDTD calculation combined with the critical points model which was found to be well adapted for particle resonance description through the entire visible range was used here. The damping of resonance is already visible for 1 nm of Cr thickness.

The effect of adhesion was further studied through fluorescence enhancement and alternative adhesion layers were proposed [65]. As shown in Fig. 9.37, a higher fluorescence enhancement is observed when replacing Cr or Ti layer by  $Cr_2O_3$  or  $TiO_2$  layer, respectively. These observations were done using fluorescent molecules going through a metallic single aperture of 120 nm of diameter (cf. 9.37b). A 10 nm  $TiO_2$  adhesion layer gives the highest enhancement factor (four times). The results were again interpreted in terms of absorption losses via the material properties or thickness.

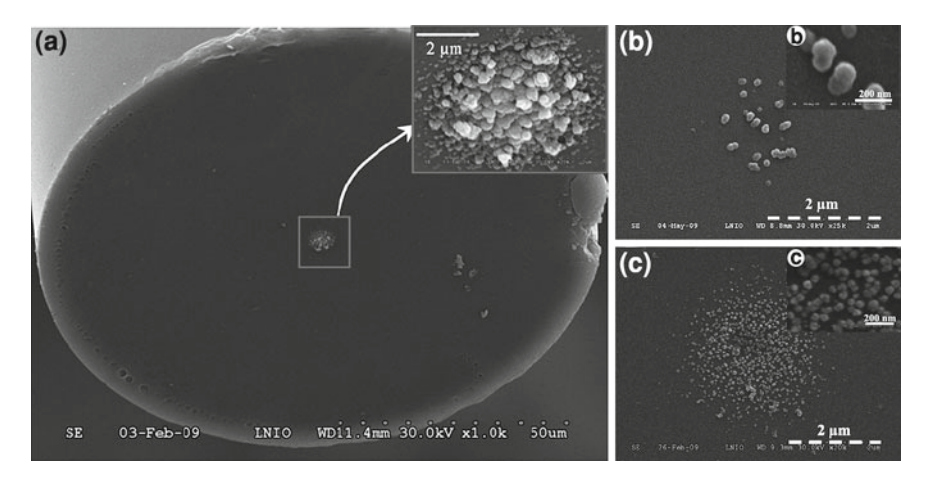
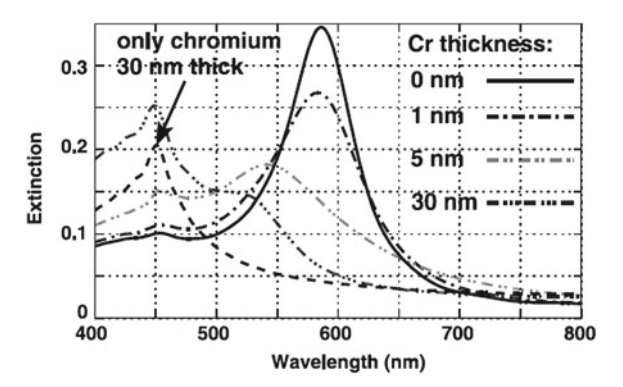


**Fig. 9.35** a Silver NPs photogenerated at the extremity of an optical fiber. Influence of the photonic conditions on the size and number of silver NPs fabricated at the extremity of single mode optical fiber. (Wavelength = 405 nm; 0.15 wt% of AgNO3; 0.30 wt% of Irgacure 819.) **b**  $P = 1 \,\mu\text{W}$ ,  $t = 12, 5 \,\text{s.}$  **c**  $P = 25 \,\mu\text{W}$ ,  $t = 0, 5 \,\text{s}$ 

**Fig. 9.36** Chromium adhesion layer effect on particle resonance. From [64]



Another material-related aspect is the crystallinity of the evaporated metals. While thermal or electron-beam evaporations are very versatile techniques, the films show a granular structure as shown in Fig. 9.7b. One of the first papers which emphasized on the importance of the crystallographic quality of the metallic structure, was published in 2005 [66]. As shown in Fig. 9.38, plasmons generated at one end of the structure can be reflected back to form a stationary wave pattern whose contrast directly depends on losses. A 10 times larger contrast is observed for a chemically synthesized nanowire than the evaporated one [66].

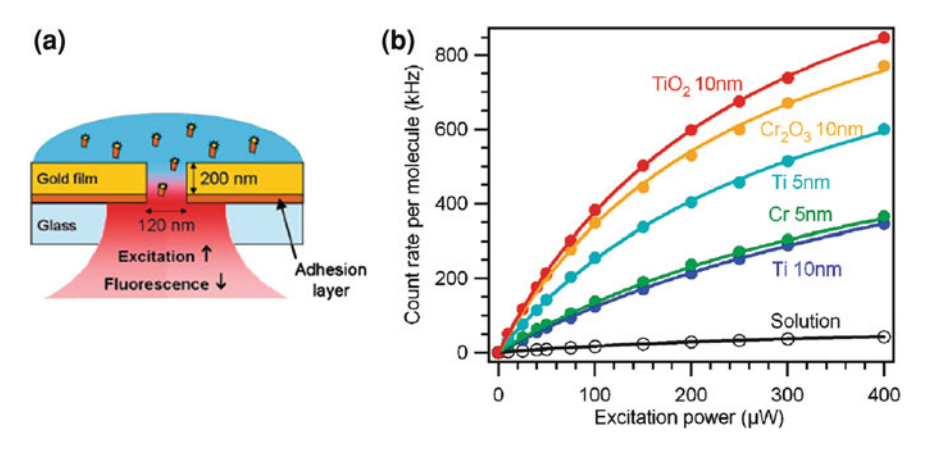


Fig. 9.37 Adhesion layer effect on fluorescence enhancement. From [65]

# 9.4.3 Large-Scale Nanostructuring: Toward Plasmonic Materials (Effective Properties) and Metamaterials

Large-scale nanolithography has become an issue in numerous fields and not only in electronics. As far as periodic patterns are concerned, laser interference lithography is definitely a technique of interest. In 2007, a high-throughput nanofabrication technique, soft interference lithography (SIL), combining the ability of interference lithography to produce wafer-scale nanopatterns with the versatility of soft lithography, was proposed and used to produce plasmonic metamaterials [67]. Metal films perforated with quasi-infinite arrays of 100-nm holes were generated over areas greater than 10 square centimeters, exhibiting sharp spectral features. In addition, soft interference lithography was also used to produce various infinite and finite-area arrays of nanoparticles, including patterns that contained optically side-by-side distinct particles and arrays that contained both metallic and dielectric materials. A sketch of the technique is shown in Fig. 9.39. An amazing aspect of this technique is that one can obtain metallic foils as shown in Fig. 9.40.

As far as high resolution, fast process, and low cost are concerned, one of the most promising techniques is to combine electron-beam lithography with nanoimprinting. While high-resolution nanoimprinting of plasmonic structures has been demonstrated, large-scale replication is still an issue. One of the issues lies in the intimate contact, which is needed on the wafer scale. An example of replicated and transferred, bow-tie nanoantenna with sub-30-nm gap is shown in Fig. 9.41. While large-scale structuring is still an issue, there is an increase in the number of papers dealing with nanoimprinting applied to plasmonics [68].

As already mentioned, large-scale nanolithography is an issue for 2D patterning. It appears even more challenging in 3D or at least 2.5D structuring. As an example of 2.5D large-scale nanostructuring, the reader may refer to Fig. 9.30 presented earlier showing an array of plasmonic glass nanotips obtained by combining interference

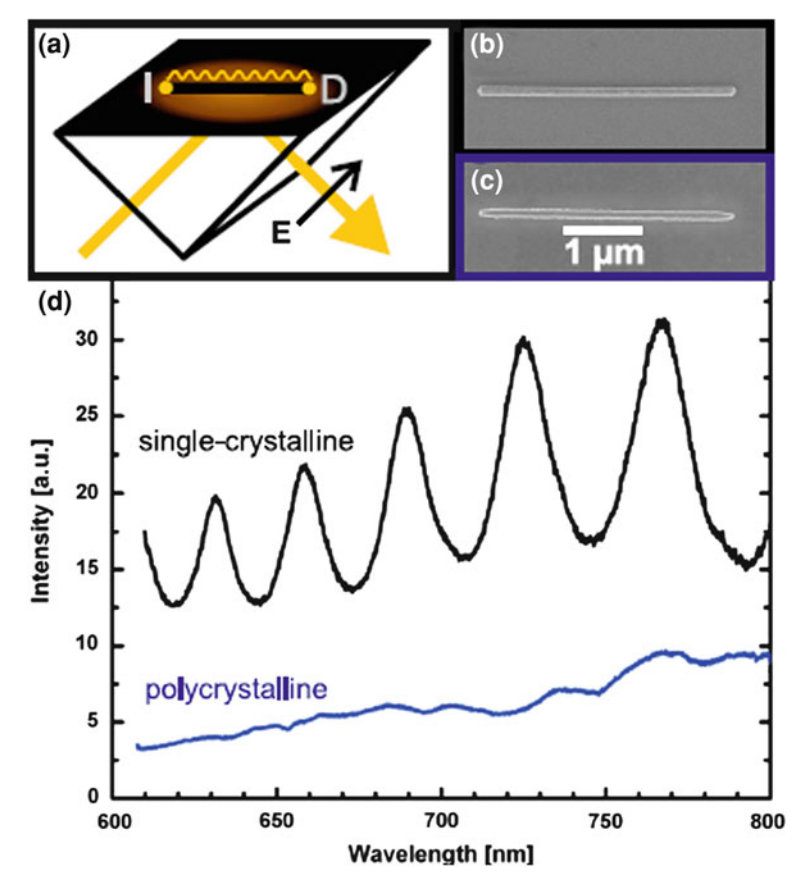
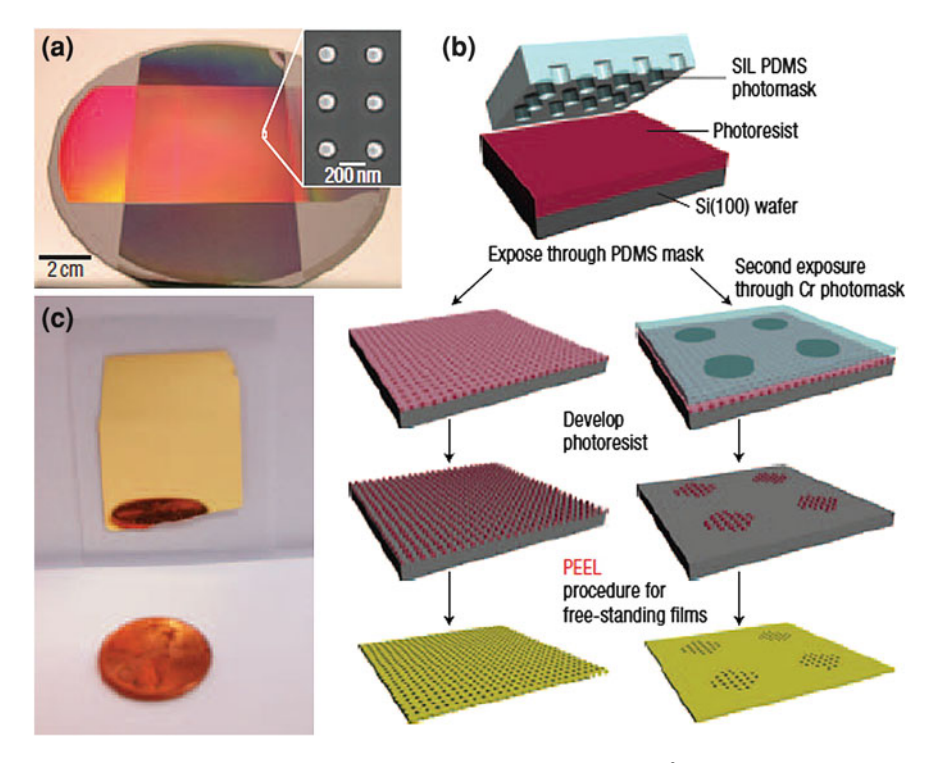


Fig. 9.38 a Schematic of the experiment. b and c Scanning electron micrographs of a chemically and an electron-beam lithographically fabricated silver nanowire, respectively. d Scattered light spectra at the end of the nanowires and resulting stationary waves. From [66]

lithography together with surface functionalization. As far as 3D nanostructuring is concerned, multistep processes based on planar nanotechnology ("wood pile" structure [69]) have already been demonstrated for the fabrication of metamaterials [70]. Alternatively 3D self-assembly of mesospheres could be used as for photonic crystals [71], but metamaterials are usually based on more elaborated elementary cells, which require even more elaborated surface chemistry with anisotropic interaction. Alternatively to self-assembly, the latter approach combining laser interference lithography with surface functionalization in order to graft to 3D nanoobjects could also be used. It is worth mentioning here that compared to plasmonics, large-scale lithography appears to be an even more important issue in the case of metamaterials.



**Fig. 9.39** Soft interference lithography. **a** Optical micrograph of a 14 cm<sup>2</sup> array of 100-nm-diameter Si posts (height and pitch = 400 nm) prepared by interference lithography. The inset shows the SEM image of the Si posts. The pattern was used as a master for preparing Simon India Ltd. polydimethylsiloxane (SIL PDMS) photomasks. **b** Scheme depicting the fabrication procedure of infinite nanohole arrays and finite-sized arrays (patches) of holes. **c** Optical micrograph of a largearea (around 3 cm times 4 cm) gold film perforated with an array of 100-nm holes supported on glass. A reflection of the penny can be seen at the bottom of the gold film. From [67]

## 9.4.4 Plasmonic Integration

Integration of plasmonic structures on glass has already been demonstrated making plasmonic platforms available for bio or chemical sensing and even more and more for imaging. In addition, plasmonic structures integration on optoelectronic devices, such as edge-emitting diodes, has also been demonstrated [56]. Plasmonic structures are also potentially of great interest for other applications and especially major ones like telecommunications and computing relying on integrated electronics and photonics. Plasmonic structures are often presented as candidates to transport both electronic and photonic information and to bridge the gap between electronic and photonic devices. Silicon photonics has become a reality thanks to the Silicon on insulator (SOI) technology which is fully compatible with CMOS processes. The same compatibility



Fig. 9.40 Folding plasmonic foil from [67]

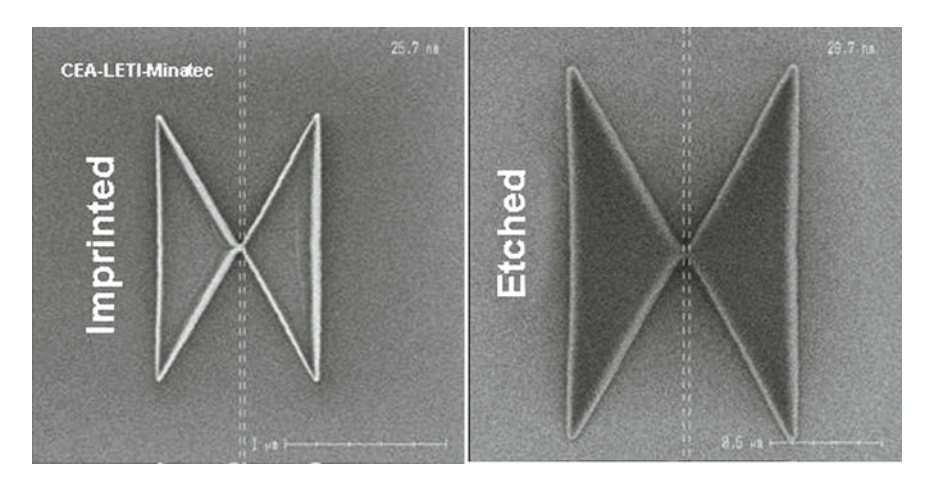


Fig. 9.41 Nanoimprinted nanoantenna (courtesy of LETI)

has to be met for plasmonic devices. Figure 9.42 shows a very recent result dealing with copper slit waveguides bridging SOI waveguides [72].

The processes used to realize the structure shown in Fig. 9.42 include deep UV photolithography, dry etching, and chemo-mechanical polishing (CMP) allowing for monolithic integration with no alignment step. Besides a very efficient optical coupling (over 50%), unexpectedly low propagation losses, and a broadband sub-50-nm optical confinement, the structure reported in this paper is of importance because

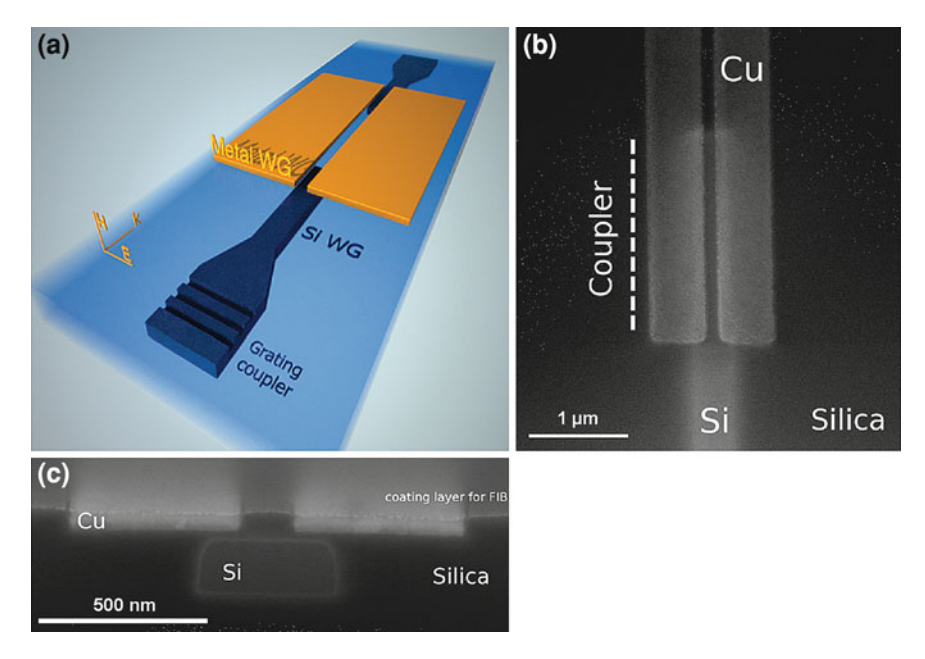


Fig. 9.42 CMOS-compatible hybrid plasmonic/photonic optical chip. From [72]

it is the first CMOS-compatible plasmonic device ever made. The use of frontline microelectronic fabrication facilities is suitable for very large-scale integration. This work follows first attempts on plasmonic waveguide integration on SOI [73] and other works on active devices [74, 75].

## 9.5 Summary

Within the past 15 years tremendous progresses have been done in the control of metallic nanostructure or particle size, shape, and distribution. Remarkable is the number of techniques and approaches that have been developed. While electron-beam lithography allows for perfect arrangement, it does not give access to the full zoology of particles that can be chemically synthesized. As a consequence if simple assemblies of well-defined structures have been demonstrated, there is still a long way to go to be able to synthesize a real plasmonic material with well-defined engineering macroscopic properties. Large-scale structuring is definitely one of the issues, together with the nanostructuring in the third direction. It is therefore most likely that depending on the application, a combination of techniques will be required including soft chemistry routes and 3D nanoobjects' assembly. Forthcoming issue, include silicon photonics integration and elaboration of (hybrid) functional Materials and Metamaterials.

#### References

- 1. M. Fleischmann, P. Hendra, A. McQuillan, Chem. Phys. Lett. 26, 123 (1974)
- 2. see for a review T. Vo-Dinh, Trends in analytical chemistry 17, 557 (1998)
- 3. J.C. Hulteen, R.P. Van Duyne, J. Vac. Sci. 13, 1553 (1995)
- J. Grand, S. Kostcheev, J.-L. Bijeon., M. Lamy de la Chapelle, P.-M. Adam, A. Rumyantseva, G. Lerondel, P. Royer. Synthetic Metals 139, 621 (2003)
- 5. K. Nozaki, T. Baba, Appl. Phys. Lett. 88, 211101 (2006)
- 6. MRS bulletin 30, 339–367 (2005)
- 7. N. Srituravanich, N. Fang, C. Sun, Q. Luo, X. Zhang, Nano Lett. 4, 1085 (2004)
- 8. Z. Liu, J.M. Steele, W. Srituravanich, Y. Pikus, C. Sun, X. Zhang, Nano Lett. 5, 957 (2005)
- 9. E. Spille, R. Feder, in X-Ray Optics applications to solid vol. 22,(Springer 1977), pp. 35
- 10. G. Mollenstedt, R. Speidel, Phys. Blatter **14**, 192 (1960)
- 11. A. N. Broers, IBM J. Res. Develop. 32, 4 502 (1988)
- 12. A.N. Broers, J. Electrochem. Soc. **128**, 166 (1981)
- C. Vieu, F. Carcenac, A. PTpin, Y. Chen, M. Meijas, A. Lebib, L. Manin-Ferlazzo, L. Couroud, H. Launois, Appl. Surf. Sci. 164, 111 (2000)
- 14. D. Brambley, B. Martin, P.D. Prewett, Adv. Mater. Opt. Electron. 4, 55 (1994)
- 15. T.W. Ebbesen, H.J. Lezec, H.F. Ghaemi, T. Thio, P. Wolff, Nature 391, 667 (1998)
- J. Gieraka, A. Madouria, A.L. Biancea, b, E. Bourhisa, G. Patriarchea, C. Ulyssea, D. Lucota, X. Lafossea, L. Auvrayb, L. Bruchhausc, R. Jedec. Microelectronic Engineering 84, 779 (2007)
- 17. M. Carter, R.C. Fleming, T.A. Savas, M.E. Walsh, T.B. OReilly, Interference Lithography. MTL Annual Report 2003: Submicron and Nanometer Structures (2003)
- 18. C.-H. Chang, Y. Zhao, R.K. Heilmann, M.L. Schattenburg, Opt. Lett. 33, 1572 (2008)
- A. Barbara, J. Le Perchec, S. Collin, C. Sauvan, J-L. Pelouard, T. López-Ríos, P. Quémerais. Opt. Express 16, 19127 (2008)
- X. Zhang, A.V. Whitney, J. Zhao, E.M. Hicks, R.P. Van Duyne, Journal of Nanoscience and Nanotechnology 6, 1 (2006)
- 21. P. Royer, D. Barchiesi, G. Lerondel, R. Bachelot, Phil. Trans. Soc. Lond. A 362, 821 (2004)
- 22. R.D. Piner, J. Zhu, F. Xu, S. Hong, C. A. Mirkin. Science **283**, 661 (1999)
- G. Lerondel, A. Sinno, L. Chassagne, S. Blaize, P. Ruaux, A. Bruyant, S. Topcu, P. Royer, Y. Alayli, Journal of Applied Physics 106, 044913 (2009)
- L. Chassagne, S. Blaize, P. Ruaux, S. Topcu, P. Royer, Y. Alayli, G. Lerondel, Rev. Sci. Instrum. 81, 086101 (2010)
- N. Silvis-Cividjian, C.W. Hagen, P. Kuit, M. A. J. v.d. Stam and H. B. Groen. Appl. Phys. Lett. 82, 3514 (2003)
- K. Edinger, H. Becht, J. Bihr, V. Boegli, M. Budach, T. Hofmann, HWP Koops, P. Kuschnerus, J. Oster, P. Spies, B.K. Weyrauch, Journal of Vacuum Science Technology B 22, 2902 (2004)
- 27. C.J. Lobo, M. Toth, R. Wagner, B. L. Thiel M. Lysaght. Nanotechnology 19, 025303 (2008)
- 28. K.S. Lee, R.H. Kim, D.Y. Yang, S.H. Park, Prog. Poly. Sci. 33, 631 (2008)
- S. Shukla, E.P. Furlmani, X. Vidal, M.T. Swihart, P.N. Prasad, Advanced Materials 22, 3695 (2010)
- 30. G.M. Whitesides, Small 1, 172 (2005)
- G. Barbillon, J.L. Bijeon, J. Plain, M. Lamy de la Chapelle, P.M. Adam, P. Royer, Surf. Sci. 601, 5057 (2007)
- 32. J. Plain, A. Pallandre, B. Nysten, A.M. Jonas, Small 2, 892 (2006)
- 33. H.J. Butt, K. Graf, M. Kappl, *Physics and Chemistry of Interfaces* (WILEY-VCH Verlag GmbH & Co. KGaA, Weinheim, 2003), pp. 206–219
- 34. A. Ulman, Chem. Rev. 96, 1533 (1996)
- 35. G. Yang, G.-Y. Liu, J. Phys. Chem. B 107, 8746 (2003)
- 36. P. Winckler, R. Jaffiol, J. Plain, P. Royer, J. Phys. Chem. Lett. 1, 2451 (2010)
- 37. G. Decher, J.B. Schlenoff, *Multilayer Thin Films* (WILEY-VCH Verlag GmbH & Co. KGaA, Weinheim, 2003), pp. 1–154

- 38. G. Decher, Science **277**, 1232 (1997)
- A.G. Curto, G. Volpe, T.H. Taminiau, M.P. Kreuzer, R. Quidant, N.F. van Hulst, Science 329, 930 (2010)
- 40. D.R. Smith, J.B. Pendry, M.C.K. Wiltshire, Science 305, 788 (2004)
- 41. J. Grand, Dissertation, University of Technology of Troyes (2004)
- L. Douillard, F. Charra, Z. Korczak, R. Bachelot, S. Kostcheev, G. Lerondel, P.-M. Adam, P. Royer, Nanoletters. 8, 935–940 (2008)
- 43. M. Consonni, J. Hazart, G. Lerondel Appl, Phys. Lett. **94**, 051105 (2009)
- 44. A. Hohenau, J.R. Krenn, A.L. Stepanov, A. Drezet, H. Ditlbacher, B. Steinberger, A. Leitner, F.R. Aussenegg, Opt. Lett. **30**, 893 (2005)
- 45. F. Chen, Q. Qing, L. Ren, Z. Wu, Z. Liu, Appl. Phys. Lett. **86**, 123105 (2005)
- 46. H.T. Miyazaki, Y. Kurokawa, Phys. Rev. Lett. 96, 097401 (2006)
- S. Bidault, F.J. Garcia de Abajo, A. Polman, Journal of American Chemical. Society. 130, 2750 (2008)
- 48. H. Wang, C.S. Levin, N.J. Halas, J. AM. CHEM. SOC. 127, 14992 (2005)
- 49. A. Pallandre, K. Glinel, B. Nysten, A.M. Jonas, Nano Lett. 4, 365 (2004)
- C.S. Dulcey, J.H. Georger, V. Krauthamer, D.A. Stenger, T.L. Fare, J.M. Calvert, Science 252, 551 (1991)
- 51. J.R. Li, K.L. Lusker, J.J. Yu, J.C. Garno, ACS Nano 3, 2023 (2009)
- C. Deeb, R. Bachelot, J. Plain, A.L. Baudrion, S. Jradi, A. Bouhelier, O. Soppera, P.K. Jain, L. Huang, C. Ecoffet, L. Balan, P. Royer, ACS Nano 4, 4579 (2010)
- 53. J.X. Huang, A.R. Tao, S. Connor, R.R. He, P.D. Yang, Nano Lett. 6, 524 (2006)
- 54. M. Mitsuishi, M. Ishifuji, H. Endo, H. Tanaka, T. Miyashita, Polym. J. 39, 411 (2007)
- 55. J.N. Farahani, D.W. Pohl, H.-J. Eisler, B. Hecht, Phys. Rev. Lett. 95, 017402 (2005)
- 56. E. Cubukcu, E. Kort, K. Crozier, F. Capasso, Appl. Phys. Lett. **89**, 093120 (2006)
- 57. G. Barbillon, J.L. Bijeon, G. Lerondel, J. Plain, P. Royer, Surf. Sci. 16, L119 (2008)
- 58. G. Barbillon, J.L. Bijeon, J. Plain, P. Royer, Thin Solid Films **517**, 2997 (2009)
- 59. C.H. Lalander, Y. Zheng, S. Dhuey, S. Cabrini, U. Bach, ACS Nano 4, 6153 (2010)
- 60. H. Ibn El Ahrach, R. Bachelot, A. Vial, G. Lerondel, J. Plain, P. Royer, O. Soppera, Phys. Rev. Lett. 98, 107402 (2007)
- 61. P. Viste, J. Plain, R. Jaffiol, A. Vial, P.M. Adam, P. Royer, ACS Nano 4, 759 (2010)
- S. Jradi, L. Balan, X.H. Zeng, J. Plain, D.J. Lougnot, P. Royer, R. Bachelot, S. Akil, O. Soppera, L. Vidal, Nanotechnology 21, 095605 (2010)
- 63. M. Schneider, H. Moehwald, S. Akari, Journal of Adhesion **79**, 597 (2003)
- 64. A. Vial, T. Laroche, J. Phys. D: Appl. Phys. 40, 7152 (2007)
- 65. H. Aouani, J. Wenger, D. Gerard, H. Rigneault, E. Devaux, T. W. Ebbesen, F. Mahdavi, T. Xu, S. Blair, ACS, Nano 3, (7) 2043 (2009)
- H. Ditlbacher, A. Hohenau, D. Wagner, U. Kreibig, M. Rogers, F. Hofer, F.R. Aussenegg, J.R. Krenn, Phys. Rev. Lett. 95, 257403 (2005)
- 67. J. Henzie, M.H. Lee, T.W. Odom, Nature Nanotech. 2, 549 (2007)
- 68. A. Boltasseva, J. Opt, A: Pure Appl. Opt. 11, 114001 (2009)
- 69. S.Y. Lin, Nature **394**, 251 (1998)
- 70. N. Liu, H. Guo, L. Fu, S. Kaiser, H. Schweizer, H. Giessen, Nature Materials 7, 31 (2008)
- 71. Y.A. Vlasov, X.Z. Bo, J.C. Sturm, D.J. Norris, Nature **414**, 289 (2001)
- C. Delacour, S. Blaize, P. Grosse, J.M. Fedeli, A. Bruyant, R. Salas-Montiel, G. Lerondel, A. Chelnokov. Nano Letters 10, 2922 (2010)
- 73. L. Chen, J. Shakya, M. Lipson Opt, Lett. **31**, 2133 (2006)
- 74. J.A. Dionne, K. Diest, L.A. Sweatlock, H. A. Atwater. Nano Lett 9, 897 (2009)
- 75. J.A. Dionne, IEEE J. Sel. Top. Quantum Electron. **16**, 295 (2010)

A	Chemical patterning, 296
Absorption cross section, 154, 192	Clausius-Mosssotti formula, 180
Acceleration voltage, 278	Coherence, 11
Adhesion layer, 308	Coherent thermal emission, 11
Adhesion, 307	Collective electron resonance, 10, 45
Adjoint structure, 71–73	Confocal microscopy, 248
Adjoint structures, 73	Correlation function, 23, 26
Airy formula, 272	Correlation length, 23–25
Anderson localization, 3, 4, 21, 26, 28	Coupled particles, 163
Anderson, 26	Crossed gratings, 10, 75
Andrewartha, 10	
Anti-Stokes, 168, 169	
Apertureless near-field optical	D
microscopy, 231	Damping, 154
Ash, 21	Dark-field optical
	microscopy, 245
	DDA, 162
В	Depolarization factors, 161
BEM, 162	Diagnostics, 217
Bergman–Milton bounds, 188	Dielectric function, 153
Biological and medical applications, 201	Differential theory, 44, 74
Biosensing, 70, 208	Differential transmission, 248
Biosensors, 70	Diffraction gratings, 3, 5, 7, 27
Bird, 45	Dimer, 249
Bloch mode, 94–99	Dimers, 165
Bonding dimer plasmon, 165	Dip pen lithography, 282
Bound modes, 230	Dipolar momentum, 155
Bowtie antenna, 165	Dipolar resonance, 155
Brewster effect, 51, 52	Dipolar, 233, 249, 259
Bruggemann effective	Dipole, 245
medium formulae, 178	Direct writing techniques, 284
Bull-eye, 90	Dispersion curve, 256
	Dispersion relation, 119, 122
	Dispersion, 152
C	DNA, 295
Cathodoluminescence, 259	Drude model, 116, 154
Cermet, 178	Dynamic, 262, 263

Holographic gratings, 6, 7, 42, 45
Hot spot, 165
Hutley, 7–10, 43–45, 60
Hyperthermia, 218
I
Image plane, 241
Immersion lithography, 280
Immunosensor, 70
Immunosensors, 70
Inelastic scattering, 252
Infrared spectroscopy, 168
Integral theory, 43–45
Integral theory, 65, 66, 68
Interstitial enhancement, 250
Intrinsic losses, 238
Ion-beam lithography, 278
J
Joule effects, 60
K
Keller's Theorem, 186
Kirchoff's Law, 191
Korringa-Kohn-Rostoker (KKR)
method, 179
Kröger, 10, 45
Kretschmann, 10, 45
,,
L
Lab-on-a-chip (LOC), 217
Landau damping, 119
Langmuir–Blodgett, 299
Laplace's equation, 186
Large scale nanolithography, 310
Laser interference lithography, 281
Lateral wave, 106, 126
Lattice sums, 184
LDOS, 129, 132–136
Leakage radiation microscopy, 235, 241, 242
Leaky mode, 235, 237, 242
Left-handed material, 16–18
Lift-off technique, 274
Light shielding, 71
Light shicking, 71 Lightning rod effect, 163
Linear dipole antenna, 167, 172
Littrow, 8, 9, 60, 74, 75 Local density of electromagnetic states, 231,
258, 260
Localiton, 27, 28

Localized plasmons, 177	0
Localized SPPs, 70	Oak Ridge National Laboratory, 10
Localized Surface Plasmon (LSP), 201	O'Donnell, 22
Localized surface plasmons, 151	Oliner, 6, 42
Lock-key systems, 304	Omnidirectional black-body emitters, 71
Longitudinal LSP, 161	Optical antenna, 21, 154, 162, 167
Lorentzian profile, 238, 241	Optical antennas, 20, 233, 260
Lorentz–Lorenz formula, 181	Optical path length, 192
LSP sensors, 209	Optical trapping, 211
Lycurgus cup, 178	Optics, 4
7 6 17	Or Rayleigh, 90
	Organosilicon, 286
M	
Maxwell-Garnett formula, 178	
Maystre, 10, 26, 43	P
Maystre, 7, 8	Particle clusters, 188
McPhedran, 7, 8, 43	Pendry, 16, 17, 19
Mean intensity, 23, 24	Perfect lens, 16
Mendez, 22	Petit, 7, 43
Metal nanoparticles, 230	Phenomenological formula, 10, 44, 65–67, 70
Metal stripe, 229	Phenomenological study, 89
Metallic nanoparticle, 152	Phenomenological theory, 9
•	Photochemical mapping, 234
Metallic nanoparticles (MNP), 201 Metamaterial, 18–20	
	Photolithography, 271  Photon induced electron microscopy, 262
Metamaterials, 19, 311	Photon -induced electron microscopy, 262
Metamaterials, superlensing,	Photopolymerization, 232, 304
near-field optics, 29	Photothermal energy, 190
Microscopic model, 90, 97, 99, 101	Photothermal imaging, 249
Microscopic, 87, 88, 90, 97	Photovoltaic cells, 71
Mie theory, 160, 194	Photovoltaic energy, 190
Multiple scattering, 98	Photovoltaic, 10
	Physisorption, 285
	Planck, 11
N	Plane-wave, 90
Nanofabrication, 270	Plasma frequency, 107
Nanoimprinting, 310	Plasmon polaritons, 269
Nanoparticles, 246	Plasmonic cloaking, 193
Nanophotonics, 3, 76, 11, 12, 14, 29	Plasmonics, 3, 4, 10–12, 19, 21, 26, 29,
Nanophotonics: metamaterials, near-field	39, 75, 269
optics, extraordinary transmission, 3	Pockrand, 10, 45
Nanorod, 231, 250	Point source, 245
Nanorods, 203	Polarizability, 153, 154, 180
Nanosphere lithography, 282	Poles, 89
Nanowire, 168	Polyelectrolytes, 288
Near field microscopy, 4	Poor man superlens, 19
Near field optical lithography, 282	Powell, 54
Near field, 11	Propagation constant, 237
Near-field optical microscopy, 12, 21	Propagation length, 239
Near-field optics, 11	
Near-field, 155	
Nevèire, 7, 43	Q
Nichols, 21	Quantum dots, 305
Non-local dispersion, 118	Quasi-CW, 93, 100
Norton wave, 93	Quasi-CWs, 99–101

<b>Q</b> (cont.)	SPP, 9, 10, 21, 26–28, 39, 44, 48, 50–52, 54,
Quasi-cylindrical wave, 93	56, 57, 59–64, 70–73, 76
Quasistatic approximation, 178	SPPs, 3, 4, 6, 9–11, 13, 14, 21, 22, 25, 28, 29,
	42, 45, 51, 56, 58–60, 70, 71, 73, 75, 76
	Stokes, 168, 169
R	Strong, 5, 41
Radiative losses, 239	Subwavelength hole, 12
Raether, 10, 45	Subwavelength holes, 12, 14, 29
Raman enhancement factor, 170	Subwavelength holes, metamaterials, 4
Raman scattering, 169	Subwavelength holes, near-field
Raman spectroscopy, 168	microscopy, 4
Randomly rough surface, 22, 24–27	Subwavelength holes, second harmonic
Randomly rough surfaces, 3, 4, 21–23,	generation, surface enhanced
27, 28	Raman scattering, 3
Rayleigh anomalies, 8	Subwavelength light lines, 20
Rayleigh anomaly, 6, 42, 74	Subwavelength light localization, 11
Rayleigh condition, 88	Subwavelength light source, 12
Rayleigh criterion, 11	Subwavelength light sources, 14
Rayleigh expansion, 59	Subwavelength light spots, 11
Rayleigh expansions, 58, 59	Subwavelength light spots, 19
Rayleigh formulae, 187	Superlens, 18, 20
Rayleigh limit, 14, 16	Superlenses, 4, 12, 19
Rayleigh, 5, 6, 40–42, 88–91, 97, 101	Superresolution, 142
Reciprocity theorem, 43	Surface functionalization, 285
Reciprocity, 8, 24	Surface modes, 157
Reflection pole method, 238	Surface phonons, 11
Rejection filter, 70	Surface plasmon coupled emission, 242
Resist, 273	Surface Plasmon Polariton, 39
Resolution, 270	Surface Plasmon Polaritons (SPPs), 3
Retardation, 159	Surface plasmon polaritons, 86, 152
Rigorous vector theories, 42	Surface plasmon resonance, 246
Rigorous vector theory, 43	Surface plasmon, 50
RMS, 22, 24–26	Surface-enhanced spectroscopies, 231
Rytov, 11	Swan, 54
Kytov, 11	Synge, 21
	Synge, 21
$\mathbf{S}$	
Saillard, 26	T
Scanning near-field optical microscope, 227	Telecommunications, 10
Scattering cross section, 154, 192, 249	Teperik, 71
SEIRA, 169, 172	Thermal emission, 11
Self-assembled monolayer, 285	Thermal radiation, 11
Self-Induced Back Action trapping, 215	Thiol, 286
Sellberg, 6	Time resolved photoemission electron
SERS, 169	microscopy, 262
Silanes, 286	Time-resolved femtosecond pulsed
Solar absorbers, 71	excitation, 229
Solar cells, 10	Total absorption, 10, 67, 68, 70, 71, 73, 75
Solar-selective surface, 191	Toxicity, 219
Sommerfeld mode, 106	Transversal LSP, 162
Sommerfeld wave, 124	Transverse wavelength, 16
Spaser, 196	Transverse wavelengths, 20
SPP studies 28	Tunneling effect, 96 Tunneling, 96
SPP studies, 28	runneling, 90

Two-photon interband absorption, 249 Two-photon polymerization, 233	Wood's anomalies, 3, 9, 14, 40–45, 70, 76 Wood's anomalies, SPP studies, 5 Wood's anomaly, 87, 90
V Veselago, 16	X X-ray lithography, 273
W Waterworth, 7, 43 Weyl formula, 14, 20 Wood, 39, 40, 42, 87–89, 101	Z Zenneck mode, 92, 124 Zeros, 89